UNIVERSITÉ DE LORRAINE | BIBLIOTHÈQUES UNIVERSITAIRES

AVERTISSEMENT

Ce document est le fruit d'un long travail approuvé par le jury de soutenance et mis à disposition de l'ensemble de la communauté universitaire élargie.

Il est soumis à la propriété intellectuelle de l'auteur. Ceci implique une obligation de citation et de référencement lors de l'utilisation de ce document.

D'autre part, toute contrefaçon, plagiat, reproduction illicite encourt une poursuite pénale.

Contact bibliothèque : ddoc-theses-contact@univ-lorraine.fr
(Cette adresse ne permet pas de contacter les auteurs)

LIENS

Code de la Propriété Intellectuelle. articles L 122. 4
Code de la Propriété Intellectuelle. articles L 335.2- L 335.10
http://www.cfcopies.com/V2/leg/leg_droi.php
http://www.culture.gouv.fr/culture/infos-pratiques/droits/protection.htm

Université de Lorraine - Ecole Doctorale SIReNa « Sciences et Ingénierie des Ressources Naturelles »

Thèse

Présentée et soutenue publiquement pour l'obtention du titre de

DOCTEUR DE l'UNIVERSITE DE LORRAINE

mention Géosciences

par Baptiste ABIVEN

sous la direction de Alexandre TARANTOLA et Antonin RICHARD

Traçage des fluides et conditions *PVTX*-déformation de mise en place des veines minéralisées d'un gisement de type porphyre-épithermal à Cu-Mo-Re-Au (Pagoni Rachi, Thrace occidentale, Grèce)

Soutenance publique le 24 février 2025

Président du jury :	
M. Damien GUILLAUME	Professeur, Université Jean Monnet, LGL TPE, Saint-Etienne
Rapporteurs :	
Mme Giada IACONO-MARZIANO	Chargée de recherche, CNRS, ISTO, Orléans
M. Philippe BOULVAIS	Maître de conférences, Université de Rennes, Géosciences Rennes, Rennes
Examinateurs :	
Mme Véronique LE ROUX	Professeure, Université de Lorraine, CRPG, Nancy
M. Julien MERCADIER	Directeur de recherche, CNRS, GeoRessources, Nancy
M. Philippe GONCALVES	Professeur, Université Bourgogne Franche-Comté Chrono-environnement, Besançon
Directeurs de thèse :	
M. Alexandre TARANTOLA	Maître de conférences, Université de Lorraine GeoRessources, Nancy
M. Antonin RICHARD	Maître de conférences, Université de Lorraine GeoRessources, Nancy

RESUME

Les gisements de type « porphyre-épithermal » représentent près de 75 % du Cu, 95 % du Mo, et près de 20 % de l'Au exploités dans le monde. Nombre de ces gisements se concentrent au sein de la Ceinture Métallogénique Téthysienne, notamment dans la région sud-est des Balkans-Rhodopes. Le nord-est de la Grèce présente une occurrence de ces gisements, qui ont pour particularité de s'être formés dans le contexte géodynamique post-collisionnel et d'être parmi les plus riches au monde en métaux accessoires. Leur étude représente une opportunité précieuse pour mieux contraindre certains processus encore peu explorés. Afin de reconstruire l'environnement et les conditions de formation de ces gisements, deux points majeurs sont traités : (i) la redistribution des éléments traces durant la recristallisation dynamique du minéral hôte et (ii) la caractérisation de la signature en éléments traces et isotopique des minéraux hôtes et des fluides.

Le site de Pagoni Rachi présente un gisement de type porphyre à Cu-Mo (Re-Au) et sub-épithermal à Pb-Zn télescopé, encaissé dans une granodiorite altérée (~32 Ma) sous la forme d'un stockwork minéralisé en métaux de base (Cu, Pb, Zn), précieux (Au, Ag) et critiques (Mo, Re, Ga, In, Te). La présence de molybdénite enrichie en Re (>4,7 wt.%) avec la présence de rhéniite (ReS_2) rend cette minéralisation atypique.

Les observations de terrain et la pétrographie montrent une succession de veines caractéristiques des systèmes porphyres et épithermaux : A/M ondulantes à quartz-hématite/magnétite-pyrite, B1 droites à quartz, C en réouverture des veines précédentes, à chalcopyrite-molybdénite±rhéniite, D à pyrite massive, B2 rubanées en stockwork massif, E1 à quartz-calcite-sphalérite-galène, et E2 à calcite-pyrite.

L'imagerie des veines de quartz par cathodoluminescence révèle des réouvertures de veines, une croissance oscillatoire des cristaux de quartz, ainsi que des textures de recristallisation dynamique témoignant d'une transition d'un domaine de déformation chaud-ductile (>400 °C) à froid-cassant (<250 °C). L'étude de ces textures et des éléments traces, montre une mobilité du titane dans le quartz lors de taux de déformation élevés caractérisés par des textures de recristallisation dynamique des cristaux. L'implication de tels processus et de la croissance rapide des cristaux de quartz rend impossible l'utilisation du thermomètre du Ti dans le quartz, rendant des valeurs de température non cohérentes avec des thermomètres indépendants. Cette mobilité du titane rend l'interprétation des diagrammes de classification géochimique (Al/Ti vs. Ge/Ti) des veines plus subtile, nécessitant une attention particulière pour éviter d'éventuelles interprétations erronées.

L'étude des inclusions fluides dans le quartz indique une circulation continue de fluides pendant la cristallisation et la recristallisation du quartz, marquée par une ébullition vers 490 °C, et le passage de conditions de pression lithostatique à hydrostatique, puis par un refroidissement et une dilution par des fluides de surface liés à l'événement épithermal.

La combinaison des compositions en isotopes stables (O, C, H) et des éléments traces des minéraux de gangue des différentes veines indique un mélange d'eau de mer et de fluides magmatiques au stade

porphyre (T = 350-500 °C, P = 200-600 bars). Le stade épithermal est caractérisé par un mélange de fluides magmatiques et météoriques (T = ~250 °C, P = 10 – 150 bars). Ces résultats sont compatibles avec les reconstitutions géologiques suggérant que la granodiorite se soit mise en place dans un bassin sédimentaire marin en contexte d'arc (stade porphyre) progressivement exhumé (stade épithermal), alors suivi par une érosion exposant le gisement à la surface.

L'ensemble de ces résultats permet de mieux comprendre les processus à l'origine de la formation de ces gisements atypiques de Grèce, et donnent également des clés pour questionner les modèles généraux de gisements de type porphyre-épithermal.

Mots clés : Porphyre-épithermal, traçage, déformation, fluides minéralisateurs, inclusions fluides.

ABSTRACT

Porphyry-epithermal type deposits account for approximately 75% of the world's exploited Cu, 95% of Mo, and about 20% of Au. Many of these deposits are concentrated within the Tethyan Metallogenic Belt, particularly in the southeastern Balkans-Rhodope region. Northeastern Greece hosts occurrences of these deposits, which are distinctive for having formed within the unique post-collisional geodynamic context and for being among the richest in accessory metals globally. Their study presents a valuable opportunity to constrain certain underexplored processes.

To reconstruct the environment and formation conditions of these mineralized systems, two major aspects are addressed here: (i) the redistribution of trace elements during the dynamic recrystallization of the host mineral, and (ii) the characterization of the trace element and isotopic signatures of host minerals and fluids.

The Pagoni Rachi site features a Cu-Mo (Re-Au) porphyry deposit telescoped by a sub-epithermal Pb-Zn system, hosted within an altered granodiorite (~32 Ma) in the form of a stockwork mineralized in base (Cu, Pb, Zn), precious (Au, Ag), and critical (Mo, Re, Ga, In, Te) metals, characteristic of such systems. The presence of Re-enriched molybdenite (>4.7 wt.%) along with rheniite (ReS_2) makes this mineralization atypical.

Field observations and petrography reveal a sequence of veins characteristic of porphyry and epithermal systems: A/M veins: wavy quartz-hematite/magnetite-pyrite/magnetite, B1 veins: straight quartz veins, C veins: reopening of previous veins, containing chalcopyrite-molybdenite±rheniite, D veins: massive pyrite, B2 veins: banded stockwork-type veins, E1 veins: quartz-calcite-sphalerite-galena, and E2 veins: calcite-pyrite.

Cathodoluminescence imaging of quartz veins reveals vein reopening, oscillatory quartz crystal growth, and dynamic recrystallization textures indicative of a progressive transition from a hot-ductile (>400 °C) to a cold-brittle (<250 °C) deformation regime. The study of this deformation, combined with trace element analysis, shows titanium mobility in quartz, associated with high strain rates and typical dynamic recrystallization textures such as grain boundary migration. The involvement of such processes and rapid quartz growth renders the Ti-in-quartz thermometer unreliable, yielding temperature values inconsistent with independent thermometers. This Ti mobility complicates the use of geochemical classification diagrams (Al/Ti vs. Ge/Ti) for veins, requiring careful interpretation to avoid potential misinterpretations.

Fluid inclusion studies in quartz indicate continuous fluid circulation during quartz crystallization and recrystallization, marked by boiling at 490 °C and a transition from lithostatic to hydrostatic pressure conditions, followed by cooling and dilution by surface-derived fluids during the epithermal event, leading to the precipitation of base (Pb, Zn, Ag) and critical (Ga, Ge, In, Te) metals.

The combination of stable isotope compositions of oxygen, hydrogen, carbon, and trace elements in gangue minerals from different veins suggests the involvement and mixing of seawater and magmatic

fluids during the porphyry stage (T = 350-500 °C, P = 200-600 bars). The epithermal stage is characterized by the interaction and mixing of magmatic and meteoric fluids (T = ~250 °C, P = 10 – 150 bars). These findings align with the geological reconstructions of the study area, indicating that the granodiorite intrusions were emplaced in a marine sedimentary basin within an arc setting (porphyry stage) and were progressively exhumed through extensional tectonics (epithermal stage), followed by erosion exposing the deposit at the surface.

These results provide new insights into the formation processes of these atypical deposits in Greece and offer valuable perspectives for refining general models of porphyry and epithermal mineralization.

Keywords: Porphyry-epithermal, tracking, Deformation, Mineralizing fluids, fluid inclusions.

REMERCIEMENTS

Une thèse se définit par un sujet, un questionnement que le doctorant tente de résoudre ou, au moins, d'apporter des éléments de réponse. Mais une thèse n'est pas que cela : c'est avant tout un laboratoire, un environnement de travail, des collaborateurs, des encadrants, des collègues, des amis, une famille.

Au laboratoire GeoRessources, merci à Anne-Sylvie André-Mayer, directrice du laboratoire, de m'avoir accueilli pendant ces trois années.

À Alexandre Tarantola et Antonin Richard, mes directeurs de thèse, qui m'ont offert cette chance : merci de m'avoir accordé cette liberté de travail, la confiance que vous m'avez donnée jusqu'à la fin, et les bons moments passés ensemble, que ce soit sur le terrain, au labo, ou lors des réunions sans fin. Merci pour tout. Sans vous, je ne serais pas le chercheur que je suis aujourd'hui.

Je tiens ensuite à remercier toutes les personnes du jury qui ont accepté de consacrer leur temps pour juger ce travail. Je tiens tout spécialement à remercier mes rapporteurs, notamment Philippe Boulvais, avec qui j'ai réalisé mon stage de cartographie de licence sur les îles d'Houat et d'Hoëdic : merci d'avoir accepté de juger ce travail. Merci à Giada Iacono-Marziano, rencontrée lors d'un congrès, d'avoir accepté d'être rapportrice de cette thèse et d'apporter son expertise dans le domaine de la géochimie des magmas et des volatils associés au magmatisme. Je souhaite également remercier mes examinateurs, Véronique Le Roux, Damien Guillaume, Philippe Goncalves et Julien Mercadier, pour leur implication dans l'évaluation de cette thèse.

Mes remerciements vont également au soutien financier du projet ARTeMIS ERASMUS+, sans lequel le travail sur le terrain n'aurait pu se faire, et qui m'a permis de développer mon réseau, de faire des rencontres, de développer mes compétences et de les mettre à l'épreuve.

I would like to extend my heartfelt thanks to the researchers whom I had the pleasure of meeting. To Manuel Keith, Panagiotis Voudouris, Vasilios Melfos, Konstantinos Mavrogonatos: for their dedication, commitment in the field, and all the help provided for the article, as well as the knowledge and experience shared, I extend my heartfelt thanks.

Je tiens également à remercier le personnel du CRPG : Thomas Rigaudier pour l'aide à l'extraction et à la mesure des isotopes de l'hydrogène, Johan Villeneuve et Nordine Bouden pour la SIMS.

Je remercie Cyril Chelle-Michou et Raphaël Pik pour leur implication dans le comité de suivi de thèse, leur constructivité et leur précieux conseils sur le déroulement scientifique et personnel de la thèse.

Je reviens maintenant au laboratoire GeoRessources pour remercier toutes les personnes qui ont contribué, d'une manière ou d'une autre, à la bonne réalisation de mon travail. Je voudrais donc citer, dans le désordre : Jean Cauzid, Andreï Lecomte, Lise Salsi, Chantal Peiffert, Christophe Ballouard, Karine Pistre, Alexandre Flammang, Julien Mercadier et Marie-Camille Caumon.

Enfin, je ne peux oublier de remercier tous les thésards, post-docs et amis avec lesquels j'ai vécu cette aventure au jour le jour : Océane Rocher, Naïla Mezoued, Saïd Sadeg, Caroline Van de Vyver, Marjolène Jatteau, Jean-Charles Fidalgo, Lucas Marulier, Célestine Berthier, Thomas Obin, Quentin Boulogne, Joffrey Corbet, Maxime Baritussio, Hugo Marek, et toutes celles et ceux que j'aurais pu oublier.

À Cédric Demeurie, qui m'a appris plein de trucs.

Aux Rennais, qui m'ont donné l'envie et le goût de la géologie, conforté dans ce projet et aidé tout au long de mon cursus. Cinq années d'études, des opportunités de stage et plein de bonnes choses : rien n'aurait été pareil sans votre soutien indéfectible.

À ma famille, mes parents, mon frère, ma belle-sœur, qui m'ont toujours soutenu et encouragé durant mes études et ma thèse, qui finalise cette étape.

À mes amis, Maxime et Anthony, pour tous les bons moments passés, le soutien, le temps, l'énergie, mais surtout l'aide apportée : sans vous, tout aurait été plus difficile.

À Greg, pour ces discussions de géologie de comptoir, sa curiosité, ses cailloux de type « bidulites » testant mes capacités.

À Katy, qui m'a suivi dans cette aventure, qui a toujours été là, et pour toute l'aide et le soutien apportés durant et surtout à la fin de la thèse.

À Saga et Téthys, pour ces moments d'évasion.

À toutes et tous, merci.

SOMMAIRE

RESUME **5**
ABSTRACT **7**

REMERCIEMENTS **11**

SOMMAIRE **15**

TABLE DES FIGURES **21**
TABLE DES TABLEAUX **25**

CHAPITRE 1. INTRODUCTION **27**
1.1. Contexte et problématique de l'étude **29**
1.2. Etat de l'art **36**
1.2.1. Systèmes de type porphyre-épithermal 36
1.2.2. Géodynamique et magmatisme 38
1.2.3. Evolution des fluides hydrothermaux d'un système de type porphyre 43
1.2.4. Génération des veines minéralisées du système de type porphyre 44
1.2.5. Altérations des roches encaissantes 45
1.2.6. Gisements épithermaux et télescopage 48
1.2.7. Brèches 50
1.2.8. Contexte géologique de la Grèce et ses gisements 50
1.2.8.1. Contexte géodynamique 50
1.2.8.2. Magmatisme 52
1.2.8.3. Le bassin de Thrace occidentale 54
A. Le bassin de Xanthi-Komotiní 57
B. Le bassin d'Évros 57
Bassin de Kirki-Esimi 57
Bassin de Maronia 58
C. Le bassin Nord-égéen (île de Límnos) 59
1.2.8.4. Ressources 59
1.2.9. Site d'études 62

CHAPITRE 2. RECONSTRUCTION OF A PORPHYRY-EPITHERMAL SYSTEM – FROM FIELDWORK TO THIN SECTION: PAGONI RACHI (GREECE) **69**
2.1. Introduction **71**
2.2. Methodology **72**
2.2.1. Sampling 72
2.2.2. Petrological observations 75
2.2.3. Cathodoluminescence (CL) imaging 75
2.3. Results **76**
2.3.1. Pagoni Rachi - Field observation, alteration and vein petrography 76
2.3.1.1. Lithologies 78
2.3.1.2. Host-rock alteration styles 79
A. Biotite/orthoclase alteration (destructive) - Potassic alteration 80
B. Sericitic alteration 81
C. Chlorite-sericite alteration 81
D. Argillic alteration 81
E. Chlorite-epidote alteration – Propylitic alteration 81
2.3.1.3. Porphyry style vein succession 82

A. Stage 1 – Early wavy quartz-pyrite/magnetite veins (A- and M-type veins) 82
B. Stage 2 – Straight banded quartz veins (B1-type veins) 85
C. Stage 3a – Reopenings associated to sulfide mineralization (C-type veins) 87
D. Stage 3b – Massive pyrite veins and pyrite filled fractures (D-type veins) 88
E. Stage 4 – Massive stockwork of barren banded quartz veins (B2-type veins) 89
2.3.1.4. Epithermal style vein succession 91
A. Stage 1 – Geodic quartz-sphalerite-galena-chalcopyrite veins (E1-type) 91
B. Stage 2 – Carbonate veins (E2-type) 93
C. Faults and breccias 95
2.3.2. Field observation of Greek Thrace deposits 97
2.3.3. Maronia 97
2.3.4. Sant Philippos 99
2.3.5. Konos Hill 101
2.4. Discussion 104
2.4.1. Alteration overprinting at Pagoni Rachi 104
2.4.1.1. Sea water influence 104
2.4.1.2. Telescoping evidence 105
2.4.2. Vein succession in Pagoni Rachi porphyry epithermal system 107
2.4.2.1. Timing reevaluation of porphyry-style mineralization 107
2.4.2.2. Chemical evolution evidence during quartz deposition and massive stockwork (B2-type veins) 109
2.4.2.3. Late epithermal style mineralization and structural control 110
2.4.2.4. Ductile to brittle deformation at Pagoni Rachi 111
2.4.3. Pagoni Rachi and structural relation to other sites – schematic figuration 113
2.4.3.1. Succession of Veins and Alterations at Pagoni Rachi 113
2.4.3.2. Observations from Other Western Thrace Sites 113
A. Maronia 114
B. Sant Philippos 114
C. Konos Hill 114
2.4.3.3. Genetic Relationships Between Pagoni Rachi and Surrounding Systems 114
2.5. Summary and conclusion 116

CHAPITRE 3. EFFET DE LA CRISTALLISATION HORS EQUILIBRE ET DE LA RECRISTALLISATION DYNAMIQUE SUR LA THERMOMETRIE DU TI DANS LE QUARTZ DANS LES GISEMENTS PORPHYRES-EPITHERMAUX : APERÇUS DE PAGONI RACHI (NE DE LA GRECE) – ARTICLE SOUMIS A LITHOS 119
3.1. Introduction 123
3.2. Geological and metallogenic context 127
3.3. Sampling and methods 132
3.3.1. Sampling selection 132
3.3.2. Cathodoluminescence (CL) imaging 132
3.3.3. Fluid inclusion analysis 132
3.3.4. Selection of previous fluid inclusion data 133
3.3.5. Laser Ablation–Inductively Coupled Plasma–Mass Spectrometry (LA-ICP-MS) 135
3.3.6. Ti-in-quartz thermometry 136
3.4. Results 138
3.4.1. Petrography–quartz microtextures and cathodoluminescence (CL) imaging 138
3.4.2. Fluid inclusion petrography and microthermometry 143
3.4.3. Trace elements in quartz 145
3.5. Discussion 149
3.5.1. Evidence for fluid inclusion overlapping and fluid evolution 149
3.5.2. Ti-in-quartz temperatures and comparison with fluid inclusion thermometry 151
3.5.3. Evidence for Ti excess in quartz during disequilibrium crystallization 152
3.5.4. Transition from lithostatic to hydrostatic conditions and from ductile to brittle conditions 155

3.5.5. Evidence for Ti diffusion during dynamic recrystallization 156
3.5.6. Implication for Ti-in quartz thermometry in magmatic-hydrothermal systems 158
3.5.7. Implication for Al/Ti vs Ge/Ti-based vein typology in porphyry-epithermal systems 159
3.6. Summary and conclusion 162
3.7. Acknowledgements 163

CHAPITRE 4. EVOLUTION OF THE PHYSICO-CHEMICAL CONDITIONS OF ORE-FORMING FLUIDS IN A PROPHYRY-EPITHERMAL SYSTEM THROUGH TRACE ELEMENTS IN QUARTZ 165
4.1. Introduction 167
4.2. Methodology 170
4.2.1. Sampling selection 170
4.2.2. Trace elements in quartz by Laser Ablation – Inductive Coupled Plasma – Mass Spectrometer (LA – ICP – MS) 170
4.2.3. Thermometry – Ti-in-quartz 171
4.3. Results 173
4.3.1. Monovalent cations 173
4.3.2. Bivalent cations 174
4.3.3. Trivalent cations 175
4.3.4. Tetravalent cation 175
4.3.5. Anions and complexes 177
4.4. Discussion 178
4.4.1. Trace element correlations 178
4.4.1.1. Trace element variations through quartz veins 178
4.4.1.2. Correlations at the porphyry scale 187
4.4.1.3. Trace element proportion per valence (absolute value) 192
4.4.2. Chemical evolution of quartz porphyry-epithermal system 192
4.4.2.1. Trace Element Evolution in Hydrothermal Quartz from Porphyry and Epithermal Veins 192
4.4.2.2. Fluid composition evolution 193
4.4.2.3. Pressure, Temperature and pH variations 194
4.4.3. Chemical diffusion during heating or deformation. 196
4.4.4. Ti-in-quartz thermometry 196
4.4.5. Trace elements: implications for ore genesis discrimination 199
4.5. Conclusion 202

CHAPITRE 5. ORIGIN AND TRACKING OF FLUID USING STABLE ISOTOPES OF OXYGEN, CARBON AND HYDROGEN 205
5.1. Introduction 207
5.2. Methodology 209
5.2.1. Oxygen and carbon isotopes – Secondary Ion Mass Spectrometer 209
5.2.2. Isotopic fractionation and fluid inclusions 210
5.2.3. Fluid inclusions data – *PTX* constraints 210
5.2.4. Hydrogen isotopes 211
5.3. Results 214
5.3.1. Oxygen in quartz and calcite veins and carbon in calcite veins 214
5.3.2. Hydrogen in quartz and carbonate veins 220
5.3.3. Fluid inclusion petrography in B2- and E2-type veins 221
5.4. Discussion 223
5.4.1. Isotopic fractionation and $\delta^{18}O_{H2O}$, $\delta^{18}O_{CO2}$, $\delta^{13}C_{CO2}$. 223
5.4.2. Influence on δD 227
5.4.3. Local temperature decreases insights of quartz overgrowths 227
5.4.4. Isotopes and fluid sources 228
5.4.5. Origin and mixing of mineralizing fluids 230

5.4.5.1. Origin of the mineralizing fluids of stages A, B1..... 231
5.4.5.2. Conditions of fluid mixing during mineralization stages A, B1 and B2. 231
5.4.5.3. Origin of the mineralizing fluids during stage E1 and E2. 233
5.4.6. Isotopic constraints and temperature estimation in fluid evolution models 234
5.5. Conclusion 236

CHAPITRE 6. DISCUSSION GENERALE : MODELE METALLOGENIQUE POUR LE GISEMENT DE PAGONI RACHI 239

CHAPITRE 7. CONCLUSIONS ET PERSPECTIVES 253

REFERENCES BIBLIOGRAPHIQUES 261

ANNEXES 283

TABLE DES FIGURES

Figure 1 : Carte mondiale des principaux gisements porphyres à Cu, et Cu-Au, ainsi que des différentes zones de subduction actuelles et anciennes (d'après Park et al. 2021). 29

Figure 2 : Cycles de l'eau (a), du soufre (b), des halogènes(c), et du carbone (d) en zones de subduction (d'après Zellmer et al., 2015). 36

Figure 3 : Subduction and collision-related tectonic settings, and their relationship to porphyry deposit formation from Richards, 2014. 39

Figure 4 : Coupe lithosphérique schématique illustrant deux évolutions possibles d'une zone de subduction typique le long d'une marge continentale (de Menant et al. 2016). 41

Figure 5 : Coupe schématique de la circulation de fluides lors de la mise en place d'un système de type porphyre et épithermal, d'après Sillitoe (2010) et Kouzmanov et al. (2012). 43

Figure 6 : Schéma chronologique des séquences de veines possible a) dans un gisement porphyre à Cu – Mo et b) dans un gisement à Cu – Au. La nomenclature des veines suit Gustafson et Hunt (1975, A, B et D) et Arancibia et Clark (1996) (d'après Sillitoe, 2010). 45

Figure 7 : Coupe schématique d'une structure porphyre et des différents styles de minéralisations et altérations associées, modifiée d'après Sillitoe (2010), Henley et al. (2015), Schaarschmidt, (2021). 47

Figure 8 : Schéma de l'évolution d'une structure d'un système de type porphyre-épithermal d'après Sillitoe, 2010. 49

Figure 9 : Carte structurale de la Grèce montrant l'empilement des nappes accrétées à la marge Européenne Sud depuis le Crétacé (d'après Schaarschmidt, 2021 ; Voudouris et al., 2018). 51

Figure 10 : Evolution géodynamique de l'Est de la méditerranée au Cénozoïque supérieur a) schéma structural dynamique de la migration du magmatisme du Crétacé supérieur au Miocène ; b) coupe structurale N-S de la région égéenne et du Rhodope et cartes paléostructurales représentant les différents types de magmatisme, d'après Menant et al. (2016). 53

Figure 11 : Cartes paléogéographiques schématiques du Bassin de l'Ouest-Thrace et de la Région Rhodope durant la période Eocène moyen-Oligocène. Les volcans sont nommés d'après leur localité respective (de Caracciolo et al. 2011). 55

Figure 12 : Bloc diagramme schématique présentant l'environnement de dépôts du bassin de Thrace de l'Eocène supérieur à l'Oligocène (de Maravellis et al. 2016). 56

Figure 13 : Colonnes stratigraphiques des bassins de Xanthi-Komotini et d'Evros (de Caracciolo et al. 2015). 58

Figure 14 : Distribution géographique des minéralisations de type porphyre (a), et épithermal (b) de l'Oligocène au Quaternaire en Grèce (de Voudouris et al. 2019). 60

Figure 15 : Carte structurale du NE de la Grèce, avec les situations des sites d'études, d'après Mavrogonatos et al. 2019. 61

Figure 16 : Cartes géologique (a) et d'altération (b) des prospects de St Philippos (au Nord de la carte) et de Pagoni Rachi au centre de la carte, d'après Mavrogonatos et al. (2019). 62

Figure 17 : Diagramme Alcalins ($Na_2O + K_2O$) vs. Silice (SiO_2) des roches magmatiques encaissant le gisement de Pagoni Rachi. 63

Figure 18 : Tableau représentant les séquences de veines/fractures, altérations et assemblages paragénétiques avec les descriptions des structures types présents à Pagoni Rachi (d'après Voudouris et al. 2013). 65

Figure 19 : Diagramme des températures d'homogénéisation en fonction de la salinité des inclusions fluides provenant des cristaux de quartz et de calcite des différents type de veines du gisement de Pagoni Rachi 66

Figure 20: Geological and alteration maps of the Sapes-Kassiteres-Kirki district, with A. Location in the NE Greece, B. the location of the Pagoni Rachi prospect at the southeastern of the map, modified from Mavrogonatos et al. (2019). 72

Figure 21: Satellite map of the Pagoni Rachi site showing sampling and exploration routes in blue (2022) and green (2023)..... 73

Figure 22: Landscapes of Pagoni Rachi. 74

Figure 23: Geological map, alteration zones, and observed/sample vein types at the Pagoni Rachi site... 76

Figure 24: Representative outcrops, macroscopic samples, and structural relationships at Pagoni Rachi. 78

Figure 25: Observed lithologies at Pagoni Rachi. 79

Figure 26: Alteration assemblages of the host-rock (granodiorite) in thin section. 80

Figure 27: Petrography of A-type veins. 83

Figure 28: Petrography of M-type veins..... 84

Figure 29: Petrography of B1-type veins. 86

Figure 30: Petrography of C-type veins and reopenings. 88

Figure 31: Petrography of D-type veins. 89

Figure 32: Petrography of B2-type veins. 90

Figure 33: Petrography of E1-type veins..... 92

Figure 34: Petrography of E2-type veins..... 94

Figure 35: Fault and silicified breccia at Pagoni Rachi. 95

Figure 36: Paragenetic sequence of the veining and alteration sequence of the porphyry-epithermal system of Pagoni Rachi 96

Figure 37: Geological map of Maronia, from Voudouris et al. 2019 97

Figure 38: Field observation of the Maronia porphyry deposit 98

Figure 39: Filed observations of Sant Philippos epithermal deposit. 101

Figure 40: Field observation of Konos Hill porphyry-epithermal deposit. 102

Figure 41: Geological, alteration, and vein distribution maps of the Pagoni Rachi prospect. The maps display the distribution of different vein types and structures..... 106

Figure 42: Schematic representation of dynamic recrystallization textures in quartz and calcite. This figure illustrates the evolution of quartz recrystallization textures, progressing from the earliest veins (type A) to the latest (type E)..... 112

Figure 43: Schematic cross-section of a porphyry-epithermal system (adapted from Sillitoe, 2010). This figure includes the localization of the porphyry-epithermal deposit at Pagoni Rachi, the Maronia porphyry deposit, and the telescoped epithermal deposit at Konos Hill, based on our observations.. 115

Figure 44: Geographical and geological context of the study area and sampling zones. 127

Figure 45: Petrography of A-, B- and E-type veins (outcrops and hand specimens) from Pagoni Rachi. 129

Figure 46: Cross-polarized (XPL) views of quartz petrography and microstructures and cathodoluminescence (CL) images of A-type veins. Ti concentration in ppm associated with the ablation spot location (white circles) are shown in E and F..... 140

Figure 47: Cross-polarized (XPL) views of quartz petrography and microstructures and cathodoluminescence (CL) images of B-type veins. Ti concentration in ppm associated with the ablation spot location (white circles) are shown in D. 141

Figure 48: Transmitted light, cross-polarized (XPL) views of quartz petrography and microstructures and cathodoluminescence (CL, “hot” and “SEM”) images of of E-type veins. Ti concentration in ppm associated with the ablation spot location (white circles) are shown in C. 142

Figure 49: Fluid inclusion petrography from A and B-type veins..... 145

Figure 50: Histograms of Ti in quartz analyzed by LA-ICP-MS. 146

Figure 51: Concentration of Ti, Al and Ge in quartz from A-, B- and E-type veins, measured by LA-ICP-MS, A. Ge vs Al. B. Ge vs Ti. C. Ti vs Al. 147

Figure 52: *PT* diagram showing our fluid inclusion data (this study and from Voudouris et al., 2013a) and *PT*[Ti] domains obtained with the Titan-in-quartz geothermometer of the A- (red), B- (blue) and E- (pink) type veins. 150

Figure 53: Synthetic sketch of the respective influence of rapid growth and dynamic recrystallization of quartz on the Ti content of quartz and on the Ti thermometer, with comparison of our Ti data and fluid inclusions..... 155

Figure 54: Ge/Ti vs Al/Ti (mass ratios) diagram based on LA-ICP-MS analyses of quartz of A-type (red), B-type veins (blue), and E-type veins (pink)..... 160

Figure 55: Quartz structure, and projection of right (P3z21) of α-quartz atomic positions onto the plane perpendicular to c-axis including the most common defect types, from Rottier and Casanova (2021). 168

Figure 56: Trace element spectrum during laser ablation ICP-MS of a B1-type vein quartz (sample AB.120.01 (no. 14)) 171

Figure 57: Boxplot of monovalent cations content in quartz. 173

Figure 58: Boxplot of bivalent cations content in quartz. 174

Figure 59: Boxplot of trivalent cations content in quartz. 175

Figure 60: Boxplot of different cations and anions content in quartz. →..... 176

Figure 61: Boxplot of tetravalent cations content in quartz. 176

Figure 62: Average abundance and variations of trace elements in quartz (from Götze et al. 2012)..... 178

Figure 63: Projection of trace elements contents measured in quartz plotted along a transect crossing an A-type vein. And CL imaging and location of the ablated spots. 179

Figure 64: Projection of trace elements contents measured in quartz plotted along a transect crossing an A-type vein. And CL imaging and location of the ablated spots. 180

Figure 65: Projection of trace elements contents measured in quartz plotted along a transect crossing an B1-type vein. And CL imaging and location of the ablated spots. 182

Figure 66: Projection of trace elements contents measured in quartz plotted along a transect crossing an B1-type vein. And CL imaging and location of the ablated spots. 183

Figure 67: Projection of trace elements contents measured in quartz plotted along a transect crossing an B1-type vein. And CL imaging and location of the ablated spots. 183

Figure 68: Projection of trace elements contents measured in quartz plotted along a transect crossing an B2-type vein. And CL imaging and location of the ablated spots. 184

Figure 69: Projection of trace elements contents measured in quartz plotted along a transect crossing an E1-type vein. And CL imaging and location of the ablated spots. 185

Figure 70: Projection of trace elements contents measured in quartz plotted along a transect crossing an E1-type vein. And CL imaging and location of the ablated spots. 186

Figure 71: Succession of diagram of sum of certain valence vs. sum of certain valence ions. 188

Figure 72 : A. K vs. Al quartz content. B. Al vs. Na quartz content. 189

Figure 73: A. Sb vs. Ge quartz content. B. Sb vs. Al quartz content 190

Figure 74: A. Al vs. Ge quartz content. B. Al vs. Ti quartz content. 190

Figure 75: A. Ti vs. Ge quartz content. B. Al vs. Mg quartz content. 191

Figure 76: Li/Al vs. Li/K diagram 191

Figure 77: *PT* diagram showing fluid inclusion data (from Muntean and Einaudi 2000 on banded veins from Maricunga Belt similar to our B2-type veins) and *PT*[Ti] domains obtained with the Titan-in-quartz geothermometer of the B2-type veins. 198

Figure 78: Al vs. Li diagram with Pagoni Rachi reported data 199

Figure 79: Ge/Ti vs Al/Ti (mass ratios) diagram based on LA-ICP-MS analyses of quartz 200

Figure 80: Handspecimen of E1 quartz veines filled by E2 calcite veins, with location of B. Cut fragment of E1 type veins after acid leaching. 212

Figure 81: CL imaging with scaled localization of SIMS analysis spots ($\delta^{18}O$), including values in ‰. 215

Figure 82: CL imaging of B1-type veins with scaled localization of SIMS analysis spots ($\delta^{18}O$), including values in ‰. A to E. 216

Figure 83: CL imaging of B2-type vein with scaled localization of SIMS analysis spots ($\delta^{18}O$), including values in ‰ 217

Figure 84: CL imaging with scaled localization of SIMS analysis spots ($\delta^{18}O$, white cercle, $\delta^{13}C$, pink circle), including values in ‰. 218

Figure 85: Fluid inclusion petrography from B2-type veins. 221

Figure 86: Fluid inclusion petrography of E2-type veins. 222

Figure 87: Histogram of T_h values for fluid inclusions, based on the synthesis by Abiven et al. (Chapter 3) 223

Figure 88: Histogram of $\delta^{18}O_{quartz}$ (grey), and calculated $\delta^{18}O_{H2O}$ value of the different quartz veins. ... 225

Figure 89: Histogram of $\delta^{18}O_{calcite}$ or $\delta^{13}C_{calcite}$ (grey), and calculated $\delta^{18}O_{H2O}$ or $\delta^{18}O_{CO2}$ value of the different quartz veins. 226

Figure 90: $\delta^{13}C$ range of extrema values of typical reservoir and of the different veins of Pagoni Rachi porphyry-epithermal system. 229

Figure 91: δD range of extrema values of typical reservoir and of the different veins of Pagoni Rachi porphyry-epithermal system. 229

Figure 92: $\delta^{18}O_{H2O}$ range of extrema values of typical reservoir and of the different veins of Pagoni Rachi porphyry-epithermal system. 229

Figure 93 : δD vs. $\delta^{18}O_{H2O}$ diagram, with the different value of the different vein types of the Pagoni Rachi porphyry epithermal system. 230

Figure 94: $\delta^{13}C_{PDB}$ vs. $\delta^{18}O_{SMOW}$ diagram, of the isotopic signature from the different calcite forming the E2-type veins. Igneous calcites box from 234

Figure 95: δD vs. δ18OH2O diagram, with the different schematic value of the different vein type of the Pagoni Rachi porphyry epithermal system, with evolution processes involved. 237

Figure 96: Schematic E-W cross section of the porphyry-epithermal system of Pagoni Rachi. 246

TABLE DES TABLEAUX

Table 1: Petrological characteristics of the different vein types, part of the mineralized stockwork of Pagoni Rachi. Abbreviations: Act= actinolite, Ab= albite, Bt= biotite, Bn= bornite, Cal= calcite, Cpy= chalcopyrite, Chl= chlorite, Eng= enargite, Ep= epidote, Fl= fluorite, Gn= galena, Hem= hematite, Kln= kaolinite, Mag= magnetite, Mol= molybdenite, Or= orthoclase, Py= pyrite, Qz= quartz, Rhn= rheniite, Ser= sericite, Sp= sphalerite, Tnt= tennantite, Ttr= tetrahedrite.....130

Table 2 : Synthesis of fluid inclusion data (this study and from Voudouris et al. 2013a), showing the different fluid events.....134

Table 3 : Ti, Al, and Ge concentrations in quartz from A-, B- and E-type veins.....148

Table 4: Synthesis of fluid events (Ttrapping and Ptrapping), Ti concentration in quartz ([Ti]), Ti-in-quartz temperatures (T[Ti]), the differences between the Ti-in-quartz temperatures and Fluid inclusion temperatures (ΔT(Ti-in-quartz–FI)) and the involved process for the different vein-types (A, B and E).....151

Table 5: PT trapping of fluid inclusions in quartz and calcite formation from the different vein type of the porphyry-epithermal system of Pagni Rachi – synthesis from Voudouris et al. 2013a and this study.....211

Table 6: presenting δ18Oquartz value from the different type of vein.....214

Table 7: presenting δ18Ocalcite value from the different E2-type veins.....219

Table 8: presenting δ13Ccalcite value from the different E2-type veins.....219

Table 9: Synthesis of δD data……...……...……...……..220

CHAPITRE 1. INTRODUCTION

1.1. CONTEXTE ET PROBLEMATIQUE DE L'ETUDE

Les métaux répondent à la demande de développement matériel et énergétique, au travers des appareils électroniques, des énergies renouvelables (panneaux photovoltaïques, éoliennes, etc… nécessaires à la vie quotidienne. Dans cette optique, la caractérisation de métaux en métaux « critiques » rend compte d'une évaluation du risque d'approvisionnement et de l'importance économique pour chacun des éléments. Cette classification évolue selon leur approvisionnement, le contexte géopolitique et la diminution de leur disponibilité (Critical Raw Materials for the EU, 2023).

Actuellement, les gisements métalliques d'importance économique sont ceux à faible teneur mais fort tonnage. Pour l'industrie, les meilleures cibles restent les gisements hydrothermaux de type porphyre et épithermal qui possèdent une minéralisation disséminée de basse teneur mais à gros volume et à de faibles profondeurs (Jebrak et Marcoux, 2008) les rendant donc accessibles. Ces gisements sont parmi les plus riches au monde en métaux. C'est pourquoi, les gisements de type porphyre-épithermal sont et resteront des ressources majeures en métaux en particulier pour le Cu, Au, Mo et Ag (Hedenquist et al. 1998 ; Richards, 2009, 2011a ; Sillitoe, 2010) parfois considérés comme étant d'une importance stratégique à l'échelle européenne ainsi que pour l'industrie française.

Les gisements de type porphyre-épithermal représentent près de 75% du Cu primaire exploité, 95% du Mo en tant que co-produit, et près de 20% de l'Au exploité dans le monde (Sillitoe, 2010). Ces gisements se situent principalement le long de systèmes linéaires tels que les zones de subduction ou les ceintures orogéniques (Sillitoe, 2010) (Figure 1), tels que la cordillère des Andes, ou la chaîne des Alpes

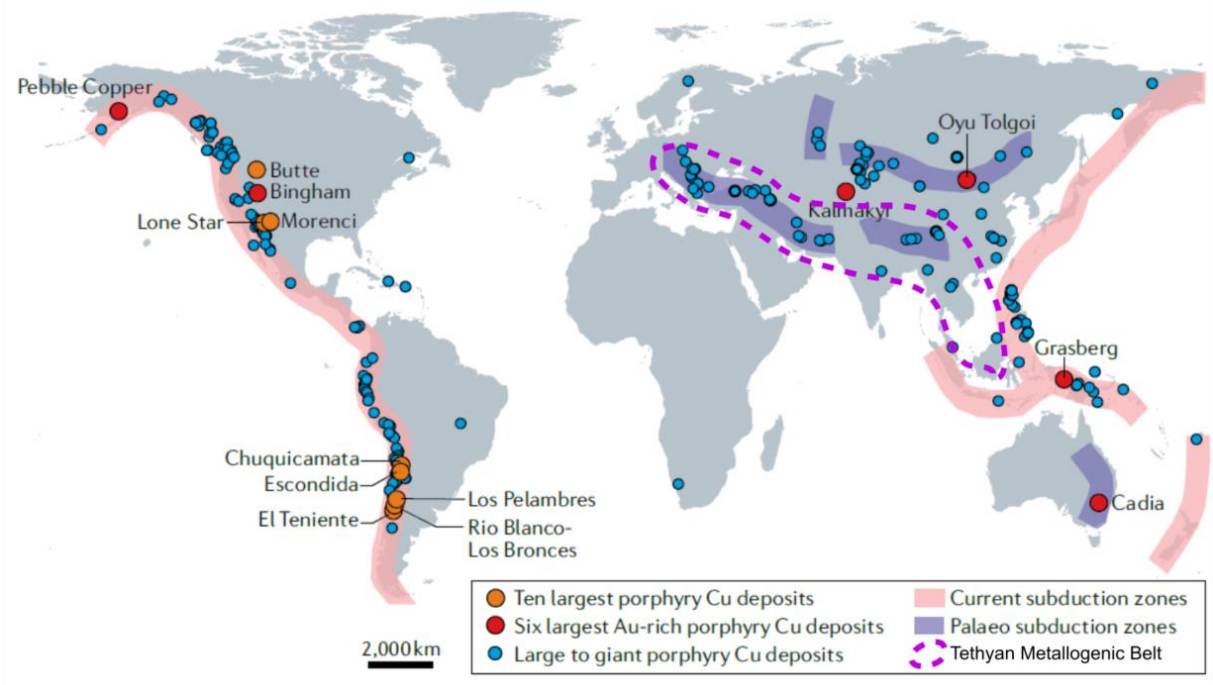

Figure 1 : Carte mondiale des principaux gisements porphyres à Cu, et Cu-Au, ainsi que des différentes zones de subduction actuelles et anciennes (d'après Park et al. 2021).

par exemple. Un grand nombre de ces gisements se concentre au sein de la Ceinture Métallogénique Téthysienne (CMT) (Richards, 2015). La CMT s'étale sur près de 10 000 km, de la chaîne alpine occidentale à la chaîne himalayenne orientale, et concentre près de 5,7% des gisements hydrothermaux mondiaux connus et de nombreuses ressources métalliques en Au, Cu, Ni, Pb et Zn (Hedenquist et al. 2017). Les concentrations métallifères en Cu – Au – Mo sont considérées comme les plus caractéristiques de cette région, formées au tertiaire lors de la subduction de l'océan Néo-Téthys et de la collision entre la plaque africaine, dans le cas de l'Europe, ou indienne, dans le cas de l'Asie, et la plaque eurasienne (Van Hinsbergen et al., 2005 ; Richards, 2015).

La région du Sud-Est des Balkans-Rhodopes (NE Grèce, SE Bulgarie, NW Turquie), où se concentrent ces gisements, est propice à la prospection de métaux critiques et à la compréhension des processus d'enrichissement dans ces types de gisements. Les gisements de type porphyre-épithermal à Cu – Mo – (Au – Ag) du Nord-Est de la Grèce sont essentiellement post-orogéniques (Menant et al., 2016, 2018). Ils se sont formés en réponse à une déformation extensive syn- et post-orogénique à l'Éocène (Jolivet et al., 2013). Un retrait du slab suit la formation des gisements à Cu – Mo (localisés plus au Nord dans les Carpates) liés à la subduction, au métasomatisme du manteau et à un magmatisme d'arc associé (Menant et al. 2018 ; Melfos et Voudouris, 2012, 2019, 2022 ; Barra et al., 2013 ; Voudouris et al. 2013b, 2019, 2021, 2022 ; Mavrogonatos et al., 2019, 2020). Cette région (Fig. 1) est alors cruciale pour de futures explorations et exploitations de métaux précieux, rares et critiques, en Grèce et en Europe (Melfos et al. 2017, Duhamel-Achin, 2022, Voudouris et al. 2022).

Les gisements de type porphyre-épithermal du NE de la Grèce sont peu riches en Cu. Ils sont petits et n'ont été que récemment caractérisés en tant que porphyres. Ils n'ont été que peu exploités depuis l'Antiquité (exploitation artisanale pour l'Au et l'Ag) et peuvent être décrits dans leur entièreté (Melfos, 2012). Actuellement ces sites sont surtout d'intérêt pour l'exploration de l'Au (Eldorado Gold – Hellas Gold) ou du Pb et Zn épithermaux de St Philippos (exploitation allemande durant la Seconde Guerre mondiale). La grande majorité de ces gisements sont liés à des intrusions magmatiques mises en place lors du retrait du slab : andésite à Pefka – granodiorite à Pagoni Rachi – granite/rhyolite à Maronia et St Philippos.

C'est à travers le Projet ARTeMIS (Action for Research and Teaching Mineral exploration Inclusive School) Erasmus+, permettant aux étudiants de Master des Universités de Lorraine - Nancy - (FR), Erlangen (DE), Athènes (GR), et Thessalonique (GR) de partir sur le terrain pour réaliser un travail d'exploration, avec des outils de spectroscopie portable (p-XRF, p-LIBS, Raman, VNIR-SWIR), que des observations et échantillonnages stratégiques et complémentaires ont été réalisés sur différents sites (Pagoni Rachi, Maronia, Konos Hill, St Philippos).

Le site de Pagoni Rachi, situé dans le district de Sapes-Kassiteres, présente un gisement de type porphyre-épithermal à Cu – Mo ± (Re – Au). La minéralisation prend la forme d'une succession de veines minéralisées organisées en stockwork encaissé au sein d'une granodiorite-tonalite altérée d'âge éocène supérieur à oligocène (Voudouris et al. 2013a). Les précédents travaux (Voudouris et al. 2009,

2013a,b, 2019, 2021) montrent des teneurs exceptionnelles en métaux : 5,1 ppm d'Au, 1,0 wt% de Cu, 40 ppm de Te, 2000 ppm de Mo, et notamment en Re avec près de 20 ppm jusqu'à sa précipitation sous forme de rhéniite (ReS_2, seul sulfure de rhénium connu) à partir de 4,7 wt% sous forme de lamelles dans la molybdénite. Ce minéral n'est observé que dans de rares gisements tels que le volcan de Kudryavy en Russie (Tessalina et al., 2005 et Tessalina, 2008). Ce qui fait de Pagoni Rachi un gisement atypique (Voudouris et al., 2013a, 2019).

Les travaux récemment publiés (Arikas, 1979, 1981 ; Voudouris et Melfos, 2006 ; Voudouris et al., 2009, 2013a, 2019, 2022 ; Mavrogonatos et al., 2019, 2020) proposent une évolution simple des conditions *PT* (*P*ression, *T*empérature) des fluides : une ébullition des fluides magmatiques vers 400 °C puis une dilution par des fluides de surface vers 250 °C avec une baisse de la salinité. Ainsi le système de type porphyre-épithermal est présenté selon un schéma classique de ces systèmes tel que décrits ailleurs dans le monde : une succession de veines et d'altérations, un télescopage des structures, une évolution des fluides marquée par le phénomène d'ébullition et de dilution par des fluides de surface ; mais qui, de par son contexte de mise en place post-subduction, voire d'arc, dont les mécanismes du magmatisme sont encore mal contraints, ainsi que ses teneurs en Mo et Re, en font un cas particulier, voire atypique. De plus, ce gisement est de petite taille (surface affleurante <1 km^2), n'a pas été exploité, n'a été caractérisé comme porphyre que récemment, et est donc parfaitement conservé. Ce système isolé représente ainsi un parfait objet d'étude pour comprendre le fonctionnement de systèmes plus complexes, avec une exposition d'éléments caractéristiques de ces systèmes, depuis les parties profondes porphyres aux parties superficielles épithermales.

Bien que les précédentes études aient établi une pétrographie détaillée et une étude préliminaire des fluides, cela ne permet pas encore de comprendre le comportement des métaux accessoires durant les processus hydrothermaux de ce gisement, en raison d'une absence : d'échantillonnage spécifique, de chronologie relative des veines, de pétrographie fine des différentes générations de quartz dans les veines et d'épisodes fluides, d'identification et de quantification des gaz ainsi que des teneurs des métaux transportés par les fluides (e.g. Voudouris et al., 2013a, 2019b). Les travaux de Bitte et al. (M2, rapport interne) ont montré qu'il était possible de quantifier les éléments traces contenus au sein des fluides des minéraux de gangue de la minéralisation. Dans ce contexte, et grâce aux résultats préliminaires, il apparaît pertinent de caractériser davantage le gisement de Pagoni Rachi.

Les systèmes de type porphyre-épithermal constituent des environnements hydrothermaux complexes, dans lesquels la circulation des fluides, les interactions fluide-roche, et les contrôles structuraux et déformations jouent un rôle clef dans la formation des gisements métallifères riches en métaux stratégiques tels que le Cu, Mo, Au et Re (e.g. Seedorf, 2005 ; Sillitoe, 2010 ; Kouzmanov, 2012 ; Richards, 2015 ; Monecke et al., 2018 ; Voudouris et al., 2019 ; Rottier and Casanova, 2021). Bien que ces systèmes soient largement étudiés, certaines questions fondamentales persistent, en particulier celles sur la reconstruction des conditions physico-chimiques, l'origine et l'évolution des

fluides, ainsi que l'influence de la recristallisation dynamique sur les processus de minéralisation. Ces incertitudes mettent en évidence à la fois la complexité des processus hydrothermaux et les limites des approches méthodologiques actuellement disponibles.

Un premier enjeu majeur réside dans la reconstitution précise des conditions *PVTX*, (*P*ression, *T*empérature, *V*olume molaire, *X* - composition des fluides). Ces paramètres contrôlent directement la dynamique des processus hydrothermaux et, par conséquent, la genèse des minéralisations associées. Une question centrale de cette recherche est donc de déterminer dans quelle mesure l'observation de terrain et de laboratoire, ainsi qu'une analyse détaillée des inclusions fluides, des isotopes stables et des éléments traces contenus dans les minéraux de gangue (quartz et calcite) permettent de contraindre ces paramètres. Il est également essentiel d'identifier les limites interprétatives et méthodologiques liées à ces approches. Ce travail a pour but de répondre à la question générale suivante : dans quelle mesure l'étude détaillée des veines hydrothermales au sein d'un système de type porphyre-épithermal permet-elle de reconstruire les conditions *PVTX* de formation, et quelles sont les implications générales pour d'autres environnements analogues ?

L'origine et l'évolution des fluides hydrothermaux impliqués dans la formation des veines constituent une autre problématique majeure. Dans les systèmes de type porphyre-épithermal, les fluides peuvent provenir de différentes sources : magmatique, météorique, marine ou d'un mélange de ces fluides (Gustafson et Hunt, 1975 ; Sillitoe, 2010 ; Kouzmanov et al., 2012 ; Richards, 2015 ; Monecke et al., 2018 ; Rottier and Casanova, 2021). Cependant, les processus de mélange ainsi que leurs effets sur la minéralisation restent mal compris. L'une des grandes questions abordées ici est donc d'identifier la contribution relative des fluides magmatiques et météoriques dans la formation des veines et leur rôle dans le transport et la concentration des métaux tels que le Cu, le Mo, l'Au ou le Re.

Une meilleure compréhension de la succession des veines et des générations de quartz et de calcite est essentielle pour reconstruire l'histoire hydrothermale complète du gisement. Les études précédentes réalisées à Pagoni Rachi, ont permis d'établir une chronologie hydrothermale préliminaire (Voudouris et al., 2009, 2013a,b, 2019 ; Mavrogonatos et al., 2019, 2020), mais une description plus fine des textures pétrographiques, des inclusions fluides et des générations successives de veines pourrait révéler une histoire plus complexe. Cela permettrait également d'identifier des épisodes jusqu'alors inobservés dans l'évolution des fluides minéralisateurs. Par ailleurs, l'analyse des isotopes stables et des éléments traces dans le quartz, qui est omniprésent dans les veines du stockwork, pourrait fournir des informations cruciales sur les fluctuations des conditions physico-chimiques tout au long de la formation du système. Une caractérisation isotopique détaillée (oxygène, hydrogène et carbone), couplée à une analyse des éléments traces dans le quartz, pourrait également révéler des variations des conditions chimiques (pH) et thermiques (température) des fluides au cours de leur circulation dans le système.

Dans la région de la Thrace occidentale, une succession de corps magmatiques avec des degrés de différenciation différents sont associés à des gisements de type porphyre (e.g. Pagoni Rachi – granodiorite, Maronia – granite, Sant Philippos – rhyolite, Pefka – andésite) et provient d'une même

source – manteau métasomatisé. Ce magmatisme migre du Nord vers le Sud, formant le Corridor Magmatique de Maronia (CMM) (Schaarschmidt et al., 2021), qui est associé au retrait de la plaque plongeant vers le sud. Quel pourrait être le rôle de la différenciation magmatique sur la formation de ces gisements, de la distribution des métaux ?

Enfin, le rôle de la déformation sur les processus hydrothermaux représente un autre point central de cette recherche. En effet, les travaux antérieurs suggèrent que les veines épithermales de Pagoni Rachi sont spatialement contrôlées par des structures tectoniques, notamment des failles orientées NNW-SSE, qui auraient permis la circulation et le mélange des fluides (Voudouris et al., 2013a). Cependant, l'effet de la déformation sur les marqueurs *PVTX*, tels que les éléments traces et les inclusions fluides dans le quartz, reste à explorer. De plus, dans d'autres systèmes de type porphyre, comme celui de Butte (Acosta et al., 2020, 2022), la déformation intracristalline et les phénomènes de recristallisation dynamique du quartz ont été observés. Ce type de microstructures cristallines, s'il est présent à Pagoni Rachi, pourrait fournir des indications précieuses sur les interactions entre la déformation et la géochimie des quartz, tout en offrant un cadre pour améliorer la compréhension des conditions hydrothermales au sein de systèmes affectés par la déformation.

Ainsi cette thèse s'appuie sur l'étude du gisement de type porphyre-épithermal de Pagoni Rachi pour répondre à ces problématiques, tout en cherchant à élaborer un modèle général intégrant des processus hydrothermaux, à la fois à l'échelle local et global applicables à d'autres contextes géologiques en combinant des approches pétrographiques, de géochimie élémentaire et isotopique. Le manuscrit est ainsi découpé en sept chapitres discutant des différents points présentés précédemment afin de répondre aux problématiques exposées :

Chapitre 1 – présentation de la littérature sur les systèmes porphyres et épithermaux, leurs contextes de mise en place et une synthèse géologique et géodynamique de la Grèce et des sites d'intérêt pour cette étude,

Chapitre 2 – étude de terrain et un échantillonnage ciblé, ainsi que la mise en place d'une chronologie et d'une pétrologie précise des veines et des altérations et des microtextures du quartz,

Chapitre 3 – rôle du processus de recristallisation dynamique et d'une croissance rapide du quartz dans l'équilibre du contenu en éléments traces et l'équilibre des inclusions fluides dans le quartz,

Chapitre 4 – quantification des éléments traces (et métaux) et la caractérisation des variations conditions physico-chimiques durant le développement du système de type porphyre-épithermal,

Chapitre 5 – traçage de l'origine des fluides hydrothermaux (magmatiques, météoriques, eau de mer) par l'utilisation des isotopes stables (oxygène, hydrogène, carbone), et la présentation de pistes de compréhension de l'évolution de la composition des fluides minéralisateurs et de géodynamique dans les systèmes porphyres et épithermaux dans le Nord-Est de la Grèce.

Chapitre 6 – discussion d'une proposition de modèle métallogénique du gisement de type porphyre-épithermal de Pagoni Rachi.

Chapitre 7 – apports et limites des différentes méthodes employées durant cette thèse, ainsi que la présentation de perspectives développées aux vues des éléments et conclusions apportées par ce travail.

Les chapitres 2, 4 et 5 avaient initialement été rédigés et construits dans l'objectif d'être valorisées dans une publication portant sur la description géologique de terrain/laboratoire ; traçages des fluides ; des conditions PTX par l'utilisation complémentaire des éléments traces dans le quartz et des isotopes stables (hydrogène, carbone, oxygène) dans le quartz, la calcite ; des inclusions fluides contenues dans les cristaux de quartz de la succession de veines de Pagoni Rachi, au sein de journaux scientifiques. Ces chapitres sont donc rédigés en anglais.

Le chapitre 3 propose une évaluation de l'effet de la recristallisation dynamique des cristaux de quartz sur la conservation des éléments traces et ces implications sur le thermomètre du Ti dans le quartz (Ti-in-Quartz) et l'utilisation de diagramme de classification géochimique. Cette partie a été valorisée sous le format d'un article actuellement soumis dans la revue Lithos et est donc également rédigée en anglais.

Vous souhaitant une bonne lecture.

1.2. ETAT DE L'ART

1.2.1. Systèmes de type porphyre-épithermal

Les gisements de type porphyre à Cu ± Mo ± Au représentent les principales réserves en Cu, Mo et Au primaire du monde (Sillitoe, 2010). Ces objets se situent principalement le long de systèmes linéaires tels que les zones de subduction ou les ceintures orogéniques (Sillitoe, 2010). Ils peuvent faire de quelques dizaines à milliers de kilomètres de long, comme pour le cas des Andes (Sillitoe et Perello, 2005). En contexte de subduction, la métallogénie observée est associée au recyclage de l'eau et d'éléments volatils du manteau de la lithosphère océanique altérée (Zellmer et al., 2015 ; Richards, 2021) (Figure 2). La remontée de ces éléments vers la surface, associée à la formation d'arcs volcaniques explosifs et de systèmes hydrothermaux superficiels peuvent alors former des gisements. Différents facteurs jouent alors sur la fertilité de tels systèmes : le magmatisme, l'hydrothermalisme, les fluides externes (météoriques, de bassin, d'eau de mer), etc. (Richards, 2021). Ces zones sont propices à la formation de gisements de type porphyre à Cu ± Mo et de provinces épithermales à Au (Sillitoe, 2010). Ces gisements se caractérisent par de gros volumes de roches (10 – 100 km^3) altérés par un hydrothermalisme centré autour du « porphyre », souvent accompagné d'autres type de corps minéralisés : skarns, remplacements de carbonates, veines épithermales de basse à haute sulfuration et/ou minéralisations à métaux précieux (Sillitoe, 2010). L'existence de quelques cas particuliers en contexte post-collision est à souligner (Sillitoe, 2010 ; Richards, 2009, 2015).

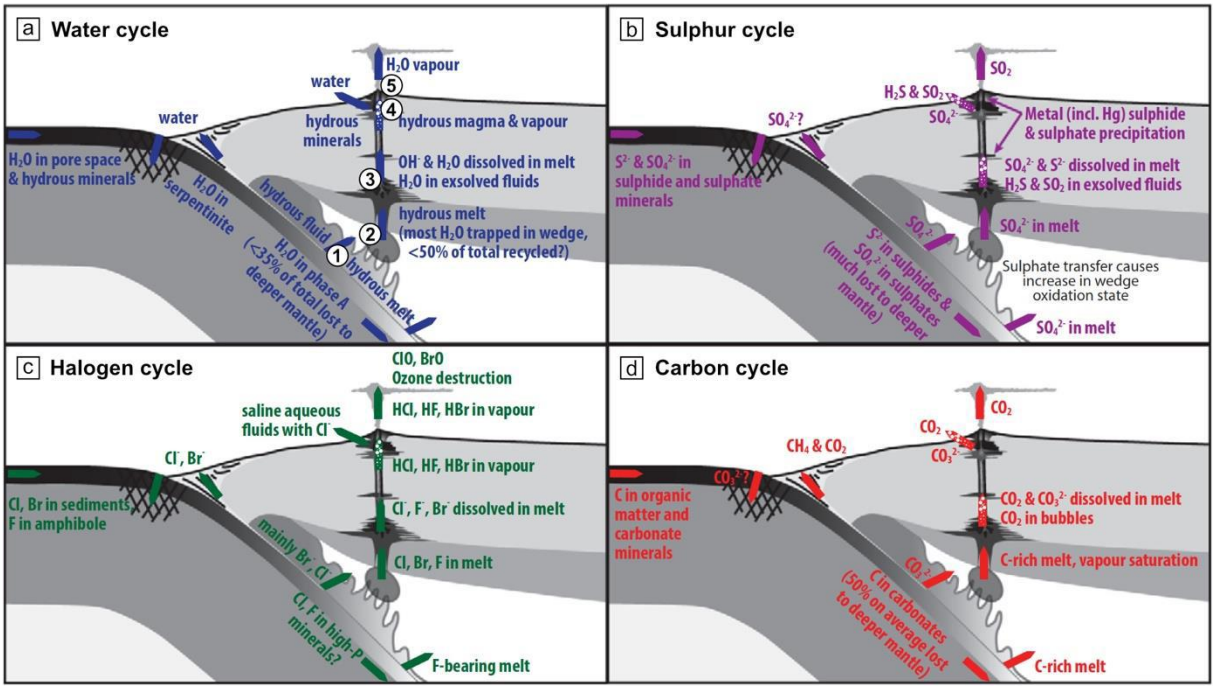

Figure 2: Cycles de l'eau (a), du soufre (b), des halogènes(c), et du carbone (d) en zones de subduction. Cinq phénomènes majeurs contrôlent le transport d'éléments volatils : (i) un/des fluide(s) passant de la croûte océanique et sédiments subduit au prisme mantellique ; (ii) le partitionnement par fusion partielle ; (iii) la remontée et la cristallisation de fluides magmatiques hydratés à éléments volatils dissous ; (iv) l'exsolution de fluides aqueux à partir de fluides magmatiques hydratés à des profondeurs superficielles ainsi que (v) le dégazage lié à des éruptions volcaniques (d'après Zellmer et al., 2015).

La fusion partielle du manteau, en zone de subduction est un milieu propice à la formation de systèmes de type porphyre. Le magma produit, enrichit en eau et éléments volatils, se différencie et circule au travers de la croûte (Figure 2) (Hildreth et Moorbath, 1988 ; Grove et al., 2003 ; Pichavant et Macdonald, 2007 ; Zimmer et al., 2010 ; Lee et al., 2014 ; Chin et al., 2018 ; Richards, 2021), entrainant une concentration progressive en métaux (Zang et Audétat, 2017 ; Audétat, 2019, 2023). Une intrusion, sous la forme d'un batholite, se forme près de la surface (entre 5 – 15 km). Celui-ci refroidit et commence à cristalliser. Les fluides magmatiques circulent et se concentrent à l'apex de cette intrusion formant une protubérance verticale, une apophyse, à texture porphyrique, riche en ligands (Cl, S) et métaux. Des fluides hydrothermaux s'exhalent de cette structure magmatique et se scindent, par décompression, en deux phases : vapeur et liquide ; c'est l'ébullition. Ces fluides traversent le système de type porphyre et altèrent les roches environnantes. La convection de fluides externes (ex. météoriques) favorisée par une mise en place d'un batholithe chaud, provoque la circulation de fluide dans la croûte. Cette circulation de fluides engendre des réactions fluides-roche provoquant des altérations des roches environnantes à grande échelle. Différentes zones d'altérations typiques peuvent se former : sodi-calcique, potassique, séricitique (ou phyllique), propylitique, argillique, etc... La précipitation des métaux provenant des fluides chargés se produit notamment lors de changement de conditions physico-chimiques (e.g. pression et/ou de température), formant la minéralisation des gisements de type porphyre et épithermal, auxquels seront associés différents styles d'altérations des roches encaissantes (Jébrak et Marcoux, 2008 ; Sillitoe, 2010 ; Richards, 2021).

Dans un système de type porphyre cuprifère, deux grandes structures sont observables : (i) une partie profonde dit hypogène avec un système dit porphyre à Cu ± Mo ± Au, pouvant s'accompagner de gisements de type skarn ; (ii) une partie superficielle avec un système dit épithermal à Au ± Ag ± Cu de Haute Sulfuration (HS, ou High Sulfidation en anglais) ou Basse Sulfuration (BS, ou Low Sulfidation – LS en anglais) (Hedenquist et al., 1998 ; Sillitoe, 2010 ; Richards 2021).

Ces systèmes existent depuis l'Archéen. Cependant, ceux observables sont majoritairement d'âges méso-cénozoïque. En effet, les systèmes de type porphyre-épithermal se mettent en place à de faible profondeur (~ 4 km), ceux-ci disparaissent alors facilement par érosion. Ainsi seuls les gisements les plus récents, n'ayant que peu subit le phénomène d'érosion sont encore conservés et observables contrairement aux systèmes anciens effacés par les affres des processus érosifs (e.g. Seedorff, 2005 ; Kesler et Wilkinson, 2006 ; Wilkinson et Kesler, 2009). Ces gisements sont de classe économique mondiale. En effet, les gisements de type porphyre à Cu ± Mo ± Au encaissent les plus importantes associations économiques de métaux. Ils représentent à eux seuls près des 75 % de Cu, 95 % de Mo et 20 % d'Au primaire exploités dans le monde, ainsi que la plupart du Re et de petites proportions d'autres métaux (Ag, Pd, Te, Se, Bi, Zn, and Pb). Les teneurs des zones minéralisées hypogènes sont d'environ : 0,5 – 1,5 % de Cu, 0,01 – 0,04 % de Mo, 0,0 – 1,5 ppm d'Au et des zones minéralisées épithermales avec 1,0 à 3,0 ppm d'Au (Sillitoe, 2010 ; USGS1-2). Il n'y a que peu de Cu et Mo par remobilisation supergène (Richards, 2021). Bien que les teneurs soient faibles, les gisements sont rentables du fait du

volume important de roche, avec un tonnage important de métaux. Ils représentent jusqu'à plusieurs millions de tonnes de métaux, notamment de Cu (203 Mt : Los Bronces-Río Blanco, Chili central ; Irarrazaval et al., 2010), Mo (2,5 Mt : El Teniente, Chili central ; Camus, 2003) et Au (Moz : Grasberg, Indonésie ; Sillitoe, 2010 ; Richards, 2021).

Il est donc primordial de comprendre l'origine et les moteurs de telles concentrations de métaux d'importances économiques, notamment dans un contexte technologique et écologique en constante évolution.

1.2.2. Géodynamique et magmatisme

Les systèmes de type porphyre à Cu ± Mo ± Au se forment en grande majorité lors de convergence lithosphérique, en contexte de subduction. La subduction permet le recyclage de l'eau et d'éléments volatils (Figure 2) (Zellmer et al. 2015 ; Richards, 2021) qui facilite le transport de métaux. En effet, la lithosphère océanique plongeante altérée, évacue l'eau et les éléments volatils qu'elle contient par déshydratation durant son enfouissement (Figure 2). L'eau évacuée, hydrate alors le manteau de la lithosphère chevauchante. Cela permet la baisse de la température du solidus du manteau et engendre sa fusion partielle (Kushiro et al., 1968; Grove et al., 2006; England et Katz, 2010; Kelley et al., 2010; Green et al., 2014 ; Richards, 2021). Ce phénomène s'accompagne d'un enrichissement du manteau en K, S, Cl, F, métaux et LILE (Large Ion Lithophile Elements) provenant du slab plongeant.

La mise en place d'un système de type porphyre nécessite une grande production de magma, qui est en grande partie contrôlée par le mécanisme de subduction. Le régime de production dépend du recul ou de l'avancée de la tranchée et du pendage de la plaque plongeant. Richards (2021) propose que pour une production de magma optimale, l'inclinaison du slab plongeant doit être comprise entre 30° et 45° et conserver un système en contrainte compressive. Cette géométrie favoriserait une localisation et une concentration spatiale et temporelle de la fusion partielle du manteau et ses produits (Richards, 2021).

Un phénomène de sous-plaquage peut se produire à la suite de la fusion partielle du manteau par une accumulation de liquide basaltique en base de croûte au niveau du Moho. Cette zone est appelée zone de MASH (Melting, Assimilation, Storage, Homogenization) (Figure 3). Ce processus de stockage de magma dans les zones MASH augmente le volume de magma disponible pour le plutonisme de la croûte supérieure. En effet cette accumulation de magma peut conduire à une augmentation de la masse totale d'éléments volatils disponibles (H_2O, S et Cl) ce qui tend à augmenter l'état d'oxydation du magma lors du processus de différenciation magmatique (Burnham, 1979 ; Candela, 1992 ; Streck et Dilles, 1998 ; Rohrlach et Loucks, 2005 ; Chambefort et al., 2008 ; Annen et al., 2009 ; Richards, 2015 ; Sparks et al. 2019 ; Hutchinson et Dilles, 2019 ; Chelle-Michou et Rottier, 2021). Ce magma basaltique, dérivé du manteau, est alors trop dense pour traverser la croûte. Un mélange se produit alors entre ce magma et un liquide magmatique issu de la fusion partielle de roches en base de croûte continentale. Ce phénomène entraine une baisse de la densité du magma par assimilation. Le magma passerait alors

d'ultramafique/mafique à intermédiaire (Hildreth et Moorbath, 1988 ; Jébrak et Marcoux 2008 ; Richards, 2021). Ce magma hybride pourra remonter et s'immobiliser dans la croûte moyenne à supérieure (Richards, 2003, 2015 ; Chiaradia et Caricchi, 2017). Il est donc favorable à la formation de gisements porphyres superficiels (Richards, 2021).

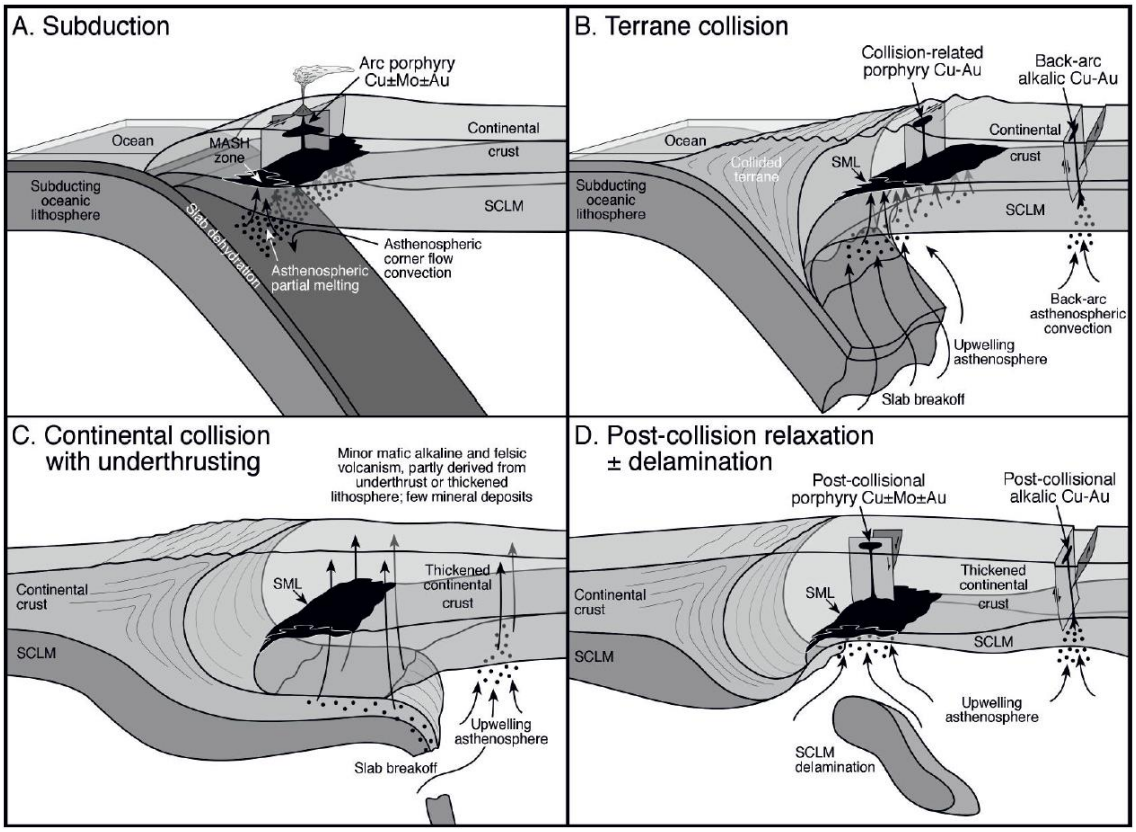

Figure 3: Subduction and collision-related tectonic settings, and their relationship to porphyry deposit formation from Richards, 2014.

Ces magmas sont riches en H_2O (4 à 10 % wt) avec un pouvoir oxydant important ($\Delta FMQ = +1$ à +2). L'état d'oxydation élevé des magmas limite la tendance à subir une saturation des sulfures, et évite la précipitation précoce des éléments chalcophiles et sidérophiles et donc favorisent dans un premier temps la conservation de ses éléments dans ces magmas (Mitchell et Keays, 1981 ; Hamlyn et al., 1985 ; Li et Audétat, 2015 ; Richards, 2011a, 2015). La forte teneur en soufre des magmas induit de petites quantités de fusion où des sulfures et des minéraux fractionnent à partir de ces magmas, même à des états d'oxydation modérés. Ce processus explique l'appauvrissement en éléments sidérophiles (Au, PGE). Néanmoins les teneurs en Cu ne peuvent être affectées (significativement) par de tels fractionnements. Ainsi le magma reste fertile en Cu, mais non en Au et PGE (Richards 2011a, 2015). La réduction du soufre de magmas riches en soufre se produit à la source et dans la croûte profonde par interaction de lithologies réductrices, diminuant la fertilité des magmas (Richards 2021). De même, la présence de matériaux carbonés dans la croûte inférieure peut entraîner la réduction des magmas dans la zone MASH, conduisant à la précipitation de sulfures et à la rétention d'éléments chalcophiles et

sidérophiles dans les cumulas (Tomkins et al., 2012). Il y aurait donc une rétention des éléments chalcophiles et sidérophiles dans la région mantellique source, diminuant la fertilité des magmas. Cependant, les métaux des phases sulfurées pourraient être remobilisés lors d'une collision ou lors d'un épaississement crustal ultérieur pouvant former des gisements de type porphyre à Cu ± Au post-subduction (e.g. Tibet, Ceinture Téthysienne Orogénique : Richards, 2009 ; Lee et al., 2012 ; Hou et al., 2015).

Des teneurs élevées en Cl dans ces magmas sont importantes dans le processus de formation d'un gisement de type porphyre à Cu (Cline et Bodnar, 1991 ; Zhu et al., 2018 ; Tattich et al. 2021). En effet le Cu migre principalement dans les fluides hydrothermaux sous forme de complexes de Cl (Cline et Bodnar, 1991). Le molybdène serait, en revanche, indépendant des concentrations en Cl et de l'état d'oxydation ($0 < QFM < +2$) des magmas et des phases aqueuses associées. Puisque le chlore n'a peu ou pas d'effet sur le partage du molybdène dans une phase aqueuse magmatique, il est possible que les concentrations en molybdène proviennent plutôt de processus géologiques (Candela et Holland, 1984). Néanmoins une teneur élevée en Cl pourrait garantir un fractionnement efficace au sein du fluide (Candela et Holland, 1984 ; Cline et Bodnar, 1991 ; Idrus et al., 2007).

Lorsque que le magma se différencie, la fraction plus différenciée, moins dense, remonte progressivement au travers la croûte continentale par équilibrage de densité. Cette différenciation se produit en majeure partie dans la croûte profonde. La composition du magma évolue depuis des compositions basaltiques à dioritiques voire granitiques. Ces magmas sont en général de type I de la série à magnétite, métalumineux, avec une affinité calco-alcaline riche en potassium, voire sub-alcalin à alcalin (Jébrak et Marcoux, 2008 ; Sillitoe, 2010 ; Richards, 2021).

Le développement de chambres magmatiques en milieu de croûte se produit durant un régime en compression structurale. Il est associé à : un fractionnement, une génération et une exhalation de fluides (Takada, 1994 ; Sillitoe, et al., 1998 ; Sillitoe, 1997, 2010). Ainsi, du magma s'accumule à des profondeurs de 5 à 15 km, proche de la transition fragile/ductile (Sillitoe, 2010 ; Richards, 2021) pour former un grand réservoir magmatique de type batholite.

La présence de failles impacte le site de formation et la géométrie du système de type porphyre à Cu. Le système de faille intra-arc actif, anté/syn-magmatique, facilite la mise en place d'un système de type porphyre à Cu, en agissant comme des drains pour la circulation des liquides magmatiques (Figure 3). Cela permet la formation de corps magmatiques en amas équidimensionnels ou le long de lignes sur des dizaines de kilomètres. Ces plutons se retrouvent soit parallèlement à l'axe de l'arc, ou de manière transverse suivant les failles majeures des zones intra-arc ou encore suivant les zones de failles traversant l'arc (Figure 4).

Lors de son ascension le magma vient à être à un équilibre de flottabilité avec la croûte. Le magmatisme est actif et le batholithe se développe par pulses magmatiques successifs. Ainsi le système reste chaud et actif. Il est la source du magma et de fluides métallifères de haute température et de haute pression qui traverseront le système (Richards, 2021). Ces intrusions, une fois cristallisées, ont une

texture porphyrique, d'où leur nom, et contiennent typiquement des phénocristaux de hornblende et/ou de biotite et/ou de plagioclase (Jébrak et Marcoux, 2008).

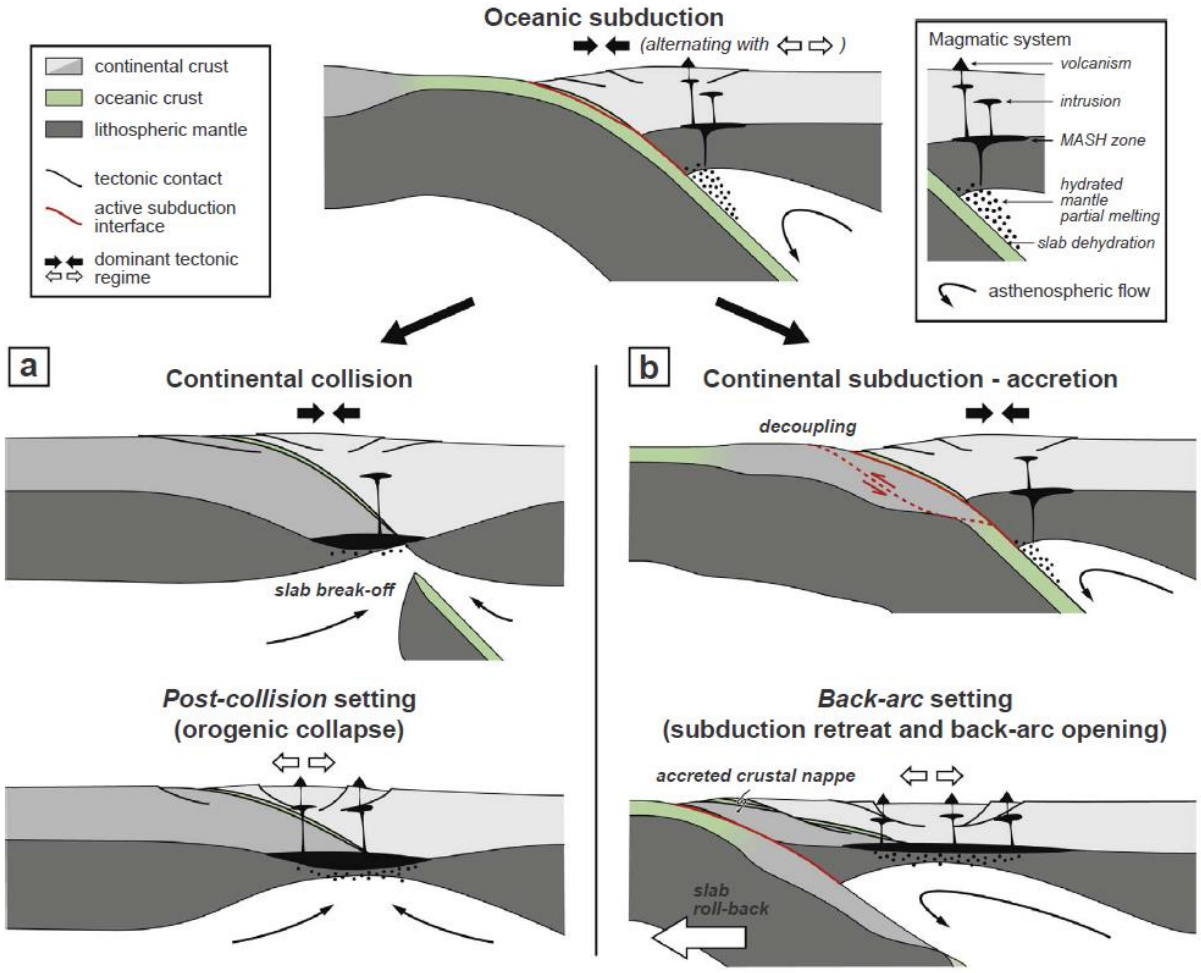

Figure 4 : Coupe lithosphérique schématique illustrant deux évolutions possibles d'une zone de subduction typique le long d'une marge continentale. (a) Zone de subduction évoluant vers une collision, suivie d'un contexte post-collision, après un détachement de la plaque plongeante (slab break-off). (b) Zone de subduction évoluant vers un contexte de rétro-arc (back-arc) en raison d'un retrait de la plaque plongeante (slab roll-back). Une accrétion continentale peut survenir par découplage des nappes crustales de la lithosphère continentale plongeante, sans interruption du processus de subduction. Zone MASH : Zone de Fusion, Assimilation, Stockage et Homogénéisation (de Menant et al., 2016).

La cristallisation fractionnée entraîne l'extraction de fluides hydratés riches en éléments volatiles et en métaux. La phase aqueuse chargée (e.g. métaux, volatils, et ligands) s'exhale de la chambre magmatique durant le refroidissement et la cristallisation du magma et se fractionne grâce à la convection magmatique. Ce mécanisme est suffisant pour délivrer une quantité importante de phase aqueuse à travers la chambre.

Le magma parent doit être riche en H_2O pour avoir un pouvoir oxydant et maximiser le contenu métallique de la phase aqueuse, cela évite la formation de pyrrhotite qui fractionne les métaux dans la phase solide (Candela et Holland, 1986). Le magma riche en soufre, alors sous forme de sulfate, avec la présence fréquente d'anhydrite magmatique (Lickfold et al., 2003 ; Audétat et al., 2004 ; Stern et al.,

2007 ; Chambefort et al., 2008 ; Sillitoe, 2010). Les volatils (H_2O, S, Cl, CO_2…) dissous dans les magmas qui peut atteindre la saturation et l'exsolution par accumulation. Les magmas finissent par se dépressuriser, se refroidir et cristalliser des minéraux anhydres pendant leur ascension dans la croûte. Les magmas de composition mafique à felsique contenant 4 à 6 % en poids de H_2O satureront en eau à des pressions de l'ordre de 2 kbars, (soit de 5 à 10 km en profondeur) dans des conditions de pression lithostatique (Burnham, 1979 ; Burnham et Ohmoto, 1980). Les fluides extraits se concentrent donc à l'apex du batholithe et forment des aspérités avec des « apophyses à texture porphyrique ». Elles peuvent être sous formes d'excroissances cylindriques verticales ou de « champs » de dyke verticaux (Sillitoe 2010 ; Richards, 2021).

Les systèmes de type porphyre à Cu sont spatialement liés à du volcanisme, avec des roches de composition intermédiaire à felsique. Dans la plupart des cas, le volcanisme s'arrête avant l'initiation de la formation du système de type porphyre à Cu. Dans de rares cas des éruptions mineures ont été observées de même que des dômes magmatiques. Souvent la partie volcanique est érodée, au moins jusqu'à la partie minéralisée. La formation d'une caldeira synchrone d'un système de type porphyre-épithermal ne peut exister. En effet les volatils s'échappent lors de l'explosion, or ce sont ces mêmes éléments (e.g. S, Cl, H_2O) qui permettent le transport de métaux et donc la formation de la minéralisation. Dans ce cas il n'y aurait pas de gisement (Sillitoe, 2010 ; Richards, 2021).

Des gisements de type porphyre peuvent également se former en contexte post-collision dans un régime extensif (Figure 3, Figure 4) (Richards, 2009, 2015). En effet une fusion par décompression peut se produire par un upwelling d'asthénosphère, alors métasomatisée par une subduction antérieure. Cela entraîne la formation de magmas mafiques alcalins voire shoshonitiques (Paquette et al., 2003 ; Richards et al., 2009). De grands accidents extensifs (détachements) pourront faire office de chenaux ou de drains pour la remontée de ces magmas (Sillitoe, 2010). Également, à la suite de la collision, un épaississement crustal survient et peut mener à de la délamination. Ce phénomène engendre une fusion partielle des parties crustales profondes, lorsque les isothermes remontent ou qu'un upwelling asthénosphérique se développe. Le magma produit sera felsique d'affinité calco-alcaline à alcaline (Richards et al., 2009).

Dans les deux cas, la source des magmas serait de la lithosphère/asthénosphère modifiée par une subduction et la fusion de résidus soufrés en base de croûte. Ils partagent une signature géochimique similaire aux magmas formés lors de cette subduction. Cependant ces magmas tendent à être spatialement isolés avec une affinité moyenne à fortement alcaline, riche en potassium (Richards et al., 2009). Les gisements associés seraient riches en Au (en comparaison avec les gisements de type porphyre en contexte de subduction) avec pour cause un faible degré de fusion partielle de la source (Richards et al., 2009) présentant une faible fugacité en soufre et une forte fugacité en oxygène.

1.2.3. Evolution des fluides hydrothermaux d'un système de type porphyre

La circulation de fluides hydrothermaux (Figure 5), ayant une origine magmatique, induit un système de fracturation avec la formation de veines successives et d'altérations des roches encaissantes. La formation des différents types de veines se fait à partir de la circulation d'un premier fluide profond (9 km) de salinité faible à intermédiaire (2 – 20 $wt\%_{equiv.NaCl.}$), avec des concentrations de métaux de base allant de quelques 1000 ppm à quelques wt.% (Richards, 2021).

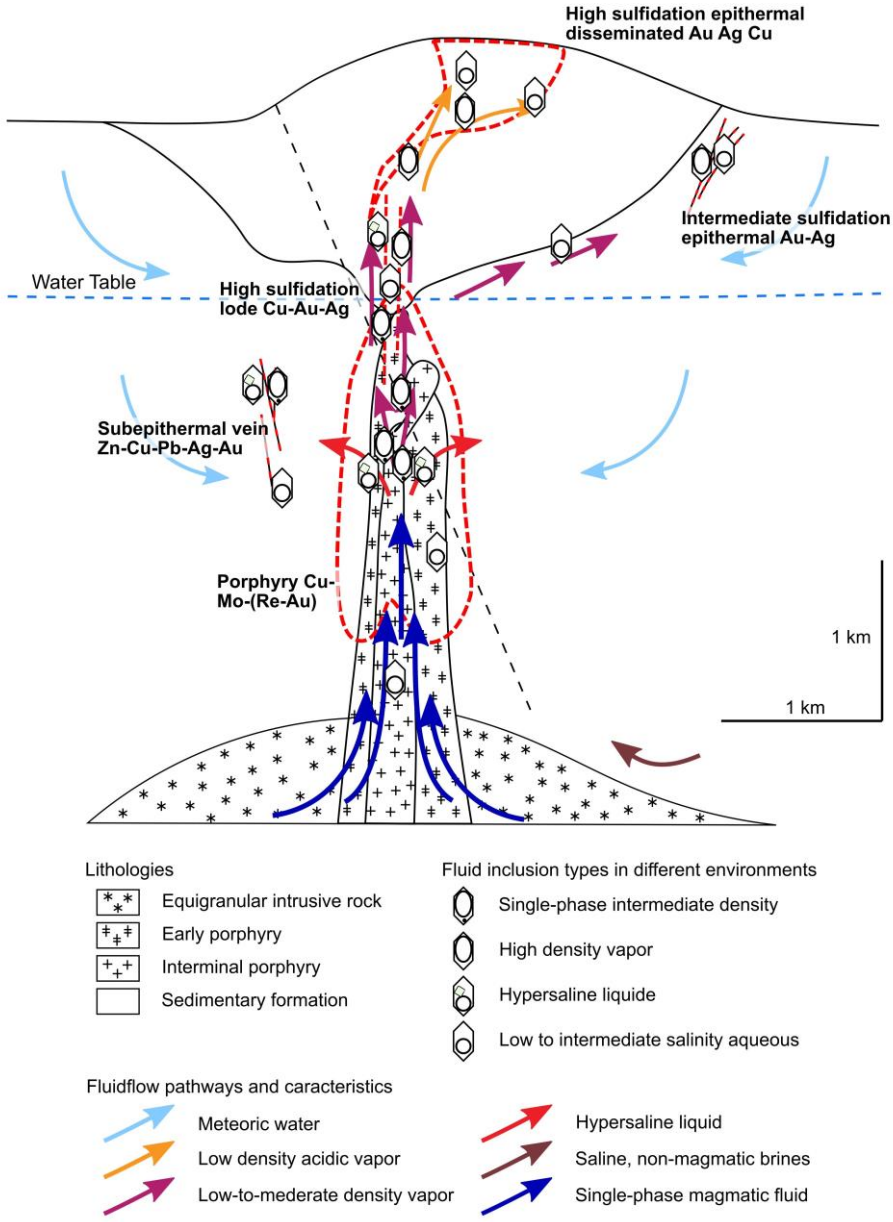

Figure 5 : Coupe schématique de la circulation de fluides lors de la mise en place d'un système de type porphyre et épithermal, modifié d'après Sillitoe (2010) et Kouzmanov et al. (2012).

Cette première phase fluide, extraite du magma, se scinde par ébullition lors de la décompression, en deux phases, liquide et vapeur concomitantes (e.g. Kouzmanov et al., 2012 ; Richards, 2021). La phase liquide, en petit volume, contient de fortes teneurs en Na, K, Fe, chlorures, avec une salinité de l'ordre de 35 – 70 $wt\%_{equiv.NaCl}$, soit une saumure hypersaline (Fournier, 1999 ; Sillitoe, 2010). La phase vapeur, en gros volume, contient majoritairement des éléments volatils, tels que des ligans, et des acides, SO_2, H_2S, CO_2, HCl, HF (e.g., Giggenbach, 1992 ; Hedenquist et al., 1998 ; Sillitoe, 2010). Des analyses du contenu élémentaire d'inclusions fluides montrent un fractionnement entre ces deux phases fluides. La phase vapeur contient principalement du Cu, Au, Ag, S, avec un peu de As, Sb, Te et B ; tandis que la phase liquide contient du Fe, Zn, Pb, Mn, Cu, S (Roedder, 1971, 1984 ; Sillitoe, 2010). Cette séparation de phase est associée à la formation de gisements métalliques qui s'initient aux conditions proches lithostatiques, avec fracturation hydraulique à haute vitesse générant un stockwork omniprésent formant des veines de type A-M et B. La décompression des fluides lors de leur remontée provoque une augmentation de volume importante, qui s'accompagne d'une augmentation de la pression fluide pouvant dépasser la pression lithostatique (e.g. Sillitoe, 2010). Les métaux se concentrent majoritairement dans la phase vapeur qui contient des ligands ($H_2S \pm SO_2 \pm Cl$). De plus, la décompression diminue la solubilité des métaux facilitant donc la précipitation de ceux-ci (Cu, Fe). La phase vapeur, moins dense, se sépare de la phase aqueuse pour remonter la colonne de roche, 1 – 2 km au-dessus de l'intrusion (Figure 5). Elle se condense dans les eaux de subsurface, formant des eaux acides riches en soufre (H_2SO_4, H_2S) responsables du haut dégrée de lessivage des roches. L'ascension se produit par le biais de failles et de niveaux perméables. Ces fluides chauds interagissent avec la roche encaissante par échange d'éléments (le potassium notamment) et provoquent une série d'altération.

1.2.4. Génération des veines minéralisées du système de type porphyre

La formation de veines avec précipitations de minéraux porteurs de métaux est associée aux minéralisations de type porphyre. Selon la dynamique des fluides du système de type porphyre ces fracturations successives peuvent légèrement varier, cependant la chronologie relative de mise en place des veines reste similaire (Figure 6). Dans le cas des porphyres à Cu – Mo, il y aura une présence possible de veines précoces à biotite (EM), puis des veines de type A à quartz granulaires accompagnés de chalcopyrite et bornite. Leurs structures sont marquées par le passage du domaine de déformation ductile à cassante avec des structures discontinues et ondulantes, puis des structures continues et linéaires. Elles seront ensuite recoupées par des veines de type B (pour Banded = rubanées, qui seront plus tard nommées B1) à quartz accompagné de molybdénite, chalcopyrite et pyrite. Elles se présenterons sous forme régulières continues. Cette succession sera ensuite recoupée par des veines de type D à pyrite et chalcopyrite (Sillitoe, 2010) (Figure 6). La formation d'un tel stockwork laissent des marqueurs du passage de fluides par la présence d'halos d'altération des encaissants qui peuvent se superposer, tel qu'explicité et décrit dans la littérature (Gustafson et Hunt, 1975 ; Hedenquist, 1995, 1998 ; Seedorf

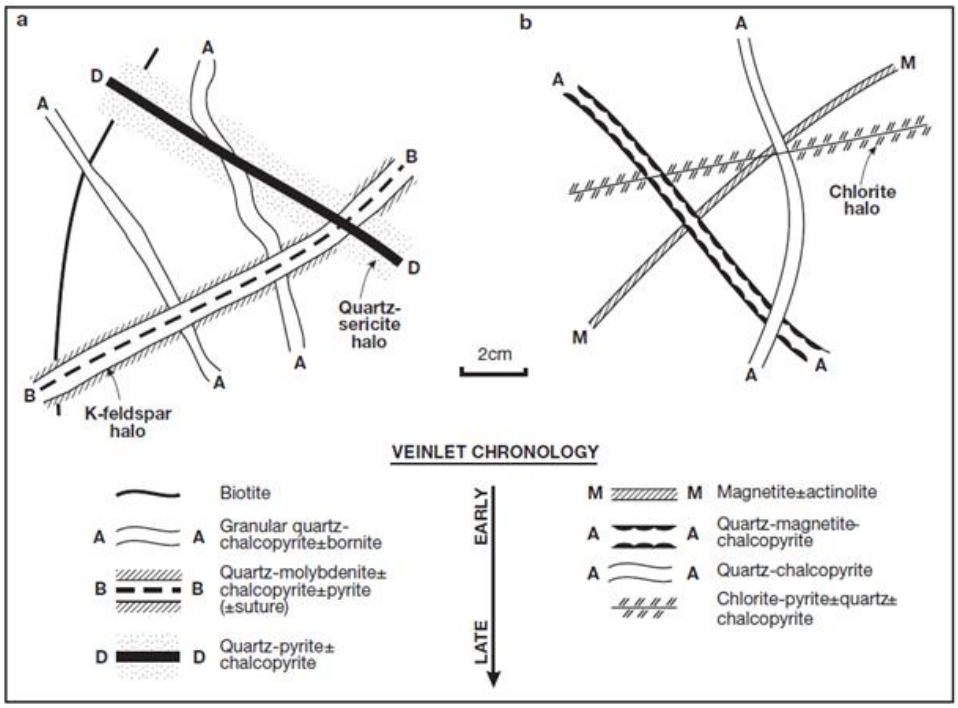

Figure 6 : Schéma chronologique des séquences de veines possible a) dans un gisement porphyre à Cu – Mo et b) dans un gisement à Cu – Au. La nomenclature des veines suit Gustafson et Hunt (1975, A, B et D) et Arancibia et Clark (1996) (d'après Sillitoe, 2010).

2005 ; Sillitoe, 2010 ; Richards, 2011, 2015 ; Halley et al., 2015 ; Voudouris et al., 2013a,b, 2019, 2022 ; Monecke et al. 2018 ; Mavrogonatos et al., 2019, 2020). D'autres veines ont été décrites comme rubanées (banded) principalement à quartz et Au (qui seront appelés B2 plus tard) qui sont associées à un phénomène de « flashing », soit une séparation de phases par décompression au sein de niveaux superficiels à des température basses à intermédiaire (Muntean et al., 2000, 2001 ; Monecke et al., 2018). Des veines nommées type C par leur contenu en chalcopyrite, pyrite, chlorite, séricite sont associées à une altération transitionnelle entre la partie de style porphyre et la partie de style épithermal (e.g. Monecke et al., 2018). Des veines dites de type E pour leur affiliation à un environnement de formation épithermal ont également été décrites et correspondent à la partie tardive d'un système de type porphyre-épithermal avec des minéralisations à galène, sphalérite, chalcopyrite, pyrite et quartz et carbonates en minéraux de gangue (e.g. Voudouris et al., 2013a, 2019).

1.2.5. Altérations des roches encaissantes

Une série d'altération des roches encaissantes favorisée par la circulation de fluides chauds (Figure 5) et chargés de métaux avec une variabilité de salinité et pH provoque une série de style d'altération évoluant depuis un domaine proximal à distal du « porphyre ».

Ainsi une altération sodi-calcique, dite précoce, se propage et est le produit de la circulation de fluide dans l'encaissant à haute température (550 à 700°C), de premiers dépôts peuvent se produire (Figure 5,

Figure 7). Une altération, dite potassique, est produite par échanges de cations (notamment le K) entre le fluide et la roche encaissante à des températures comprises entre 400 et 600 °C. Ainsi, les plagioclases s'altèrent en feldspaths potassiques (ex. orthose), par la réaction suivante : $NaAlSi_3O_8 + KCl_{fl} = KAlSi_3O_8 + NaCl_{fl}$. La hornblende est altérée en biotite (ou phlogopite) hydrothermale pouvant présenter une texture dite « shredded » et est accompagnée de quartz, magnétite, rutile et anhydrite.

Ces altérations sont accompagnées des premières précipitations de sulfures dans et autour des intrusions porphyriques (Sillitoe, 2010 ; Richards, 2021) et de la formation des premières veines de stockwork (veines type A, M, et B) (Figure 6). Les températures sont alors comprises entre 350 et 500 °C, soit des températures propices à la précipitation du Cu dans de tels systèmes superficiels supérieur à 4 km de profondeur (Redmond et al., 2004 ; Landtwing et al., 2005 ; Klemm et al., 2007 ; Cernuschi et al., 2018 ; Richards, 2021). L'assemblage minéralogique de l'encaissant est alors composé de biotite, magnétite, sulfures de cuivre, de fer et d'or (Sillitoe, 2010).

Durant l'altération potassique, les fluides externes (i.e. météoriques, eau de mer, eaux de bassin), provoquent une altération propylitique (Figure 7) par hydratation des roches à une température modérée (230 – 400 °C). Ce processus favorise le refroidissement de l'intrusion et du système de type porphyre à Cu par des mouvements convectifs des fluides plus froids au sein de roches poreuses adéquates (Sillitoe, 2010 ; Richards, 2021). Les plagioclases seront altérés en albite, la hornblende en biotite, épidote, chlorite, calcite, voire actinote et sont accompagnés de magnétite et de pyrite.

Des fluides plus froids (350 – 250 °C) acides, de faible salinité (5.0 wt%), passent par des fractures, des stockworks (veines de type D), des brèches, et engendrent une altération chlorite-séricite (Figure 7) (NB : dans la littérature : altération séricitique = altération phyllique) avec une gangue à quartz, tourmaline, pyroclaste et brèches séricitisées (Shinohara and Hedenquist, 1997 ; Hedenquist et al., 1998 ; Sillitoe, 2010). L'altération séricitique de l'encaissant se produit par un processus de neutralisation de l'acide par la formule suivante : $3KAlSi_3O_8 + 2H^+ = KAl_3Si_3O_{10}(OH)_2 + 6SiO_2 + 2K^+$, ou les feldspaths potassiques sont détruits par l'acide pour former de la séricite, la biotite est altérée en chlorite voire séricite également à des températures comprises entre 230 °C et 400 °C. Les brèches phréatiques minéralisées, plus perméables, sont généralement plus riches en métaux par rapport au reste du système de type porphyre à Cu (Sillitoe et Sawkins, 1971 ; Norton and Cathles, 1973 ; Burnham and Ohmoto, 1980 ; Burnham, 1985 ; Sillitoe, 1985 ; Carrigan et al., 1992 ; Maimon et al., 2012 ; Richards, 2021). Les niveaux les plus superficiels sont souvent caractérisés par une minéralisation de type épithermal entrainent la formation de sulfures massifs, composés de sulfosels (Sillitoe, 2010) souvent sous forme de veines tabulaires, surimprimant le « porphyre ». Dans les roches les plus superficielles la minéralisation sera le plus souvent disséminée (Sillitoe, 2010 ; Richards, 2021).

Dans les parties les plus superficielles, les gisements sont plus étendus et se surimpriment aux parties types porphyres, par la propagation d'une altération argillique avancée (Figure 7) avec des gisements à Au – Ag – Cu, qui sont souvent des zones dénudées (Sillitoe, 2010 ; Richards, 2021). Ces gisements sont dits épithermaux. L'altération argillique se produit par neutralisation de l'acide tout comme l'altération séricitique, par les réactions suivantes : $2KAlSi_3O_8(OH)_2 + 2H^+ = 3Al_2Si_2O_5(OH)4 + 2K^+$ et $2KAlSi_2O_5(OH)_4 + 2K^+ + 6H^+ + 4SO_4^{2-} = 2KAl(SO_4)(OH)_6 + 6SiO_2$ soit une altération de la séricite en alunite, accompagnée de quartz et pyrophyllite, jusqu'à l'altération de la kaolinite en alunite et quartz à des températures situées entre 180 °C et 270 °C. Cette altération intense forme des sommets topographiques. Lors du lessivage de la roche, seul le quartz est conservé sur place préservant le squelette des textures primaires de la roche encaissante, un massif de quartz avec de nombreux espace est alors formé, nommé vuggy silica (Figure 7), cette partie est alors appelée le lithocap.

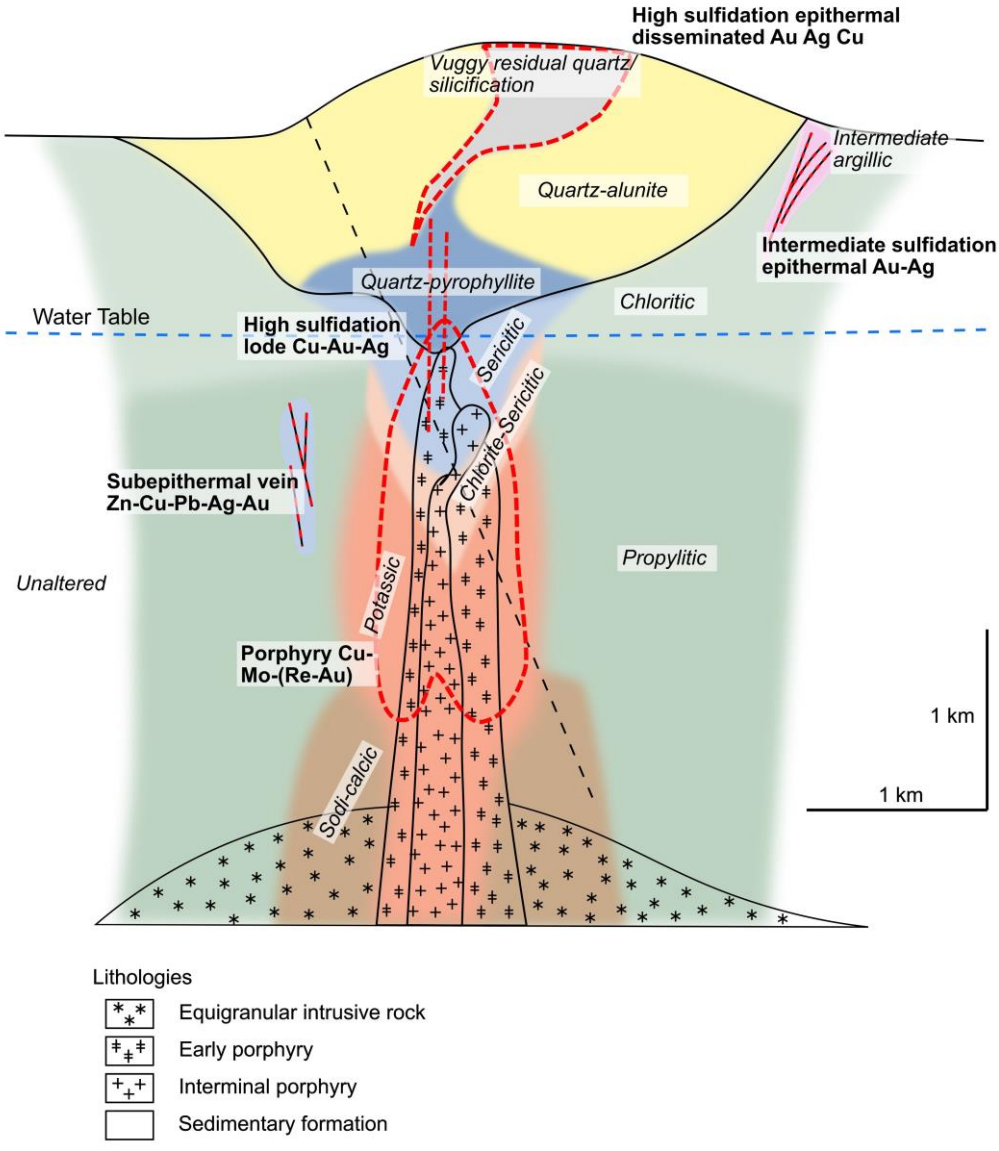

Figure 7 : Coupe schématique d'une structure porphyre et des différents styles de minéralisations et altérations associées, modifiée d'après Sillitoe (2010), Henley et al. (2015), Schaarschmidt, (2021).

1.2.6. Gisements épithermaux et télescopage

Les fluides acides peuvent atteindre la surface en interagissant avec les roches encaissantes lors de leur remontée : ils restent chauds (de 200 à 300 °C), riches en SO_2, CO_2 et HCl, salés (de 2.0 à 30 % NaCl), acides et oxydants. Ils engendrent la formation de gisements de type épithermal (profondeur <2 km) acides par réaction avec les fluides superficielles en convection (Figure 5) (Jebrak et Marcoux, 2008). Le mélange de fluides conduit à une acidification entraînant la formation d'un lithocap à alunite – kaolinite – quartz ± illite. (Jebrak et Marcoux, 2008). Dans ce cadre, trois grands types de minéralisations épithermales sont décrites, avec des cas intermédiaires, selon leur fugacité en soufre (Sillitoe et Hedenquist, 2003 ; Einaudi, 2003 ; Simmons, et al. 2005 ; Jébrak et Marcoux, 2008 ; Sillitoe, 2010, 2015 ; Hedenquist et al., 2000, 2017):

- les minéralisations disséminées épithermales de haute sulfuration (HS), à Au – Ag – Cu ± Bi ± Te sous la forme d'énargite, covellite, pyrite, bornite, digénite, tétraédrite, tennantite, avec un assemblage minéralogique de gangue à quartz + alunite ± pyrophyllite ± dickite ± kaolinite, associé à la circulation d'un fluide acide, oxydant, de salinité faible à modérée. Elles sont associées à une altération par silicification, vuggy quartz, à quartz-alunite (Figure 7). Elles apparaissent au sein d'un lithocap au-dessus du gisement de type porphyre au sein des 500 premiers mètres avec une moyenne de 1 – 3 ppm d'Au ;
- les minéralisations épithermales de sulfuration intermédiaire (SI ou IS = Intermediate Sulfidation), à l'Ag – Au – Pb – Zn ± Cu, sous la forme de tétraédrite, tennantite, chalcopyrite, sphalérite, galène et sulfosels d'Au – Ag avec un assemblage minéralogique de gangue à quartz ± calcite ± baryte ± rhodochrosite ± adulaire ± illite, associé au passage d'un fluide au pH neutre, de salinité faible à modérée. Elles se présentent majoritairement sous forme de veines en périphérie du lithocap ;
- les minéralisations épithermales de basse sulfuration (BS ou LS = Low Sulfidation) à Au ± Ag – Se – Mo, sous la forme de pyrite, pyrrhotite, arsénopyrite, sulfosels d'Au – Ag, et sphalérite, avec des minéraux de gangue de quartz ± calcédoine ± adulaire ± illite, associés à la circulation de fluides à pH neutre, réducteurs, et de très faible salinité. Elles se présentent sous la forme de veines, ou en dissémination dans la roche encaissante. L'altération associée se présente sous la forme d'une silicification, à quartz-adulaire-illite, ou de carbonatation.

Une succession de minéralisation/altération au sein d'un gisement porphyre à Cu est possible et montre alors une zonation spatiale depuis des régions non minéralisées, à des régions minéralisées à altération potassique à sodi-calcique précoce, à des régions minéralisées à altération chlorite-séricitique-séricitique à argillique avancée. La dernière région est constitutive du lithocap qui peut atteindre près de 1 km d'épaisseur s'il est peu affecté par l'érosion (Sillitoe, 2010) (Figure 7).

La formation de gisements distaux est possible par l'intermédiaire de systèmes de failles et de fractures qui permettent la formation de veine sub-épithermales à Zn – Pb – Cu – Ag ± Au (e.g., Mineral Park : Eidel et al., 1968 ; Los Bronces-Río Blanco : Sillitoe, 2010). Les métaux précieux et le soufre sont alors vraisemblablement issus du magma, tandis que les métaux de base dériveraient du lessivage des roches crustales (Camprubi et al., 2003, 2006).

Dans certains cas d'érosion ou de décapage rapide, le système de type porphyre remonte vers la surface durant sa formation, engendrant un télescopage des structures où les altérations et minéralisations épithermales superficielles se superposent au système minéralisé précoce de type porphyre (Figure 8) (Sillitoe, 1994, 2010 ; Houston and Dilles, 2013 ; Catchpole et al., 2015 ; Richards, 2021). Ainsi la distribution verticale des types de minéralisations/altérations des gisements de types porphyre-épithermaux dépendent du degré de télescopage (Sillitoe, 2010).

Dans le cas de systèmes hautement télescopés, l'altération argillique avancée du lithocap se superpose à la partie supérieure du porphyre minéralisé. Là où le télescopage reste limité, le lithocap est

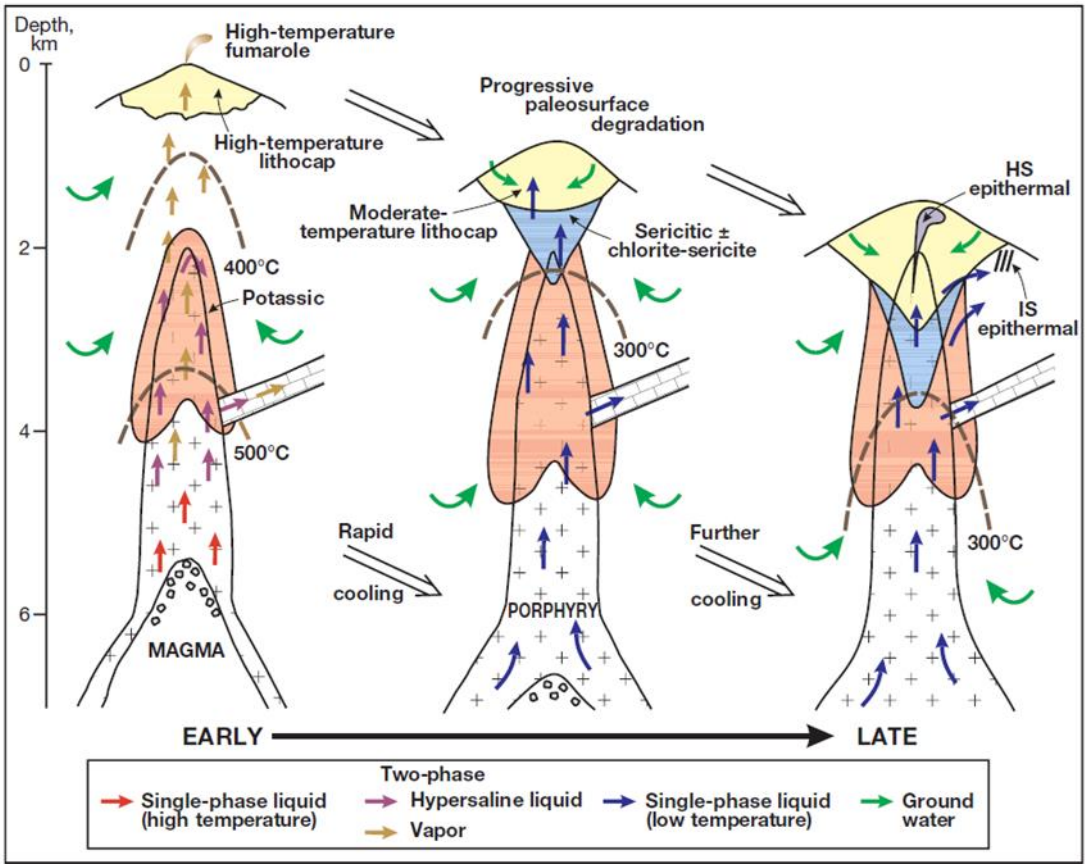

Figure 8: Schéma de l'évolution d'une structure d'un système de type porphyre-épithermal. De gauche à droite : (i) système de type porphyre se refroidissant et cristallisant avec ébullition de fluide et séparation de phase avec la formation de zone d'altération potassique et de formation du lithocaps ; (ii) érosion progressive de la paléosurface avec début de phénomène de télescopage, l'altération séricitique commence à se superposer à l'altération potassique et au porphyre magmatique, le lithocaps se rapproche de la zone d'altération potassique ; (iii) télescopage des structures d'altération avec mise en place de gisements épithermaux de haute sulfuration et de sulfuration intermédiaire, le lithocaps est superposé au porphyre magmatique et à l'altération potassique, la zone d'altération séricitique fait office de zone de transition. Les fluides magmatiques/hydrothermaux circulent et se mélangent (flèches bleues – mauves et jaunes) aux fluides de surfaces (flèches vertes), d'après Sillitoe, 2010.

séparé du porphyre ayant subi l'altération potassique, par un espace vertical (0,5 – 1 km) typiquement assujettie à de l'altération chloritique à séricitique (Sillitoe, 2010) (Figure 8).

1.2.7. Brèches

Quand le batholithe refroidit, un fluide hydrothermal riche en éléments volatils est exhalé. Ce fluide de basse salinité remonte vers la surface (Figure 5), puis passe de conditions de pression lithostatique à hydrostatique à une même profondeur, et subit une diminution brutale de la pression, passe sous le solvus, entre en ébullition et se scinde en deux phases : une petite phase aqueuse de type saumure et une grosse phase vapeur peu saline. Ces changements importants et brèves de contraintes seraient propices à la génération de gisements de porphyre à Cu. La remontée des fluides magmatiques-hydrothermaux entraîne une augmentation de la pression fluide, lors de la formation de l'arc, et de celle du batholithe. Cela provoque un uplift et engendre une érosion rapide de la région précurseur d'un relâchement des contraintes tectoniques (Richards, 2021).

La présence de cônes phréatomagmatiques (= diatrèmes) est répandu dans les systèmes de type porphyre à Cu. Ces cônes peuvent faire près d'un kilomètre de large en surface et au moins 2 km de profondeur. Ils sont formés de brèches avec clastes de type andésitique à dioritique. La structure est alors peu indurée, friable et une argilisation intense engendre la formation d'une dépression topographique (Jebrak et Marcoux, 2008). De telles brèches se forment par un relâchement soudain de pression (lithostatique) ou lorsque la pression de fluide devient supérieure à la pression lithostatique (Hedenquist et al., 1998 ; Sillitoe, 2010 ; Richards, 2021). Les brèches magmatiques-hydrothermales sont également communes en profondeur. Elles se différencient des brèches de diatrème par l'absence de tuf, ou par la présence d'une matrice à ciment hydrothermal, ou à grain fin magmatique, ou combinaison des trois (Sillitoe, 2010 ; Richards, 2021).

1.2.8. Contexte géologique de la Grèce et ses gisements

1.2.8.1. Contexte géodynamique

Les Hellénides, partie de l'orogène alpin-himalayen, se sont formées par la collision des plaques africaine et eurasienne. Elles représentent le lien géotectonique entre la partie Sud de la péninsule balkanique (e.g. les Dinarides/Albanides) et la Turquie (e.g. les Pontides, Anatolides). La convergence des deux plaques entraine l'empilement de nappes des blocs Pélagonia, Adria et Rhodopes, associée à la fermeture des océans Vardar, Pindos et de la Néotethys (Schmid et al., 2008 ; Jolivet and Brun, 2010 ; Ring et al., 2010 ; Kydonakis et al., 2015a,b). Les nappes comprennent de nombreux terrains géotectoniques hérités des évènements géodynamiques de la région - avec la présence des océans Paléotethys et Néotethys -, incluant la subduction, la collision, la post-collision et le magmatisme de post-collision, de subduction et de post-subduction (Pe-Piper et Piper, 2002) (Figure 9).

La Grèce est marquée par une ouverture puis une fermeture d'océans et par la formation de croûte continentale du Précambrien tardif au Jurassique supérieur au-dessus des zones de subduction (Anders

et al., 2006 ; Himmerkus et al., 2006 ; Reischmann et Kostopoulos, 2007). Un épisode magmatique permo-carbonifère associé à la subduction à vergence Nord de la Paléotethys sous la marge Sud de l'Europe, a été mis en évidence dans les régions de la Pélagonia, du Rhodope et de l'Attico-Cycladique (Figure 9). Cet événement reflète l'évolution d'une marge continentale active dans le socle précambrien-silurien (Anders et al., 2006; Reischmann and Kostopoulos, 2007). Du Trias supérieur au Jurassique inférieur, les continents Rhodopes et Pélagonia se scindent lors de l'ouverture de l'océan Vardar (Robertson et al., 2013). Au Jurassique supérieur une subduction à vergence Nord-Est créé un arc magmatique le long de la marge Sud du continent Rhodope. Cette convergence engendre un chevauchement de des blocs continentaux des Rhodopes, de Pélagonia et d'Adria (Robertson, 2002 ; Schmid et al., 2008 ; Jolivet et Brun, 2010 ; Ring et al., 2010 ; Kydonakis et al., 2015a,b). A la fin du Crétacé, la collision entre l'Europe et la Pélagonia entraîne la fermeture de l'océan Néotethys le long de la zone de suture de l'océan Vardar (Robertson et al., 2013). Entre 60-55 Ma, l'accrétion du bloc Pélagonia à la marge Européenne est suivie par la subduction de l'océan Pindos, puis par sa fermeture vers 35 Ma avec l'accrétion du microcontinent Adria à Pélagonia (Brun et Faccenna, 2008 ; Ring et al., 2010 ; Jolivet et al., 2013 ; Menant et al., 2016) (Figure 9).

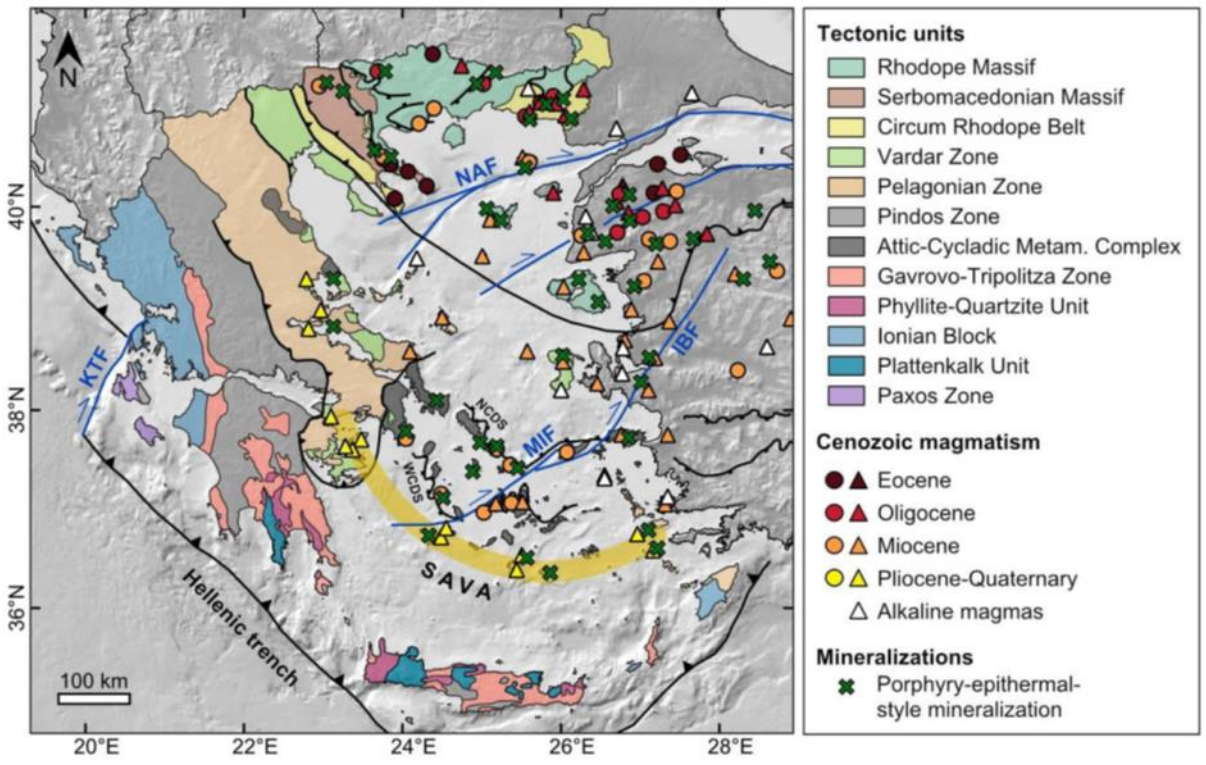

Figure 9 : Carte structurale de la Grèce montrant l'empilement des nappes accrétées à la marge Européenne Sud depuis le Crétacé. Les plutons magmatiques cénozoïques (cercles), le volcanisme (triangles), et les minéralisations type porphyre-épithermal associées sont représentées sur cette carte (Rabayrol & Hart, 2021; Voudouris et al., 2019). SAVA = South Aegean Volcanic Arc, KTF = Kephalonia Transform Fault, NAF = North Anatolian Fault, MIF = Myrthes-Ikaria Fault, IBF = Izmir-Balikeshir Fault, N/WCDS = North/West Cycladic Detachment System. (d'après Schaarschmidt, 2021 ; Voudouris et al., 2018).

Au Nord, le massif de Rhodopes est bordé par la zone de cisaillement de Maritza le séparant du massif de Srednogorie en Bulgarie ; au Sud ce dernier est limité par la zone de Suture Vardar (Figure 9). Dans le domaine du Rhodope Nord, une exhumation précoce, liée au processus orogénique, débute à l'Éocène (~55 Ma) et s'est prolongée jusqu'à ~42 Ma (Éocène moyen). Ce phénomène coïncide avec l'accrétion de la Pélagonie, survenue après la fermeture de l'océan Vardar (Wüthrich, 2009 ; Menant et al., 2016). Deux phases de déformations majeures se distinguent dans ce massif cristallin au Paléogène-Néogène (Bonev et al., 2006a,b) : (i) un stade compressif, contemporain de la subduction de l'océan Pindos, suivi par l'accrétion du bloc continental de Pélagonia à la marge européenne. Entre 42-35 Ma une rupture profonde du slab (océan Vardar) déclenche une remontée asthénosphérique qui est suivie d'une exhumation et d'un premier épisode de formation de MCC (Metamorphic Core Complex) dans les Rhodopes (Marchev et al., 2013). Ainsi, les dômes migmatitiques d'Arda, de Biala Reka-Kechros et de Kesebir-Kardamos sont progressivement exhumés le long de plusieurs zones de cisaillement ductile/cassante active de 40-35 Ma ; (ii) un stade extensif marqué par un retrait du slab vers le Sud, qui provoque l'effondrement du prisme d'accrétion orogénique et engendre l'ouverture de bassin d'arc à la suite de fermeture de l'océan Pindos vers 35 Ma (Bonev et al., 2006a,b, 2010, 2013 ; Wüthrich, 2009 ; Márton et al., 2010 ; Moritz et al., 2010 ; Kaiser-Rohrmeier et al., 2013).

Cette extension en contexte d'arc est alors rendue possible par l'exhumation post-orogénique de parties profondes de la croûte amincie que sont les MCC. Le retrait du slab entraîne également la migration progressive de l'activité magmatique du Nord vers le Sud, depuis la ceinture magmatique du Timok-Banat-Srednogorie au Crétacé, au Massif des Rhodopes au Tertiaire, à l'Arc Volcanique Sud-égéen (Fytikas et al., 1984 ; Pe- Piper and Piper, 2002, 2006 ; Jolivet et Brun 2010 ; Jolivet et al., 2013, 2015).

Dans les régions centrale et orientale du Rhodope, en Bulgarie et en Grèce (e.g. MCC du Domaine Nord Rhodope), les MCC de Biala Reka-Kechros et Kesebir-Kardamos sont progressivement exhumés le long de zones de cisaillement ductiles à fragiles, entre ~42 et 35 Ma (Bonev et al., 2006a, b, 2010, 2013 ; Wüthrich, 2009 ; Márton et al., 2010 ; Moritz et al., 2010 ; Kaiser-Rohrmeier et al., 2013).

Dans le Core Complexe Sud Rhodope (CCSR), le refroidissement et l'exhumation des roches métamorphiques se produisent le long de deux failles de détachement majeures (Brun et Sokoutis, 2007 ; Wüthrich, 2009 ; Kounov et al., 2015) : (i) le détachement ductile de Kerdylion, actif entre ~42 et 24 Ma, lié à l'exhumation du CCSR ; et (ii) le détachement ductile à fragile de Strymon, actif entre ~24 et 12 Ma (Brun et Sokoutis, 2007 ; Kydonakis et al., 2015a,b ; Brun et al., 2016 ; Jolivet et al. 2016).

1.2.8.2. Magmatisme

La subduction type andin de l'océan Sava-Vardar-Izmir-Ankara est associée au magmatisme d'arc du Crétacé supérieur (~92 – 67 Ma) dans les ceintures magmatiques Apuseni-Banat-Timok-Srednogorie-Pontides (von Quadt et al., 2005 ; Gallhofer et al., 2015) avec le développement d'un

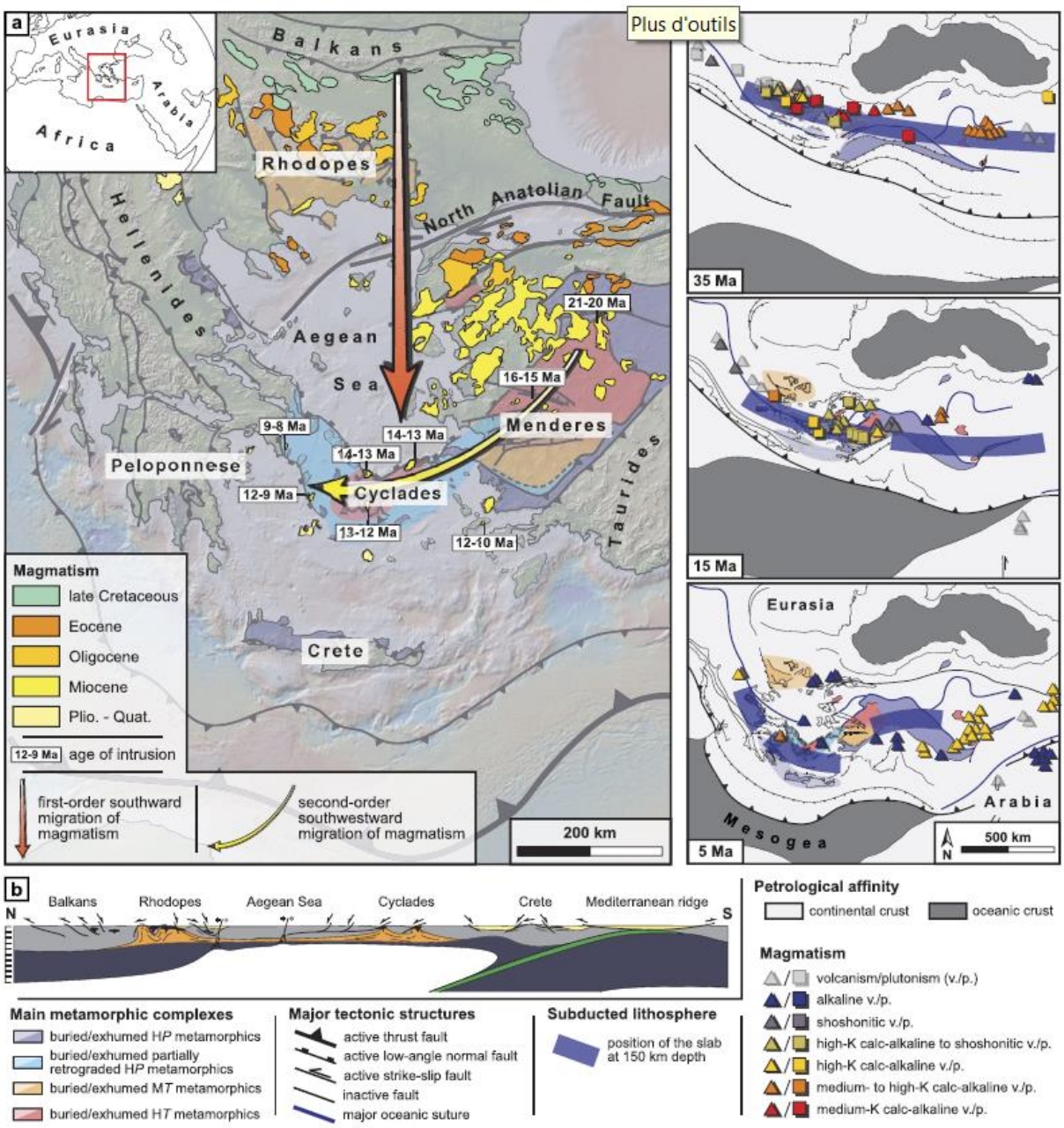

Figure 10 : Evolution géodynamique de l'Est de la méditerranée au Cénozoïque supérieur a) schéma structural dynamique de la migration du magmatisme du Crétacé supérieur au Miocène ; b) coupe structurale N-S de la région égéenne et du Rhodope et cartes paléostructurales représentant les différents types de magmatisme, d'après Menant et al. (2016).

magmatisme adakitique post-collisionnel au Paléocène-Éocène (56,0–40,4 Ma) dans les régions du Rhodope, Kraishte et Ouest-Srednogorie. Ce magmatisme résulterait d'une rupture profonde de la plaque de l'océan Vardar, suivie d'une remontée asthénosphérique, d'un réchauffement, d'une exhumation rapide entre 42 et 35 Ma, et de la première phase de formation de MCC dans les Rhodopes et le Kraishte (Marchev et al., 2013). Cette phase a été suivie par un effondrement orogénique, des déformations et un magmatisme de l'Éocène tardif au Miocène (Marchev et al., 2013).

De l'Oligocène au Quaternaire, l'effondrement orogénique des Hellénides et l'amincissement lithosphérique en mer Égée est favorisé par une accélération du retrait du slab vers le Sud (Jolivet et Brun, 2010). La remontée asthénosphérique, due à une extension à grande échelle, entraîne une perturbation thermique dans la croûte et le manteau sous-jacent, et mène à la formation de roches magmatiques plutoniques (Marchev et al., 2005). Un mécanisme de délamination lithosphérique, accompagné d'une remontée du manteau et combiné à un détachement de plaque, aurait causé une remontée de l'asthénosphère et entrainé une fusion des métabasaltes en sous-plaquage de la croûte continentale subduite (Christofides et al., 1998 ; Marchev et al., 2005 ; Pe-Piper et Piper, 2006 ; Pe-Piper et al., 2009).

Les roches magmatiques de l'Éocène supérieur à l'Oligocène présentent des affinités calco-alcalines, shoshonitiques à ultrapotassiques, avec des compositions allant de basiques à acides (Innocenti et al., 1984 ; Christofides et al., 1998 ; Pe-Piper et Piper, 2002 ; Perugini et al., 2004 ; Marchev et al., 2004, 2005, 2013 ; Dilek et Altunkaynak, 2007 ; Ersoy et Palmer, 2013) (Figure 10). Le magmatisme a évolué depuis des trachybasaltes riches en potassium (~34 Ma) vers des shoshonites, des basaltes calco-alcalins (~33–31 Ma), puis des basaltes alcalins (~28–26 Ma), avec une activité volcanique s'étendant entre ~33,4 et 19,1 Ma (Christofides et al., 2004 ; Pecskay et al., 2006) (Figure 10). Une contribution d'une source mantellique métasomatisée par des processus de subduction antérieurs, ainsi que de sources crustales, a été proposée pour ces magmas (Altherr et Siebel, 2002 ; Stouraiti et al., 2010 ; Ersoy et Palmer, 2013). Cette évolution montre une réduction de l'influence de la contamination crustale au fil du temps et une augmentation de la contribution mantellique, culminant avec des éruptions de magmas purement asthénosphériques (Voudouris et al., 2019 ; Schaarschmidt, 2021).

Le retrait du slab a entraîné une migration progressive du Nord vers le Sud de l'activité magmatique, passant des ceintures magmatiques du Crétacé (Timok-Banat-Srednogorie) dans le Massif du Rhodope (~35–30 Ma) jusqu'à l'arc volcanique de la mer Égée, correspondant à la position de la zone de subduction actuelle (Fytikas et al., 1984 ; Pe-Piper et Piper, 2002, 2006 ; Jolivet et Brun, 2010 ; Jolivet et al., 2013) (Figure 10). Une signature d'arc pour les roches ignées oligocènes a été identifiée dans la région de Thrace occidentale, marquée par un enrichissement en K, LILE et HFSE dans la source mantellique, avec des composants dérivés de la plaque (tels que les produits de fusion des sédiments) (Schaarschmidt et al., 2021a, b).

1.2.8.3. Le bassin de Thrace occidentale

Le bassin de Thrace est considéré comme l'un des plus grands bassins tertiaires de la région Nord de la Grèce et s'étend du Sud-Est de la Bulgarie, au Nord-Est de la Grèce et jusqu'au Nord-Ouest de la Turquie. Il est bordé au Sud par la zone de Sakarya (Turquie) et la mer Égée, au Nord et à l'Ouest par les massifs des Rhodopes et de Sakar-Strandzha, à l'Est par la mer Noire (Figure 11). Il s'est formé au cours de l'exhumation-extension et de la segmentation du Massif des Rhodopes. Cette formation est attribuée soit à la création de petits grabens, soit à un contexte supra-détachement lors de la migration

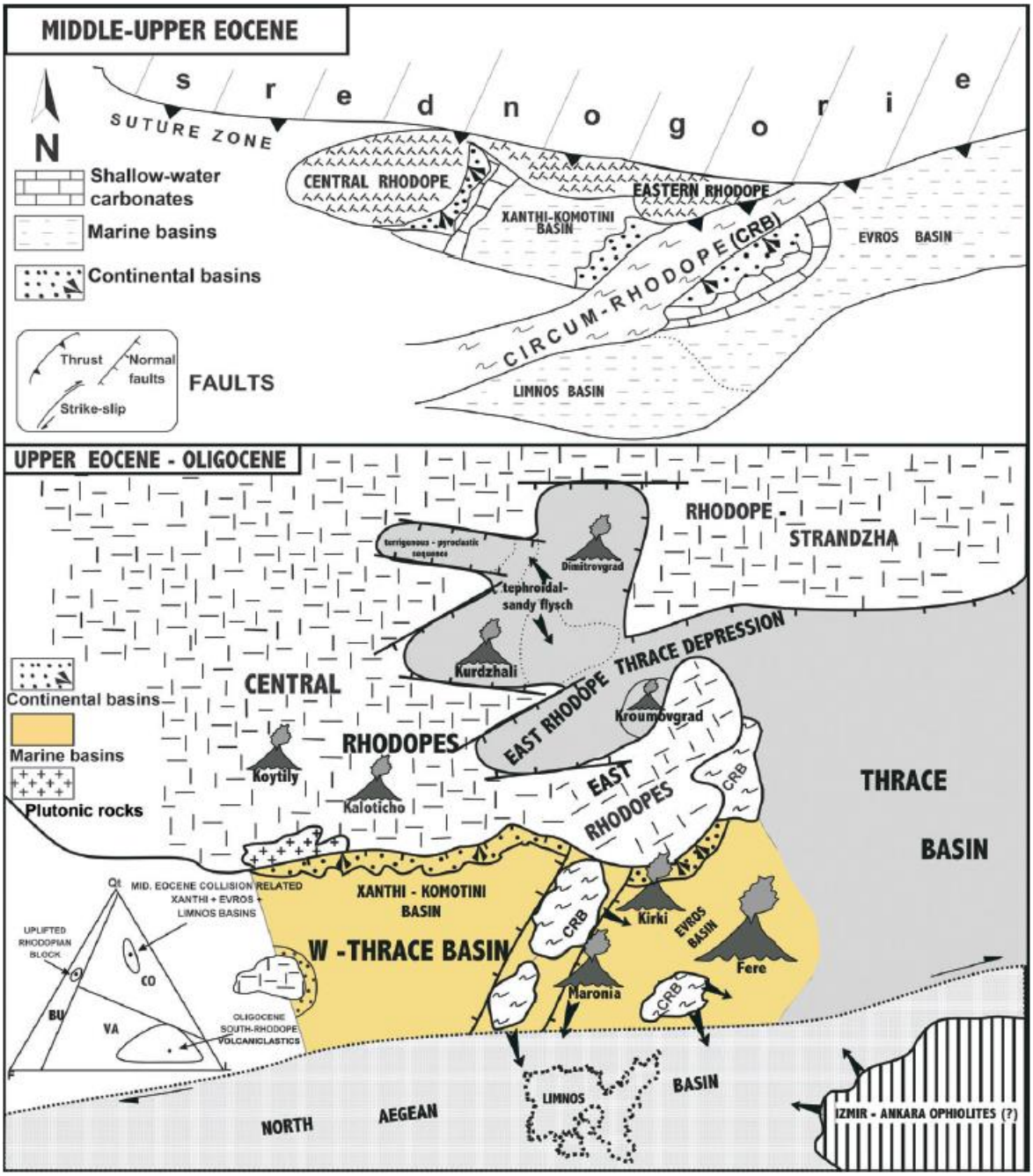

Figure 11 : Cartes paléogéographiques schématiques du Bassin de l'Ouest-Thrace et de la Région Rhodope durant la période Eocène moyen-Oligocène. Les volcans sont nommés d'après leur localité respective (de Caracciolo et al. 2011).

tertiaire vers le Sud-Sud-Ouest du Massif des Rhodopes, après la fermeture des domaines océaniques de Vardar et Pindos (Burg, 2012 ; Kilias et al., 2013). Une connexion marine entre la mer Noire et le bassin de Thrace, au cours de l'Éocène supérieur à l'Oligocène inférieur (38–31 Ma) existait par le passage de Çatalca, situé à l'Ouest d'Istanbul. Des corridors marins associés à la zone de faille de la mer Noire occidentale, ont permis des échanges marins entre la mer Noire et le bassin de Thrace durant cette période. Par cette connexion, les deux bassins étaient considérés comme faisant partie de la Paratéthys à l'Oligocène inférieur. Cependant, des séquences marines complètes, riches en foraminifères, se sont

déposées dans les deux bassins au début de l'Oligocène moyen. Cette connexion marine a finalement été interrompue au début de l'Oligocène moyen en raison d'un chevauchement le long de la marge de la mer Noire. La fermeture de ce passage a conduit à l'établissement de conditions paraliques dans le bassin de Thrace (Okay et al., 2017). Ce bassin s'est développé en discordance sur les roches métamorphiques du Massif des Rhodopes, au Nord de la Grèce (Kopp, 1965 ; Lescuyer et al., 2003 ; Tranos, 2009), ainsi que sur les massifs de Strandja et de Sakarya, au Nord-Ouest de la Turquie (Turgut et al., 1991 ; Turgut et Eseller, 2000 ; Siyako et Huvaz, 2007 ; Okay et al., 2010). Il est principalement composé de sédiments datés de l'Éocène inférieur-moyen à l'Oligocène supérieur, atteignant une épaisseur maximale de 9 000 mètres en Turquie et comprenant des successions jusqu'au Quaternaire (e.g., Turgut et Eseller, 2000 ; d'Atri et al., 2012). Le bassin est subdivisé en secteurs oriental (Thrace turque) et occidental (Thrace grecque).

Le bassin de la Thrace occidentale, comprend trois principaux sous-bassins : les bassins de Xanthi-Komotiní, d'Évros, et de Límnos dans la mer Égée septentrionale (Figure 11). Durant le Lutétien, la sédimentation dans les bassins de Xanthi-Komotiní et d'Évros a commencé par des dépôts alluviaux grossiers progrades vers l'Est, associés à des sédiments fluviaux-deltaïques distaux et des dépôts deltaïques (Caracciolo et al., 2012). Ils seraient associés au développement d'un bassin d'avant-arc dans cette région (e.g. Caracciolo et al., 2011, 2012 ; Maravellis et al., 2016) (Figure 12).

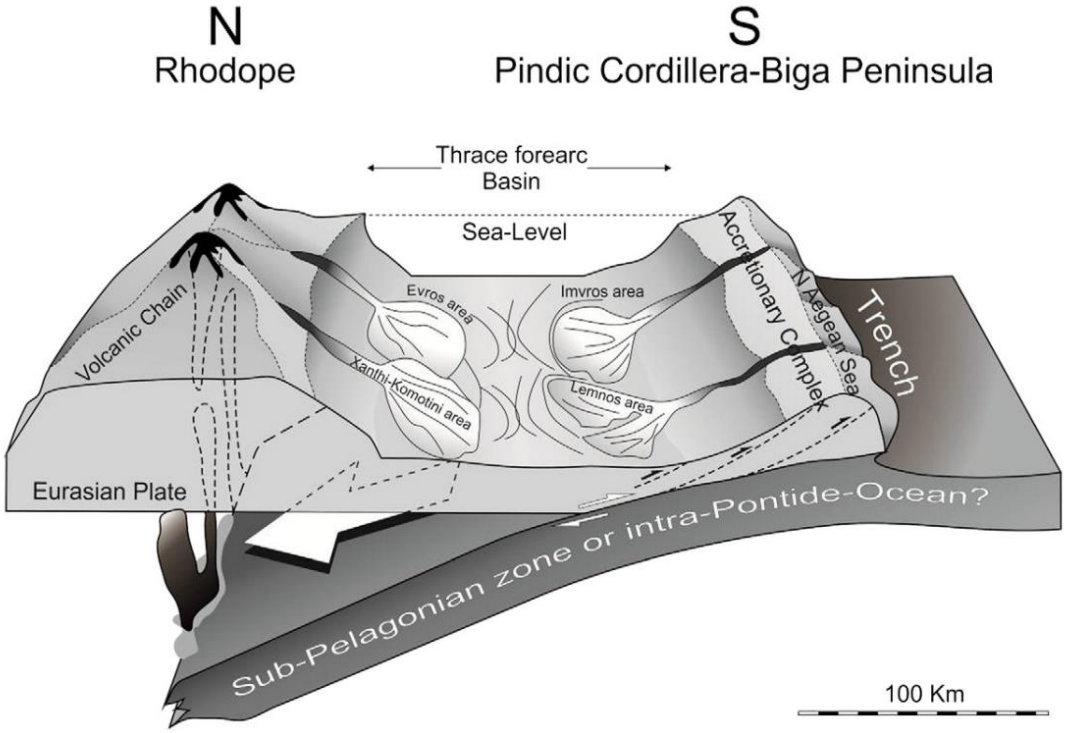

Figure 12 : Bloc diagramme schématique présentant l'environnement de dépôts du bassin de Thrace de l'Eocène supérieur à l'Oligocène (de Maravellis et al., 2016).

A. Le bassin de Xanthi-Komotiní

Le bassin de Xanthi-Komotiní est délimité par des failles normales et présente une structure de graben. Un approfondissement régional vers le Sud-Est est observé en lien avec la faille de Kavala-Xanthi-Komotiní (Tsokas et al., 1996). La succession sédimentaire repose directement sur le socle métamorphique du Massif des Rhodopes et s'étend de l'Éocène moyen (Lutétien) au Néogène. Les assemblages fossiles dans les niveaux argileux situés entre les dépôts continentaux et les carbonates marins peu profonds, comprenant des nummulites, miliolides, orbitolites et foraminifères, indiquent un âge lutétien pour le récif carbonaté. Cependant, des données sur les foraminifères benthiques des calcaires coralliens au Sud du bassin, suggèrent que la sédimentation récifale carbonatée s'est prolongée jusqu'à l'Éocène supérieur, voire l'Oligocène (Caracciolo et al., 2012, 2015).

B. Le bassin d'Évros

Le bassin d'Évros, le plus oriental des bassins de Thrace grecque, dépasse les 3 000 mètres d'épaisseur et inclut les plus anciennes unités sédimentaires des Rhodopes méridionales, réparties dans les sous-bassins de Maronia, Kirki-Esimi et Fères-Soufli-Pétrota (ce dernier ne sera pas présenté, puisque hors de la zone d'étude). Le bassin d'Évros s'est développé sur les unités métamorphiques (Makri et Drimon-Malia) du CRB (Circum Rhodope Belt) et présente des dépôts silicoclastiques grossiers intercalés avec des grès charbonneux et des calcaires nummulitiques marins peu profonds (Caracciolo, 2009). Les grès et conglomérats alluviaux lutétiens sont recouverts de dépôts fluvio-deltaïques et côtiers. Des niveaux volcaniques et volcanoclastiques, comprenant des coulées de lave, des coulées pyroclastiques et des lahars, caractérisent la section de Maronia (Innocenti et al., 1984). Entre l'Éocène supérieur et l'Oligocène inférieur, des taux de subsidence accrus ont favorisé une évolution vers des dépôts en eaux profondes accompagnée par une activité volcanique (Innocenti et al., 1984).

Une phase transgressive dans les bassins de Xanthi-Komotini et d'Évros, marquée par des carbonates peu profonds riches en nummulites et en coraux-algues, indique une subsidence rapide et une transition des tectoniques collisionnelle à extensionnelle, conduisant à un approfondissement général du bassin et au dépôt de turbidites d'eaux profondes (Caracciolo et al., 2015 ; Maravellis et al., 2012).

Bassin de Kirki-Esimi

Le bassin de Kirki-Esimi a connu une subsidence rapide durant l'Éocène supérieur à l'Oligocène, après des dépôts alluvio-fluviaux lutétiens. Sa succession sédimentaire, épaisse de 2 000 mètres, passe de marnes, argilites et turbidites peu profondes à des turbidites d'eaux profondes. Des dômes volcaniques et des conglomérats (Innocenti et al., 1984) sont intercalés avec les dépôts oligocènes d'eaux profondes (Caracciolo et al., 2011a ; Maravelis et Zelilis, 2012) (Figure 13). La base de la section de Kirki-Esimi est interprétée comme un système de cônes alluviaux fluviaux, présentant un enchaînement grossier-fin vers le haut, traduisant une transition proximale-distale. La partie supérieure, marquée par des siltites sombres intercalées avec des niveaux charbonneux, indique une influence

marine. Les carbonates stratifiés, comprenant des calcaires coralliens et algaux, sont interprétés comme des récifs corallo-algaires et sont surmontés de marnes et de turbidites profondes (Caracciolo et al., 2011a ; Maravelis et Zelilis, 2012) (Figure 13).

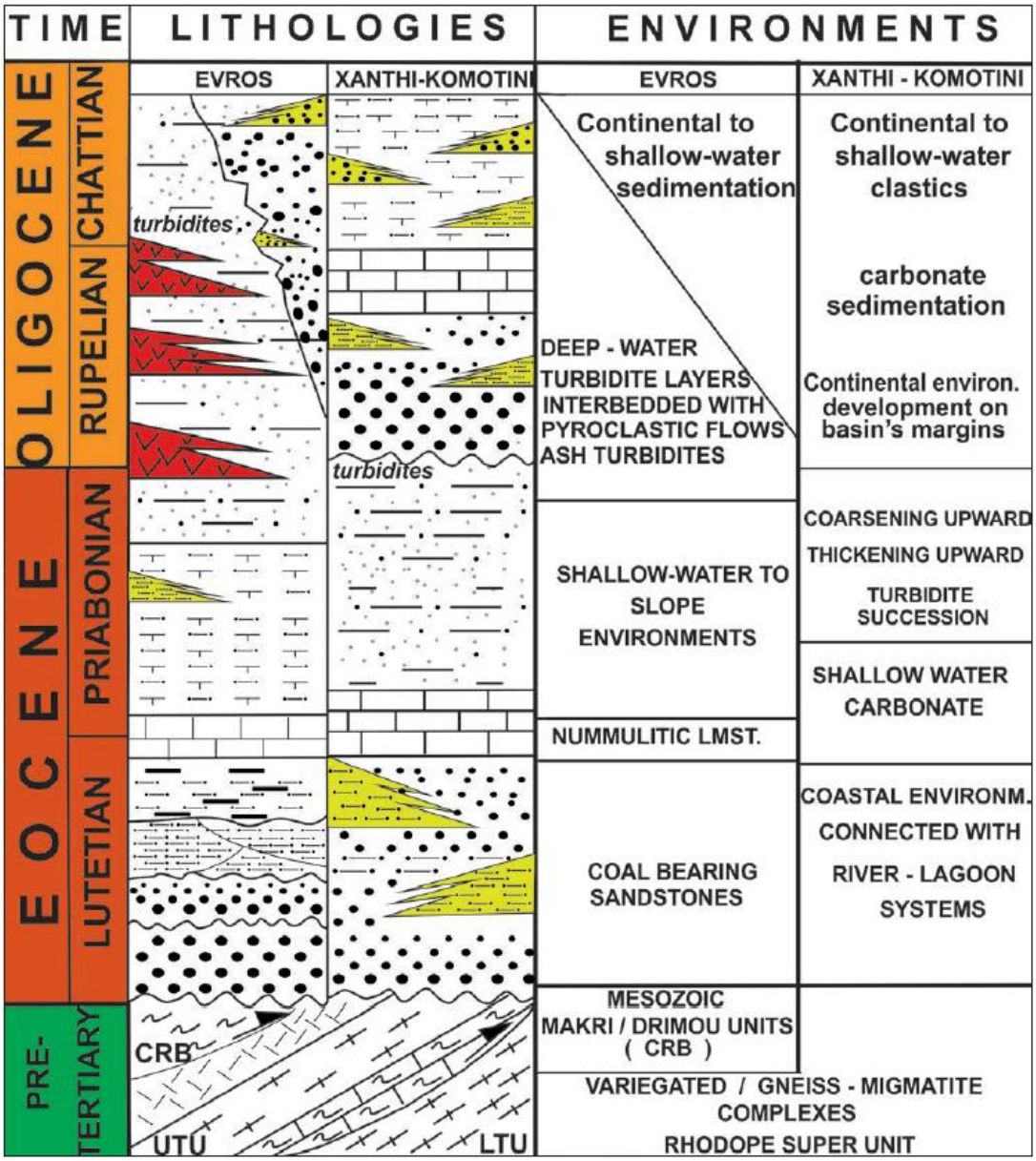

Figure 13 : Colonnes stratigraphiques des bassins de Xanthi-Komotini et d'Evros. La colonne présente les tendances d'approfondissement généraux, avec une évolution d'environnement de dépôt sédimentaire depuis des conditions en domaine continental, puis marin peu profond à marin profond (de Caracciolo et al., 2015).

Bassin de Maronia

La section de Maronia contient des grès et conglomérats alluviaux lutétiens recouverts de dépôts fluviaux et deltaïques, ainsi que des niveaux volcaniques rupéliens comprenant des coulées de laves et pyroclastes intercalées avec des conglomérats. Les niveaux supérieurs incluent des ignimbrites et des coulées de lave (Innocenti et al., 1984 ; Maravelis et Zelilis, 2012).

C. Le bassin Nord-égéen (île de Límnos)

La succession sédimentaire (Lutétien-Priabonien au Miocène inférieur) exposée à Límnos est intrudée par des corps volcaniques de 21 à 18 Ma (Innocenti et al., 1994). La succession (Éocène moyen-supérieur à Oligocène moyen) comprend des turbidites marines profondes, avec des slumps, des olistolithes calcaires nummulitiques et des niveaux de tufs, accompagnés de conglomérats et marnes (Caracciolo et al., 2012). Les assemblages de nanofossiles calcaires reflètent une baisse progressive de température, de salinité, d'oxygénation et de nutriments au passage Éocène-Oligocène. Les nanoflores de l'Éocène supérieur témoignent d'eaux de surface chaudes et bien oxygénées (Maravelis et Zelilis, 2012).

1.2.8.4. Ressources

Dans ce cadre géodynamique, de larges gisements de minerais d'importance économique se sont formés durant le Tertiaire, en relation avec du magmatisme, la formation de bassins sédimentaires et l'évolution de systèmes magmatique-hydrothermaux extensifs (Melfos et al., 2002 ; Voudouris et Alfieris, 2005 ; Bonsall et al., 2011 ; Melfos et Voudouris, 2012 ; Voudouris et al., 2013a, 2019, 2022).

La Grèce est traditionnellement un pays minier avec de nombreux gisements de minéraux à métaux de base (Pb, Zn, Cr, Ni, Mn, Al, Fe, Cu), précieux (Au, Ag, PGE), rares (Mo, Re, Bi, Te, Ti) et critiques (Mg, Sb, W, Co, Ga, Ge, In, ETR) (Melfos et Voudouris, 2012, 2019, 2022). L'activité magmatique tertiaire dans le Nord-Est de la Grèce (Figure 14) a conduit à la formation de divers types de gisements, notamment des skarns, des remplacements de carbonates, des veines polymétalliques, des sulfures disséminés, des veines épithermales et des systèmes porphyres. Des systèmes de minéralisation tels que les porphyres à Cu – Mo et les systèmes épithermaux à Au – Ag se trouvent dans des localités comme St. Barbara–Kassiteres, St. Demetrios, Viper-Sapes, Pagoni Rachi, Sant Philippos-Kirki, Ktismata-Maronia et Perama Hill. Ces systèmes, ainsi que de nombreuses veines riches en métaux de base, sont génétiquement liés à des intrusions magmatiques telles que des microdiorites, microgranites, andésites et dacites porphyriques (Arikas et Voudouris, 1998 ; Melfos et al., 2002, 2003 ; Voudouris et al., 2006). L'orientation et la distribution des roches magmatiques ainsi que les minéralisations hydrothermales associées sont contrôlées par des structures tectoniques, notamment des failles avec des veines orientées NW-SE, NE-SW et NNW-SSE. Ces fractures se sont développées simultanément avec des failles décrochantes sénestres alignées selon un axe NNW-SSE (Nesbitt et al., 1988). Une minéralisation en tellures a été identifiée dans plusieurs gisements et prospects, notamment à St. Barbara, St. Demetrios, Pagoni Rachi, Pefka, Perama Hill et Viper (Voudouris et al., 2019, 2022).

Les bassins tertiaires et l'environnement magmatique dans le massif de Rhodope sont associés à des gisements qui prennent la forme de gisements de type skarns, veines polymétalliques, porphyres-épithermaux qui sont occasionnellement riche en Au et métaux critiques (Mo et Re) (Melfos et al., 2002, 2018 ; Voudouris, 2006 ; Voudouris et al., 2009, 2011, 2013b, 2018, 2019, 2022), constituant une part

de la province métallogénique du massif du Rhodope au sein de la Ceinture Métallogénique Téthysienne. Cette région est cruciale pour de futures explorations et exploitations de métaux précieux, rares et critiques, en Grèce (Melfos et al., 2017 ; Voudouris et al., 2022) et en Europe.

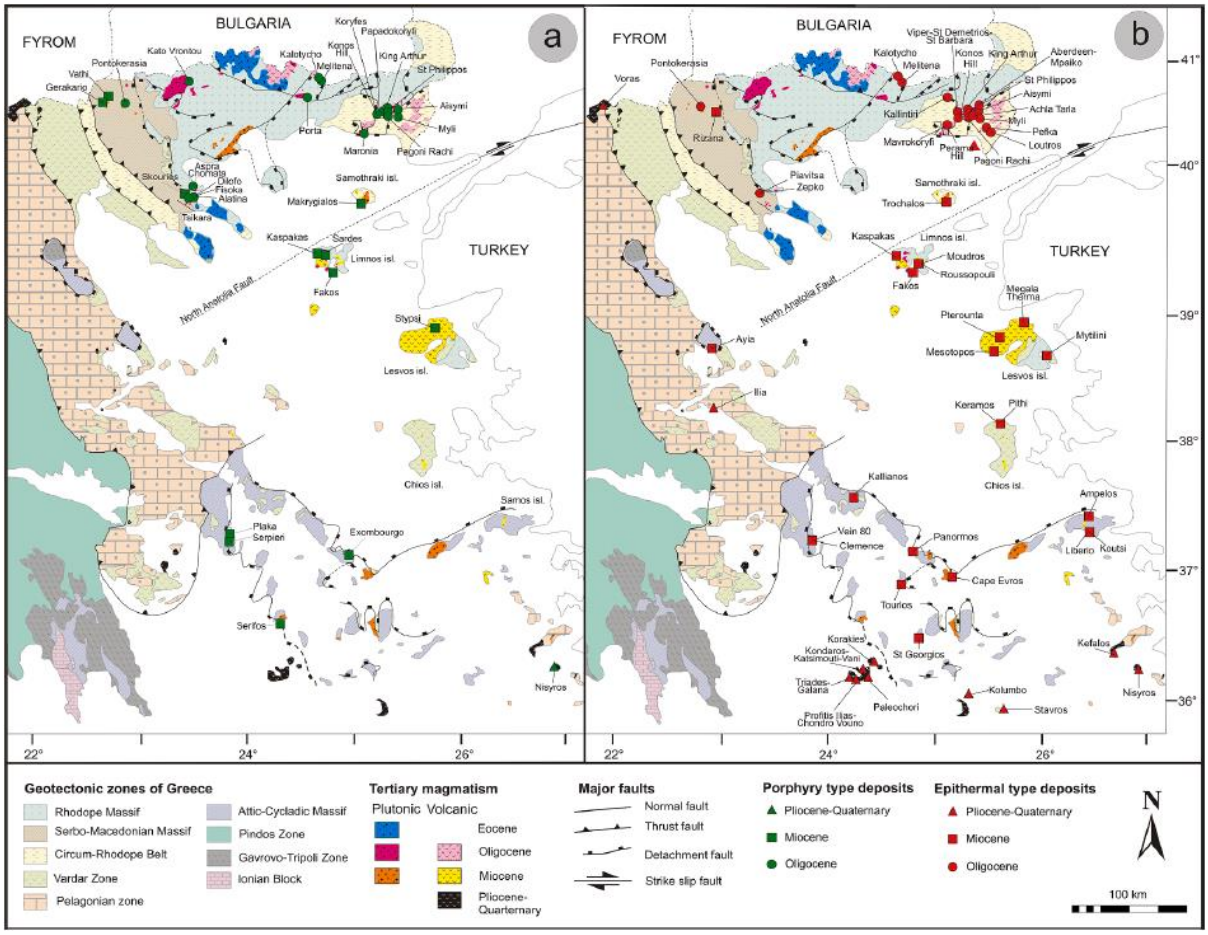

Figure 14 : Distribution géographique des minéralisations de type porphyre (a), et épithermal (b) de l'Oligocène au Quaternaire en Grèce (de Voudouris et al., 2019).

Trois prospects de porphyres à Cu – Mo enrichis en Re localisés dans le Nord de la Grèce (Maronia, Konos Hill, Pagoni Rachi) (Figure 15) se seraient développés dans un contexte géodynamique de retrait du slab et post-collision (Voudouris et al., 2009a). La fusion partielle d'une lithosphère mantellique ayant subi une métasomatose préalable, déclenchée par une remontée ponctuelle du manteau asthénosphérique, serait identifiée comme le processus responsable de l'enrichissement métallique. Cette hypothèse permet d'expliquer les teneurs exceptionnellement élevées en Re observées dans la molybdénite et suggère une contribution directe de matériaux mantelliques dans les magmas de Thrace occidentale (Voudouris, 2006, 2009a, 2019). Les gisements minéraux de type porphyre-épithermal, associés à un magmatisme lors d'un retrait du slab en post-collision, montrent une concentration plus élevée en Au et en éléments fortement sidérophiles par rapport à ceux liés aux arcs magmatiques classiques. Ce phénomène pourrait s'expliquer par la remobilisation de petites quantités de sulfures résiduels laissés dans la lithosphère profonde par les épisodes de magmatisme d'arc (Richards, 2009).

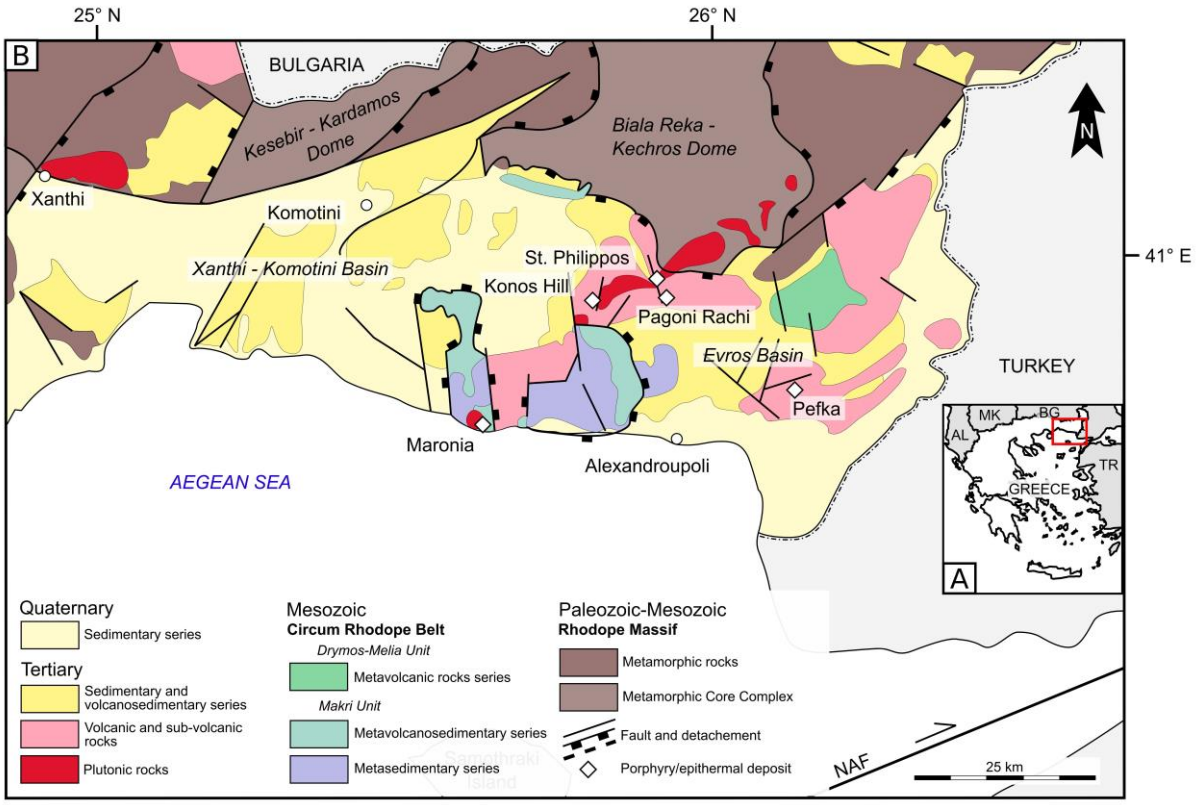

Figure 15 : Carte structurale du NE de la Grèce, avec les situations des sites d'études, d'après Mavrogonatos et al., 2019.

Cependant, la minéralogie et les mécanismes de concentration de ces éléments au sein des gisements hydrothermaux du Nord-Est de la Grèce sont mal contrains, en particulier le rôle des fluides. Ces gisements sont le résultat de plusieurs intrusions magmatiques successives et de plus en plus différenciés (granodiorite-andésite à granite) et une évolution des fluides hydrothermaux dans le temps.

Le travail se base dans le NE de la Grèce. Il portera sur l'étude de différents systèmes de type porphyre-épithermal localisés dans la Thrace occidentale, allant de Maronia au Sud, au District de Sapes-Kassiteres-Kirki au Nord (Konos Hill, **Pagoni Rachi**, St Philippos) qui présentent (1) des systèmes magmatiques différents, (2) une zonalité de minéralisation/altération pour chacun des systèmes, (3) de relativement faibles teneurs en Cu, les gisements du NE de la Grèce n'ont été que peu exploités et proposent un accès et des affleurements préservés de ces objets, et une préservation des structures, des parties porphyres profondes aux parties les plus superficielles épithermales (4) les objets et sites sont connus et d'ores et déjà étudiés. Cela en fait donc de parfaites cibles pour une étude d'évaluation et de caractérisation des fluides dans les différentes générations de veines associées.

1.2.9. Site d'études

Le prospect de Pagoni Rachi (= Nervure de plume de paon, en grec) (Figure 16) présente le gisement porphyre-épithermal à Cu – Mo – Re – Au et se situe à environ 18 km au Nord-Nord-Est d'Alexandroúpolis (Figure 15), dans un paysage de collines recouvert par une végétation dense et ruisseaux, avec un dénivelé pouvant atteindre 200 m. Ce prospect a été décrit pour la première fois par Arikas (1979) avec un gisement affleurant en surface représentant une surface proche de 4 km^2. Le prospect de Pagoni Rachi se compose d'un système porphyre et d'un système de type sub-épithermal télescopés, associé à un pluton de granodiorite-tonalite (Voudouris et al., 2013a,b) . Le système de type porphyre est encaissé dans une granodiorite-tonalite à texture porphyrique Oligocène, qui intrude une formation clastique basale. Cette séquence, formant le bassin de Kírki-Aísymi, est composée de conglomérats, marnes, grès, série volcanosédimentaire datée de l'Éocène moyen à supérieur (Priabonien) (Figure 13). Elle recouvre de manière discordante le socle métamorphique de la ceinture Circum-Rhodope (Melfos et Voudouris, 2001). Cette formation est surmontée par une séquence volcanique constituée de dômes, coulées et pyroclastes volcaniques de composition andésitique à dacitique, avec plus au Sud des calcaires nummulitiques Éocène à Oligocène (Arikas, 1979, 1981 ; Caracciolo et al., 2012).

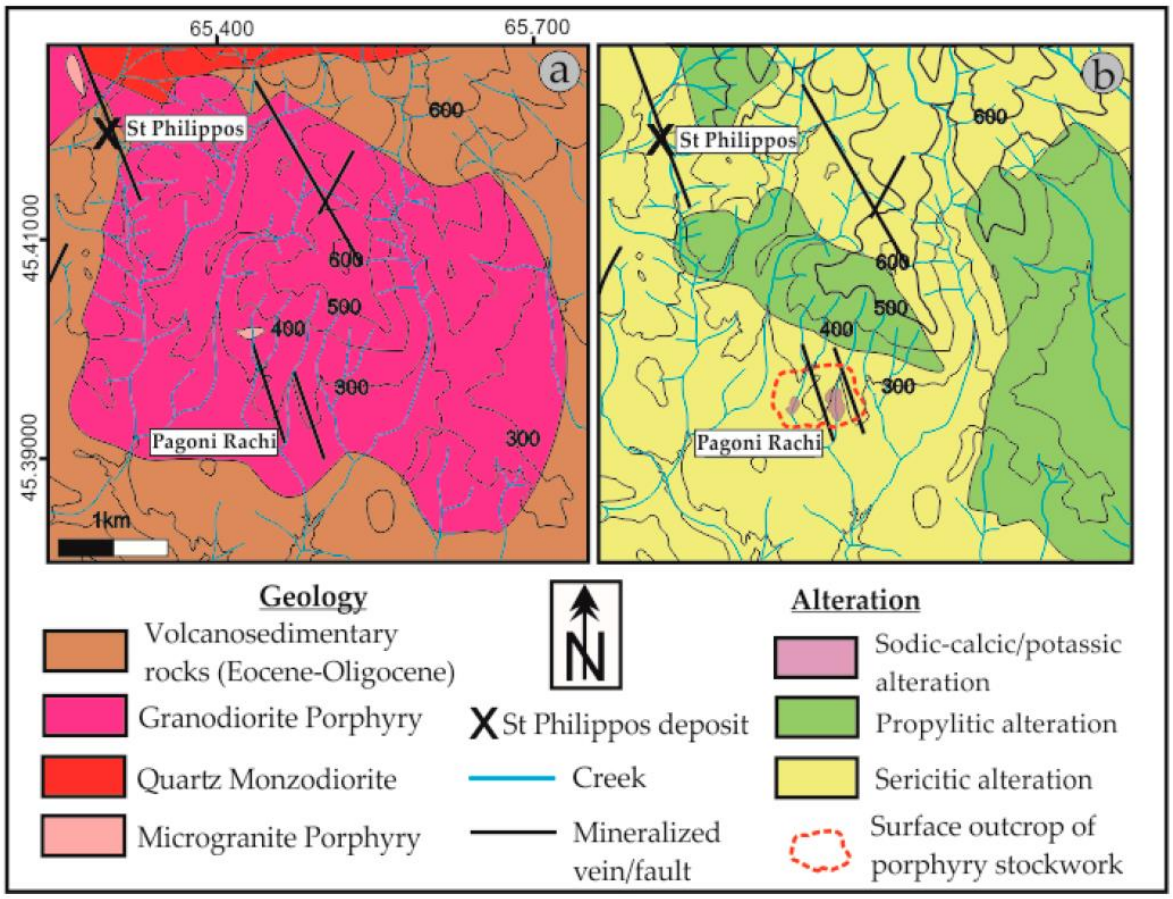

Figure 16 : Cartes géologique (a) et d'altération (b) des prospects de St Philippos (au Nord de la carte) et de Pagoni Rachi au centre de la carte, d'après Mavrogonatos et al. (2019).

La granodiorite-tonalite porphyrique est la principale lithologie de la zone étudiée (Figure 16). Elle est constituée de phénocristaux de plagioclase, amphibole, biotite, quartz et titanite dans une matrice microlithique de quartz, orthose, plagioclase et magnétite (Voudouris et al., 2013a ; Mavrogonatos et al., 2019). Cette roche à texture porphyrique, présentant une affinité calco-alcaline riche en potassium et un caractère sub-alcalin (Figure 17, Voudouris et al., 2013a), est la roche intrusive la plus ancienne de la région (Ortelli, 2009).

La partie Nord de la zone d'étude est occupée par une grande intrusion de quartz monzodiorite, qui recoupe à la fois la séquence volcanosédimentaire et la granodiorite-tonalite porphyrique. La monzodiorite présente une texture allant de moyennement grenue à porphyrique, composée de plagioclase, ainsi que des proportions variables de pyroxène, amphibole, biotite, quartz et oxydes de Fe-Ti. La mise en place de la monzodiorite a été datée à 31,9 ± 0,5 Ma par Rb/Sr sur biotite (Del Moro et al., 1988) et à 32,05 ± 0,07 Ma par U – Pb sur zircon (Perkins et al., 2018).

Des dykes tardifs de microgranites porphyriques de composition sub-alcaline (Figure 17) orientés NNO (Figure 16) recoupent les roches magmatiques précédemment décrites et représentent le dernier stade intrusif de la région (Voudouris et al., 2019). Ces dykes ont une texture porphyrique et se composent de phénocristaux de quartz résorbés et de feldspaths grossiers, souvent remplacés par de la séricite en raison d'une altération séricitique pervasive (Voudouris et al., 2019).

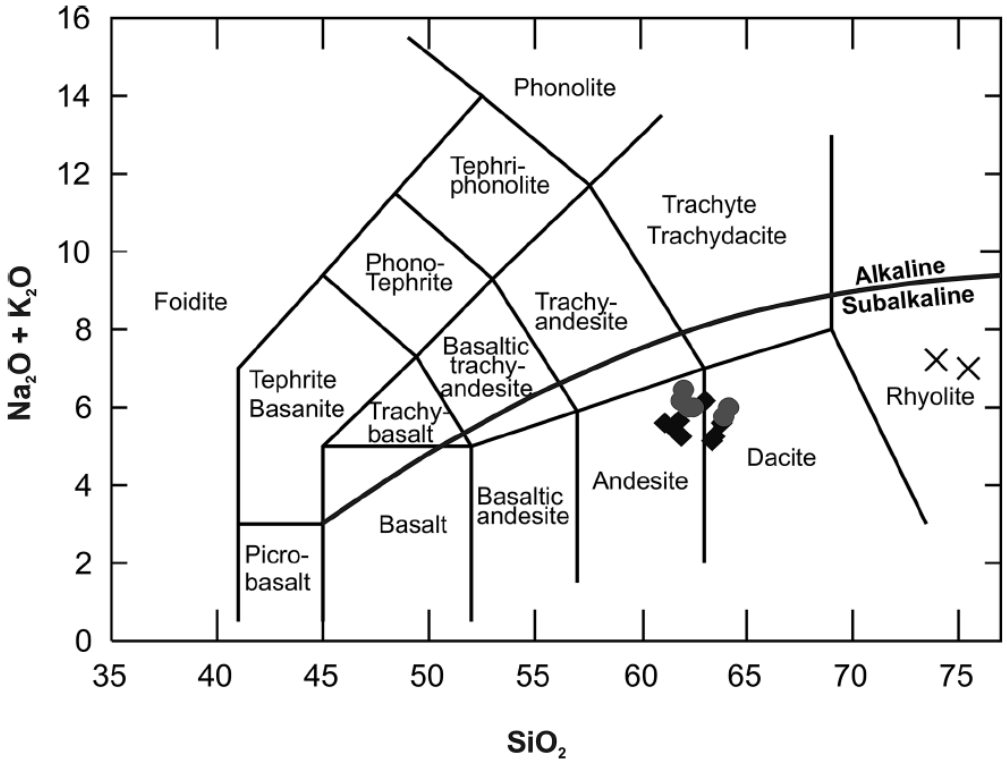

Figure 17 : Diagramme Alcalins ($Na_2O + K_2O$) vs. Silice (SiO_2) des roches magmatiques encaissant le gisement de Pagoni Rachi. Les analyses géochimiques de roche totale proviennent de Arikas et Voudouris (1998) (losange) et de Voudouris et al. (2013a) (disque). Les rhyolites (croix) encaissant la minéralisation Pb – Zn – Cu – Ag – Bi – Sn – In de St Philippos est de Voudouris et al. (2013a). Les catégories pétrographiques sont d'après Le Bas et al. (1986), et domaines alcalins et sub-alcalins proviennent d'Irvine et Baragar (1971).

Le gisement de Pagoni Rachi est un système de type porphyre-épithermal à sulfuration intermédiaire. Les analyses chimiques en roche totale du site montrent des concentrations importantes en Cu (jusqu'à 0,5 %), Mo (jusqu'à 2000 ppm), Au (jusqu'à 5 ppm) et Re (jusqu'à 20 ppm). L'enrichissement extrême en rhénium du système de Pagoni Rachi est associé à la présence de rhéniite (ReS_2) et de molybdénite riche en Re (jusqu'à 4.7wt.%) (Voudouris et al., 2009, 2013a). Montrant alors un enrichissement atypique de la minéralisation en Re. Le gisement de Pagoni Rachi a été décrit comme la cinquième occurrence connue de rhéniite (i.e. le volcan de Kudriavy (Korzhinsky et al., 1994), au gisement de type porphyre à Cu – Au – Mo de Kalmakyr (Ouzbékistan), et aux gisements de Voronov Bor (sables cuprifères) et Rybozero (Cu-Ni) en Carélie (Lavrov & Kuleshevich, 2010)) (Voudouris et al., 2009). La minéralisation de style porphyre-épithermal se présente sous la forme d'un stockwork de quartz et est associée à une zonation d'altérations hydrothermales de la granodiorite (Figure 18). L'introduction de métaux précieux, de molybdénite et de rhéniite caractérise tous les stades de la minéralisation. Ainsi la formation de la minéralisation est assimilée à quatre stades paragénétiques successifs (Voudouris et al. 2013a ; Voudouris et al., 2019) :

- des veines à magnétite + bornite + chalcopyrite + molybdénite + or natif (veine de type M) d'épaisseur inférieur à 1 cm, discontinues et des veines à quartz + magnétite + actinote avec des cristaux de quartz vitreux granulaires (veine de type A). Une altération sodi-calcique/potassique est caractérisé par une recristallisation et oblitération complète des textures primaires de la roche avec un assemblage composé d'albite, calcite, chlorite, quartz, white mica, épidote, apatite, hématite, titanite and pyrite, et une altération propylitique distale contemporaine ;
- des veines à quartz + pyrite + chalcopyrite + molybdénite (veine de type B) planaire de 1 à 50 cm d'épaisseur, avec épontes parallèles et textures en quartz en peigne avec une texture rubanée. Une altération sodique/potassique similaire à celle des veines de type M-A est associée à cette veine, avec une plus grande proportion en orthose, biotite, chlorite, épidote, séricite, pyrite, hématite, magnétite et une structure primaire effacée ;
- des veines à quartz + pyrite + chalcopyrite + molybdénite, or natif et un assemblage de sulfures et sulfosels de Ag, Bi, Te et Se avec une texture des épontes régulières à sinueuses et sont d'épaisseur millimétrique à pluridécimétrique avec des ouvertures centrales à remplissage de pyrite, molybdénite, chlorite, fluorite, micas blancs et à carbonates (veine de type D). Une altération séricitique pervasive est associée à une destruction des textures primaires de la roche encaissante avec un assemblage à quartz, séricite, chlorite, albite, orthose, reliquat de biotite hydrothermale et carbonates. Cette altération séricitique atteint également les dykes magmatiques tardifs recoupant la granodiorite ;
- une altération argillique avec des veines épithermales, riches en métaux précieux et de base avec Au, Ag et Te (veines de type E). Ces veines épithermales tardives, orientées NNO, recoupent la minéralisation de type porphyre et sont associées à une zone d'altération argillique (quartz-séricite-carbonates), jusqu'à argillique avancée (quartz-kaolinite-séricite), alors

associées à un télescopage du système épithermal sur le système de type porphyre. Les veines à quartz carbonates sont considérées comme épithermale profondes (Voudouris, 2006).

Ore mineralization style	Vein types/ stage	Vein assemblage	Alteration assemblage	Form, texture, zonation
Porphyry style	A-type M-type (stage I)	Qz + Mag + Py + Hem + Bt + Or/ Ab + Act + Ep + Ccp ± Bn ± Mol ± Au ± Po ± Chl ± Fl	Qz + Bt + Or/Ab + Act + Ep + Mag ± Chl ± Cal ("Sodic/Potassic-Calcic")	Sinuous, wavy quartz or magnetite veins, to continuous straight-sided, quartz veins with parallel walls. In some A-type veins centerlines of magnetite and/or pyrite.
	B-type (stage II)	Qz + Py + Ccp + Mol ± Rhn ± Hem ± Po ± Mag ± Ab ± Chl ± Fl ± Cal ± Ser	Qz ± Ab/Or ± Chl ± Cal ("Sodic/potassic")	Continuous straight-sides, quartz veins with sharp parallel walls, sulfides at vein margins, within quartz and along vein centers. Banded veins black quartz at margins, grey at center. Ab, Cal, Chl, Fl, minor Ser, fill open spaces.
	D-type (stage III)	Py + Ccp ± Mol + Ser ± Qz ± Cal ± Hem ± Po ± Rhn ± Bn ± Ilm ± Ttd ± Alt ± $Gn_{s.s.}$ ± unnamed phases along the PbS-$AgBiS_2$ joint	Qz ± Ser ± Py ± Cal ("Sericitic")	Continuous pyrite-quartz veins and pyrite-chalcopyrite-molybdenite veins reopening and overprinting B-type veins
Epithermal style	E-type (stage IV)	Qz + Cal + Sp + Gn + Ccp + Py ± Tnt ± Ttr ± Eng ± Hes ± Ptz ± Stz ± Alt ± Ag-Au ± Aik ± Hmr ± Lnd ± Wtc ± Ber ± Ser ± Kln	Qz ± Cal ± Ser ± Kln	Continuous straight-sides, quartz-carbonate veins with sharp parallel walls.

Figure 18 : Tableau représentant les séquences de veines/fractures, altérations et assemblages paragénétiques avec les descriptions des structures types présents à Pagoni Rachi (d'après Voudouris et al., 2013).

Ces veines à quartz ± calcite contiennent des inclusions fluides (IF) (Figure 19), marqueurs de la circulation de fluides minéralisateurs. Trois types d'inclusions fluides sont décrits dans la littérature (Voudouris et al., 2013a, 2019). Les Types 1 biphasées (V+L) sont les plus tardives et sont liées à l'épisode épithermal du gisement, ceci reste cependant à démontrer pétrographiquement (seules les T_h (Température d'homogénéisation) et des salinités faibles ont été mesurées). Les Types 2 triphasées (H+L+V±S) et les Types 3 biphasées (V+L±S) résultent de l'ébullition d'un fluide avec séparation des phases vapeur et liquide. Leurs proportions sont variables dans les différents types de veine. Les Types 3 représentent près de 80 % des populations d'inclusions fluides dans les veines type A et B (Voudouris et al., 2013a).

Les données d'analyses d'inclusions fluides suggèrent que la minéralisation se soit formée entre 360 °C et 510 °C par ébullition de fluides hydrothermaux, avec la vapeur en phase dominante. L'ébullition produit des fluides, coexistant, de faible à moyenne salinité (1,7 à 10,7 $wt\%_{equiv.NaCl.}$) et de haute salinité (36 à 74 $wt\%_{equiv.NaCl.}$) (Voudouris et al., 2019). Les inclusions fluides tardives (des veines de type E) sont caractérisées par des T_h allant de 210 à 340 °C, avec de faibles salinités (1,4 à 2,9 $wt\%_{equiv.NaCl.}$). Ces dernières seraient associées à une dilution et/ou refroidissement des fluides magmatiques-hydrothermaux, par des fluides de surface (Figure 19). Ceci est comparable avec ce qui est observé dans les minéralisations du district de Sapes-Kassiteres-Kirki (Voudouris et al., 2013a).

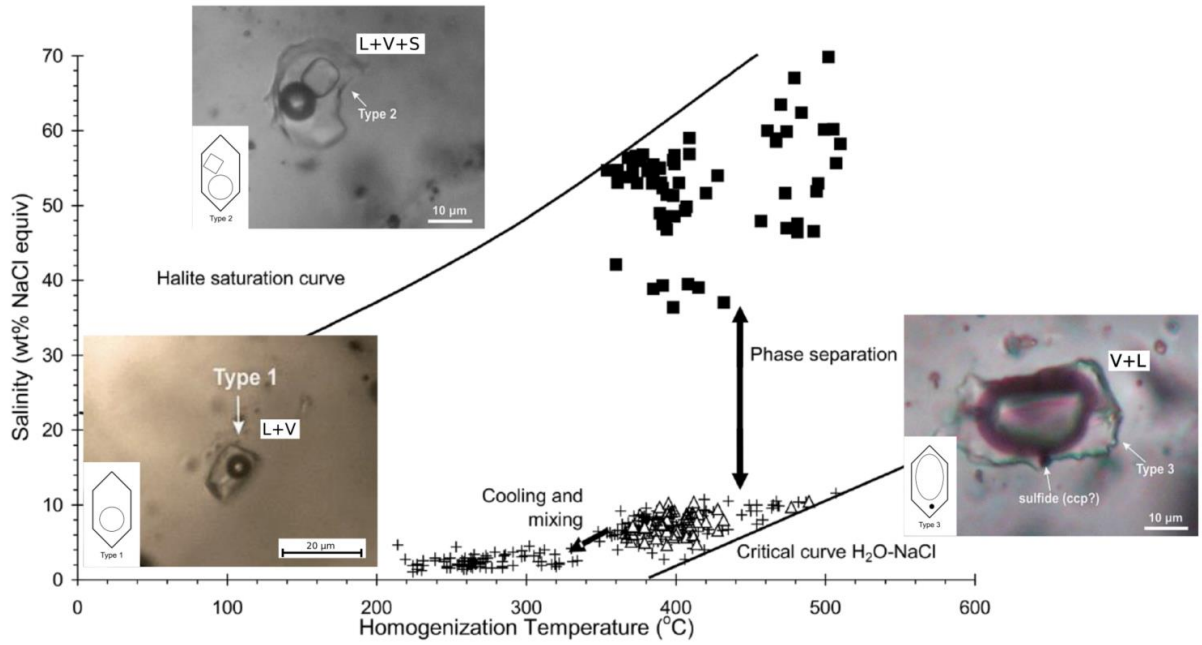

Figure 19 : Diagramme des températures d'homogénéisation en fonction de la salinité des inclusions fluides provenant des cristaux de quartz et de calcite des différents types de veines du gisement de Pagoni Rachi : Type 1 = croix, Type 2 = triangle, et Type 3 = carré noir (de Voudouris et al., 2013a). Avec photographie des différents types d'inclusions fluides (provenant de Voudouris et al., 2013a).

Le gisement de Pagoni Rachi a donc déjà été étudié à travers les études de Arikas (1979 et 1981), Voudouris et Melfos (2006), Voudouris et al. (2009, 2013, 2019, 2022), Mavrogonatos et al. (2019, 2020). Ainsi de premières descriptions et interprétations de la minéralisation et la succession paragénétique formées lors les différentes phases d'altération ont été réalisées. La salinité et les températures d'homogénéisation des inclusions fluides ont permis de contraindre les conditions *PT* des minéralisations. De plus, des analyses préliminaires (discutées), réalisées à GeoRessources Nancy, sur IF des veines de type A par la méthode d'ablation laser ICP-MS montrent des valeurs extrêmes de concentration en K, Mn, Mg, Mo, Ag qui pourraient être expliquées par la présence de solides non identifiés au sein des inclusions, des chlorites ou biotites par exemple. Les rapports Cu/Mo sont très faible en comparaison avec d'autres gisement de types porphyres tels que El Teniente au Chili ou encore Haftchesmeh en Iran. Il a été montré que pour ces veines à quartz-Mo-Re, il est possible de proposer une chronologie fine des événements fluides, de mesurer la présence de phases vapeurs de CO_2 pur ainsi que des solides tels que la chalcopyrite et l'anhydrite dans le fluide, et d'établir la teneur en métaux des fluides par LA-ICP-MS avec des teneurs importantes en Cu, Mo, Mn, Zn, Pb (+ Te, Bi, Sb et Sn jusque plusieurs centaines de ppm). En revanche aucune donnée quantitative par LA-ICP-MS n'a été produite en ce qui concerne les veines de type B et type E (Bitte M., 2019, *rapport interne*).

Néanmoins les travaux déjà effectués sont encore à compléter : la pétrologie des assemblages minéralogiques des veines, des encaissants et des altérations sont précises mais celles concernant la structure des cristaux de quartz (recristallisation, générations) est à réaliser ainsi qu'une pétrologie des

inclusions fluides précises (type d'inclusion, assemblages, type de quartz, type de veine), une quantification élémentaire des cristaux de quartz, et analyses isotopiques des cristaux de quartz et de calcite. Cela permettra d'aboutir de nouvelles contraintes sur les conditions *PVTX* de formation du gisement, la source et l'évolution des fluides au cours de la vie du porphyre de Pagoni-Rachi.

Le site de Pagoni Rachi est privilégié pour cette thèse : objet connu, présence d'échantillons, de lames minces et épaisses et structure complète et conservé à l'affleurement du système. Ce travail se base sur des échantillons collectés lors d'une mission de terrain à Pagoni Rachi en octobre 2018, complétés par une collection de lames épaisses fournie par V. Melfos (Univ. Thessalonique) et P. Voudouris (Univ. Athènes) sur lesquelles les inclusions fluides ont déjà été travaillées (Voudouris et al., 2009, 2013), qui seront complétés par deux campagnes d'échantillonnages réalisées en 2022 et 2023. De plus l'imagerie et la pétrologie réalisées ont permis de poser les bases d'analyses in situ que sont l'isotopie stable dans les minéraux de gangue (quartz, calcite) des veines ainsi que la mesures d'éléments traces dans les cristaux de quartz et de calcite. Elles donnent des perspectives d'analyses complète du site avec des taux de croissance des veines, évolutions des fluides avec une mise en parallèle des données quantitatives des fluides associés à la mise en place de la minéralisation et un traçage de ces mêmes fluides.

CHAPITRE 2. RECONSTRUCTION OF A PORPHYRY-EPITHERMAL SYSTEM – FROM FIELDWORK TO THIN SECTION: PAGONI RACHI (GREECE)

2.1. INTRODUCTION

Porphyry and epithermal systems represent geologically significant environments due to their economic importance, particularly in the formation of metal-rich deposits containing copper, gold, molybdenum, and silver. These systems are inherently linked to active magmatic and hydrothermal processes occurring in diverse tectonic settings. Their formation results from interactions between magmatic intrusions and circulating hydrothermal fluids within rocks, leading to specific alterations and mineralized deposits. Understanding these complex processes requires a thorough analysis of associated structures, alterations, and morphologies to reconstruct the spatiotemporal evolution of the system. The conceptual model proposed by Sillitoe (2010) establishes a clear correlation between deep porphyry zones and shallow epithermal environments. This model highlights the vertical zoning of alterations and mineralization styles, offering a crucial theoretical framework for interpreting field observations and petrographic data.

The understanding of porphyry-epithermal systems largely relies on the study of veins, alteration types, and associated structures. Veins, which serve as drains for hydrothermal fluids, are valuable archives of the physicochemical conditions of the system during its evolution. Their spatial distribution, textures, and mineralogical compositions provide insights into metal transport processes, fluid-host rock interactions, and fluctuations in pressure, temperature, and fluid chemistry. Similarly, hydrothermal alterations, manifested as distinct mineralogical transformations, help reconstruct the evolution of physicochemical conditions and fluid dynamics within the system. The morphology and texture of minerals, particularly gangue minerals, offer clues about successive events of opening, filling, and fluid circulation.

Reconstructing these complex processes requires a methodology that combines field observations, petrographic analyses, and advanced imaging techniques. Field observations are critical for identifying major vein types, and their orientations. Petrographic analyses of thin and thick sections provide higher resolution insights into the mineralogical content of individual veins and mineral textures. Additionally, cathodoluminescence (CL) imaging is a powerful tool to reveal internal mineral zoning, potential chemical variations, and growth textures that are often invisible under ordinary light. Integrating these approaches enables the deciphering of successive alteration and mineralization stages while linking microscopic, macroscopic, and field-scale characteristics (e.g., geomorphology).

This chapter aims to explore and characterize the veins, alteration types, and associated morphologies within a porphyry-epithermal system. A multi-scale methodology, guided by the models proposed by Sillitoe (2010), was implemented to reconstruct the structural and hydrothermal history of the Pagoni Rachi porphyry-epithermal system. By integrating field and microscopy observations, this study contributes to a deeper understanding of the formation and evolution processes of porphyry and epithermal systems, providing new perspectives on the dynamics of these complex geological environments.

2.2. METHODOLOGY

2.2.1. Sampling

The work is carried out on a set of (i) field observations, (ii) hand specimen descriptions, and (iii) thin and thick sections with successive veins at the Pagoni Rachi prospect located in the Sapes-Kassites-Kirki District (Figure 20). The samples were chosen because they show all typical macroscopic characteristics of different vein types of the Pagoni Rachi magmatic-hydrothermal system (Voudouris et al., 2013a, b ; Mavrogonatos et al., 2019, 2020). Three sampling campaigns took place from 2018 to 2023 at the Pagoni Rachi site. This allowed for the implementation of strategic sampling and the establishment of a detailed mapping of the site, based on observed vein types, alteration types, and structures, to have a representative basis of the porphyry-epithermal system. Thus, around thirty samples of different vein types associated with various alteration styles were collected. Several sets of thin and thick sections were produced for petrological studies, geochemical analyses, and fluid inclusion studies.

The first sampling campaign was carried out by Marie Bitte, who collected 10 samples. These samples primarily represent the various geological objects at the Pagoni Rachi site, although with some

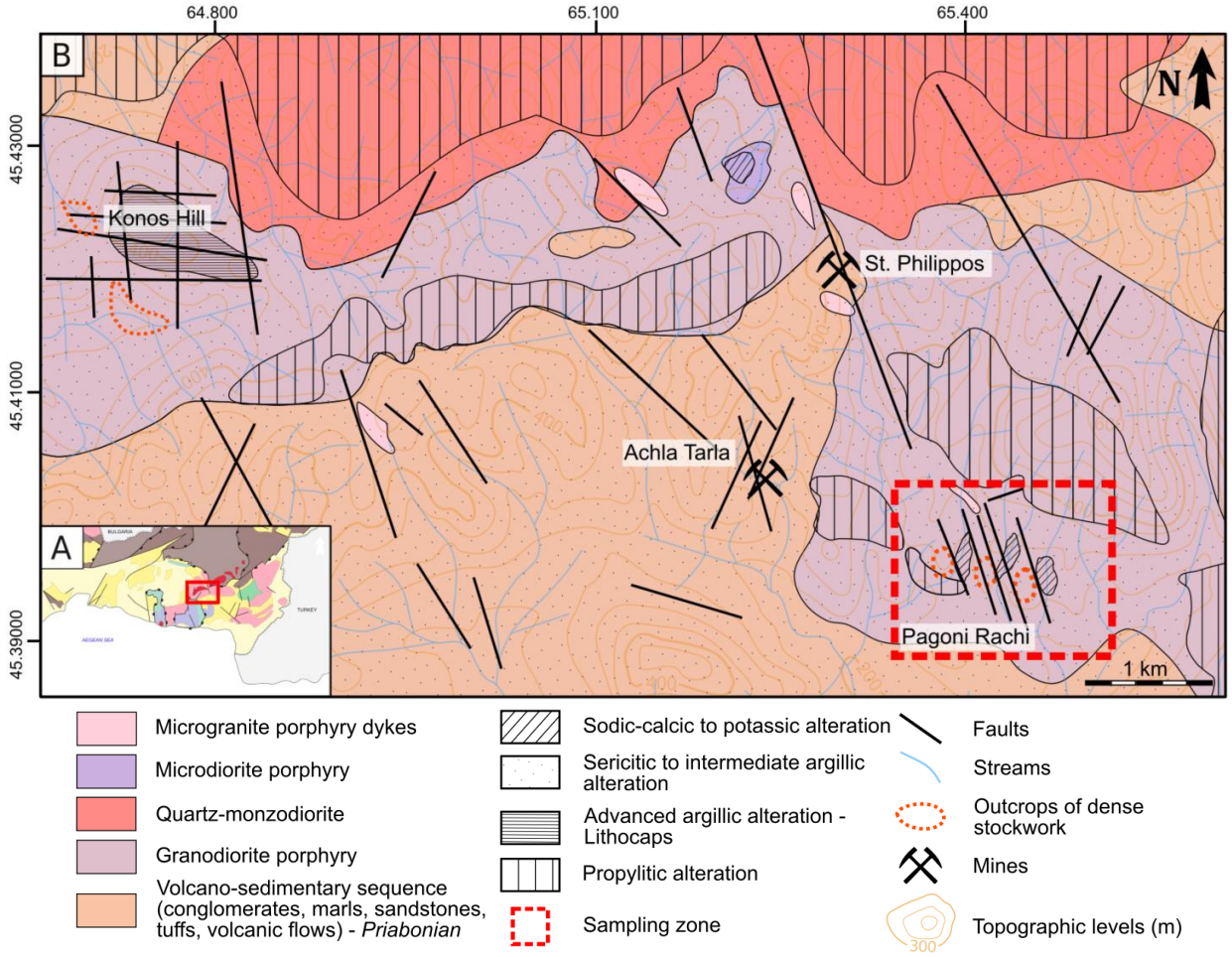

Figure 20 : Geological and alteration maps of the Sapes-Kassiteres-Kirki district, with A. Location in the NE Greece, B. the location of the Pagoni Rachi prospect at the southeastern of the map, modified from Mavrogonatos et al. (2019).

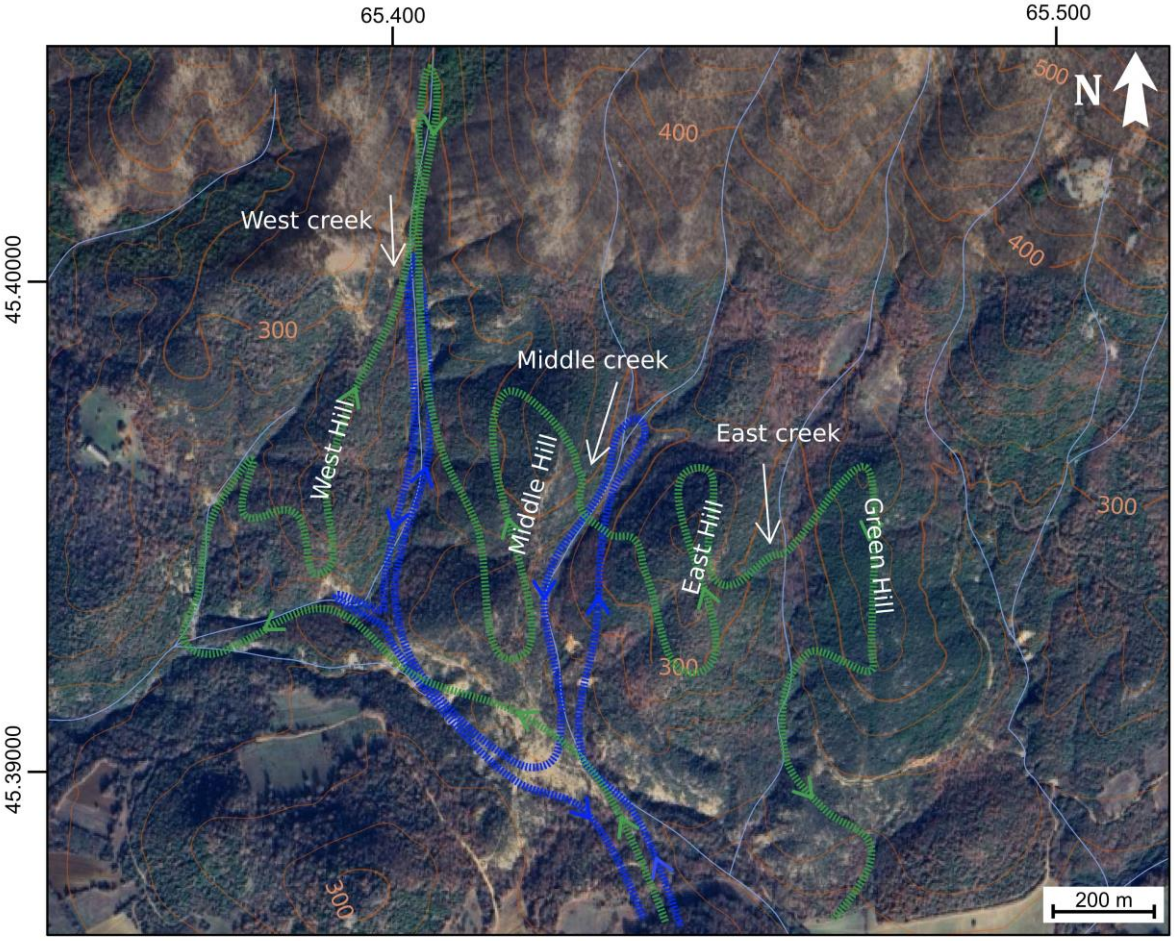

Figure 21 : Satellite map of the Pagoni Rachi site showing sampling and exploration routes in blue (2022) and green (2023).

inaccuracies (spatial location, absence of GPS points, sample descriptions, etc.), the sampling strategy was not targeted on our subject, it was specifically focused on the chlorite presence, and only the two central creeks (Middle and West) were explored. However, this sample series provided, at the beginning of the thesis, an initial petrographic observation base for the Pagoni Rachi site, improved the localization of geological objects in the Pagoni Rachi porphyry-epithermal system, and helped refine the geological and alteration map of the site. The loan of thick-sectioned samples of similar fragments from V. Melfos (University of Thessaloniki) and P. Voudouris (University of Athens) allowed for the initiation of fluid inclusion microthermometry descriptions and analyses in the quartz and calcite of the various veins at the Pagoni Rachi site; however, most of the fluid inclusions in these samples had already decrepitated and decrepit easily during microthermometry, making the description and analyses of fluid inclusions difficult.

The next two sampling campaigns, carried out during the thesis, aimed to establish better constraints on the relative chronology between the different vein stages (mineralization) and the associated alteration, and to provide petrographic constraints, with 23 new samples (see Tableau des échantillons des différents sites avec commentaires et positions associées.). These campaigns also provided new

insights into the distribution of the various structures in the Pagoni Rachi porphyry-epithermal system and enabled the collection of better-constrained samples for fluid inclusion observations (see Abiven et al., 2025, submitted).

The second campaign, in September 2022, followed a similar approach to the first carried out in 2018 with a more exhaustive and strategic sampling focused on the different alteration associations and observable veins (Figure 21). The macroscopic field indicators for these differences are mainly the rock colors, the relief of structures and objects within the host rock, as well as the hardness and friability of the rocks—particularly due to texture variations in the granodiorite, which is the only observable lithology in the field (excluding the rhyolitic dykes to the north of the site, which are described later, and the unobserved enclosing sedimentary series). Thus, the two creeks (Middle and West) were resampled (Figure 21). The surrounding vegetation is dense, limiting visibility both at a distance and on the ground, with a thick cover. The only accessible outcrops are indeed located along the creek beds, promoting the erosion of the exposed rocks (Figure 22 A-E). On the day of exploration, the end of September, there was no actual stream, only a thin trickle of water or small puddles. The vegetation is

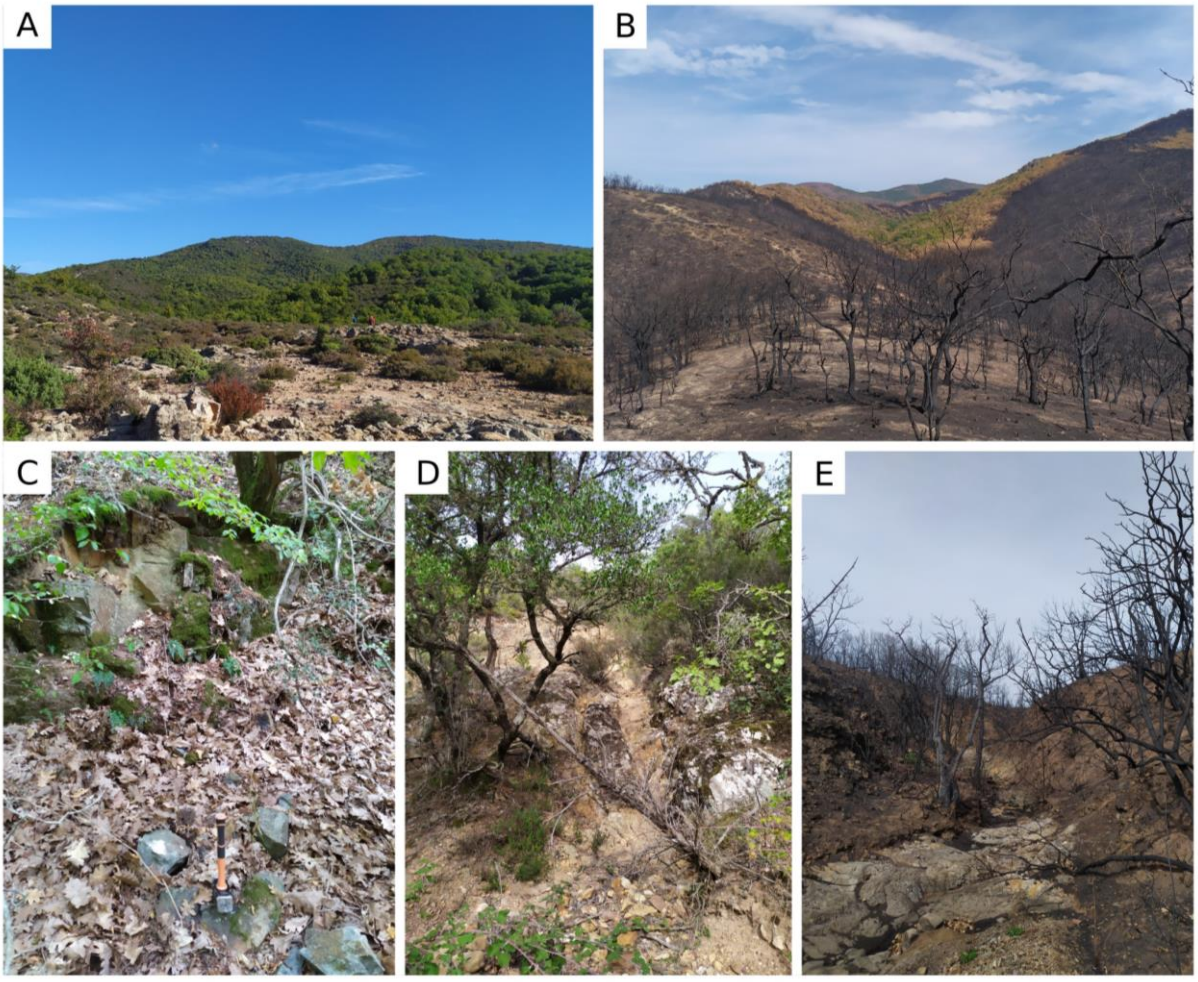

Figure 22 : Landscapes of Pagoni Rachi. A. Landscape at the starting point in the southern part of the map (Figure 46). B. View from the summit of West Hill after the fire. C. Representative outcrop along streams before the fire (Middle Creek). D. Clay zone before the fire (West Creek). E. Stream after the fire (East reek).

mainly composed of dense, thorny shrubs, oak, and brambles, with moss also present at the bases of trees and on the few rocks that can outcrop.

During the third and last field exploration, the end of September 2023, of the site, a large wildfire ravaged the area a few days before (Figure 22, B, E). Although the surface of the site was completely blackened by flames and ashes, the vegetation removal caused by the fire provided excellent exposure. It was now possible to explore the various hills along the creeks, which had never been explored before. This exploration allowed for the observation of rocks at the tops of the hills. (Additionally, along all the creeks many tortoise shells, those that did not manage to run as fast as the rabbits, litter the ground. On the valley floor your feet sink about thirty centimeters into layers of cold ash).

2.2.2. Petrological observations

Petrographic observations of thin and thick section were made using an Axioscope Zeiss (x10 to x100) with transmitted and reflected light, and quarter wave filter (as a help to appreciate the different crystal orientation) for paragenesis sequence, microstructures/texture of minerals (especially quartz and calcite). Macroscopic scale photographies of thin and thick sections were made using a Macroscope Keyence VHX 2000, with transmitted and reflected light. This observational work allows the development of relative chronological criteria by cross-checking features, to provide paragenetic sequences between the different geological structures and objects.

2.2.3. Cathodoluminescence (CL) imaging

The (CL) imaging of quartz from the different vein-types was performed by (i) an OPEA Cathodyne using the following parameters: P = 50 – 60 mTorr, T = 11.0 – 14.0 mV, I = 250 – 480 μA and a 5 – 10 s obturation duration, (ii) a Newtech Scientific Cathodyne was for the imaging, with the following parameters: P = 50 – 70 mTorr, T = 10 – 12 kV, I = 300 μA, and 10 s obturation duration per zone. For the CL imaging of a complete thin/thick section, 40 – 80 CL images were acquired and (iii) an SEM TScan was used with the following parameters: T = 15 kV, I = 2 – 3 nA, x300 magnification, 4 min obturation. The (i) and (ii) methods gave same results; in this paper we propose a collection of the pictures. The (iii) method allows obtaining more precise imaging compared to the previous methods. This is particularly advantageous for observing zoned quartz next to carbonates exhibiting strong yellow-red luminescence.

It is unrealistic to compare the CL intensity on different photographs with varying acquisition parameters (voltage tension, intensity, pressure, and device). Fortunately, the presence of different types of veins with varying CL and dynamic recrystallization domains in the same sample allows us to compare these relationships to some extent. A combination of CL photographies is presented further.

2.3. RESULTS

2.3.1. Pagoni Rachi - Field observation, alteration and vein petrography

This section is based on a brief field description resulting from the various field missions (see Sampling), aiming to present the possible limitations encountered in the field and to outline the methods of observation used, along with some preliminary results. These include field observations with a preliminary description of the different types of veins, alteration styles, the development of a more detailed map showing the spatial extent of the vein succession, alteration zones, and their relationships with tectonic and lithological structures (Figure 23, Figure 24). This provides the groundwork for further detailed laboratory observations of hand specimens, including microscopy, cathodoluminescence imagery, trace elements and stable isotopes analyses for fluid tracking which are presented in the next chapters.

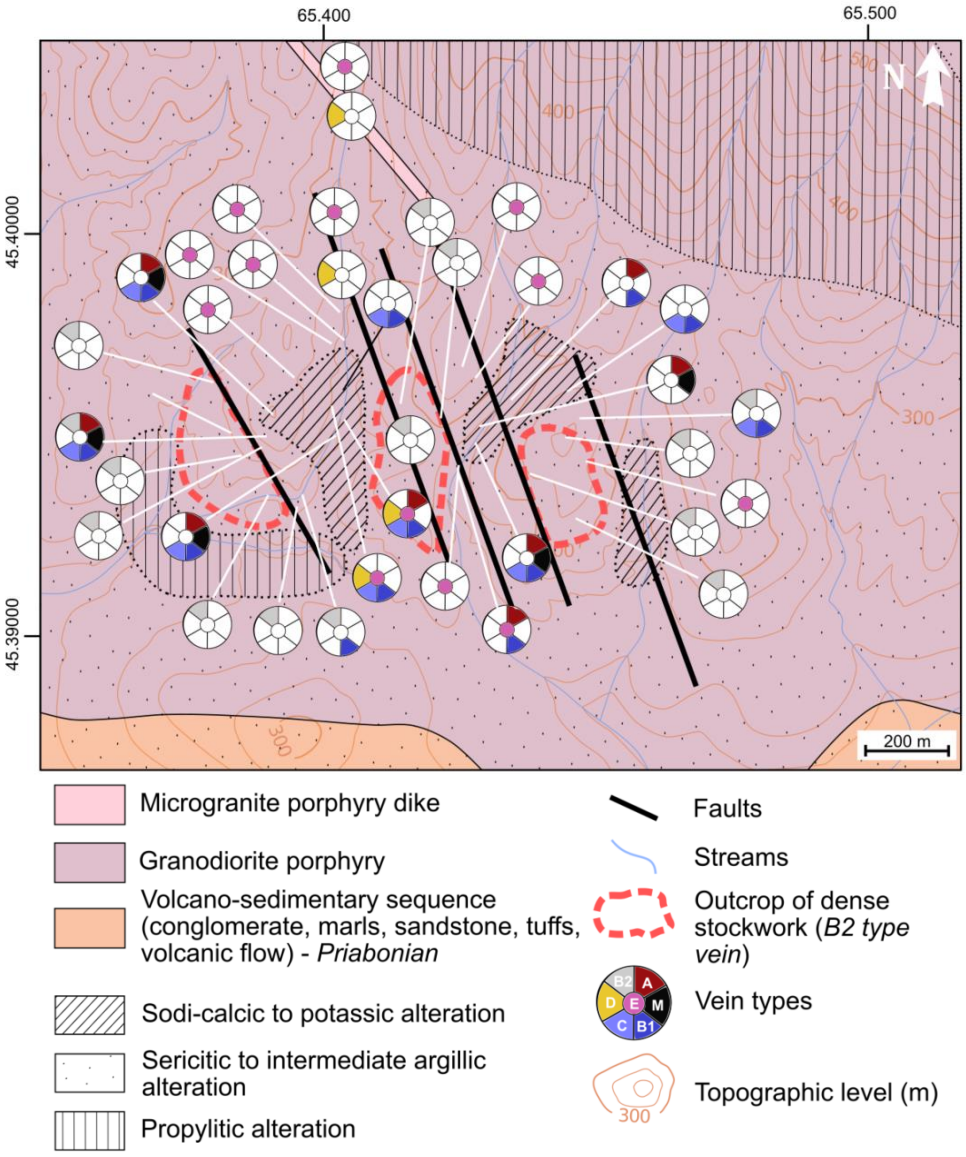

Figure 23 : Geological map, alteration zones, and observed/sample vein types at the Pagoni Rachi site.


A
MB12
Propylitic altered granodiorite porhyry
2.5 cm
B
MB02
M-type
B1-type
A-type
M-type
Mag+Hem
2.5 cm
C
AB120.01
E2-type
B1-type
D
AB123.01
D-type
2 cm
E
B2-type
F
AB116
Massive stockwork of B2-type
10 cm
G
AB122.03
E1-type
4 cm
H
AB122.01
E2-type (2)
E2-type (1)
E2-type (3)
E2-type (2)
3 cm
I
B1-type
J
Sericitic alteration
Potassic alteration, propylitic overprinting
30 cm
K
Sericitic alteration to argillic alteration
L
Sericitic alteration
Argillic alteration
30 cm
M
B2-type SW zone
A/M-B1-type zone
50 cm

Figure 24: Representative outcrops, macroscopic samples, and structural relationships at Pagoni Rachi. A. Sample of fresh granodiorite with low-intensity propylitic alteration, featuring phenocrysts of hornblende, plagioclase, quartz, rare biotite, epidote, chlorite, and calcite. B. Wavy quartz-pyrite vein (A-type) crosscut by magnetite-hematite-pyrite veins (M-type) and ribboned quartz-chalcopyrite-molybdenite veins (B1-type) within granodiorite with potassic alteration overprinted by propylitic alteration. C. Type B1 vein with pyrite-filled fractures (D-type) crosscut by calcite veins (E2-type), hosted in recrystallized rock with potassic and propylitic alteration. D. Massive pyrite vein with host rock exhibiting intense sericitic alteration, containing sericite, quartz, and disseminated pyrite. E. Sterile ribboned quartz vein (B2-type) associated with intense sericitic to argillic alteration. F. Stockwork mass with ribboned veins. G. Epithermal miarolitic vein (E1-type) with comb quartz, sphalerite, galena, chalcopyrite, pyrite, and calcite infill (E2-type), associated with argillic alteration. H. Epithermal veins with multiple calcite sequences (1) to (3) containing disseminated pyrite. I. Ribboned quartz vein outcrop (B1-type). J. Transition zone between sericitic alteration at the summit and potassic alteration with a propylitic overprint. K. Argillic-sericitic alteration zone associated with Type B2 veins. L. Transition zone from sericitic alteration (yellow) to argillic alteration with kaolinite (white). M. Summit of West Hill, showing a transition zone between stockwork with Type B2 veins and intense sericitic alteration (south) and stockwork with A/M- and B1-type veins with potassic alteration overprinted by propylitic alteration.

Alteration assemblages and vein types are recognized based on relationships and distinguished according to the terminology summarized by Seedorff et al. (2005) and Sillitoe (2010). The veins observed at Pagoni Rachi are equivalent but not identical to the vein terminology proposed by Gustafson & Hunt (1975), Sillitoe (2000), Muntean & Einaudi (2001) and Seedorff et al. (2005) for A-M , B (our B1-type), D veins, by Dilles and Einaudi (1992), Monecke et al. (2018) for C veins and by Arancibia & Clark (1996) for M veins, Muntean et al. (2000, 2001) and Monecke et al. (2018) for banded veins (our B2-type veins), and Vouduris et al. (2013a, 2019) for the E-type veins.

Descriptions of the different lithologies, veins, alterations, and structural and spatial relationships are presented in detail in the following sections of the paper, and the details of the samples are provided in the appendix.

2.3.1.1. Lithologies

The Pagoni Rachi deposit occurs as a mineralized stockwork enclosed within an altered granodioritic body (Figure 23). The granodiorite displays a porphyry texture with a fine-grained matrix ranging from 200 μm (10%) to < 10 μm (90 %). When fresh it consists of plagioclase (30 %) amphibole (hornblende) (15 %), and biotite (20 %) phenocrysts, in a matrix consisting of microlithic quartz (30 %), plagioclase, orthoclase, and magnetite (5 %) (Figure 25 A, B).

To the north of the site, a subvertical rhyolitic dyke crosscut the granodiorite, with a width of 3 meters, oriented E-W (Figure 23, Figure 25 C, D). The rhyolite consists of quartz-embayed phenocrysts having sizes from few millimeters to 1cm diameter, plagioclase phenocrysts, muscovite, sericite and euhedral disseminated pyrite. It is crosscut by thin pyrite veins.



Figure 25: Observed lithologies at Pagoni Rachi. A. Fresh granodiorite outcrop on the western side of the site. B. Granodiorite sample with phenocrysts of hornblende, plagioclase, quartz, and rare biotite. C. Altered rhyolite dyke, 3 m thick. D. Rhyolite sample with phenocrysts of quartz, plagioclase/orthoclase, rare biotite, disseminated pyrite, and supergene malachite (indicative of probable chalcopyrite presence).

2.3.1.2. Host-rock alteration styles

The sulfide mineralization at Pagoni Rachi occurs as disseminated grains (pyrite + molybdenite ± rheniite ± chalcopyrite ± galena ± sphalerite) in the altered granodiorite and in the porphyry and epithermal veins. Based on the mineral assemblage and association with distinct succession of mineralized veins and associated alteration style of host-rocks defining the relative chronological sequences, the hydrothermal quartz-sulfide veins can be separated into an early to late formation as part of the distinct consecutive hydrothermal stages exhibiting a spatial zoning.

Observations suggest that there is a significant overprinting of alterations, particularly from the epithermal system onto the porphyry system, complicating the differentiation of alteration styles. The relative proportions of certain minerals, such as sericite, chlorite, and the presence of pyrite, epidote, or calcite, are the primary means of distinguishing them. Indeed, it is exceedingly difficult to differentiate between the various types of feldspars, which are typically altered into micas or clays. Similarly, mafic minerals are altered to varying degrees, from weak to intense, often preserving their structural framework despite mineralogical changes or, in some cases, the complete disappearance of the primary structure. Only few photographs will be presented due to the near ubiquity of common minerals (sericite, calcite, biotite, chlorite, feldspar, amphibole). The most effective approach for distinguishing these alterations remains the combination of microscopic observations with field observations.

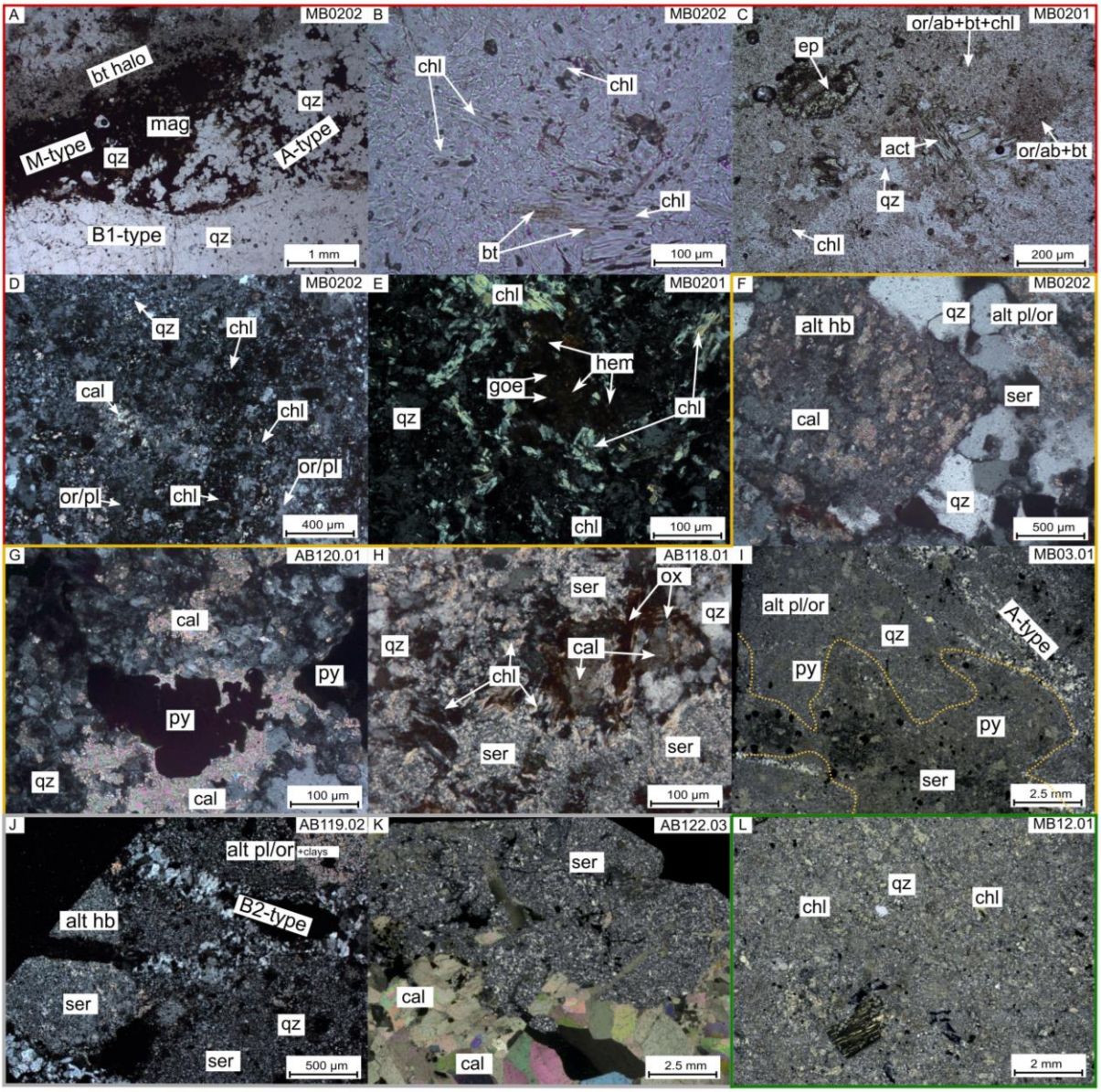

Figure 26: Alteration assemblages of the host-rock (granodiorite) in thin section. A–E. Potassic alteration associated with A/M- and B1-type veins, overprinted by propylitic to sericitic alteration around C/D-type veins. Biotite halos are common around A/M- and B1-type veins, with hornblende altering to biotite, chlorite, epidote, and calcite. Biotite itself is altered to chlorite, while plagioclase transitions to orthoclase or albite. F–I. Sericitic alteration associated with D-type veins, overprinting earlier potassic alteration, with sericite replacing amphiboles and phyllosilicates along with disseminated pyrite and calcite. Thin sections often show alteration fronts (yellow dashed lines). J–K. Sericitic to argillic alteration with feldspar and phyllosilicate replaced by sericite and indistinct clay (kaolinite), pervasive with quartz, pyrite, and calcite. This alteration is commonly associated with E1/E2-type veins. L. Propylitic alteration characterized by quartz, chlorite, actinolite, epidote, calcite, albite, and magnetite.

A. Biotite/orthoclase alteration (destructive) - Potassic alteration

The rock is light brown, with recrystallized quartz grains, secondary biotite (shredded), rare relicts of phenocryst hornblende, rare actinolite, plagioclase altered in orthoclase/albite (Figure 24 A-C, I, Figure 26 A-E). The magmatic texture is absent. It is spatially linked to the porphyry stock. The observation of “fresh” potassic altered rocks is rare, often an association of sodium to calcium minerals (epidote, chlorite, calcite) is present with a greenish color (Figure 24 A). Overprinting is common in this porphyry.

B. Sericitic alteration

The outcropping rock is yellow to whitish and formed some topographic depression, with friable outcrop, muddy, with a surrounding smell of sulfur (Figure 24 D, E, K). Sericite and pyrite are the diagnostic phases, but kaolinite and secondary quartz can be present. K-feldspars are altered to sericite. Sulfide minerals, mainly pyrite, are widespread throughout the sericitic zone and are spatially related to hydrothermal quartz veins (Figure 26 J-K). It is particularly intense, pervasive and extends into the adjacent lithologies (e.g. rhyolite). This alteration style surrounds the center of the porphyry stock and is partly overprinted by an argillic alteration (see below) (Figure 24 K, L).

C. Chlorite-sericite alteration

Some spatial textures and mineral transitions between potassic and sericitic alteration can be observed with a transition of concentration of chloritization of primary and secondary biotite (and amphiboles) to a more intense alteration with sericite which can be described as chlorite-sericite alteration (Figure 25 B-E). They are spatially linked to the reopening of quartz veins part of the stockwork. The altered rock is displaying a dark green color and can be confused by potassic alteration overprinted by propylitic alteration (see below) (Figure 24 B, C).

D. Argillic alteration

White, yellow to pink colored rocks, are associated to topographic depression, with muddy friable outcrop (Figure 24 K, L). It is particularly well developed at the north porphyry stock. This alteration is spatially linked to late epithermal veins and NNW-SSE fractures associated with silicified breccia. Petrographic evidence indicates that it superimposed on earlier alteration. The boundary between argillic and sericitic alteration is not well defined; this is the reason why the alteration map only displays the sericitic alteration (Figure 23). The major constituents of the argillic zone alteration are kaolinite, quartz, sericite and less abundant calcite with disseminated pyrite. The characteristic replacements are those of biotite, amphiboles, and feldspars by kaolinite, sericite and calcite.

E. Chlorite-epidote alteration – Propylitic alteration

Light to dark green colored outcrop, displaying magmatic textures in the outer part of the porphyry stock, particularly at the West side of the site (Figure 23, Figure 24 A). This alteration is characteristic of the outer part of the hydrothermal system and is well developed in the western part of the granodiorite (Figure 23). The major constituents of the alteration assemblage are microcrystals of quartz (30 %), amphibole, biotite mostly altered into chlorite, epidote and calcite (40 %), plagioclase/orthoclase altered in albite/anorthite (25 %), disseminated magnetite and pyrite (5 %). Mafic minerals (hornblende, biotite) have been altered to chlorite, epidote and calcite, whereas plagioclase is replaced mainly by sericite (Figure 26 L). It seems relevant that the center part of the porphyry system where potassic alteration can be observed, is mostly overprinted by this alteration, and shows a mixture between both types of

alteration. These zones display sodi/calci-potassic minerals, as mixed feldspars (plagioclase/orthoclase/albite), rare hornblende mixed with actinolite, biotite (and secondary biotite) altered into chlorite, epidote, calcite, magnetite, some sericite and calcite, and disseminated without any conservation of the magmatic texture.

2.3.1.3. Porphyry style vein succession

A re-evaluation of alteration types and vein crosscutting relations at Pagoni Rachi conducted in this study suggests that six main stages of hydrothermal circulation were associated with the formation of mineralization.

A. Stage 1 – Early wavy quartz-pyrite/magnetite veins (A- and M-type veins)

The early quartz veins are continuous to discontinuous, wavy, with variable thickness (Figure 24 B, Figure 27 A, B). They can rarely display reopened features in the central part. Most of vein are barren and consist primarily of quartz (90 – 95 %), magnetite with hematite rim, rare biotite, chlorite, and epidote. When mineralized they can comprise metal bearing minerals consisting of pyrite, chalcopyrite (5-10%) (Figure 27 A-F). Oxides and sulfides are disseminated within the veins or along discontinuous lines/planes visible in thick sections, they may also be parallel to the edge of certain quartz grains. The presence of orthoclase, secondary biotite accompanied by chlorite in the host-rock and an absence of magmatic texture at the contact suggest a potassic alteration of the granodiorite (Figure 27 A, B). There are mostly observed at the bottom of the creeks (Figure 23).

Quartz crystals are granular, xenomorphic, and lack any preferential orientation. Their size ranges from tens of microns to several hundred microns, displaying a seriate distribution (Figure 27 C, H). The edges of the quartz grains are continuous and may be either sharp or rounded. Under plane-polarized light, individual grains may appear uniform, but under cross-polarized light, they may reveal several distinct domains with varying extinction orientations. Grain boundaries can appear either diffuse or well-defined, with polygonal boundaries indicating the presence of sub-grains. These features are characteristic of dynamic recrystallization of quartz via SubGrain Rotation (SGR), a process that is widespread and intense throughout the vein (Figure 27 G, I). Locally, quartz grains ranging from a few microns to tens of microns show xenomorphic shapes with interlobate edges, where opening angles can reach extremes. These grains exhibit sinuous boundaries, associated with dynamic recrystallization by Grain Boundary Migration (GBM) (Figure 27, I). These quartz microtextures serve as indicators of deformation conditions during dynamic recrystallization, typically occurring at relatively high temperatures or rapid deformation rates (Stipp et al., 2002a, b; Passchier and Trouw, 2005).

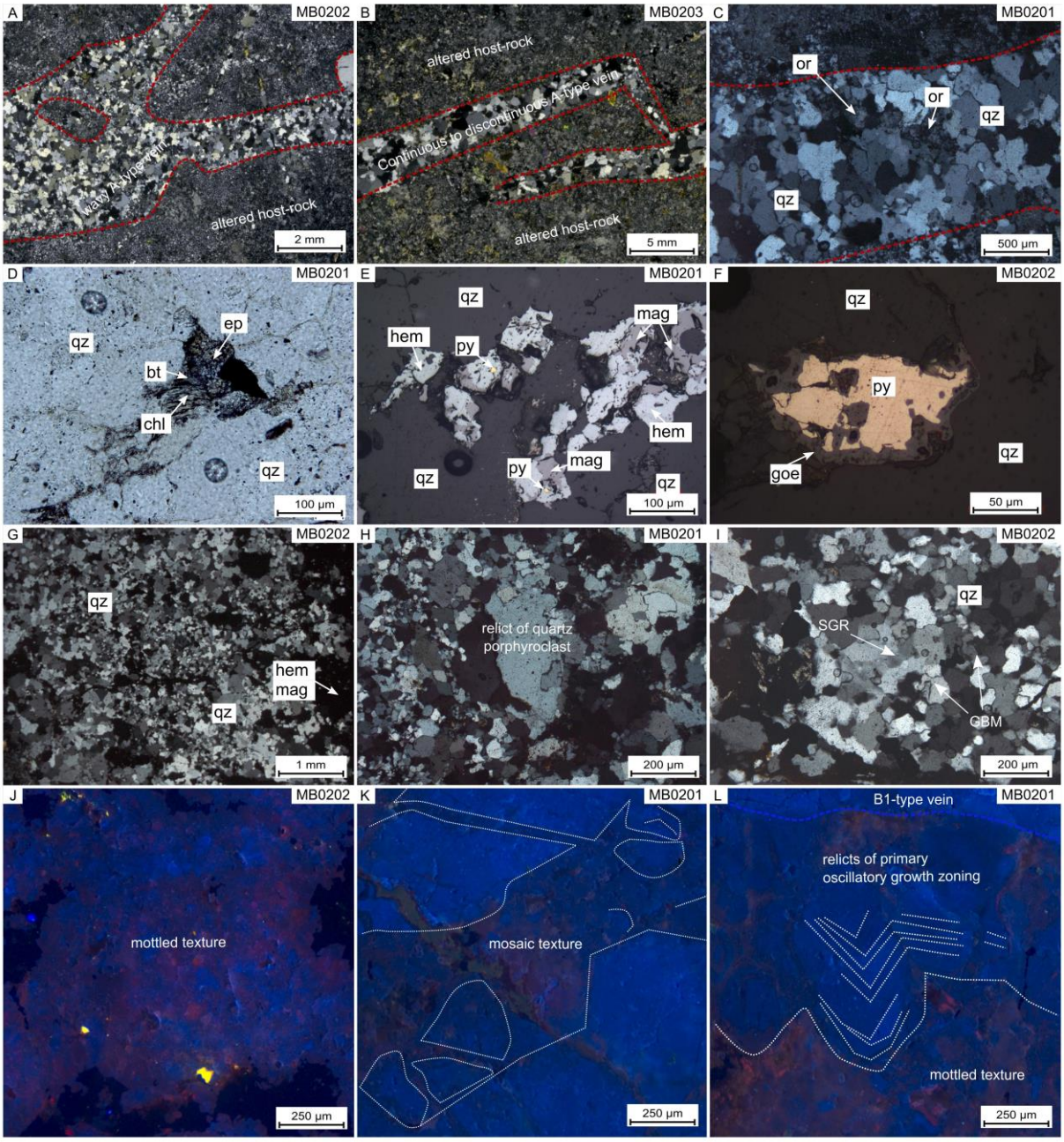

Figure 27: Petrography of A-type veins. A. Continuous, undulating A-type veins with irregular, asymmetrical edges and variable thickness (millimeter to centimeter scale) (XPL). B. Discontinuous A-type vein (XPL). C. A-type vein with orthoclase in the core (XPL). D. Quartz inclusions containing biotite, epidote, and chlorite (TL). E. Magnetite inclusions with hematite rims surrounded by quartz margins (RL). F. Pyrite with goethite rims between quartz margins (RL). G. A-type veins consisting of granular quartz (XPL). H. Relicts of quartz crystals surrounded by dynamically recrystallized quartz (XPL). I. Subgrain rotation texture and grain boundary migration in dynamically recrystallized quartz grains (XPL). J. Mottled cathodoluminescence (CL) texture in quartz grains associated with dynamically recrystallized quartz. K. Mosaic CL texture of quartz associated with recrystallized quartz and fluid circulation. L. Relicts of primary oscillatory growth zones in CL-textured quartz adjacent to B1-type veins (north) and mottled CL-textured quartz domains (south).

Quartz crystals display a range of color hues (from reddish to blue) and varying intensities (from dark to bright) by using CL-imaging (Figure 27 J-L). The luminescence and associated structures are heterogeneous within wavy quartz-veins. Several zones can be distinguished based on the previously described microtextural domains of quartz: (i) Some areas exhibit mottled and mosaic CL patterns in dark red tones (brown), with occasional bluish streaks. Zones with chaotic red zoning are spatially

associated with areas of intense dynamic recrystallization, particularly SubGrain Rotation (SGR) and, notably, Grain Boundary Migration (GBM) (Figure 27 J); (ii) Other areas show ghost band textures, primarily at grain boundaries, near domains with moderate dynamic recrystallization intensity, especially of the SGR type (Figure 27, K); (iii) In rare cases, chevron zoning textures are observed, suggesting oscillatory growth patterns in quartz, with shades of blue. Domains displaying chevron zoning, which lack any clear orientation within the vein, are spatially linked to areas with little to no dynamic recrystallization or with moderate intensity. These CL textures may represent remnants of oscillatory growth zonation in original quartz during vein formation (Figure 27 H, K, L). The texture and elemental composition could have been inherited from older quartz that underwent dynamic recrystallization, leading to the formation of subgrains, or altered by deformation, resulting in the homogenization of the chemical signal. It is important to note that wavy quartz-veins veins may have been influenced by subsequent fluid circulation, which formed later vein generations.

At the center of the site (Middle creek), a sparse stockwork of A-type veins is intersected by granular, discontinuous M-type veins, which are cut by straight banded quartz veins with copper sulfides (Figure 23).

Thin magnetite-veins varying in thickness (1 – 5 mm), discontinuous to continuous, irregularly shaped, asymmetrical, with sinuous and diffuse edges crosscut the previous quartz veins (Figure 24 B, Figure 28 A-C). They are composed of magnetite with hematite rims (95 %), and small amount of biotite, chlorite, epidote, - and pyrite, chalcopyrite included in magnetite. Epidote and biotite altered into chlorite are located between oxide grains. The magnetite grains are approximately 50µm in size (Figure 28 D-F). The oxide grains take the shape of the quartz margins of previous quartz veins, suggesting a sub-contemporaneous to posterior emplacement (Figure 28 A, C). Quartz from wavy quartz-veins at

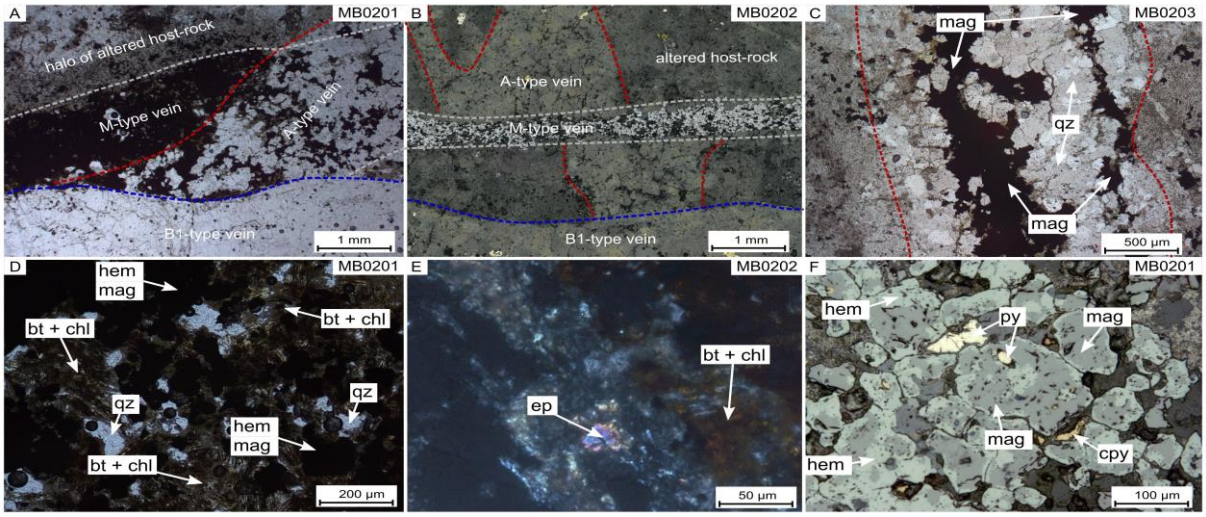

Figure 28: Petrography of M-type veins. A. Magnetite-hematite vein crosscutting A-type veins (TL). B. M-type vein crosscutting and offsetting a wavy A-type vein. Associated with potassic alteration (RL). C. M-type vein reopening an A-type vein; magnetite grains conform to the shapes of quartz grains in the A-type vein (TL). D. M-type vein with magnetite and hematite rim, accompanied by biotite, chlorite, and quartz filling the spaces between magnetite grains (TL). E. M-type vein with epidote, biotite, and chlorite between magnetite grains (XPL). F. M-type vein with magnetite rimmed by hematite, including pyrite and chalcopyrite inclusions (RL).

contact with the magnetite vein present a dark red luminescence in CL-imaging. The presence of orthoclase and secondary biotite accompanied by chlorite in the host-rock with an absence of magmatic texture at the contact of magnetite veins suggests a potassic alteration of the granodiorite. They are in the same area as the quartz-pyrite type veins and the potassic alteration zone.

B. Stage 2 – Straight banded quartz veins (B1-type veins)

Straight banded quartz veins crosscut the wavy quartz-veins and magnetite veins. They host most of the minerals forming the mineralization of interest at Pagoni Rachi. They are continuous, planar, with constant thickness (millimetric to centimetric), sharp edges, and sometimes slightly wavy (Figure 24 B, C, Figure 29 A-C). They exhibit central axial symmetry and have a banded texture, emphasized by the presence of chevron-like opaque minerals lines suggesting a syntaxial structure. They often display reopening features in the central part of the vein, linked to quartz extremity fractured and attributed to

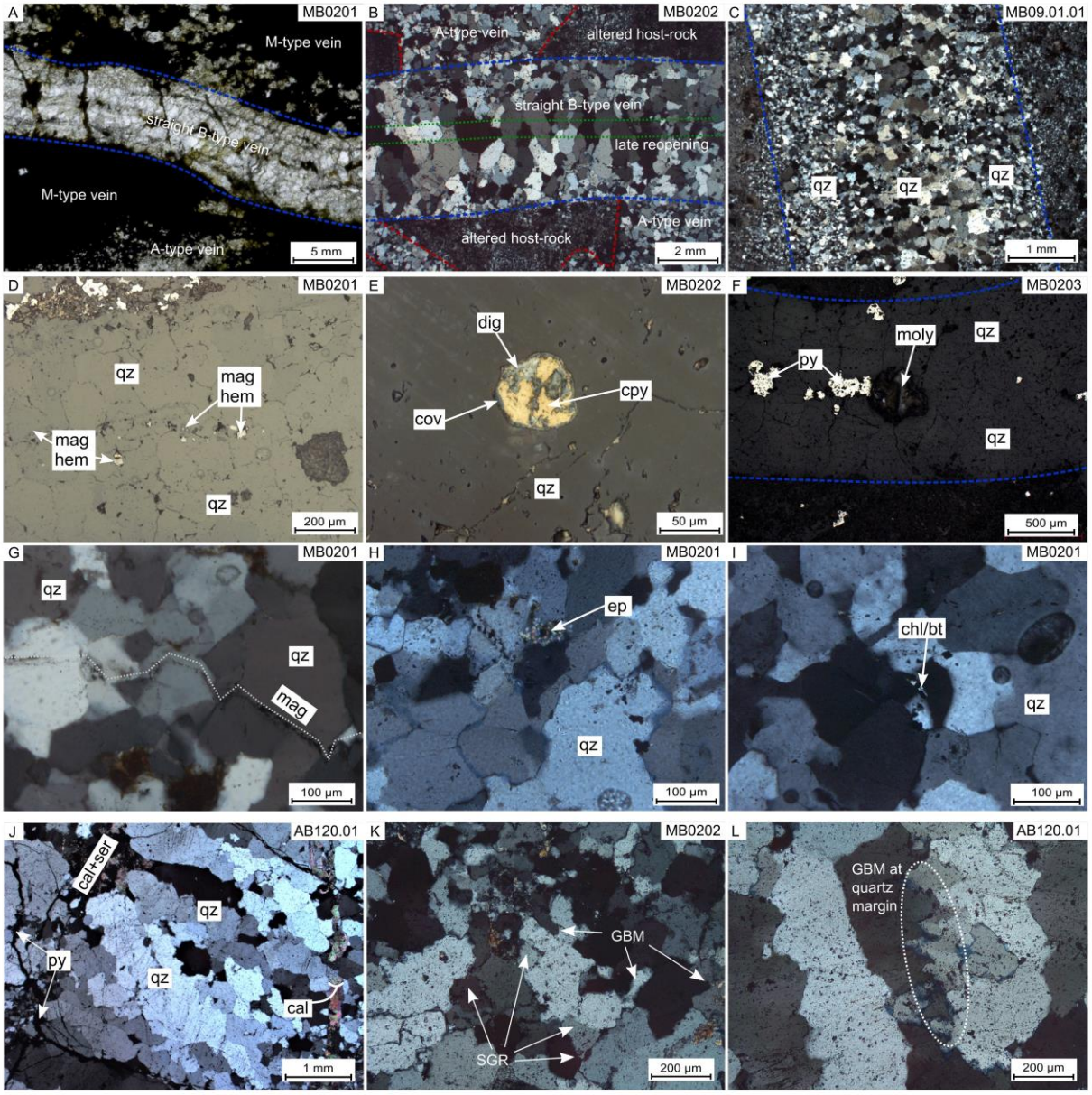

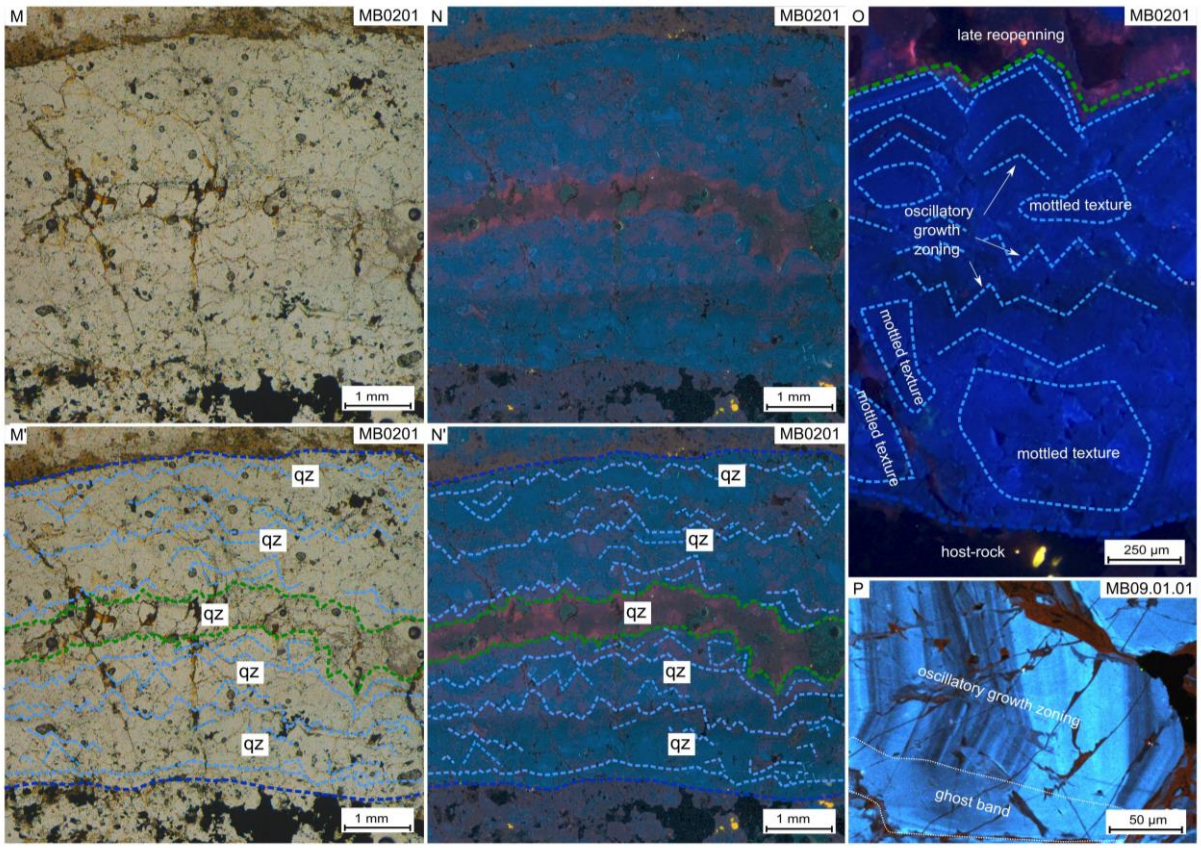

Figure 29: Petrography of B1-type veins. A. Ribbon-textured quartz vein crosscutting M-type and A-type veins, with a central axial symmetry (TL). B. Straight B1-type quartz vein with late reopening (green) crosscutting and offsetting an A-type vein. Associated with potassic alteration (possibly overprinted by propylitic alteration) (XPL). C. B1-type vein with straight edges and a grain size evolution in quartz, from granular grains (~tens of microns) at the margins to elongated grains (~hundreds of microns) in the central portion (XPL). D. Magnetite, hematite, and pyrite grains (a few microns to tens of microns in diameter) aligned between quartz grains in B1-type veins (RL). E. Chalcopyrite grains between quartz grains, altered to digenite and covellite (RL). F. Pyrite and molybdenite located in the central portion of a B1-type vein (RL). G. Chevron-shaped magnetite inclusions aligned with quartz growth zoning, highlighting the ribbon texture of these veins (XPL). H. Epidote inclusions in quartz (XPL). I. Chlorite/biotite inclusions in quartz (XPL). J. Central portion of a B1-type vein with elongated quartz grains featuring irregular, interlobate boundaries. A reopening filled with calcite and sericite is visible in the NW part of the image, with a calcite vein crosscutting the quartz vein in the eastern portion of the image. Preferential mineral orientations are orthogonal to the vein edges (XPL). K. Quartz crystal with extinction variation, highlighting a subgrain rotation (SGR) texture, common in quartz but rarely interlobate with grain-boundary migration (GBM) texture (XPL). L. Elongated quartz grains at the edges with interlobate GBM texture in the central portion of the vein (XPL). M. Straight-edged B1-type veins, and M' ("bare") (TL). B1-type veins with oscillatory growth zoning (dashed blue lines) visible in cathodoluminescence (CL). N. Bare vein; N'. B1-type vein with oscillatory growth zoning in blue chevron patterns within quartz crystals, indicating growth from the margins toward the vein core and subsequent reopening with reddish quartz in the central portion (green dashed lines). O. Cross-section of a B1-type vein showing oscillatory growth zoning in chevron patterns with blue color bands. Mottled textures are associated with dynamically recrystallized quartz (CL). P. Quartz crystals with oscillatory growth zoning and "ghost bands" at grain boundaries, linked to dynamically recrystallized zones with GBM textures (see L) (CL-SEM).

latter veins (see below) (Figure 29 A, M, M'). They consist of quartz (90 – 95 %), along with magnetite, hematite, pyrite, chalcopyrite, molybdenite (interlayered with rheniite sheets – Voudouris et al. 2013a), bornite, covellite, digenite, chlorite, epidote, and biotite (Figure 29 D-I). Covellite and digenite form rims of bornite or chalcopyrite grains. Most metal bearing minerals such as chalcopyrite and molybdenite are often located in the central part of the veins and associated with the reopening features or between the quartz margins and but rarely in inclusion of quartz (Figure 29 D-F). They are constitutive of the central porphyry stock with the same alteration assemblage of the A- and M-type veins.

Multiple structural and microtextural domains are observed in quartz of the straight banded quartz-veins: (i) At the edges of the veins or in contact with zones of weakness (e.g., fractures or latter veins), quartz crystals are anhedral to granular and lack any preferential crystallographic orientation (Figure 29 C). Their size ranges from a few tens of microns to around one hundred microns, with a seriate distribution. The granular quartz shows no preferential crystallographic orientation and may contain quartz subgrains with diffuse to well-defined boundaries, forming contiguous grains. These subgrains are associated with SubGrain Rotation (SGR) dynamic recrystallization (Figure 29 K). Locally, interlobate boundaries between quartz grains are visible, suggesting dynamic recrystallization by grain boundary migration (GBM); (ii) In the central part of the veins, quartz crystals are elongated, subhedral to euhedral, with frequent interlobate boundaries, and display a preferential orientation of the c-axis orthogonal to the vein margins (Figure 29 J). Their sizes range from a few hundred microns to several millimeters with a homogeneous distribution. Elongated quartz display, with the CL imaging, oscillatory growth zoning, in a chevron pattern with variations of hues and intensity of blue which follow the opaque chevron-like bands. This suggests the growth of quartz crystals from the border towards the center of the vein, so a syntaxial growth within the vein (Figure 29 M-O). The interlobate grain structures indicate intense and localized dynamic recrystallization by GBM (Figure 29 L). These structures are spatially associated with CL-ghostband texture domains (Figure 29 P).

Progressive evolution from undulous discontinuous veins to straight planar, continuous veins from wavy quartz-veins to straight banded-quartz veins.

C. Stage 3a – Reopenings associated to sulfide mineralization (C-type veins)

In the central part of the B1-type veins, CL imaging revealed reopening quartz-sulfides-structures in straight banded quartz veins (Figure 29 M-N', Figure 30 A-E'). These veins are regularly reopened and exhibit two distinct types of fillings. The first type consists of alteration minerals such as chlorite, sericite, altered K-feldspar, calcite, and magnetite (Figure 30 A-D). The second type contains quartz and small fluorite crystals (approximately 10 microns) located at the interfaces with the straight B1-type veins quartz crystals (Figure 29 M-N', Figure 30 E-F'). Both types of filling also contained most of the metal-bearing minerals, such as chalcopyrite, pyrite, chalcopyrite, bornite and molybdenite, which constitute the mineralization of Pagoni Rachi. These reopening structures obliterate the extremities of the B1-type vein quartz (Figure 29, O, Figure 30 A). Quartz crystals do not show any dynamic recrystallization features and display faint red luminescence with subtle growth zoning, characterized by minimal variations in CL intensity, in contrast to the blue luminescent straight banded quartz-veins quartz with distinct oscillatory growth zoning (Figure 29 M-O, Figure 30 D', E'). The distinction between the quartz in the reopening structures and the one of the banded quartz veins is most noticeable in CL but difficult to observe under natural light. The growth zoning in the reopening quartz is weakly

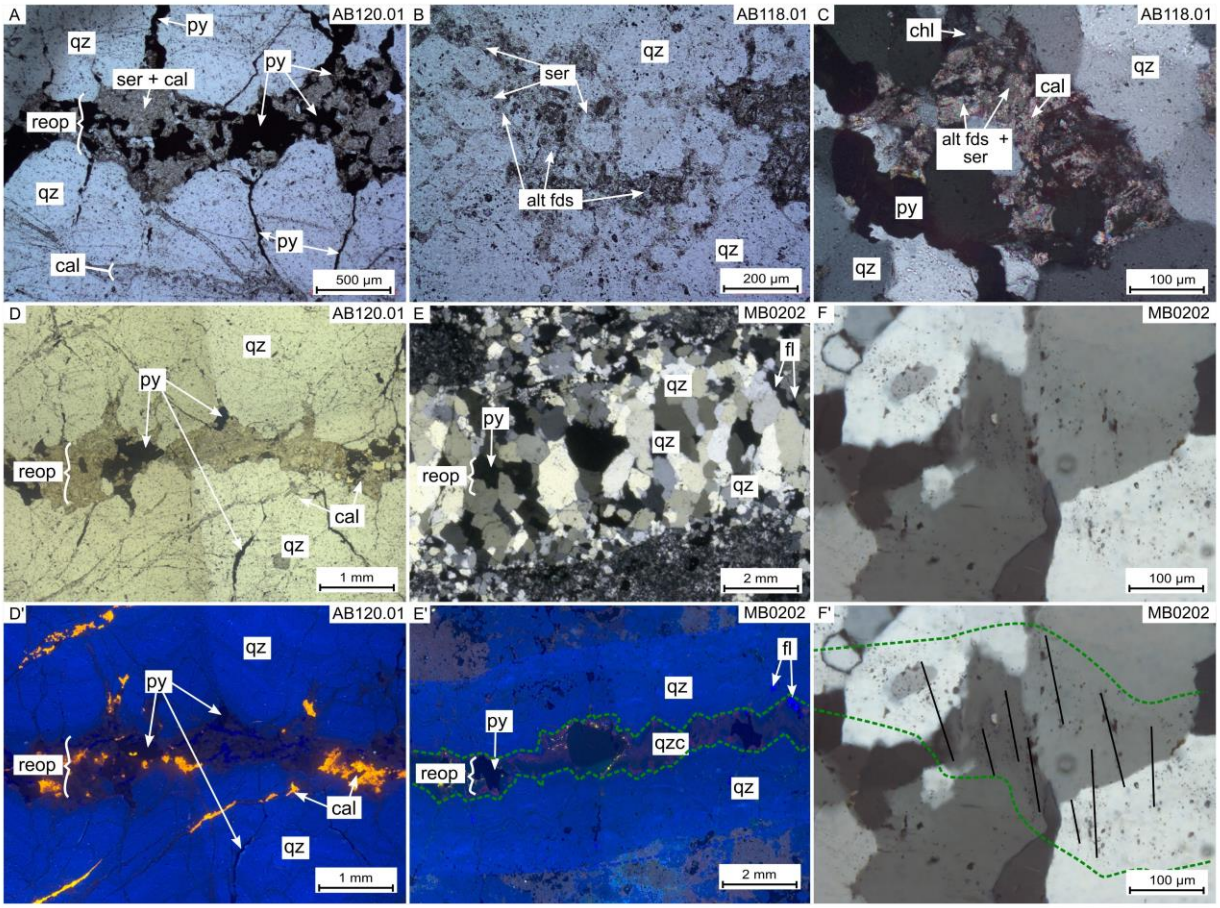

Figure 30: Petrography of C-type veins and reopenings. A. Reopening of B1-type veins with sericite, calcite, and disseminated pyrite, associated with fractures along the vein margins (TL). B. Sericite-filled reopenings resulting from feldspar alteration (TL). C. Reopenings filled with altered feldspar (to sericite) and calcite, with pyrite grains (XPL). D. Reopening filled with pyrite, calcite, and sericite (TL). D'. Reopening crosscutting the quartz terminations in B1-type veins with truncated oscillatory growth zoning (CL). E. B1-type veins with central reopenings (green margins), associated with pyrite and sulfides (XPL). E'. Reopenings visible in CL as a contrast between the reddish quartz (associated with sulfides) in the central part of the vein and the truncated oscillatory growth zones at the quartz terminations, suggesting fracturing during the reopening. F. Fluid inclusion planes near the micron scale, appearing biphasic (liquid-vapor) and oblique to the vein walls in reopening zone (XPL). F'. Bare image, annotated image with green margins for reopenings and black lines for fluid inclusion planes (XPL).

perceptible and suggests crystal growth from the boundary toward the center of the reopening. No veins have been observed corresponding to this reopening event in the surrounding rock. They are spatially linked to the concomitant straight banded quartz veins and the porphyry stock. But this event is spatially linked to a chlorite-sericite alteration style assemblage, with chlorite in alteration of biotite and amphiboles, small amount of sericite in alteration of feldspars, calcite and epidotes, no magmatic structures are observable within the host granodiorite (Figure 26 A-E).

D. Stage 3b – Massive pyrite veins and pyrite filled fractures (D-type veins)

To the north of the site (Figure 23), massive pyrite veins (D-type) of varying thickness and discontinuous, with friable white to yellow host rock, emanate a strong sulfur smell (Figure 24, D, Figure 31). Massive pyrite veins crosscut the previously existing veins. These veins are irregularly shaped, with variable thickness (ranging from millimeter to centimeter), sharp and irregular borders, slightly

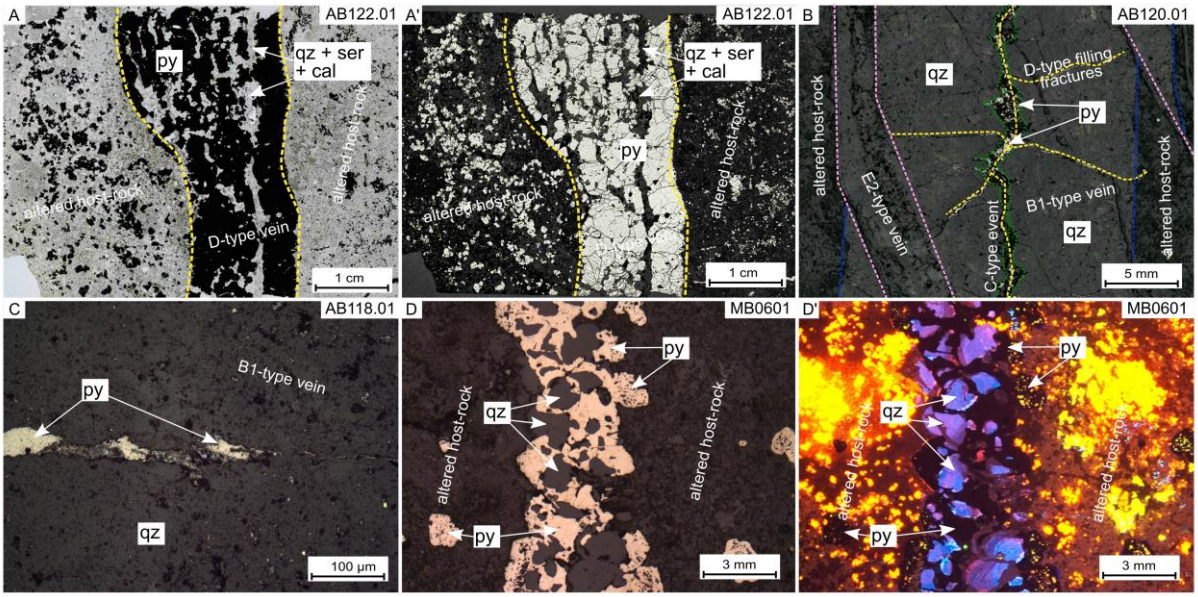

Figure 31: Petrography of D-type veins. A. Massive granular pyrite vein associated with sericitic alteration (sericite, pyrite, quartz) (TL: Transmitted light). A'. Same in reflected light (RL). B. B1-type vein with C-type reopening, introducing sericite, calcite, and fractures filled with pyrite orthogonal to the vein walls and in the central portion. This may be confused with C-type reopenings and is crosscut by a carbonate vein (E2). C. Thin pyrite veins crosscutting B1-type veins. D. Short pyrite veins incorporating quartz grains with oscillatory growth zoning (possibly B1-type vein?) in RL. D'. Same in CL, associated with sericitic alteration (sericite, pyrite, calcite, quartz).

undulating, and sometimes discontinuous (Figure 24, D, Figure 31 A, A'). They consist mainly of massive granular pyrite, with small amounts of magnetite/hematite, and rarely quartz. These veins are also found filling fine fractures that crosscut earlier veins, often following preexisting weakness planes, typically located in the central parts of straight banded quartz veins or between quartz grain boundaries, as seen in sample AB120.01 (Figure 31 B, C). Occasionally, the pyrite encompasses fragments of quartz from small quartz veins, and the quartz retains its oscillatory growth zoning in CL (Figure 31 D, D'). These veins are observed from the center of the porphyry stock as fracture fillings, extending northward where they are more developed. The alteration assemblage of the surrounding rock consists of quartz, sericite, pyrite, and calcite, suggesting sericitic alteration, with the initial rock structure being nearly unrecognizable. A gradation in the intensity of alteration is visible from the porphyry stock, with low intensity at the central part of the site and increasing intensity and pervasive development toward the north (Figure 23, Figure 24 K).

E. Stage 4 – Massive stockwork of barren banded quartz veins (B2-type veins)

Along the creek beds, falling rocks consisting of dense stockworks (>90% by volume) of banded quartz veins (B2-type) with wavy texture cover the ground (Figure 24 F). No outcrop of such objects has yet been observed either by me or by colleagues who participated in previous explorations.

Banded quartz veins form a massive stockwork at summit part of the three principal hills of Pagoni Rachi and spatially at the summit of the porphyry structure (Figure 23, Figure 24, E). They are irregular and display sharp borders, constant thickness which run from 0.5 to 5.0 cm width, central axial pseudo-

symmetry, continuous, slightly undulous, sharp margins, and numerous sporadic openings in central parts (old, altered mineral disappeared or real open space?), giving them the banded appearance (Figure 24 E, F, Figure 32 A). They mainly consist of quartz (95 %), minor sericite, calcite, and supergene minerals (e.g. goethite and hematite).

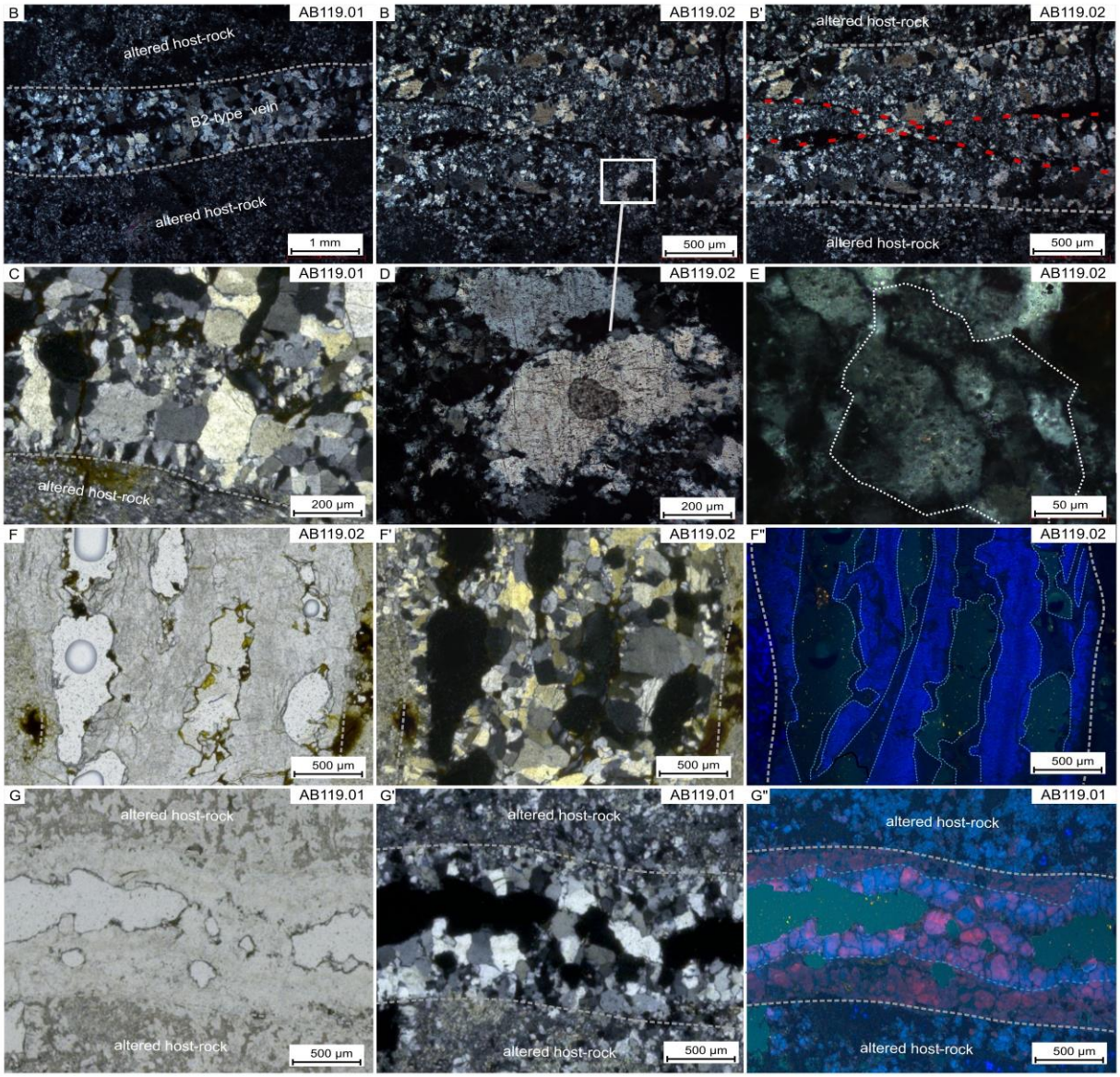

Figure 32: Petrography of B2-type veins. A. Straight to slightly wavy veins with sporadic central openings, quartz with seriate distribution (XPL). B. B2-type vein with irregular edges and curvilinear fractures in the central portion, causing offsets of several tens of microns. Bare image. B'. Annotated image: gray lines (vein edges) and red dashed lines (fractures) (XPL). C. Variations in quartz size and texture at the vein margins, ranging from comb quartz (~tens of microns) to blocky quartz, with variable grain sizes in the central portion (XPL). D. Dynamically recrystallized quartz with bulging (BLG) texture, showing small grains with orientations differing from the main central grain (XPL). E. Quartz grains with subgrain boundaries exhibiting variable orientations, visible through extinction angles (XPL). F. B2-type vein in TL (Transmitted Light) with sporadic openings, several hundred microns long and wide, unfilled, with botryoidal quartz textures. F'. Same vein in XPL, with seriate quartz distribution, ranging from a few microns to several hundred microns. F''. In CL, showing zoning from intermediate-blue hues in the central vein portion to lighter-blue hues, transitioning progressively and homogeneously to dark-blue or extinguished zones at the edges, appearing as quartz overgrowths not discernible in F and F'. G. B2-type vein in TL, with botryoidal quartz textures. G'. Same vein in XPL (cross polarized light), showing seriate quartz distribution as in F'. G''. In CL, showing intermediate-blue to reddish hues in the central vein portion, transitioning progressively to heterogeneous light-blue zones, and finally to dark blue/red extinguished zones, interpreted as quartz overgrowths not discernible in G and G'.

These massive stockworks, several hundred meters in diameter and tens of meters thick, dominate the landscape with local topographic summit (Figure 23). A clear boundary is visible from south to north, with the massive stockwork to the south and a stockwork similar to that observed along the creeks (Middle and West creeks) to the north, with A-type veins, granular, M-type veins, and B1-type veins (Figure 24 M). The associated host rock is darker greenish but lighter than that found in the valley floor. This boundary is observable due to the abrupt transition from a relatively irregular rocky environment to a "smooth" flat area. The smell of burning and remnants of the fire make it difficult to distinguish any sulfur odor.

The quartz grains exhibit seriate distribution, ranging from a few tens to several hundred of microns with a shape going from subhedral to xenomorphic with locally rounded or acicular shape, with smaller grains at margin of bigger quartz grains Figure 32 B-C). They present weakly recrystallized structures with generalized BLG to weak SGR textures which are locally observed within the veins at proximity of fractures (Figure 32D, E). In CL-imaging, quartz display dark blue luminescence in central part progressively going medium bright blue at veins margins to a sharply dark blue band. This supports the macroscopic "banded" texture (Figure 32 F-G"). The variation of CL hues and intensity is not linked to quartz texture, even when quartz show dynamic recrystallization features. Numerous fractures crosscut these veins associated with a grain size reduction of nearby quartz and possibly associated with dynamic recrystallization (Figure 32, B, B').

No clear link has been made with the other type of vein due to an absence of relative chronology features, crosscutting. However, they are always linked to a pervasive sericitic alteration. They are associated with intense pervasive sericitic alteration, containing sericite, quartz, minor amount of chlorite, calcite, clays, and supergene iron oxide. The magmatic texture is preserved thanks to the framework of quartz skeleton primary minerals constituting the rock (Figure 24 E, K Figure 26 J). They are structurally at the apex part of the porphyry structure (Figure 23), and the density of B2-type veins forming the massive stockwork do not allowed the differentiation of the thin crosscutting sequence of vein formation.

2.3.1.4. Epithermal style vein succession

A. Stage 1 – Miarolitic quartz-sphalerite-galena-chalcopyrite veins (E1-type)

To the north of the site (Figure 23), quartz-galena-sphalerite-chalcopyrite and calcite veins are observed (E1- and E2-type), with a host rock that is grayish to pinkish and sometimes slightly friable (Figure 24 G). Miarolitic quartz-sphalerite-galena-chalcopyrite-veins constitute the first epithermal stage of the Pagoni Rachi system. They crosscut the previous vein types. They are straight, continuous, planar, with frequent branching (Figure 33A, A', B). They present constant thickness, sharp borders, a miarolitic texture with comb quartz at the walls and frequently contain millimetric to centimetric host-rock enclaves (Figure 24 G, Figure 33 A, A', B). The veins consist of elongated euhedral quartz and

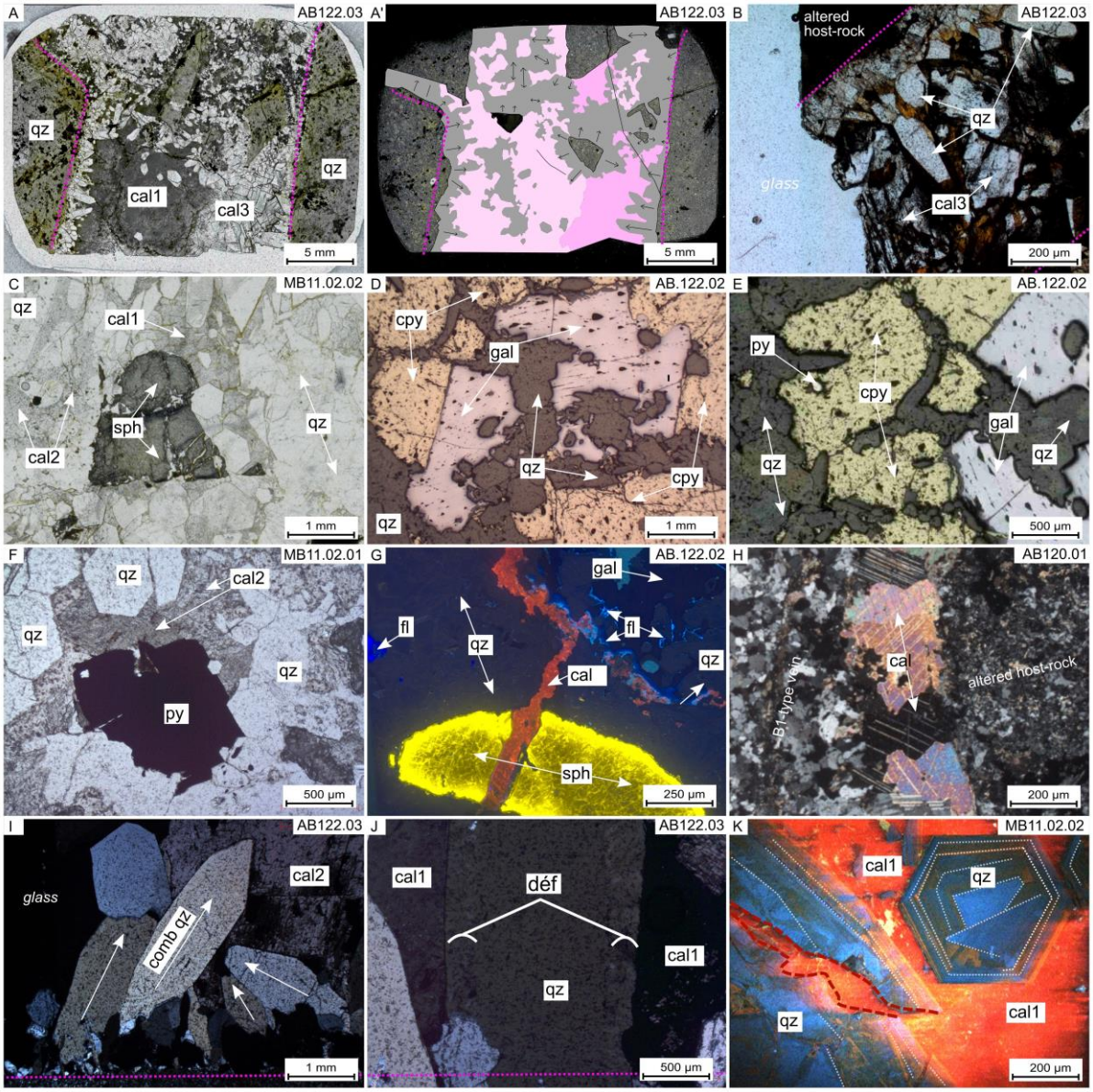

Figure 33: Petrography of E1-type veins. A. Thin section of E1-type veins with geodic texture and comb quartz, calcite fillings (cal1, cal2) with some host rock inclusions on which the quartz grows TL). A'. Same as A, annotated image: gray = quartz; black arrows = quartz growth direction; light pink and dark pink zones = carbonate generations; dashed pink lines = vein margins. B. Thick section of E1-type vein showing elongated, euhedral comb quartz in contact with calcite (TL). C. Subhedral sphalerite conforming to the contours of euhedral quartz grains, with calcite surrounding the sphalerite (TL). D. Euhedral galena incorporating quartz grains and conforming to their contours, with chalcopyrite enveloping the galena and following its shapes (RL). E. Chalcopyrite surrounding quartz grains, including pyrite inclusions (~10 µm in diameter (RL)). F. Subhedral pyrite conforming to quartz contours, with calcite conforming to the pyrite outlines (TL). G. Sphalerite grain located between quartz grains, crosscut by a thin calcite vein. Fluorite is present at the contact between quartz and galena grains (CL). H. Calcite from an E2-type vein crosscutting B1-type veins, showing deformation-associated twinning (XPL). I. Comb quartz at vein margins, with grain size ranging from ~10 µm to 1 mm (XPL). J. Euhedral quartz showing extinction variations at grain boundaries under cross-polarized light (XPL). K. Quartz crystals exhibit oscillatory growth zoning from the core to the grain boundaries. Calcite (cal1) fractures these quartz grains (CL).

oriented orthogonally to the vein margins, base metal minerals, such as sphalerite, galena, pyrite, and chalcopyrite (Figure 32 C-G) (± tennantite ± tetrahedrite ± enargite can be found according to Voudouris et al., 2013a), are found associated to the quartz, as well as small fluorites (10 microns). Quartz sizes range from 100 to x100 microns. Quartz also grows on enclaves of host-rock contained within the veins.

Quartz can be fractured but they do not display any internal deformation (e.g. no dynamic recrystallization textures, no undulous extinction) (Figure 33 A, A', B, I, J). Quartz displays low contrasted growth oscillatory zoning in red tones with low using CL-imaging (Figure 33 K).

The miarolitic cavities are filled by late carbonates veins (Figure 33 A, A') which also crosscut the previous veins in the AB.120.01 sample (Figure 24 C, G, Figure 33 H). They are straight, continuous, with constant thickness, and sharp parallel walls. They consist of euhedral to xenomorphic calcite.

Different generations of calcite are easily discernable, notably thanks to CL-imaging. Indeed, oscillatory growth zonation, altering, bright orange to yellow, to dark red, brown. Possible extinction, no luminescence. There is no preferential orientation of chevron zoning. Some xenomorphic calcite crystals display heterogeneous reddish zones.

The quartz exhibits oscillatory growth zoning in CL, in reddish to bluish tones (Figure 33 K). It is difficult to discern the zoning due to the presence of calcite in contact with the quartz, which presents a high-intensity luminescence that can blur the quartz signal. They are associated with sericitic to argillic alteration (quartz, sericite, kaolinite).

B. Stage 2 – Carbonates veins (E2-type)

These veins are straight, with sharp wall and a constant thickness (0.2-1.0 cm), sometimes filling fractures in porphyry quartz vein types (Figure 24 H, Figure 33 H, Figure 34 A). When they intersect the wavy and straight banded quartz veins, the calcite crystals they contain show cross-twinning or simple twinning typical of the deformation of calcite crystals (Figure 33 H). They consist of calcite, disseminated pyrite within the vein, with sericite (Figure 34 A, A'). Four types of calcite crystal based on CL zoning allow differentiation of different generations/types of calcite crystals, by distinguishing domains with homogeneous CL in red or yellow hues, crystals with oscillatory growth zoning (without preferential orientation). Calcite 1 (cal1) contains euhedral pyrite and small fluorite at the contact of E1-type quartz crystals (Figure 34 B-C'). They show heterogeneous CL zoning in red hues. Calcite (cal2) displaying oscillatory growth zoning (red to brown hues) and euhedral texture. Fluorite is present at the contact between the two first calcite generations (Figure 34 C, C', E, E'). Calcite 3 (cal3) are euhedral and have well-defined oscillatory growth zoning, with zones extending over hundreds of microns (Figure 34 D-F'). Calcite (cal4) are subhedral, crosscut earlier calcite crystals and includes fluorite grains (~10 µm in diameter), without showing any CL-zoning (Figure 34 E-F'). When filling the open space of miarolitic quartz-veins they often break the euhedral quartz crystal.

They are associated with a sericitic alteration (sericite, quartz, pyrite) to intermediate argillic alteration (quartz, kaolinite, sericite), with ghost structures of feldspar filled with kaolin and surrounded by a quartz skeleton, with disseminated pyrites.

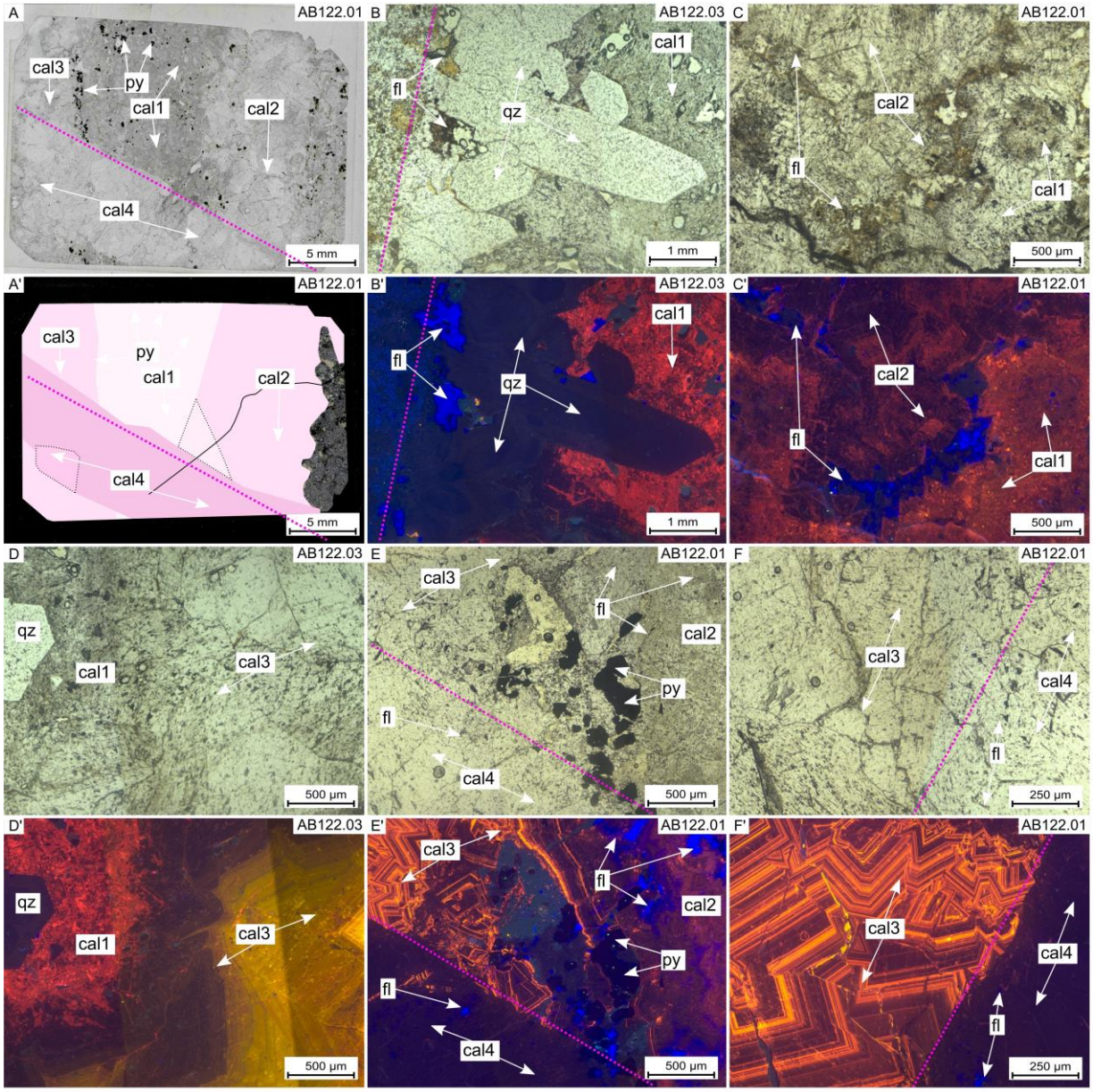

Figure 34: Petrography of E2-type veins. A. Unannotated photo (TL). A'. Annotated photo showing multiple sequences of E2-type veins with calcite: cal1 containing euhedral pyrite is crosscut by cal2, then by cal3, and finally by cal4. (XPL) B (TL), B'. Margin of an E1-type vein with euhedral quartz, including fluorite at the base of quartz crystals in contact with the host rock. Some grains are also located between quartz and calcite (cal1) and show heterogeneous CL zoning in red hues. C, (TL) C'. Calcite (cal1) with heterogeneous CL and cross-polarized textures, in contact with calcite (cal2) displaying oscillatory growth zoning (red to brown hues) and euhedral texture. Fluorite is present at the contact between the two calcite generations. D (TL), D'. Contact between calcite (cal1) and calcite (cal3) with a gradual transition from heterogeneous to euhedral texture, showing oscillatory growth zoning (brown/black to yellow hues). E (TL), E'. Contact between calcite generations with oscillatory growth zoning in red and brown hues. Fluorite is observed at the interface between calcite (cal3) and pyrite. Calcite (cal3) has well-defined oscillatory growth zoning, with zones extending over hundreds of microns. Calcite (cal4) crosscuts earlier structures and includes fluorite grains (~10 µm in diameter). F (TL), F'. Calcite (cal3) with well-defined oscillatory growth zoning crosscut by euhedral calcite (cal4), which shows no CL zoning.

C. Faults and breccias

A few faults, cutting the vein structures, show an NNW/SSE orientation with vertical dip. Although striations were observed on the fault mirrors, the displacement direction could not be determined (Figure 35 A).

At the tops of the hills, large, rather planar quartz masses, of meter-thick and decametric length, slightly protrude from the landscape (Figure 35 B). These "small" topographic walls appear as massive silicified breccias and are oriented NNW-SSE. Massive, silicified brecciated faults crosscut any of the previous veins, even the massive stockwork. This later structure is discernable from the landscape by walls a few meters high and wide. These are observable specifically on the hill sides. A thin section displays a complex vein succession with numerous reopening (Figure 35 C). They display a similar NNW/SSE orientation to epithermal veins which display similar orientation which are parallel to major local faults.

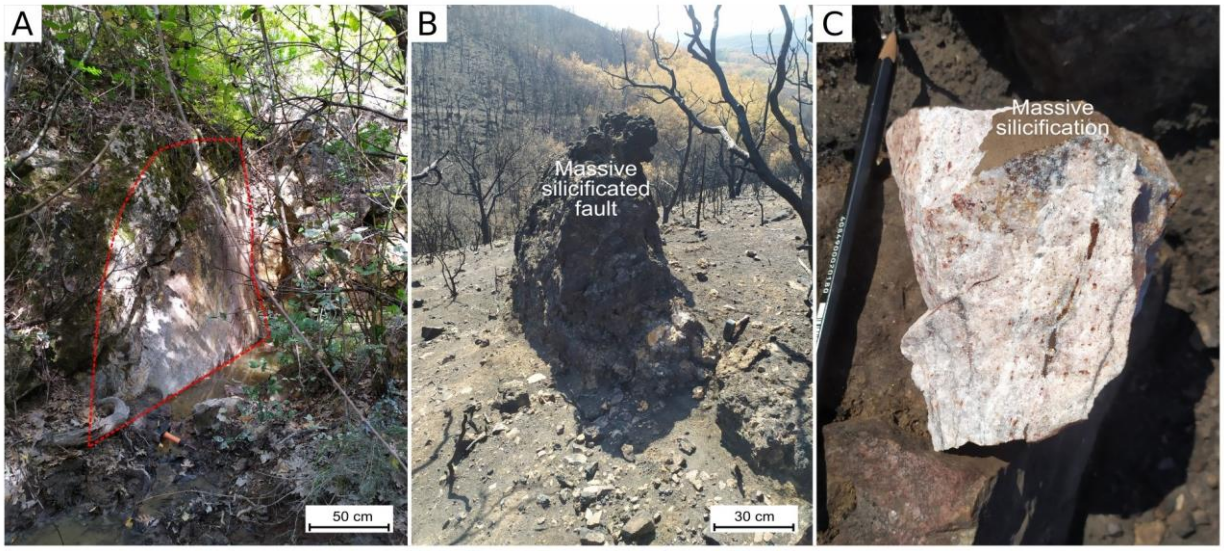

Figure 35: Fault and silicified breccia at Pagoni Rachi. A. Fault plane (red dashed lines) oriented N160, 80E. B. Meter-thick silicified fault zone cutting the topography, oriented N160, subvertical. C. Silicified fault fragment with milky quartz and iron oxides.

All these previous observations lead to the following paragenetenic sequence, which will be discussed later.

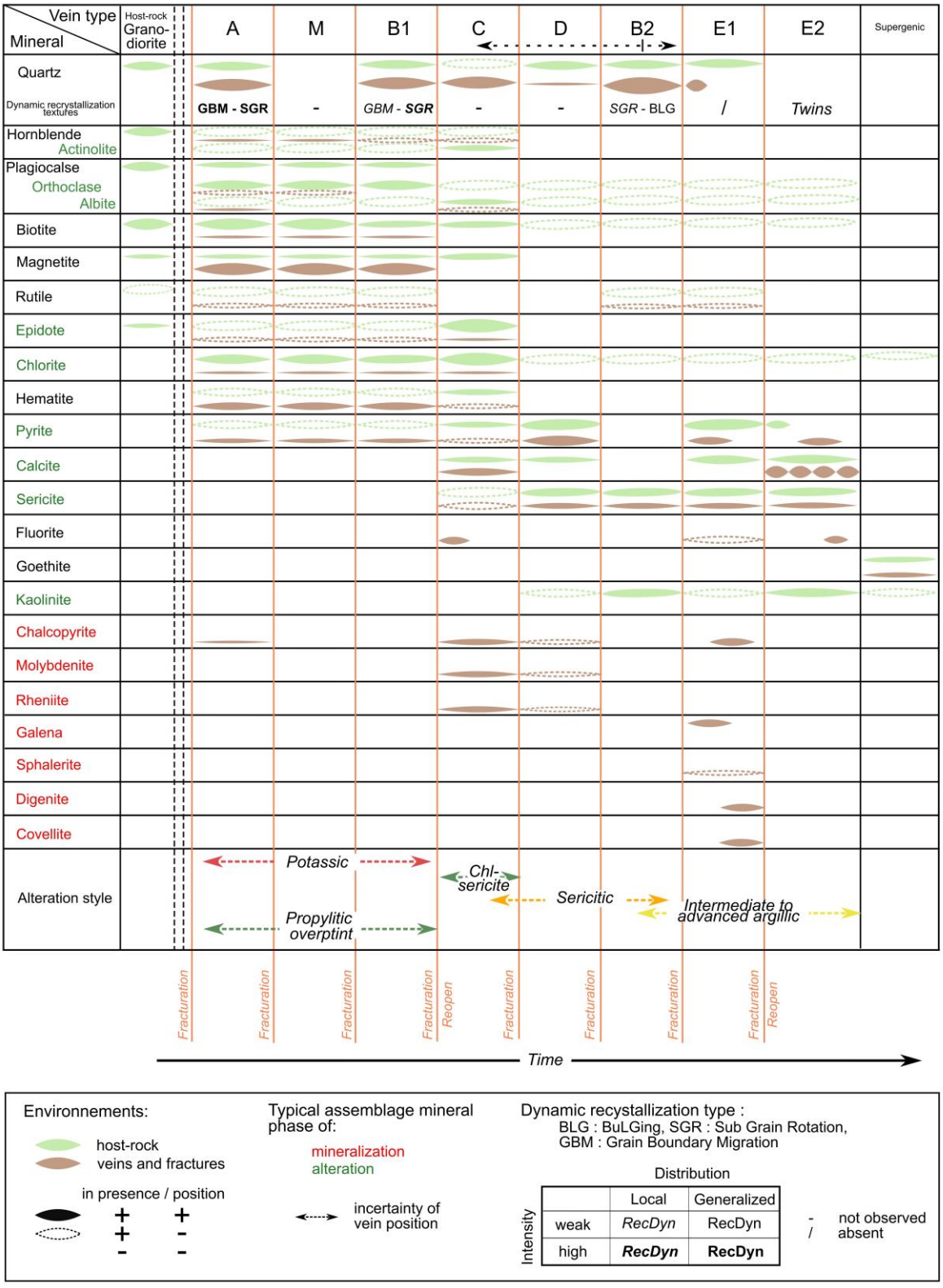

Figure 36: Paragenetic sequence of the veining and alteration sequence of the porphyry-epithermal system of Pagoni Rachi

2.3.2. Field observation of Greek Thrace deposits

This section of the results presents field observations conducted on other mineralized sites in Greek Thrace (e.g., the Maronia porphyry system, the Konos Hill epithermal system, and the Saint Philippos epithermal system). These descriptions will only be briefly discussed later for educational purposes, serving as a foundation for the description and photographic documentation of typical structures associated with these small systems (a few hundred meters in diameter). These systems often exhibit a self-collapsing hydrothermal structure, characterized by the superposition of vein structures and overprinting alterations (telescoping process), occasionally influenced significantly by weathering. For each site, a brief description of the literature is provided, followed by observations illustrated with photographs.

2.3.3. Maronia

Synthesis - The Maronia intrusions are located on the western edge of the Evros Basin, which is filled with Eocene-Oligocene sediments (Caracciolo et al., 2011; Maravelis et al., 2016) (Figure 15, Figure 37). The main pluton is a shoshonitic monzogabbro dated to 29.8 Ma (Perkins et al., 2018). This monzogabbro is intruded by a microgranite, which hosts a porphyry-type Cu±Mo (±Re±Au) mineralization associated with minerals such as chalcopyrite, molybdenite (up to 2.9 wt% Re), pyrrhotite, and pyrite (Melfos et al., 2002; Voudouris et al., 2017, 2019). The mineralization occurs in the form of a stockwork of quartz-sulfide veins (A-B type veins) associated with potassic and propylitic alteration of the host rock, overprinted by sericitic alteration associated with quartz-pyrite veins (D-type veins). The primary mineralizing process likely involved the boiling of mineralizing fluids interacting with surface fluids (Melfos et al., 2002). Hydrothermal fluid boiling is thought to have occurred during metal deposition,

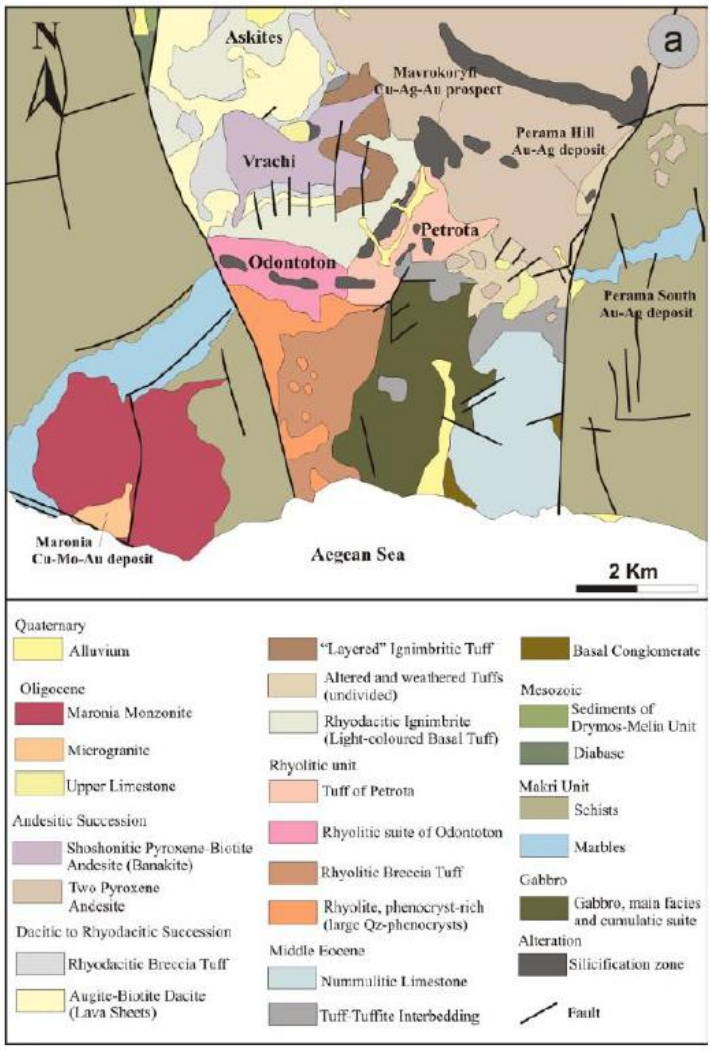

Figure 37: Geological map of Maronia, from Voudouris et al. 2019

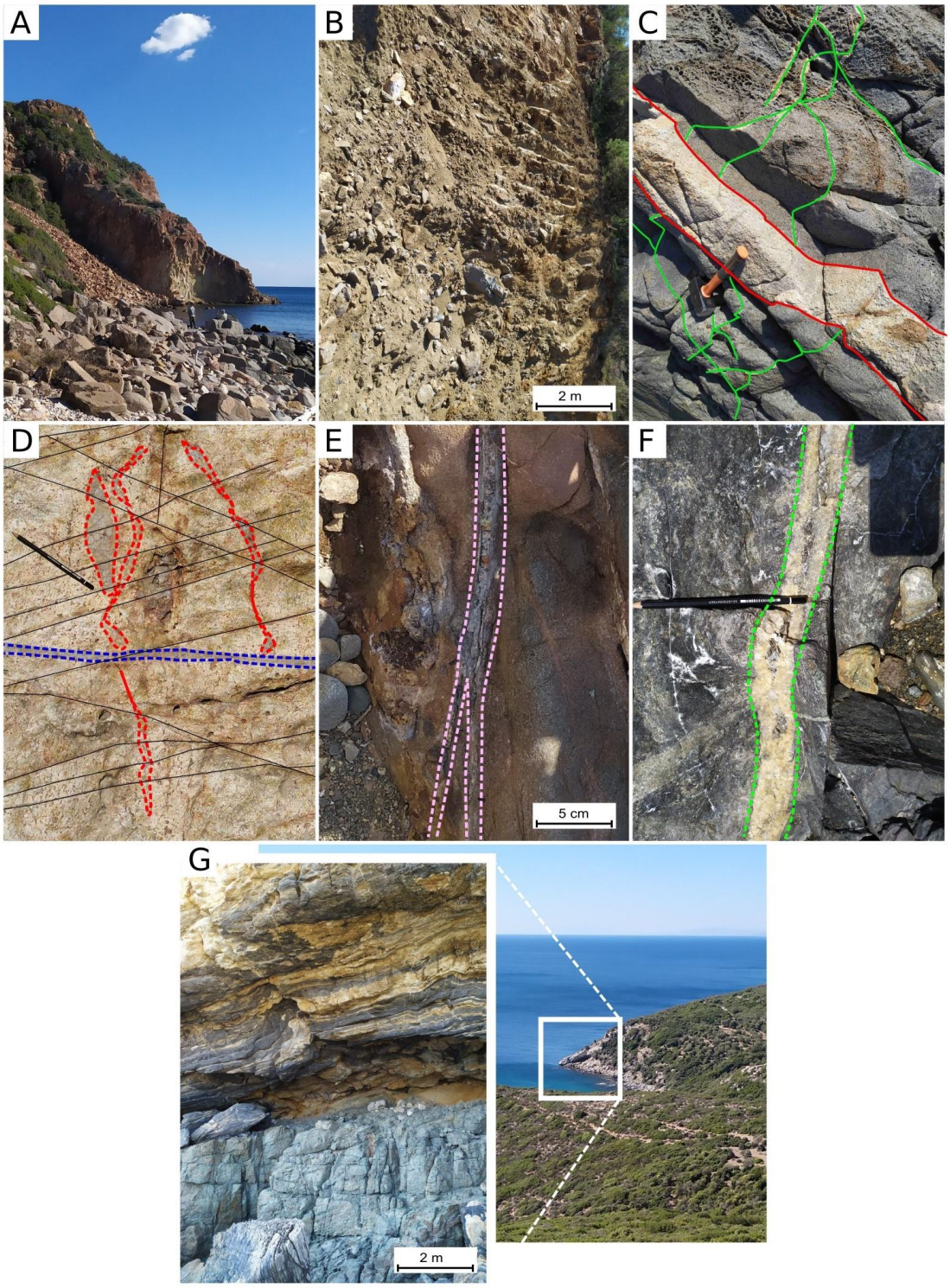

Figure 38:Field observation of the Maronia porphyry deposit A. Outcrop of mineralized Maronia porphyry (west-facing exposure). B. Outcrop of rhyolite with sericitic alteration and pyrite/chalcopyrite veins. C. Syenite dyke (red border) crosscutting monzogabbro, hosting geodic veins (green lines). D. Outcrop of microgranite hosting A-type veins (red dashed lines) of variable thickness, undulating and discontinuous, crosscut by straight B-type veins of consistent thickness (blue dashed lines). Thin biotite veins also crosscut these structures. E. Epithermal vein (E-type) with quartz, calcite, chalcopyrite, pyrite, galena, and supergene minerals (malachite), located several hundred meters east of the Maronia porphyry. F. Geodic quartz vein hosted in monzogabbro. G. Detachment fault west of the Maronia porphyry, juxtaposing schist (top) against marble (bottom), with landscape location provided. Photo taken from the summit of the Maronia microgranite pluton.

with fluid salinities ranging from 5.5 to 16.4 wt%$_{equiv.NaCl.}$ and 28 to 55 wt% $_{equiv.NaCl.}$, and temperatures between 320°C and 460 °C. The possibility of an overprint by a high-sulfidation (HS) epithermal alteration is suggested due to high concentrations of metals (Mo <0.8 wt%, Cu <0.5 wt%, and Au <1 ppm) in surface rocks (Voudouris et al., 2019).

Observations - North of the Maronia pluton (Figure 38 A), along the road (N40°51'57"; E25°32'57"), a light-colored rock with large phenocrysts of quartz and plagioclase (mostly altered) along with biotite is exposed. This is a porphyritic rhyolite/microgranite showing sericitic alteration. Various veins cut through this rock, including planar quartz veins with molybdenite, chalcopyrite, and pyrite, likely corresponding to B-type veins. A second type of vein, fine-grained and containing pyrite and sulfides (chalcopyrite, molybdenite?), may represent D-type or possibly C-type veins. The rhyolite exhibits sericitic alteration, with feldspars replaced by sericite, consistent with the presence of D-type veins (Figure 38, B). A monzogabbro is cut by horizontal geodic veins, possibly a syn-detachment, and is intruded by a syenite body (Figure 38, C).

The Maronia porphyry is intersected by numerous successive veins, the chronology and vein textures being notable in the field: (i) A-type veins: Quartz veins that are barren, wavy, and discontinuous, associated with potassic alteration; (ii) B-type veins: Mineralized quartz veins (chalcopyrite, pyrite, pyrrhotite, molybdenite), straight and sheeted, cross-cutting A-type veins, often showing reopening events (e.g., N40°51.678'; E25°32.780' - TA03.143.02 and N41°51'45"; E25°32'44" - AB.01.132.01) (Figure 38, D). Some B-type veins with vitreous quartz and vacuoles may be epithermal veins; (iii) D-type veins: Mineralized (chalcopyrite, pyrite, pyrrhotite) veins visible only under a microscope, with late massive pyrite associated with sericitic alteration; (iv) Early Biotite veins (EMB?): Present and observable only microscopically. (v) E-type veins: Found further east (Figure 38, E). These include veins (N160, 40°W) (N40°51'34"; E25°33'00" - AB.01.135.01) containing comb quartz, carbonates, pyrite, chalcopyrite, sericite, and supergene malachite, which appear to be E-type veins. Other E-type veins with chalcedony, quartz, and sulfides are observed on the western flank of the Maronia pluton (Figure 38, A). It is possible that these vein types are not directly related to the Maronia porphyry due to their distance from the main porphyry body. (vi) Numerous geodic veins (N40°51'58"; E25°32'98" - AB.01.112.01) are observed as one moves away from the mineralized Maronia porphyry, with no structural link identified (Figure 38, F).

A detachment is observed west of the Maronia pluton (N40°51'49"; E25°32'23") (Figure 38, G).

2.3.4. Sant Philippos

Synthesis - In the Kirki district, north to the Pagoni Rachi deposit (Figure 20), the Sant Philippos site, located within Eocene sediments, hosts an epithermal deposit of the IS-HS type in the form of breccias with Quartz-Pb-Zn-Ag-Bi-Sn-Ga-Ge-In mineralization (Dimou, 1994; Skarpelis, 1999; Voudouris et al., 2005). This deposit is thought to be genetically linked to a microgranite porphyry like the one at

Pagoni Rachi (Voudouris et al., 2013a). The deposit contains an unusual mineral assemblage with various sulfides and sulfosalts of Pb-As-Cu-Ag-Bi-Sn (Moelo et al., 1985; Vavelidis et al., 1989; Michailidis et al., 1989; Skarpelis, 1999a; Voudouris et al., 2013b). The mineralization occurs within a breccia/stockwork system and formed through successive stages: (i) HS stage with pyrite containing inclusions of enargite, stannite, cassiterite, bismuthinite, and pyrophyllite (T = 300 °C), (ii) IS stage with galena, barite, and tennantite (T = 250 °C), (iii) IS-LS stage with wurtzite and barite (T = 150 °C), (iv) calcite deposition (T = 100 °C). The gangue minerals include quartz, dickite, alunite, pyrophyllite, and barite (Skarpelis, 1999a; Voudouris et al., 2019), associated with early-stage ores and late-stage calcite. Whole-rock analyses of the ore show the following maximum metal concentrations: 62 ppm Mo, 100 ppm Ag, 2.5 ppm Au, 2000 ppm Bi, 35 ppm Se, 43 ppm Te, 100 ppm Sn, 221 ppm In, 466 ppm Ga, and 100 ppm Ge (Voudouris et al., 2013a; Voudouris et al., 2019). This deposit shows spatial and likely genetic relationships with the quartz-feldspar porphyry dykes at Pagoni Rachi (Schaarschmidt, 2021; Voudouris et al., 2019). The primary mineralization can be interpreted as derived from a sub-epithermal HS lode system from the Sillitoe (2010) models.

Observations - Near an open pit, stratified sandstone resulting from shallow marine turbiditic Eocene deposits is present (Figure 39 A, B, C). Ash layers have been identified in these sediments, indicating volcanic activity in the region related to subduction in an arc setting. The Sant Philippos region is characterized by multiple rhyolitic dykes (N41°00'56"; E25°49'16" – AB.01.102.01) of variable thickness (3–6 m) intruding sediments that have undergone metamorphism (hornfels) with propylitic alteration. These rhyolites are like those observed at the Pagoni Rachi site. The dykes frequently display irregular barren quartz veins of variable thickness, with frequent branching and a mineralogical assemblage suggesting sericitic alteration (Figure 39 D).

Mineralized breccias crosscut the sedimentary sequences. This breccia is observed north of the open pit. The main Sant Philippos deposit consists of silicified breccias located north of the open pit, crosscutting the sedimentary series (Figure 39 B, C). These breccias host multiphase mineralization, including pyrite, enargite, cassiterite, pyrophyllite, and dickite, characteristic of a High-Sulfidation (HS) epithermal system (GPS: N41°01'06"; E25°49'07" - AB.01.104.01; GPS: N41°01'11"; E25°49'04" - AB.01.129.01-02). This is followed by galena, wurtzite, pyrite, barite, sphalerite, and tennantite mineralization, indicative of an Intermediate-Sulfidation (IS) to Low-Sulfidation (LS) system, as well as sub-epithermal veins (N41.00163°; E25.82385°) (50 cm thick) (N175, 80°W; N12, 68°W) containing galena, pyrite, chalcopyrite, sphalerite, calcite, and quartz (Figure 39 E, F). These veins are associated with sericitic alteration and are crosscut by second-generation N90, 90° veins. Many of these veins are localized along bedding planes of the host sedimentary rocks (marls, sandstones, conglomerates) with orientations of N0, 50°W.

The breccia shows a progressive alteration pattern from proximal to distal zones. Near the breccia, alunite and barite veins occur, close to an alteration zone with potassic feldspar, quartz, amethyst, adularia (chalcedony + Au), and arsenopyrite. The violet/white appearance of the outcrop is due to the

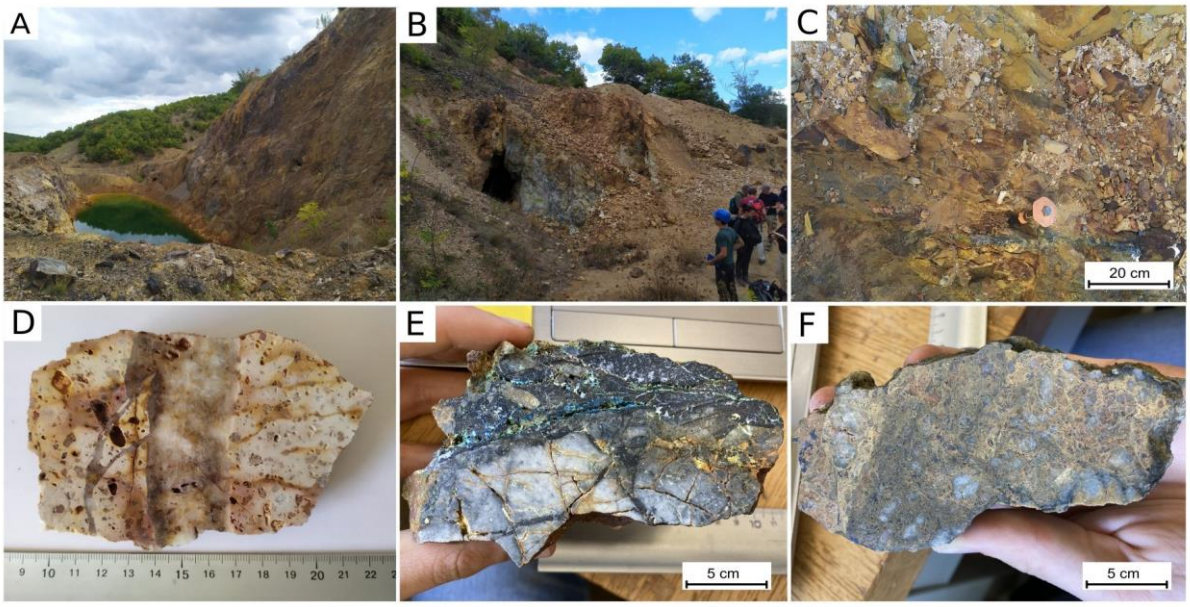

Figure 39: Filed observations of Sant Philippos epithermal deposit. A. Open pit at the Sant Philippos quarry showing Pb-Zn mineralization. B. Tunnel entrance leading to Pb-Zn silicified breccia mineralization hosted in sediments. C. Silicified breccia with quartz and Pb-Zn sulfides. D. Rhyolite with sericitic alteration and quartz veins of variable thickness and frequent branching. E. Mineralized breccia with black quartz, sphalerite, galena, chalcopyrite, dickite, and host rock fragments. F. Mineralized breccia with quartz, barite, sphalerite, and host rock fragments.

presence of alunite, kaolinite, and sericite. Fluid circulation in this area appears to be controlled by brittle structures (faults).

2.3.5. Konos Hill

Synthesis - In the Kassiteres-Sapes area, adjacent to Pagoni Rachi, porphyritic diorite-monzodiorite (Figure 20) host porphyry-type mineralization and exhibit sodic/potassic alteration (Voudouris et al., 2006). The quartz- and plagioclase-bearing monzodiorite contains variable amounts of pyroxene, amphibole, biotite, and Fe-Ti oxides. All rocks are crosscut by porphyritic dikes with quartz and feldspar, which are themselves cut by numerous NNW-trending faults. These porphyries exhibit hydrothermal alteration and porphyry-type Cu-Au mineralization, overlain by epithermal mineralization with rare and precious metals (Voudouris et al., 2006).

Observations - In this area, several lithologies with varying degrees of alteration were observed along a transect from a hilltop down to the base of a stream. The observations are summarized as follows:

Hilltop:

A lithocap of HS-type dacite consists mainly of vuggy silica, alunite, diaspore, APS, pyrophyllite, zunyite, barite, and pyrite. Notably, plumose alunite within veins is typical of magmatic origin (TA03.141.04, GPS: N41°01.301’; E25°45.269) (Figure 40 A, B).

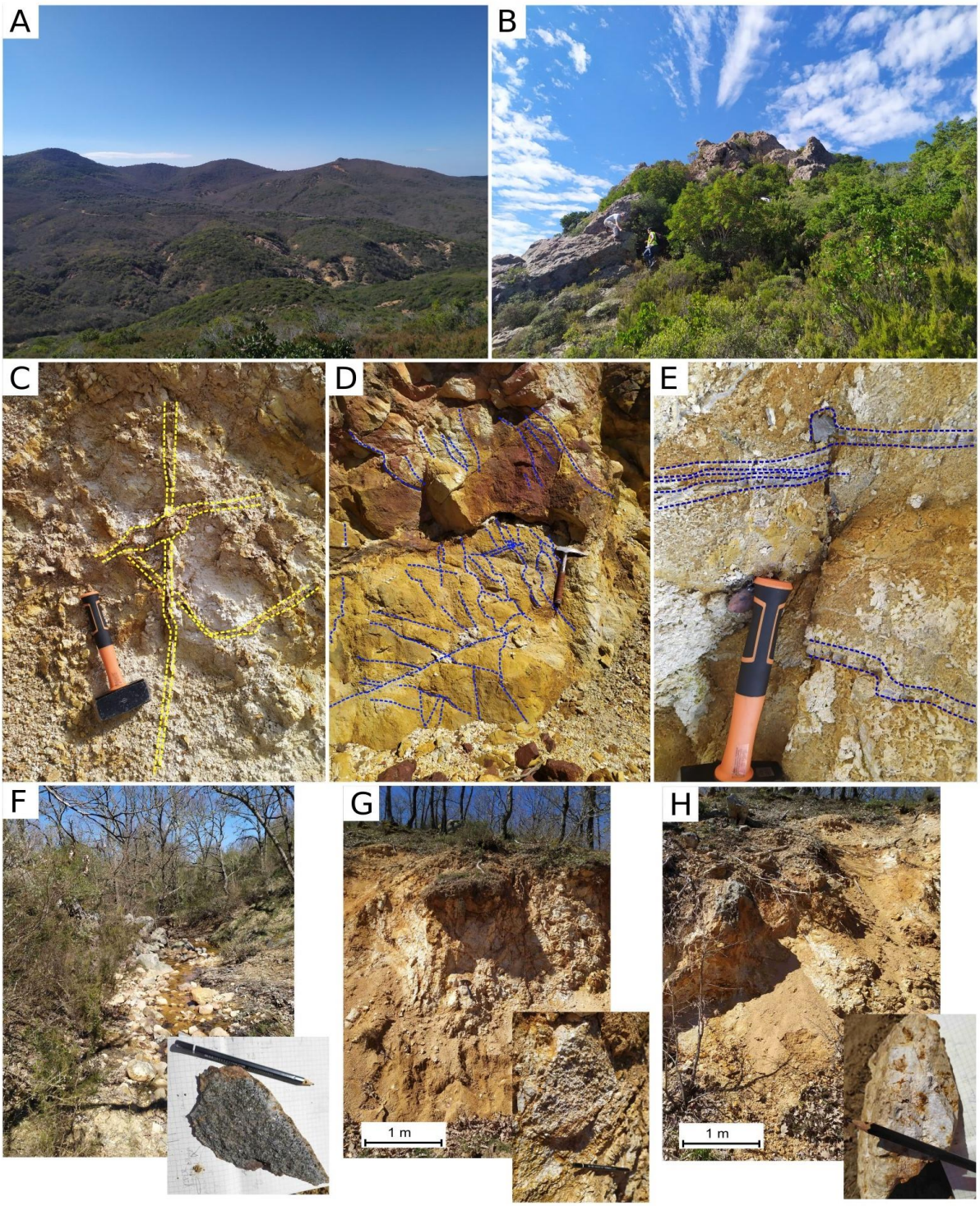

Figure 40: Field observation of Konos Hill porphyry-epithermal deposit. A. Landscape view from the summit of Konos Hill (southward). B. Topographic summit associated with a lithocap structure with vuggy silica. C. Straight, planar vein (centimeter-scale thickness) with hematite/goethite/magnetite, associated with intense sericitic alteration. Likely a weathered (oxidized) D-type vein originally composed of pyrite. D. Outcrop of a stockwork with ribbon quartz veins (B-type) associated with sericitic overprint on potassic alteration. Ribbon quartz veins exhibit macroscopic textures similar to B2-type veins at Pagoni Rachi. E. Outcrop along a stream of monzodiorite with propylitic alteration and characteristic sample type. F. Outcrop of monzodiorite with sericitic alteration and ribbon quartz veins, with characteristic sample type. G. Outcrop of granodiorite/dacite with sericitic alteration, with characteristic sample type.

Descending from the Hilltop:

Kaolinite is detected via VNIR-SWIR spectroscopy. The rock becomes friable, poorly consolidated, and displays a white to pinkish-yellow coloration, indicative of advanced argillic alteration (white) overprinting sericitic alteration (yellow) (GPS: N41°01.176'; E25°45.059') (Figure 40).

Approaching the Ravine:

A stockwork structure of hematite/goethite/pyrite is recognizable within the rock. These veins resemble D-type veins (with pyrite) that have been altered into iron oxides (Figure 40 C) (GPS: N41°01'10''; E25°45'01''). Progressive detection of sericite via VNIR-SWIR suggests a transition from advanced argillic alteration to sericitic alteration.

A stockwork with A/M- and B-type veins shows sericitic alteration, possibly overprinted onto earlier potassic alteration (telescoping phenomenon) (Figure 40 D) (GPS: N41°00'58''; E25°45'05'' - AB.01.82.01) (GPS: N41°00.994'; E25°45.077').

Sericitic alteration overprints potassic alteration and is associated with a stockwork of banded quartz veins (Figure 40 E). These quartz veins contain molybdenum, as confirmed by XRF analysis (sample TA03.141.01; GPS: N41°01.135'; E25°45.041') (TA03.141.02; GPS: N41°00.973'; E25°45.076').

Further Down the Slope:

Significant goethite is present, derived from acid drainage and pyrite oxidation (pyrite → goethite + sulfuric acid). This massive goethite is considered epigenetic and is of limited relevance for this study (no photographs were taken of these occurrences).

Base of the Ravine (Northern Site), several altered rocks were observed:

A monzodiorite with propylitic alteration, appearing almost fresh (Figure 40 F). Sample: TA03.140.01; GPS: near N41°01.184'; E25°46.047'.

A monzodiorite with sericitic alteration and banded quartz veins, possibly weathered (Figure 40 G). Sample: TA03.140.02; GPS: N41°01.184'; E25°46.047'. This rock is in contact with the monzodiorite displaying propylitic alteration. Nearby, a contact is visible between the monzodiorite and a subvolcanic granodiorite/dacite with sericitic alteration (Figure 40 H). Sample: TA03.140.03; GPS: N41°01.184'; E25°46.047'.

The monzodiorite and sericitic altered dacite are distinguished by their internal structures. The monzodiorite retains a coarser, granular texture compared to the dacite, despite the alteration.

2.4. DISCUSSION

The following sections aim to discuss the relative chronology of vein formation and the associated alteration types, highlighting the importance of integrating field observations with mineral texture analyses and CL imaging techniques. This approach seeks to evaluate the timing of events and provide initial constraints on the physicochemical evolution of the mineralized stockwork at Pagoni Rachi.

2.4.1. Alteration overprinting at Pagoni Rachi

At Pagoni Rachi, determining the precise style of alteration observed is challenging. It is essential to integrate multiple scales of analysis, from outcrop observations to thin-section studies. Mineralogical assemblages in the host rocks rarely display the endmember types commonly described in the literature. This complicates the presentation of typical images for alterations such as potassic alteration, as its assemblage is often overprinted by other mineral assemblages associated with different formation conditions and fluid circulations.

2.4.1.1. Sea water influence

Most of the porphyry stockwork zone consists of granodiorite, where hydrothermal biotites are extensively replaced by chlorite, hornblende by actinolite, and potassic feldspars by albite. These are often associated with calcite, epidote, and occasionally pyrite. Such transformations can be attributed to alteration overprinting, where the primary magmatic texture is completely obliterated by successive alteration events. This alteration has been described as potassic-sodic/calcic by Voudouris et al. (2013a), based on the coexistence of K- and N-rich silicate minerals along with Ca- phases such as epidote and calcite. However, propylitic alteration, even though isochemical, can also produce sodium- and calcium-bearing minerals similar to those observed in these assemblages. Albite-chlorite alteration assemblages are widespread in many porphyry copper deposits located in island-arc tectonic settings (e.g., Southwest Pacific, British Columbia) and are thought to result from interactions with seawater (Carson e al., 1976; Chivas, 1978; Gustafson, 1978). In example at Ann Mason deposit, the hydrogen isotopic data indicate that meteoric water components were associated to sodic-calcic fluids circulation, linked to interactions with evaporites, marine volcaniclastic and sedimentary rocks (Gustafson, 1978). Moreover, the formation waters within the Jurassic-Triassic volcanic and sedimentary rocks at Yerington likely represent mixtures of trapped meteoric and marine waters (Gustafson, 1978). At Pagoni Rachi, this may be consistent with the geodynamic context and geological environment during the formation of the deposit, which has been associated with the emplacement of granodiorite prior to ~ 32 Ma (Del Moro et al., 1981). This predates the Priabonian sediments, whereas the sedimentary column of the Kirki Basin suggests a marine depositional environment at that time (Figure 13) (Caracciolo et al., 2015). Moreover,

this context is interpreted as a back-arc setting (Figure 12) (Caracciolo et al., 2011; Maravelis et al., 2016).

2.4.1.2. Telescoping evidence

The propylitic alteration appears to be linked to potassic alteration, commonly observed as a progression from distal to proximal zones. It can be assumed here that potassic alteration is associated with high-temperature fluids, whereas propylitic alteration results from lower-temperature conditions. In a system where structural telescoping has occurred, or simply during the system's cooling phase, alteration assemblages may progressively overprint the original potassic alteration. This mechanism, in which the system "collapses" upon itself, appears likely given the availability of reactants to produce the mineralogical assemblages currently observed in A-, M-, and B1-type veins which may be linked to the presence of seawater. Moreover, it is common to observe the reopening of C-type veins within B1-type veins, indicating that the rock may have undergone chlorite-sericite alteration, associate to chlorite-sericite-biotite-magnetite-pyrite assemblage. Then such assemblage is hard to associate to a specific veining stage. Indeed, the presence of very similar alteration mineral assemblage does not expose an assemblage "endmember" specifically associated to only one vein-type.

Sericitic alteration is particularly intense at Pagoni Rachi and so pervasive that it shapes parts of the landscape. However, determining its precise extent or whether it is exclusively associated with D- or B2-type veins remains challenging. There are currently no clues to identify the primary textures or assemblages in the rocks hosting the B2-type veins. The high density of the stockwork, combined with advanced alteration and possible leaching of the host rock, has largely obliterated residual rock. This is often accompanied by widespread argillic alteration. This overprint seems plausible, particularly given the spatial association with sub-epithermal veins and the transition between porphyry and epithermal systems. In contrast, no deep telescoping of high-grade (advanced argillic or vuggy silica) alteration into porphyry-style veins has been observed. Voudouris et al. (2019) suggested that such structures might have existed but were eroded over time. However, only sub-epithermal mineralization or structures characteristic associate to NNW-SSE faults have been identified at Pagoni Rachi. Telescoping is generally interpreted to occur as a response to significant surface degradation caused by uplift-induced erosion or, less commonly, volcanic collapse during the lifespans of hydrothermal systems (Sillitoe, 1994). The presence of syntectonic minerals at Chuquicamata (Lindsay et al., 1995) and a hydrothermal breccia pipe at Agua Rica (Perelló et al., 1998) exemplify telescoping processes controlled by zones of high permeability. At Agua Rica, the process involves a hydrothermal breccia pipe and a NE-oriented fault, which is projected to cut through the center of the deposit and interact with the ore body (Peregrine Metals Ltd., 2011).

Although alteration overprints are common—even ubiquitous—at Pagoni Rachi, distinct boundaries have been observed (Figure 24 J, L) at different location where, sericitic alteration is in contact with the potassic to propylitic altered granodiorite, and the sericite alteration in contact with an argillic altered

granodiorite, with in both case a possible overprinting. Furthermore, while telescoping has affected the B2-type vein system, no minerals other than sericite have been observed, making it difficult to determine whether other minerals were present during vein formation, particularly within the central spaces of the veins.

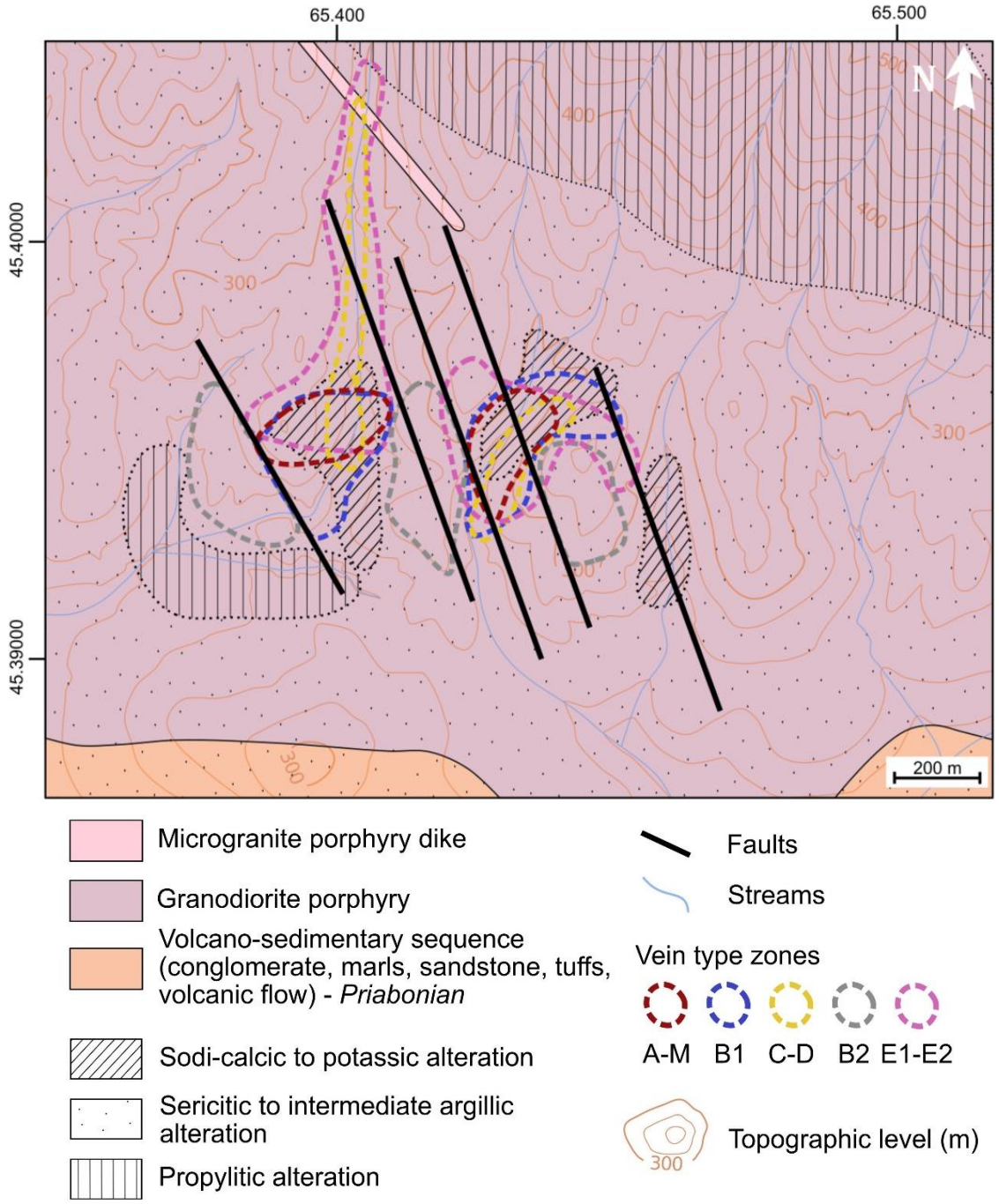

Figure 41: Geological, alteration, and vein distribution maps of the Pagoni Rachi prospect. The maps display the distribution of different vein types and structures. A-, M-type veins are contemporaneous and are therefore presented as a single zone. Similarly, C-, D-type veins are grouped due to the difficulty in defining their chronological and genetic differences. E1 and E2-type veins are also contemporaneous, associated with the epithermal stage.

A significant indicator of telescoping is the co-occurrence of minerals representative of different alteration types within the same zone. For instance, in a typical porphyry system, potassic alteration (marked by secondary biotite and orthoclase) and sericitic alteration (characterized by quartz, sericite, and pyrite) dominate in deeper zones near the magmatic intrusion. In contrast, epithermal systems are often associated with argillic alteration (e.g., alunite and kaolinite) or intermediate argillic alteration (e.g., smectites and illites), which are typically linked to more superficial conditions.

Telescoping complicates geological interpretations because the classic boundaries between porphyry and epithermal zones become blurred. Multi-proxy analytical techniques, including isotopic mass spectrometry and thermodynamic modeling, are thus essential for unraveling these complex systems. The sub-epithermal veins crosscuting earlier porphyry-style mineralization and are spatially associated with argillic alteration (kaolinite-sericite-stable) in the wall rocks.

In conclusion, telescoping in porphyry and epithermal systems reflects the dynamic interplay of magmatic, tectonic, and hydrothermal processes. Identifying hybrid signatures offers significant opportunities for resource exploration but requires a deep understanding of the underlying mechanisms.

2.4.2. Vein succession in Pagoni Rachi porphyry epithermal system

2.4.2.1. Timing reevaluation of porphyry-style mineralization

Several similarities can be identified with the studies conducted by Voudouris et al. (2013a) and Mavrogonato et al. (2019, 2020), which examined the Pagoni porphyry system. However, the observations presented in this study led to another vein succession and mineralization timing.

A-type quartz is predominantly present in early-stage veins that are either straight or slightly wavy. These veins generally lack visible internal symmetry and are typically linked to potassic alteration. Classified as A-veins (Gustafson and Hunt, 1975), this type of quartz displays high-intensity cathodoluminescence (CL) and is either unzoned or exhibits weak concentric zoning (Rusk, 2012). At Pagoni Rachi, these characteristics align with observations by Voudouris et al. (2013a), although differences may exist in the quartz microtextures. CL imaging provides detailed insights that can distinguish domains and reveal dynamic recrystallization textures in the quartz, with the presence of mottled, ghostband or mosaic CL-texture of quartz crystals (Figure 27 G-L).

B1-type quartz, also associated with potassic alteration, is found in early-stage veins commonly referred to as B-veins (Voudouris et al. 2019 and reference therein). These veins are more regular than A-veins and display visible internal symmetry (Gustafson and Hunt, 1975). Quartz of this type also shows high-intensity CL and features distinct growth oscillatory zoning suggesting a syntaxial growth (Figure 29 M-O). CL imaging has helped refine the timing of sulfide deposition, highlighting possible associations with vein reopening events or the infiltration of later-stage fluids through A- and B1-type veins. While Voudouris et al. (2013a) suggested such phenomena, they did not demonstrate them. Observations suggest a more complex sequence than previously described, especially regarding the

reopening of B1-type veins. These reopenings, identified only through CL imaging, are associated with the emplacement of metal-bearing minerals, which fill these reopened veins (Figure 29 F).

The reopening of B1-type veins appears to be tied to the deposition of ore-hosting minerals, resembling processes seen in C-type veins, which represent reactivations of B1-type structures. However, certain aspects remain ambiguous. Two main types of reopening have been identified. Both result in the deposition of gangue minerals and sulfides, as well as fracturing of central quartz crystals in B1 veins. These fractures disrupt the oscillatory growth zoning visible under CL. In one instance, quartz is the dominant infill, likely deposited at lower temperatures than the B1 quartz. In the other, the infill includes alteration-related minerals such as chlorite, sericite, calcite, and quartz. It remains unclear why quartz dominates in some cases, while alteration minerals are predominant in others. Voudouris et al. (2013) reported feldspar in the central portions of some B-type veins (here, B1), although this study found it only in minor quantities. If fluids linked to chlorite-sericite alteration moved through these veins, it is plausible that the feldspars were altered, forming alteration minerals along with sulfides. What remains unresolved is the specific set of conditions determining whether feldspars are deposited in the vein centers—an observation not made in this study. More targeted sampling could help clarify this phenomenon.

The terminology used in this study aligns with the literature, where C-type quartz is characterized by dull CL intensity and crosscuts or grows over earlier high-CL quartz (A- and B1-types) in early high-temperature veins (Figure 30 A-E'). C-type quartz, typically unzoned, is widely reported in porphyry deposits and is frequently associated with sulfides such as pyrite, chalcopyrite, and bornite within mineralized veins (e.g., Fournier, 1967; Nielsen, 1968; Landtwing and Pettke, 2005; Landtwing et al., 2005). Occasionally, traces of molybdenite are also observed in the Pagoni Rachi system. The term "C-type" reflects its spatial association with chalcopyrite and bornite in mineralized veins, suggesting a possible genetic link to "paint veins" (Fournier, 1967). Chalcopyrite and pyrite are typically dispersed along fracture surfaces, while quartz is found only where C-type veins intersect B1-type veins. In such cases, quartz predates sulfide deposition based on textural evidence (Tsuruoka et al., 2021). At Pagoni Rachi, C-type quartz is variable in abundance, ranging from scarce to almost absent, and is sometimes associated with minor chlorite and sericite (Monecke et al., 2018; Driesner and Heinrich, 2019). The genetic relationship between dull-CL C-type quartz and copper sulfides remains debated (Monecke et al., 2018; Schirra et al., 2019). There is also ambiguity regarding the relative contributions of C-type and D-type veins at Pagoni Rachi. These two vein types have been deliberately distinguished based on several factors. Their compositions differ: C-type veins contain quartz, alteration minerals, and sulfides, whereas D-type veins are predominantly composed of pyrite. Their textures also vary, with C-type veins exhibiting infill and reopening patterns (Figure 30), while D-type veins display massive pyrite deposition along fractures (Figure 31). Furthermore, their associated alteration styles are distinct, with C-type linked to chlorite-sericitic alteration and D-type to sericitic alteration.

This raises the question of whether these veins represent a single fluid circulation event with chemical evolution over time or distinct events from separate pulses. D-type quartz is predominantly found in straight-walled quartz veins up to a few centimeters thick (Gustafson and Hunt, 1975). These veins are typically rich in pyrite with minor chalcopyrite and are associated with quartz-sericite-pyrite (sericitic) alteration. D-type quartz also occurs as infill in reopened high-temperature veins (Monecke et al., 2018). It generally exhibits moderate CL intensity with well-defined oscillatory growth zones. However, our observations indicate that D-type veins are primarily associated with massive pyrite deposition along fractures in earlier veins. In telescoped porphyry-epithermal systems, such as those in Thames, New Zealand (Brathwaite et al., 2001), La Caridad, Mexico (Valencia et al., 2008), and Agua Rica, Argentina (Franchini et al., 2011), molybdenite formation often coincides with D-type vein events. This process likely involves remobilization from B-type veins and is linked to high- and intermediate-sulfidation base and precious metal mineralization that overprints the porphyry systems. A similar mechanism may explain the formation of C-type veins at Pagoni Rachi. Molybdenite formation during the D-type vein event is unusual in porphyry Cu-Mo-Au deposits linked to alkaline and calc-alkaline magmatism (e.g., Bingham Canyon, Utah, and Butte, Montana). In these systems, molybdenite is typically associated with B-type veins and is either absent or minimally present in D-type quartz-pyrite-sericite veins, which are surrounded by sericitic alteration (Seedorf et al., 2005; Redmond and Einaudi, 2010). Consequently, the molybdenite at Pagoni Rachi is more likely linked to C-type vein formation.

Determining the sequence of these veins and the stockwork within the framework established by Voudouris et al. (2013a) is challenging. No definitive textural connections have been observed with previously described vein types. However, a geomorphological shift is evident, transitioning from the summit of the hill to its lower slopes. Unfortunately, pervasive sericitic to argillic alteration has obscured the vein textures. Despite this, these veins are crosscut by silicified faults and breccias associated with epithermal veins, placing them within the epithermal ore sequence. Surprisingly, these veins and their host rocks lack sulfides, rendering them entirely barren.

2.4.2.2. Chemical evolution evidence during quartz deposition and massive stockwork (B2-type veins)

B2-type veins at Pagoni Rachi correspond to the “banded” veins described by Voudouris et al. (2013). The historical nomenclature refers to “B” as banded, though these veins differ from earlier banded veins that follow A-type veins. The texture remains consistent, hence the B2 designation. These veins are associated with "banded " veins typically found in shallow, gold-rich porphyry deposits of the Maricunga belt (Vila et al., 1991; King, 1992; Muntean and Einaudi, 2000, 2001; Koděra et al., 2014; Rottier et al., 2016). Their banded texture is attributed to the high concentration of vapor inclusions and micrometer-sized magnetite grains within quartz, aligned parallel to vein walls they are usually described with quartz exhibiting a broad range of cathodoluminescence (CL) intensities and various textures, including botryoidal and comb-like forms (Rottier et al., 2016). The dark bands often display

botryoidal structures in quartz, suggesting recrystallization from a silica gel (e.g., Boydell, 1924; Ramdohr, 1980; Sander and Black, 1988). At Verde (Maricunga Belt) the banded veinlets typically account for 1 – 4 % of the rock volume, with a maximum of 20 %. These veinlets contain quartz with a fine-grained (< 0.25 mm) granular texture, sometimes elongating perpendicular to vein walls. Quartz fills fractures of various widths, ranging from hairline cracks to millimeter-scale openings (up to 2 cm wide), with slightly wavy and closely aligned walls (e.g., At Verde: Muntean and Einaudi, 2000, 2001). King (1992) proposed that banded veinlets at Marte formed from silica gel due to silica supersaturation triggered by sudden pressure drops—a hypothesis later supported by Muntean et al. (2001). The structures observed at Pagoni Rachi align with field data, quartz textures, potential recrystallization, and CL intensity variations. Their shallow emplacement is consistent with stockwork veins occurring at higher elevations in the porphyry system (Figure 23, Figure 41). The CL textures also suggest silica gel formation. However, B2 veins at Pagoni Rachi appear barren on a macroscopic scale, and the stockwork density is significantly higher than that of the Maricunga Belt, with veinlet volumes reaching up to 80 %. Whole-rock analyses or micro-XRF could help detect metals as micro-inclusions within quartz or as disseminations in the host rock. Yet, the intense sericitic to argillic alteration of the host rock complicates such investigations, as it renders the rock friable. CL-zoning within the quartz crystals indicate a change in fluid chemistry during formation (Götze, 2005), and a diffuse transitioning from a dark blue to clear blue, then to a final weakly luminescent domain with sharp boundaries, implying polyphase vein growth from core to vein margin (Figure 32 F-G”). There are no apparent relations between CL domains (color and intensity variation) and quartz microtextural domains within these veins. CL varies along the vein's growth. The signal is not destabilized or re-equilibrated by ductile/brittle deformation, unlike A- and B1-type veins.

2.4.2.3. Late epithermal style mineralization and structural control

Voudouris et al., 2013a, described E-type quartz has associated with late, low-temperature (< 350 °C) veins that often accompany base metal mineralization. These veins range from cryptocrystalline to euhedral, have glassy, straight-walled appearances, and vary in thickness from millimeters to meters, extending over several meters (Voudouris et al., 2013a). They are associated with sericitic to argillic alteration. Quartz in these veins exhibits pronounced oscillatory growth zoning with low CL intensity (Monecke et al., 2018), maintaining straight, sharp, parallel walls. Accompanying minerals include pyrite, sphalerite, galena, chalcopyrite, enargite, tennantite, tetrahedrite, and gold-bearing minerals. Our new sequence of E1- and E2-type veins resembles carbonate-base metal veins observed in the southwest Pacific (Corbett and Leach, 1998) and late-stage polymetallic veins at deposits such as Golden Sunlight, Montana (Spry et al., 1996), and the Central City alkaline porphyry molybdenum system (Spry, 1987), as proposed by Voudouris et al., 2013a). At Pagoni Rachi, late-stage calcite in E2-type veins is interpreted as the result of overprinting and the gradual neutralization of hydrothermal fluids (Voudouris et al., 2013a). This process is common in other epithermal systems of western Thrace (e.g.,

Kassiteres/Sapes, Pefka; Voudouris, 2006; Maronia, this study). These veins are frequently identified in telescoped porphyry systems (Masterman et al., 2005; Voudouris et al., 2013; Maydagan et al., 2015; Catchpole et al., 2015) and are often considered equivalent to porphyry-related sub-epithermal polymetallic veins (e.g., Sillitoe) At Pagoni Rachi these epithermal veins show a structural similarity with a similar orientation than observed faults-oriented NNW-SSE. Massive, silicified faults observed in the field appear to represent the final veining phase associated with major faulting. They look like the description of epithermal vein of Maydagan et al. (2015). No clear connection has been established between these faults and E1- or E2-type veins, although they share structural controls related to regional NNW-SSE faulting. Due to the lack of detailed descriptions across scales, these structures are excluded from this discussion.

2.4.2.4. Ductile to brittle deformation at Pagoni Rachi

The structure of the veins, from A-type veins, with undulating and discontinuous characteristics, to B1- and B2-type veins, which are planar, continuous, and finally to E1 and E2-type veins, which are continuous, planar, contain fractured quartz suggests an evolution of the deformation system from ductile to brittle conditions.

This evolution is also evidence by the quartz and calcite crystals microtextures and CL-textures: (i) A-type veins display highly recrystallized quartz evidence by GBM textures associated to ghostbands, and mottled-CL textures (Figure 27 I-L), (ii) B1-type veins have intermediate recrystallized quartz evidence by SGR textures to none associated with mottled and growth oscillatory zoning (Figure 29 K, O, P)), (iii) B2-type veins have weakly recrystallized quartz evidence by BLG textures to none, no CL-texture is particularly linked to these structures (Figure 32 D-E), and (vi) finally E1- and E2-type veins contain euhedral quartz, associated with CL-growth oscillatory zoning (Figure 33 I-K), which are frequently fractured and twinned calcite crystals (Figure 33 H), respectively. This sequence of textures is associated with theoretical quartz deformation temperatures ranging from 400 to 600 °C (Stipp et al., 2002a,b) for A-type veins, characterized by the presence of GBM textures; from 400 to 500 °C (Stipp et al., 2002a,b) for B1-type veins, indicated by the presence of SGR textures; from 250 to 400 °C (Stipp et al., 2002a,b) for B2-type veins, marked by BLG textures; and below 200 °C for E1 and E2-type veins, evidenced by quartz crystal twinning and fracture textures (Stipp et al., 2002a,b; Lacombe, 2022) (Figure 42 A and B). This suggests that the quartz and calcite record a progressive temporal and spatial evolution of deformation, transitioning from a high-temperature ductile domain (~ 600 °C) to a low-temperature brittle regime (< 200 °C).Then, following the veins sequence show a decrease in the intensity of deformation during the formation of the veins sequence, going from GBM type dynamic recrystallization texture of quartz to preserved primary quartz textures.

Underformed quartz or fractured ones, associated with a decrease of theoretical temperature of deformation going to 600°C to < 300 °C (Figure 42) which is coherent with the ductile-to-brittle transition temperature range for quartz considered ranging from 400 to 500 °C (Monecke et al., 2018).

The spatial zoning of veins can also explain this evolution, considering a hot central porphyry stock where the A-type veins are formed, to a lateral extension (to the north i.e.) with cold distal epithermal

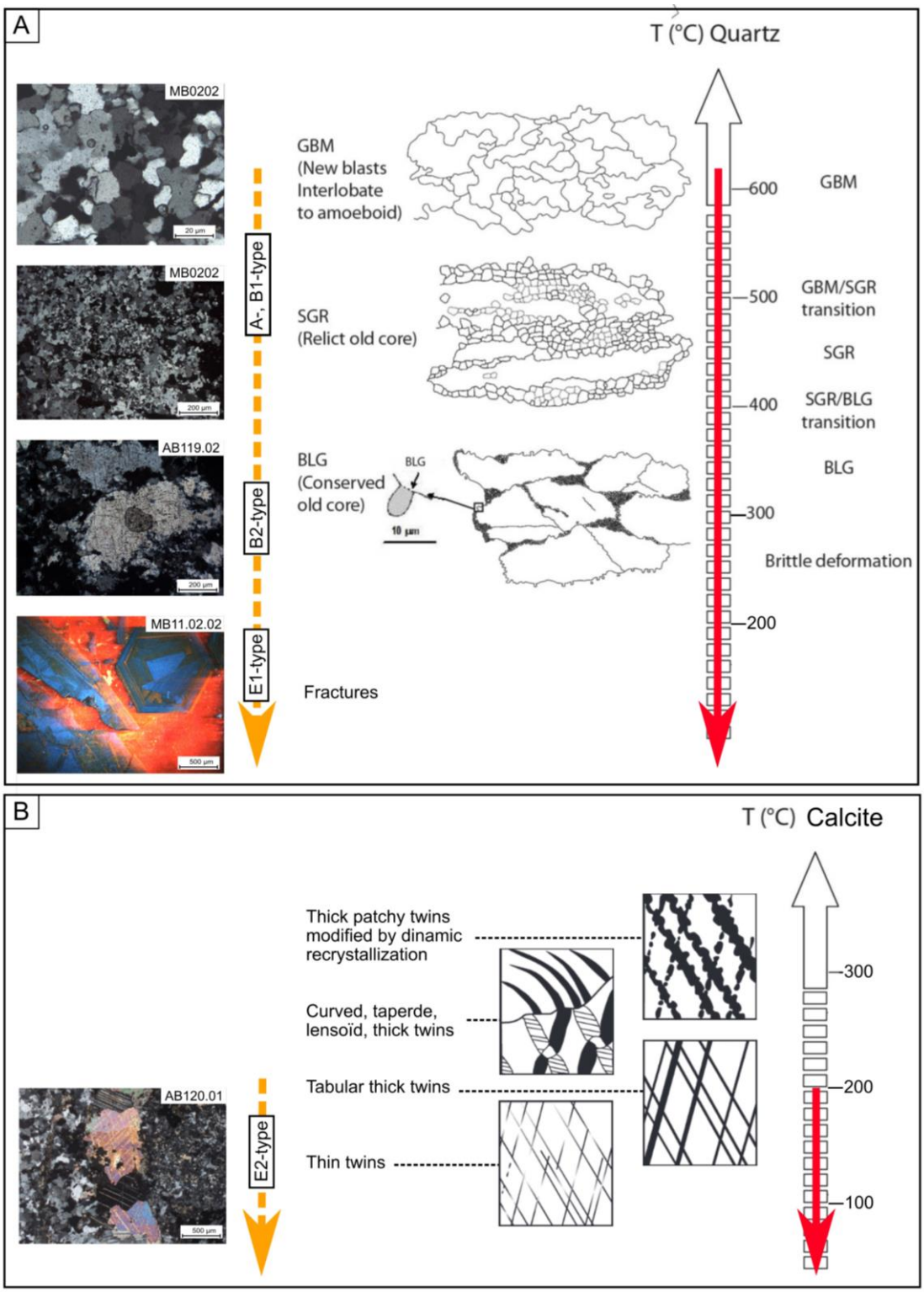

Figure 42: Schematic representation of dynamic recrystallization textures in quartz and calcite. This figure illustrates the evolution of quartz recrystallization textures, progressing from the earliest veins (type A) to the latest (type E). The sequence shows (A): GBM (Grain Boundary Migration), SGR (Subgrain Rotation), BLG (Bulging Recrystallization), Fractures. The corresponding deformation temperatures are annotated, adapted from Passchier and Trouw (2005). Additionally (B), different types of calcite twinning are depicted, ranging from fine twinning to planar twinning, based on Ferrill et al. (2004) and Vrabec et al. (2018). (Modified from Owona et al., 2013; Stipp et al., 2002; Passchier and Trouw, 2005).

veining (Figure 23). It is also surprising that the hosting rock (granodiorite) does not display any textures of deformation, no preferential orientation of minerals, fractures etc. Only the veins display deformation features, mostly with the quartz dynamic recrystallization textures – from GBM/SGR to fractured quartz. This suggests deformation during the crystallization and the formation of the veins/quartz sequence. This deformation evolution may therefore involve a transition from a warm, ductile environment to a cold, brittle one, from a high deformation rate to a low deformation rate, or a combination of these deformation conditions.

2.4.3. Pagoni Rachi and structural relation to other sites – schematic figuration

2.4.3.1. Succession of Veins and Alterations at Pagoni Rachi

The succession of veins and associated alterations at Pagoni Rachi appears more complex than previously described in the literature (Voudouris et al., 2013a, b, 2019, 2022; Mavrogonatos et al., 2019, 2020). Microtextures observed through cathodoluminescence (CL) provide insights into the formation mechanisms of most veins, along with a qualitative evaluation of deformation processes based on quartz and calcite grain structures.

Based on Sillito (2010) model's, the Pagoni Rachi system shows an evolution from a Cu-Mo porphyry system to a sub-epithermal Pb-Zn system (Figure 43). The system appears to be intermediate between Sillitoe's Cu-Au and Cu-Mo poles, based on the mineralization assemblage and successive vein types. This transition from porphyry to sub-epithermal system is characterized by telescoping of veins and alterations in the proximal porphyry system. For example, A-, B-, C-, and D-type veins are superimposed near the porphyry center, while intermediate-epithermal D-type veins extend distally, as seen in their presence to the north of the site. The spatially limited distribution of these veins aligns with the pervasive overprinting of different alteration types, making it difficult to precisely distinguish individual alteration phases or confidently link specific alteration types to distinct vein types.

In the central part of the site, the mineralogical assemblage of chlorite, biotite, orthoclase/albite, calcite, epidote, magnetite, and pyrite suggests a propylitic alteration overprint (associated with sodic-calcic assemblages) on earlier potassic alteration. The omnipresence of sericite, combined with disseminated pyrite, further indicates an overprint of sericitic alteration.

2.4.3.2. Observations from Other Western Thrace Sites

Field descriptions from other sites in Western Thrace generally align with prior studies (e.g., Voudouris et al., 2019, 2022). However, some recent observations offer new insights and remain under discussion. Below, a brief synthesis situates these sites within Sillitoe's (2010) theoretical model and highlights their similarities with the Pagoni Rachi system.

A. Maronia

The Maronia deposit features mineralization in the form of successive A-, B-, and D-type quartz veins with chalcopyrite and molybdenite (Cu-Mo), centered on the porphyry. There is evidence of a sericitic alteration overprint on a probable central potassic alteration. As in Pagoni Rachi, epithermal system has been observed, with veins bearing quartz/carbonate base metals. Based on Sillitoe's model, the mineralization corresponds to a Cu-Mo porphyry system with minor alteration overprinting (Figure 43).

B. Sant Philippos

The Sant Philippos deposit consists of a breccia hosting high- to intermediate-sulfidation Pb-Zn mineralization. Nearby rhyolitic dykes exhibit pervasive sericitic alteration and host barren quartz veins. Based on Sillitoe's model (2010), this corresponds to a high-sulfidation lode associated with a deeper porphyry system (Figure 43). The proximity of Sant Philippos to Pagoni Rachi suggests a genetic relationship, as proposed in the literature notably due NNW-SSE structural trends and similarities in epithermal mineralization suggest a common genesis (Voudouris et al., 2013a, 2019). The high barite content in breccias and sedimentary sequences indicates the involvement of seawater, as suggested by salinities of 3.5 $wt\%_{equiv.NaCl}$ with significant barium content (*internal communication Voudouris et al.*). This is consistent with the sodic-calcic overprint observed at Pagoni Rachi, implying that both systems may have formed simultaneously within the same geodynamic and geological context.

C. Konos Hill

At Konos Hill, vuggy silica and diaspore-rich summit structures suggest the presence of a lithocap, a typical feature of porphyry systems (e.g., Sillitoe, 2010). The association of porphyry-style veins with rocks exhibiting intense sericitic and argillic alteration implies significant telescoping, in deeper parts. Massive hematite-goethite veins likely represent weathered remnants of once-massive pyrite veins. Konos Hill appears to host a porphyry Mo-(Re?) system that experienced intense telescoping (Figure 43). The summit lithocap forms a prominent topographic feature typical of the Sapes-Kassiteres-Kirki district.

2.4.3.3. Genetic Relationships Between Pagoni Rachi and Surrounding Systems

The Pagoni Rachi deposit is likely a multi-centered system resulting from two successive magma pulses, like the nearby Sapes porphyry-epithermal deposit. A correlation between the rhenium (Re) content of molybdenite and the Cu, Mo, and Au grades emphasizes Pagoni Rachi’s extreme Re enrichment compared to other porphyry deposits worldwide (Voudouris et al., 2013; Mavrogonatos et al., 2019, 2020). The genetic relationship between the porphyry and epithermal mineralization at Pagoni Rachi cannot be conclusively established due to a lack of chronological data. However, the similarities in structural trends and mineralogical assemblages between Pagoni Rachi and Sant Philippos suggest

they may represent either distinct hydrothermal systems related to separate porphyry events or lateral metal transitions within a single, evolving magmatic-hydrothermal system (Voudouris et al., 2005).

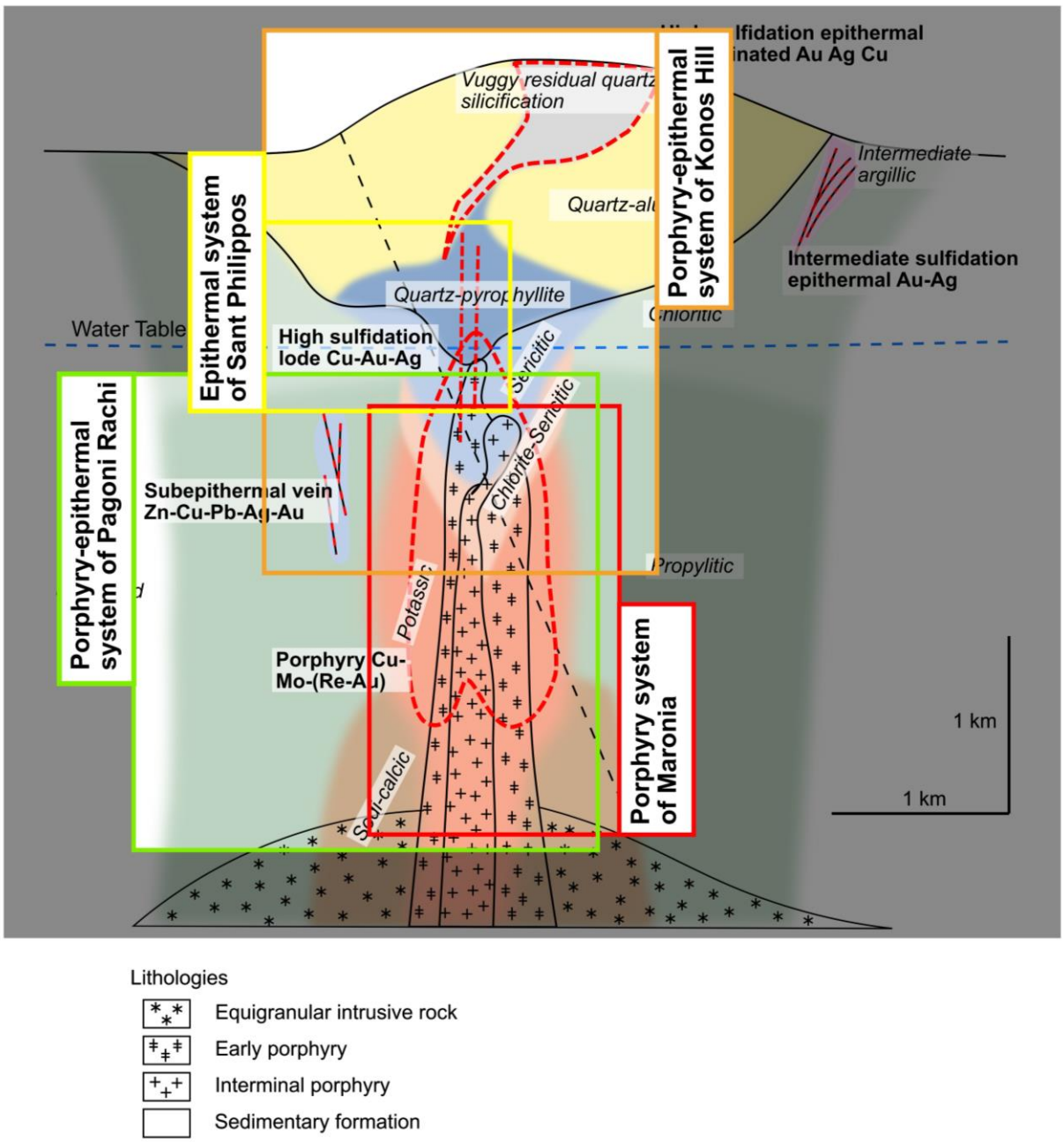

Figure 43: Schematic cross-section of a porphyry-epithermal system (adapted from Sillitoe, 2010). This figure includes the localization of the porphyry-epithermal deposit at Pagoni Rachi, the Maronia porphyry deposit, and the telescoped epithermal deposit at Konos Hill, based on our observations.

2.5. SUMMARY AND CONCLUSION

The Western Thrace region presents a range of deposits aligned with Sillitoe's porphyry-epithermal model: (i) Maronia represents a classic porphyry Cu-Mo system with limited alteration overprinting, (ii) Pagoni Rachi shows a telescoped porphyry-epithermal system, with overlapping porphyry and epithermal veins and alterations, (iii) Sant Philippos features a high-sulfidation lode within a breccia, likely associated with a deeper porphyry, (iv) Konos Hill represents the upper part of a porphyry system, with intense telescoping and a lithocap marked by vuggy silica.

These deposits collectively illustrate the diverse expressions of magmatic-hydrothermal systems in the Sapes-Kassiteres-Kirki and Maronia districts, with varying degrees of telescoping and mineralization styles.

Pagoni Rachi is an excellent example of overlapping of porphyry Cu-Mo-Re-Au and sub-epithermal Pb-Zn veins. Metallic mineralization at Pagoni Rachi deposit precipitated in six main stages of veins with quartz. The new classification proposed in this study suggests a redefinition of fluid circulation and mineralization events. The first and second stages are represented by an evolution from undulating quartz veins (A-type) to straight and rectilinear veins (B1-type), associated with potassic alteration and propylitic alteration overprinting resulting in a mixing of alteration type between potassic and sodi-calic alteration. The sodi-calcic alteration may be linked to the presence of sea water in the system. The third stage corresponds to reopening phases characterized by quartz or alteration minerals typical of a chlorite-sericite alteration assemblage, and the deposition of metal-bearing minerals forming the mineralization in C-type veins with chalcopyrite, pyrite, and molybdenite, potentially genetically linked to the emplacement of massive pyrite veins, sometimes filling fractures within earlier veins (D-type veins). The fourth stage veins are associated with pervasive sericitic alteration with massive stockwork of barren B2-type veins, located in topographic highs and showing textural evidence of fluid chemistry changes during vein formation. However, the direct association of these veins with earlier types requires further study. The two last stages are subsequently crosscut by epithermal quartz-carbonate veins containing base-metal minerals, structurally related to NNW-SSE-oriented faults and the siliceous ledges that formed at low temperatures equivalent or transitional to the epithermal environment. An uplift of the land of the Sapes-Kassiteres-Kirki district would have increased the overlapping of late low-temperature and early high-temperature veins. Similar telescoping processes have been recognized in other porphyry deposits (e.g., Pudack et al., 2009; Franchini et al., 2011, 2012).

Cathodoluminescence imaging is a powerful technique for revealing internal mineral zoning, potential chemical variations, and growth textures that are often invisible under ordinary light. Integrating CL imaging with other analytical approaches has allowed for a redefinition of the timing of mineralization events and has highlighted potential fluid chemistry evolution during quartz formation, particularly in B2-type veins. This technique, combined with observations of microtextures in different

quartz generations, has revealed evidence of quartz deformation within the veins. The deformation evolves from high-temperature ductile environments (A-type veins) to low-temperature brittle environments (E1- and E2-type veins), with intermediate deformation conditions observed in B1- and B2-type veins. The combination of CL imaging and quartz texture analysis is crucial for understanding the relationships between mineralization and alteration events. This makes it a valuable tool for exploring hydrothermal systems, particularly those characterized by the complex overprinting of multiple mineralization events.

These observations establish a foundational framework for integrating field and laboratory studies to evaluate the physicochemical conditions that led to the formation of the Pagoni Rachi system. By bridging detailed fieldwork with advanced analytical techniques, this approach enables a deeper understanding of the processes driving the evolution of this complex hydrothermal system.

CHAPITRE 3. EFFET DE LA CRISTALLISATION HORS EQUILIBRE ET DE LA RECRISTALLISATION DYNAMIQUE SUR LA THERMOMETRIE DU TI DANS LE QUARTZ DANS LES GISEMENTS PORPHYRES-EPITHERMAUX : APERÇUS DE PAGONI RACHI (NE DE LA GRECE) – ARTICLE SOUMIS A LITHOS

La compréhension de l'évolution des températures dans les systèmes porphyriques-épithermaux qui est un facteur est essentiel pour décrypter les processus de formation des gisements, tels que la séparation des phases fluides et la solubilité des métaux. Le quartz, un minéral commun dans ces systèmes, fournit des informations précieuses grâce à ses textures de croissance, ses inclusions fluides et la distribution de ses éléments traces. La thermométrie basée sur le titane dans le quartz (Ti-in-quartz) et l'analyse des inclusions fluides permettent de reconstituer l'histoire des fluides et les conditions thermiques. Cependant, la recristallisation dynamique du quartz, qui modifie sa texture et sa composition en éléments traces, peut compliquer les interprétations géochimiques.

Des taux de croissance plus rapides augmentent les concentrations de titane, tandis que la recristallisation peut réinitialiser ces concentrations et effacer les inclusions fluides, ce qui affecte les estimations de température. Les processus de déformation influencent les textures en cathodoluminescence (CL) du quartz et la distribution des éléments traces, la recristallisation modifiant les caractéristiques des inclusions fluides et l'état d'équilibre du titane. Ces facteurs peuvent introduire des biais dans les analyses géochimiques, en particulier dans les environnements magmato-hydrothermaux. C'est le cas ici pour le gisement de Pagoni Rachi (Grèce), exemple représentatif où de multiples générations de quartz et veines fournissent des informations clés sur l'évolution des fluides et la formation des gisements.

Comprendre ces processus est crucial pour une classification et une interprétation précise des gisements. L'impact potentiel de cette étude est donc significatif pour mieux contraindre les conditions de formation des gisements magmato-hydrothermaux.

Ce chapitre de discussion a fait l'objet d'une publication sous format article et vous sera présenté comme tel. Il a été soumis au Journal *Lithos* le 11/12/2024.

Effect of disequilibrium crystallization and dynamic recrystallization on Ti-in-quartz thermometry in porphyry-epithermal deposits: Insights from Pagoni Rachi (NE Greece)

Article soumis le 10/12/2024 à Lithos

Baptiste Abiven*[a], Alexandre Tarantola[a], Antonin Richard[a], Manuel Keith[b], Vasilios Melfos[c] and Panagiotis Voudouris[d]

*: baptiste.abiven@univ-lorraine.fr

[a]*GeoRessources, UMR 7359, Université de Lorraine, CNRS, Nancy 54000, France*

[b]*GeoZentrum Nordbayern, Friedrich-Alexander-Universität (FAU) Erlangen-Nürnberg, Schlossgarten 5, Erlangen 91054, Germany*

[c]*Department of Mineralogy, Petrology, Economic Geology, School of Geology, Aristotle University of Thessaloniki, GR-54124, Greece*

[d]*Department of Mineralogy and Petrology, Faculty of Geology and Geoenvironment, National and Kapodistrian University of Athens, 15784, Athens, Greece*

A B S T R A C T

Understanding the temperature evolution of magmatic-hydrothermal systems is key to unraveling fluid-rock-deformation interactions and related ore-forming processes. Ti-in quartz thermometry has been widely used to estimate temperatures in these systems, but its reliability may be significantly affected by disequilibrium crystallization and recrystallization of hydrothermal quartz veins. melting

Here, we use the Pagoni Rachi deposit (NE Greece) to provide insight into these processes. Typical A-type (ductile, 450–530 °C), B-type (ductile/brittle, 350–440 °C) and E-type (brittle, 210–340 °C) veins are developed in a continuum of deformation, forming from boiling fluids followed by cooling and dilution by surface waters. In A-type veins, intense recrystallization leads to variable Ti concentrations (10–60 ppm), yielding Ti-in-quartz temperatures (350–500 °C) that are lower than fluid inclusions trapping temperatures (~485 °C), likely due to Ti loss by diffusion during dynamic recrystallization. In later B-type veins, rapid growth under disequilibrium conditions results in overestimated Ti-in-quartz temperatures (460–740 °C), higher than fluid inclusions trapping temperatures (~395 °C). However, late-stage E-type veins show better agreement between Ti-in-quartz (120–310 °C) and fluid inclusions trapping (~260 °C) temperatures, as no recrystallization occurred.

Our results obtained for the Pagoni Rachi deposit show that disequilibrium crystallization and dynamic recrystallization processes can shift the Ti concentration in quartz leading to potential misinterpretation of the cooling path of magmatic-hydrothermal systems. This may lead to erroneous classification of vein types of porphyry-epithermal systems using Al/Ti and Ge/Ti ratios. More

generally, careful examination of quartz veins microtexture is key for reliable use of Ti concentration in quartz as a petrogenetic indicator.

Keywords: Porphyry-epithermal, Ti-in-quartz, thermometry, disequilibrium crystallization, dynamic recrystallization, fluid inclusions

3.1. INTRODUCTION

Understanding the temperature evolution of porphyry-epithermal systems is essential for elucidating ore-forming processes, including fluid-phase separation, metal solubility and the associated alteration and deformation history. Quartz, one of the most abundant minerals in the Earth's crust (Götze 2009), is particularly prevalent in hydrothermal ore deposits, including porphyry-epithermal mineralization (Seedorf et al. 2005; Sillitoe 2010). Due to its widespread presence and complex growth textures, which record multiple fluid and deformation events, quartz provides critical insights into the evolution and history of ore deposit formation (e.g., Casanova et al., 2021; Wilkinson, 2001; Bennett, 2014; Landtwing et al., 2005, 2010; Redmund et al., 2004; Monecke et al., 2018; Kouzmanov et al., 2012; Cernuschi et al. 2023; Acosta et al., 2022; Rusk and Reed, 2017; Rusk et al., 2006, 2012; Stipp et al., 2002a, b; Huang et al., 2012; Pan et al., 2019; Hong et al., 2024). Quartz is also a robust host for fluid inclusions, making it a useful tool for reconstructing fluid histories (e.g. Bodnar, 1995; Kouzmanov et al., 2012; Monecke et al., 2018). The combination of petrographic observations, including cathodoluminescence (CL), LA-ICP-MS analysis and fluid inclusion microthermometry, is widely used to discriminate fluid provenance and to constraint various physico-chemical fluid parameters, which are crucial for the genetic interpretation and classification of different mineralizing events (e.g., Tanner et al., 2013; Maydagan et al., 2015; Breiter et al., 2017, 2020; Mao et al., 2017; Schrön et al., 1988; Götze, 2009; Rottier and Casanova, 2021; Falkenberg et al., 2024). Indeed, trace elements are considered as CL-activators are quenchers, such as Ti which is considered as the main CL activator (Götze, 2009, 2012; Rusk et al., 2012). Consequently, fluid temperature constraints are commonly based on fluid inclusions (Bodnar, 1985, 2014; Wilkinson, 2001; Kouzmanov et al., 2012; Monecke et al., 2018) and Ti-in-quartz thermometry (e.g., Grujic et al., 2011; Zhang et al., 2020; Rottier et al., 2021; Rottier and Casanova, 2021; Hong et al., 2023; Falkenberg et al., 2024), which are both applied to the same quartz grains in barren and ore veins.

The incorporation of Ti in quartz during out-of-equilibrium crystallization is significantly influenced by the growth rate of the crystal. Research indicates that as the growth rate increases, Ti concentrations in quartz can more than double compared to equilibrium conditions (e.g. Huang and Audétat, 2012;; Cernuschi et al., 2018). For instance, Huang and Audétat (2012) demonstrated that fast growth leads to higher-than-equilibrium levels of impurities, specifically Ti, in quartz crystals. This is evidenced by the presence of euhedral oscillatory growth zones in quartz which show a wide range of Ti concentrations, indicating non-equilibrium growth (e.g. Butte porphyry deposit – Cernuschi et al., 2018). The variability in Ti content also suggests that trace element incorporation depends on crystallization kinetics, with faster growth allowing for enhanced Ti uptake, potentially linked to fluid dynamics during magma ascent (Cernuschi et al., 2018). Importantly, while uniform Ti distributions are often seen as indicative of equilibrium, studies show that they can also occur in rapidly grown crystals (e.g. Huang and Audétat,

2012). This nuanced understanding emphasizes the need for caution when applying Ti-in-quartz geothermometry in hydrothermal settings, as growth rates can vary widely (up to 100°C (Huang and Audétat, 2012), leading to inaccuracies in inferred formation conditions.

Shortly after veins filled, high temperature dynamic recrystallization preferentially changed the CL-euhedral quartz in vein centers to CL-mottled texture for reasons explained below. That the Ti concentration in CL-mottled crystals is the same as that in the dark bands in the adjacent CL-euhedral crystals indicates that the temperature of the strain that accompanied grain boundary migration was roughly the same as the temperature of the primary crystallization of the euhedral crystals, because recrystallization anneals quartz to its equilibrium Ti concentration. Ti diffusion through quartz is very slow (Jollands et al., 2020) but grain boundary migration induces Ti homogenization in quartz and allows it to reset to the equilibrium value at a rate that is much faster (Van der Kerkhof et al., 2004; Nachlas and Hirth, 2016).

However, deformation processes or growth rates may affect the distribution of elements, CL imagery and fluid inclusion constraints in quartz (Nachlas et al., 2015; Cernuschi et al., 2018; Acosta et al., 2022, Liu et al., 2023). The state of intragranular deformation provides key information on the strain rate at a given temperature (Stipp et al., 2002a, b). Thus, a high-temperature (500–600 °C) and low-strain rate system will result in high-intensity dynamic recrystallization of the grain boundary migration (GBM) type with interlobate quartz structures, for example and a heterogeneous grain size distribution, associated with an increase in grain boundary surface areas (Passchier and Trouw, 2005). By contrast, a low-temperature (250–400 °C) but high-strain rate system will result in low-intensity dynamic recrystallization of the bulging (BLG) type, with a reduction in grain size, associated with a bimodal grain size distribution with large quartz grains surrounded by smaller grains (Stipp et al., 2002a, b; Passchier and Trouw, 2008). Intermediate intensity structures, such as subgrain Rotation (SGR), present straight grain boundaries and a rotation of quartz crystal/subgrain orientations are linked to moderate temperature of 400–500 °C. In general, three major parameters control the dynamic recrystallization of quartz: the temperature, the deformation rate and the influence of circulating fluids (Stipp et al., 2002a, b; Passchier and Trouw, 2005; Grujic et al., 2011; Nachal and Hirth, 2015; Bromiley and Hiscock, 2016). In the same way the effects of non-equilibrium crystallization can play on the interpretation of Ti data (Nachlas and Hirth, 2015; Cernuschi et al., 2018; Acosta et al., 2022,) but not quantified or evaluated.

The recrystallization of quartz influences the equilibrium of contained fluid inclusions (structure, chemical composition) (Kerrich, 1976; Audétat and Günther, 1999; Tarantola et al., 2010, 2012; Lecumberri-Sanchez et al., 2012; Diamond and Tarantola, 2015; Eglinger et al., 2014; Audétat, 2023). Recrystallisation may stretch fluid inclusions, generate volume modification (increase of homogenization temperature) and water loss, increase of salinity, so an increase of T_m(hal) observed during microthermometric measurements. Extreme recrystallization can erase fluid inclusions from the host mineral (Kerrich, 1976; Audétat and Günther, 1999; Tarantola et al., 2010; Voudouris et al., 2013a; Audétat, 2023). Recrystallization of quartz may also affect the element distribution by diffusion,

potentially leading to a loss of elements into the surrounding matrix. Titanium can diffuse within quartz crystals especially during such processes (Cherniak et al., 2007; Ashley et al., 2014; Bromiley and Hiscock, 2016; Nachlas and Hirth, 2015). Additionally, Nachlas and Hirth (2015, 2018) concluded that dislocation creep facilitated by GBM enhances the resetting of Ti in quartz. Titanium partitioning into dislocations can accelerate overall diffusivity, helping to equilibrating quartz during deformation through SGR and GBM mechanisms. This allows mineral compositions to re-equilibrate more rapidly than through static volume diffusion, explaining such re-equilibration across different geological contexts, including hydrothermal environments. Grujic et al. (2011) proposed that GBM conditions reset the quartz Ti signal, whereas weaker deformation associated with SGR or BLG does not. Accordingly, Ti diffusion may also impact the temperatures obtained by Ti-in-quartz thermometry and the luminescence of quartz and thereby the CL imagery (Huang and Audétat, 2012; Acosta et al., 2020). The CL textures of quartz are thus not only indicative of fluid circulation and quartz growth, but also record potential disequilibrium conditions (Götze, 2012; Monecke et al., 2018; Acosta et al., 2020, 2022). When well crystallized, quartz shows marked oscillatory growth zoning, while recrystallized quartz may show specific CL textures like ghost bands, mosaic, or mottled patterns — characterized by erased or darkened CL signals (Landtwing and Pettke, 2005; Rusk et al., 2014; Monecke et al., 2018; Acosta et al., 2022).

Dynamic recrystallization was predominantly studied under metamorphic conditions and in experiments (e.g., Urai, 1986, Stipp et al., 2002a, b; Grujic et al., 2011; Nachlas et al., 2014, 2018; Nachlas and Hirth, 2015). Although the duration of recrystallisation processes is much shorter in magmatic-hydrothermal systems, recent studies demonstrated that quartz exhibits the same types of recrystallization patterns within hydrothermal systems (e.g. Acosta et al., 2022), which may also help to explain potentially biasing geochemical interpretations and classifications of vein-types in porphyry-epithermal systems. Most research on CL textures and trace element chemistry in porphyry deposits has focused on common Cu-Mo sub-types (e.g., Redmond et al., 2004; Landtwing and Pettke, 2005; Rusk et al., 2006, 2008; Rusk, 2012; Muller et al., 2010; Tanner et al., 2013; Maydagan et al., 2015; Mao et al., 2017; Monecke et al., 2018; Rottier and Casanova, 2021; Rottier et al., 2021; Gao et al., 2022; Falkenberg et al., 2024). However, the effects of dynamic recrystallization on Ti concentration in quartz under the temperature conditions typical of porphyry-epithermal systems (150–500 °C) are not well understood and are still understudied.

The use of trace elements in quartz is commonly accepted for retracing fluid evolution in hydrothermal systems and veins classification, notably Al, Ge, and Ti (e.g. Götze et al., 2012; Rottier and Casanova, 2021; Falkenberg et al., 2024), whose incorporation into quartz during crystallization depends on *PTX* conditions (pressure, pH, temperature). This allows for the interpretation of vein formation environments through the geochemistry of quartz, which is ubiquitous in these systems. However, in the case of out-of-equilibrium crystallization and dynamic recrystallization leading to concentration changes, to what extent would the geochemical interpretation (Al, Ti, Ge) be affected?

The Pagoni Rachi porphyry-epithermal Cu-Mo (Re-Au) deposit in NE Greece is a prime example, where multiple quartz generations are preserved, closely associated with Cu-Mo (± Re ± Au) deposition. Here, typical A-type (ductile, 450–530 °C), B-type (ductile/brittle, 350–440 °C) and E-type (brittle, 210–340 °C) veins are developed in a continuum of deformation, forming from the same boiling fluids followed by cooling and dilution by surface waters (Voudouris et al., 2013a). By combining textural observations with fluid inclusions and in-situ trace element analysis of quartz from A-, B- and E-type veins, this study investigates the potential disturbing effects of deformation on trace element composition, fluid inclusion constraints and Ti-in-quartz thermometry. The dynamics and kinetics of the complex growth histories of quartz, arranged in a relative chronological order, provide new insights into magmatic-hydrothermal processes. As such, the approach has significant implications for porphyry ore formation, as disequilibrium crystallization and dynamic recrystallization of quartz is a commonly observed but often overlooked process.

3.2. GEOLOGICAL AND METALLOGENIC CONTEXT

The Tethyan Metallogenic Belt (TMB) stretches from the Alps to the Himalayas and hosts numerous hydrothermal deposits, rich in metals like Au, Cu, and Mo. These deposits formed during the subduction of the Neo-Tethys Ocean and collisions between tectonic plates. In the Southeast Balkans-Rhodopes region (NE Greece, SE Bulgaria, NW Turkey), magmatic-hydrothermal deposits are notable for their rare and precious metal content. Post-orogenic processes and slab rollback also contributed to Cu-Mo deposit formation in the Balkans during the Eocene. The Pagoni Rachi porphyry-epithermal system is part of the Sapes-Kirki ore district in Western Thrace, NE Greece. The mineralization is centered in a high-K calc-alkaline biotite-amphibole granodiorite porphyry (Figure 44).

The Cu-Mo-(Re-Au) mineralization occurs in the form of a succession of mineralized veins, organized in a stockwork pattern, with typical successive hydrothermal stages (Voudouris et al., 2013a) (Figure 44, *Table 1*). The nomenclature of vein- and alteration-types, based on structural criteria (vein shapes, structures) and mineralogical composition (mineral assemblage of vein or alteration), is

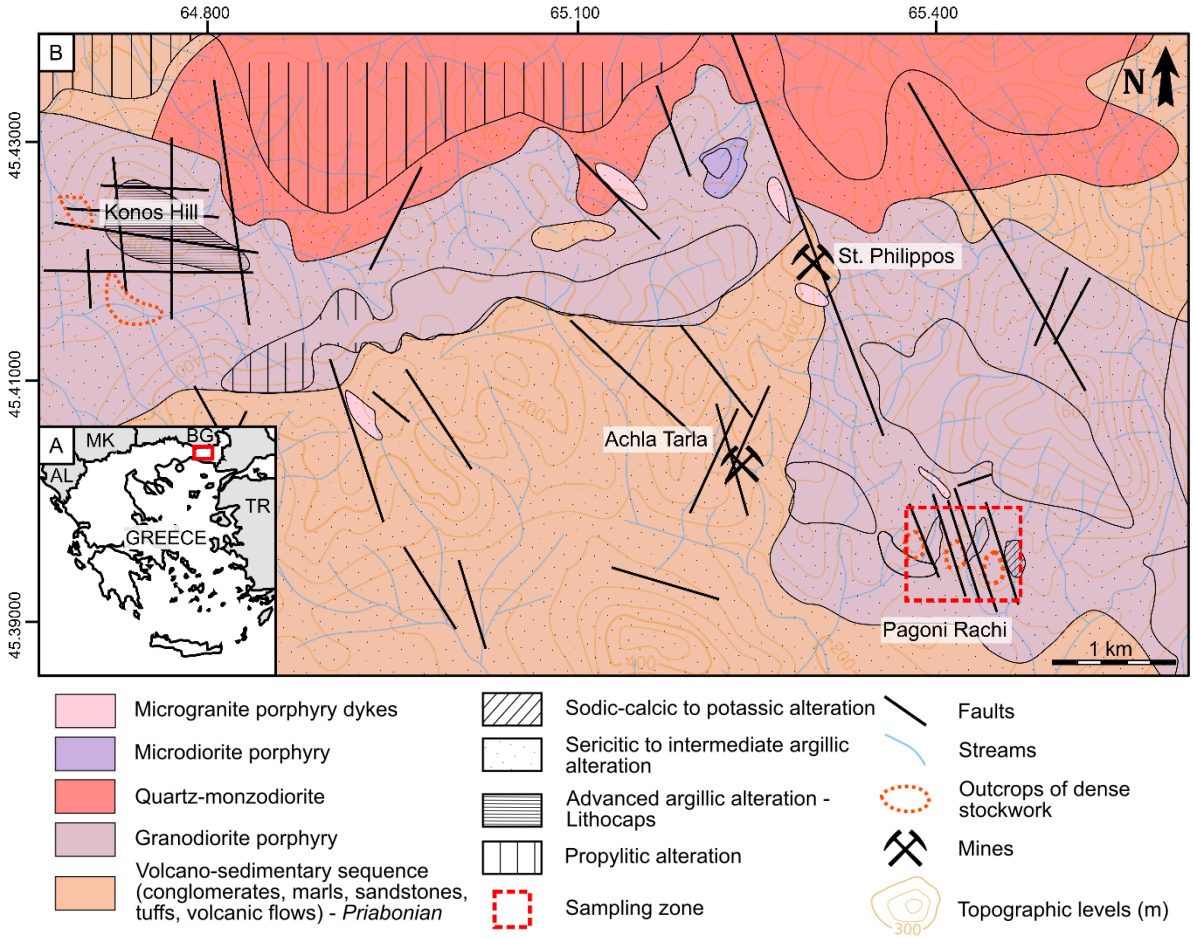

Figure 44 : Geographical and geological context of the study area and sampling zones. A. Geographic location (red rectangle) of the Sapes-Kirki district in Thrace, NE Greece – AL= Albania, BG= Bulgaria, MK= Macedonia, TR= Turkey. B. Geological and alteration map of the Sapes-Kirki district. The porphyry-epithermal mineralization at Pagoni Rachi is found within a granodioritic body at the Southeastern part of the map. Early potassic to sodic-calcic alteration are frequently overprinted by other alterations, as propylitic, sericitic or advanced argillic alteration (based on Mavrogonatos et al., 2020).

consistent with previous studies of porphyry and epithermal systems (i.e. Sillitoe, 2010; Voudouris et al., 2013a, b; Monecke et al., 2018):

(i) The earliest stage is represented by A- and M-type veins, which are sinuous and discontinuous. They are dominated by quartz and magnetite, respectively, with only little sulfide occurrence. In some A-type veins, magnetite and pyrite form a mineralized line in the center of the gangue quartz. A-type veins contain saccharoidal quartz, magnetite, pyrite, hematite, as well as minor biotite, feldspars (albite, orthoclase), chalcopyrite, bornite, molybdenite and native Au. The veins are associated with proximal sodic-calcic to potassic alteration with quartz, biotite, orthoclase/albite, actinolite, magnetite, epidote and chlorite, where the two latter minerals are possibly the result of an inner propylitic overprint (Figure 45 A–C). (ii) The second stage consists of parallel B-type veins that are continuous quartz-bearing and have a sinuous to straight shape with sharp boundaries. Sulfides occur at the vein margins, disseminated in quartz or along the center of the vein. The B-type veins contain quartz (anhedral to euhedral), pyrite, chalcopyrite, molybdenite (with high Re content as evidenced by intercalated sheets of rheniite, ReS_2) and minor hematite, magnetite, albite, chlorite, fluorite, sericite and calcite (Voudouris et al., 2009, 2013a, b). Some reopening filled by albite, calcite, fluorite and sericite can appear in the center of the veins. The host-rock alteration assemblage is composed of quartz, albite/orthoclase, chlorite and calcite, corresponding to a sodic-potassic alteration (Figure 45 A–C). (iii) The third stage consists of massive straight continuous pyrite-chalcopyrite-molybdenite veins (D-type) cross-cutting previous veins, especially the B-type veins. They are associated with pervasive sericitic alteration, consisting of pyrite, quartz, sericite and calcite. This marks the transition from the porphyry to the epithermal environment (Richards, 2015) where the latter is reflected by (iv) straight continuous quartz-carbonate veins (E-type) with base metal sulfides, such as galena, sphalerite and chalcopyrite that contain elevated concentrations of critical and precious (semi-)metals (Te, Bi, Au, Ag, Se) (Voudouris et al., 2009, 2013a, b) (Figure 45 C, D). The E-type veins are associated with advanced argillic alteration assemblages characterized by kaolinite, sericite, calcite, quartz and disseminated pyrite.

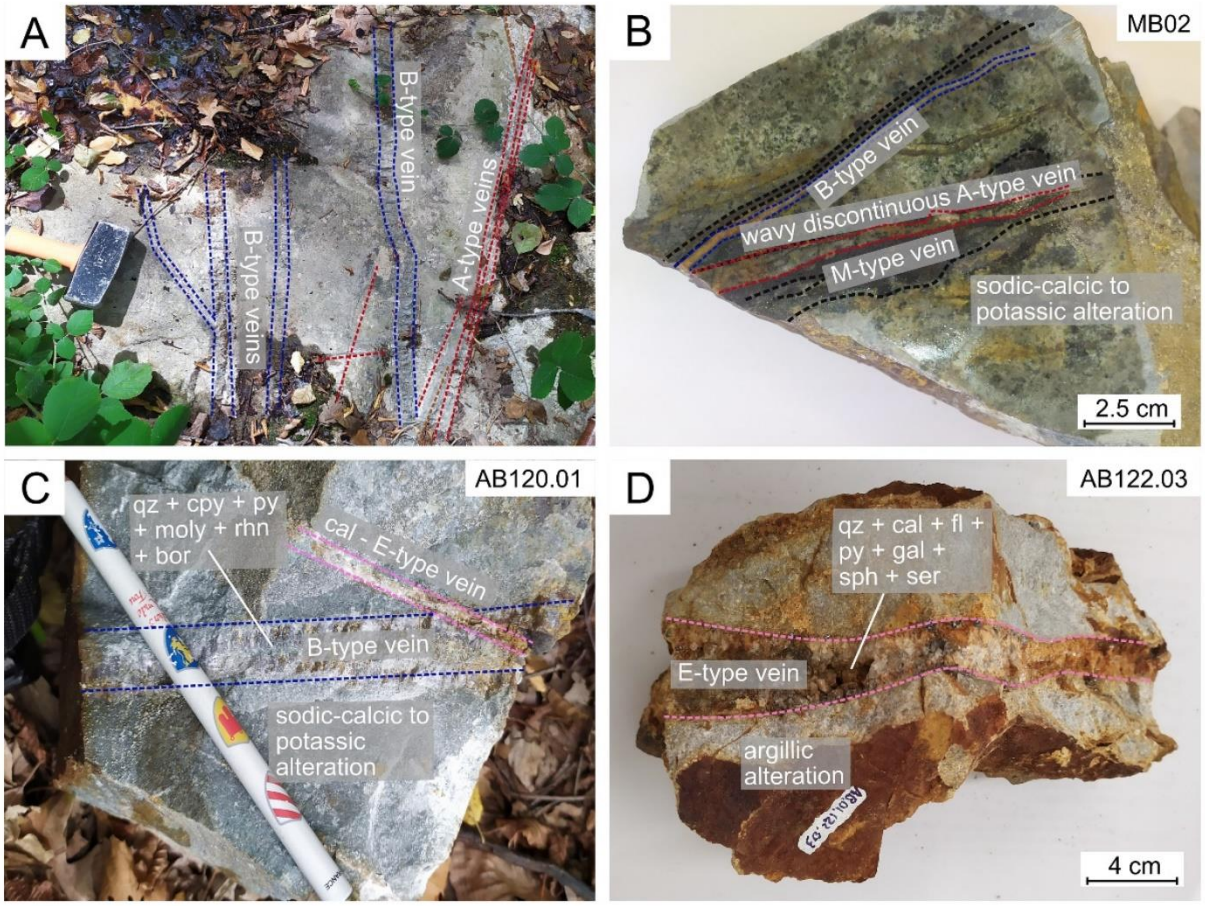

Figure 45: Petrography of A-, B- and E-type veins (outcrops and hand specimens) from Pagoni Rachi. A. Outcrop of a stockwork of A- and B-type veins enclosed within a potassic altered granodiorite. B. Granodiorite with propylitic alteration overprinting potassic alteration hosting a stockwork of A-, M-, and B-type vein (quartz-chalcopyrite-molybdenite). C. Potassic altered granodiorite with propylitic overprint enclosing a B-type vein (quartz-chalcopyrite-pyrite-bornite-molybdenite-rheniite) and E-type vein (calcite). D. Granodiorite with sericitic/argillic alteration cut by an E-type vein with comb quartz filling, containing base metal minerals (pyrite, sphalerite, galena) and calcite. Red dashed lines= A-type veins, black= M-type veins, blue= B-type veins, pink= E-type veins. Abbreviations: bor= bornite, cal= calcite, cpy= chalcopyrite, fl= fluorite, gal= galena, moly= molybdenite, py= pyrite, qz= quartz, rhn= rheniite, ser= sericite, sph= sphalerite.

Table 1: Petrological characteristics of the different vein types, part of the mineralized stockwork of Pagoni Rachi. Abbreviations: Act= actinolite, Ab= albite, Bt= biotite, Bn= bornite, Cal= calcite, Cpy= chalcopyrite, Chl= chlorite, Eng= enargite, Ep= epidote, Fl= fluorite, Gn= galena, Hem= hematite, Kln= kaolinite, Mag= magnetite, Mol= molybdenite, Or= orthoclase, Py= pyrite, Qz= quartz, Rhn= rheniite, Ser= sericite, Sp= sphalerite, Tnt= tennantite, Ttr= tetrahedrite.

Ore mineralization style	Vein type	Vein assemblage	Alteration assemblage (type)	Vein textures	Quartz structures	CL textures	Deformation textures *(temperatures from Stipp et al. 2002a,b)*	Sample (GPS)
Porphyry	A	Qz + Mag + Hem + Py + Bt + Or/Ab + Act + Ep + Cpy + Bor + Moly + Chl + Ser	Qz + Bt + Or/Ab + Act + Ep + Mag + Hem + Chl (potassic - propylitic overprint)	Irregular and sharp borders, variable thickness, asymmetric, discontinuous to continuous, undulating	Anhedral, granular, with subgrains and lobate margins - 10 to 100 microns size, seriate distribution, no preferential crystal orientation	Dark to medium bright CL from dark red to blue, with mosaic texture, rare ghostbands, and rare oscillatory growth zoning relict	Intense generalized SGR; intense local to generalized GBM *(400 - 600 °C)*	MB02 (N40°59,744' E25°50,144')
	B	Qz + Py + Cpy + Mol + Rhn + Hem + Bt +Chl + Ep + Ab + Fl + Cal + Ser	Qz + Bt + Ab/Or + Chl + Cal + Ep (potassic - propylitic overprint)	Regular and sharp borders, constant thickness, central axial symmetry, continuous, planar, syntaxial	Anhedral to subhedral, at margins or near fractures, elongated in central parts, growing stripes of opaque minerals, preferential orientation of crystal elongation orthogonal to the walls - 10 to x100 microns size	Dark to medium bright CL from dark red to blue, oscillatory growth zoning showing syntaxial opening, with frequent ghostbands at elongate quartz margins, mosaic textures near fracture and deformation zones	SGR at vein margins or at fractures contacts, local GBM at elongate quartz margins, rare local, weak to moderate BLG *(250 - 400 °C)*	MB02 (N40°59,744' E25°50,144') AB120.01 (N40°59'46"; E25°49'56")
Epithermal	E1	Qz + Fl + Py + Gal + Sph + Cpy + Ser + Kln + Tnt + Ttr + Eng	Qz + Cal + Ser + Kln (advanced argillic)	Straight veins, regular and sharp borders, constant thickness, continuous, frequent branching, comb quartz	Undeformed elongated euhedral quartz, orthogonally oriented to the vein walls, comb quartz - 100 to x100 microns in size	Oscillatory growth zoning from center to margins of quartz crystals	Fractures *(< 250 °C?)*	AB.122.03 (N40°58'29"; E25°49'56")
	E2	Cal + Fl + Py + Gal + Sph + Ser + Kln	Qz + Cal + Ser + Kln (advanced argillic)	Straight veins, irregular and sharp borders, constant thickness, continuous with frequent branching	Calcite: Subhedral to euhedral, frequent twins when crosscutting older veins	Calcite: Oscillatory growth zoning from center to margins	Twins when crosscutting older veins	AB.122.03 (N40°58'29"; E25°49'56")

Major NNW-SSE trending faults crosscut the magmatic body, which are linked to the E-type veins and to some late-stage veins associated with silicified breccias following the same trend at Sant Philippos (Figure 44). This consecutive vein sequence was the basis for previous fluid inclusion and micro-analytical studies of the vein stockwork at Pagoni Rachi (Voudouris et al., 2009, 2013a, Mavrogonatos et al., 2019, 2020). In these studies, three types of fluid inclusions were described, including: (i) Type 1 two-phase (at room temperature) liquid + vapor (LV) inclusions with low salinity (1.4 to 2.9 $wt\%_{equiv.NaCl.}$), homogenizing to the liquid phase at ~ 250 °C. (ii) Type 2 three-phase (at room temperature) liquid + vapor + halite (LVH) inclusions with high-salinity (36 to 74 $wt\%_{equiv.NaCl.}$), homogenizing to the liquid phase at temperatures from 400 to 500 °C. Post-entrapment modification was suggested for some Type 2 inclusions that homogenize by dissolution of halite. (iii) Type 3 two-phase (at room temperature) liquid + vapor (LV) inclusions of low to intermediate salinity (1.7 to 10.7 $wt\%_{equiv.NaCl.}$), homogenizing at temperatures in the range from 400 to 500 °C to the vapor phase. The type 2 and 3 fluid inclusions were only observed within quartz of the A- and B-type veins, whereas the Type 1 inclusions were found in all vein-types, but particularly in the E-type veins. Voudouris et al. (2013a) proposed an evolution of fluid *PT* conditions with phase separation at 400 to 500 °C associated with the A- and B-type veins. This was suggested to be followed by a progressive dilution of magma-derived fluids by surface waters causing cooling to 250 °C and decreasing fluid salinity (Voudouris et al., 2013a).

3.3. SAMPLING AND METHODS

3.3.1. Sampling selection

The sample selection for this study aimed at covering the deformational history and magmatic-hydrothermal evolution of Pagoni Rachi, with a focus on quartz-bearing vein types. The samples were chosen because they show all typical macroscopic characteristics of A-, B- and E-type veins of the Pagoni Rachi magmatic-hydrothermal system (Voudouris et al., 2013a, b; Mavrogonatos et al., 2019, 2020) (*Table 1*). A set of five samples hosting A-, B- and E-type veins, all cutting altered granodiorite were cut for thin and doubly-polished thick (150 μm) section preparation at GeoRessources (Figure 45): MB0201 (A- and B-types), MB0202 (A- and B-types), AB120.01 (B-type), AB.122.03 (E-type) and MB11.02.01 (E-type).

3.3.2. Cathodoluminescence (CL) imaging

The (CL) imaging of quartz from the different vein-types was performed on thin sections at GeoRessources by (i) an OPEA Cathodyne using the following parameters: P = 50–60 mTorr, T = 11.0–14.0 mV, I = 250–480 μA and a 5–10 s obturation duration and (ii) a SEM TScan was used with the following parameters: T = 15 kV, I = 2–3 nA, x300 magnification and 4 min obturation. The former provided CL imagery on the section scale, while higher resolution imaging was performed by the latter. Combining the two approaches is particularly suitable for investigating zoned quartz next to carbonates, exhibiting strong yellow-red luminescence. It is noteworthy that the CL intensity of different images with varying acquisition parameters (voltage tension, intensity, pressure and device) can usually not be compared. However, the presence of different vein-types in the same sample with varying CL intensity allowed such a comparison to some extent.

3.3.3. Fluid inclusion analysis

Fluid inclusions hosted in quartz of the different vein-types were studied on thick sections at GeoRessources. After a detailed petrographic study, primary fluid inclusions were analyzed by a Linkam THMS600 cooling-heating stage, designed to work in the temperature range –180 to +600 °C, linked to an Olympus BX50 microscope equipped with several objectives (x10 to x100) and a camera for image caption.

The stage was calibrated prior to each analytical session by measuring the phase transition temperatures of natural and synthetic standard fluid inclusions: the triple point of CO_2 at –56.6 °C, the melting point of pure water at 0.0 °C (synthetic sample) and the homogenization temperature of natural fluid inclusions at +165 °C. A heating rate of 10 °C/min was first adopted and then reduced to 2.0–0.1 °C/min approaching the phase transitions of interest, with stabilization steps of 2 minutes. The

temperature accuracy was 0.1 °C for temperatures <31.0 °C and 1 °C for high temperatures. The samples were first cooled to –100 °C, then gradually heated. The following phase transition temperatures were reported: T_e the first melting temperature (eutectic); T_m(ice) the ice melting temperature; T_h (L+V→L), T_h (L+V→V) the temperature of total homogenization by disappearance of the vapor or liquid phase, respectively; T_m(hal) the dissolution temperature of halite.

Although fluid inclusions along growth zones were noticed, they were too small to be analyzed. Fluid inclusions were identified due to similarities in size and shape and constant phase ratios based on petrographic observations and were interpreted accordingly as primary, pseudo-secondary or secondary fluid inclusion assemblages (FIAs) (Goldstein and Reynolds, 1994a, b; Bodnar et al., 2014). Only fluid inclusions that are most probably of primary origin were measured, which were either evenly clustered, isolated or forming quartz intragrain trails. Fluid inclusion petrography was supplemented by the CL-imaging to determine more accurately the geometric relationships between fluid inclusions and the host quartz growth zoning.

The salinity was calculated from T_m(hal) using the Sterner et al. (1988) equation for Type 1 (LV) and Type 3 (VL) fluid inclusion and the Bodnar et al. (1993) equation for Type 2 (LVH) fluid inclusion. Based on this description of Type 2 and Type 3 fluid inclusion trapping, they concluded there was boiling (Voudouris et al., 2013a). In the case of boiling, the T_h represents the trapping temperature, and the P_h represents the trapping pressure ($P_{trapping}$) (e.g., Diamond, 2001). Trapping pressures are obtained from these pressures.

The trapping pressure was graphically determined using the *PTX* diagram from Bodnar et al. (1993) showing the isotherm curves (representing the T_h of fluid inclusion) (Supplementary), using salinity and T_h values as entry data. The T_h and salinity of each fluid inclusion has been used (i.e. a fluid inclusion with T_h = 500 °C and a salinity of 35.0 wt%$_{equiv.NaCl.}$). A vertical line passing through the salinity scale at the salinity value of the fluid inclusion (35.0 wt $_{equiv.NaCl.}$) is draw and plot the fluid inclusion point at the intersection between the corresponding isothermal curves (T_h = 500 °C) and the vertical line (salinity = 35.0 wt%$_{equiv.NaCl.}$). Then, the pressure value is found by drawing a horizontal line from the crossing the fluid inclusion point and *P* scale and report the pressure value at the intersection between both lines (~ 500 bars). In addition, the pressure of NaCl-H_2O fluid inclusions was also estimated using the Atkinson (2002) equation in the HokieFlincs_H2O-NaCl spreadsheet (Steele-MacInnis et al., 2012), which yielded similar pressure estimates (within 5% difference) as those obtained by the above-described method.

3.3.4. Selection of previous fluid inclusion data

Fluid inclusion data from Voudouris et al. (2013a) were used to supplement the measurements from this study. This is possible because the measurements were made on the same or similar samples. The selected data correspond to fluid inclusions for which T_h, T_m(ice), T_m(hal) and the salinity values were

available, allowing to calculate the trapping pressure using the method described above (following Bodnar et al. (1993)).

Then, the main observation of the dataset from Voudouris et al. (2013a) is that Type 2 and Type 3 fluid inclusions, associated to a phase separation, from A-type vein display a bimodal T_h dispersion : one population centered at 486 ± 17 °C ranging from 457 to 510 °C at a $P_{trapping}$ ranging from 273 to 497 bars (mean at ≈ 333 ± 55 bars) and a second population centered around 388 ± 15 °C ranging from 360 to 412 °C, at $P_{trapping}$ ranging from 120 to 295 bars (mean at ≈ 222 ± 53 bars). In the B-type vein, the $T_{h,}$ of Types 2 and 3 fluid inclusion, show a unimodal dispersion, overlapping the second population of A-type veins, that is centered around 396 ± 16 °C at a range $P_{trapping}$ from 190 to 357 bars (*Table 2*). E-type veins (Voudouris et al. 2013a) present a unimodal population of Type 1 fluid inclusions (named E), with minimal T_h ranging from 219 to 334 °C (mean at ≈ 264 ± 35 °C) and a minimal $P_{trapping}$ from 22 to 133 bars (mean at ≈ 55 ± 34 bars). However, dozens of their measurements, on A- and B-type veins, display evidence of reequilibration, these data are not considered in this study. Secondary Type 1 fluid inclusions in A and B-type veins are not considered in this study, indeed they are late and associated to a cooling and mixing of derived surface fluids, while we are only interested in the contemporary fluid of a type of vein and not in secondary fluids. The selected fluid inclusion data are available from Supplementary file and summarized in Table 2.

Table 2 : Synthesis of fluid inclusion data (this study and from Voudouris et al. 2013a), showing the different fluid events.

Vein type	Fluid inclusion	T_h (°C)		T_m (°C)		Sal. (wt%$_{equiv.NaCl.}$)		$P_{trapping}$ (bar)		n
		Range	Mean ± 1σ	Range	Mean ± 1σ	Range	Mean ± 1σ	Range	Mean ± 1σ	
A	Type 2	457–510	486 ± 12	394–502	440 ± 40	46.5–60.0	52.0 ± 5.0	273–497	333 ± 55	12
	Type 3	470–490	483 ± 11	–5.7– –4.4	–4.8 ± 0.7	7.0–8.8	7.6 ± 1.1	495–605	564 ± 60	3
	A - event	457–510	486 ± 16	/	/	/	/	273–605	379 ± 110	15
	Type 2	360–391	379 ± 16	315–347	327 ± 17	39.3–42.1	40.4 ± 1.5	120–173	152 ± 29	3
	Type 3	371–419	391 ± 15	–7.0– –0.4	–5.2 ± 3.0	0.8–10.4	8.0 ± 2.6	201–319	239 ± 40	14
	later - event	*360–419*	*389 ± 15*	/	/	/	/	*120–319*	*234 ± 51*	*17*
B	Type 2	418–436	420 ± 13	274–323	293 ± 18	36.2–39.9	37.6 ± 1.4	190–260	228 ± 44	8
	Type 3	366–428	394 ± 15	–6.3– –2.8	–4.5 ± 0.9	4.6–9.6	7.2 ± 1.3	191–357	259 ± 40	47
	B - event	366–436	398 ± 17	/	/	/	/	190–357	255 ± 40	55
E	E - event	219–334	264 ± 35	–1.7– –0.6	–1.2 ± 0.3	1.1–2.9	2.0 ± 0.5	22–134	55 ± 34	29

Voudouris et al. 2013a described Type 2 fluid inclusions that homogenize by halite dissolution in quartz of the A- and B-type veins. According to Bodnar (2003), Lecumberri et al. (2012) and Audétat (2023) this suggests (i) the reequilibration of fluid inclusions by stretching and H_2O loss during host-quartz recrystallization, or (ii) the incorporation of halite crystals during trapping of a heterogeneous fluid. Most of the fluid inclusions show typical textures of deformation or elongation along subgrain boundaries within recrystallized quartz crystals (Tarantola et al., 2010; Eglinger et al., 2014). Numerous

fluid inclusions were deformed due to plastic deformation of the host crystals according to petrographic criteria reported in Kerrich (1976) and Tarantola et al. (2010) as evidence by homogenization by halite disappearance (T_m(hal) > T_h) (Lecumberi et al. 2012). Due to potential post-entrapment effects (e.g., water loss, density change) (Audétat and Günther, 1999; Audétat, 2023), we thus assert that the fluid inclusions showing homogenization by halite dissolution were reequilibrated by stretching, likely during the recrystallization of the host quartz crystals and do not represent the *VX* properties of the original mineralizing fluid. Because of the non-representative information of the trapping condition, these data are discarded from this paper.

3.3.5. Laser Ablation–Inductively Coupled Plasma–Mass Spectrometry (LA-ICP-MS)

The strategy for defining LA-ICP-MS spots was to select different microtextural domains of quartz (i.e. growth zoning, microtextures linked to deformation, undeformed grains) within the different vein types based on optical microscopy and CL imaging. Only spots with low variability in CL intensity were chosen on order to limit the possibility of mixing variable elemental concentrations, particularly for Ti, which is considered as the main CL activator (Götze, 2009, 2012; Rusk et al., 2012). Also, CL variations linked to partial recrystallization of fluid inclusions might cause a geochemical marking of the host quartz, as indicated by CL trails with low Ti concentration (Lambrecht and Diamond, 2014), which were also avoided. As far as reasonably possible, areas with visible fluid and solid inclusions were also avoided.

The LA-ICP-MS setup operated at GeoRessources consists of Agilent 7900 quadrupole ICP-MS coupled with a 193 nm ArF excimer laser (GEOLAS Pro). Laser ablation was performed with a constant frequency of 5 Hz and a fluence of 12 J.cm^{-2}, focused on the thick section surface. The ablation diameter was 50 μm. Helium was used as the carrier gas to transport the ablation-generated particles from the ablation cell to the ICP-MS. Argon was added as an auxiliary gas through a flow adapter before the ICP-MS torch. The reference materials NIST SRM 610 (primary) and NIST SRM 612 (secondary) were used for the external standardization (Jochum et al., 2011; Pearce et al., 1997). The standards were analyzed twice before and after each sample or every 20–30 measurements. The acquisition time included 30 s of background measurement, 60–90 s of ablation and 30 s of wash-out time. Thanks to the generally low trace element contents of quartz, stoichiometric Si content of quartz was assumed as a reasonable approximation for internal standardization (e.g. Müller et al., 2003; Monnier et al., 2018).

A total of 38 isotopes were measured with an integration time of 10 ms: ^{7}Li, ^{9}Be, ^{11}B, ^{23}Na, ^{24}Mg, ^{27}Al, ^{29}Si, ^{35}Cl, ^{39}K, ^{44}Ca (instead of ^{40}Ca to avoid isobaric interference with ^{40}Ar) , ^{47}Ti, ^{55}Mn, ^{56}Fe, ^{59}Co, ^{63}Cu, ^{66}Zn, ^{71}Ga, ^{72}Ge, ^{75}As, ^{85}Rb, ^{88}Sr, ^{90}Zr, ^{93}Nb, ^{95}Mo, ^{107}Ag, ^{115}In, ^{118}Sn, ^{121}Sb, ^{125}Te, ^{133}Cs, ^{137}Ba, ^{181}Ta, ^{182}W, ^{185}Re, ^{197}Au, ^{208}Pb, ^{209}Bi and ^{238}U. The different isotopes were selected for the following reasons: (i) they represent the most abundant isotope of a given element in order to maximize the

obtained signal (except for ^{44}Ca and ^{57}Fe, as significant interferences between ^{40}Ca and ^{40}Ar and between ^{56}Fe and $^{40}Ar^{16}O$ may occur) (ii) they represent metals and semi-metals that are known to be important constituents of the mineralization at Pagoni Rachi (Voudouris et al. 2013a), (iii) they represent elements that allow to discriminate the ablation of quartz from possible fluid/solid inclusions, such as K, Na, Cl, Fe and Ca and (iv) they represent elements commonly substituting into quartz (Al, Li, Ti, Ge) and may serve as markers for temperature, pressure, pH and growth rate (e.g., Götze et al., 2012, 2021; Raimbourg et al., 2022; Casanova and Rottier, 2021).

A total of 211 measurements were carried out, which were subsequently processed using the Iolite software (https://iolite-software.com) for data reduction. The limits of detection (LOD) of each element were calculated according to Longerich (1987) using the 3σ criterion. Initially, the retained spectra were those showing a stable signal over time. Signals showing intensity spikes of elements potentially representing fluid inclusions (K, Na, Cl) or solid inclusions such as silicates and oxides (Al, Ca, Fe, Mg, etc.) or sulfides (Cu, Re, Mo), were excluded from further data processing.

3.3.6. Ti-in-quartz thermometry

Several calibrations of Ti-in quartz thermometers are available from the literature (Wark and Watson, 2006; Thomas et al., 2010; Huang and Audétat, 2012; Zhang et al., 2020; Osborne et al., 2022). Recent studies have favored the calibration of Zhang et al. (2020) (Cernuschi, 2018; Rottier and Casanova, 2021; Hong et al., 2023). Indeed, it was shown to minimize the difference in temperature relative to genetically related fluid inclusions (Rottier and Casanova, 2021). The Ti-in-quartz thermometer also depends on the pressure conditions, since the Ti^{4+} substitution into quartz increases with decreasing pressure. Even though the calibration of Zhang et al. (2020) was initially valid for temperatures between 700–900 °C and pressures between 0.5–4.0 kbars, it was suggested to be also the best calibration for hydrothermal system at lower *PT* conditions), based on empirical observations demonstrating which show the lowest temperature difference (less than 30 °C) between temperature given by the calibration and the fluid inclusion (Rottier and Casanova, 2021).

The temperature of quartz crystallization was thus obtained using equation (1) (Zhang et al., 2020).

(1) $$T[\mathrm{Ti}] = \frac{1948.4 + 981.4 \times P^{0.2}}{5.3226 - \log_{10}([\mathrm{Ti}]_{\mathrm{Qz}})} - 273.15$$

where T[Ti] is the temperature of quartz crystallization (in °C), P is the pressure of quartz crystallization (in kbar) and $[\mathrm{Ti}]_{\mathrm{Qz}}$ is the Ti concentration in quartz (in ppm).

All Ti-in-quartz thermometers are *PX* dependent. The Ti content was measured, and the used data are the maximum Ti range for each population of each vein type (as $[\mathrm{Ti}]_{\mathrm{min}}$ and $[\mathrm{Ti}]_{\mathrm{max}}$), and the maximum P range for each vein type (as P_{min} and P_{max}), to constrain a range of T[Ti] for each vein type. This approach naturally introduces a bias in the reported values, but allows for the presentation of potential variations, which are also influenced by various processes to which Ti is sensitive. The pressure

of quartz crystallization was obtained from the trapping pressure of fluid inclusions population for each quartz generation (e.g. Tanner et al., 2013), from a merging of fluid inclusion dataset of this study and Voudouris et al. (2013a). Consequently, the *T*[Ti] domains are bounded by the minimal and maximal Ti concentration and pressure values for each vein type, $[Ti]_{min}$ and P_{min} giving the $T[Ti]_{min}$ and, $[Ti]_{max}$ and P_{max} giving the $T[Ti]_{max}$.

3.4. RESULTS

3.4.1. Petrography–quartz microtextures and cathodoluminescence (CL) imaging

The Pagoni Rachi deposit occurs as a mineralized stockwork enclosed within an altered granodioritic body (Figure 45 B). The granodiorite typically has a fine-grained matrix. When fresh, it consists of hornblende phenocrysts, biotite, plagioclase, quartz and disseminated magnetite. The succession of mineralized quartz veins and the associated alteration style of the host-rock allow defining a relative chronological sequence (Figure 45, Table 1).

The early A-type veins are mostly associated with potassic alteration assemblages, visible by the presence of hydrothermal biotite and K-feldspar, that locally shows signs of propylitic overprinting indicated by the presence of epidote, magnetite and chlorite that replaces biotite. The A-type veins are either continuous or discontinuous, undulating, with irregular edges, asymmetrical and variable thickness (mm to cm) (Figure 45 A, Figure 46 A). The veins are dominated by quartz (90–95%), as well as minor magnetite-hematite, pyrite, chalcopyrite, molybdenite and bornite (5–10%) (Voudouris et al. 2013a). Oxides and sulfides are disseminated within the A-type veins, along the vein selvage or form discontinuous lines. The quartz crystals range in size from a few microns to tens of microns and are granular, xenomorphic and do not exhibit any preferential orientation. Their size varies from tens of microns to several hundreds of microns with a seriate distribution (Figure 46 A-D). The edges of the quartz grains are straight and can be either sharp or not. In crossed-polarized light, several domains with distinct extinction are visible in individual quartz crystals (Figure 46 C), with well-developed to diffuse and polygonal grain boundaries forming sub-grains. These structures are typical for dynamic recrystallization of quartz through SGR (Stipp et al., 2002a, b; Passchier and Trouw, 2005), which is commonly intense and can be observed throughout the vein. Locally, the quartz shows interlobate edges with other quartz grains and sinuous edges that suggest dynamic GBM recrystallization (Figure 46 D) (Stipp et al., 2002a, b; Passchier and Trouw, 2005). These quartz micro-textures are markers of quartz deformation by dynamic recrystallization at elevated temperatures (400–600 °C) or relatively low deformation rates (Stipp et al., 2002a, b; Passchier and Trouw, 2005). The CL imaging of quartz crystals in A-type veins exhibits different color hues (reddish to blue) and intensities (dark to bright) (Figure 46 E-G). Luminescence and associated quartz structures are heterogeneous within the A-type veins. Several zones can be distinguished by microtextural domains in quartz: (i) mottled and mosaic CL patterns with dark red colors and some bluish streaks, where zones with chaotic red zoning are spatially associated

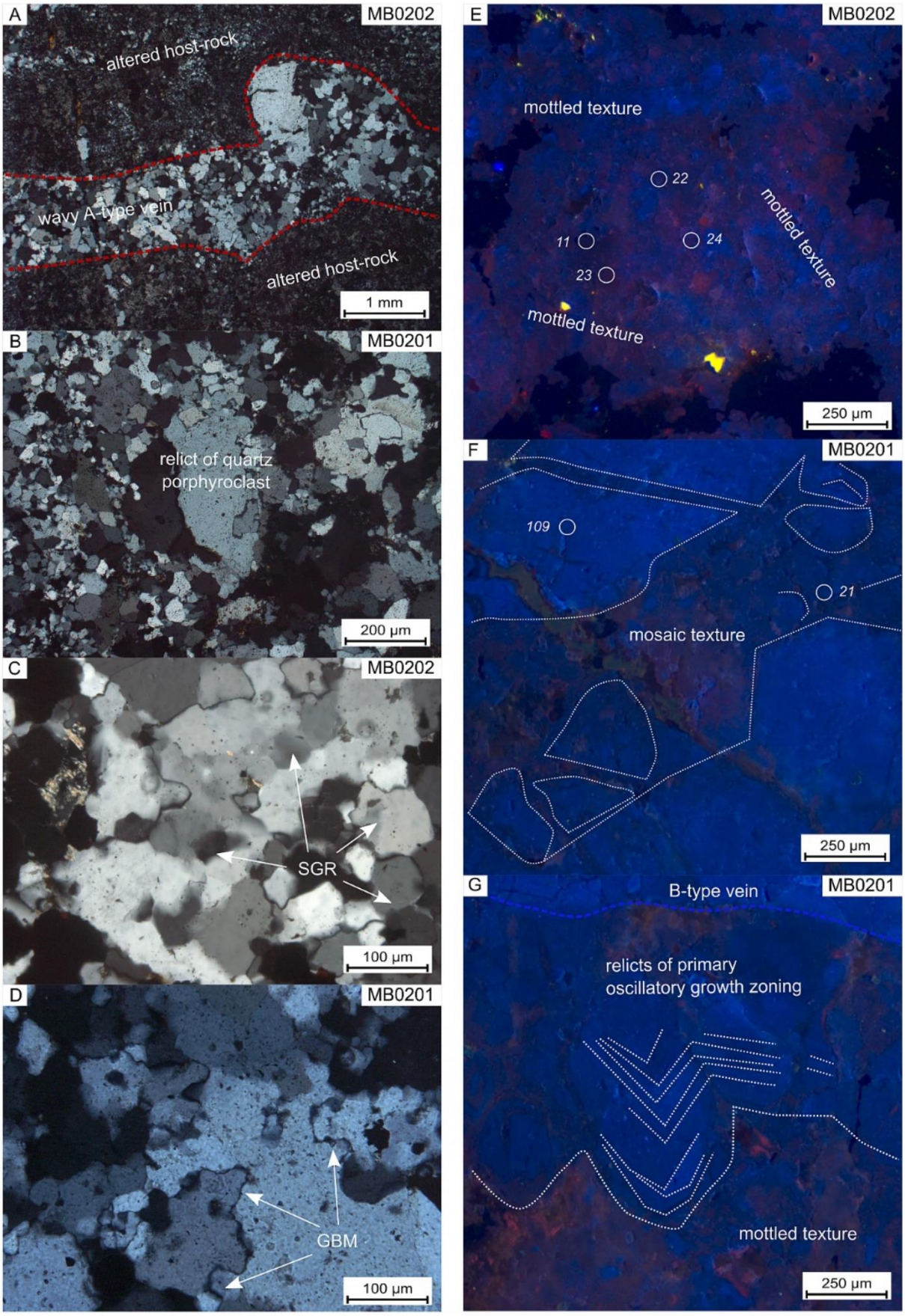
A
MB0202
altered host-rock
wavy A-type vein
altered host-rock
1 mm
B
MB0201
relict of quartz
porphyroclast
200 µm
C
MB0202
SGR
100 µm
D
MB0201
GBM
100 µm
E
MB0202
mottled texture
22
11
24
23
mottled texture
mottled texture
250 µm
F
MB0201
109
21
mosaic texture
250 µm
G
B-type vein
MB0201
relicts of primary
oscillatory growth zoning
mottled texture
250 µm

Figure 46: Cross-polarized (XPL) views of quartz petrography and microstructures and cathodoluminescence (CL) images of A-type veins. Ti concentration in ppm associated with the ablation spot location (white circles) are shown in E and F. A. Wavy A-type vein consisting of recrystallized quartz crystals crosscutting the granodiorite host rock. B. Quartz porphyroclast showing typical relicts of primary oscillatory growth zoning in contact with recrystallized quartz crystals with misorientation and a seriate size distribution (see details E and G). C. Dynamically recrystallized quartz crystals showing Sub-Grain Rotation (SGR). D. Dynamically recrystallized quartz crystals showing typical interlobate margins due to Grain Boundary Migration (GBM). E. CL imaging showing relicts of primary oscillatory growth zoning of quartz crystals in contact with mosaic and mottled CL texture linked to SGR- to GBM-type dynamic-recrystallization of quartz crystals. F. CL imaging of quartz crystal showing a mosaic texture linked to dynamically recrystallized quartz crystals. G. Relicts of primary oscillatory growth zoning domain in contact with a B-type vein, and a domain of quartz crystals with a mottled texture.

with domains of high intensity of dynamic recrystallization, particularly SGR and notably GBM, (ii) ghost band textures mostly at grain boundaries, near domains with moderately dynamic recrystallization intensity, especially of GBM type (Figure 46 D-F) and (iii) rare chevron zoning related to oscillatory growth textured quartz, with shades of blue luminescence. Domains with chevron zoning, without any defined orientation within the vein, are spatially associated with domains which display quartz textures associated to a lack of dynamic recrystallization or at a moderate intensity (Figure 46 B, G).

B-type veins are mostly associated with potassic alteration assemblages that locally shows signs of propylitic overprinting as also described above for A-type veins. The B-type veins that crosscut the earlier A-type veins (Figure 45 B; Figure 47 A) are continuous, planar, with sharp edges and show syntaxial textures (Figure 47 A). Quartz (90–95%) dominates the B-type veins, which also contain magnetite, hematite, pyrite, chalcopyrite, molybdenite (interlayered with rheniite sheets), bornite, covellite, digenite, chlorite, epidote and biotite (Voudouris et al. 2013a). In addition, the B-type veins exhibit a central axial symmetry and have a banded texture, emphasized by the presence of oxides and sulfides in the center of vein and a central quartz suture (Figure 47 A). Multiple structural and microtextural domains can be observed in quartz within the B-type veins, based on CL imaging. (i) Xenomorphic to granular quartz without preferred crystallographic orientation at the vein edges or in contact with fractures. Their size ranges from a few tens to a hundred microns with a seriate distribution. The granular quartz sometimes shows subgrain boundaries with diffuse to clear edges forming contiguous subgrains. These subgrains are associated with SGR dynamic recrystallization (Figure 47 B, C). Locally, interlobate borders of quartz grains are observable, suggesting GBM dynamic recrystallization (Figure 47 B, C). Small grains show CL ghost bands or mottled red colors of low intensity and some rare oscillatory growth zoning in discontinuous bluish chevrons. These chevrons are highlighted by discontinuous lines of magnetite/hematite. (ii) Sub-euhedral to euhedral quartz crystals

in the central part of the veins have interlobate borders and are oriented orthogonal to the vein selvage with a homogeneous sizes distribution ranging from a few hundred microns to some millimeters. The interlobate grain structures suggest an intense and localized dynamic recrystallization process of the GBM type. These elongated quartz grains may host discontinuous oxide chevron lines, suggesting a syntaxial growth of the vein. The CL imaging of this quartz-type shows oscillatory growth zoning in a chevron pattern with variations in hues and the intensity of blue, suggesting an oriented quartz growth

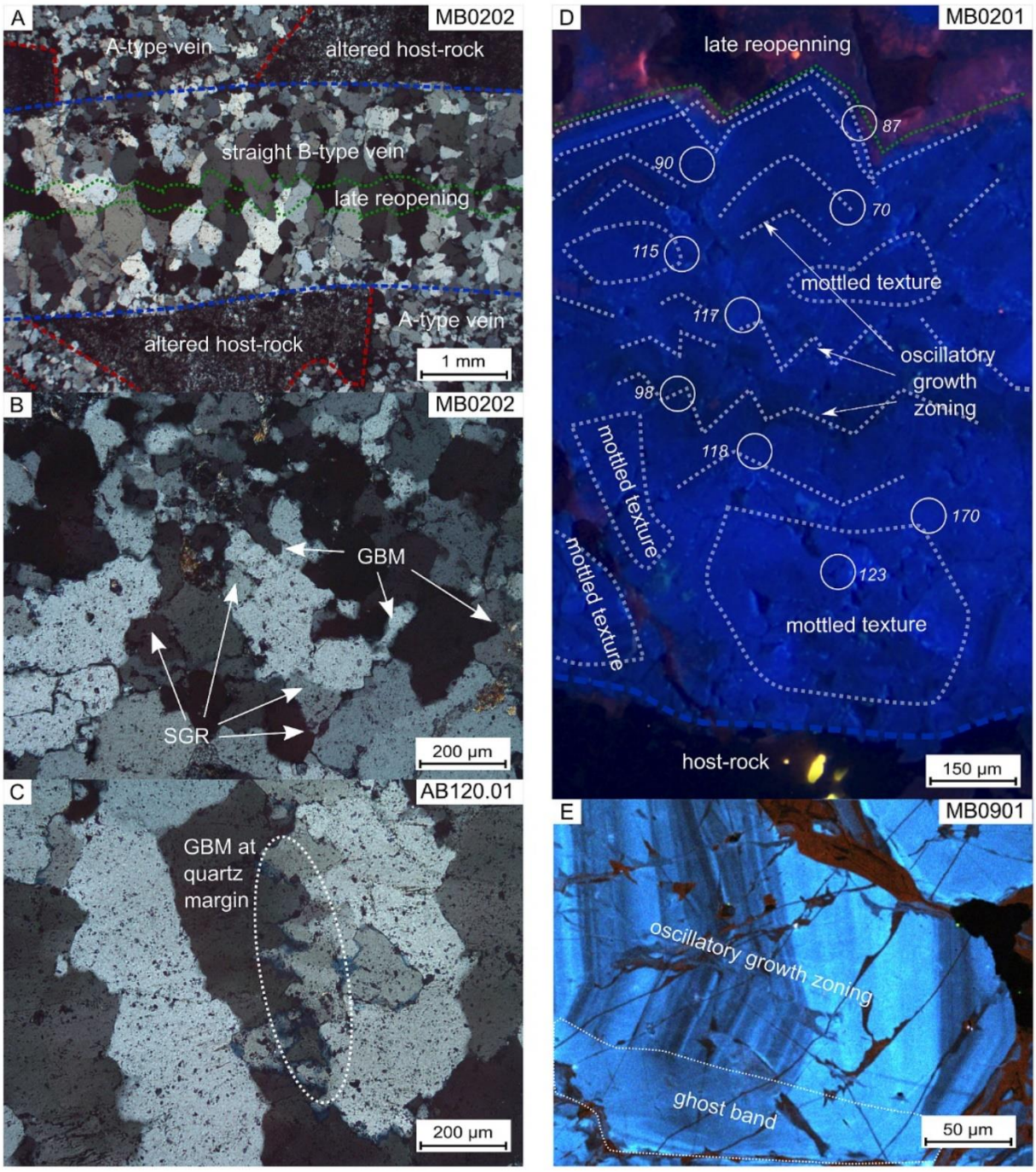

Figure 47: Cross-polarized (XPL) views of quartz petrography and microstructures and cathodoluminescence (CL) images of B-type veins. Ti concentration in ppm associated with the ablation spot location (white circles) are shown in D. A. Continuous and planar B-type vein with parallel walls and sharp margins, crosscutting a wavy A-type vein. The B-type vein shows a late reopening in the center of the vein (green dotted line) visible in CL (see details in B). Quartz grains show different types of dynamic recrystallization textures detailed in B and C. B. Dynamically recrystallized quartz crystals with SGR and GBM textures, typical of B-type vein margins. C. Dynamically recrystallized quartz crystals with GBM textures at margins, typical of the center of B-type vein. D. CL imaging of a half B-type vein showing oscillatory growth zoning orientated perpendicular to the wall, with a growth direction from the vein wall to the center of the vein, and with a late reopening with dark red CL. Few bright homogeneous domains show a mottled texture especially at vein margins. E. CL(-SEM) imaging of a euhedral quartz, from a B-type vein, showing primary oscillatory growth zoning and ghost band at contact with another grain and quartz-filled fracture.

towards the center of the vein, where the opaque mineral linings are developed. The boundaries of grains with oscillatory growth zoning show CL textures in ghost bands, which are spatially associated with GBM type dynamic recrystallization (Figure 47 D, E). (iii) Reopening structures of the B-type veins were commonly observed by CL imaging (Figure 47 D), with two distinct types of later infills. The first one shows minerals, such as chlorite, sericite, K-feldspar, calcite, pyrite, molybdenite and magnetite, while the second one consists of quartz and small fluorite crystals mainly at the contact with the B-type vein quartz. In the latter case the quartz crystals do not exhibit any dynamic recrystallization features, such as SGR or GBM. The quartz present in this reopened part of the B-type veins is faintly luminescent in red tones, distinguishing them from the quartz crystals of the earlier B-type vein stage (Figure 47 A, D). Some growth zoning is observable, suggesting oriented quartz growth towards the center of the reopening. No alteration has been identified and linked to this reopening event, but it can be suggested as a transition from potassic to sericite-chlorite and sericitic alteration.

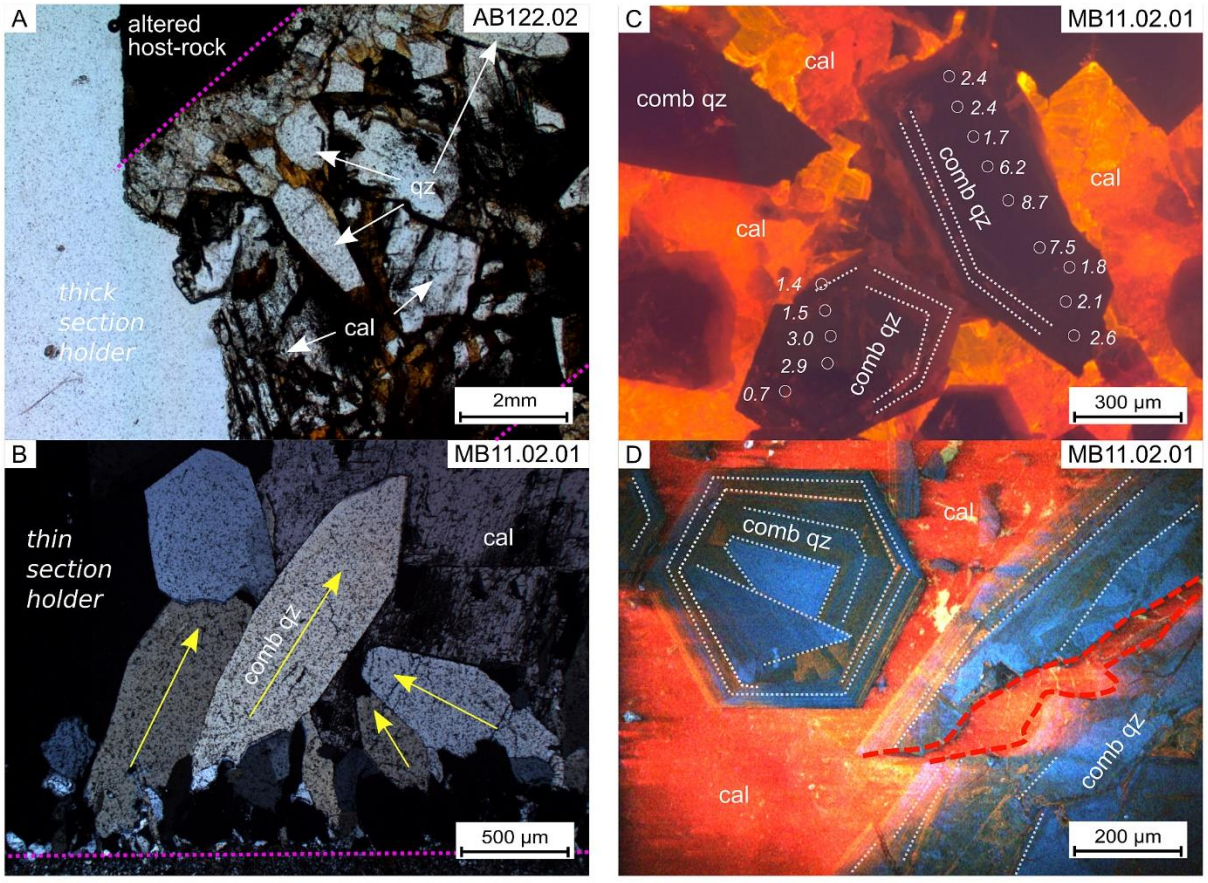

Figure 48: Transmitted light, cross-polarized (XPL) views of quartz petrography and microstructures and cathodoluminescence (CL, "hot" and "SEM") images of of E-type veins. Ti concentration in ppm associated with the ablation spot location (white circles) are shown in C. A. Thick section (for better contrasts compared to a thin section) of E-type vein with comb quartz at vein margins and calcite filling. B. Comb quartz at vein margins, with preferential orientation (white arrow) of growth, from the vein wall to the center. C. CL imaging of euhedral comb quartz with oscillatory growth zoning from the center to the boundaries of the quartz crystal with surrounding calcite (yellow/orange/red). D. CL-SEM imaging of euhedral comb quartz crystals (± fractured) with oscillatory growth zoning (and internal reflections) cut by and surrounded with calcite cement Abbreviations: cal= calcite, qz= quartz. Pink dotted line= E-type vein margins, red dashed line= fractured quartz surface, white dotted line= CL zoning, yellow arrow= growth direction.

The E-type veins are associated with sericitic to advanced argillic mineral alteration and crosscut the earlier A and B-type veins. They are straight, continuous, with sharp boundaries and show a miarolitic texture. The quartz is elongated, euhedral, oriented orthogonally to the vein selvages and precipitated on host-rock fragments that are enclosed in the E-type veins (Figure 45 D; Figure 48 A, B). Miarolitic cavities are infilled by carbonates. Base metal sulfides, such as sphalerite, galena, pyrite and chalcopyrite, are associated with the gangue quartz (Figure 45 D). The quartz exhibits oscillatory growth zoning, as revealed by CL imaging in reddish to bluish tones. It is difficult to discern the zoning due to the presence of calcite in contact with the quartz, which results in high-intensity luminescence artifacts that blur the quartz signal (Figure 48 C, D). The quartz can be fractured, but no other deformation features are observable, as supported by the lack of undulous extinction (Figure 48 A-D).

Variations in CL intensity (bright to dark) and color (blue to red) of the quartz crystal from the A- and B-type veins spatially correlate with the intensity and the location of different microtextural domains (e.g. GBM, SGR). In these veins, the CL intensity seems to decrease with increasing deformation, which is also recorded by a shift from blue to red CL colors and from well preserved growth zoning to ghostbands, mottled or mosaic textures. In E-type veins, where there is no evidence of deformation, growth zoning is well preserved.

3.4.2. Fluid inclusion petrography and microthermometry

The A-, B- and E-type veins contain clear and transparent quartz. Primary fluid inclusions that are isolated or arranged in clusters or trails along quartz growth zoning (Hein and Van den Kerkhof, 2001) reach 20 μm in size but are mostly between 5 and 15 μm in size. Locally, in A- and B-type veins, recrystallized quartz grains are devoid of primary inclusions or show partial re-equilibration (Kerrich et al. 1976; Tarantola et al. 2010). Numerous Type 2 and Type 3 fluid inclusions showed high T_h or T_m(hal) (>550 °C) or are stretched and are contained in dynamically recrystallized quartz. As for Voudouris et al. (2013a) data these data or not used in the rest of the paper.

Three types of primary fluid inclusions were identified: Type 1, two-phase (LV) aqueous inclusions, are characterized by a vapor bubble occupying 10 to 50 vol.%, that disappears upon homogenization to liquid. They are secondary in A and B-type veins, since they intersect the oscillatory growth zoning of quartz, but are primary in E-type veins. Type 2 inclusions are three phases (LVH) and contain a vapor phase occupying 5 to 50 vol.% of the inclusion and a halite crystal (Figure 49 A). They homogenize by bubble disappearance into the liquid state or by dissolution of halite after bubble disappearance. Type 3 inclusions are two-phase (VL) inclusions that are vapor-dominated (70–90 vol.%) and homogenized by disappearance of the liquid phase and homogenize to the vapor phase (Figure 49 B). Locally, they can contain daughter or accidentally trapped opaque crystal, possibly chalcopyrite or hematite (*Table 2*).

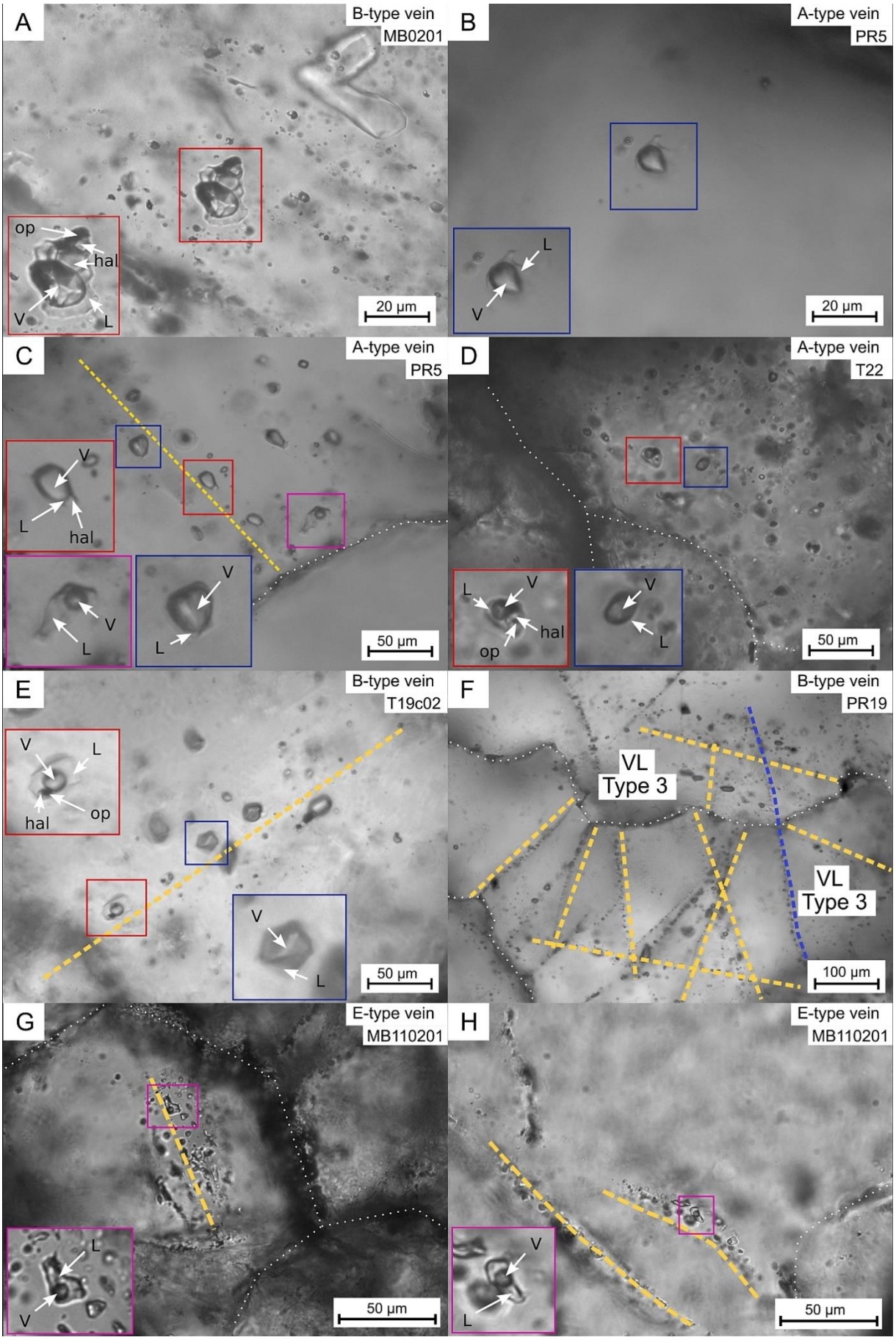
A
B-type vein
MB0201
op
hal
V
L
20 µm
B
A-type vein
PR5
L
V
20 µm
C
A-type vein
PR5
V
L
hal
V
L
V
L
50 µm
D
A-type vein
T22
L
V
hal
op
V
L
50 µm
E
B-type vein
T19c02
V
L
hal
op
V
L
50 µm
F
B-type vein
PR19
VL
Type 3
VL
Type 3
100 µm
G
E-type vein
MB110201
L
V
50 µm
H
E-type vein
MB110201
V
L
50 µm

Figure 49: Fluid inclusion petrography from A and B-type veins. A. Isolated Type 2 fluid inclusion (VLH) in a B-type vein. B. Isolated Type 3 fluid inclusion (VL) in an A-type vein. C. Intragrain plane of Type 3 and Type 2 fluid inclusions ending at a contact of a quartz subgrain margin in a A-type vein. D. Type 2 and Type 3 fluid inclusions in a A-type vein. E. Intragrain plane of Type 3 and Type 2 fluid inclusions in a B-type vein. F. Intragrain planes of Type 3 fluid inclusions in a B-type vein. G. Primary plane of Type 1 fluid inclusion in an E-type vein. H. Primary plane of Type 1 fluid inclusion in a E-type vein. V= vapor phase, L= aqueous liquid phase, H= halite crystal, op= opaque mineral. Yellow (intragrain), blue (secondary), lines indicate the strikes of the fluid inclusion planes, White dotted lines= quartz grain/subgrain margins.

Fluid inclusion planes in A-type veins were rarely observed and are, if present, without any preferential orientation (Figure 49 C). The planes can be interpreted as primary to secondary. The three main types of fluid inclusions were distinguished: (i) secondary Type 1 show a T_m(ice) –1.7 ± 0.4 °C and low salinity (1.4 to 3.3 wt%$_{equiv.NaCl.}$) and homogenize at 373 ± 74 °C (320–425 °C). (ii) no T_h or T_m(hal) has been measured for Type 2, due to lack of apparent phase ratio variation during heating (up to 550 °C) (Figure 49 D). (iii) two populations of Type 3 inclusions are discernable : the first population shows high T_h with a mean at 483 ± 11 °C (470–490 °C), mean T_m(ice) at –4.8 ± 0.7 °C, with medium salinity (7.0–8.8 wt%$_{equiv.NaCl.}$), and a second population shows a lower T_h with a mean at 392 ± 18 °C (376–419 °C), mean T_m(ice) at –3.3 ± 2.9°C, with medium salinity (0.8–9.1 wt%$_{equiv.NaCl.}$).

In the B-type veins, fluid inclusion planes were observed in quartz, including Type 1 secondary and Type 2 and Type 3 primary to rarely pseudo-secondary inclusions (Figure 49 E, F). Sometimes, the inclusions are isolated in the core of the grains or have no spatial relationship within the host grains. B-type veins show: (i) secondary Type 1 inclusions show a T_m(ice) at –3.3 ± 2.3°C and a low salinity (1.1–7.4 wt%$_{equiv.NaCl.}$) with a T_h of 238 ± 98 °C (125–301 °C). (ii) primary Type 2 show a T_m(hal) 282 ± 7°C and are hypersaline (36.2–37.2 wt%$_{equiv.NaCl.}$). During heating they homogenize either by vapor disappearance at 426 ± 8 °C (418–436 °C). (iii) primary Type 3 show a T_m(ice) –4.8 ± 1.3 °C, are of medium salinity (6.3–9.6 wt%$_{equiv.NaCl.}$) and homogenize by disappearance of the liquid phase at 391 ± 6 °C (386–398 °C).

E-type veins showed only primary Type 1 inclusions occurring along trails following the growth zoning of the host quartz (Figure 49 G, H). Type 1 fluid inclusions show a T_m(ice) –0.8 ± 0.1 °C and have a low salinity (1.2–1.4 wt%$_{equiv.NaCl.}$), no T_h has been determined in this study due to decrepitation.

3.4.3. Trace elements in quartz

Hydrothermal quartz from the different vein types shows distinct trace element compositions. The most prominent elements are Mg, Cl, Al, Ca, Ti and Fe with concentrations between 50 and 100 ppm for A-type veins, 100–200 ppm for B-type veins and 10–50 ppm in the E-type veins. The other elements such as B, Na, K, Mn, Cu, Zn, Ge, Mo, Sn and Ba generally show concentrations close to the detection limit (see Supplementary). By contrast, quartz from the E-type veins commonly contains 10 times more Li than from earlier A- and B-type veins (25.8 ± 17.9 ppm). Only, Al, Ti and Ge content will be presented in detailed and discussed in this paper as a vein classifier (e.g. Rottier and Casanova, 2021; Falkenberg et al., 2024) (Figure 50), the rest of the trace element data will be discussed in another paper.

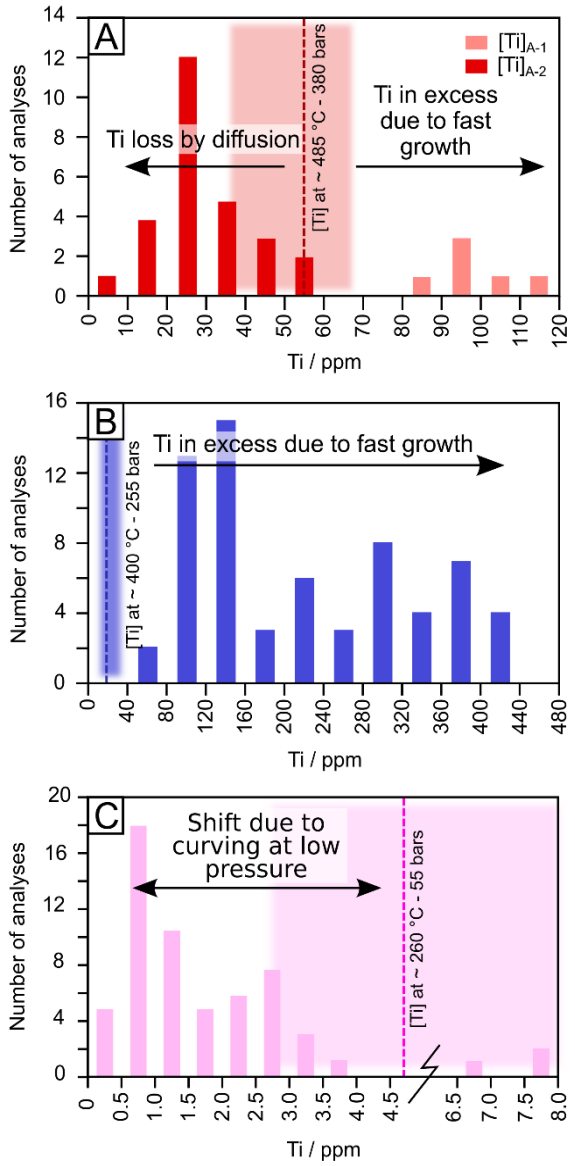

Figure 50: Histograms of Ti in quartz analyzed by LA-ICP-MS, for A. A-type veins, B. B-type veins, C. E-type veins and the expected Ti concentration (colored dotted line) in quartz obtained using the (1) calculation and typical fluid inclusion data with T_{mean} and P_{mean} trapping from respective vein type (see Table 4).

In the A-type veins, the Ti concentration values show two populations: a first one ($[Ti]_{A-1}$) ranging from 83.6 to 114 (mean ± 1σ at 99.7 ± 11.5 ppm, n = 6) ppm mainly linked to light blueish CL quartz domain, and second one ($[Ti]_{A-2}$) ranging from 9.7 to 56.4 ppm (mean at 28.3 ± 12.2 ppm, n = 37) mainly linked to dark reddish CL quartz domain (Figure 50 A). The $[Ti]_{A-1}$ population is spatially linked to well-preserved growth zoning domain without any evidence of recrystallization of the quartz grains, while the $[Ti]_{A-2}$ population is spatially linked to low-intensity CL with mottled, mosaic texture and with high intensity textures of dynamic recrystallization as GBM to SGR (Figure 46 E, F). The Ge concentration ranges from 1.5 to 4.5 ppm (mean at 2.8 ± 1.6 ppm, n = 18) with an outlier at 8.7 ppm. Aluminum ranges from 63.9 to 233 ppm (mean at 131 ± 75 ppm, n = 17) with an outlier at 371 ppm.

In the B-type veins the Ti values ($[Ti]_B$) range from 44.6 to 416 ppm (mean at 201 ± 111 ppm, n = 65) and display some variability within the veins (Figure 50 B), but no link has been observed with CL textures (e.g. growth zoning, mottled) or quartz microtextures (SGR to well-crystallized) (Figure 47 D, E). The Ge data range from 0.7 to 3.3 ppm (mean at 1.6 ± 0.5 ppm, n = 53) and the Al data range from 77.7 to 677 ppm (mean at 273 ± 175 ppm, n = 55).

In E-type veins Ti values ($[Ti]_E$) range from 0.2 to 8.7 ppm (mean at 2.0 ± 1.9 ppm, n = 57) ppm, and is variable (less than 10 ppm) (Figure 50 C) within the veins but not along the growth zoning (Figure 48 C, D). The Ge data range from 0.7 to 1.7 ppm (mean at 1.3 ± 0.3 ppm, n = 17), Al ranges from 77.7 to 677 ppm (mean at 1073 ± 793 ppm, n = 59) with three outliers at concentrations >3100 ppm (Figure 51) (*Table 3*). Sometimes the calculated LOD for trace element measuring is equal to 0 ppm. This can be

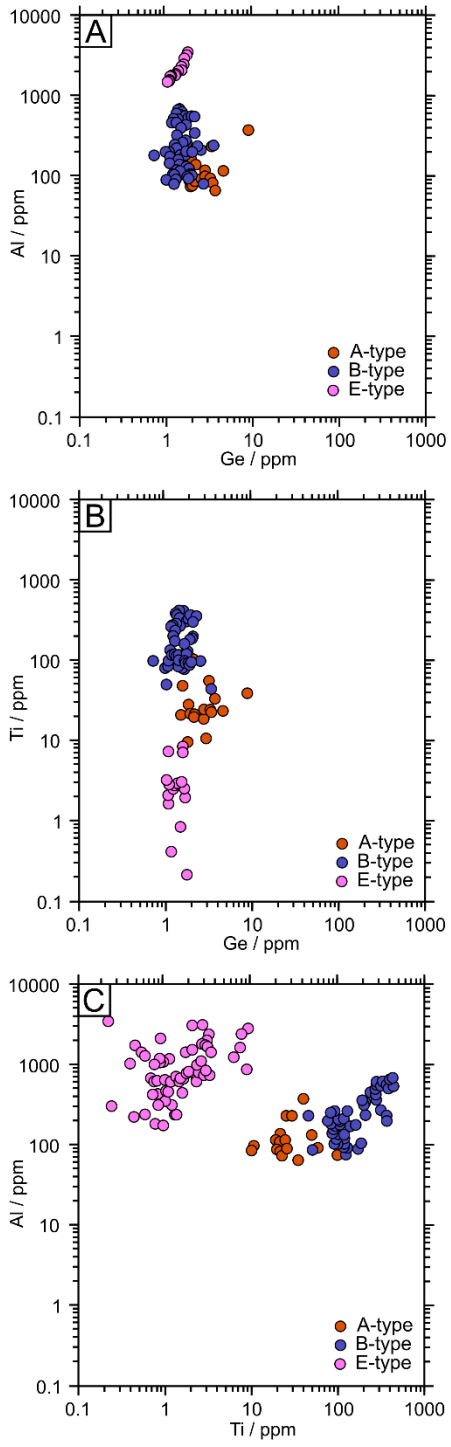

Figure 51: Concentration of Ti, Al and Ge in quartz from A-, B- and E-type veins, measured by LA-ICP-MS, A. Ge vs Al. B. Ge vs Ti. C. Ti vs Al.

explained by the extremely low background signal for Ti and Ge during LA-ICP-MS. According to the used LOD calculation from Longerich (1987), this returns to a LOD of 0 ppm. Then, the element is considered as detected. This is supported when a LOD value is calculated, which is always lower than the concentration of the element (see Supplementary).

The Ge concentrations are very similar between the different types of veins and show only slight variations and short range (Figure 51 A, B), on the order of 1 ppm. A- and B-type veins have similar Al concentration values, within the same range (Figure 51 A, C) and show only slight variation within each vein type. However, E-type veins show higher Al concentrations than A- and B-type veins and display a significant variation within the vein and quartz grain (Figure 51). The B-type veins show higher Ti concentrations than A-type veins, which in turn show high Ti concentration than E-type veins (Figure 50 and Figure 51). The number of visible points in Figure 51 A-C is variable since the data is incomplete for all the analysis points, particularly regarding Ge and Ti in E-type veins. In E-type veins, Ti concentrations are low, and Al concentration is high, and are linked to low CL-intensity. In A- and B-type veins, the trace elements considered as CL activators (e.g. Ti) or inhibitors (i.e. Al, Li, (Phelps et al. 2020)) do not show any clear correlation even within a specific vein. Al and Ge values do not display any trend regarding CL domain or recrystallized domains. However, the Ti concentration in quartz increases with increasing CL intensity. Accordingly, Ti is interpreted here as the main element responsible for quartz luminescence signal and its concentration may be affected by dynamic recrystallization.

Table 3 : Ti, Al, and Ge concentrations in quartz from A-, B- and E-type veins.

Vein type	[Ti] (ppm)				[Al] (ppm)				[Ge] (ppm)			
	Range	Median	Mean ± 1σ	n	Range	Median	Mean ± 1σ	n	Range	Median	Mean ± 1σ	n
A	83.6–115	99.4	99.7 ± 11.5	6	63.9–372	104	131 ± 75	18	1.5–8.7	2.3	2.8 ± 1.6	18
	9.7–56.4	24.0	28.3 ± 12.2	27								
B	44.6–416	170.5	201 ± 111	65	77.8–677	205	273 ± 175	55	0.7–3.3	1.4	1.6 ± 0.5	53
E	0.2–8.7	1.3	2.0 ± 1.9	63	172–3458	790	1073 ± 793	62	0.7–1.7	1.3	1.3 ± 0.3	16

3.5. DISCUSSION

3.5.1. Evidence for fluid inclusion overlapping and fluid evolution.

Presenting a relative chronology based on fluid inclusion petrography offers challenges that can lead to valuable insights. In the quartz of the A- and B-type veins, both Type 2 and Type 3 fluid inclusions may coexist within the same planes (very rare) with similar T_h (~ 400 °C). This heterogeneous entrapment below the H_2O-NaCl solvus suggests a boiling event (Figure 49 C-E). And the presence of primary and pseudo secondary planes suggesting a continuous trapping during crystallization and recrystallisation. This is, in some point, coherent with the dynamic recrystallization occurrence during the crystallization of the quartz grain, mostly in B-type veins, which is evidenced by the GBM of elongate quartz grain, and the associated ghost bands-CL textures (Acosta et al., 2020). At boiling, T_h and P correspond to the trapping temperature and pressure ($T_{trapping}$ and $P_{trapping}$) (Diamond, 2001). In a shallow crustal environment, as for E-type veins, it is assumed that the pressure correction is <10 bars and hence the trapping pressure correction was negligible (e.g. Bodnar et al. 1985). Then, different fluid events related to the different fluid inclusion population for each vein type are distinguished. In A-type veins two population are discernable: (i) have high temperature and pressure with a $T_{trapping}$ range from 470 to 490 °C (mean ± 1σ at ≈ 483 ± 11 °C) and a $P_{trapping}$ ranging from 495 to 605 bars (mean at ≈ 564 ± 60 bars), (ii) have low temperature and pressure with a $T_{trapping}$ range from 376 to 419 °C (mean at ≈ 392 ± 18 °C) and a $P_{trapping}$ range from 220 to 319 bars (mean at ≈ 255 ± 41 bars). In B-type veins only one population of fluid is discernable with a $T_{trapping}$ ranging from 386 to 436 °C (mean at ≈ 411 ± 20 °C) and a $P_{trapping}$ ranging from 225 to 267 bars (mean at ≈ 244 ± 15 bars) (Figure 52, *Table 2*).

Our major fluid populations are comparable to the ones of the A-, B- and E-type veins from Voudouris et al. (2013a). Merging of both datasets allows us to distinguish and describe three major fluid events. The low temperature and pressure population of the A-type veins are very similar to the one of B-type veins. We then assume these fluid inclusions may be associated to the fluid trapping during a later fluid incursion which does not represent the condition of A-type quartz formation and will not be considered in the rest of the paper. Only the “high temperature and pressure” population is considered, as the associated fluid event forming the A-type vein, trapped from 457 to 510 °C (mean at ≈ 486 ± 16 °C) and from 273 to 605 bars (mean at ≈ 379 ± 110). The B-type veins show a fluid event population trapped from 366 to 436 °C (mean at ≈ 398 ± 17 °C) and from 190 to 357 bars (mean at ≈ 255 ± 40 bars). A last fluid event is represented by Type 1 fluid inclusions related to the E-type vein formation. Which, in E-type veins yields $T_{trapping}$ ranging from 219 to 334 °C (mean at ≈ 264 ± 35 °C) and a minimal $P_{trapping}$ from 22 to 133 bars (mean at ≈ 55 ± 34 bars) (*Table 2*, Figure 51). Only the merged fluid inclusion data will then be used in the rest of the discussion (Figure 52, Table 4).

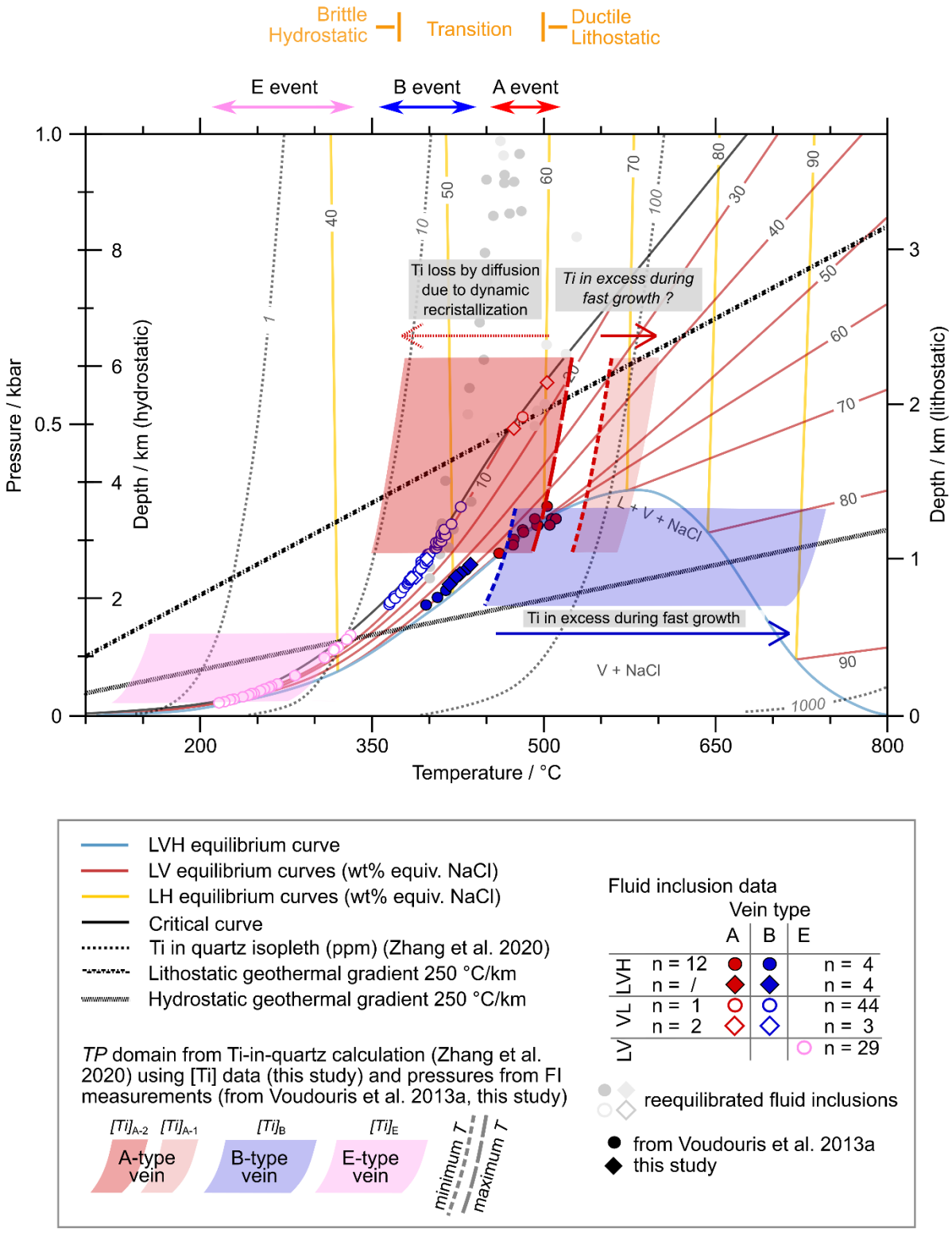

Figure 52: PT diagram showing our fluid inclusion data (this study and from Voudouris et al., 2013a) and PT[Ti] domains obtained with the Titan-in-quartz geothermometer of the A- (red), B- (blue) and E- (pink) type veins. LVH, LV, LH and critical curve are from Bodnar (1993, 1995), Ti isopleths are coming from Ti-in-quartz calculation (Zhang et al. 2020).

Table 4: Synthesis of fluid events ($T_{trapping}$ and $P_{trapping}$), Ti concentration in quartz ([Ti]), Ti-in-quartz temperatures (T[Ti]), the differences between the Ti-in-quartz temperatures and Fluid inclusion temperatures (ΔT(Ti-in-quartz–FI)) and the involved process for the different vein-types (A, B and E).

Vein type	$T_{trapping}$ (°C)		$P_{trapping}$ (bar)		[Ti] (ppm)		*T*[Ti] range (°C)	Δ*T*(Ti-in-quartz–FI) (°C)	Involved process
	Range	Mean ± 1σ	Range	Mean ± 1σ	Range	Mean ± 1σ			
A	457–510	486 ± 16	273–605	379 ± 110	83.6–115	99.7 ± 11.5	522–596	+12– +86	*Fast growth?*
					9.7–56.4	28.3 ± 12.2	351–521	–106– +11	Dynamic recrystallization
B	366–436	398 ± 17	190–357	255 ± 40	44.6–416	201 ± 111	449–743	+15– +300	Fast growth
E	219–334	264 ± 35	22–134	55 ± 34	0.2–8.7	2.0 ± 1.9	126–277	–93–0	/

3.5.2. Ti-in-quartz temperatures and comparison with fluid inclusion thermometry

The occurrence of rutile and titanite inclusions associated with the hydrothermal quartz and the host rocks (Voudouris et al., 2013a) suggests a TiO_2 activity of ~ 1. This allows the estimation of quartz formation temperatures by Ti-in-quartz thermometry (Zhang et al., 2020). The extrema of Ti concentrations provided by our quantitative analyses of trace elements in quartz of both vein types are used for the Ti-in-quartz calculation with $[Ti]_{A\text{-}2}$ = [9.7–56.4] ppm and $[Ti]_{A\text{-}1}$ = [83.6–114.8] ppm, $[Ti]_B$ = [44.6–416.4] ppm and $[Ti]_E$ = [0.2–3.9] ppm, as well as the trapping pressure of fluid inclusions for the three types of veins (Figure 50 A-C). For the A-type veins, the extreme pressures (range 273–605 bars) given by the high-temperature fluid inclusions. For the B-type veins the pressure range of 190–357 bars are used, from the fluid inclusion data of the B-type veins. For the E-type veins the extrema pressure range of 22–134 bars are used, from the fluid inclusion data of the E-type veins (Table 3 and Table 4).

Then, the Ti-in-quartz geothermometer gives the following calculated temperatures (*T*[Ti]) for A-, B- and E-type veins, respectively: $T[Ti]_{A\text{-}2}$ = 351–521 °C, $T[Ti]_{A\text{-}1}$ = 522–596 °C, $T[Ti]_B$ = 449–743 °C and $T[Ti]_E$ = 126–277 °C (Table 4, Figure 52). This results in an increasing calculated precipitation temperature of quartz formation from the A-type to the B-type veins, which agrees with the higher Ti contents in quartz in the B- compared to the A-type veins and decreasing temperatures from the B-type to the E-type veins. $T[Ti]_{A\text{-}2}$ partially covers trapping temperature from fluid inclusion of the A-type veins (457–510 °C) and extend to lower values and $T[Ti]_{A\text{-}1}$ are higher than the fluid inclusions of A-type veins. $T[Ti]_B$ (432–727 °C) are higher than fluid inclusion trapping temperatures of the B-type veins (366–436 °C). $T[Ti]_E$ (126–277 °C) are within the fluid inclusion trapping temperatures of the E-type veins (219–334 °C) (Table 4, Figure 52).

Using the formula of Zhang et al. (2020), we can recalculate the expected quartz concentration based on the *PT* data of fluid inclusions from the different types of veins. The maximum and minimum *PT* values are used to obtain [Ti] ranges for each type of quartz veins. As such, we obtain the following ranges: $[Ti]_A$ = 34.4–67.0 ppm (mean at 50.5 ± 10.7 ppm), $[Ti]_B$ = 14.8–32.9 ppm (mean at 20.7 ± 4.3

ppm), $[Ti]_E$ = 2.7–10.8 ppm (mean at 5.3 ± 2.5 ppm) (Figure 50 A-C). For A-type veins, the expected [Ti]A values are higher and do not overlap with the range of values $[Ti]_{A-2}$, which were analyzed only for the higher values. In contrast, the expected concentrations are lower than those of the $[Ti]_{A-1}$ population. For B-type veins, the expected $[Ti]_B$ values derived from fluid inclusions are lower than the analyzed $[Ti]_B$ values. For E-type veins, the expected values mostly overlap the measured ones; the small difference (on the ppm scale) may be attributed to the low-pressure conditions, which could induce an error (Figure 50 A-C).

3.5.3. Evidence for Ti excess in quartz during disequilibrium crystallization

The Ti incorporation in quartz is linked to the *PT* precipitation conditions, where high temperatures imply higher Ti content (Götze et al., 2009, 2012). Yet, the Ti concentration evolution and *T*[Ti], given by Ti-in-quartz thermometer, through the different types of veins at Pagoni Rachi is not consistent with the expected evolution regarding the trapping temperature given by the fluid inclusions, which show a decrease from the A- to the E-type veins (Figure 52). Here, a decrease of the *T*[Ti] and [Ti] in quartz from the A- to the B-type veins was expected according to the decreasing fluid inclusions temperatures, which is not the case. Instead, the estimated Ti-in-quartz temperatures of the B-type veins are higher than that of the A-type veins and which may thus indicate an enrichment or a post-crystallization modification of the Ti contents, particularly in quartz of the B-type veins, where the measured $[Ti]_B$ are higher than the expected Ti content, up to one order of magnitude (Figure 50 A, B and Figure 52).

Huang and Audétat (2012) suggested that the quartz crystallization rate influences the Ti incorporation. At slow crystallization rates, the Ti incorporation is typically in equilibrium with the fluid, while during high crystallization rates less time is available for a re-organization of the crystal lattice resulting in disequilibrium conditions. This may generate adequate condition to a substitution of Si^{4+} by Ti^{4+} in quartz crystals, resulting in a Ti in excess in quartz compared to Ti concentration expected for equilibrium conditions. As a result, it is usually recommended consider the lower [Ti] value of a given quartz to calculate the temperature of crystallization using Ti-in-quartz thermometer (Huang and Audétat, 2012; Hong et al., 2023; Cernuschi et al., 2018, 2023).

Quartz crystals of the B-type veins at Pagoni Rachi are elongated euhedral to subhedral shaped (Figure 47 C) and most CL textures consist of alternating dark and bright growth zones revealing euhedral crystal faces (Figure 47 D, E), and thus reflecting primary crystal growth from a hydrothermal fluid. This observation is particularly evident in the central parts of the veins, which were not affected by dynamic recrystallization (Figure 53 B, H). However, the presence of the intermediate ghost band textures of subhederal quartz crystals in the central part of the B-type veins (Figure 47 A, D) can be interpreted as CL-euhedral crystals that already underwent partially recrystallization during the initial precipitation due to growing competition among different adjacent quartz crystals, which is consistent

with a fast growth rate. One possibility is that CL-bright bands form during pressure fluctuations that are relatively short-lived, but which can cause fast quartz growth (Raimbourg et al., 2022; Acosta et al., 2022). Moreover, the elongated habit of subhedral quartz was suggested to be controlled by fast growth rates of quartz along the c-axis compared to the a-axis, which may be linked to oscillatory growth zoning with alternating high and low CL intensity zoning (Swanson and Fenn, 1986; Yang et al., 2015) (Figure 47 D, E). Hence, fast crystal growth may be the best candidate to explain the excess Ti contents in quartz from the B-type veins at Pagoni Rachi. Falkenberg et al. (2024) mentioned the implication of such a process during the formation of B-type quartz veins at the Maronia porphyry-epithermal system, located some 30 km SW of Pagoni Rachi (Figure 50). They measured Ti concentration near 75 ± 32 ppm (up to 135 ppm) linked to the fast formation of B-type quartz veins at the Maronia porphyry-epithermal system, located some 30 km SW of Pagoni Rachi. Their Ti concentrations are lower than for B-type veins from Pagoni Rachi, but they are still higher than what is expected for this kind of vein (~ 30 ppm; Rottier and Casanova, 2021) (Figure 51). Höss et al. (2024) also involved a fast growth rate which generate a Ti incorporation in excess in the porphyry quartz veins at the Skouries deposit (N. Greece) with high Ti content in quartz (up to 332 ppm for their B1-type vein), although, they described a decrease in temperature from their A- to B-type veins using the minimal Ti (~ 25 ppm) and their Ti-in-quartz temperatures are then corresponding to the expecting temperatures from fluid inclusion data and are within our expected temperature. At Butte porphyry Cu-Mo deposit, Acosta (2020) implied that their high Ti concentrations (from 32 to 332 ppm) in quartz are inconsistent with a quartz growth out of equilibrium. This Ti concentration dispersion is consistent with that of the B-type vein of Pagoni Rachi. And due to a fast precipitation rate, they used the lowest Ti contents to reconstruct crystallization temperature.

If this Ti excess is due to fast crystallization of B-type veins, it is also possible that similar Ti excess is found in non-recrystallized parts of A-type veins. Indeed, the A-type veins show relicts of primary oscillatory growth zoning (rarely), with high CL contrast (Figure 46 B, G). If a fast crystallization process occurred during the A-type vein formation, this could imply an excess Ti incorporation, leading to a higher $[Ti]_{A\text{-}1}$ than expected by the

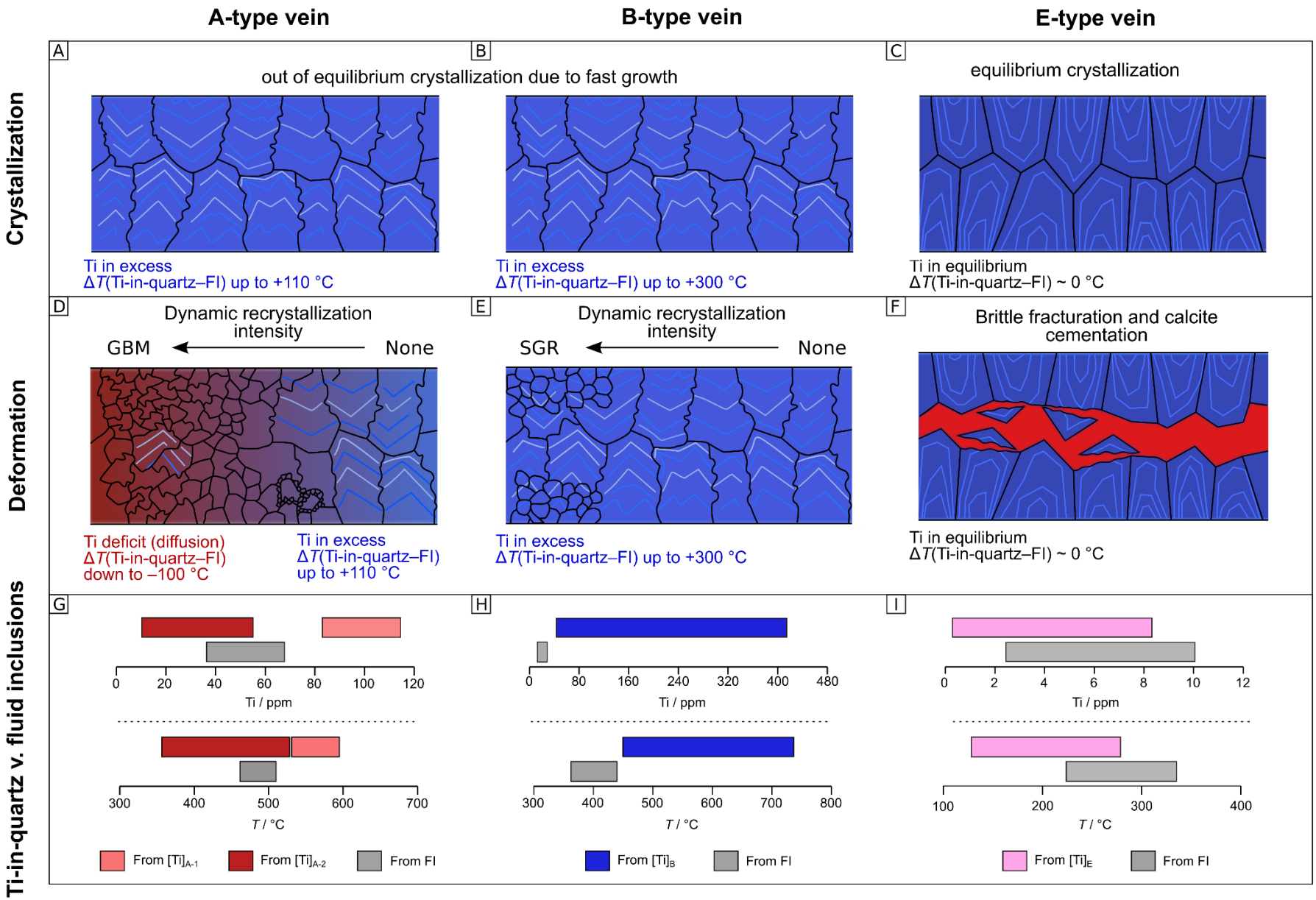
A-type vein
B-type vein
E-type vein
Crystallization
Deformation
Ti-in-quartz v. fluid inclusions
A
B
C
out of equilibrium crystallization due to fast growth
equilibrium crystallization
Ti in excess
ΔT(Ti-in-quartz–FI) up to +110 °C
Ti in excess
ΔT(Ti-in-quartz–FI) up to +300 °C
Ti in equilibrium
ΔT(Ti-in-quartz–FI) ~ 0 °C
D
E
F
Dynamic recrystallization intensity
GBM
None
SGR
None
Brittle fracturation and calcite cementation
Ti deficit (diffusion)
ΔT(Ti-in-quartz–FI)
down to –100 °C
Ti in excess
ΔT(Ti-in-quartz–FI)
up to +110 °C
Ti in excess
ΔT(Ti-in-quartz–FI) up to +300 °C
Ti in equilibrium
ΔT(Ti-in-quartz–FI) ~ 0 °C
G
H
I
0 20 40 60 80 100 120
Ti / ppm
300 400 500 600 700
T / °C
From [Ti]A-1
From [Ti]A-2
From FI
0 80 160 240 320 400 480
Ti / ppm
300 400 500 600 700 800
T / °C
From [Ti]B
From FI
0 2 4 6 8 10 12
Ti / ppm
100 200 300 400
T / °C
From [Ti]E
From FI

Figure 53: Synthetic sketch of the respective influence of rapid growth and dynamic recrystallization of quartz on the Ti content of quartz and on the Ti thermometer, with comparison of our Ti data and fluid inclusions. A. Out-of-equilibrium crystallization of quartz in A-type veins. The quartz shows a significant contrast in CL intensity with oscillatory growth zoning from the edge of the vein to the center. In some cases, dynamic recrystallization occurs simultaneously with crystallization, with the presence of GBM at the grain boundaries. Titanium is in excess due to the rapid growth of quartz, implying a ΔT(Ti-in-quartz – FI) of up to +110°C. B. Out-of-equilibrium crystallization of quartz in B-type veins. The quartz shows a significant contrast in CL intensity with oscillatory growth zoning from the edge of the vein to the center. In some cases, dynamic recrystallization occurs simultaneously with crystallization, with the presence of GBM at the grain boundaries, associated with a ghostband texture (see Figure 47 E). Titanium is in excess due to the rapid growth of quartz, implying a ΔT(Ti-in-quartz – FI) of up to +300°C. C. Equilibrium crystallization of automorphic quartz in E-type veins. The quartz shows a low CL intensity contrast with oscillatory growth zoning from the center of the vein grains to the rim. Titanium is at equilibrium, implying a ΔT(Ti-in-quartz – FI) close to 0°C within error. D. Ductile deformation of quartz in A-type veins with intense generalized dynamic recrystallization, with GBM and associated CL textures in ghostbands, mottled, of low intensity, and a Ti deficit, implying a ΔT (Ti-in-quartz – FI) down to –100°C. In some cases, quartz porphyroclasts with little to no deformation can be observed, preserving their CL textures (oscillatory growth zoning with intensity contrast) and an excess Ti signal, implying a ΔT(Ti-in-quartz – FI) of up to +100°C. E. Ductile deformation of quartz in B-type veins with low-intensity dynamic recrystallization, with SGR and an excess of Ti, implying a ΔT(Ti-in-quartz – FI) of up to +300°C. F. Brittle deformation of quartz in E-type veins with quartz fracturing and cementation by calcite (orange). The quartz shows unmodified oscillatory growth zoning in CL with low-intensity CL. Their Ti signal is at equilibrium, implying a ΔT(Ti-in-quartz – FI) close to 0°C. G. Expected (gray rectangle) and actual (red rectangles) Ti concentrations in quartz from A-type veins. The expected values are calculated from the Ttrapping of the fluid inclusions (FI), using the extreme pressure values (Pmin = 273 bars, Pmax = 605 bars). H. Expected (gray rectangle) and actual (blue rectangles) Ti concentration in quartz from B-type veins. The expected values are calculated from the Ttrapping of the fluid inclusions, using the extreme pressure values (Pmin = 190 bars, Pmax = 357 bars). I. Expected (gray rectangle) and actual (pink rectangles) Ti concentrations in quartz from E-type veins. The expected values are calculated from the Ttrapping of the fluid inclusions, using the extreme pressure values (Pmin = 22 bars, Pmax = 134 bars). ΔT(Ti-in-quartz – FI)= temperature difference between Ti-in-quartz thermometer and fluid inclusion data, FI= fluid inclusion.

fluid inclusion data, which is the case (Figure 50 A, Figure 53 A). These results are linked to high CL intensity and spatially associated with low to no dynamic recrystallization microtextures of quartz, and a $T[\mathrm{Ti}]_{\mathrm{A\text{-}1}}$ higher than the fluid inclusion temperature related to A-type veins (Figure 53 A, D, G). In contrast of such processes, the measured [Ti]E are within the expected Ti from fluid inclusion, with low concentration down to 0.2 ppm and 2.1 ppm, respectively. Quartz of E-type veins display low CL-intensity with well-formed growth zoning. Thes can support equilibrium crystallization (Figure 50 C, Figure 53 C, I). [Ti] and associate $T[\mathrm{Ti}]$, is subsequently decreasing due to an intense deformation allowing a process responsible for a decrease of the Ti content in quartz (e.g. as diffusion, see next section). Thus, even if fast quartz growth can imply a Ti excess to other processes linked to one magnitude of order higher than expected, deformation may influence the preservation of this Ti enrichment in quartz, potentially leading to misinterpretations.

3.5.4. Transition from lithostatic to hydrostatic conditions and from ductile to brittle conditions

The fluid inclusions show a clear temperature and pressure decrease from A- to B- to E-type veins. With a pressure drop from B- to E- type veins, with an overlap of B- in the A-type vein (“low temperature and pressure” of B-type vein population present in A-type veins), and same for the E-type which overlap the A and B-type veins evidenced by the presence of Type 1 fluid inclusions in A- and B-type veins. The shallow emplacement of the system between 3 and 0.2 km at temperatures ranging from ~ 485 °C (A-type) to ~ 260 °C (E-type) implies high geothermal gradients on the order of 250 °C/km (Figure 52). This high value is consistent with the emplacement of hot magma (granodiorite type) at shallow depths,

precursor to the porphyry-epithermal system (Sillitoe, 2010; Richards, 2015; Monecke et al., 2018). Thus, fluid inclusion data mostly fall between hydrostatic and lithostatic geothermal gradients of around 250 °C/km (Figure 52). This is consistent with the boiling phenomenon, involving a rapid pressure drop and intense fracturing, represented by stockwork veins (such as A-, B- and E-type veins), suggesting a shift in the pressure regime, transitioning from lithostatic to hydrostatic. This linked to a spatial overprinting of the alteration and vein structures with a co presence of epithermal vein cross cutting porphyry vein types (Figure 45 C), with frequent alteration overprinting. Then this is consistent with a telescoping process with an epithermal system following within the porphyry body (Sillitoe, 2010).

Moreover, the structure of the veins, from A-type veins, with undulating and discontinuous characteristics and highly recrystallized quartz evidence by GBM textures, to B-type veins, which are planar, continuous, and have weakly recrystallized quartz (SGR to none), and finally to E-type veins, which are continuous, planar, and contain fractured quartz (Figure 45, Figure 46, Figure 47, Figure 48), suggests an evolution of the deformation system from ductile to brittle conditions. This is highlighted by the temperature range of formation for A- and B-type veins, which corresponds to the ductile-to-brittle transition range for quartz (Monecke et al., 2018) (Figure 52).

3.5.5. Evidence for Ti diffusion during dynamic recrystallization

The presence of a quartz population with low Ti concentrations (down to 9.7 ppm), which is lower than the expected Ti concentration, near to 1 order of magnitude, and low Ti-in-quartz temperatures (351–521 °C) compared to what is expected from fluid inclusion data (457–510 °C) suggests a phenomenon of post-crystallization Ti loss (Table 4, Figure 50 A, Figure 52 and Figure 53 D, G). The microtextural domain of quartz, indicating high deformation intensity through the presence of GBM (to SGR) and CL texture with ghost bands and mottled textures of low CL intensity display low Ti content, suggest that the dynamic recrystallization may be associated with this Ti anomaly, potentially involving a deficit in Ti concentration (Figure 46 C-F). Grain Boundary Migration textures are such an example, which were described as a possible factor of Ti diffusion during deformation and dynamic recrystallization by Nachlas and Hirth (2015). Even if volume diffusion of Ti through quartz is known to be very slow (Cherniak et al., 2007; Jollands et al., 2020), Ti in quartz can be reset by stress-induced GBM to a new equilibrium at a faster stress rate (Van den Kerkhof et al., 2004; Nachlas and Hirth, 2015; Bromiley and Hiscock, 2016), particularly in fluid-rich systems such as porphyry-epithermal systems (like Pagoni Rachi). Then, A-type vein quartz underwent a Ti loss through deformation to highly deformed quartz showing widespread GBM and SGR textures, responsible of the lowering of the CL intensity with due to a low $[Ti]_{A\text{-}2}$ (<56.4 ppm). The given $T[Ti]_{A\text{-}2}$ values are derived from Ti loss and therefore, they may not reflect the expected temperatures based on fluid inclusions. The presence of mosaic textured quartz in the A-type veins may be indicative of late fluid circulation (Rusk et al., 2012; Acosta et al., 2022) (Figure 47 F). Because this CL texture is spatially associated to GMB/SGR textures

and low Ti quartz contents, this suggests that low Ti contents are due to a fluid-assisted Ti diffusion in quartz, as proposed by Audétat et al. (2015). This can support the implication of fluid circulation during the deformation conditions, so the Ti deficit in A-type vein quartz. Thus, the observed Ti deficit by diffusion may be partially linked to different processes, such as dynamic recrystallization by deformation or fluid-assisted. The A-type veins may have undergone one or more sequences of recrystallization with the later crosscutting veins (e.g. B-type veins, Figure 47 A).

Currently, the variations in Ti concentrations in quartz, associated with dynamic recrystallization, are consistent with the values reported in the literature, a reduction on the order of one magnitude, possibly reaching an intermediate value and a new equilibrium level. Indeed, Kidder et al. (2013) observed no variation in Ti concentration between recrystallized (with GBM) and undeformed quartz, with low values ranging from 0.2 to 2 ppm in their quartz veins. However, they present a significant decrease in Ti concentrations between recrystallized and undeformed quartz from a quartzite, ranging from 1–100 ppm to 1–10 ppm. They conclude that Ti diffused to an intermediate value, or to another equilibrium concentration. Bestmann et al. (2021) showed that Ti concentrations in quartz are variable and associated with the recrystallization texture of the quartz, with a decrease in Ti concentration from the core (2–50 ppm) to the recrystallized borders, which display a lower Ti content ranging from 40–60% of the core content. Newly recrystallized quartz had even lower concentrations (2–10 ppm), showing nearly an order of magnitude difference. This reduction in Ti induces a decrease in Ti temperature from the center of the quartz to the recrystallized borders.

Low temperature recrystallization (e.g. SGR and BLG) has been described as possible mechanisms to reset Ti to lower equilibrium values in certain *PT* conditions (Bestmann et al., 2021; Grujic et al., 2011). Experimental studies (Nachlas and Hirth, 2015) proposed that Ti diffusion is possible during SGR deformation under metamorphic conditions. However, during the exhumation of syn-kinematic quartz veins that underwent retrograde BLG and SGR at temperatures less than 350 °C, the quartz preserved its Ti concentration (Haertel et al., 2013). At Pagoni Rachi, combining quartz micro- and CL textures, as well as its trace element composition does not show any evidence of Ti diffusion in B-type vein quartz (Figure 47 D). Indeed, quartz display spatial variations in degree and type of recrystallization through the vein with rare BLG and minor SGR indicators, as well as rare GBM structures in central parts of the vein, and present similar Ti concentrations through the veins irrespective of the presence, intensity and type (e.g., SGR) of deformation and CL domains (Figure 47 B-E). Thus, it can also be assumed that the CL-mottled texture occurred during low temperature BLG and SGR recrystallization must have occurred during vein cooling and exhumation, but did not further facilitate Ti loss and equilibration. The E-type vein quartz does not show any evidence indicative of dynamic recrystallization, which is supported by its euhedral shape and well-preserved CL-oscillatory growth zoning, lacking also signs of disequilibrium reactions (Figure 48, A-D). This suggests that no intracrystalline deformation was involved at lower temperature (~ 250 °C).

The present investigation of the Pagoni Rachi deposit indicates that Ti diffuses during dynamic recrystallization of quartz at high intensity (GBM) and present a Ti deficit (to one order of magnitude) to a possible new equilibrium state, but not at lower intensity which in these case preserves the Ti signature of the quartz formation, even if Ti is in excess in the quartz (Figure 50 A, Figure 52 and Figure 53 A, D, G). This hypothesis is interesting regarding the stability of the geochemical signature along the lifespan and deformation of the porphyry-epithermal system. Then a potential Ti sink, when Ti diffusion, could be the surrounding magnetite/hematite or biotite present in the host rock or directly included in the quartz.

3.5.6. Implication for Ti-in quartz thermometry in magmatic-hydrothermal systems

Where a quartz forming out-of-equilibrium dur to fast growth rate this results to a Ti in excess in quartz and high inferred crystallization temperature. Conversely, a decrease in Ti concentration in quartz, due to diffusion during dynamic recrystallization of the host quartz, results in lower inferred temperatures. It is important to note that the maximum values of $[Ti]_{A-1}$ align with the primary trace element signature of the quartz crystals, whereas the lowest $[Ti]_{A-2}$ values correspond to recrystallized quartz crystals, where Ti was lost by diffusion. Grujic et al. (2011) reported similar observations in the context of deformation in metamorphic systems for quartz crystals exhibiting grain boundary migration (GBM). At Pagoni Rachi, this leads to an unusual evolution from intermediate temperatures for $T[Ti]_{A-2}$ = 351–521 °C, to higher temperatures $T[Ti]_{A-1}$ = 522–596 °C, $T[Ti]_{B}$ = 449–743 °C and then lower temperatures $T[Ti]_{E}$ = 126–277 °C, in veins (Table 4, Figure 52, Figure 53 G-I).

In the case of fast quartz growth, the use of the lowest temperature values is recommended (e.g., Huang et al., 2012; Acosta et al., 2022; Hong et al., 2024) to minimize the impact of potential Ti excess in quartz. For the B-type veins, this suggests a possible temperature range based on Ti-in-quartz geothermometry (449–475 °C, Figure 51). This same reasoning can be applied to the $[Ti]_{A-1}$ quartz population by assuming that (i) the Ti has not diffused and (ii) considering rapid quartz growth with Ti excess, which would yield the interval [522–561] °C (Figure 52, Figure 53 G). This analysis also underlines the pressure dependency of the thermometer, potentially leading to a broad range of temperature values, particularly at low pressures.

Furthermore, Cernuschi et al. (2018) and Hong et al. (2024) suggested that minimum Ti contents provide more realistic temperature estimates. This is consistent with the fact that the temperatures for $[Ti]_{A-1}$, which retains the primary Ti signature of quartz, are higher than those for $[Ti]_{A-2}$, which exhibits partial Ti loss due to diffusion during dynamic recrystallization. Thus, the temperatures should decrease from $T[Ti]_{A-1}$ to $T[Ti]_{A-2}$. In this context, the evolution appears more consistent with a transition from (ia) high temperatures A-type veins, where quartz retains the primary signal pre-recrystallization, with (ib) low Ti temperatures when Ti has diffused during high-intensity dynamic recrystallization, to (ii)

intermediate temperatures B-type veins, where the quartz is moderately deformed to undeformed, and to (iii) low temperatures E-type veins, without plastic deformation (Figure 52 and Figure 53 A-I).

Moreover Nachlas et al. (2015) suggested that Ti temperature of highly recrystallized quartz grains give the temperature of the deformation conditions. Noting that, it is still interesting to look at these low temperatures due to Ti loss during deformation, which go from 351 to 521 °C in the A-type veins. They may represent the possible range of temperature deformation, which are consistent with the deformation texture, as widespread GBM and SGR that give a range of theoretical deformation temperatures from 250 to 600 °C (Stipp et al., 2002a, b), also with the presence of later fluid circulation forming B-type veins at around 400 °C and the formation temperature of A-type veins quartz at ~ 500 °C. This may indicate a possible temperature of deformation from 350 to 500 °C consistent with fluid circulation conditions and thus with recrystallization during quartz crystallization.

An artificial underestimation of $T[\mathrm{Ti}]_E$ is conceivable for E-type veins which are lower than those expected from fluid inclusion data (Figure 53 I). At low pressures, the isopleth curves flatten (Figure 52), so even slight variations in pressure can significantly alter the associated temperature. This artificial phenomenon exists at high pressure as well, but less pronounced.

Therefore, for the specific case of the Pagoni Rachi system, the Ti-in-quartz thermometer is not suitable for calculating the temperature of Ti incorporation in quartz when recrystallized, or when the Ti incorporation in quartz is related to fast growth. In the first case, the given $T[\mathrm{Ti}]$ may represent the temperature of deformation, and in the second case the use of the lowest Ti content may be done to avoid an overestimation of the quartz crystallization. It is interesting regarding the stability of the geochemical signature along the lifespan and deformation of the porphyry-epithermal system.

3.5.7. Implication for Al/Ti vs Ge/Ti-based vein typology in porphyry-epithermal systems

It is common to distinguish different vein types in porphyry-epithermal systems based on distinct Al/Ti and Ge/Ti ratios in quartz (e.g. Schrön et al., 1988; Götze, 2012; Rottier and Casanova, 2021; Falkenberg et al., 2024), which, however, can be disturbed by dynamic recrystallization and rapid crystal growth (Nachlas et al., 2015; Cernuschi et al., 2018). For instance, the quartz data from Pagoni Rachi of the A-type veins fall within the range of other B-type veins from the literature, while our data from the B-type veins overlaps with data from the A-type veins data from the literature (Figure 53 G-I). This suggests that particular attention should be paid to the concentration variations of the different involved elements. Germanium appears to be relatively stable within the veins and does not show any resetting due to deformation, like the Al content (Figure 51). Some authors have already described Al as immobile or only slightly mobile at the micrometer scale (Tailby et al., 2018). Moreover, this variability in element concentrations, particularly Al, reflects broader geochemical changes within the system, as evidenced by the shift in Al content from A- to E-type veins, which is closely linked to alterations in fluid pH. This

is evidenced by the changing Al content of the quartz, which increases from A- to E-type veins. This trend is associated with a decrease in fluid pH, as Al concentration in hydrothermal quartz is known to increase with decreasing pH (Rusk et al., 2008a, b; Müller et al., 2018). The shift from sericitic to advanced argillic alteration assemblages in the host rocks further supports this acidification process, which is typical of the late stages of porphyry to epithermal transitions (Sillitoe, 2010).

Therefore, Ti appears to be the main factor for these anomalous features, being more impacted during dynamic recrystallization and its incorporation sensitive to the crystallization rate. This again indicates that the Ti contents in these quartz types from Pagoni Rachi do not reflect the actual precipitation conditions at equilibrium but rather the history of deformation and recrystallization and out-of-equilibrium crystallization processes.

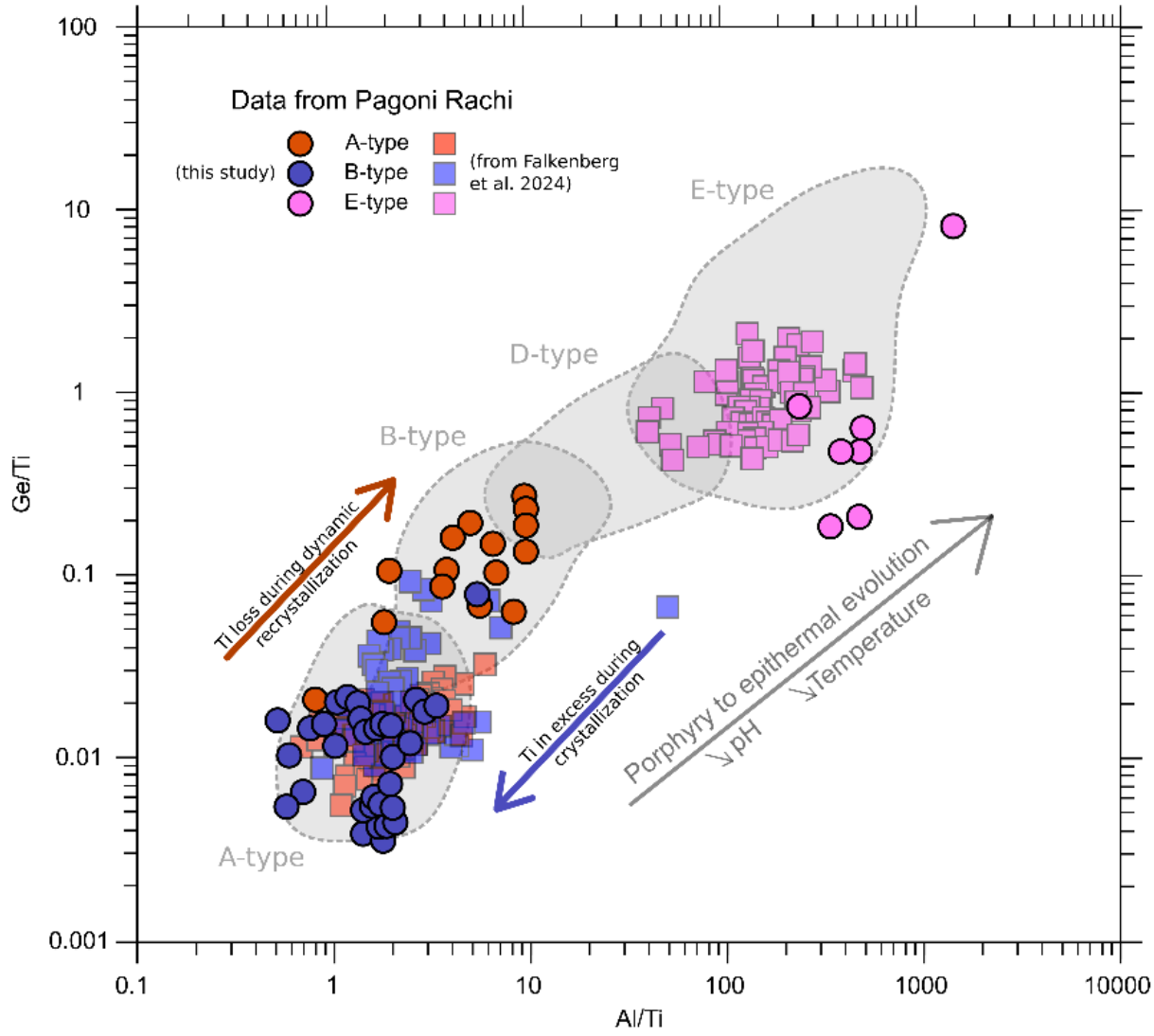

Figure 54: Ge/Ti vs Al/Ti (mass ratios) diagram based on LA-ICP-MS analyses of quartz of A-type (red), B-type veins (blue), and E-type veins (pink). Compilation of data from the literature is shown by the grey shaded aeras (from Casanova and Rottier, 2020), and by the shaded colored squares for similar vein in Maronia porphyry system (from Falkenberg et al. 2024).

For the A-type vein quartz, it is likely that Ti diffusion is controlled and possibly enhanced by deformation processes causing quartz recrystallization. This results in an underestimation of quartz precipitation temperatures by the Ti-in-quartz thermometer (Figure 53 G) and unexpectedly high Ge/Ti and Al/Ti ratios in quartz (Figure 54). This likely explains why the trace element data of A-type veins fall within the B-type vein domain from the literature (Figure 54). On the other hand, a fast precipitation rate, which implies an excess of Ti in quartz, leads to high Ti concentrations in quartz (Figure 53 H) and an underestimation of Ge/Ti and Al/Ti

ratios. This likely explains why our B-type vein trace element ratios fall within the A-type vein data from the literature. Where veins which do not show any evidence of Ti in excess or a Ti loss like the E-type veins which are within the expected domain (Figure 54). In Falkenberg et al. (2024), this anomaly is also observable through their data. Indeed, the analysis of the Al/Ti vs. Ge/Ti ratios of their B-type vein quartz falls within the range of A-type veins. This is consistent with the implication of excess Ti due to rapid, out-of-equilibrium growth of the quartz. However, in their case, the data for the A-type vein quartz are consistent with what is expected from the literature, showing no evidence of imbalance due to recrystallization of their quartz.

Therefore, this suggests that specific attention must be paid to the petrographic textures and trace element compositions of quartz to interpret such geochemical classification of hydrothermal quartz veins from porphyry-epithermal systems. In other words, the Al/Ti vs Ge/Ti-based typology of Rottier and Casanova (2021) may be valid only for quartz veins formed under equilibrium conditions and preserved from dynamic recrystallization.

3.6. SUMMARY AND CONCLUSION

Overall, the Pagoni Rachi system serves as a case study illustrating how the interplay between deformation, fluid chemistry and thermal conditions can impact the development of quartz veins in porphyry-epithermal systems. The evolution from ductile to brittle deformation and from lithostatic to hydrostatic conditions (Figure 52), coupled with fluid boiling and Ti diffusion, fast growth rate, suggests that careful attention must be paid to the petrographic textures and trace element compositions of quartz when reconstructing the history of such systems. It is interesting regarding the stability of the geochemical signature along the lifespan and deformation of the porphyry-epithermal system.

Quartz veins within the system demonstrate varying degrees of dynamic recrystallization, reflecting changes in the deformation environment over time. A-type veins are marked by widespread grain boundary migration (GBM) and subgrain rotation (SGR) textures, indicative of ductile deformation under high-temperature conditions (600–450 °C) (Stipp et al., 2002a, b; Passchier and Trouw, 2008) with for the most deformed part showing lower Ti content than expected. These textures suggest intense deformation processes, which not only impacted the microstructure of the quartz but also influenced its geochemical properties, particularly the Ti diffusion. The Ti content in quartz, affected by dislocation creep, results in discrepancies when using Ti-in-quartz thermometry, leading to temperature estimates that may not accurately reflect the conditions of quartz precipitation with a underestimation down to –100 °C (Figure 52 and Figure 53 A, D and G).

B-type veins show a different deformation history, with localized SGR textures suggesting lower temperatures of deformation (450–350 °C) (Stipp et al., 2002a, b). The formation of these veins likely marks the transition from ductile to brittle deformation within the system (Monecke et al., 2018) (Figure 52). The relatively straighter and more continuous character of B-type veins, compared to the sinuous and discontinuous A-type veins, reflects this transition. Additionally, the rapid quartz precipitation out of equilibrium associated with B-type veins can result in a Ti excess, further complicating the interpretation of Ti-in-quartz data with an overestimation up to +300 °C (Figure 52 and Figure 53 B, E and H).

E-type veins, in contrast, did not experiment with dynamic recrystallization, indicating that they formed under brittle conditions at temperatures below 300 °C. These veins are characterized by euhedral, undeformed quartz crystals and their formation in equilibrium is consistent with the final stages of the system evolution, where brittle fracturing was predominant. Here, the Ti content does not display any excess or deficit, and the Ti-in-quartz thermometer yields the expected temperature from fluid inclusions (Figure 50 C, Figure 52 and Figure 53 C, F and I).

Crystallization and deformation processes can alter or modify the expected Ti signature in quartz, leading to potential misinterpretation of the geochemical signatures of quartz in different veins of a porphyry-epithermal system. Therefore, careful attention must be paid to the petrographic texture of quartz and CL imaging. This study highlights the importance of considering these deformation histories

when interpreting geochemical signatures, as processes like GBM and SGR can significantly alter the Ti content and other trace elements in quartz, and out-of-equilibrium crystallization due to fast crystal grow which can imply a Ti in excess, leading to potential misinterpretations (Figure 54 if not properly accounted for. This study highlights the importance of deformation on the geochemical signature and emphasizes all the processes that must be considered to avoid errors in interpretation.

3.7. ACKNOWLEDGEMENTS

We would like to acknowledge Chantal Peiffert for her assistance during the LA-ICP-MS measurements. Alexandre Flammang for the thin and thick sections from the lithopreparation plateform of Otelo and the ERASMUS+ ARTeMIS (Action for Research and Teaching Mineral exploration Inclusive School) project number KA220-HED-B1B19447, which supported field trip to Northern Greece and part of the analytical work. This work was supported by the French National Research Agency through the national program “Investissements d’avenir” with the reference ANR-10-LABX-21–RESSOURCES21.

CHAPITRE 4. EVOLUTION OF THE PHYSICO-CHEMICAL CONDITIONS OF ORE-FORMING FLUIDS IN A PROPHYRY-EPITHERMAL SYSTEM THROUGH TRACE ELEMENTS IN QUARTZ

4.1. INTRODUCTION

The quantitative analysis of trace elements in quartz serves as a proxy for the content of these elements in the fluids from which they originated. Data on trace element concentrations in quartz across a series of veins allow for assessing concentration variations during fluid circulation, and thus the partitioning of metals across different veins (Müller et al., 2003; Landtwing et al., 2005; Beurlen et al., 2011; Götze et al., 2012; Tanner et al., 2013; Maydagan et al., 2015; Mao et al., 2017, 2018; Rottier et al., 2017; Cernuschi et al., 2018; Monnier et al., 2018; Rottier et al., 2020; Rottier and Casanova, 2021).

The study of trace elements in minerals is a crucial field in geoscience, offering insights into the complex processes underlying the formation of hydrothermal deposits. Quartz serves as an exceptional recorder of the physicochemical conditions of the fluids that precipitate it. Due to its chemical stability and resistance to alteration, quartz preserves, at the microscopic scale, chemical signatures that reflect the conditions under which hydrothermal veins formed (Monecke et al., 2002; Götze et al., 2004; Rusk et al., 2008; Gotte et al., 2011). These veins, prevalent in porphyry-epithermal systems, are critical in concentrating economically important metals, such as gold, silver, copper, and molybdenum (Sillitoe, 2010; Voudouris et al., 2019). Tracing fluid circulation and changes in physicochemical parameters, including temperature, pressure, chemical composition, and pH, is essential for understanding the formation of these systems and guiding mineral exploration strategies (Rottier and Casanova, 2021; Dong et al., 2022).

In porphyry-epithermal hydrothermal systems, trace elements incorporated into quartz provide valuable data about crystallization conditions. Titanium is one of the most extensively studied trace elements. The titanium concentration in quartz is controlled by temperature and the chemical activity of titanium in the fluid. Using thermometric calibrations, such as those suggested by Zhang et al. (2020), the crystallization temperature of quartz veins can be estimated. Other trace elements, such as boron and lithium, offer additional insights into fluid composition and chemical evolution. Boron, for example, serves as an indicator of pH and salinity variations, while lithium can reveal interactions between hydrothermal fluids and host rocks (Müller et al. 2000).

Quartz, a common mineral in hydrothermal ore deposits, is a widely distributed gangue mineral in magmatic-hydrothermal deposits, including porphyry Cu-Mo systems (Rusk et al., 2008; Maydagan et al., 2015; Mao et al., 2017) and epithermal Pb-Zn and Au-Ag deposits (Tanner et al., 2013; Rottier and Casanova, 2021). Many studies have used laser ablation-inductively coupled plasma-mass spectrometry (LA-ICP-MS) to analyze trace elements in quartz in these types of deposits, providing insights into ore-forming processes (Rusk et al., 2008; Tanner et al., 2013; Mercer et al., 2015; Monnier et al., 2018; Hong et al., 2019; Breiter et al., 2020; Rottier and Casanova, 2020). However, the causes of trace element variations in quartz remain debated. For example, in porphyry systems, high aluminum concentrations in late-stage quartz veins have been attributed to cooling, rapid depressurization,

compositional changes in hydrothermal fluids (e.g., mixing with meteoric water), pH, or precipitation rate (Allan and Yardley, 2007; Rusk et al., 2008; Rottier and Casanova, 2020).

Quartz consists of a three-dimensional network of [SiO4]4− tetrahedra, creating small and large channel-like structures along the c-axis (Figure 55; Weil 1984). The most common point defects in quartz structures include the substitution of an Si^{4+} cation with a trivalent cation, such as Al^{3+}, Fe^{3+}, B^{3+}, As^{3+}, and Ga^{3+} (Götze et al., 2004). This charge imbalance is compensated either by the incorporation of a monovalent cation in an interstitial position (Figure 55), such as Li^{+}, Na^{+}, K^{+}, H^{+}, Cu^{+}, and Ag^{+}, by substituting a neighboring $Si4^{+}$ with a pentavalent cation like P^{5+} (Müller and Koch-Müller, 2009), or by the absence of an electron in a non-bonding orbital of an oxygen anion adjacent to the trivalent cation (Weil, 1984; Stevens-Kalceff, 2009). Si^{4+} can also be substituted by tetravalent cations such as Ti^{4+}, Ge^{4+}, or Sn^{4+}. Divalent cations such as Mn^{2+}, Ca^{2+}, Mg^{2+}, and Sr^{2+} may be incorporated to compensate for the substitution of two Si^{4+} by two trivalent cations, though this mechanism is rare (Weil, 1984; Götze et al., 2004).

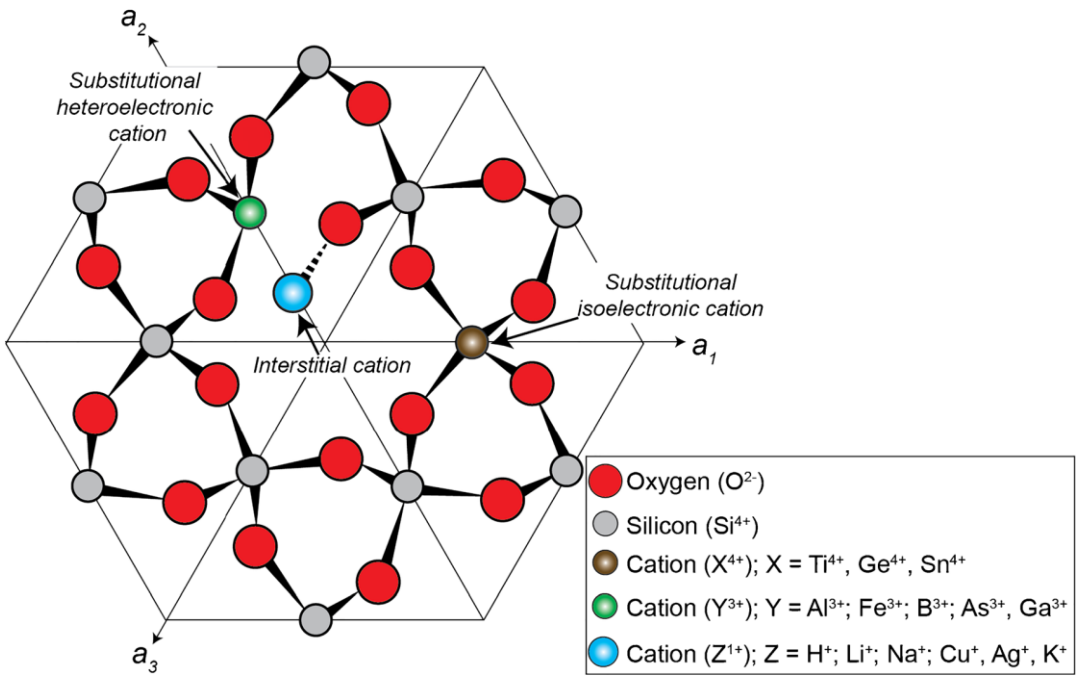

Figure 55: Quartz structure, and projection of α-quartz atomic positions onto the plane perpendicular to c-axis including the most common defect types, from Rottier and Casanova (2021).

The inconsistent explanations surrounding trace element variations in quartz hinder efforts to use quartz trace elements to constrain fluid sources and evolution in magmatic-hydrothermal deposits. There are two primary reasons for these inconsistencies. Multiple episodes of quartz precipitation and dissolution generate varied textures visible in cathodoluminescence (CL) images. For example, multiple stages and complex cross-cutting relationships are found in veins from porphyry and epithermal systems, ranging from early quartz veins formed at high temperatures (>500 °C) to late quartz veins precipitating at lower temperatures (<300 °C) (Gustafson and Hunt, 1975; Dilles and Einaudi, 1992; Rusk and Reed,

2002; Müller et al., 2010; Maydagan et al., 2015; Zhang et al., 2020; Rusk et al., 2008, 2011; Gotze, 2009; Gao et al., 2021). Fluid circulation, deformation, dynamically recrystallized quartz, fracturing, dissolution, precipitation, and reopening all contribute to these complexities.

The various in situ methods used for analysis differ in analytical precision, detection limits, and spatial resolution. For instance, electron probe microanalysis (EPMA) cannot detect light elements such as H, He, or Li (Müller et al., 2003; Audétat et al., 2015). Laser ablation-ICP-MS has emerged as the most popular method for obtaining reliable trace element compositions in quartz (e.g. Tanner et al., 2013; Rottier et al., 2017). To advance understanding of quartz trace element compositions in evolving magmatic-hydrothermal systems, we analyzed trace elements in several textural types and generations of quartz from different quartz vein types in the Pagoni Rachi porphyry-epithermal system. Geochemical diagrams are presented to distinguish hydrothermal stages, and we demonstrate how quartz trace elements can be applied in the exploration of magmatic-hydrothermal deposits, with the necessary precautions.

This article aims to explore in detail how trace elements in quartz from hydrothermal veins can help reconstruct fluid circulation pathways in porphyry-epithermal system of Pagoni Rachi and the physicochemical conditions that led to the formation of metallic deposits. By combining advanced analytical techniques such as laser ablation inductively coupled plasma mass spectrometry (LA-ICP-MS) with sophisticated geochemical modeling, this study contributes to a deeper understanding of hydrothermal processes. A better understanding of these systems has broader implications, not only for fundamental scientific knowledge but also for practical applications in mineral exploration.

4.2. METHODOLOGY

4.2.1. Sampling selection

The sample selection for this study was designed to encompass the history and hydrothermal evolution of Pagoni Rachi, with an emphasis on quartz vein types. Samples were selected based on their representation of the characteristic macroscopic features of A-, B1-, B2-, and E1-type veins within the Pagoni Rachi magmatic-hydrothermal system (Voudouris et al., 2013a, b; Mavrogonatos et al., 2019, 2020). A set of six samples, each containing different vein types hosted by altered granodiorite, were prepared for thin sections and doubly polished thick sections (150 μm) at GeoRessources: MB0201 (A- and B1-types), MB0202 (A- and B1-types), AB120.01 (B1-type), AB.119.02 (B2-type), AB.122.03 (E1-type), and MB11.02.01 (E1-type).

4.2.2. Trace elements in quartz by Laser Ablation – Inductive Coupled Plasma – Mass Spectrometer (LA – ICP – MS)

The strategy for selecting LA-ICP-MS spots involved targeting distinct microtextural domains within quartz, including growth zoning, deformation-related microtextures, and undeformed grains, across the various vein types. This selection was guided by optical microscopy and CL imaging (optical and SEM) presented in Chapter 1. Spots exhibiting minimal variability in CL intensity were prioritized to reduce the risk of incorporating regions with variable elemental concentrations. Additionally, CL variations associated with partial recrystallization of fluid inclusions, which can cause geochemical anomalies in the host quartz (e.g., CL trails with low Ti concentrations; Lambrecht and Diamond, 2014), were intentionally avoided. Where feasible, regions containing visible fluid or solid inclusions were also excluded.

The LA-ICP-MS system at GeoRessources comprises an Agilent 7900 quadrupole ICP-MS coupled with a 193 nm ArF excimer laser (GEOLAS Pro). Laser ablation was conducted at a constant frequency of 5 Hz and a fluence of 12 $J \cdot cm^{-2}$, focused on the surface of the thick section. The ablation spot size was set to 50 μm. Helium was used as carrier gas to transport ablated particles from the ablation cell to the ICP-MS, with argon added as an auxiliary gas via a flow adapter before the ICP-MS torch. External standardization was performed using NIST SRM 610 (primary) and NIST SRM 612 (secondary) as reference materials (Jochum et al., 2011; Pearce et al., 1997). The standards were analyzed twice before and after each sample, or approximately every 20–30 measurements. Acquisition times included 30 seconds for background measurement, 60–90 seconds for ablation, and 30 seconds for washout. Given the typically low trace element concentrations in quartz, the stoichiometric Si content of quartz was assumed to be a reasonable approximation for internal standardization (e.g., Müller et al., 2003; Monnier et al., 2018).

A total of 38 isotopes were measured with an integration time of 10 ms: ^{7}Li, ^{9}Be, ^{11}B, ^{23}Na, ^{24}Mg, ^{27}Al, ^{29}Si, ^{35}Cl, ^{39}K, ^{44}Ca (used instead of ^{40}Ca to avoid isobaric interference with ^{40}Ar), ^{47}Ti, ^{55}Mn, ^{56}Fe, ^{59}Co, ^{63}Cu, ^{66}Zn, ^{71}Ga, ^{72}Ge, ^{75}As, ^{85}Rb, ^{88}Sr, ^{90}Zr, ^{93}Nb, ^{95}Mo, ^{107}Ag, ^{115}In, ^{118}Sn, ^{121}Sb, ^{125}Te, ^{133}Cs, ^{137}Ba, ^{181}Ta, ^{182}W, ^{185}Re, ^{197}Au, ^{208}Pb, ^{209}Bi, and ^{238}U. These isotopes were selected for the following reasons: (i) they represent the most abundant isotope of each element to maximize signal intensity (except for ^{44}Ca and ^{56}Fe, which were chosen to avoid significant interferences between ^{40}Ca and ^{40}Ar and between ^{56}Fe and ^{40}Ar^{16}O, respectively); (ii) they include metals and semi-metals known to be key constituents of the mineralization at Pagoni Rachi (Voudouris et al., 2013a); (iii) they include elements such as K, Na, Cl, Fe, and Ca, which help distinguish quartz ablation from potential fluid or solid inclusions (e.g. Kouzmanov and Pokrovski 2012); and (iv) they include elements commonly substituting into quartz (e.g., Al, Li, Ti, Ge) that can serve as markers for temperature, pressure, pH, and growth rate (e.g., Götze et al., 2012, 2021; Raimbourg et al., 2022; Casanova and Rottier, 2021).

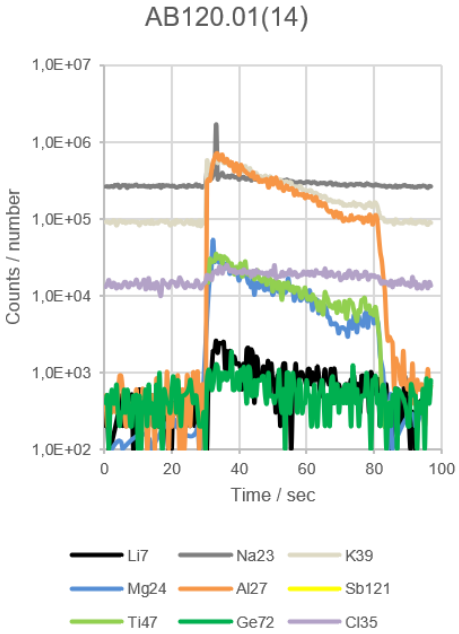

Figure 56: Trace element spectrum during laser ablation ICP-MS of a B1-type vein quartz (sample AB.120.01 (no. 14)), showing Li, Na, K, Mg, Al, Sb, Ti, Ge, and Cl.

A total of 211 measurements were performed and subsequently processed using Iolite software (https://iolite-software.com) for data reduction. Detection limits (LOD) for each element were calculated following the method of Longerich (1987) using the 3σ criterion. Initially, only spectra exhibiting a stable signal over time were retained (Figure 56). The precision (%RSD) is between 1.6 for Be and 20.2 % for Fe, with a mean of all elements at 4.6 %. The accuracy is between 82% for Mg and 175 % for Cl, the mean accurcy for all element is 100 % (See Table of ICP-MS quartz analyses for different elements in G_NIST610 standard.Table of ICP-MS quartz analyses for different elements in G_NIST612 standard.). Signals displaying intensity spikes for elements indicative of fluid inclusions (e.g., K, Na, Cl) or solid inclusions, such as silicates and oxides (e.g., Al, Ca, Fe, Mg) or sulfides (e.g., Cu, Re, Mo), were excluded from further data processing.

4.2.3. Thermometry – Ti-in-quartz

Recent studies have favored the calibration of Zhang et al. (2020) in hydrothermal systems (Cernuschi, 2018; Rottier and Casanova, 2021; Hong et al., 2023; Abiven et al., submitted). The Ti-in-quartz thermometer depends on the pressure and temperatures conditions, since the Ti^{4+} substitution into quartz increases with decreasing pressure and increasing temperature. Even though the calibration of

Zhang et al. (2020) was initially valid for temperatures between 700 – 900 °C and pressures between 0.5 – 4.0 kbars, Rottier and Casanova (2021) suggested to be the best calibration for lower *PT* hydrothermal system. The temperature of quartz crystallization was thus obtained using the following equation (Zhang et al. 2020):

$$T[\mathrm{Ti}] = \frac{1948.4 + 981.4 \times P^{0.2}}{5.3226 - \log_{10}\left([\mathrm{Ti}]_{\mathrm{Qz}}\right)} - 273.15$$

where T[Ti] is the temperature of quartz crystallization (in °C), P is the pressure of quartz crystallization (in kbar) and $[\mathrm{Ti}]_{\mathrm{Qz}}$ is the Ti concentration in quartz (in ppm).

The measured Ti content, and used data are the maximum Ti range for each population of B2-type veins (as $[\mathrm{Ti}]_{\mathrm{min}}$ and $[\mathrm{Ti}]_{\mathrm{max}}$), and the maximum P range (as P_{min} = 10 and P_{max} = 150 bars), to constrain a range of T[Ti] for each vein type. This approach naturally introduces a bias in the reported values, but allows for the presentation of potential variations, which are also influenced by various processes to which Ti is sensitive. The pressure of quartz crystallization is commonly obtained from the trapping pressure of fluid inclusions (e.g. Tanner et al. 2013). However, due to a lack of fluid inclusions data of B2-type vein in this study, a pressure range from Muntean and Einaudi (2000) from fluid inclusion analyses in banded veins in the Maricunga Belt which are similar to B2-type veins have been used. Consequently, the T[Ti] domains are bounded by the minimal and maximal Ti concentration and pressure values for each vein type, $[\mathrm{Ti}]_{\mathrm{min}}$ and P_{min} giving the $T[\mathrm{Ti}]_{\mathrm{min}}$ and, $[\mathrm{Ti}]_{\mathrm{max}}$ and P_{max} giving the $T[\mathrm{Ti}]_{\mathrm{max}}$.

4.3. RESULTS

Quartz crystals from the different veining stages display variable trace element concentrations. In the A-, B1-, B2- and E1-type veins, many analyses yielded usable B, Be, Ag, Te, Ta, Re, As, Bi, Zn, Zr, In, and Au values mostly due to concentrations falling below limit of detection (< LOD) in quartz (Longerich et al., 1987), or because they were not measured. As a result, these elements are excluded from this study. The full dataset is presented in Table of ICP-MS quartz analyses for different elements in A-type vein. Table of ICP-MS quartz analyses for different elements in B1-type veins. Table of ICP-MS quartz analyses for different elements in B2-type vein. Table of ICP-MS quartz analyses for different elements in E1-type vein. and in boxplots.

Mass interferences and/or signal contamination from the sample chamber are known to affect the LA-ICP-MS quantification of Ca and Sn (Müller et al., 2008; Flem and Müller, 2012; Schlöglova et al., 2017; Rottier et al., 2021); therefore, these elements will not be discussed. Additionally, Mo, Au, and U, which theoretically exhibit hexavalence (6+), are not readily incorporated into the quartz lattice. Instead, they are more likely associated with inclusions, potentially forming oxides such as MoO_4^{2-} or complexing with K or Ca. Similarly, UO_2^{2+} and gold may serve as indicators of ablated microinclusions. Divalent cations (such as Mg, Mn, Ba, Co, Zn, Sr, and Pb) are usually incorporated into the quartz structure only in small amounts, as predicted by theoretical models (Weil, 1984; Götze et al., 2004). Although these elements are frequently found within unidentified inclusions (Götze et al., 2004), a notable relationship has been identified between their concentrations and the aluminum content of quartz.

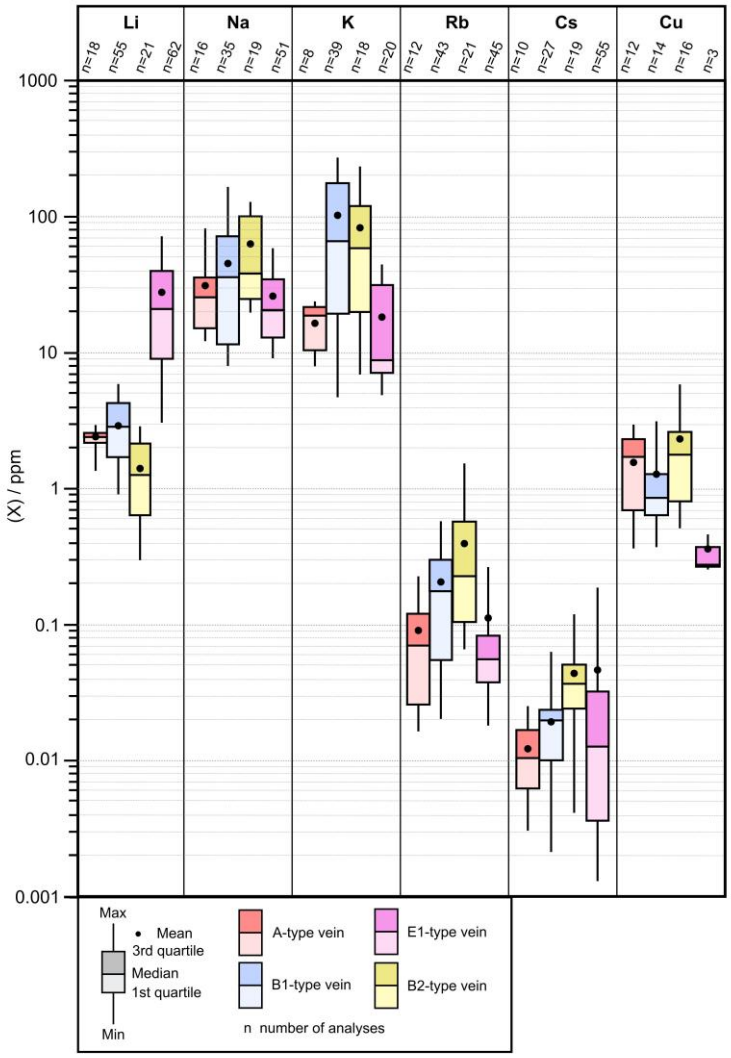

Figure 57: Boxplot of monovalent cations content in quartz.

4.3.1. Monovalent cations

Li content in quartz varying from 0.20 to 98.6 ppm, with > 6 ppm content only in E1-type veins quartz. It shows a

decrease from A- to B2-type veins. Sodium concentration and potassium concentrations are between 3.69 and 293 ppm (Figure 57). Na content slightly increases from A to B2-type veins quartz, and K content is higher in B1- and B2-type veins quartz than in A- and E1-type veins quartz. Rubidium is mostly < 1 ppm, it increases from A- to B2-type veins quartz, it is less abundant in epithermal quartz (Figure 57). Cesium concentrations are low with most values below 0.20 ppm, they increase from A- to B2-type veins quartz, and it display high variation in E1-type veins (Figure 57). Copper concentration is between 0.25 to 8.00 ppm. Epithermal quartz displays a lower Cu content than porphyry quartz and is generally < 0.4 ppm (Figure 57).

4.3.2. Bivalent cations

Magnesium content in quartz is between 0.20 and 25.3 ppm (Figure 58). A slight decrease of Mg concentration is visible from the B1-type quartz to the E1-type quartz. Magnesium content of A-type

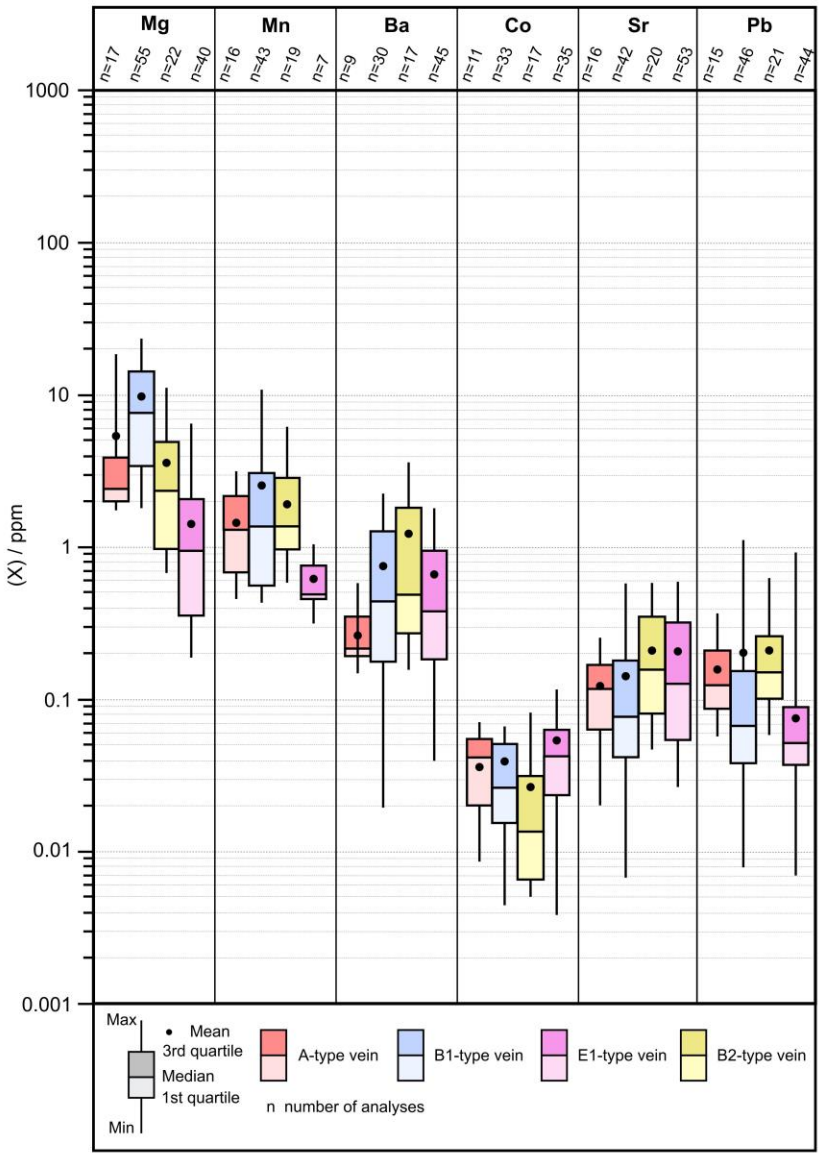

Figure 58: Boxplot of bivalent cations content in quartz.

quartz is within the range of B1- and B2-type quartz (Figure 58). The concentration of manganese ranges from 0.24 to 14.0 ppm and does not display visible variation within the porphyry type quartz, it is mostly < 1 ppm in E1-type quartz (Figure 58). Barium concentration ranges from 0.007 to 5.00 ppm within the vein sequence (Figure 58). Cobalt is low concentrated in quartz, it is generally < 0.1 and does not display any trend of evolution in vein sequence. Strontium concentration is between 0.004 ppm and 1.02 ppm and appears constant within the vein sequence (Figure 58). A small amount of Pb has been measured ranging from 0.003 to 1.4 ppm in the different veins (Figure 58).

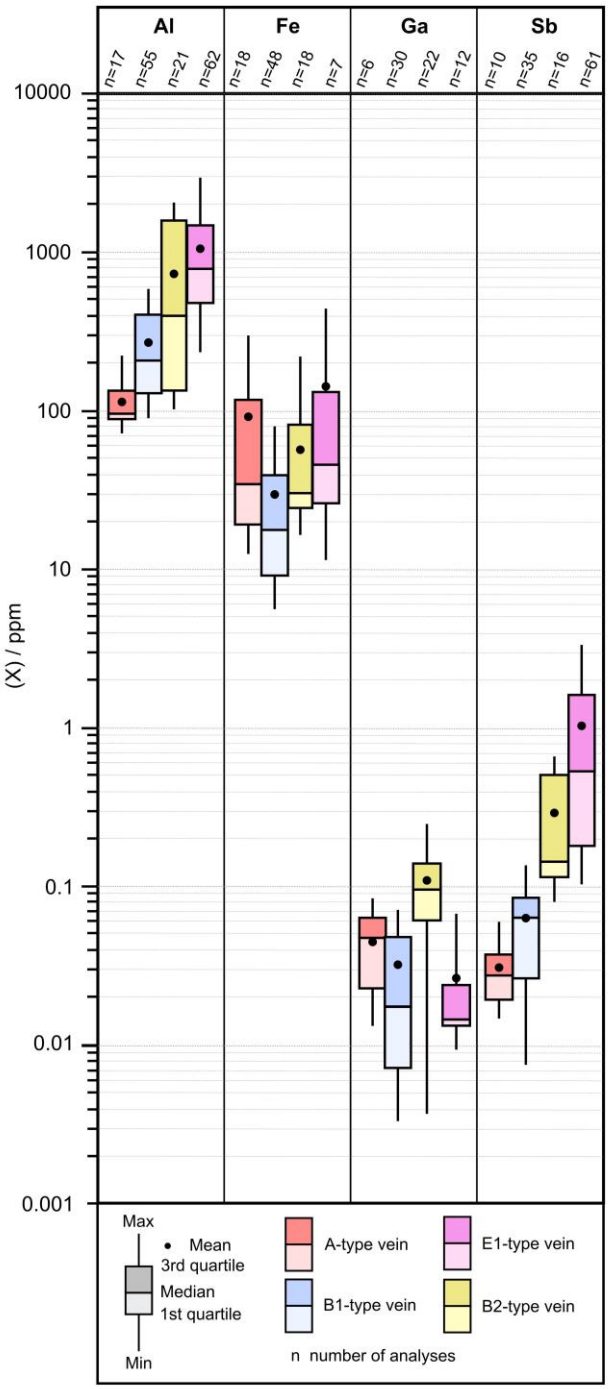

Figure 59: Boxplot of trivalent cations content in quartz.

4.3.3. Trivalent cations

Aluminum is the most abundant and variable trace element, with concentrations ranging from 63.9 to 3459 ppm, with values < 700 ppm restricted to stages A and B1 (Figure 59). The Al content increases from A to E1-type veins. Iron is the second most concentrated element with 3.08 to 513 ppm. Gallium is rare in quartz and its concentration is between 0.002 and 0.34 ppm (Figure 59). It was detected more in B2-type quartz. Antimony concentrations are between 0.001 and 4.43 ppm, and high concentrations (> 1 ppm) are only recorded in E1-type quartz (Figure 59).

4.3.4. Tetravalent cation

Titanium content in quartz ranges from 0.24 to 416 ppm. A clear increase and decrease of Ti content is visible in the different types of porphyry quartz, with an increase from A- to B1-type and then a decrease from B1-type to B2-type, and E1-type quartz which is always < 9 ppm (Figure 61). Variation of Ti content has been found within the different veins regarding microtextural behavior and CL

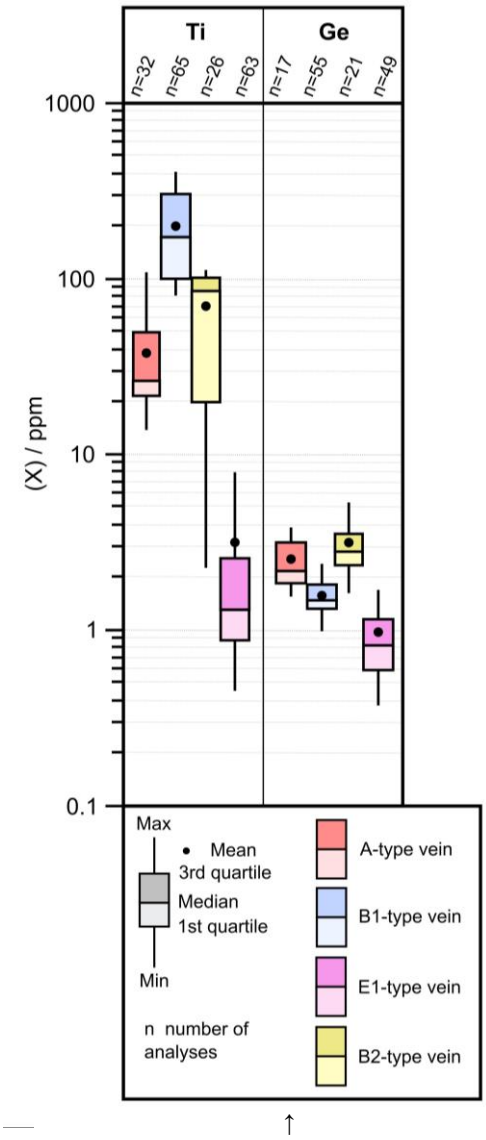

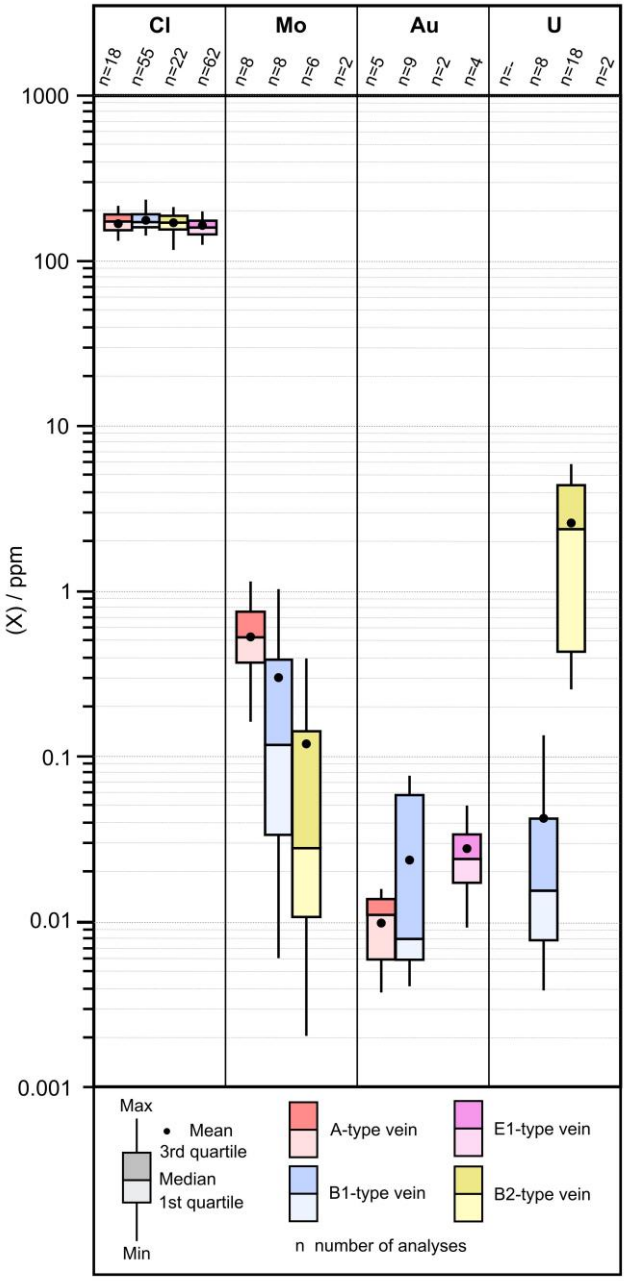

Figure 61 : Boxplot of tetravalent cations content in quartz.

Figure 60: Boxplot of different cations and anions content in quartz.

imaging, has been observed in A-type vein and in B2-type veins. In A-type veins, quartz which displays GBM texture with low CL intensity in red tones presents lower Ti content than the ones which display SGR textures or quartz displaying growth oscillatory zoning CL-textures, which going from 28.3 ± 12.2 ppm (from 9.7 to 56.4 ppm) to 99.7 ± 11.5 (from 83.6 to 115 ppm), respectively (Figure 61). The B2-type veins which display two sequences of quartz forming display a trace element variation from the central structures of the vein to the margin. Indeed, the central parts displaying a granular brighter blue CL intensity have Ti concentration near 96.5 ± 17.2 ppm (ranging from 46.4 to 122 ppm) and external parts in homogeneous dark blue tones CL intensity have a Ti concentration of 18.7 ± 29.2 ppm (ranging

from 1.6 to 90.2 ppm) (Figure 61). Germanium concentrations in quartz are mostly between 0.4 and 6 ppm, with the highest concentrations recorded in A-type quartz and B2-type quartz (Figure 61).

4.3.5. Anions and complexes

Chlorine content is constant within the system, considering the whole vein sequence, and ranges from 99.0 to 261 ppm. Uranium has been detected and above the LOD in the B2-type quartz 2.62 ± 2.27 ppm (ranging from 0.04 to 6.91 ppm), it was always under LOD or not calculated for the other stages. Molybdenum is rarely detected and only appears at concentration < 1 ppm and down to 0.002 ppm, some high concentrations have been measured but are mostly due to the presence of microinclusions in quartz. (Figure 60)

4.4. DISCUSSION

The substantial heterogeneity observed in the trace element content of hydrothermal quartz is consistent with previous studies (Suttner and Leininger, 1972; Goguel, 1983; Perny et al., 1992; Heynke et al., 1992; Monecke et al., 2002; Müller et al., 2003b; Landtwing and Pettke, 2005; Rusk et al., 2006; Götze et al. 2012; Rottier and Casanova, 2021). All Pearson correlation coefficients are in Annexe (Tables of pearson correlation coefficient (Trace Element in quartz).

4.4.1. Trace element correlations

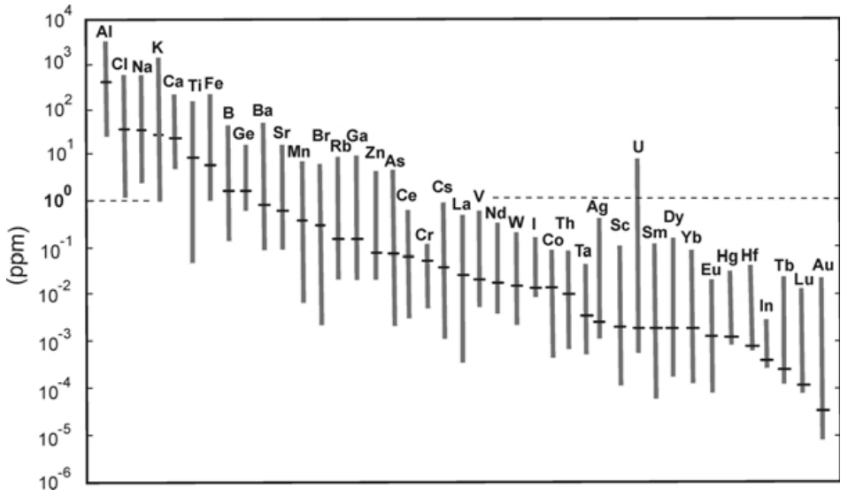

Figure 62: Average abundance and variations of trace elements in quartz (from Götze et al. 2012).

4.4.1.1. Trace element variations through quartz veins

The trace element analyses in quartz were conducted along transects across the veins, from edge to edge whenever feasible, and according to CL zoning. This approach allows for an assessment of the relative evolution of trace elements measured along with the growth of the veins and quartz crystals.

For A-type veins, aside from relative variations within the different veins analyzed, no clear covariation is observed between the various elements, except for Na and Al (Figure 63, Figure 64), which appear to be positively correlated. The lack of complete data for individual analysis points may explain the difficulty or inability to identify such correlations (Figure 63, Figure 64). No clear relationship has been observed between CL textures and the microtextural features of quartz, except for Ti, which shows lower concentrations in strongly recrystallized quartz associated with CL zones of low intensity and textures such as ghostbands or mottled patterns (Figure 63, Figure 64) (presented and discussed in detail in Chapter 3).

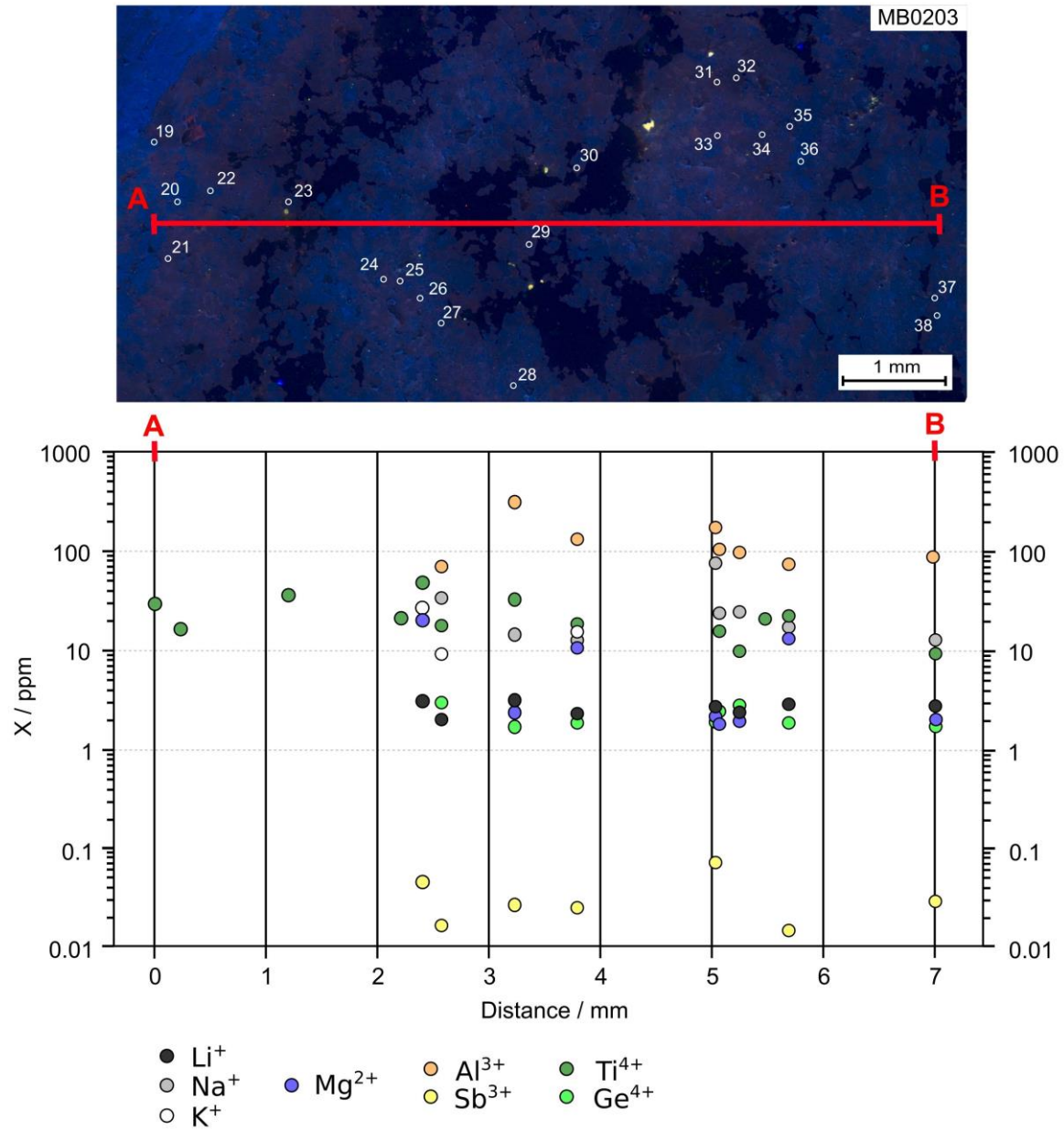

Figure 63: Projection of trace elements contents measured in quartz plotted along a transect crossing an A-type vein. And CL imaging and location of the ablated spots.

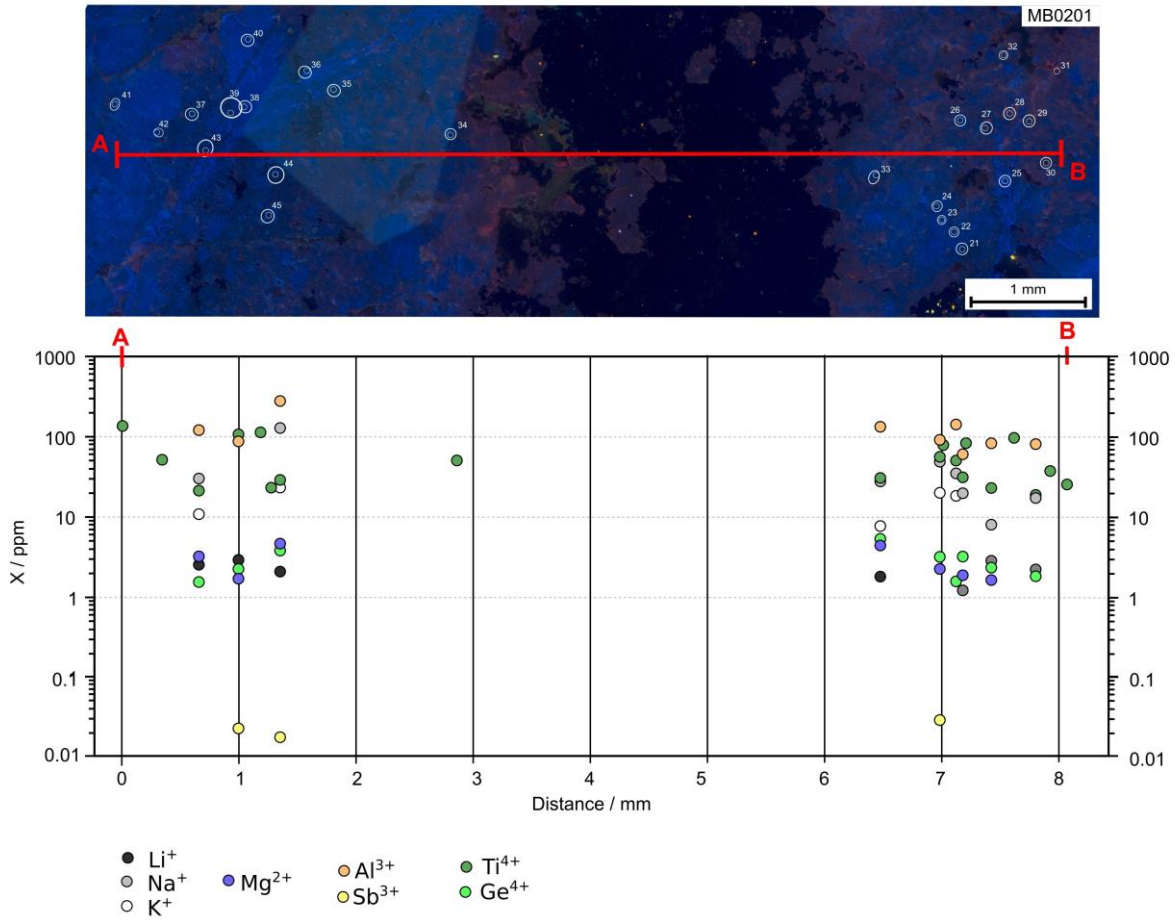

Figure 64: Projection of trace elements contents measured in quartz plotted along a transect crossing an A-type vein. And CL imaging and location of the ablated spots.

For B1-type veins, three transects were performed on veins exhibiting quartz crystals with well-defined oscillatory growth zoning from edge to edge (Figure 65, Figure 66, Figure 67). Several elements, including Al, Ti, Li, Na, K, Mg, and Sb, are positively correlated (Figure 65, Figure 66, Figure 67). The relationship between Ge and the other elements is inconsistent, as Ge sometimes increases alongside other elements and sometimes decreases inversely (Figure 65, Figure 66, Figure 67). Although the general variation trends of Li and Ti are associated with Al, there are instances where their signals decrease as Al increases (Figure 65, Figure 66, Figure 67). No clear link exists between the microtextural domains of quartz, their CL textures, and the trace element content along the vein.

A single transect was performed on B2-type veins (Figure 68). First, a covariation of Al, Sb, K, Li, Na, Mg, and Ge is observed along the vein (Figure 68). However, Ti and Al are inversely correlated, with Ti decreasing as Al increases (Figure 68). Unlike the previous veins, trace element content in B2-type veins is associated with variations in texture and CL intensity (Figure 68). Border zones of void spaces or veins with dull to non-luminescent blue CL exhibit higher trace element concentrations than the rest of the vein, except for Ti, which shows lower signals in these zones. In regions where the CL imagery shows bright blue luminescence, although the CL signal is heterogeneous, no trends beyond those already described are apparent (Figure 68). No clear relationship has been observed between the trace element content of quartz crystals and their microtextural domains.

For E1-type veins, transects from the base to the edge of quartz or from edge to edge were performed when possible, as complete edge-to-edge transects were not always feasible (Figure 69, Figure 70). Al, Li, Na, and Sb appear to be positively correlated along the quartz, whereas Ge and Mg show no correlation with other elements (Figure 69, Figure 70), except in rare cases where Ge is positively correlated with Al variations (Figure 69, Figure 70). Ti sometimes appears to correlate with Al and sometimes correlates inversely with Al, Li, Na, and Sb. No trends are observed between CL zoning and the trace element signal, nor along the quartz transects (Figure 69, Figure 70). Even though concentrations vary from point to point, no clear relationship has been identified.

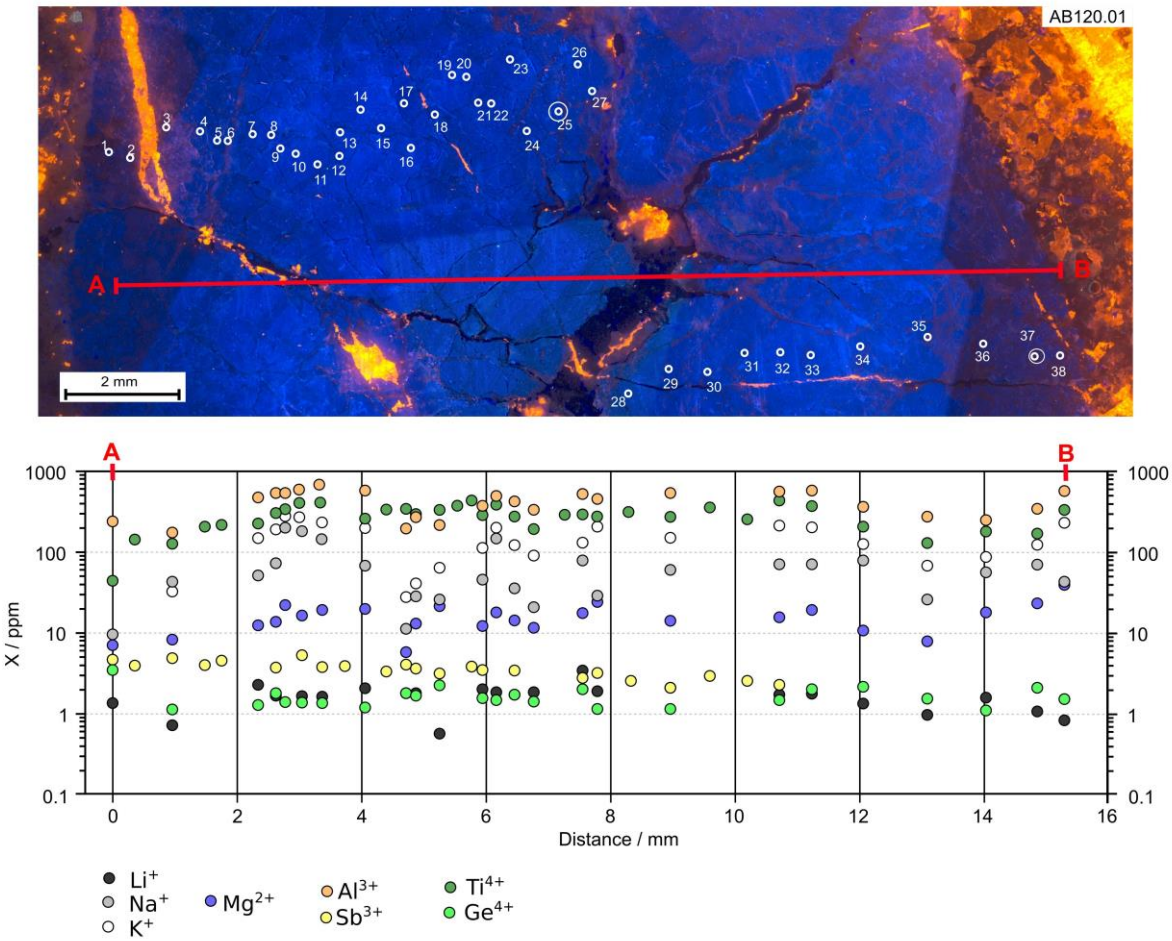

Figure 65: Projection of trace elements contents measured in quartz plotted along a transect crossing an B1-type vein. And CL imaging and location of the ablated spots.

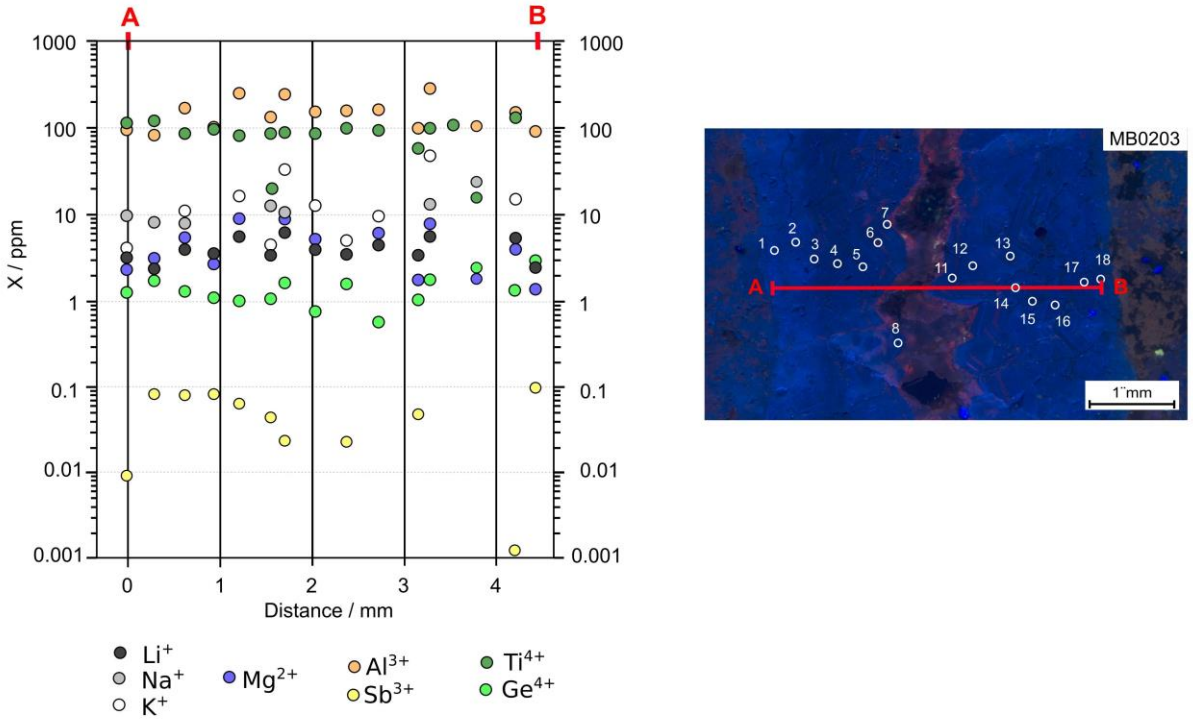

Figure 67: Projection of trace elements contents measured in quartz plotted along a transect crossing an B1-type vein. And CL imaging and location of the ablated spots.

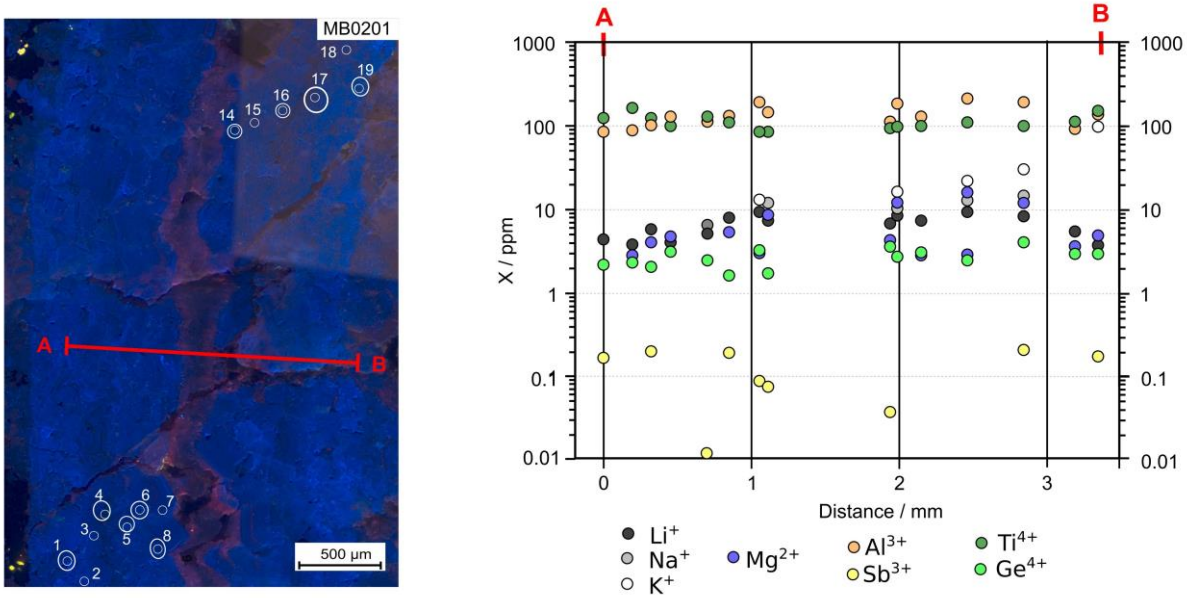

Figure 66: Projection of trace elements contents measured in quartz plotted along a transect crossing an B1-type vein. And CL imaging and location of the ablated spots.

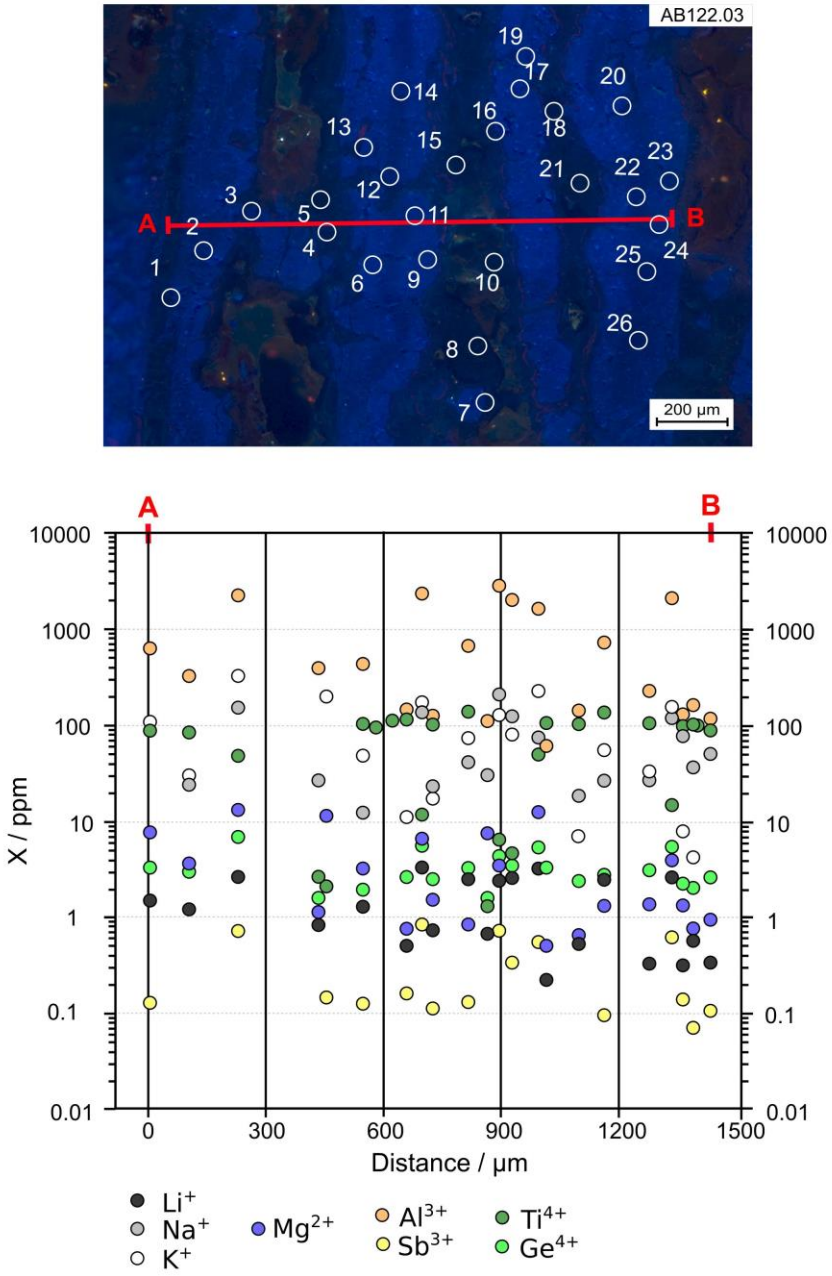

Figure 68: Projection of trace elements contents measured in quartz plotted along a transect crossing an B2-type vein. And CL imaging and location of the ablated spots.

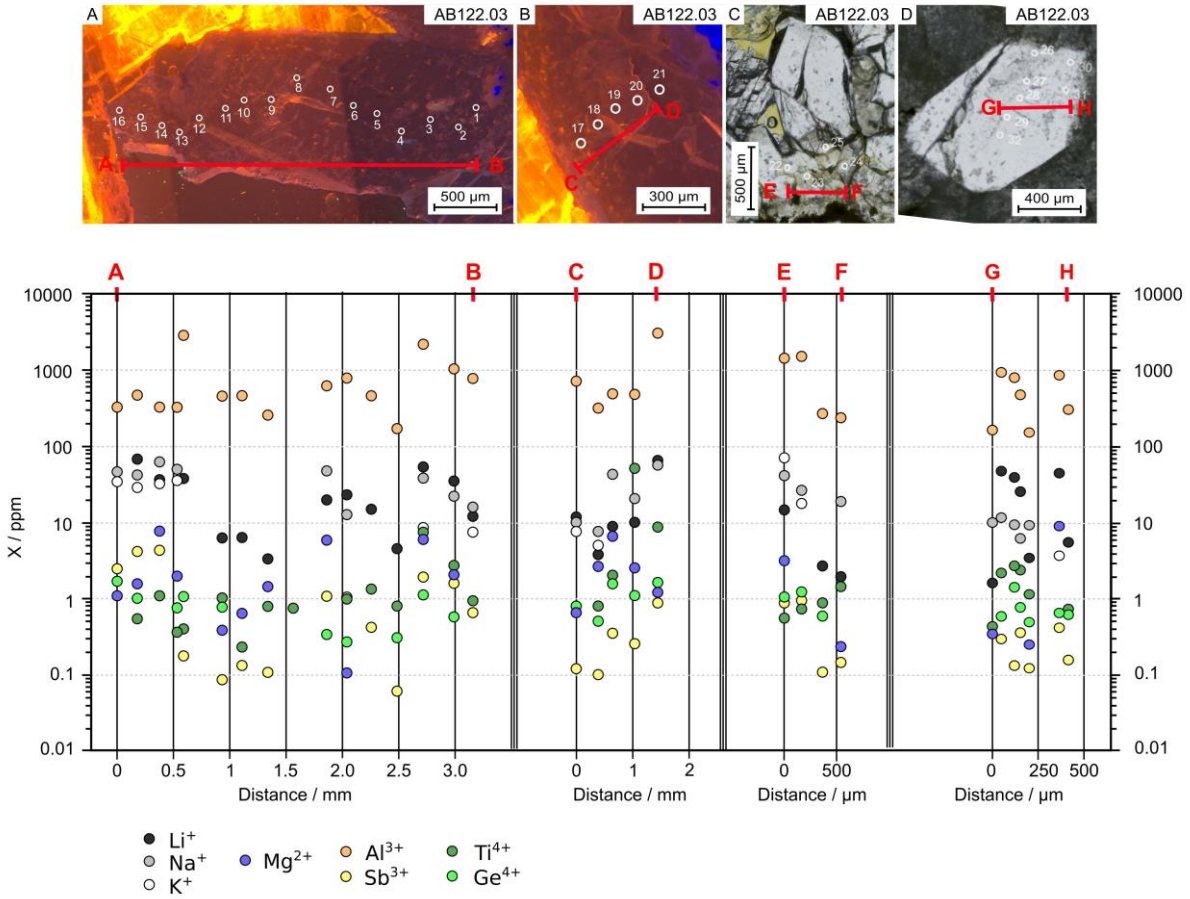

Figure 69: Projection of trace elements contents measured in quartz plotted along a transect crossing an E1-type vein. And CL imaging and location of the ablated spots.

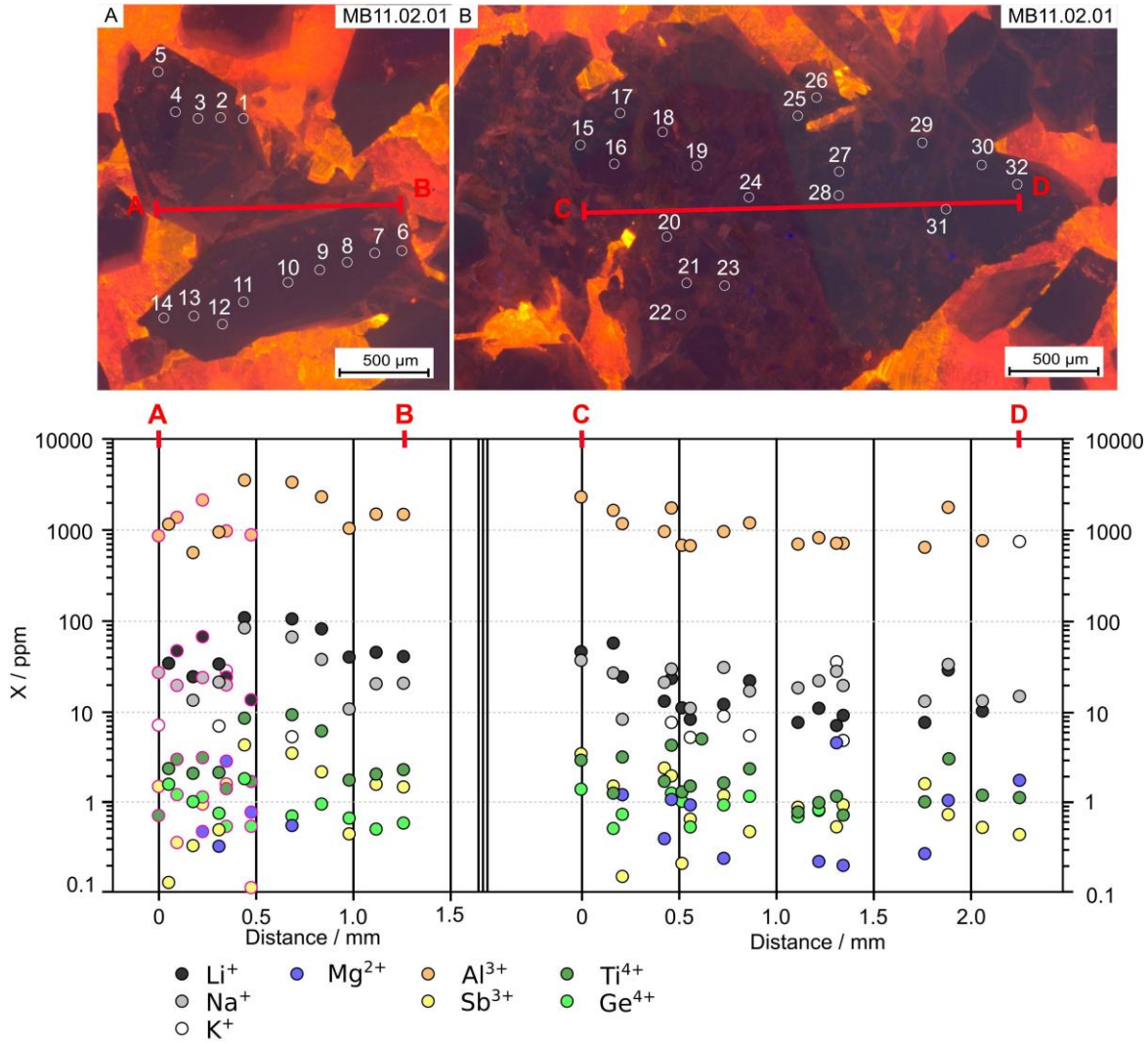

Figure 70: Projection of trace elements contents measured in quartz plotted along a transect crossing an E1-type vein. And CL imaging and location of the ablated spots.

4.4.1.2. Correlations at the porphyry scale

For helping the correlation and trace element content along the prophy-epithermal system several diagrams combining the sum of same valence ions are presented.

At first order, it is interesting to observe how the cations interact with one another. The bivalent and trivalent cations exhibit a positive linear trend for B1-type vein, unlike the others, which show a dispersion. However, there is a progression from high values in trivalent cations and low values in bivalent cations to high values in bivalent cations and low values in trivalent cations.

The bivalent and trivalent cations exhibit a positive linear trend for B1-type vein, but not for the others, which display a dispersion. However, there is a progression from high values starting from low trivalent values and high bivalent values toward high trivalent values and low bivalent values.

Monovalent, bivalent, trivalent, and tetravalent cations do not show any trend, only a decrease in tetravalent concentrations from B1-type veins to A-type veins and finally to E1-type veins, with B2-type veins spreading between B1- and E1-type veins. Monovalents exhibit a positive linear trend in relation to monovalents for B1-type vein. The data for E1-type veins are scattered, but otherwise, there is an overlap of values for A-, B1-, and B2-type veins.

Trivalent and monovalent elements show a linear trend across all vein types. There is an evolution from A- and B1- to B2-type veins, and finally to E1-type veins, associated with a decrease in monovalents and an increase in trivalents.

Lithium shows good correlation with Al; values of quartz crystals from A-type veins, part of B1-type veins, and E1-type veins plotting along a same broad trend, and those from second part of B1- and B2-type veins plotting along a parallel trend characterized by lower Li contents. Potassium shows a clear correlation with Al in B1- and B2- stages, plotting along a broad trend (Figure 72). Al and Li are relatively homogeneous in A and B1 type veins and are more heterogenous in B2- and E1- type veins. Aluminum content tends to increase from A- (~63 to ~300 ppm) and B1-type (~77 to ~700 ppm) veins to B2-type (~55 to ~4000 ppm) and E1- (~70 to ~3500 ppm) veins (Figure 61). The Al and Li contents increase in B2 and E1-type veins quartz from the central part to the margins. For A-, B1-, B2-, and E1-type quartz, Li and Al concentrations are well correlated.

Titanium, Sb, and Ge exhibit a rough correlation with Al for quartz from B1- and B2-type veins (Figure 73, Figure 74). The increase of Ti is also associated to an increase of Al from 403 ± 407 ppm (range from 104 to 1564 ppm) to 1312 ± 963 ppm (range from 57 to 2447 ppm), Na from 40.2 ± 24.4 ppm (range from 12.9 to 86.6 ppm) to 83.2 ± 56.7 ppm (range from 26.2 to 170 ppm), K from 49.4 ± 61.0 (range from 4.4 to 220 ppm) to 150 ± 82.6 (range from 76.6 to 256 ppm) content in quartz.

Antimony and Ge also correlate, where most variations are due to Ge variation (1 to 10 ppm), associated with a small Sb variation within the different stages (1 ppm) (Figure 73 A). Sodium correlates with Al for A-, B1- and B2-type veins plotting along two parallel broad trends (Figure 72 B). A correlation between Al and Mg is observed only for the B1 stage (Figure 75 B). However, a slight

increase of the Al, Li, Ge, and Sb content is observed from the inner part of the systems to its external parts.

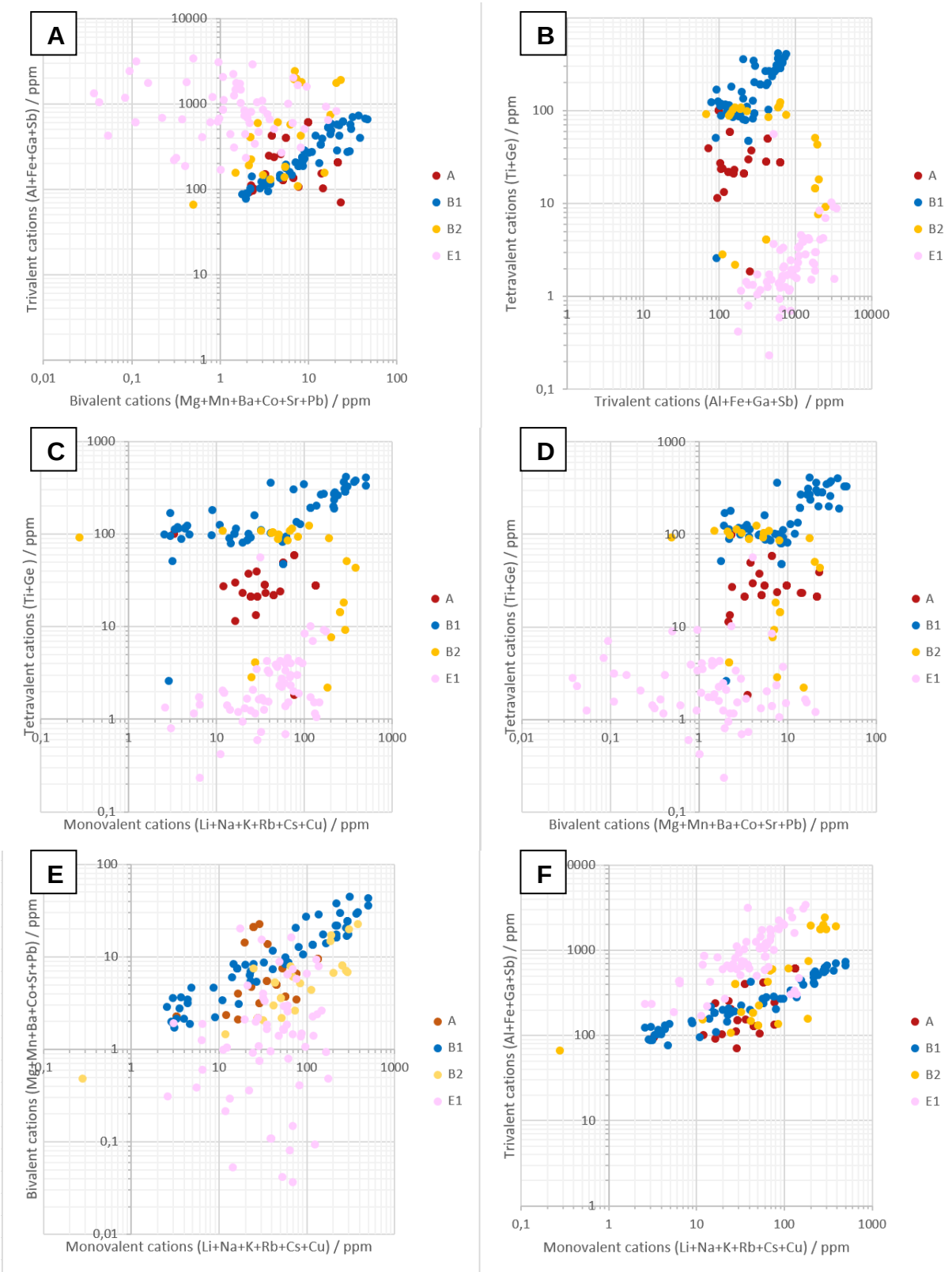

Figure 71: Succession of diagram of sum of certain valence vs. sum of certain valence ions. A. Trivalent cations vs. Bivalent cations B. Tetravalent cations vs. Trivalent cations C. Tetravalent cation vs. Monovalent cations D. Tetravalent cations vs. Bialent cations E.Bivalent cations vs. Monovalent cations F. Trivalent cations vs. Monovalant caions.

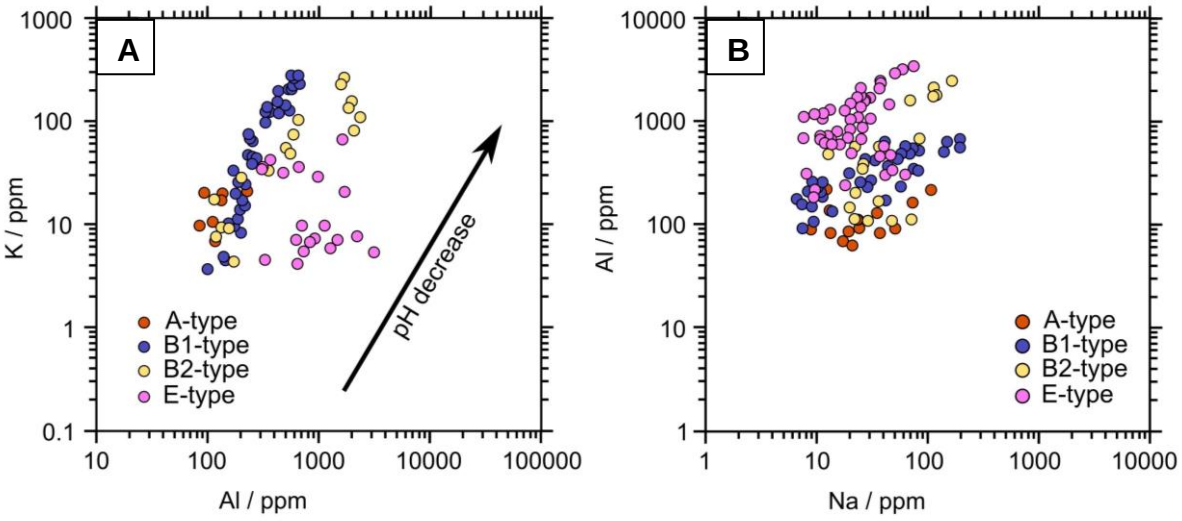

Figure 72 : A. K vs. Al quartz contents. B. Al vs. Na quartz contents.

Two populations of data in B1-type are observable, one with relatively high Li and low Al content and another with high Al, and low Li content (Figure 76). This may be due to growth rates which can produce imbalance in element incorporation during crystallization. There are too few coupled data in A-type veins to appreciate any trend.

The observed good linear correlation between Al and K in A-, B1-, B2-type, suggests that either K is present in the quartz structure or K- and Al-rich solid inclusions such as K-feldspar or sericite which are alteration minerals commonly associated with porphyry veins (Figure 72 A).

Germanium and Ga concentrations in quartz are unlikely to be affected by solid inclusions as they usually are trace elements (< few ppm) in most common minerals found in porphyry veins. In addition, they show no correlation with Na or Cl suggesting that they are not related to the presence of fluid inclusions. Therefore, they are most likely present in the structure of the analyzed quartz., and their signal is constant during quartz ablation.

A correlation is visible between the Al concentrations and those of Sb or Ge in the different quartz generation (Figure 73, Figure 74), but not with Ga, where too few data allow any good interpretation. A trend follows the vein sequence from A-type quartz with low Sb and Al content to E1-type with high Sb and Al contents. Titanium and Ge do not show specific trend, only the Ti decrease from B1- to E1-type veins (Figure 75 A).

Iron concentration can be easily affected by either the presence of fluid or solid (magnetite, biotite, chlorite, pyrite) inclusions. For the different quartz types, Fe does not correlate with Na or with any elements that can suggest that it is related to solid inclusions of biotite or chlorite (Al, Ti, K). However, contamination by small inclusions of magnetite or pyrite cannot be ruled out, and magnetite contamination likely explains the high Fe content (> 400 ppm) of some type of quartz.

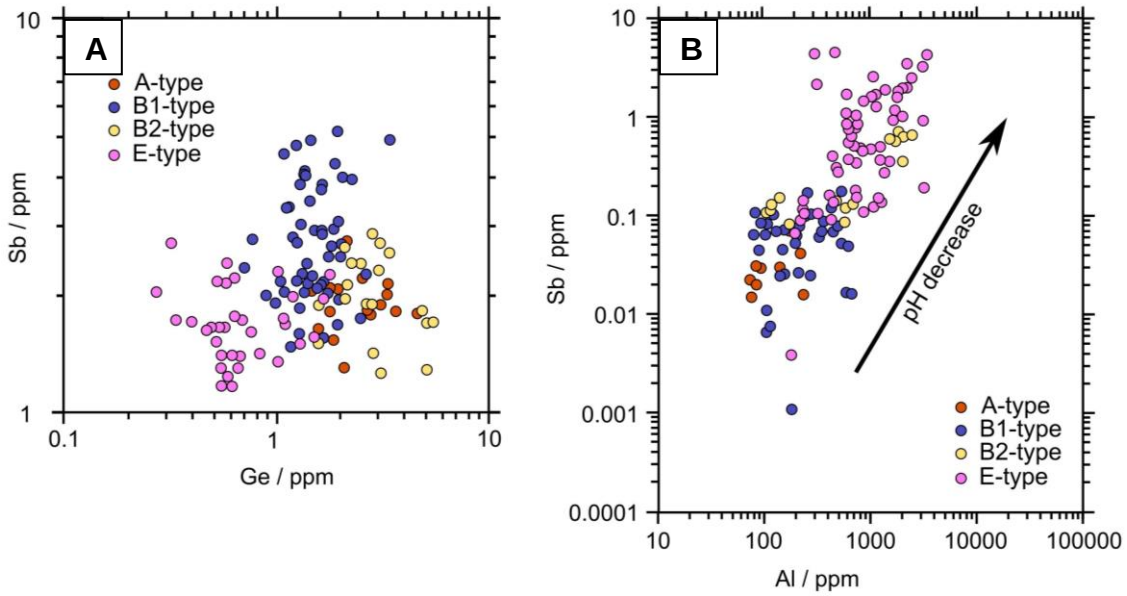

Figure 73: A. Sb vs. Ge quartz content. B. Sb vs. Al quartz contents.

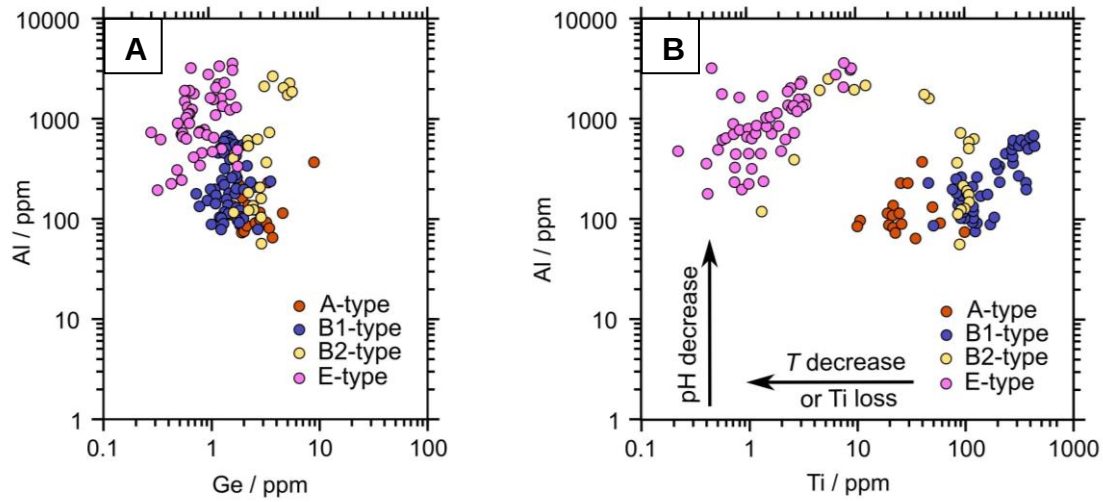

Figure 74: A. Al vs. Ge quartz content. B. Al vs. Ti quartz content.

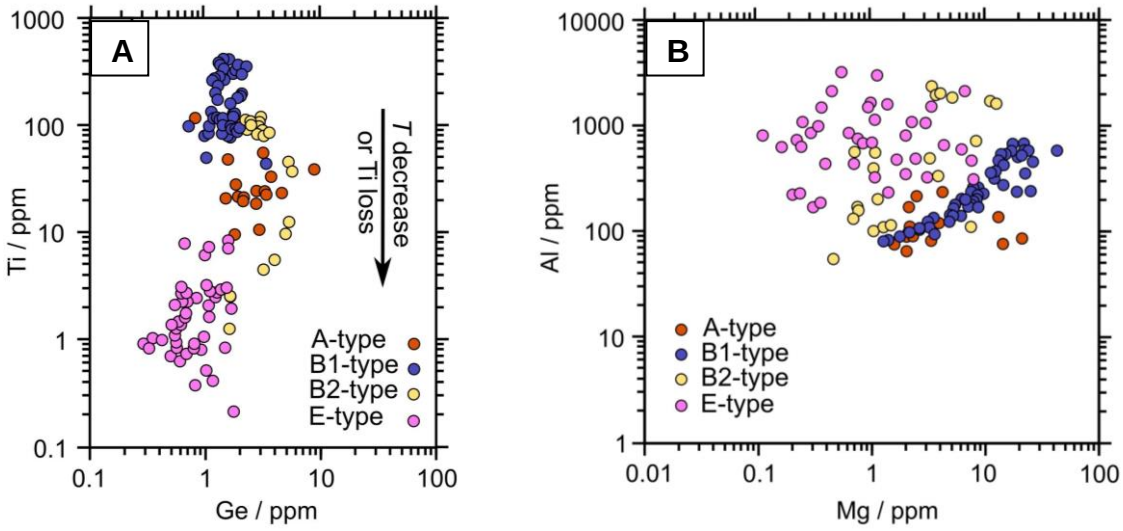

Figure 75: A. Ti vs. Ge quartz content. B. Al vs. Mg quartz content.

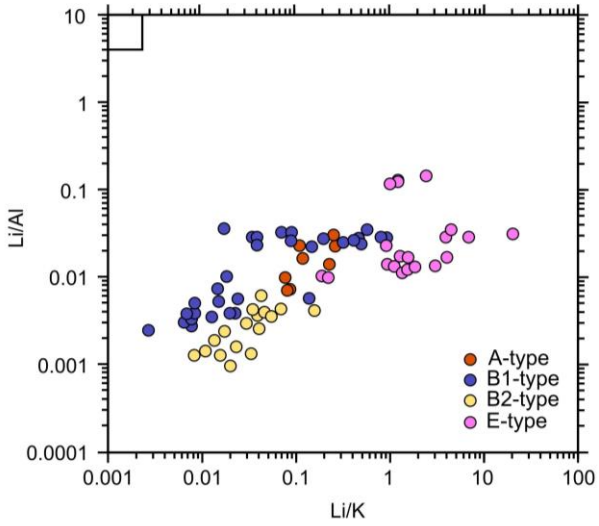

Figure 76: Li/Al vs. Li/K diagram

4.4.1.3. Trace element proportion per valence (absolute value)

In the compilation of the trace element content in all types of vein Na counts for 42 ± 23 % of the sum of the monovalent cations, while Li represents 13 ± 35 %. The large dispersion of Li data is mainly due to the low Li content in porphyry type quartz and its higher content in epithermal quartz.

Potassium contributes to 42 ± 24 % of the total, while Rb, Cu, and Cs contribute less than 1 %. Consequently, when correlations are observed between monovalent cations and other elements, they are predominantly related to the Ti, Na, and K content, which are the most abundant measured monovalent cations. Although correlations between the sum of elements and other valence cations groups indicate monovalent cations substitution behavior, they do not reflect specific chemical variations between individual elements. It is therefore important to examine how each element varies individually.

For divalent cations, Mg accounts for 57 ± 27 % of the total, while Mn contributes 16 ± 14 %. Cobalt, Ba, Sr, and Pb each account for less than 12 %. Thus, when correlations are observed, they are primarily associated with variations in Mg or Mn. Given the limited variation in Mn within the system, any correlations or possible variations observed among divalent cations are mainly linked to Mg.

Aluminum accounts for approximately 90 ± 14 % of the total trivalent cations (Al + Fe + Ga + Sb) in quartz crystals. Therefore, the strongest correlations observed between this group of cations and other valence groups are primarily associated with the high aluminum content relative to other elements in its category. While a similar analysis could be performed using the three other trivalent elements, Fe shows little variation across the vein sequence. Only Sb and Al could therefore be used, but separately due to the concentration scale difference, to identify any meaningful trends. However, as these two elements are positively correlated, the outcome would be effectively the same.

For tetravalent cations, Ti accounts for approximately 87 ± 17 % of the total. Thus, when variations or correlations are observed within the vein sequence, they are primarily driven by variations in Ti, as Ge has only a minimal impact.

4.4.2. Chemical evolution of quartz porphyry-epithermal system

4.4.2.1. Trace Element Evolution in Hydrothermal Quartz from Porphyry and Epithermal Veins

Quartz from porphyry and epithermal veins exhibits trace element compositions that reflect the evolution of hydrothermal fluids over time (Monecke et al., 2018; Rottier and Casanova, 2021). The CL intensity variations observed in hydrothermal quartz are attributed to compositional differences, which indicate the incorporation of trace elements, where Ti is generally considered the main CL activator (Landtwing and Pettke, 2005; Jourdan et al., 2009b; Lehmann et al., 2011; Rusk et al., 2011; Rusk, 2012).

The incorporation of trace elements into quartz is influenced by various physical (pressure, temperature) and chemical parameters (pH, Eh, fluid composition), as well as the crystal growth rate

(Rottier and Casanova, 2020). At smaller scales, minor fluctuations in pressure, temperature, and growth rates can locally alter trace element incorporation (e.g. Raimbourg et al., 2022). At larger scales, successive quartz formation events under distinct physical and chemical conditions result in trace element variation between veins (e.g. Rottier and Casanova, 2021). A combination of these factors likely explains the observed compositional variations. However, the interpretation of data is constrained by the spot size of LA-ICP-MS measurements, which often exceed the thickness of quartz CL growth bands (e.g. Landtwing and Pettke, 2005; Jourdan et al., 2009b; Lehmann et al., 2011; Rusk et al., 2011; Rusk, 2012).

Rapid crystal growth rates tend to incorporate higher concentrations of impurities than slow growth rates (Ihringer and Zink, 2000; Cernushi et al., 2018; Huang and Audétat, 2012). In dynamic hydrothermal systems, quartz precipitation rates are influenced by factors such as pressure fluctuations (Raimbourg et al., 2022). Precipitation rates are, in turn, related to quartz solubility gradients, driven by temperature and pressure changes (Rimstidt and Barnes, 1980; Helgeson et al., 1978). For instance, quartz overgrowths with high Al concentrations, such as B2-type quartz (Figure 68), likely form during fluid mixing events influenced by changes in temperature, pH, or pressure. The Ti and Al signatures in B2-type quartz margins resemble those of E1-type quartz, suggesting fluid evolution (Figure 74 B).

Titanium, Sb, Ge, Al, Li, Na, and Cs exhibit systematic variations among different quartz types in porphyry systems (Figure 71). These variations are influenced by pressure, temperature, pH, fluid composition, and growth rates during quartz formation. However, isolating the influence of individual parameters remains challenging.

4.4.2.2. Fluid composition evolution

E2-type quartz veins exhibit significant variations in monovalent cation and Al contents (Figure 69, Figure 70), similar to those observed in the margins of B2-type quartz veins. Such observations have been previously reported by numerous authors (Allan and Yardley, 2007; Jourdan et al., 2009; Tanner et al., 2013). The correlation between Li and Al in most quartz samples can be explained by the tetrahedral substitution of $[SiO4]^{0}$ sites by $[AlO4]^{-}$, with charge compensation provided by monovalent cations in neighboring interstitial sites (Götze et al., 2001; Landtwing and Pettke, 2005; Heaney, 1994; Weil, 1984; Jourdan et al., 2009; Rusk, 2012). Due to its small ionic radius, Li^{+} is expected to cause less lattice distortion compared to larger monovalent cations (Na, K, Rb, and Cs). At PAgoni Rachi, during the evolution of quartz from A- to E1-type veins, as Al content increases, the overall content of monovalent elements also increases (Figure 59). However, a decoupling is evident: (i) From A- to B2-type quartz, Li decreases while K, Na, and Cs contents increase slightly (Figure 57), (ii) From B2- to E1-type quartz, Li increases while K, Na, and Cs contents decrease slightly (Figure 57). Li content is negatively correlated with other monovalent cations (Na, K, Rb, Cs). Its concentration decreases as the others increase, and vice versa, particularly during the transition from A- to B2-type veins. Interestingly,

Li content is high in E1-type veins, while Na, K, Rb, and Cs concentrations are low, coinciding with high Al content. This pattern may be consistent with changes in the fluid composition.

A negative correlation exists between quartz precipitation temperatures and Li, Al, Sb concentrations, with E1-type quartz forming from Li-Al-Sb-enriched fluids compared to porphyry brines or intermediate-density fluids (Kouzmanov and Pokrovski, 2012; Rottier et al., 2018b). This suggests that Li, Al, Sb concentrations in quartz reflect those in the hydrothermal fluid. Similarly, Ge concentrations increase with decreasing temperature, indicating temperature-dependent incorporation. The Ge/Ti ratio also correlates strongly with precipitation temperature.

4.4.2.3. Pressure, Temperature and pH variations

Aluminum concentrations in quartz exhibit significant variability across different quartz types. Although the relationship between aluminum content and temperature remains ambiguous, studies indicate a negative correlation between aluminum concentration and the apparent pH of mineralizing fluids (Allan and Yardley, 2007; Rusk et al., 2008; Müller et al., 2018). This is corroborated by the observed pH decrease from stages A, B1, B2, to E1, as inferred from alteration assemblages and spatial distribution. These patterns are consistent with a telescoping system (Voudouris et al., 2013a; Mavrogonatos et al., 2019, 2020), transitioning from feldspar-stable (potassic) to feldspar-destructive alteration (sericitic, argillic, chlorite-sericite) (see Telescoping evidence). The increase in aluminum concentration may then reflect the cooling and pH decrease of hydrothermal fluids over time (Sillitoe, 2010). Previous studies have interpreted this evolution because of variations in the aluminum concentrations of the hydrothermal fluids (Perny et al., 1992; Allan and Yardley, 2007; Rusk et al., 2008a; Jourdan et al., 2009; Lehmann et al., 2011; Rusk, 2012). While processes such as the infiltration of external aluminum-rich fluids, pH changes (Perny et al., 1992; Rusk et al., 2008; Müller et al., 2010), pressure fluctuations, and quartz growth rate (Allan and Yardley, 2007; Huang and Audétat, 2012) can theoretically increase the aluminum concentration in quartz, they fail to account for the observed two orders of magnitude increase in aluminum content from A- to E1-type veins. The pressure range of 10 – 650 bars within the porphyry-epithermal system at Pagoni Rachi (Voudouris et al., 2013a; this study) is considered too narrow to exert a significant influence on Al concentrations in quartz (Huang and Audétat, 2012). Similarly, rapid crystal growth may lead to the incorporation of impurities in quartz, yet experimental data suggest that Li/Al ratios are not governed by growth rates (Allan and Yardley, 2007; Huang and Audétat, 2012). An alternative mechanism is required to explain the observed two to three orders of magnitude enrichment in aluminum within quartz. It is proposed that the most likely factor driving systematic changes in trace elements in quartz is the increase in the partition coefficient of trace elements between fluid and quartz as temperature decreases, despite the lack of available partition coefficient data (e.g. Rottier et al., 2021).

Titanium concentrations in quartz decrease with precipitation temperature (Figure 74, Figure 75), consistent with studies showing a general decline in Ti during hydrothermal fluid cooling (Mercer and

Reed, 2013; Maydagan et al., 2015; Mao et al., 2017; Rottier et al., 2018a), from A-type veins (*T* ~ 500 °C), to B1-type veins (*T* = ~ 400 °C), to *B2-type veins (T = ~ 300 °C from Muntean and Einaudi, 2000)* and finally to E1-type veins (*T* = < 250 °C) (from Voudouris et al. 2013a and this study see Fluid inclusion petrography and microthermometry). Experimental data confirm the sensitivity of Ti^{4+} incorporation to temperature variations (Wark and Watson, 2006; Thomas et al., 2010; Huang and Audétat, 2012). Consequently, the Ti-in-quartz geothermometer is widely applied to estimate diagenetic and metallogenic temperatures (Lehmann et al., 2009; Huang and Audétat, 2012; Zhang et al. 2020; Rottier and Casanova, 2021). This is evidence in Pagoni Rachi with a clear Ti content decrease from B1- to E1 type veins from 1 to 2 orders of magnitude (Figure 61). A possible decrease in temperature may have happened between the central B2-type quartz and B2-type quartz margins, with a clear decrease from 1 order of magnitude. However, A-type veins display low Ti content which is consistent with low CL imaging and may be due to a Ti loss by diffusion during quartz recrystallization (following section and see chapter 3). For B2-type vein quartz, it is likely that titanium (Ti) content is primarily associated with temperature and remains in equilibrium (or only out of equilibrium crystallization occurred). Indeed, the CL-textures of B2-type quartz are linked to low deformation-related microtextures to fractures. Ti content appears to be predominantly controlled by the decrease in crystallization temperature, as observed from the central part of the vein to the overgrown quartz crystals, this is associated with a clear reduction in CL intensity. This decrease in CL intensity is characteristic of a corresponding decline in Ti content. However, when using Ti as a tracer, its concentration in quartz is not solely dependent on crystallization temperature. Two additional factors can influence Ti incorporation: (i) quartz growth rates, which can lead to excess Ti incorporation, and (ii) quartz deformation, which can induce disequilibrium and reduce Ti concentration through diffusion. Ti can serve as an effective tracer of geological events, but its use requires careful association with observations of microtextures and CL textures in the analyzed quartz crystals.

Trace element data provide initial insights into the qualitative physico-chemical evolution of vein formation. Specifically, Sb and Al are primarily pH-dependent and are associated with a decrease in system pH, generally observed from A- to E1-type veins. In contrast, Ti is largely controlled by temperature and decreases as the system temperature decreases, following the same A- to E1-type vein progression (the differences between successive vein types are further discussed in the following sections and in Chapter 3). The variations in monovalent cations, whose total concentrations are closely linked to changes in Al and Sb, and thus to pH variations, further suggest a change of fluid composition, particularly between B2- and E1-type veins (Figure 73).

The trace element composition of quartz provides critical insights into the evolution of hydrothermal fluids in porphyry and epithermal systems. Temperature and pH fluctuations play dominant roles in trace element incorporation, while dynamic factors like precipitation rates also contribute. While caution is necessary in interpreting trace element data due to measurement limitations and disequilibrium effects,

the trends observed highlight quartz as a valuable proxy for reconstructing fluid conditions during mineralization.

4.4.3. Chemical diffusion during heating or deformation.

- This part completes the discussion of Abiven et al. submitted Chapter 3 -

The heterogeneous trace element signal in A-type veins, for which no correlation between elements could be demonstrated, is possibly due to the presence of microtextural evidence in quartz indicative of high-temperature deformation conditions, with GBM mechanism observed throughout the veins (see Ductile to brittle deformation at Pagoni Rachi). In contrast, in quartz from other vein types, clear correlations have been observed along transects, with co-variations of trace elements. These quartz crystals do not exhibit microtextures indicative of potential trace element disequilibrium, either in their dominant microtextural domains or their CL-textures. Generally, these quartz textures indicate the absence of deformation and are interpreted as primary.

Abiven et al. (*submitted – Chapter 3*) discussed the potential diffusion of elements like Al and Ge, Ti during recrystallization processes and demonstrated that, in their case, only Ti could have diffused under conditions of intense dynamic recrystallization driven by GBM. They also showed that such diffusion did not occur under SGR or BLG recrystallization mechanisms. It is therefore unlikely that significant trace element diffusion occurred in quartz from B1-, B2-, and E1-type veins. Nevertheless, a detailed analysis of all microtextural domains in these quartz crystals would be necessary to further support this hypothesis. Additionally, since quantitative trace element data for A-type veins are incomplete, it is difficult to deduce any spatial relationship between deformation domains and potential decreases in trace element content (*see Chapter 3*).

Rottier et al. (2017) suggest that the diffusion of many monovalent cations, including Cu^+, Li^+, Na^+, Ag^+, and possibly K^+ and the trivalent cation B^{3+} may happen by heating. They record a modification of K concentration demonstrated that diffusing Cu, Li, Na, and B could be accommodated by or be removed from the quartz structure during heating experiments (Rottier et al., 2017).

Trace element disequilibrium and post-crystallization processes (element incorporation) can significantly alter the geochemical signature, potentially leading to misinterpretations of fluid evolution in terms of temperature, pressure, pH, and elemental content associated with quartz deposition and the mineralization stage. Therefore, careful attention must be paid to microtextures, CL-imaging should be conducted prior to any chemical interpretation.

4.4.4. Ti-in-quartz thermometry

- This part completes the discussion of Abiven et al. submitted Chapter 3 -

The occurrence of rutile and titanite inclusions associated with the hydrothermal quartz and the host rocks (Voudouris et al., 2013a) suggests a TiO_2 activity of ~ 1. This allows the estimation of quartz

formation temperatures by Ti-in-quartz thermometry (Zhang et al., 2020). The extrema of Ti concentrations provided by our quantitative analyses of trace elements in quartz of both vein types are used for the Ti-in-quartz calculation with $[Ti]B2_{center}$ = [1.3–13.3] ppm and $[Ti]B2_{margin}$ = [38.6–123] ppm. For the B2-type veins, the extreme pressures (range 10 – 150 bars) are given by the fluid inclusions (Muntean and Einaudi, 2000). Then, the Ti-in-quartz geothermometer gives the following calculated temperatures (*T*[Ti]) for B2-type veins: $T[Ti]B2_{center}$ = 423 – 573 °C, $T[Ti]B2_{margin}$ = 226 – 386 °C Figure 77). This results in a decrease in the calculated precipitation temperature of quartz formation from the center to the margin of the B2-type veins, which agrees with the higher Ti contents in quartz in the center than in the margin of the B2-type veins.

Using the formula of Zhang et al. (2020), we can recalculate the expected quartz concentration based on the *PT* data of the fluid inclusions from the B2-types of veins (Muntean and Einaudi, 2000) if applied to the B2-type veins of Pagoni Rachi. The maximum and minimum *PT* values are used to obtain [Ti] ranges for each type of quartz veins. As such, we obtain the following ranges: [Ti]A = [3.8–13.1] ppm. The expected [Ti]B2 values are lower and do not overlap with the range of values $[Ti]B2_{center}$. In contrast, the expected concentrations are within the range than those of the $[Ti]B2_{margin}$ population.

Low temperatures associated with quartz overgrowths at grain boundaries are consistent with a low incorporation of Ti during quartz crystal formation (Figure 68), resulting in low Ti concentrations. This is also consistent with a weak CL signal – which is not linked to any deformation or dynamic recrystallisation texture of quartz –, as Ti is considered the main activator of CL in quartz. A precise description of fluid inclusions in these veins should help characterize this quartz sequence (cf. Chapter 5 on isotopes).

However, the difference between the theoretical and measured concentrations of titanium is significantly close to an order of magnitude which leads to a notable discrepancy between the calculated and theoretical temperatures for the B2-type veins. Several hypotheses can be considered to explain these differences: (i) Ti-in-excess during quartz crystal formation, made possible by rapid quartz growth. However, unlike B1-type veins (Chapitre 3.), B2-type veins do not exhibit rapid quartz growth structures that would allow for such over-incorporation. Nevertheless, it should be noted that the proposed formation process for these veins is associated with a flashing phenomenon, during which the stockwork forms following a rapid pressure drop and cooling. It is possible that the quartz was formed from a silica gel capable of incorporating significant amounts of Ti. (ii) The pressure-temperature data used (Muntean and Einaudi, 2000) may not correspond to the actual conditions of B2-type veins at Pagoni Rachi. Indeed, other authors (Monecke et al., 2018; Rottier et al., 2016; Rottier and Casanova, 2021) have proposed that these structures formed at higher temperatures, around 600 °C, which are hotter than the A- and B1-type veins at Pagoni Rachi. While this might align with the temperatures indicated by Ti-in-quartz (albeit at the maximum values), it seems unlikely that this model aligns with the deformation succession model presented in Chapter 2. In this case, how can we explain that A-type and B1-type veins exhibit deformation textures associated with higher temperatures than those of the B2-type veins,

despite the latter being supposedly hotter than the former? A study of fluid inclusions in these B2-type veins is evidently required, particularly in light of the CL texture differences and quartz overgrowths, to determine better *PT* conditions of quartz formation.

None of the calibrations provide a perfect match with the reported temperatures, which can be explained by (1) the inaccuracy of the reported temperatures and pressures, (2) an actual Ti activity of the mineralizing fluid lower than 1, (3) quartz disequilibrium precipitation, and (4) by the inaccuracy of the different Ti-in-Quartz calibrations for hydrothermal quartz (Acosta et al., 2020).

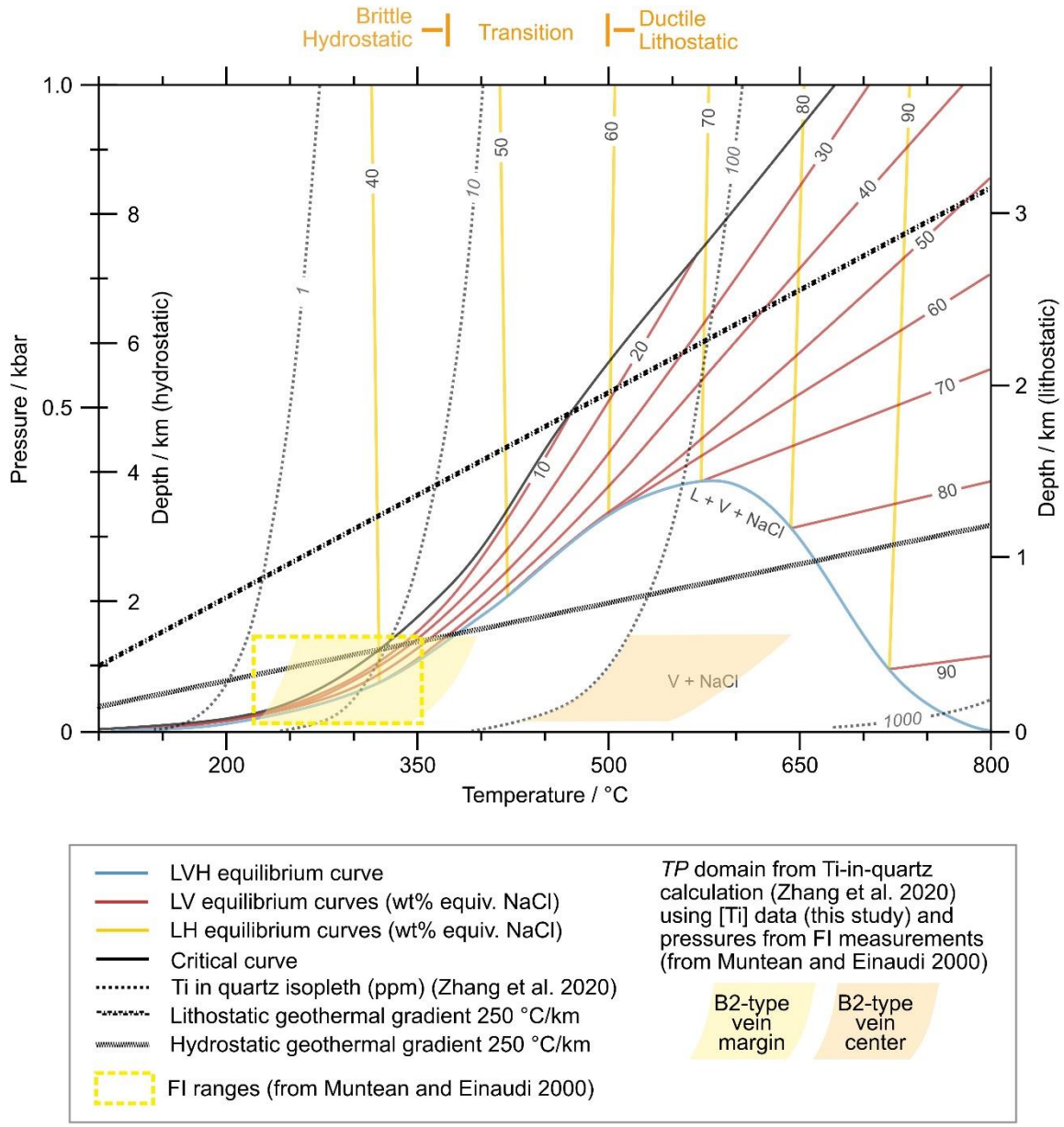

Figure 77: PT diagram showing fluid inclusion data (from Muntean and Einaudi 2000 on banded veins from Maricunga Belt like B2-type veins of this study) and PT[Ti] domains obtained with the Titan-in-quartz geothermometer of the B2-type veins. LVH, LV, LH and critical curve are from Bodnar (1993, 1995), Ti isopleths are coming from Ti-in-quartz calculation (Zhang et al. 2020)

4.4.5. Trace elements: implications for ore genesis discrimination

- This part completes the discussion of Abiven et al. submitted Chapter 3 -

It is commonly admitted (e.g. Rottier and Casanova, 2021; Dong et al., 2022) that quartz from different types of deposits can be distinguished by their trace element signature and that the information can be used as a tracer for different modes of ore genesis, which is a useful tool for prospecting and exploration of different types of ore deposits.

Vein quartz from Pagoni Rachi shows Li/Al ratios < 0.05 (Figure 78. The independence of the Li/Al ratio from quartz precipitation temperature contrasts with Hurst and Storch's (1981) observation that the ratio of impurities decreases with increasing formation temperature. The low average Li/Al ratio across the Pagoni Rachi samples may relate to the availability of Li^+ in the hydrothermal fluid relative to other charge-balancing impurities such as H^+, Na^+, and K^+. Changes in the proportions of these elements may influence interpretations of the genesis process. The trace element data from Pagoni Rachi fits well with porphyry Cu-related Pb-Zn-Ag veins (Figure 78). Some B1- and B2-type veins align well with the expected Li/Al ratios, while E1-type veins fall at the extreme end of the range, closer to Sn-related Pb-Zn veins (Figure 78). This may be linked to an evolution in the oxidation state of the fluid, transitioning between Cu and Sn endmembers. Additionally, the vein succession at Pagoni Rachi may demonstrate an evolution from more reduced to more oxidizing conditions. This is consistent with the previously observed changes in fluid composition between the B2- and E1-type veins.

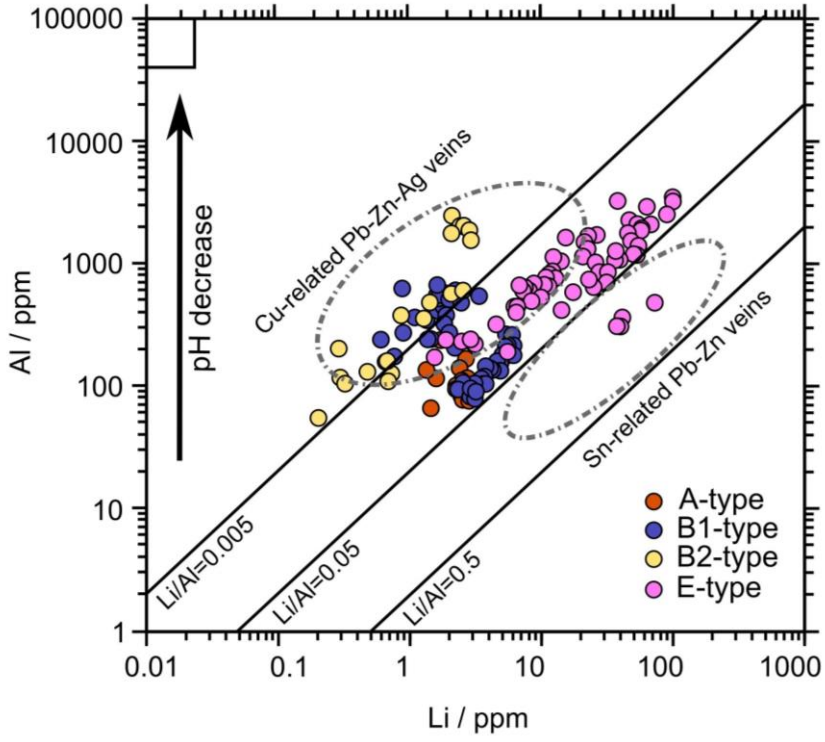

Figure 78: Al vs. Li diagram with Pagoni Rachi reported data, with reported Li/Al ratios; and Cu-related Pb-Zn-Ag veins domain ar from Cerro de Pasco, Peru (Rottier et al. 2016, Rottier and Casanova, 2021), and Sn-related Pb-Zn veins from are from Heemskirk, Australia (Hong et al. 2016), from Gao et al., 2022.

It is also common to distinguish different vein types in porphyry-epithermal systems based on distinct Al/Ti v. Ge/Ti ratios in quartz (e.g. Schrön et al., 1988; Götze, 2012; Rottier and Casanova, 2021; Falkenberg et al., 2024), which, however, can be disturbed by dynamic recrystallization and rapid crystal growth (Nachlas et al., 2015; Cernuschi et al., 2018) or changing in fluid composition or precipitation physic-chemical conditions (. For instance, the quartz data from Pagoni Rachi of the A-type veins fall within the range of other B-type veins from the literature, while our data from the B1-type veins overlaps with data from the A-type veins data from the literature (Figure 79). Quartz data from B2-type veins are within both A-type veins and partially B1-type veins. This suggests that particular attention should be paid to the concentration variations of the different involved elements. Germanium appears to be relatively stable within the veins sequence (1 to 3 ppm) and does not show any evidence of post-crystallization reequilibrium. Therefore, Ti appears to be the main factor for the anomalous features for the A- and B1-type veins, being impacted during dynamic recrystallization and its incorporation sensitive to the crystallization rate. This again indicates that the Ti contents in these quartz types from Pagoni Rachi do not reflect the actual precipitation conditions at equilibrium but rather the history of deformation and recrystallization and out-of-equilibrium crystallization processes.

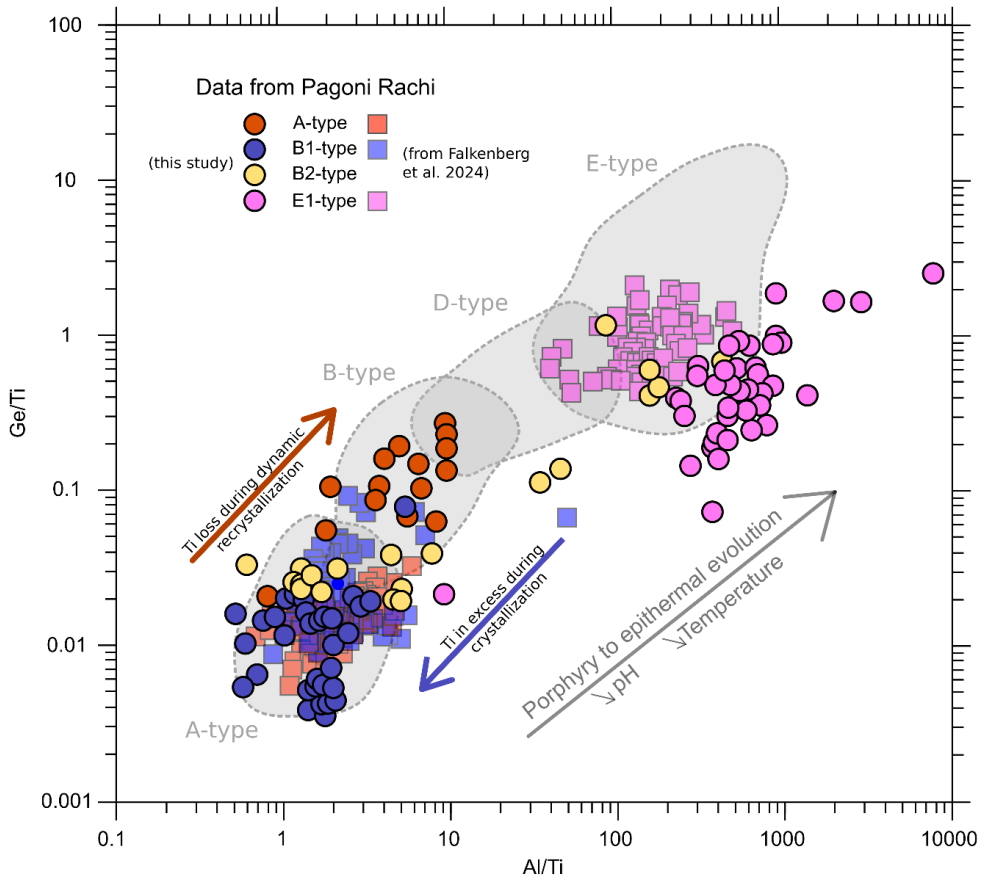

Figure 79: Ge/Ti vs Al/Ti (mass ratios) diagram based on LA-ICP-MS analyses of quartz of A-type (red), B1-type veins (blue), B2-type (yellow) and E1-type veins (pink). Compilation of data from the literature is shown by the grey shaded aeras (from Casanova and Rottier, 2020), and by the shaded colored squares for similar vein in Maronia porphyry system (from Falkenberg et al., 2024).

For B2-type veins, it is initially reasonable to assume that the formation conditions of B2-type veins are like those of A-type veins, as they belong to the same associated categories. However, although the elemental ratios of A-type and B1-type quartz from Pagoni Rachi exhibit anomalies (see next chapter), the B2-type vein quartz still falls within the A-type category for the central part of the vein (Figure 79).

This results in unexpectedly high Ge/Ti and Al/Ti ratios in quartz margins. Although the Ge/Ti ratio is presented as Ti-dependent and, by extension, temperature-dependent, the Al/Ti ratio also increases, not only due to a decrease in Ti concentration but also due to an increase in Al content.

Therefore, this suggests that specific attention must be paid to the petrographic textures and trace element compositions of quartz to interpret such geochemical classification of hydrothermal quartz veins from porphyry-epithermal systems. In other words, the Al/Ti vs Ge/Ti based typology of Rottier and Casanova (2021) may be valid only for quartz veins formed under equilibrium conditions and preserved from dynamic recrystallization.

Quartz shows different distribution characteristics in the Al/Ti and Li/Al diagrams due to the fluctuations of temperature, pressure and pH of the fluid during its precipitation. Therefore, it has been proposed that these compiled trace elements data can be potentially used to distinguish different modes of ore genesis.

4.5. CONCLUSION

For Pagoni Rachi, a trend is evident from the center of the system, showing an evolution in trace element concentrations in quartz along the vein sequence. This progression corresponds to a decrease in temperature, pressure, pH, and changes in fluid composition, with a general decline in Ti (except during disequilibrium crystallization), an increase in Al, Sb, and Li, and a decrease in monovalent cations in favor of Li, as well as a reduction in Mg. Elemental fractionation appears to occur in the more oxidizing parts at the onset of the system.

The analysis of trace elements in quartz from various veins within the Pagoni Rachi porphyry-epithermal system highlights chemical composition changes in quartz during successive stages of formation. These elemental variations, whether within a single vein or across different veins, reveal that the variations in certain elements are tied to changes in the physicochemical conditions of quartz formation. Specifically, Al, Sb, and monovalent cations appear to be associated with a decrease in pH and possibly temperature.

From the hot A-type veins (~500 °C), characterized by a potassic feldspar-bearing assemblage, to the cooler E1-type veins (~250 °C), with assemblages dominated by sericite or even kaolinite, there is a shift in fluid composition. This is particularly evident in veins transitioning from type B2- to E1-type, marked by an increase in Li content and a decline in other monovalent cations (Na, K, Rb, Cs). Additionally, there is a change in CL-textures of B2-type veins, which exhibit a central chemical signature like porphyry-type veins and overgrowth rims with a chemical signature similar to E1-type veins signature.

Finally, there is a clear decrease in temperature, as indicated by a reduction in Ti concentrations from B1- to E1-type veins. However, crystallization and deformation processes can alter or modify the expected Ti signature in quartz, leading to potential misinterpretation of the geochemical signatures of quartz in different veins of a porphyry-epithermal system. Therefore, careful attention must be paid to the petrographic texture of quartz and CL imaging. This study highlights the importance of considering these deformation histories when interpreting geochemical signatures, as processes like GBM and SGR can significantly alter the Ti content and other trace elements in quartz, and out-of-equilibrium crystallization due to fast crystal growth which can imply an excess of Ti, leading to potential misinterpretations if not properly accounted for. This study highlights the importance of deformation on the geochemical signature and emphasizes all the processes that must be considered to avoid errors in interpretation.

In this context, it is (i) first important to observe the variations and potential relationships between the different cation groups, each having their own substitution mechanism; then (ii) to consider the major elements that could independently impact these variations, and explore whether preferential substitutions occur between elements of the same valence; (iii) to observe their respective evolution/variation as a function of elements of different valence; and (iv) to correlate this with the

microstructural and petrographic relationships of the different quartz types across the various veins, after which variations can be interpreted as resulting from changes in physicochemical conditions during quartz and vein crystallization, and post-crystallization processes that could destabilize the systems.

At present, trace elements in quartz do not directly allow for the clear identification of the physicochemical parameters that may vary and modify the trace element content of quartz during crystallization, particularly in porphyry-epithermal systems. Structural element clues can help evaluate which of these parameters are involved in the incorporation of elements into quartz: (i) growth rate—slow/fast—associated with a preferential orientation of the quartz C-axis, sometimes with dynamic recrystallization textures at grain boundaries due to competitive growth between grains (Acosta et al., 2022), which is linked to excess Ti; (ii) fluid pressure fluctuations, which are responsible for the contrasting CL colors and variations in Al concentration (low pressure induces low Al content); (iii) crystallization temperatures, as indicated by the decrease in Al, Ti, Ge, and the equilibrium texture of quartz, without re-equilibration and without excess elements; (iv) pH—evaluating the evolution of fluid pH by observing alteration types and their progression, particularly in porphyry-epithermal systems, which can shift from potassic to advanced argillic alteration.

Thus, it is likely that one or more of these factors fluctuate during fluid circulation, leading to the crystallization of quartz. This is in addition to the variation in the chemical composition of the fluid itself, which affects fluid-rock fractionation and stability conditions, as well as equilibrium.

Furthermore, rare earth elements (REE), though present in low concentrations, can signal variations in redox conditions and fluid mixing. REE fractionation patterns, particularly europium (Eu) anomalies, can indicate transitions between oxidizing and reducing environments, a crucial factor in the precipitation of many metals (data from Monecke et al., 2000, 2002; Götze et al., 2004, 2016, 2017)

In addition to these elements, stable isotopes and fluid micro-inclusions trapped in quartz provide complementary data. For example, oxygen isotope ratios ($\delta^{18}O$) in quartz, when combined with trace element data, offer critical information on the origin of the fluids (magmatic, meteoric, or mixed)

and their interactions with host rocks (e.g. Rottier et al., 2020). Fluid inclusion analyses enable direct determination of fluid salinity, homogenization temperature, and composition—essential parameters for reconstructing the fluid history in hydrothermal systems (Roedder, 1984).

Understanding porphyry-epithermal systems requires an integrative approach, combining elemental and isotopic data obtained from quartz with thermodynamic and geochemical modeling. Previous research has identified correlations between thermal gradients, pH variations, and metal precipitation in hydrothermal systems (Cooke et al., 2014). Nevertheless, several questions remain unresolved, particularly regarding the mechanisms of fluid mixing, chemical re-equilibration, and the selective transport of metallic elements.

CHAPITRE 5. ORIGIN AND TRACKING OF FLUID USING STABLE ISOTOPES OF OXYGEN, CARBON AND HYDROGEN

5.1. INTRODUCTION

In porphyry-epithermal hydrothermal systems, fluids circulating through fractures and veins transport metals that concentrate to form ore deposits. These fluids, often derived from a combination of magmatic, meteoric, and sometimes metamorphic sources, undergo complex interactions with host rocks and with each other, altering their physicochemical properties (temperature, pH, salinity, redox) and triggering metal precipitation. The study of stable isotopes of hydrogen (δD), oxygen ($\delta^{18}O$), and carbon ($\delta^{13}C$) in gangue minerals such as quartz and calcite is a key method for tracing these fluids and reconstructing their evolution. These isotopes allow identification of fluid sources, mixing mechanisms, and physicochemical processes controlling mineralization.

Oxygen isotopes are among the most widely used to trace hydrothermal fluids because oxygen is a major constituent of water and minerals such as quartz (SiO_2) and calcite ($CaCO_3$). The oxygen isotopic composition of a mineral ($\delta^{18}O$) reflects the isotopic equilibrium between the fluid and the mineral at the time of crystallization, which depends primarily on the temperature and isotopic composition of the fluid (e.g., Zheng, 1999; Rottier et al., 2020). By combining $\delta^{18}O$ values measured in quartz and calcite with experimental calibrations of isotopic fractionation as a function of temperature (e.g., Clayton et al., 1972; Zheng, 1993), it is possible to estimate the $\delta^{18}O$ values of the fluid from which different mineral phases formed. Variations in $\delta^{18}O$ within a hydrothermal system can also reflect changes in fluid origin. For instance, magmatic fluids typically exhibit $\delta^{18}O$ values ranging from +5 to +10 ‰, whereas meteoric fluids have much lower values, often near –10 ‰ and sometimes as low as –30 ‰ (Craig, 1961; Hoefs et al., 2009). Mixing between these two fluid types in a porphyry-epithermal system results in progressive variations in $\delta^{18}O$ values measured in precipitated minerals. Additionally, interactions between hydrothermal fluids and host rocks can enrich or deplete the fluid in heavy isotopes, further modifying the isotopic signature of quartz or calcite.

Hydrogen, present in the water of hydrothermal fluids, also plays a crucial role in tracing fluid origins. δD values measured in fluid inclusions trapped within quartz directly reflect the isotopic composition of circulating fluids. Magmatic fluids, for example, typically exhibit δD values between –80 and –60 ‰, whereas meteoric fluids show much lower values, often below –100 ‰. Seawater, by contrast, has a δD value near 0 ‰. These differences enable the distinction of magmatic, meteoric, and seawater contributions in a hydrothermal system. The hydrogen isotopic signature can evolve due to several processes. Mixing between magmatic and meteoric fluids is a dominant factor, but evaporation or vapor condensation can also alter isotopic ratios. For instance, in high-temperature epithermal systems, a vapor phase enriched in light isotopes may separate from the fluid, leading to a relative increase in δD values in residual fluids and corresponding fluid inclusions (Giggenbach, 1992).

Carbon, present as CO_2, carbonates, or bicarbonate ions in hydrothermal fluids, is essential for tracing fluid-rock interactions. Stable carbon isotopes ($\delta^{13}C$) in calcite reflect not only the isotopic composition

of the hydrothermal fluid but also the physicochemical processes affecting the system. Magmatic fluids rich in CO_2 typically exhibit $\delta^{13}C$ values near –5 to –7 ‰, corresponding to a source linked to magma decarbonation (Taylor, 1979). In contrast, hydrothermal fluids circulating in carbonate-rich environments may have higher values, close to 0 ‰, due to the incorporation of carbon from dissolved carbonates (Hoefs et al., 2009). The carbon isotopic signature can evolve with changes in pH and temperature. For instance, a decrease in pH promotes calcite precipitation and isotopic fractionation favoring light isotopes, thereby enriching the fluid phase in heavy isotopes. Additionally, significant $\delta^{13}C$ variations can occur in environments with redox reactions, such as organic matter oxidation or CO_2 reduction.

By combining isotopic data for oxygen, hydrogen, and carbon, it is possible to reconstruct the fluid history in porphyry-epithermal systems. These approaches allow for: Identifying the sources of fluids (magmatic, meteoric, or metamorphic). Tracing fluid mixing and interactions with host rocks. Determining variations in physicochemical parameters (temperature, pH, redox) during fluid circulation. Linking these processes to metal precipitation conditions and the mechanisms controlling mineralization. This chapter explores the use of stable isotopes in gangue minerals from the Pagoni Rachi porphyry-epithermal system, highlighting their applications in tracing fluid pathways and understanding the evolution of hydrothermal conditions.

5.2. METHODOLOGY

5.2.1. Oxygen and carbon isotopes – Secondary Ion Mass Spectrometer

The stable isotopes of $\delta^{18}O$ and $\delta^{13}C$ were analyzed on the different generations of quartz and calcite. The in-situ isotopic analyses were carried out at the LG-SIMS platform (Large Geometry – Secondary Ions Mass Spectrometry) at the CRPG in April 2023, in collaboration with J. Villeneuve and N. Bouden of CRPG, using an IMS 1280-HR2 equipped with a high-resolution RF (radio frequency) Hyperion oxygen source.

A total of 199 in-situ SIMS $^{18}O/^{16}O$ analyses were performed on 7 thin sections from 6 samples that exhibit typical structures as described in the literature and representative of those found in the Pagoni Rachi porphyry-epithermal system, of A-, B1-, B2, E1- and E2-type veins. No suitable stage C or D quartz was found. Several spots were analyzed on each vein type: 69 on A-type veins, 88 on B1-type veins, 14 on B2-type veins, and 28 on E1-type veins. All values are normalized to V-SMOW. A total of 47 in-situ SIMS $^{18}O/^{17}O$ analyses were performed on 3 thin sections of calcite from E2-type veins from 3 samples. All values are normalized to V-SMOW. A total of 29 in-situ SIMS $^{13}C/^{12}C$ analyses were performed on 2 thin sections of calcite from E2-type veins from 2 samples: MB110201 and AB122.01. The analysis points were placed near the $^{18}O/^{16}O$ analysis spots on the same thin sections and within the same textural domains. All values are normalized to PDB. Analysis spots were placed along vein transects or in half-transects when veins exhibited central axial symmetry (especially B1 and B2-type veins). For E1-type veins, transects from the edge to the center of the quartz were carried out. Special attention was given to variations in texture of the quartz and calcite crystals (microtexture or CL zoning). The CL zoning are thinner than the analyzed areas, so there is a risk of analyzing multiple zoning in a single point; considerable effort was made to address this.

During the analysis, internal natural quartz standards (Brazil2) with a $\delta^{18}O = +19.62$ ‰ relative to V-SMOW and calcite standards (CCigA) with a $\delta^{18}O = +18.94$ ‰ and $\delta^{13}C = +1.04$ ‰ were used to monitor machine drift and correct for matrix effects. These standards were measured six times at the beginning and end of each day. Subsequently, an Instrumental Mass Fractionation (IMF) correction was applied to obtain the corrected $\Delta^{18}O$ values with a 2σ uncertainty. The measurement of carbon isotopes was carried out using a multi-collector, which involves significant drift over the course of the day; linear regression was used for correction. A primary Cs^+ ion beam of 1.8 nA for oxygen and 2.2 nA for carbon, accelerated to 20 kV, was focused onto a spot approximately 5x5 microns. For each analysis point, 40 cycles of 5 seconds per mass, preceded by a 15x15 micron presputtering for surface cleaning, were performed. For $\delta^{18}O_{quartz}$, the internal error is 0.06 ‰, the reproducibility is 0.21 ‰, and the reported analytical uncertainty is 0.43 ‰. For $\delta^{18}O_{calcite}$, the internal error is 0.07 ‰, the reproducibility is 0.21 ‰, and the reported analytical uncertainty is 0.45 ‰. For $\delta^{13}C_{calcite}$, the internal error is 0.25 ‰, the reproducibility is 0.48 ‰, and the reported analytical uncertainty is 1.08 ‰. The estimated $\delta^{18}O_{quartz}$ values were obtained using SIMS analyses performed on quartz that exhibits growth bands or minor Cl-

texture variations. When multiple analyses were available, a mean value was used. This approach relies on two key assumptions: (i) that the $\delta^{18}O_{quartz}$ values are representative of the quartz precipitated during fluid entrapment, and (ii) that $\delta^{18}O_{quartz}$ remains consistent along the same growth band.

5.2.2. Isotopic fractionation and fluid inclusions

Values of $\delta^{18}O$fluid and $\delta^{13}C$fluid were calculated from $\delta^{18}O_{quartz}$, $\delta^{18}O_{calcite}$, $\delta^{13}C_{calcite}$ assuming that isotopic equilibrium was maintained between quartz and fluid (H_2O) during quartz precipitation, and between calcite and fluid (H_2O and CO_2) during calcite precipitation. The quartz-water fractionation equations of Zheng (1993a) for oxygen isotopes considering T = [0; 1200] °C (1), the calcite-water fractionation equation of Zheng (1999) for oxygen isotopes considering T = [0; 1200] °C (2), the calcite-CO_2 fractionation equations of Zheng (1999) for oxygen isotopes considering T = [0; 1200] °C (3) and Golysh et al. (1981) for carbon isotopes considering T = [0; 1273] °C (4), are used to calculate the $\delta^{18}O_{H2O/CO2}$ and $\delta^{13}C_{CO2}$ at specific temperatures (T) :

$$1000ln\alpha = 4{,}48 \times (10^6 / T^2) - 4{,}77 \times (10^3 / T) + 1{,}71 \quad (1)$$

$$1000ln\alpha = 4{,}01 \times (10^6 / T^2) - 4{,}66 \times (10^3 / T) + 1{,}71 \quad (2)$$

$$1000ln\alpha = -1.71 \times (10^6 / T^2) + 10.01 \times (10^3 / T) - 3.45 \quad (3)$$

$$1000ln\alpha = 0{,}05855 \cdot (10^{18} / T^6) - 4{,}09568 \cdot (10^{12} / T^4) + 20{,}776421 \cdot (10^9 / T^3) - 35{,}8984 \cdot (10^6 / T^2) + 19{,}1975 \cdot (10^3 / T) + 0{,}2204 \quad (4)$$

5.2.3. Fluid inclusions data – *PTX* constraints

The $\delta^{18}O_{H2O}$ values were calculated using the extreme homogenization temperatures of fluid inclusions from each mineralization stage, as measured and discussed by Voudouris et al. (2013a) and Abiven et al. (submitted – see Chapitre 3.). The *PT* fluid inclusions data are summarized in Table 5. In the case of A- and B1-type veins, Abiven et al. (see Fluid inclusion petrography and microthermometry) showed that phase separation occurs during boiling, associated with continuous trapping during the crystallization and recrystallization of host quartz. Thus, the T_h values correspond to the fluid trapping temperatures and are assumed to represent the formation temperatures of quartz crystals. These temperatures will be used for calculations, with quartz formation temperatures for A-type veins ranging between 457 and 510 °C, and between 366 and 436 °C for B1-type veins. In shallow environments (< 1 km), the homogenization temperatures of fluid inclusions can be considered a good approximation of quartz crystallization temperature (i.e., trapping temperatures; Rottier et al., 2018a), as observed for E1- and E2-type veins. In these cases, the T_h values correspond to trapping temperatures and are assumed to represent the formation temperatures of both quartz and calcite. Therefore, the quartz formation temperatures for E1-type veins are between 219 and 334°C, and the calcite formation temperatures for E2-type veins range from 239 to 277°C.

No temperature data were produced for B2-type veins; however, we will use the temperatures reported by Muntean et al. (2000, 2001) from their study of a porphyry system in the Maricunga belt, Chile, which shows strong petrographic similarities in terms of vein structures, deposit environment (structural level in a porphyry system, alteration, etc.), quartz microtextures, and the petrography of fluid inclusions within quartz. This yields the following extreme formation temperatures for quartz (220–350°C) from B2-type veins.

Thus, the temperatures used will be the minimum and maximum homogenization temperatures, which are assumed to represent the trapping temperatures. These values will be used in this paper to evaluate and discuss the temperature variations in relation to the isotopic values of the fluids, all the used fluid inclusion data are in Table of analyses of fluid inclusion in A-type vein.Table of analyses of fluid inclusion in B1-type vein.Table of analyses of fluid inclusion in E1- and E2-type veins.

Table 5: PT trapping of fluid inclusions in quartz and calcite formation from the different vein type of the porphyry-epithermal system of Pagni Rachi – synthesis from Voudouris et al. 2013a and this study.

Vein type	$T_{trapping}$ (°C)		$P_{trapping}$ (bar)	
	Range	Mean ± 1σ	Range	Mean ± 1σ
A	457–510	486 ± 16	273–605	379 ± 110
B1	366–436	398 ± 17	190–357	255 ± 40
B2	220-350	/	10-150	/
E1	219–334	264 ± 35	22–134	55 ± 34
E2	239-277	260 ± 10	23-60	46 ± 7

5.2.4. Hydrogen isotopes

Fluids trapped in the hydrothermal quartz and calcite were extracted by crushing under vacuum (Rigaudier, 2010). The same samples as those analyzed by SIMS ($\delta^{18}O$, $\delta^{13}C$) were selected for data complementarity, allowing the combination of hydrogen data with oxygen data and providing better constraints on the tracing and evolution of fluids. These samples consist of quartz and calcite from the different veins forming the complete porphyry-epithermal system: A-, B1- (+C- to D- as it is inseparable), B2-, E1- and E2-ype veins. Two extraction series were carried out (August 21-28, 2023, and January 19-26, 2024). For this, the quartz veins (A, B1, B2, and E1) were mechanically reduced into grains of small size. The cutting of A-, B1-, B2-, E1- and E2-type veins to extract quartz and calcite was done using a diamond saw, cutting them into small fragments of less than one centimeter in diameter. The cutting was done to obtain approximately ten grams of quartz for each measurement. Special attention was paid to avoid the presence of contaminants (e.g., fragments of surrounding rock in contact with the vein walls, presence of mineral-bearing water (e.g., phyllosilicates), and quartz from other veins). The samples were then dried for 12 hours at 50 °C to remove residual H_2O.

In the case of veins of type E1, which consist of quartz in miarolitic space filled with calcite, slices were cut along the border of the vein walls and then reduced into small pieces (<1 cm), carefully removing as much of the surrounding rock and carbonates as possible (Figure 80). The fragments were then immersed in a hydrochloric acid bath (23 % – pH ≈ - 0.5) for 24 hours at room temperature under a fume hood to dissolve the calcite and keep only the quartz. The quartz fragments were subjected to several successive water baths with baking soda to neutralize the residual acid, and the remaining quartz was rinsed. They were then dried for 12 hours in a 50 °C oven. It should be noted that certain minerals associated with the quartz do not dissolve under such conditions (e.g., pyrite and galena). The fume hood is important because, unlike the previously mentioned sulfides, sphalerite dissolves to form volatile H_2S.

Then, for each sample, 4.0 to 13.7 g of quartz or calcite, were loaded into stainless steel tubes and degassed overnight under vacuum to release adsorbed water (down to $1.0.10^{-5}$ mbars. The tube and sample are crushed, and the liberated H_2O was collected in a liquid nitrogen cold trap at –170 °C. Non condensable volatiles (e.g., H_2, O_2, CH_4, and N_2) were evacuated. The separated H_2O was subsequently reduced to H_2 in a uranium reactor at 800 °C. The CO_2 was also trapped to trigger out its presence and its vol.% but no isotopic analyses were carried out on this material - CO_2 was separated from H_2O, using the liquid nitrogen trap was warmed up to –80 °C, it is then described in the sample as present or absent.

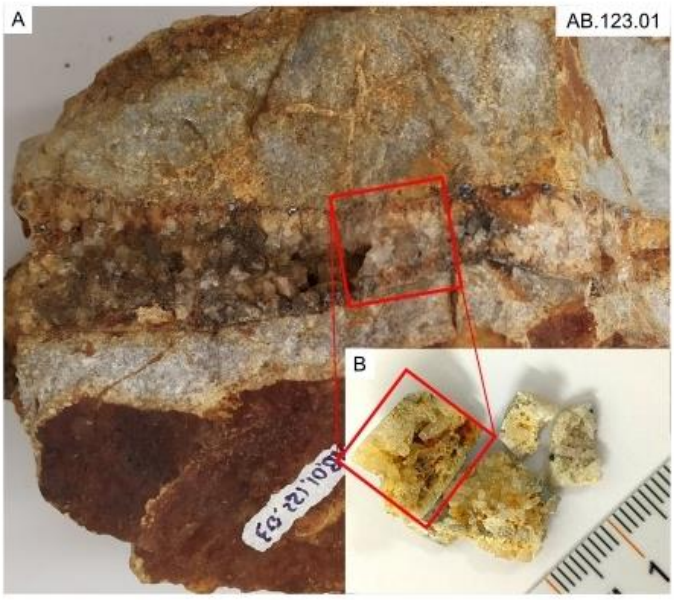

Figure 80 : Handspecimen of E1 quartz veins filled by E2 calcite veins, with location of B. Cut fragment of E1 type veins after acid leaching.

The D/H ratios were measured using a GV IsoPrime/ ThermoFisher MAT253 mass spectrometer at CRPG by T. Rigaudier (Vandoeuvre-lès-Nancy, France). Water standards were analyzed along with each weekly batch of water samples obtained from the fluid inclusions: THALASSA (0.0 ‰), IAEA OH-29 Tropical (+1.8 ‰), ED4 (-54.0 ‰) et IAEA OH-26 Vienna (-78.0 ‰). The reproducibility for the

standards was estimated to be lower than 2 ‰. To detect potential memory effect on the D/H ratios within the uranium reactor, the samples were duplicated to triplicated whenever possible. However, this effect was not detected, but slight variations in δD for some samples were recorded. Given that these variations probably reflect variations in the δD composition within the fluid inclusion population, the data displaying an amount of matter less than 30 µmol are discarded from the presented results due to possible bias caused by low content during analyses which tend to lower the measured isotopic value (Tarantola et al. – *internal communication*).

5.3. RESULTS

5.3.1. Oxygen in quartz and calcite veins and carbon in calcite veins

The oxygen isotope values of quartz ($\delta^{18}O_{quartz}$) in the A- and B-types veins show minimal variability, remaining close to a plateau near 10 ‰, whether within the grains, across the vein, or following the oscillatory growth zoning (Figure 81, Figure 82). The mean values are given with 1σ uncertainty. Quartz from A and B1-type veins display $\delta^{18}O_{quartz}(A) = 9.9 \pm 0.9$ ‰ (median = 9.9 ‰, n = 69) and $\delta^{18}O_{quartz}(B1) = 9.9 \pm 0.6$ ‰ (median = 9.9 ‰, n = 87). In contrast, the quartz from B2-type veins exhibit a correlation between $\delta^{18}O_{quartz}$ values and CL domains. The central, heterogeneous bright blue zones present $\delta^{18}O_{quartz}(B2)_{central} = 8.7 \pm 0.7$ ‰ (median = 8.6 ‰, n = 12), while the darker outer zones show higher values at the margin, with $\delta^{18}O_{quartz}(B2)_{margin} = 12.1 \pm 0.6$ ‰ (n = 2) (Figure 83). Quartz from E1-type veins show a clear variation between the core and the nearby margin, with values ranging from 6.5 ‰ to 12.5 ‰, no linkage has been observed regarding the CL-zoning. There is an increase in the isotopic signature from the core to the margin (a few tens of microns), from $\delta^{18}O_{quartz}(E1)_{center} = 8.8 \pm 0.8$ ‰ (median = 8.8 ‰, n = 22) to $\delta^{18}O_{quartz}(E1)_{margin} = 11.9 \pm 0.5$ ‰ (median = 11.7 ‰, n = 6) (Figure 84). Data are summarized in Table 6.

Table 6: presenting δ18Oquartz value from the different type of vein.

Vein type	Min - Max / ‰	Median / ‰	Mean ± 1σ / ‰	n
A	7.1 – 11.6	9.9	9.9 ± 0.9	69
B1	8.5 – 11.7	9.9	9.9 ± 0.6	88
$B2_{center}$	7.6 – 9.9	8.6	8.7 ± 0.7	12
$B2_{margin}$	11.8 – 12.5	12.1	12.1 ± 0.6	2
$E1_{center}$	7.0 – 10.0	8.8	8.8 ± 0.8	22
$E1_{margin}$	11.4 – 12.7	11.7	11.8 ± 0.5	6

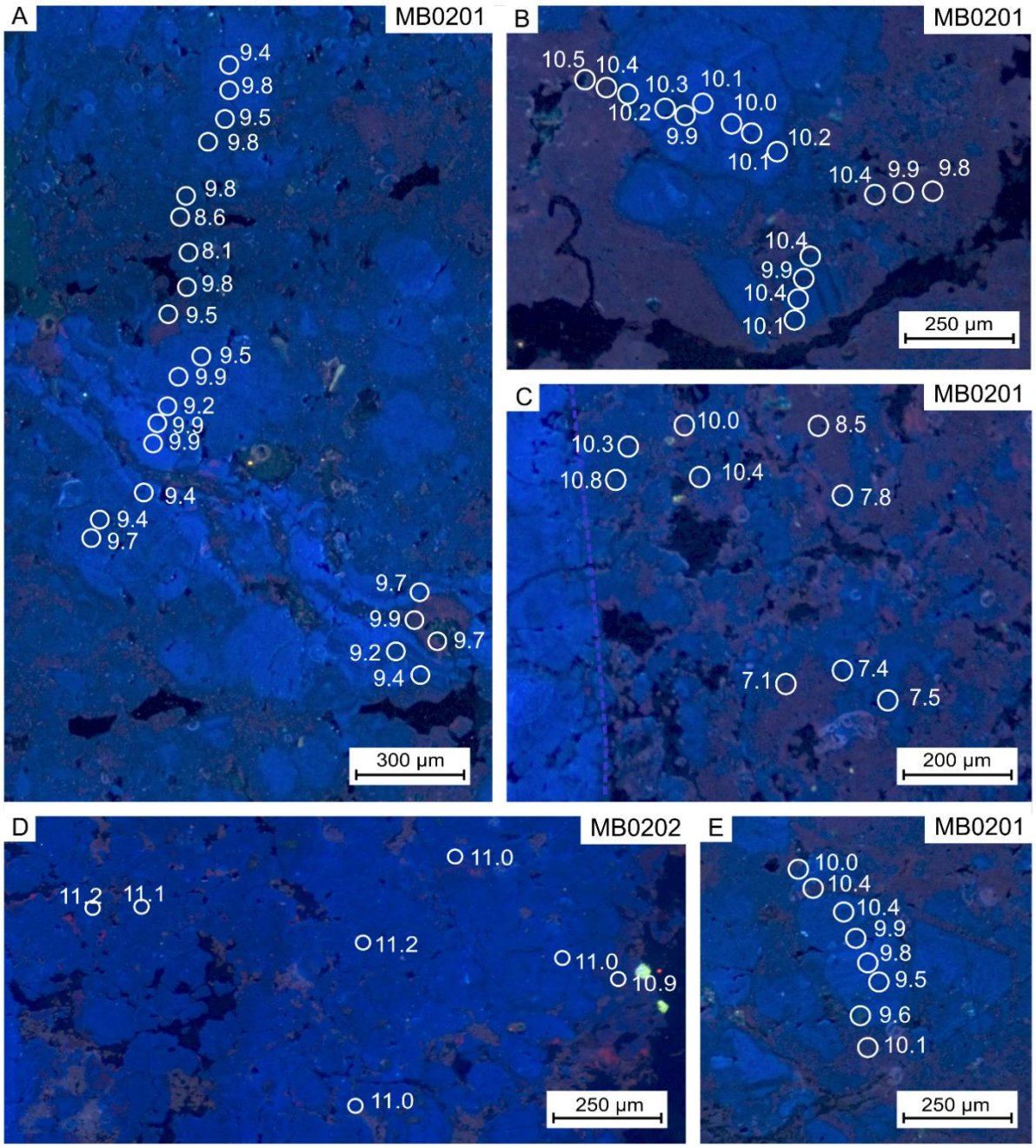

Figure 81 : CL imaging with scaled localization of SIMS analysis spots ($\delta^{18}O$), including values in ‰. A to E. Different locations with varying CL intensities; the isotopic values on quartz show no correlation with CL zonation.

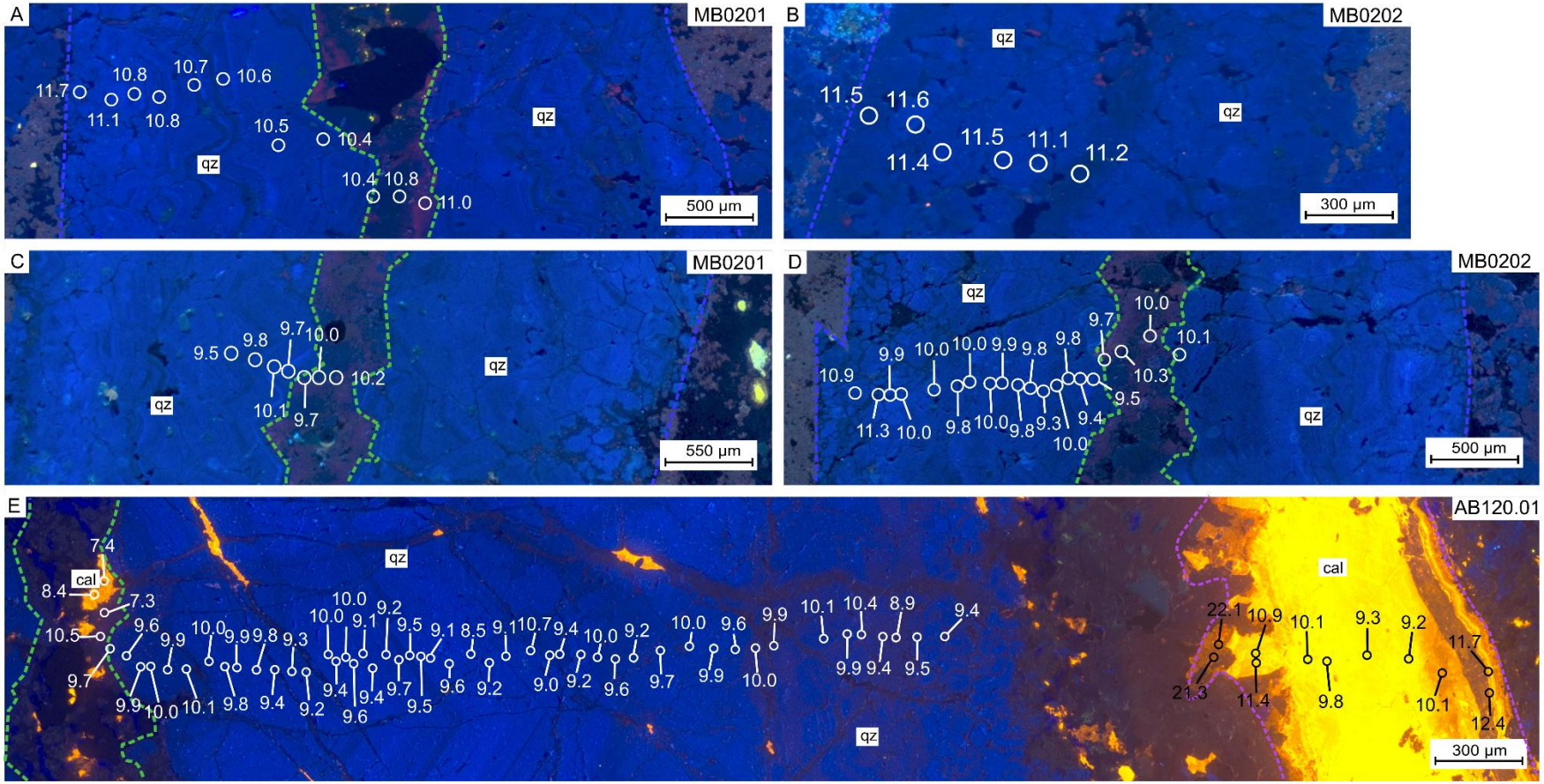

Figure 82: CL imaging of B1-type veins with scaled localization of SIMS analysis spots ($\delta^{18}O$), including values in ‰. A to E. Different locations with varying CL intensities; the isotopic values on quartz show no correlation with CL zoning. Blue dotted line = B1-type vein margin, Pink dotted line = E2-type veins margins, Green dotted line = C-type veins margins.

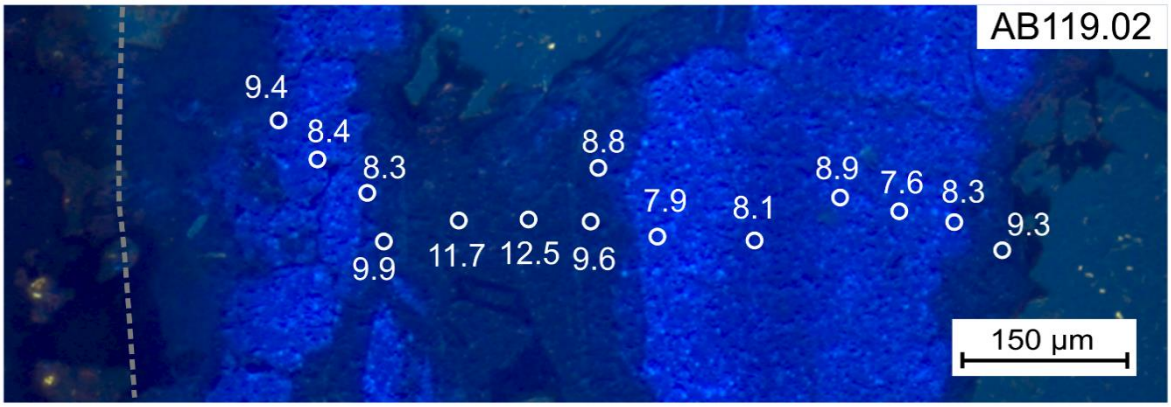

Figure 83: CL imaging of B2-type vein with scaled localization of SIMS analysis spots ($\delta^{18}O$), including values in ‰. The isotopic values on quartz show a correlation with CL zoning. Dark quartz shows heavier isotopic value than high intensity CL.

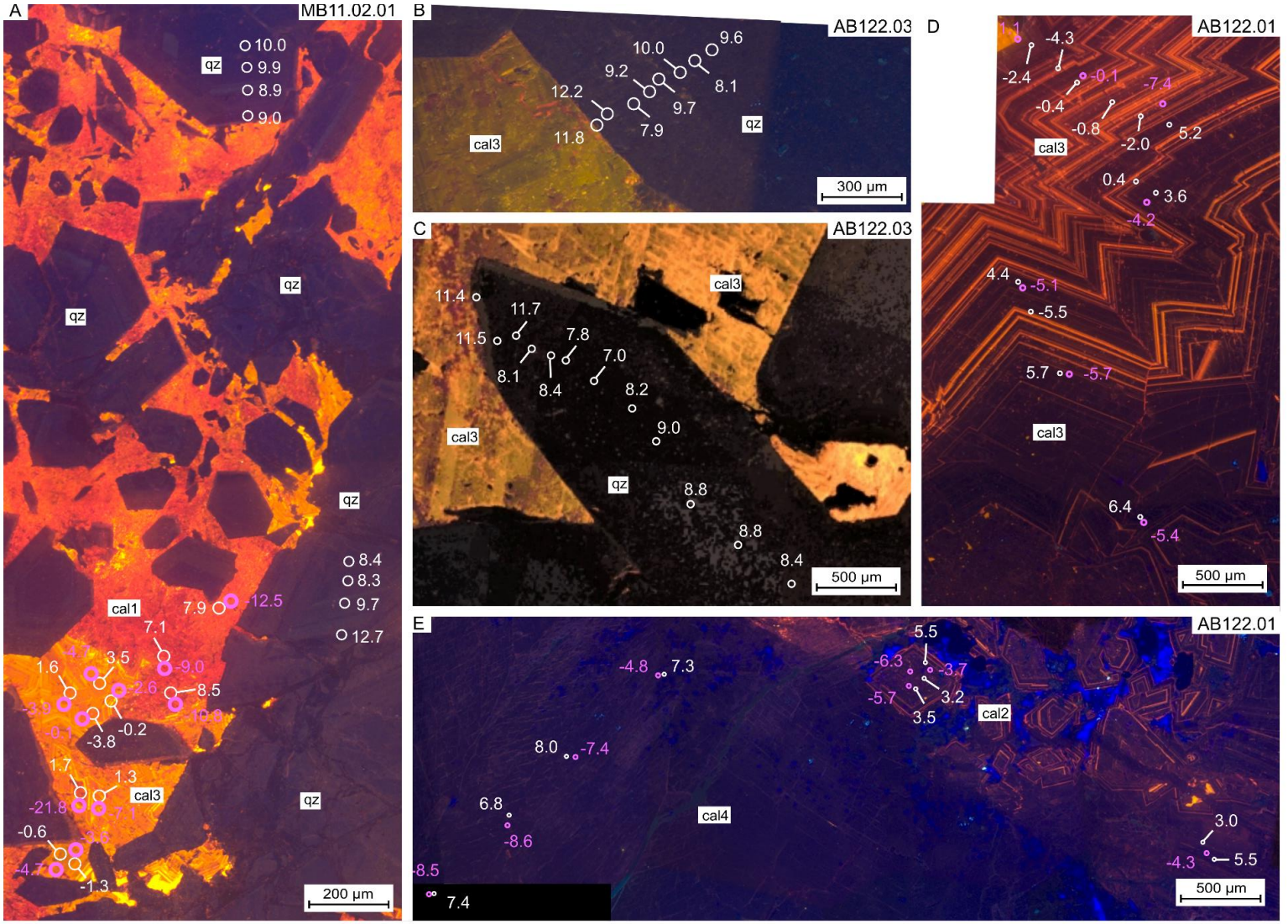

Figure 84: CL imaging with scaled localization of SIMS analysis spots ($\delta^{18}O$, white cercle, $\delta^{13}C$, pink circle), including values in ‰. A. Isotopic value in quartz of E1-type vein and Calcite 1 and Calcite 3from E2-type veins. B. Isotopic value in quartz of E1-type vein. C Isotopic value in quartz of E1-type vein. D. Isotopic value in Calcite 3from E2-type veins. E. Isotopic value Calcite 2 and Calcite 4 from E2-type veins.

The $\delta^{18}O_{calcite}$ values show significant variability within a calcite crust and, by extension, across the vein scale: $\delta^{18}O_{calcite}$(E2) = 5.8 ± 6.4 ‰ (median = 5.4, n = 48). No systematic trends were observed whether in relation to CL intensity. However, the different textures from the different calcite crystals display different range of value $\delta^{18}O_{calcite}$(E2): $\delta^{18}O_{calcite}$(Cal1) range from 7.1 to 8.5 ‰ (n=3), $\delta^{18}O_{calcite}$(Cal2) range from 3.0 to 5.6 ‰ (n=5), $\delta^{18}O_{calcite}$(Cal3) range from -5.5 to 6.4 ‰ (n=20), and $\delta^{18}O_{calcite}$(Cal4) range from 6.8 to 8.0 ‰ (n=4) (Figure 84). Data are summarized in Table 7*: presenting δ18Ocalcite value from the different E2-type veins.*

Table 7: presenting $\delta^{18}O_{calcite}$ value from the different E2-type veins.

Vein type	Min - Max / ‰	Median / ‰	Mean ± 1σ / ‰	n
E2 Cal1	7.1 to 8.5	7.9	7.8 ± 0.7	3
E2 Cal2	3.0 to 5.5	3.5	4.2 ± 1.3	5
E2 Cal3	-5.5 to 6.4	0.7	1.1 ± 3.0	20
E2 Cal4	6.7 to 8.0	7.4	7.4 ± 0.5	4

A tendency towards mean values is discernible for the veins of types A, B1, $B2_{margin}$, $B2_{center}$, $E1_{margin}$, and $E1_{center}$, with value ~ 9.0 ‰ for A- and B1-type veins and center parts of B2 and E1 type veins. where quartz margins of B2- and E1-type display $\delta^{18}O_{quartz}$ ~ 12 ‰. This is not the case for calcite crystals in E2-type veins, where the distribution appears sub-uniformly between the two extreme values.

Euhedral to anhedral calcite from 2 different samples of mineralization stages E2 were selected for in-situ SIMS carbon isotopes. The obtained $\delta^{13}C_{calcite}$ values range from -12.5 to -0.1 ‰. Spatial variations are important even at small distances (less than 100 microns). There are no clear links between the isotopic value and the CL-textures of the different calcite generations forming the E2-types veins. However, the different textures from the different calcite crystals display different ranges of value $\delta^{13}C_{calcite}$(E2): $\delta^{13}C_{calcite}$(Cal1) range from -12.5 to -9.0 ‰ (n=3), $\delta^{13}C_{calcite}$(Cal2) range from -6.3 to -3.7 ‰ (n=3), $\delta^{13}C_{calcite}$(Cal3) range from -7.4 to -0.1 ‰ (n=14) and $\delta^{13}C_{calcite}$(Cal4) range from -8.6 to -4.8 ‰ (n=4). Data are summarized in Table 8: presenting δ13Ccalcite value from the different E2-type veins.

Table 8: presenting $\delta^{13}C_{calcite}$ value from the different E2-type veins.

Vein type	Min - Max / ‰	Median / ‰	Mean ± 1σ / ‰	n
E2 Cal1	-12.5 to -9.0	-10.7	-10.7 ± 1.7	3
E2 Cal2	-6.3 to -3.7	-5.0	-5.0 ± 1.2	4
E2 Cal3	-7.4 to -0.1	-4.3	-4.3 ± 1.8	15
E2 Cal4	-8.6 to -4.8	-8.0	-7.3 ± 1.8	4

5.3.2. Hydrogen in quartz and carbonate veins

Over two extraction sessions, leading to a total of 28 analyses, 7 measurements showed traces of contamination. Among the 21 remaining values, 7 are associated with a material quantity of less than 30 µmol, which may introduce analytical bias, and were therefore excluded. The remaining 14 values range from -49.6 to +2.8 ‰. The variation within the same vein type reaches up to 36.8 ‰ for the E2-type vein. The δD(A) values range from -25.4 to -21.0 ‰ (mean – 23.5 ± 2.3 ‰) n=3, δD(B1) values range from -23.8 to -2.8 ‰ (mean – 11.8 ± 7.3 ‰) n=5, and only one δD(B2) value is retained (for the reasons mentioned previously), which is +2.0 ‰. The δD(E1) values range from -41.6 to -35.4 ‰ (mean – 38.9 ± 3.2 ‰) n=3, and δD(E2) values range from -49.6 to -12.8 ‰ (mean - 34.8 ± 16.0 ‰) n=5. The detailed values are presented in Table 9: Synthesis of δD data (Full dataset is in Tableau d'analyses du δD par broyage des différentes veines de quartz).

Table 9: Synthesis of δD data

Vein type	Min - Max / ‰	Mean ± 1σ / ‰	n
A	-25.4 to -21.0	-23.5 ± 2.3	3
B1	-23.8 to -2.8	-11.2 ± 7.9	5
B2	/	+ 2.0	1
E1	-41.6 to -35.4	-38.9 ± 3.2	3
E2	-47.0 to 12.8	-34.8 ± 16.0	5

The values increase from A-type veins to B1-type veins, with δD(A) = -23.5 ± 2.3 ‰ (n = 3) to δD(B1) = -11.8 ± 7.3 ‰ (n = 5), respectively, and then increase further towards B2-type veins with δD(B2) = +2.0 ‰ (n = 1). E1-type veins show more negative values, with a drop in δD values: δD(E1) = -38.9 ± 3.2 ‰ (n = 3), and δD(E2) = -34.8 ± 16.0 ‰, which are similar within the different range of values.

During the extraction of H_2, a procedure was conducted to determine the presence or absence of CO_2 in the fluid inclusions. This led to the observation of CO_2 presence, notably in association with carbonates. The formation of carbonates and CO_2 can be assessed through the equilibrium between calcite and CO_2 for oxygen isotopes or calcite and H_2O. Both methods were applied, and the results revealed a linear relationship in the measured data. This suggests that the two fluids were in equilibrium during the precipitation of calcite.

5.3.3. Fluid inclusion petrography in B2- and E2-type veins

The petrological details and microthermometry results for the A-, B1- and E1-type vein fluid inclusions are exposed in chapter 3. The B1-type vein is same as the B-type vein, the E1-type vein is same as the E-type vein in chapter 3. In the following section, only the petrological description of the B2- and E2-type veins fluid inclusions is exposed.

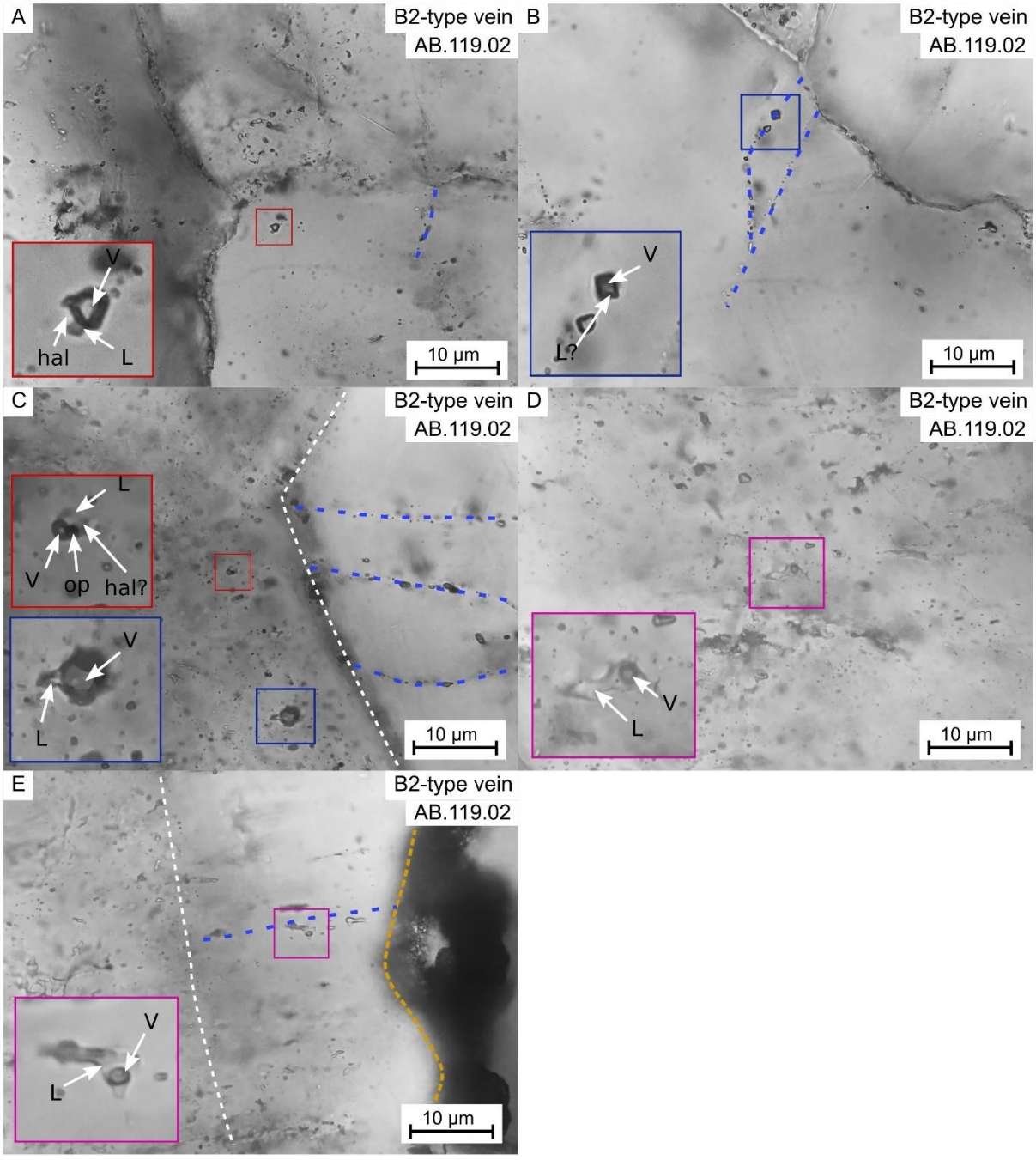

Figure 85: Fluid inclusion petrography from B2-type veins. A. Isolated Type 2 fluid inclusion (VLH). B. Isolated Type 3 fluid inclusion (VL) along FI planes. C. Type 3 and Type 2 fluid inclusions at a contact of a quartz margin. D. Isolated Type 1 fluid inclusion in quartz grain. E. Type 1 fluid inclusions in plane in clear overgrowth quartz. V= vapor phase, L= aqueous liquid phase, H= halite crystal, op= opaque mineral. Blue dots = intragrain plane, yellow dots = open space margin in central part of B2-type vein), white dotted lines = quartz grain margins.

The B2-type veins contain clear, transparent to inclusion-rich (solid/fluid) quartz. Primary fluid inclusions that are isolated or arranged in clusters or trails along quartz growth zoning (Hein and Van den Kerkhof 2001) reach 15 µm in size but are mostly < 10 µm in size (Figure 85). Three types of fluid inclusions were identified: Type 1, two-phase (LV) aqueous inclusions, are characterized by a vapor bubble occupying 10 to 50 vol.%. They are mostly secondary, since they intersect the CL-zoning of quartz, but are primary in the quartz overgrowths, where they are the only fluid inclusion (Figure 85). Type 2 inclusions are three phases (LVH) and contain a vapor phase occupying 5 to 50 vol.% of the inclusion and a halite crystal (Figure 85). Type 3 inclusions are two-phase (VL) inclusions that are vapor-dominated (70–90 vol.%). Locally, they can contain daughter or accidentally-trapped opaque crystal, possibly chalcopyrite or hematite (Figure 85).

In the B2-type veins, fluid inclusion planes were observed in quartz, including Type 1 secondary and Type 2 and Type 3 primary to rarely pseudo-secondary inclusions. Sometimes, the inclusions are isolated in the core of the grains or have no spatial relationship within the host grains. The Type 1 fluid inclusion is observable all along the vein, however, it is the only one in clear quartz overgrowth zones. Where they can be found along plane which are orthogonally oriented to the vein's margins. These overgrowths are devoid of Type 2 and Type 3 fluid inclusions (Figure 85).

The E2-type veins contain near transparent calcite. Primary fluid inclusions that are isolated or arranged in clusters or trails along quartz growth zoning (Hein and Van den Kerkhof 2001) reach 50 µm in size but are mostly < 10 µm in size (Figure 86). Only one type of fluid inclusion was identified: Type 1, two-phase (LV) aqueous inclusions, are characterized by a vapor bubble occupying 10 to 50 vol.%. They are primary, since they follow the CL-zoning of quartz, and in calcite overgrowths. In the E2-type veins, fluid inclusion planes were observed in quartz, including Type 1. Sometimes, the inclusions are isolated in the core of the grains or have no spatial relationship within the host grains (Figure 86).

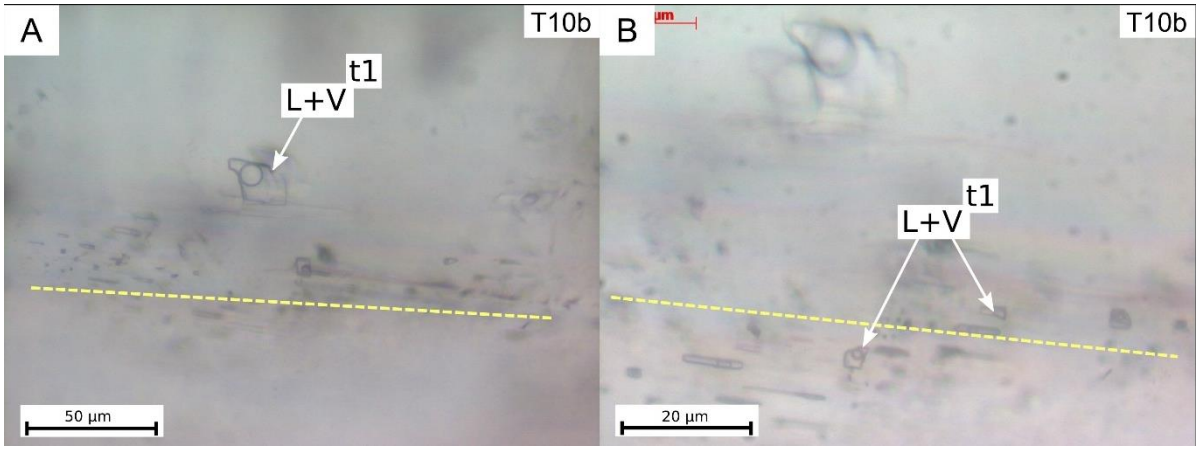

Figure 86: Fluid inclusion petrography of E2-type veins. A: two-phase fluid inclusion (L+V) (type1) near an intragrain B. plane of fluid inclusions like the previous one, in a calcite crystal. Legend: V = vapor, L = Liquid.

5.4. DISCUSSION

5.4.1. Isotopic fractionation and $\delta^{18}O_{H2O}$, $\delta^{18}O_{CO2}$, $\delta^{13}C_{CO2}$.

The $\delta^{18}O_{H2O}$, $\delta^{18}O_{CO2}$, $\delta^{13}C_{CO2}$ are the estimated isotopic composition of the fluid (water) in equilibrium with quartz or calcite during precipitation. The isotopic value of the fluid has been calculated using each time the maximum and minimum value of temperature given by the respective fluid inclusion T_h, from the works of Voudouris et al. 2013a and Abiven et al. (see Chapitre 3. and Figure 87).

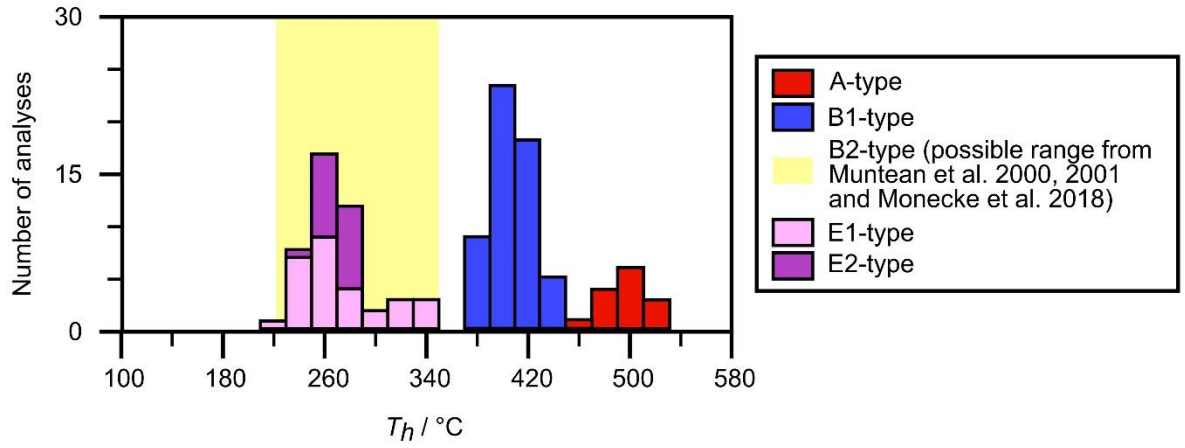

Figure 87: Histogram of T_h values for fluid inclusions, based on the synthesis by Abiven et al. (Chapter 3), with the addition of data from E2-type veins and the temperature range of B2-type veins according to Muntean and Einaudi (2000).

This led to the calculation of two ranges of isotopic value of fluid for each type of vein and is presented in Figure 88 and Figure 89. (Full dataset is available in Tableau de valeurs du δ18O dans les veines de type A. Tableau de valeurs du δ18O dans les veines de type B1.Tableau de valeurs du δ18O dans les veines de type B2.Tableau de valeurs du δ18O dans les veines de type E1.Tableau de valeurs du δ18O dans les veines de type E2. And Tableau de valeurs du δ13C dans les veines de type E2.). With their high formation temperatures >350 °C corresponding to A- and B1-type veins are very similar, with less than 1.6 ‰ of difference (Figure 87, Figure 88). However, when temperatures of vein formation are <350°C, as for B2-, E1- and E2-type veins, this difference is much higher, and is up to 10.3 ‰ (Figure 87 and Figure 88). This is consistent with a greater spread in temperature data for B2-, E1-, and E2-type veins (up to 115 °C) compared to A- and B1-type veins (up to 70 °C) and with increasing isotopic fractionation as temperature decreases. Although these differences exist, the evolution of isotopic values remains the same when considering the minimum or maximum formation temperatures of quartz and calcite, with a decrease in $\delta^{18}O_{H2O/CO2}$ along the porphyry-epithermal system. Mean values were calculated by averaging the $\delta^{18}O_{quartz}$ values for each vein type and applying isotopic fractionation calculations based on quartz crystallization temperatures derived from the synthesis of fluid inclusion data (see fluid inclusions data). The isotopic values of fluids evolve from A-type veins with $\delta^{18}O_{H2O}$(A)=

3.9–8.4 ‰ (mean 6.7 ± 0.9‰) (Figure 88 A) to B1-type veins with $\delta^{18}O_{H2O}$(B1)= 3.9–7.2 ‰ (mean 5.3 ± 0.6 ‰) (Figure 88 B) to B2-type veins with $\delta^{18}O_{H2O}(B2_{center})$ = [-2.9 – 4.3] ‰ and $\delta^{18}O_{H2O}(B2_{margin})$ = [1.3 – 7.0] ‰ (Figure 88 C), to E1-type veins with d $\delta^{18}O_{H2O}(E1_{center})$ = [-3.5 - 4.0] ‰ (mean 1.1 ± 0.7 ‰) and $\delta^{18}O_{H2O}(E1_{margin})$ = [1.2 - 6.7] ‰ (Figure 88 D) and to E2-type veins with $\delta^{18}O_{H2O}$(E2)= [-14.8 - 6.6] ‰ (mean -3.8 ± 2.0 ‰) (Figure 89 A) and $\delta^{18}O_{CO2}$(E2) = [-15.4 - 3.6] ‰ (mean -4.5 ± 2.0 ‰) (Figure 89 B). The data distribution follows normal laws for A- and B1-type veins, while two populations are observable for B2- and E1-type veins, which are associated with differences between central quartz and marginal quartz values. The spread of isotopic values for calcite is highly variable and does not display any specific mode (Figure 89).

The spread of isotopic values for calcite is highly variable and does not display any specific mode. The calculated $\delta^{18}O$ values for H_2O and CO_2 as fluid, show a shift of approximately 1.5 ‰, which, on the scale of $\delta^{18}O_{calcite}$ variations, represents only a 5 % difference (Figure 89 A, B). For $\delta^{13}C$, the variations between the values for quartz and the calculated fluid values are minimal and suggest a possible mode close to -4 ‰. The values presented here represent the bulk composition of the calcite veins (Figure 89 C).

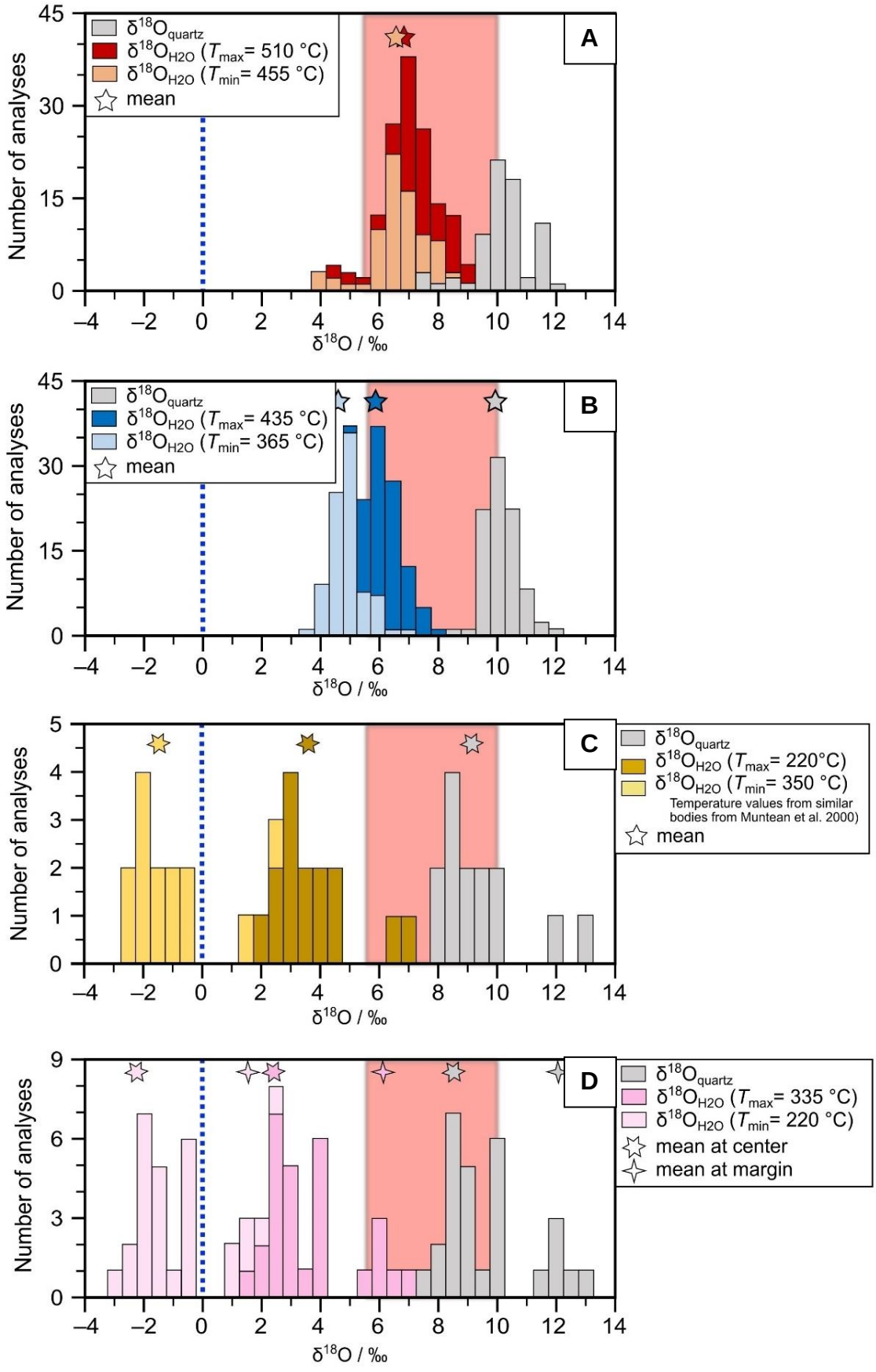

Figure 88: Histogram of $\delta^{18}O_{quartz}$ (grey), and calculated $\delta^{18}O_{H2O}$ value of the different quartz veins. A. A-type veins. B. B1-type veins. C. B2-type veins. D. E1-type veins. Blue dotted line: SMOW value, red domain: primary magmatic water (from Taylor, 1979), range of B2-type veins temperature according to Muntean and Einaudi (2000), the other is from fluid inclusions synthesis of Pagoni Rachi in Chapter 3.

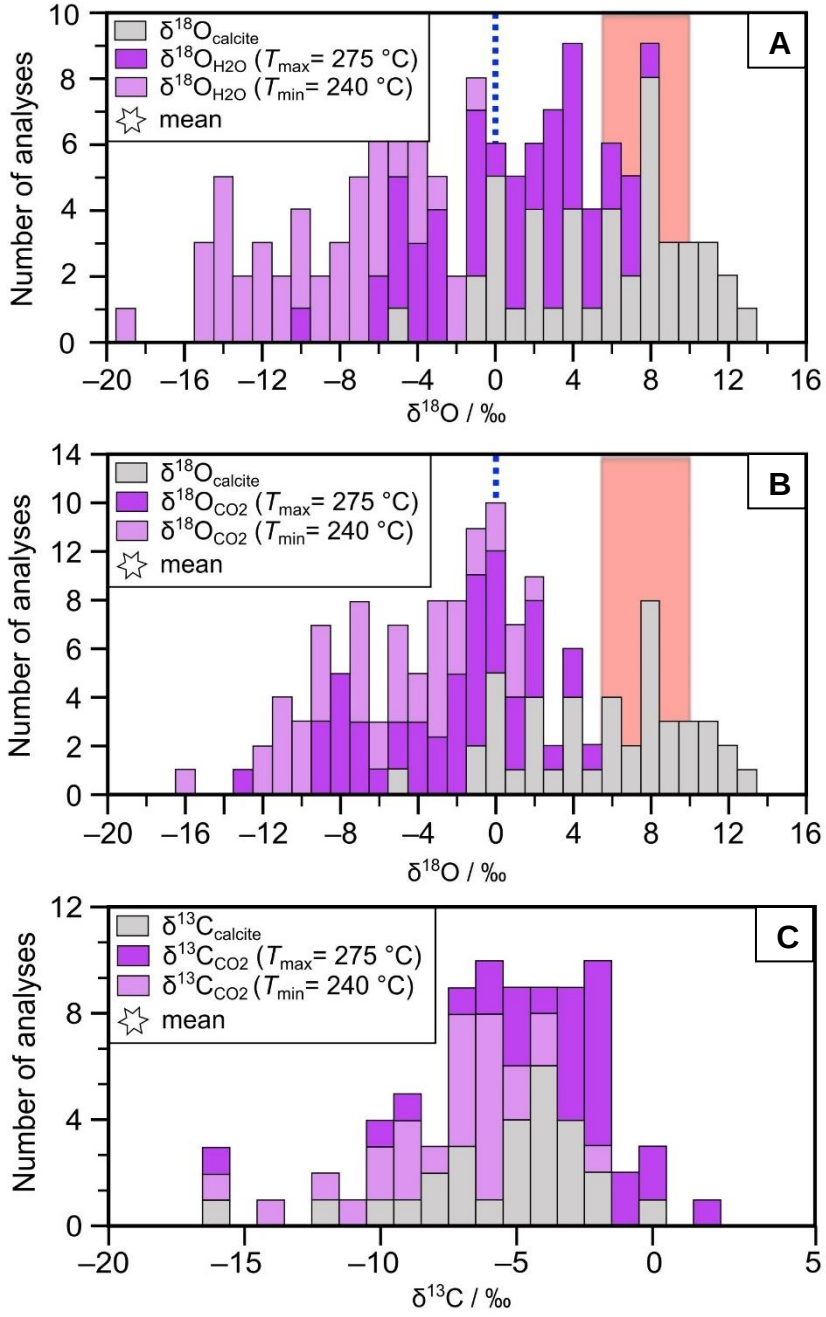

Figure 89: Histogram of $\delta^{18}O_{calcite}$ or $\delta^{13}C_{calcite}$ (grey), and calculated $\delta^{18}O_{H2O}$ or $\delta^{18}O_{CO2}$ value of the different quartz veins. A. E2-type veins with calculated $\delta^{18}O_{CO2}$. B. E2-type veins with calculated $\delta^{18}O_{H2O}$. C. E2-type veins with calculated $\delta^{13}C_{CO2}$. Blue dotted line: SMOW value, red domain: primary magmatic water (from Taylor, 1979).

5.4.2. Influence on δD

δD data for samples with material quantities below or near 30 micromoles were excluded from the discussion. The analysis of such small amounts of material leads to an underestimation of the actual isotopic value, making the inclusion of these data incongruous.

Several issues were also encountered during the experimental procedures, which may have impacted the final δD signal: (i) Incorporation of hydrated minerals (e.g., sericite, biotite, amphibole) as inclusions within quartz or in contact with the host rock. Despite efforts to minimize such contaminants, their presence or the reopening of quartz veins (e.g., C-type veins in B1-type veins) could not always be avoided. This resulted in a mixed δD signal from quartz and these other minerals. (ii) Mixing of quartz generations with varying degrees of dynamic recrystallization. This could have led to elemental diffusion in fluid inclusions, causing a loss of material or even the complete destruction of inclusions. Consequently, the resulting populations may not be representative of the primary fluid composition. (iii) Loss of fluid during the reduction of large samples into smaller fragments (e.g., via diamond sawing or crushing with a hammer). This process could have caused the analyzed fluid inclusion populations to be unrepresentative of the original samples. (iv) Mixing of multiple fluid generations. Secondary fluid inclusions (e.g., Type 1 in all vein types, which overlap with Type 2 and Type 3 inclusions in A-, B1-, and B2-type veins) can constitute up to 20 vol% of the total fluid inclusion assemblage. This non-negligible proportion may have shifted the δD_{H2O} signal, blending it with the isotopic value of the fluid responsible for these secondary inclusions. (v) System contamination due to leaks could have altered the δD_{H2O} signature.

5.4.3. Local temperature decreases insights of quartz overgrowths

A significant increase in $\delta^{18}O_{quartz}$ values is observed from the center of the quartz crystals to their edges, with a particularly pronounced rise near the edges. In quartz from B2 and E1-vein types, $\delta^{18}O_{quartz}$ values generally increase from approximately 9‰ at the center to 12‰ at the edges (Figure 83, Figure 88 C). In the B2 veins, this increase coincides with specific CL-zoning, characterized by a lower luminescence intensity near the edges of the quartz grains or veins (Figure 83, Figure 88 C). This isotopic variation can be explained by a greater fractionation associated with a decrease in temperature during crystallization, a phenomenon consistent with thermodynamic models reported in the literature.

Assuming a constant isotopic composition of the fluid during quartz precipitation, isotopic fractionation increases as temperature decreases, resulting in higher $\delta^{18}O_{quartz}$ signatures at the edges compared to the centers of the crystals. This suggests that the crystallization temperature decreases abruptly toward the end of quartz growth. In the E1-type veins, a similar increase in $\delta^{18}O_{quartz}$ values at the edges is associated with variable optical extinction, supporting the hypothesis of changing physicochemical conditions during the final stages of quartz precipitation (Figure 84, Figure 88 D, Figure 33 J).

Based on the measured oxygen isotopic values and thermal data from fluid inclusions (Table 6*: presenting δ18Oquartz value from the different type of vein.*), the temperatures associated with B2-type veins, where $\delta^{18}O_{quartz}$ values show a difference of 3.5 ‰ between central quartz (mean $\delta^{18}O_{quartz}(B2)_{center}$ = 8.7 ‰) and edge quartz (mean $\delta^{18}O_{quartz}(B2)_{margin}$ = 12.2 ‰). Fractionation is estimated at 7.5 ‰ for a central quartz temperature of 285 °C. Although no average temperature is available for B2-type veins, for this exercise, a central temperature of 285 °C, based on the proposed extremes, is assumed. The fractionation at the edges should then be approximately 11.0 ‰, corresponding to an edge crystallization temperature of about 210 °C. A similar trend is observed in E1-type veins reveal a $\delta^{18}O_{quartz}$ difference of 3 ‰ between the center (mean $\delta^{18}O_{quartz}(E1)_{center}$ = 8.8 ‰) and the edge (mean $\delta^{18}O_{quartz}(E1)_{margin}$ = 11.8 ‰). The average fractionation at 264 °C, the crystallization temperature of central quartz, is 8.36 ‰, leading to a theoretical fractionation of 11.36 ‰ for edge quartz. This corresponds to a crystallization temperature of approximately 195 °C at the edges.

These results highlight a thermal dynamic for the B2- and E-type1 veins, reflecting a progressive decrease in temperature during their formation. This isotopic and thermal evolution reveals a fluid-crystal system subjected to significant thermal variations, likely driven by fluctuating geochemical and hydrodynamic conditions.

5.4.4. Isotopes and fluid sources

Traditionally, the range of $\delta^{18}O_{H2O}$ from quartz is thought to reflect changes in temperature and fluid source under equilibrium conditions (e.g., Taylor, 1974). For example, magmatic waters have an isotopic signature of 5.5 – 10 % as they equilibrate with crystallizing plutons (Taylor, 1974) (Figure 92,Figure 91), commensurate with measurements of undiluted magmatic water (700 °C) expelled from high-temperature fumaroles (e.g., Goff and McMurty, 2000). Incursion of groundwater and mixing in hydrothermal systems results in lower $\delta^{18}O_{H2O}$ values, as ocean water has a value of 0 %, and meteoric waters range from 0 to -55 % at high latitudes (Taylor 1974). The sequence of data in Figure 92 reveals a clear evolutionary trend. The $\delta^{18}O_{H2O}$ values transition from A/B1-type veins, where fluid signatures are indicative of a magmatic origin (5.0 – 10.0 ‰) (Hedenquist and Lowenstern, 1994), to B2- and E1-type veins, which display $\delta^{18}O_{H2O}$ values close to 0 ‰. This suggests the presence of surface-derived fluids, such as seawater ($\delta^{18}O_{SMOW}$ = 0), or a mixing of magmatic fluids with surface fluids like meteoric waters ($\delta^{18}O_{meteoric} \approx$ -13.0 ‰) or seawater. This interpretation is further supported by the $\delta^{18}O$(E2) and $\delta^{18}O$(E2) values measured in the later calcite-rich veins, which reach as low as -14.8 and -15.5 ‰, respectively (Figure 89 C, Figure 92, Figure 90).

Then, the most likely fluid sources in Pagoni Rachi system are hydrous magmas, meteoric groundwater and seawater (Figure 92, Figure 91, Figure 90). Interpreting fluid sources based on oxygen, hydrogen, carbon isotopic composition of hydrothermal quartz and calcite, however, is nontrivial, even

with fluid inclusion estimates of palaeotemperature. The problem is only tractable if there is reasonable evidence to assume equilibrium (or alternatively, that isotopic exchange rates are far from equilibrium).

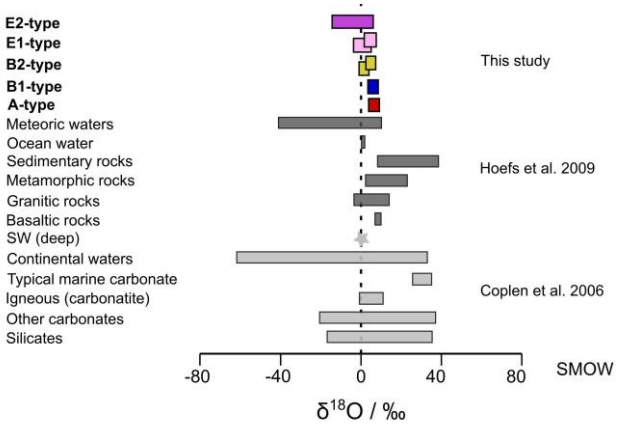

Figure 92: $\delta^{18}O_{H2O}$ range of extrema values of typical reservoir and of the different veins of Pagoni Rachi porphyry-epithermal system. When to boxes are superposed, the right one is associated with the quartz /veins margins value and the left one of the quartz in center of the vein.

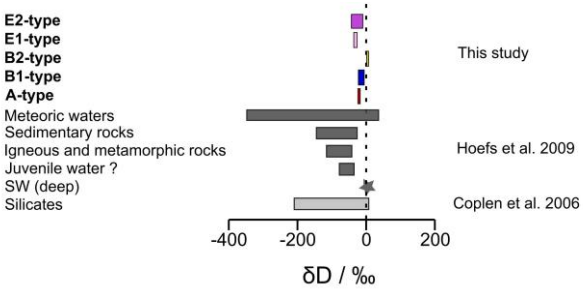

Figure 91: δD range of extrema values of typical reservoir and of the different veins of Pagoni Rachi porphyry-epithermal system. When to boxes are superposed, the right one is associated to quartz /veins margins value and the left one of the quartz in center of the vein.

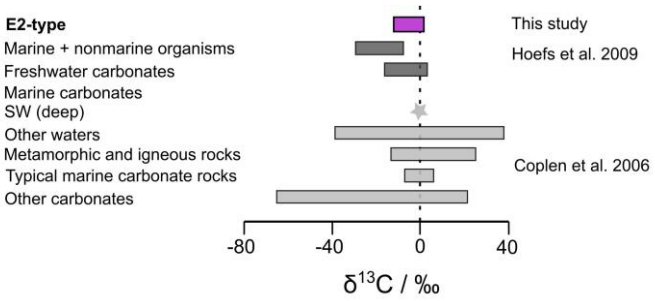

Figure 90: $\delta^{13}C$ range of extrema values of typical reservoir and of the different veins of Pagoni Rachi porphyry-epithermal system. When to boxes are superposed, the right one is associated to quartz /veins margins value and the left one of the quartz in center of the vein.

5.4.5. Origin and mixing of mineralizing fluids

The results of hydrogen and oxygen isotope analyses are reported in Figure 93. Further, they are plotted in Figure 3 together with two reference lines: the first line is the GMWL (Craig, 1961) identifying the world meteoric water line while the second one is the Mediterranean meteoric water line (MMWL) (Gat and Carmi, 1970). As can be seen, almost all the samples E2-type fall within the two reference lines reported, thus indicating a marked meteoric origin. All the other samples, but one, lie to the right of the MWL reference lines, thus indicating a different origin of water and/or that other groundwaters have modified their pristine isotopic composition due to: (1) mixing between groundwaters and heavy isotope-rich waters such as Mediterranean seawater (δD = +10 ‰, $\delta^{18}O$ = +1 ‰), condensate fumarolic steam on Vulcano Island (Capasso et al., 1997); (2) secondary processes causing an isotopic fractionation as a consequence of evaporation process (D and ^{18}O -enrichment); (3) ^{18}O-shift during water-gas rock interaction.

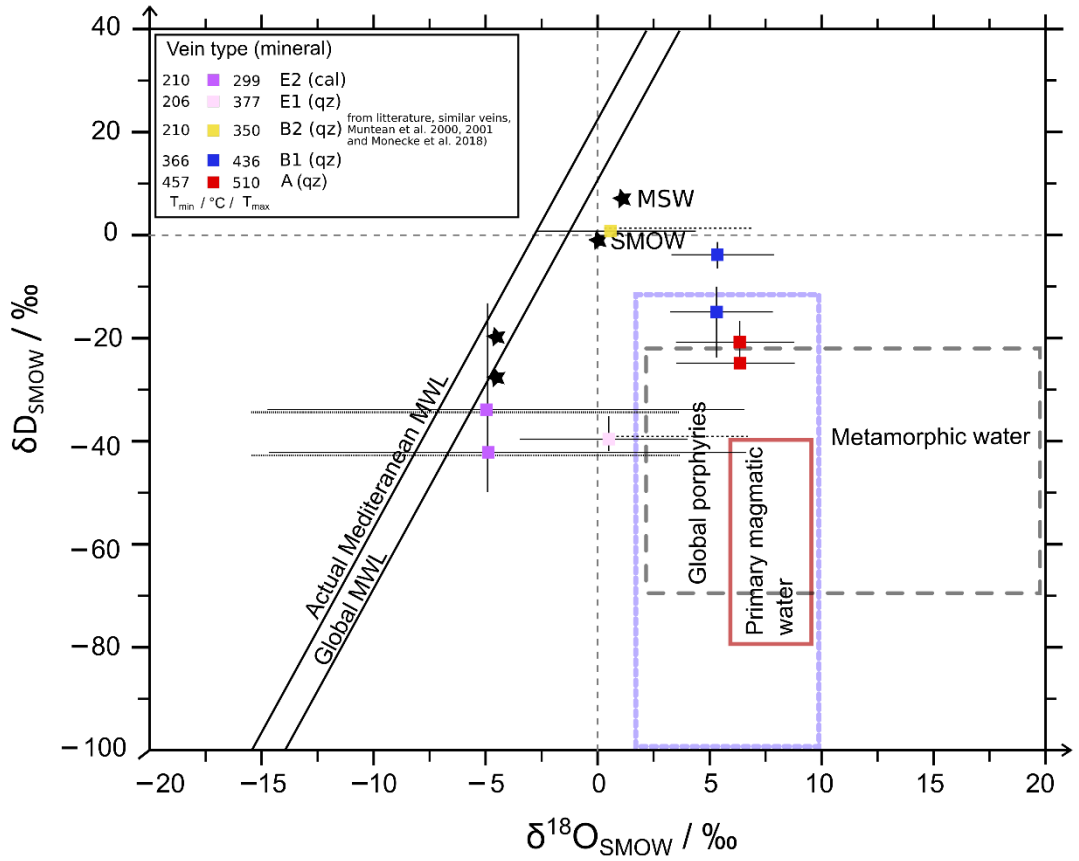

Figure 93 : δD vs. $\delta^{18}O_{H2O}$ diagram, with the different value of the different vein types of the Pagoni Rachi porphyry epithermal system. MMWL is from Gat and Carmi (1970) global porphyry fluid data from Sheppard et al. (1971), Sheppard and Gustafson (1976), Ford and Green (1977), Bowman et al. (1987), and Zaluski et al. (1994), , GMWL, from Graig 1961, MSW (mediterranean Sea Water is from Farrell et al. 1995, Milos meteoric water and from Tutum Bay Price et al. 2013, primary magmatic water is from Taylor, (1974).

5.4.5.1. Origin of the mineralizing fluids of stages A, B1.

The calculated fluid compositions for A, B1-type veins yield a $\delta^{18}O_{H2O}$ compositions of ~3.9 to 8.4‰ at equilibrium. This range is typical of felsic igneous rocks (e.g. Campbell and Larson, 1998) and overlaps with the 5.0–10.0 ‰ range. These δD values evolve from a low signature of -25 ‰ for A-type veins to around -10 ‰ for B1-type veins. This evolution is therefore decoupled. This could be consistent with mixing with a secondary fluid. Unfortunately, isotopic equilibration of the fluid with rock at high rock-to-fluid ratios tends to erase the original fluid composition, thereby obscuring evidence of the fluid source (Taylor, 1974). However, the geological context, with an emplacement within a granodiorite, demonstrates a genetic link between the two features (Voudouris et al., 2013a).

The salinity of the original fluid before boiling could be estimated using fluid inclusion salinity data provided by microthermometry and the relative volumetric proportion of Type 2 and Type 3 fluid inclusions. While this is achievable for B1-type veins, it is much more challenging for A-type veins. Quartz in A-type veins shows evidence of fluid overlap from B-type veins, with two generations of Type 2 and Type 3 inclusions. This makes it difficult, if not impossible, to reliably evaluate the volumetric proportions of fluid inclusions associated with the formation of A-type veins. This estimation can be attempted by considering volumetric phase proportions reported in the literature (e.g., Bodnar, 1993) and observations from A and B1-type veins, with a proportion of approximately 15 % (type 2) to 85 % (type 3). This yields an original salinity of 14.6 $wt\%_{equiv.NaCl}$ for A-type veins and 11.8 $wt\%_{equiv.NaCl}$ for B1-type veins. Thus, there is a decrease in salinity values, though the first theoretical value remains poorly constrained. A detailed petrography study and fluid inclusion counting could be conducted, with an evaluation of the volume of each FI type, distinguishing the various present types. This would involve microthermometry and Raman spectroscopy to assess the salinity of each inclusion, while also accounting for potentially re-equilibrated or recrystallized FIs. The estimated salinity range aligns with a magmatic fluid origin (0 to 15 $wt\%_{equiv.NaCl}$ for primary magmatic fluid (Sharma and Srivastava, 2014). A decreasing salinity trend from A- to B1-type veins suggests mixing with lower-salinity fluids.

5.4.5.2. Conditions of fluid mixing during mineralization stages A, B1 and B2.

A mixture, in varying proportions, between low-salinity surface-derived fluids ($\delta^{18}O \approx 0$ ‰) and moderately saline fluids with a magmatic isotopic signature ($\delta^{18}O \approx 10$ ‰) could explain the majority of the $\delta^{18}O_{quartz}$ variations observed in A-, B1-, and B2-type veins. Quartz crystals reflect distinct histories of fluid mixing, with isotopic signatures specific to each mineralization stage.

In stages A and B1, the $\delta^{18}O_{quartz}$ values are relatively homogeneous, indicating that their formation was largely controlled by fluid mixing at constant proportions. In contrast, quartz crystals from stage B2 exhibit lower isotopic values ($\delta^{18}O_{H_2O}$ = -2.0 to 5.0 ‰; δD = 2 ‰), which are below the typical ranges for magmatic fluids or those in isotopic equilibrium with igneous rocks. These light isotopic signatures suggest the intrusion of surface-derived fluids through the pore spaces of the Pagoni Rachi rocks, likely

sourced from seawater, given the paleogeographic context of the Early Oligocene. The rapid flux of these fluids likely prevented complete isotopic exchange with the host rocks.

The low $\delta^{18}O_{quartz}$ values (< 9 ‰) can be attributed to the progressive infiltration of seawater into the aquifer, consistent with the increase in δD values from -25 ‰ (A-type veins) to -12 ‰ (B1-type veins) to +2 ‰ (B2-type veins). These observations illustrate a chronological transition from a magmatic fluid endmember to a seawater-dominated fluid. The fluid mixing during stages A, B1, and B2 was thus a continuous process, marked by the progressive injection of moderately saline, metal-bearing fluids into an aquifer dominated by low-salinity surface-derived fluids.

Following the incursion of seawater, the system transitioned from a regime dominated by magmatic fluids to one largely controlled by seawater. This transition is consistent with the structural position of B2 veins at higher levels compared to the A and B1 veins, aligning with the model proposed by Muntean and Einaudi (2000) for similar systems in the Maricunga Belt. The salinities of the fluids responsible for the B2 veins are expected to be intermediate between those of seawater (~3.5 wt% NaCl) and the moderately saline fluids (~11 wt% NaCl) associated with the preceding B1 veins, prior to phase separation.

This mixing model is also consistent with a shallow environment linked to a surface water aquifer. The geological and geodynamic context suggests the establishment of a porphyry-epithermal system in a "foreland" setting, which could explain these characteristics (Caracciolo et al., 2011, 2015).

In stages A and B1, the veins resulted from the mixing of ascending magmatic fluids with low- to medium-salinity surface-derived fluids (~3.5 wt% NaCl) at shallow depths. This mixing occurred prior to fluid boiling, as boiling would have produced distinct fluid inclusions indicative of separate vapor and liquid phases rather than a homogeneous mixture.

Using a typical magmatic fluid with $\delta^{18}O$ = 10 ‰ (e.g., Rottier et al., 2021) and seawater with $\delta^{18}O$ = 0 ‰, the fluid mixture in the A veins implies ~35% seawater, while in the B1 veins, this proportion increases to ~45%, indicating a growing seawater contribution between these two stages.

It should also be noted that the positive δD value of the B2-type vein can be explained by paleoseawater with a more positive δD signature, as has been measured on Milos Island, where δD values is +7‰ and $\delta^{18}O_{H_2O}$ value is +2 ‰ (e.g. Price et al., 2013). Mixing with such water could contribute to the positive δD_{H_2O} values of the B2-type veins. These positive values are primarily attributed to evaporation processes, which result in Rayleigh distillation and favor heavier isotopic compositions in the residual seawater. This interpretation is consistent with the geological framework during the formation of the porphyry system, which is situated in a forearc basin. However, the sedimentary sequences in this region do not exhibit any evidence of high levels of evaporation, which would typically be indicated by evaporite layers within the sedimentary record.

5.4.5.3. Origin of the mineralizing fluids during stage E1 and E2.

The values of $\delta^{18}O_{H_2O}$ and δD decrease abruptly from B2- to E1- and E2-type veins. The unique presence of fluid inclusions associated with quartz overgrowths in the B2-type vein suggests a geochemical and geological affinity between this overgrowth and the later formation of E1-type veins. All generations of E1 quartz crosscut earlier magmatic-associated quartz veins (A, B1, B2). Central values for $\delta^{18}O_{H_2O}$ and δD for E2-type veins tend to align with those of meteoric water lines (both Global and Mediterranean), which are assumed to best represent the fluid values at the origin of the epithermal veins (E1- and E2-type).

In contrast, the E1-type vein exhibits higher $\delta^{18}O_{H_2O}$ values than E2-type vein, suggesting fluid-rock interaction from a meteoric water reservoir or mixing between meteoric water and magmatic fluid. This observation aligns with the presence of low-salinity fluids in E1- and E2-type veins, which are likely partially mixed with surface-derived low-salinity fluids. The salinity of the fluids forming quartz and calcite, in these veins, ranges between 1.2 and 2.7 $wt\%_{equiv.NaCl}$ for E1-type veins and 1.4 to 2.9 $wt\%_{equiv.NaCl}$ for E2-type veins, which are significantly lower than those observed in stages A, B1, and possibly B2. For the epithermal fluids, the lowest salinity value corresponds to the oxygen isotope signature of a meteoric fluid endmember, while the highest value can be explained by water-rock interaction or mixing between magmatic fluid and meteoric water. This mixed-fluid proportion also accounts for the observed decrease in salinity recorded by fluid inclusion assemblages, as studied by Voudouris et al. (2013a).

Quartz crystals from stages B2 and E1 show an increase in $\delta^{18}O_{quartz}$ during crystal growth, suggesting that they crystallized during periods when the two endmember fluids were not mixed, but instead, the fluid source evolved. B2-type veins likely crystallized from seawater, while E1- and E2-type veins originated from meteoric water associated with epithermal processes. The model suggests that re-equilibrated meteoric water would achieve an oxygen isotope composition greater than 0‰ only at low water-rock ratios in shallow environments.

For E2-type veins, the isotope signature of calcite crystals ($\delta^{13}C_{calcite}$ and $\delta^{18}O_{calcite}$) shows an evolution in vein succession, with lighter $\delta^{13}C_{calcite}$ and heavier $\delta^{18}O_{calcite}$ values transitioning to heavier $\delta^{13}C_{calcite}$ and lighter $\delta^{18}O_{calcite}$ values from cal1 to cal3. This shift may reflect an evolving system with increasing meteoric water influence on magmatic calcite, followed by a reversal of this trend during the formation of cal4, possibly indicating a reversal in the meteoric water and magmatic fluid proportion dynamics (Figure 94). The low overall δ^{13}Ccalcite values may result from the influence of organically derived carbon, which reduces the carbon isotope signal in fluids that have circulated through organic-rich sediments.

The combination of the three stable isotope signatures tends to demonstrate that the fluids forming the E1-type quartz veins and E2-type calcite veins originate from a mixture of magmatic fluid and meteoric water. The magmatic fluids may have derived from a late magmatic pulse or a succession of pulses. This is consistent with the development of epithermal veins controlled by structural features

along NNW-SSE-oriented faults, which could act as conduits for the fluids, allowing for the mixing of meteoric surface fluids with deeper magmatic fluids. Initially, there is an increasing influence of meteoric water, followed by a late stage return to a stronger magmatic fluid influence. The mixing could range from a 50% meteoric and magmatic fluid contribution for E1-type veins to nearly 100% meteoric fluids for E2-type veins.

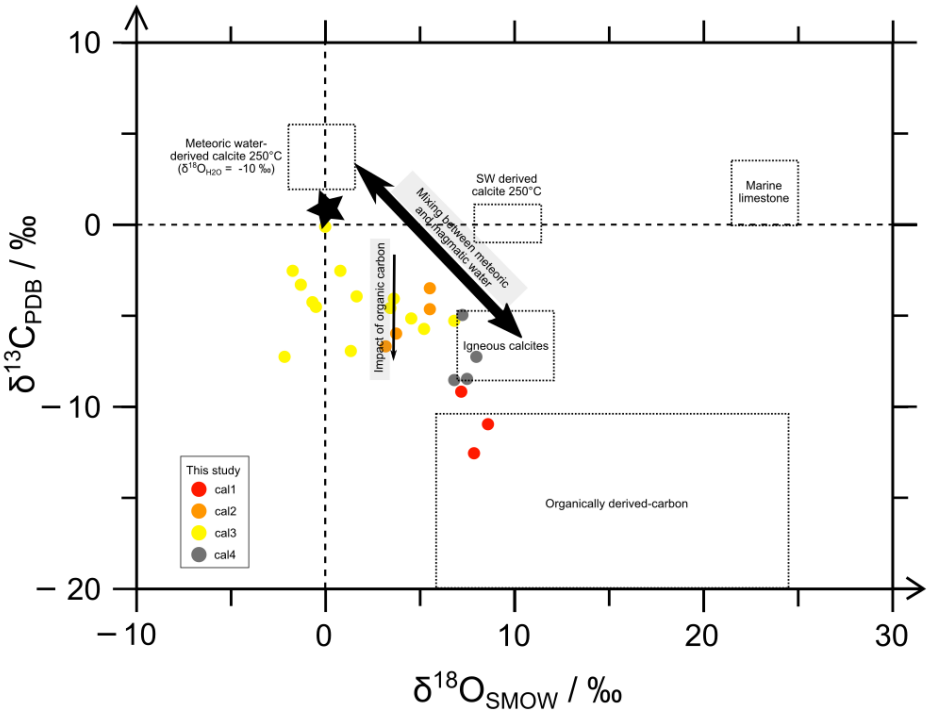

Figure 94: $\delta^{13}C_{PDB}$ vs. $\delta^{18}O_{SMOW}$ diagram, of the isotopic signature from the different calcite forming the E2-type veins. Igneous calcites box from Bowman 1998, Meteoric water derived calcite box from a meteoric water at $\delta^{18}O_{H2O}$ = -10‰ from which a calcite precipitates at 250°C, Sea water derived calcite box from a seawater at $\delta^{18}O_{H2O}$ = 0‰ from which a calcite precipitate at 250°C.

5.4.6. Isotopic constraints and temperature estimation in fluid evolution models

Based on the previously presented fluid evolution model, it is evident that isotopic values located to the left of the meteoric water line appear inconsistent and significantly underestimated. This discrepancy can partially be attributed to the broad range of fluid formation temperatures, particularly in low-temperature fluid inclusions. At low temperatures, isotopic fractionation increases. Therefore, constraining these fractionation values would provide more precise restrictions on temperature estimates. A similar approach to that used for determining the growth temperatures of quartz in E1- and B2-type vein could be applied here.

To simplify this analysis and better frame the isotopic values, we will rely on the intersection limits between the Mediterranean meteoric water line (which is more representative of the studied geologic context than the global meteoric water line) and the isotopic value ranges of the fluids that formed the

calcite crystals. For E2-type veins, two intersection points for oxygen isotopes are obtained: -6.8 ‰ and -5.5 ‰.

This analysis is complex due to the substantial variability in oxygen isotopic values, with a maximum difference of 11.9 ‰. This variability introduces significant biases, as a mean oxygen isotope value is used for all veins combined, despite interactions between meteoric water and organic matter within sedimentary rocks. A weighted average, accounting for the number of data points analyzed for each vein, would provide a more accurate value, approximately 5.1 ‰.

Using this method, fractionation coefficient values of 10.6 ‰ and 11.9 ‰ correspond to temperatures of 160 °C and 145 °C, respectively. The difference between these results is primarily due to the presence of low $\delta^{18}O_{calcite}$ values (and associate $\delta^{18}O_{H2O}$), which reduce the mean isotopic value of the fluids regardless of the method applied. This discrepancy limits the reliability of the thermal constraints obtained, particularly due to the wide spread of isotopic data.

Moreover, the temperature ranges derived from fluid inclusions typically provide more robust constraints than this inverse method, which is subject to numerous biases. It is also worth noting that no distinction has been made in literature between different generations of calcite veins. It is therefore possible that some of these veins formed at lower temperatures than those suggested by the synthesis of *PT* data from fluid inclusions (Voudouris et al., 2013a; this study). A detailed study of calcite veins is required to refine the thermal constraints and trace the succession of formation events.

5.5. CONCLUSION

Since the physical and chemical properties of circulating fluids passing through rocks can change over time, it is expected that a single quartz vein will record a range of conditions throughout its growth history. Oxygen isotope and trace element analyses conducted along growth bands of selected quartz crystals and veins highlight the complexity of hydrothermal processes during the different mineralization stages at the Pagoni Rachi deposit.

During mineralization stages A, B1, and B2, the relative proportions of two fluid types (moderate-salinity and low-salinity) exhibited significant variation. This suggests that these stages were formed by multiple, transient pulses of a rising moderate-salinity magmatic fluid, which infiltrated an aquifer dominated by low-salinity fluid (seawater) (Figure 95). These pulses of magmatic fluid provided the base metals, and their dilution led to sulfide precipitation during hydrothermal events. Quartz overgrowths from stage B2 align with the formation of banded quartz stockwork from flash events, like those observed in the Maricunga Belt (Muntean and Einaudi, 2000). In this study, quartz grains from different mineralization stages generally show only a small difference (around 2 ‰) in $\delta^{18}O_{quartz}$ values, which is interpreted as the result of early mixing of magmatic and seawater fluids in varying proportions (Figure 95).

The distinct variation in $\delta^{18}O_{quartz}$ values (up to 4 ‰) observed along a quartz vein, particularly in B2 and E1-type veins at Pagoni Rachi, underscores the usefulness of in-situ analysis over bulk isotope analysis for reconstructing the origins of mineralizing fluids in epithermal ore deposits. Furthermore, sharp $\delta^{18}O_{quartz}$ decreases identified by SIMS in-situ oxygen isotope analysis in B2-type veins are likely indicative of transient meteoric water recharge into the aquifer. At Pagoni Rachi, the significant variations in $\delta^{18}O_{quartz}$ values are attributed to fluctuations in precipitation temperatures and are explained by a fluid change at the site of mineralization. This involved a rising, low-salinity, surface-derived fluid with a $\delta^{18}O_{fluid}$ signature of 30 ‰ δD and -5 ‰ $\delta^{18}O$. The low-salinity fluid is believed to have originated from meteoric water, which underwent fluid-rock interactions and was re-equilibrated with the surrounding rocks; this event is linked to faulting.

The variability in $\delta^{13}C$ and $\delta^{18}O$ values of calcite veins is associated with a mixing between meteoric water and magmatic fluid. The δD and $\delta^{18}O$ values of the epithermal veins controlled by low-salinity fluid may represent the transition between a marine environment to a continental environment of the Pagoni Rachi porphyry-epithermal system. By combining the identification of different fluid reservoirs (magmatic, seawater, meteoric) and fluid mixing process, we can infer the evolution of local geological environment (Figure 95). The early vein formation likely occurred in a submarine porphyry system near sea level, with seawater elevation, progressing to a continental epithermal environment. This represents a possible uplift of several hundred meters, a relative sea level decrease, or a decrease of eustatic level.

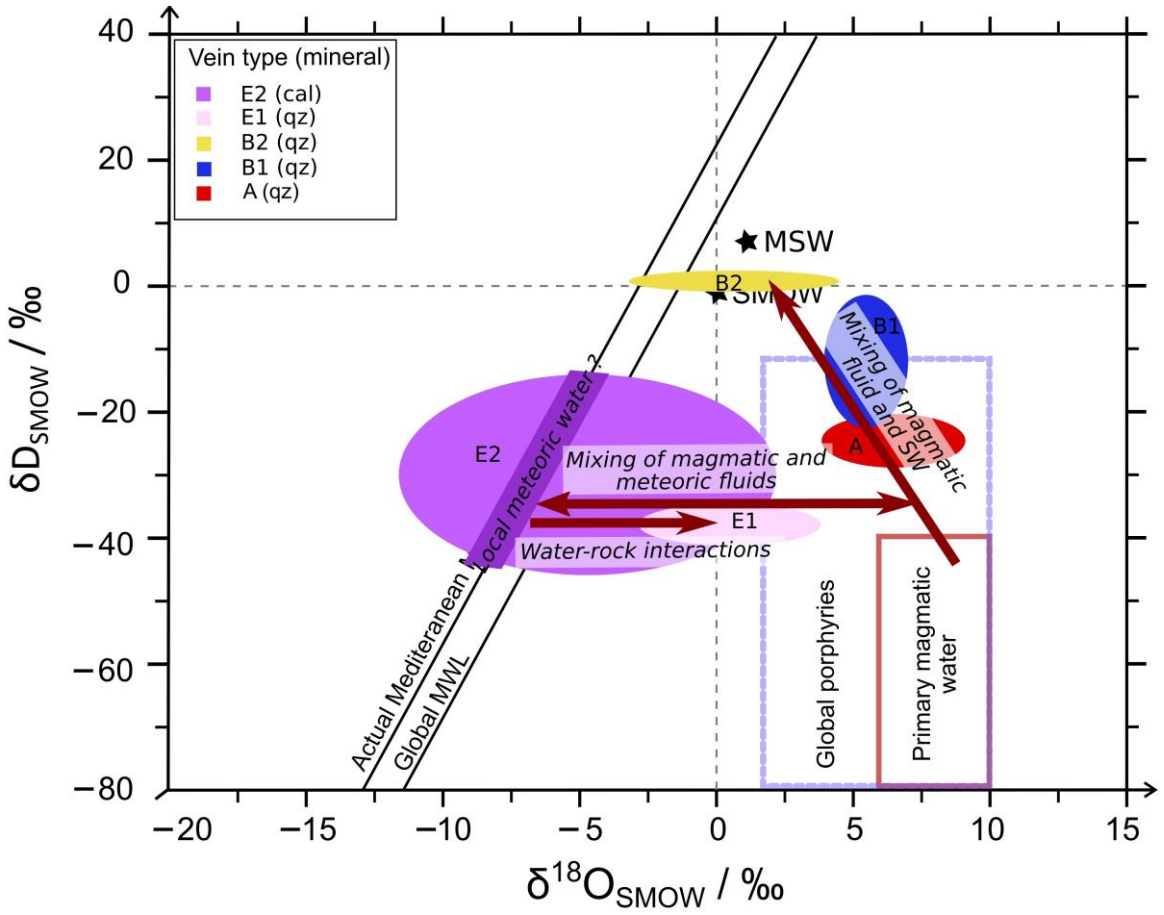

Figure 95: δD vs. δ18OH2O diagram, with the different schematic value of the different vein type of the Pagoni Rachi porphyry epithermal system, with evolution processes involved. (1) ascent of magmatic fluid, (2) mixing between magmatic fluid and seawater, (3) fluid incursion of possible meteoric water which underwent water rock interactions and/or mixing between meteoric and magmatic waters. MMWL is from Gat and Car global porphyry fluids data from Sheppard et al. (1971), Sheppard and Gustafson (1976), Ford and Green (1977), Bowman et al. (1987), and Zaluski et al. (1994)MI (1970), GMWL, from Graig 1961, MSW (mediterranean Sea Water is from Farrell et al. (1995), Milos meteoric water and from Tutum Bay Price et al. (2013), Primary magmatic water is from Taylor, (1974).

This process was followed by surface erosion, allowing the formation of the current outcrops of the Pagoni Rachi porphyry-epithermal system.

In conclusion, this study demonstrates that tracing the mineralizing fluids responsible for forming epithermal deposits in the shallow part of a porphyry system requires high spatial resolution in-situ oxygen isotope analyses of multiple quartz grains from the same mineralization stage. This approach provides a more comprehensive understanding of the fluid's origins and the mixing processes leading to the mineralization deposition.

CHAPITRE 6. DISCUSSION GENERALE : MODELE METALLOGENIQUE POUR LE GISEMENT DE PAGONI RACHI

Le développement d'un modèle métallogénique pour les systèmes de type porphyre-épithermal est d'une importance scientifique et économique, ces systèmes représentent certaines des plus grandes sources mondiales de Cu, Mo et Au (Sillitoe 2010, Richards 2015). La compréhension des processus qui régissent la formation de tels gisements, nécessite une approche intégrée combinant observations de terrain, pétrographie, géochimie et analyses isotopiques. Les avancées récentes dans l'analyse des éléments traces du quartz, les études sur les inclusions fluides, la géochimie isotopique des minéraux de gangue (par exemple le quartz et la calcite), ainsi que les observations détaillées sur le terrain, offrent de nouvelles perspectives sur l'évaluation des conditions physico-chimiques (pression, température, composition des fluides) qui contrôlent la mise en place des minéralisations (e.g. Schrön et al., 1988 ; Götze, 2009 ; Tanner et al., 2013 ; Maydagan et al., 2015 ; Breiter et al., 2017, 2020 ; Mao et al., 2017 ; Rottier et al., 2018, 2020 ; Rottier and Casanova, 2021 ; Falkenberg et al., 2024). Ces approches sont essentielles pour affiner la compréhension de l'évolution spatiale et temporelle des systèmes de type porphyre-épithermal, ainsi que des processus influençant le transport et la précipitation des métaux.

Le quartz est un minéral de gangue omniprésent dans les systèmes de type porphyre-épithermal, et constitue une archive des conditions de cristallisation des fluides hydrothermaux. L'incorporation d'éléments traces dans le quartz reflète les variations de la chimie des fluides, de la température et de la pression lors de sa formation (Thomas et al., 2010 ; Breiter et al., 2017). Les inclusions fluides piégées dans le quartz fournissent une fenêtre directe sur la composition et la salinité, permettant de mieux comprendre leur évolution et leurs interactions (Roedder, 1984 ; Bodnar et Sterner, 1987). L'analyse des isotopes stables tels que l'oxygène et de l'hydrogène dans le quartz, et de l'oxygène, de l'hydrogène et du carbone dans la calcite, permet d'identifier les sources des fluides (magmatiques, météoriques, marins ou mixtes) et les processus de mélange ou d'interactions fluide-fluide ou fluide-roche (Sheppard et al., 1971 ; Taylor, 1974 ; Hoefs, 2018).

Les études de terrain restent fondamentales pour contextualiser les données géochimiques et isotopiques dans le cadre structural et textural des gisements. Les observations portant sur la paragenèse des veines, les textures des minéraux et les relations de recoupement fournissent des contraintes temporelles cruciales sur l'évolution des systèmes hydrothermaux (Gustafson et Hunt, 1975 ; Wilkinson et al., 2015). Ces observations, lorsqu'elles sont intégrées aux analyses en laboratoire, permettent de démêler les interactions complexes entre les processus magmatiques, la circulation des fluides et les déformations dans les systèmes porphyres-épithermaux.

Cependant, des questions fondamentales restent ouvertes quant à la dynamique des fluides et aux mécanismes qui conduisent à la précipitation des métaux. Cette partie vise à proposer un modèle métallogénique du gisement de Pagoni Rachi en intégrant les éléments discutés dans les parties précédentes du manuscrit, soit : les observations de terrain, la quantification des éléments traces du quartz, des inclusions fluides, et des isotopes stables dans les minéraux de gangue. En appliquant ces méthodes à un système porphyre-épithermal bien caractérisé, l'objectif est d'affiner le modèle métallogénique et de fournir un cadre applicable à d'autres systèmes similaires dans le monde. Cette

approche intégrée contribue non seulement à une meilleure compréhension des processus de formation des gisements mais aussi au développement de modèles d'exploration prédictifs.

Le système porphyre-épithermal de Pagoni Rachi illustre une dynamique hydrothermale, en contexte d'arc (Maravellis, 2010, 2012 ; Caracciolo et al., 2012) avec un retrait du slab et un affinement lithosphérique, marqué par une succession d'événements magmatiques, hydrothermaux et tectoniques (e.g. Voudouris et al., 2013a, 2019). Des zones d'altération potassique à sodi-calcique ainsi que des veines de type A, B1 et B2 sont bien développées à Pagoni Rachi. Les veines de type B2 prédominent au sommet des collines de Pagoni Rachi. Ainsi, un spectre de gisements de type porphyre-épithermal qui partage de nombreuses caractéristiques essentielles avec les gisements de type porphyre à Cu–Mo, Cu–Au et épithermal à Pb–Zn décrits dans la littérature, est défini par la présence des veines successives de quartz et de calcite (e.g. Gustafson, 1978 ; Muntean et Einaudi, 2000, 2001 ; Seedorf, 2005 ; Sillitoe, 2010 ; Richards, 2015 ; Monecke et al., 2018 ; Rottier and Casanova, 2021). Pagoni Rachi est un système télescopé dans lequel la relation spatiale entre les veines de type B2 et celles de type A et B1 est significative. Cependant, l'altération séricitique associée aux veines de type B2 pourrait avoir recouvert les zones d'altération potassique et sodi-calcique associées aux veines de type A et B1. La partie épithermale, sous forme de lithocaps, pourrait avoir été érodée à Pagoni Rachi, tandis qu'à Konos Hill, elle serait encore conservée (e.g. Voudouris et al., 2019).

L'interprétation du développement spatial et temporel du système magmatique-hydrothermal étudié est illustrée dans la Figure 96. Le système de Pagoni Rachi présente l'évolution suivante: l'intrusion de granodiorite porphyrique est suivie par une altération potassique, puis par une surimpression d'altération sodi-calcique généralisée et la formation de veines de type A, B1 et B2 sous influence de fluides magmatiques et d'une progressive infiltration d'eau de mer. L'évolution du système se termine par des veines de type C/D qui recoupent les précédentes veines avec le dépôt de la minéralisation à Cu-Mo-Re associé à une altération séricitique pervasive et de veines de quartz et de calcite (E1 et E2) de type sub-épithermal, sous influence mixte de fluide magmatique et d'eau météorique. Cette évolution a été favorisée par la mise en place d'accidents NNW-SSE, contrôlant structurellement les veines épithermales en agissant comme drains pour la circulation fluide. Ces fluides ont ainsi formés la minéralisation Pb-Zn. Les accidents régionaux peuvent être associés à de l'étirement induit par le retrait du slab vers le Sud. Le système évolue depuis des conditions de formation en contexte chaud/ductile/lithostatique à froid/cassant/hydrostatique (Figure 96). La minéralisation tardive est définie comme une période d'activité hydrothermale ayant eu lieu avant la cessation de l'activité magmatique et est associée à de la tectonique. Les veines de type D marquent le début de la minéralisation tardive : aucune veine de type A/M, B1 ou B2 ne recoupe les veines de type D, à l'exception des veines épithermales tardives, qui recoupent l'ensemble des veines du système. Le système de Pagoni Rachi a connu des cycles répétés de pulses magmatiques suivis de la formation de veines de quartz. Pour ce gisement, les événements d'altération et de minéralisation se sont produit par de nombreux cycles, bien que leur intensité ait pu varier d'un cycle à l'autre (Figure 96). Un modèle en érosion, est proposé par défaut, puisqu'aucune donnée de paléoaltitude n'ont été trouvé dans la littérature, et peut être associé à un cas simple de télescopage.

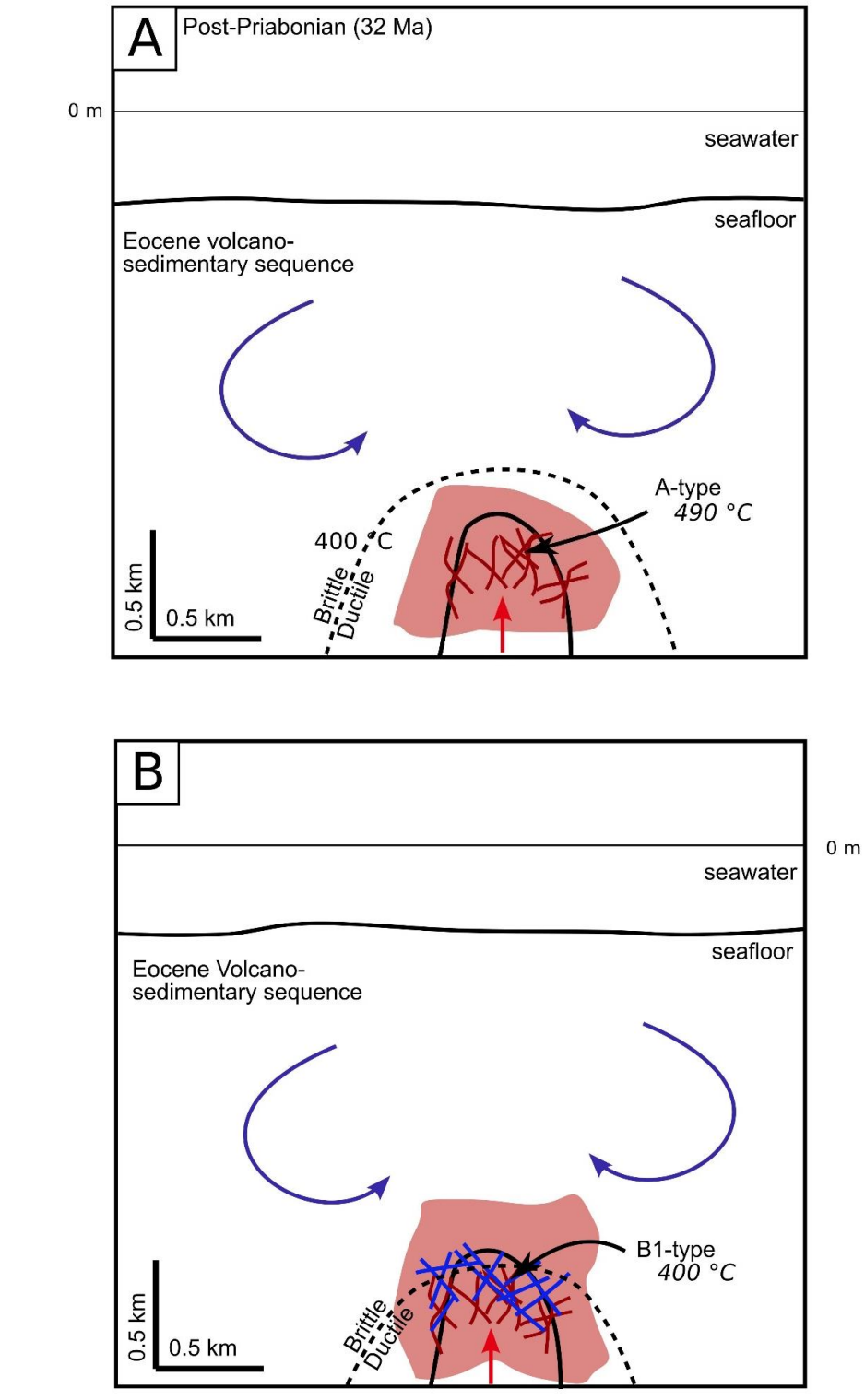
A
Post-Priabonian (32 Ma)
0 m
seawater
seafloor
Eocene volcano-
sedimentary sequence
A-type
490 °C
400 °C
Brittle
Ductile
0.5 km
0.5 km
B
0 m
seawater
seafloor
Eocene Volcano-
sedimentary sequence
B1-type
400 °C
Brittle
Ductile
0.5 km
0.5 km
Alteration
Argillic
Sericitic
Chlorite-sericitic
Potassic-sodi/calcic
Vein type
A-type
B1-type
C/D-type
B2-type
E1/2-type
Granodiorite
?
Theorical lithocaps
Brittle/ductile transition
Sea water
Meteoric water
Magmatic fluids

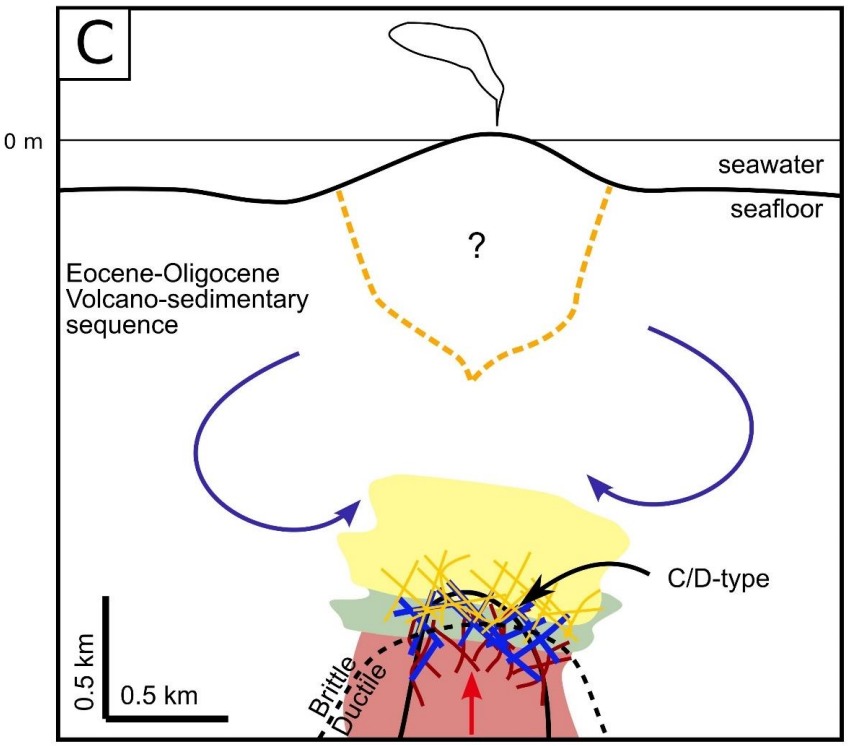
C
0 m
seawater
seafloor
?
Eocene-Oligocene
Volcano-sedimentary
sequence
C/D-type
0.5 km
0.5 km
Brittle
Ductile

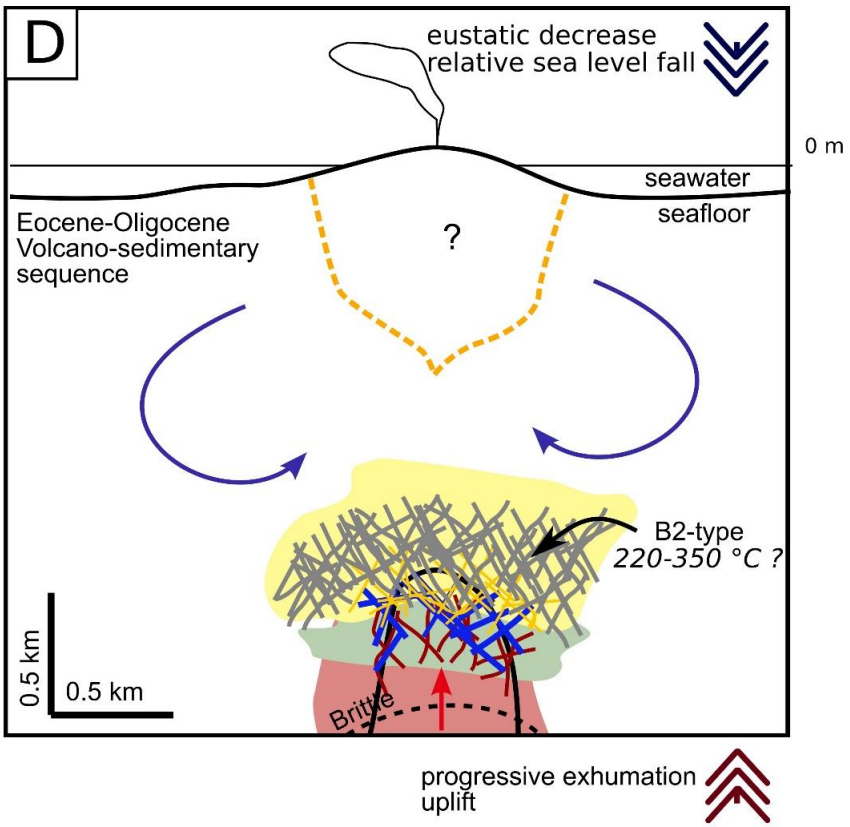
D
eustatic decrease
relative sea level fall
0 m
seawater
seafloor
?
Eocene-Oligocene
Volcano-sedimentary
sequence
B2-type
220-350 °C ?
0.5 km
0.5 km
Brittle
progressive exhumation
uplift

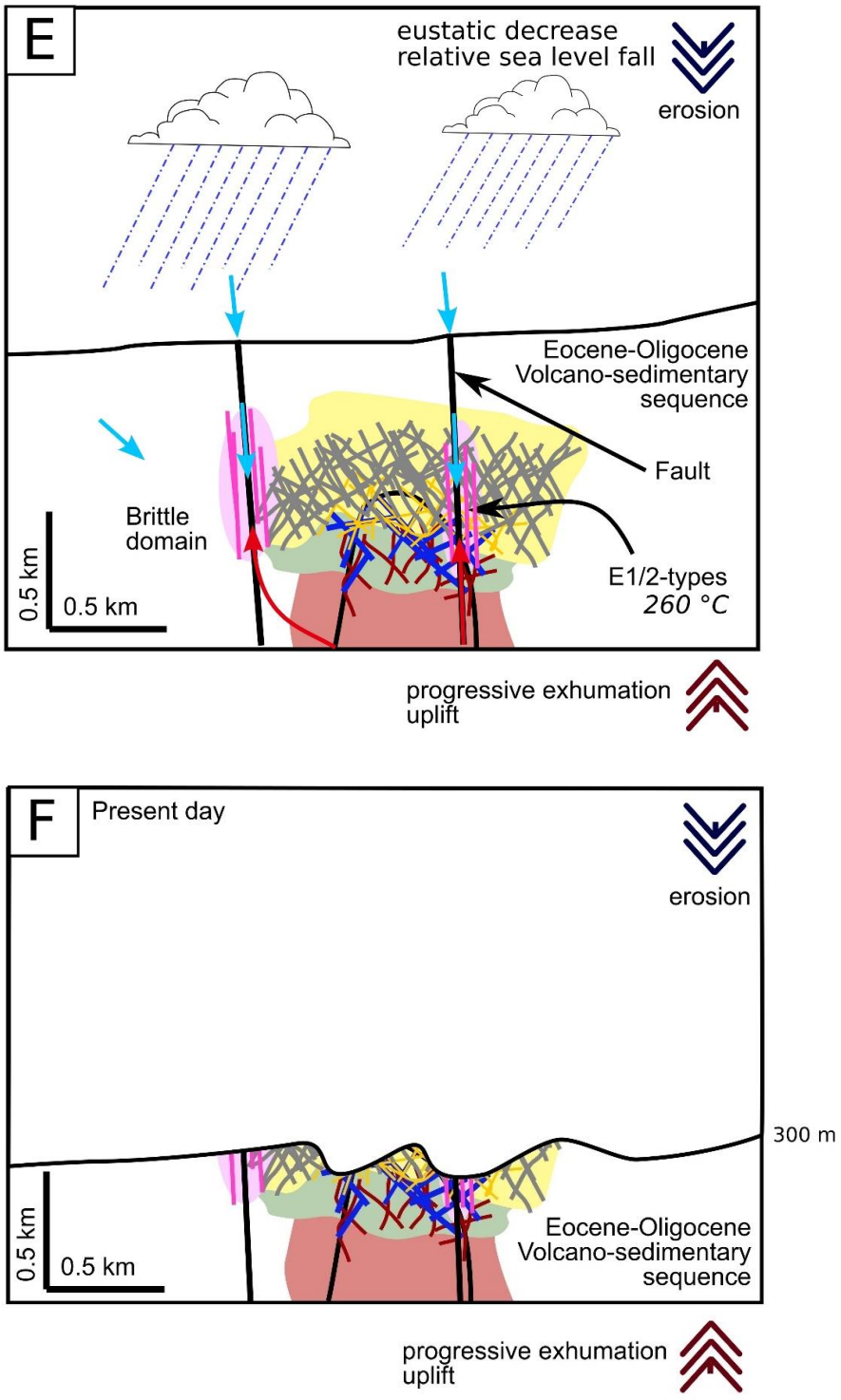

Figure 96: Coupe schématique E-O du système porphyre-épithermal de Pagoni Rachi. A. Des fluides magmatiques sont exsolvés à des températures élevées et sous des pressions passant du régime lithostatique au régime hydrostatique. Dans ces conditions, les veines précoces de type A se forment. B. Les veines de type B1 se forment à partir de fluides similaires qui subissent un refroidissement et une dépressurisation à des températures et pressions plus basses. C. Les fluides continuent à se refroidir sous des pressions hydrostatiques, ce qui favorise une diminution de leur pH. Cela conduit au développement des altérations chlorite-séricitique et séricitique ainsi qu'à la formation des veines de types C et D, associées à la précipitation de la minéralisation à Cu-Mo-Au-Re. D. Un phénomène de « flashing » des fluides engendre la formation d'un stockwork dense massive de quartz stérile, représenté par les veines de type B2. E. Les veines sub-épithermales de type E1/2 précipitent des sulfures, principalement associés à des minéralisations de Pb-Zn-Cu. Ces veines se forment à des températures et pressions plus basses, en lien avec des zones de failles. F. Situation à l'actuel, après érosion

Les premières manifestations hydrothermales sont liées à l'incursion d'un fluide magmatique de haute température (~ 490°C), montrant une séparation de phase, formant des veines précoces à quartz et à magnétite (type et A et M) (e.g. Sillitoe, 2010 ; Seedorf, 2005 ; Richards, 2015) (Figure 96 A). Ces veines présentent des textures ondulantes, discontinues, typiques de conditions ductiles avec recristallisation dynamique des cristaux de quartz (e.g. GBM, SGR). Ce fluide se caractérise par une salinité originelle proche de ~ 14 $\%wt_{équivalentNaCl}$, une signature isotopique proche de celle des eaux primaires magmatiques (δD = ~ -25 ‰, $\delta^{18}O$ = ~ +7 ‰) (e.g. Taylor, 1974), et une association avec une altération potassique de la roche encaissante reflète une origine magmatique dominante (Sillitoe, 2010). La textures des veines, traduisent des conditions lithostatiques à une profondeur estimée entre 1,5 et 2,0 km (Figure 96 A). En effet à des températures supérieures à 400 °C et des taux de déformation inférieurs à 10^{-14}/s, les roches de composition quartz-diorite se comportent de manière quasi-plastique, ce qui rend la fracturation fragile difficile et permet aux pressions des fluides d'approcher les valeurs lithostatiques (Fournier, 1991, 1999 ; Muntean and Einaudi, 2001). L'altération associée est majoritairement potassique, bien que des signatures d'altération sodi-calcique soient également observées, témoignant de l'influence de plusieurs sources hydrothermales (Figure 96).

Un deuxième épisode fluide de plus basse température (~ 400 °C) est accompagné d'une séparation de phase. La mise en place de veines droites, continues, avec des structures de croissance syntaxiale, avec des quartz présentant des textures de recristallisation dynamique d'intensité intermédiaire et local (SGR, BLG) est interprété comme le résultat d'un régime de déformation à la transition ductile/cassant, et d'un régime de pression évoluant depuis des conditions lithostatiques à hydrostatiques (e.g. Stipp et al., 2002a,b ; Monecke et al., 2018 ; Acosta et al., 2020, 2022) (Figure 96 B). A mesure que l'intrusion magmatique refroidit, cette transition ductile/cassant se déplace progressivement vers de plus grandes profondeurs (Figure 96 B). Cette transition est également marquée par un mélange progressif entre des fluides magmatiques et de l'eau de mer. L'origine de l'eau de mer peut être de la présence d'une tranche d'eau de mer en surface, avec une percolation au travers les sédiments ou bien d'eau de mer piégée dans les sédiments marins éocènes (anté-Priabonien), remobilisée par une convection hydrothermale par des circulations induites lors de la mise en place du pluton (Figure 96 B). La salinité des fluides, passant de ~14 à ~11 $\%wt_{équivalentNaCl}$, témoigne d'une dilution progressive comme en témoigne les valeurs isotopiques de fluides (δD = ~ -10 ‰, $\delta^{18}O$ = ~ +5 ‰), se rapprochant du pôle de l'eau de mer. L'altération sodi-calcique, marquée par la présence d'albite, de chlorite, d'épidote et d'actinote, est omniprésente, confirmant une influence croissante de l'eau de mer dans l'évolution du système hydrothermal (e.g. Gustafson 1978). Ceci est cohérent avec la mise en place du système situé (avant 32 Ma) au sein du bassin sédimentaire marin de Kirki-Esimi (e.g. Caracciolo et al., 2011, 2012, 2015 ; Mavrogonatos et al., 2020).

Les conditions de températures, pressions, et pH de circulation fluide diminuent tout en restant en domaine hydrostatique et cassant. Cette variation de conditions physico-chimiques est associée au développement d'une altération séricitique intense, pervasive observée sur le terrain, et à la mise en

place des veines et réouvertures minéralisées de type C/D (Figure 96 C). La formation de telles structures est souvent interprétée comme la transition entre la partie porphyre et la partie épithermale. La partie épithermale évoluée avec une minéralisation de haute sulfuration et vuggy silica, comme observée dans les prospects voisins (e.g. Konos Hill, St Demetrios, Viper, St Barbara), aurait complétement été érodé à Pagoni Rachi. Aujourd'hui aucune observation permet d'affirmer si une telle structure ait ou non existée (e.g. Voudouris et al., 2013a) (Figure 96 C).

Par une baisse de température des conditions de circulation de fluide, le système évolue vers un environnement hydrostatique à plus faible profondeur, entre 0.5 et 1.5 km. À ce stade, des veines de type B2 se forment à des températures comprises entre 220 et 350°C (e.g. Muntean and Einaudi, 2001) (Figure 96 D). Comme proposé par Muntean et Einaudi (2000), les veines de quartz rubanées comme les type B1 et B2 se forment lors de la rupture de la frontière ductile-fragile à basse pression (Figure 96 B, D). Ces veines, stériles, traduisent des conditions de « flashing » et de séparation de phases (e.g. Muntean and Einaudi, 2000, 2001), où l'influence de l'eau de mer devient dominante. La signature isotopique de ces fluides est proche de celle de l'eau de mer contemporaine, ce qui suggère une dilution importante de fluides magmatiques par des fluides marins. Ceci est cohérent avec le développement du système porphyre sous une tranche d'eau de mer, ou alors au sein de sédiments dont les eaux connées ont une signature marine (Figure 96 D). Les fluides associés aux veines type B2 devraient présenter une salinité plus faible que les veines type B1. Les veines de la partie porphyre présente une signature isotopique traduisant un mélange continu et progressif entre des fluides magmatiques et de l'eau de mer. Le contexte géologique au Priabonien en Thrace occidentale paraît très similaire au contexte actuel des Cyclades. Ainsi il est possible que l'eau de mer en Thrace occidentale lors de la formation du système porphyre de Pagoni Rachi ait des valeurs isotopiques similaire à celle de l'actuelle Mer Egée eau de mer (Eau de mer mesurée à lîle de Mylos est à $\delta D \sim +7$ ‰ et $\delta^{18}O \sim +2$ ‰ (Price et al., 2013)) et donc montre un mélange entre un pôle de mer impactée par de l'évaporation (valeurs isotopiques positives), et du fluide magmatique en faible quantité. La salinité originelle du fluide devrait donc se situer entre celle de l'eau de mer, soit 3.5 wt% equiv NaCl et celle des veines de type B1, au vu de la proportion croissante de l'eau de mer dans les mélanges des fluides. La composition du fluide calculée serait proche de 90% d'une eau de mer, ce qui par ailleurs, en considérant l'origine des métaux comme étant magmatiques, est cohérent avec une absence (ou une faible concentration) de métaux dans les veines type B2 décrites comme stériles.

Lorsque le système atteint des conditions superficielles, l'influence des eaux météoriques devient prédominante cette fois-ci. La circulation d'eaux météoriques dans un contexte continental, participent à la mise formation de veines épithermales à quartz (E1) et à calcite (E2) (Figure 96 E). Les fluides présentent des salinités comprises entre 1,0 et 3,0 $wt\%_{équivalentNaCl}$ et des températures proches de 250 °C. Les signatures isotopiques des fluides à l'origine des veines épithermales indiquent une dilution progressive des fluides magmatiques par des eaux météoriques à faible et δD, $\delta^{18}O$, s'accompagnant alors d'une diminution du δD, $\delta^{18}O$ et une légère augmentation du $\delta^{13}C$. La dernière génération de calcite

suggère un retour vers une signature magmatique, montrant une dynamique des fluides et des conditions transitoires de circulation de fluide et donc de formation de veine. La signature météorique de ces fluides est cohérente avec la signature actuelle des eaux météorique de l'île de Mylos, dans le Péloponnèse, avec des valeurs δD = -25 ‰ et $\delta^{18}O$ = -4 ‰ (e.g. Price et al., 2013). Bien que ces données n'apportent que de larges contraintes, les valeurs isotopiques des réservoirs impliqués dans la formation successive de veines sont similaires aux valeurs isotopiques des réservoirs actuels, dans un contexte géologique similaire. Les accidents tectoniques locaux, orientés principalement NNW-SSE, jouent un rôle clé en favorisant la localisation et l'orientation des veines épithermales, dans un contexte de contrainte locale favorable à la formation de fractures en ouvertures et à faciliter la circulation des fluides et leurs mélanges en faisant office de drains (Figure 96 E). Il est envisageable que la succession dynamique des veines à calcite puisse faire suite au rejeu des accidents locaux, à des pulses magmatiques, et à des relâchements des contraintes permettant la précipitation de veines à calcite. Cet événement entraine la formation des veines tardives épithermales recoupant l'ensemble des précédentes veines (Figure 96 E), avec l'omniprésence d'inclusions fluides biphasées (overlap) à dominante liquide de faible salinité et basse température dans le quartz des veines associées au système porphyre.

Les fluides hydrothermaux responsables des minéralisations dans ce système porphyre-épithermal télescopé proviennent d'un mélange complexe de sources magmatiques, marines et météoriques. Les métaux tels que le cuivre, le molybdène et le rhénium peuvent trouver leur origine dans des fluides magmatiques profonds, avec un enrichissement par des processus de contamination crustale ayant pu impliquer des sédiments encaissants (Schaarschmidt et al., 2021). Il est peu probable que la source de ces métaux puisse être les eaux météoriques ou alors l'eau de mer (peu chargés), il est néanmoins possible que des interactions fluide-roche des eaux de surface aient permis un enrichissement en métaux, notamment par la circulation de fluides au sein de sédiments riches en matière organique (ex. charbon) (e.g. Caracciolo, 2015). La concentration en métaux tels que le plomb, le zinc et l'argent associés à la minéralisation de type sub-épithermal semble résulter d'une interaction entre des fluides magmatiques et météoriques, avec un processus de fractionnement des métaux lors d'une séparation de phase (en profondeur), circulation et condensation de la phase vapeur.

Le modèle proposé pour le système porphyre-épithermal de Pagoni Rachi repose sur une succession d'événements de pulses magmatiques et hydrothermaux (Figure 96). Les phases magmatiques initiales, associées à la mise en place (1) d'une granodiorite et (2) à des pulsations répétées de fluides magmatiques, pouvant être associée à une succession d'intrusions en partie plus profonde ou de petite taille ayant engendrés des veines minéralisées à haute température (veines de type A et B2) puisque le système n'est pas réchauffé à chaque influx de fluides magmatique. Ce qui est géologiquement cohérent avec la mise en place d'un batholite profond et l'incursion d'autres magmas dans la région (e.g. dykes rhyolitiques, Figure 16, Figure 23), en lien avec l'amincissement crustal, une subduction et retrait du slab vers le Sud (Schaarschmidt et al., 2021) en contexte d'arc (Maravellis, 2012, 2015 ; Caracciolo, 2015). Les métaux présents dans la partie porphyre et la partie épithermal proviennent

vraisemblablement de fluides magmatiques profonds. Ce modèle rejoint celui suggéré par Muntean and Einaudi (2001) pour des gisements de la Maricunga Belt, bien que des particularités locales telles que l'influence omniprésente de l'eau de mer et le télescopage des structures (altérations et veines) à Pagoni Rachi. Ces veines sont suivies par des événements superficiels où l'influence d'eaux météoriques devient dominante, aboutissant à la formation de veines épithermales.

CHAPITRE 7. CONCLUSIONS ET PERSPECTIVES

Ce travail de thèse a permis d'apporter de meilleures connaissances et contraintes sur la structure du site de Pagoni Rachi qui présente alors un gisement de type porphyre à Cu-Mo (Re-Au) et sub-épithermal à Pb-Zn, télescopé, et se présente sous la forme d'un stockwork minéralisé en métaux caractéristiques de ces systèmes, alors encaissé dans une granodiorite altérée. L'étude de terrain et pétrographique ont permis la description et la spatialisation d'une succession de veines caractéristiques des systèmes de type porphyre-épithermal, plus complexe que ce qui est décrit dans la littérature (e.g. Voudouris et al., 2013a) avec des veines type : A/M ondulantes à quartz-hématite-pyrite/magnétite-hématite, B1 droites à quartz, C en réouvertures des veines précédentes, à chalcopyrite-molybdénite ± rhéniite, D à pyrite massive, B2 rubanées en stockwork massif en partie sommitale du système, E1 à quartz-calcite-sphalérite-galène, et E2 à calcite-pyrite associées à un système sub-épithermal tardif.

L'imagerie des veines de quartz par cathodoluminescence, combinée à une observation des microtextures des cristaux de quartz des veines de Pagoni Rachi, révèle la présence de réouvertures de veines, une croissance oscillatoire des cristaux de quartz, ainsi que des textures de recristallisation dynamique des cristaux de quartz témoignant d'une transition progressive d'un domaine de déformation chaud-ductile (~600 °C) à froid-cassant (<250 °C). Il en a été conclu que cette déformation, lorsque de haute intensité, implique une mobilité du titane dans le quartz qui présentent alors des textures typiques de recristallisation dynamique des cristaux de quartz, comme les textures GBM, et des textures CL en ghostbands et mottled. La mobilité du Ti par diffusion et la cristallisation du quartz hors équilibre rend impossible l'utilisation du thermomètre du Ti-in-quartz, qui donne des valeurs de température calculé de formation de quartz incohérente avec les données d'inclusions fluides. De plus, ce décalage a pour effet de produire des observations impliquant de mauvaises interprétations, lors de la lecture de diagramme de classification élémentaire utilisant les rapports Al/Ti et Ge/Ti, communément utilisé dans la littérature (e.g. Rottier and Casanova 2021).

L'étude des inclusions fluides dans le quartz indique une circulation continue de fluides pendant la cristallisation et la recristallisation du quartz, marquée par une ébullition autour de 490 °C, pour les veines de type A, vers des températures pouvant être inférieur à 350°C pour les veines de type B2 (d'après le modèle de Muntean and Einaudi, 2001), puis par un refroidissement et une dilution par des fluides météoriques liés à l'événement épithermal à métaux critiques. L'évolution des fluides montrent et une mise en place de veine de conditions de pression lithostatique à hydrostatique, associée à la formation de la minéralisation à Cu, Mo, et Re.

La combinaison des données d'isotopes stables de l'oxygène, de l'hydrogène, et du carbone ainsi que la quantification des éléments traces des minéraux de gangue des différentes veines montre que la mise en place du système de type porphyre évolue d'un domaine de magmatisme sous-marin en contexte d'arc vers un domaine continental dominé par les eaux météoriques. En effet, la signature géochimique des fluides évolue depuis un pôle magmatique vers un pôle d'eau de mer, avec un mélange progressif des veines de type A à B2. Cette variation d'origine et de composition de fluide est soutenu par le

développement d'une altération sodi-calcique en partie centrale du porphyre en surimpression d'une altération potassique de la granodiorite encaissante. Une incursion de fluides mixtes est alors responsable des réouvertures des précédentes veines, et de la précipitation des minéraux porteurs de métaux, tels que la chalcopyrite, bornite, molybdénite, et la rhéniite. Une incursion tardive d'eau météorique et d'un mélange avec des fluides magmatiques associée à la formation de failles et à un phénomène d'uplift avec les veines type E1 et E2. Cette incursion de fluide est également marquée par une de baisse de température, de pH, et de pression des fluides, qui est alors associé au développement d'une altération séricitique intense pervasive voire à de l'altération argillique associée à la présence. Ce processus est ensuite suivi par une érosion exposant le gisement à la surface.

Les systèmes hydrothermaux sous-marins, déjà décrits dans des travaux classiques (Gustafson et Hunt 1975 et références), sont essentiels pour comprendre la formation des gisements porphyres-épithermaux. À Pagoni Rachi, les observations récentes ont mis en lumière la présence de processus tels que la recristallisation dynamique des cristaux de quartz (e.g. Acosta et al., 2020, 2022), identifiés grâce à l'imagerie CL et l'étude des microtextures associées. Les observations de textures caractéristiques de cristallisation hors équilibre, évoquée notamment par Rottier and Casanova (2021), montrent l'influence significative de tels processus dans l'incorporation et de la distribution des éléments traces dans les cristaux de quartz. Cependant, définir précisément les conditions pression-température-chimie (*PTX*) reste un défi, tout comme déterminer dans quelle mesure le quartz est un bon traceur du contenu en éléments traces des fluides hydrothermaux.

Le rôle des éléments traces dans le quartz, exploré (Rottier and Casanova, 2021 ; Tanner et al., 2013 ; et d'autres), offre une perspective précieuse pour comprendre les interactions fluide-minéral. Toutefois, ces études révèlent que les conditions influençant un élément ou un cortège d'éléments sont multiples et complexes. Ainsi, les analyses doivent être systématiquement complétées par des observations de terrain et d'autres approches géologiques. Bien que le quartz soit considéré comme un bon traceur, des limites apparaissent, notamment liées aux déséquilibres lors de sa cristallisation et à la variabilité des conditions de formation et de déformation.

Pour compléter l'étude, plusieurs pistes de recherche peuvent être explorées afin d'apporter de meilleurs contraintes *PVTtX*:

Chronologie absolue : À Pagoni Rachi, la chronologie des événements reste mal contrainte. Ni la granodiorite hôte, ou corps magmatiques à proximité (rhyolite), ni les sédiments associés, ni les minéraux directement liés à la minéralisation n'ont été datés. Une datation U-Pb sur zircon dans la granodiorite ou sur calcite dans les veines de type E2 ou datation Re/Os de la molybdénite, une datation Ar-Ar ou K-Ar sur des minéraux d'altération (ex. biotite) permettrait de dater l'altération associé à la minéralisation, souvent contemporaine du magmatisme et de la minéralisation pourrait fournir des bornes temporelles précises.

Étude structurale détaillée : Des mesures systématiques des linéations et des plans de fracture permettraient de mieux comprendre le contrôle structural éventuel et spatiale sur la minéralisation. Une observation détaillée sur terrain du contact entre les veines de type B2 et les veines antérieures de type A et B1, permettrai d'améliorer la chronologie de la formation des veines successives.

Géochimie des altérations : Une analyse élémentaire des roches encaissantes, permettrait de contraindre le type d'altération et l'évolution des concentrations élémentaires, alors témoins des interactions fluide-roche (e.g. Höss et al., 2024). Des études sur les sulfures, comme celles de Höss et al. (2024) et Falkenberg et al. (2024), pourraient également apporter des informations sur les processus métallogéniques.

Inclusions fluides : Les différents types de veines issus de la nouvelle classification dont les conditions de formations sont également mal contraintes (e.g. type B2). Une étude plus approfondie des inclusions fluides pourrait clarifier l'évolution des fluides et notamment déterminer les conditions *PT* de formation (T_h, *P*, salinité) des veines.

Origine des métaux : La quantification des éléments traces (et notamment les métaux) dans les inclusions fluides (e.g. M. Bitte (*rapport interne*) contenu dans les cristaux de quartz des différentes veines permettrai d'évaluer le fractionnement élémentaire entre le fluide et les cristaux de quartz, alors associé à la minéralisation, tout au long de la formation du système de type porphyre-épithermal de Pagoni Rachi. La caractérisation des événements magmatiques décrit comme responsables de l'apport de métaux devraient également être étudié. L'étude des différents corps magmatiques, montrant des degrés de différenciation différent et formés dans un contexte d'amincissement de croute et d'une origine commune, qu'est le manteau métasomatisé, permettrait l'évaluation de l'impact cette différenciation magmatique sur la distribution en métaux des gisements porphyre-épithermaux de la région.

Ces différents points d'intérêt, portant sur la chronologie des différents corps magmatiques et des minéralisations, les relations géométriques des différentes structures (microstructurale et échelle régionale), l'évolution du contenu en métaux des fluides depuis les parties profondes (magma) jusqu'aux parties les plus superficielles (systèmes épithermaux), et une caractérisation des sources des fluides (du prospect à la région de la Thrace occidentale) vont être étudiées et évaluées à travers le projet ANR-DFG HERMES (Hydrothermal Economic Resources in Magmatic EnvironmentS) et qui permettra à deux doctorants des Universités de Lorraine (Nancy - FR) et d'Erlangen (DE) d'apporter de nouvelles contraintes sur les modèles de formation de ces systèmes atypiques.

Bien que des progrès significatifs aient été réalisés dans la compréhension des systèmes de type porphyre-épithermal, chaque méthode présente des limites. Une approche intégrative, combinant observations de terrain, analyses pétrographiques, datations absolues, et géochimie des altérations, reste essentielle pour résoudre les questions ouvertes. Ces recherches permettront non seulement d'affiner la

compréhension des processus hydrothermaux, mais aussi de développer des outils plus robustes pour explorer et exploiter les ressources minérales.

RÉFÉRENCES BIBLIOGRAPHIQUES

Abiven, B., Tarantola, T., Richard, A., Keith, M., Melfos, V., Voudouris, P., submitted in December 2025. Effect of Disequilibrium Crystallization and Dynamic Recrystallization on Ti-in-Quartz Thermometry in Porphyry-Epithermal Deposits: Insights from Pagoni Rachi (NE Greece). Lithos.

Acosta, M.D., 2020. Titanium in quartz during growth and deformation under hydrothermal-magmatic conditions – Thesis.

Acosta, M.D., Reed, M.H., & Watkins, J.M., 2022. Quartz Vein Formation and Deformation during Porphyry Cu Deposit Formation: A Microstructural and Geochemical Analysis of the Butte, Montana, Ore Deposit. Lithosphere, 2022(1), 3196601.

Allan, M.M., & Yardley, B.W., 2007. Tracking meteoric infiltration into a magmatic-hydrothermal system: A cathodoluminescence, oxygen isotope and trace element study of quartz from Mt. Leyshon, Australia. Chemical Geology, 240(3-4), 343-360.

Altherr, R., & Siebel, W., 2002. I-type plutonism in a continental back-arc setting: Miocene granitoids and monzonites from the central Aegean Sea, Greece. Contributions to Mineralogy and Petrology, 143(4), 397-415. https://doi.org/10.1007/s00410-002-0352-y.

Anders, B., Reischmann, T., Kostopoulos, D., 2006. The oldest rocks of Greece: first evidence for a Precambrian terrane within Pelagonian Zone. Geol. Mag. 143, 41-58.

Annen, C., 2009. From plutons to magma chambers: Thermal constraints on the accumulation of eruptible silicic magma in the upper crust. Volume 284, Issues 3-4, p409-416. https://doi.org/10.1016/j.epsl.2009.05.006.

Arancibia, O.N., & Clark, A.H., 1996. Early magnetite-amphibole-plagioclase alteration-mineralization in the Island Copper porphyry copper-gold-molybdenum deposit, British Columbia. Economic Geology, 91(2), 402-438.

Arikas, K., 1979a. Geologische und petrographische Untersuchungen in der Umgebung von Kirki (Thrakien, Nordgriechenland). Mitt. Geol.-Paläont. Inst. Univ. Hamburg49, 1-26.

Arikas, K., 1979b. Ein porphyrisches Mo−Cu-Vorkommen bei Kirki (Thrakien, Nordgriechenland). N. Jb. Min. Abh.137, 74-82.

Arikas, K., 1981. Subvulkanisch-hydrothermale Mo− Cu− Zn− Pb-Vererzungen, SE Rhodopen, Nordgriechenland: Petrographie und Geochemie. Tschermaks mineralogische und petrographische Mitteilungen, 28(3), 189-205.

Arikas, K., & Voudouris, P., 1998. Hydrothermal alterations and mineralizations of magmatic rocks in the southeastern Rhodope massif. Acta Vulcanologica, 10, 353-366.

Ashley, K.T., Carlson, W.D., Law, R.D., & Tracy, R.J., 2014. Ti resetting in quartz during dynamic recrystallization: Mechanisms and significance. American Mineralogist, 99(10), 2025-2030.

d'Atri, A., Zuffa, G.G., Cavazza, W., Okay, A.I., & Di Vincenzo, G., 2012. Detrital supply from subduction/accretion complexes to the Eocene–Oligocene post-collisional southern Thrace Basin (NW Turkey and NE Greece). Sedimentary Geology, 243, 117-129.

Audétat, A., & Günther, D., 1999. Mobility and H2O loss from fluid inclusions in natural quartz crystals. Contributions to Mineralogy and Petrology, 137(1), 1-14.

Audétat, A., Pettke, T., and Dolejš, D., 2004. Magmatic anhydrite and calcite in the ore-forming quartz-monzodiorite magma at Santa Rita, New Mexico (USA): Genetic constraints on porphyry-Cu mineralization: Lithos, v. 72, p. 147-161.

Audétat, A., and Simon, A. C., 2012. Magmatic controls on Porphyry Copper Genenis. Society of Economic Geologists, Inc. Special Publication 16, pp. 553–572

Audétat, A., Garbe-Schönberg, D., Kronz, A., Pettke, T., Rusk, B., Donovan, J.J., & Lowers, H.A. 2015. Characterisation of a natural quartz crystal as a reference material for microanalytical determination of Ti, Al, Li, Fe, Mn, Ga and Ge. Geostandards and Geoanalytical Research, 39(2), 171-184.

Audétat, A. 2019. The Metal Content of Magmatic-Hydrothermal Fluids and Its Relationship to Mineralization Potential. Society of Economic Geologists, Inc. Economic Geology, v. 114, no. 6, pp. 1033–1056

Audétat, A., 2023. A plea for more skepticism toward fluid inclusions: part II. Homogenization via halite dissolution in brine inclusions from magmatic-hydrothermal systems is commonly the result of postentrapment modifications. Economic Geology, 118(1), 43-55.

Le Bas, M.L., Maitre, R.L., Streckeisen, A., Zanettin, B., & IUGS, 1986. Subcommission on the Systematics of Igneous Rocks. A chemical classification of volcanic rocks based on the total alkali-silica diagram. Journal of petrology, 27(3), 745-750.

Barra, F., Alcota, H., Rivera, S., Valencia, V., Munizaga, F., & Maksaev, V., 2013. Timing and formation of porphyry Cu–Mo mineralization in the Chuquicamata district, northern Chile: new constraints from the Toki cluster. Mineralium Deposita, 48(5), 629-651.

Beane, R. and Titley, S., 1981. Economic Geology, Seventy-fifth Anniversary Volume, 1905-1980, 214.

Bennett, M.M., 2014. Cathodoluminescence and fluid inclusion characteristics of hydrothermal quartz from porphyry deposits. Colorado School of Mines.

Bestmann, M., Pennacchioni, G., Grasemann, B., Huet, B., Jones, M.W., and Kewish, C.M., 2021. Influence of deformation and fluids on Ti exchange in natural quartz. Journal of Geophysical Research: Solid Earth, vol. 126, no. 12.

Beurlen, H., Muller, A., Silva, D., & Da Silva, M.R.R., 2011. Petrogenetic significance of LA-ICP-MS trace-element data on quartz from the Borborema Pegmatite Province, northeast Brazil. Mineralogical Magazine, 75(5), 2703-2719.

Blevin, P.L., & Chappell, B. W., 1995. Chemistry, origin, and evolution of mineralized granites in the Lachlan fold belt, Australia; the metallogeny of I-and S-type granites. Economic Geology, 90(6), 1604-1619.

Blevin, P.L., 2004. Redox and compositional parameters for interpreting the granitoid metallogeny of eastern Australia: Implications for gold-rich ore systems. Resource Geology, 54(3), 241-252.

Blevin, P., Chappell, B., & Jeon, H., 2010. Heat generating potential of igneous rocks within and underlying the Sydney Basin: some preliminary observations. In Proceedings of the 37th symposium of the geology of the Sydney Basin.

Bodnar, R.J., 1993. Revised equation and table for determining the freezing point depression of H2O-NaCl solutions. Geochimica et Cosmochimica acta, 57(3), 683-684.

Bodnar, R.J., Lecumberri-Sanchez, P., Moncada, D., & Steele-MacInnis, M., 2014. Fluid inclusions in hydrothermal ore deposits. Treatise on geochemistry, 13, 119-142.

Bonev, N., Burg, J.P., Ivanov, Z., 2006a. Mesozoic-Tertiary structural evolution of an extensional gneiss dome – the Kesebir-Kardamos dome, E. Rhodopes, Bulgaria. Int. J. Earth Sci. 95, 318-340.

Bonev, N., Marchev, P., Singer, B., 2006b. 40Ar/39Ar geochronology constraints on the Middle Tertiary basement extensional exhumation, and its relation to oreforming and magmatic processes in the Eastern Rhodope (Bulgaria). Geodin. Acta 19, 265–280.

Bonev, N., Moritz, R., Márton, I., Chiaradia, M., Marchev, P., 2010. Geochemistry, tectonics, and crustal evolution of basement rocks in the Eastern Rhodope Massif, Bulgaria. Int. Geol. Rev. 52, 269-297.

Bonev, N., Spikings, R., Moriz, R., Marchev, P., 2013. 40Ar/39Ar age constraints on the timing of Tertiary crustal extension and its temporal relation to ore-forming and magmatic processes in the Eastern Rhodope Massif, Bulgaria. Lithos 180-181, 264-278.

Bonsall, T.A., Spry, P.G., Voudouris, P., Tombros, S., Seymour, K., Melfos, V., 2011. The geochemistry of carbonate-replacement Pb-Zn-Ag mineralization in the Lavrion District, Attica, Greece: fluid inclusion, stable isotope, and rare earth element studies. Econ. Geol. 106, 619-651.

Bowman, J.R., Willett, S.D., & Cook, S.J. 1987. Oxygen isotopic transport and exchange during fluid flow: One-dimensional models and applications. American Journal of Science, 287(7), 755-787. DOI: 10.2475/ajs.287.7.755.

Bowman, J.R., 1998. Stable-isotope systematics of skarn. In: Lentz, D.R. (Ed.), Mineralized Intrusion-Related Skarn Systems. vol. 26. Mineralogical Association of Canada, pp. 99–145 (Short Course).

Boydell, H.C., 1924. The role of colloidal solutions in the formation of mineral deposits. Massachusetts Institute of Technology, Department of Mining, Metallurgy and Geology.

Brathwaite, R.L., Simpson, M., Faure, K., & Skinner, D.N.B., 2001. Telescoped porphyry Cu-Mo-Au mineralisation, advanced argillic alteration and quartz-sulphide-gold-anhydrite veins in the Thames District, New Zealand. Mineralium Deposita, 36, 623-640.

Breiter, K., Ďurišová, J., & Dosbaba, M., 2017. Quartz chemistry–A step to understanding magmatic-hydrothermal processes in ore-bearing granites: Cínovec/Zinnwald Sn-W-Li deposit, Central Europe. Ore Geology Reviews, 90, 25-35.

Breiter, K., Ďurišová, J., & Dosbaba, M., 2020. Chemical signature of quartz from S-and A-type rare-metal granites–A summary. Ore Geology Reviews, 125, 103674.

Bromiley, G.D., & Hiscock, M., 2016. Grain boundary diffusion of titanium in polycrystalline quartz and its implications for titanium in quartz (TitaniQ) geothermobarometry. Geochimica et Cosmochimica Acta, 178, 281-290.

Brun, J.P., & Sokoutis, D., 2007. Kinematics of the southern Rhodope core complex (North Greece). International Journal of Earth Sciences, 96, 1079-1099.

Brun, J.P., Faccenna, C., 2008. Exhumation of high-pressure rocks driven by slab roll-back. Earth Planet. Sci. Lett. 272, 1-7.

Brun, J.P., Faccenna, C., Gueydan, F., Sokoutis, D., Philippon, M., Kydonakis, K., & Gorini, C., 2016. The two-stage Aegean extension, from localized to distributed, a result of slab rollback acceleration. Canadian journal of earth sciences, 53(11), 1142-1157.

Brun, J.P., & Sokoutis, D., 2018. Core complex segmentation in North Aegean, a dynamic view. Tectonics, 37(6), 1797-1830.

Burg, J.P., 2012. Rhodope: From Mesozoic convergence to Cenozoic extension. Review of petro-structural data in the geochronological frame. J. Virtual Explor, 42(1).

Burnham C.W., 1979. Magmas and hydrothermal fluids. Geochemistry of Hydrothermal Ore Deposits. 71-136.

Burnham, C.W., and Ohmoto, H., 1980. Late-stage processes in felsic magmatism: Mining Geology Special Issue, No. 8, p. 1-11.

Burnham, C.W., 1985. Energy release in subvolcanic environments; implications for breccia formation. Economic geology, 80(6), 1515-1522.

Campbell, A.R., & Larson, P.B. 1998. Introduction to stable isotope applications in hydrothermal systems. In J.P. Richards & P.B. Larson (Eds.), Techniques in Hydrothermal Ore Deposits Geology (pp. 1-12). Society of Economic Geologists.

Camprubí, A., Ferrari, L., Cosca, M.A., Cardellach, E., and Canals, À., 2003. Ages of epithermal deposits in Mexico: Regional significance and links with the evolution of Tertiary volcanism: ECONOMIC GEOLOGY, v. 98, p. 1029-1037.

Camprubí, A., & Albinson, T., 2006. Depósitos epitermales en México: actualización de su conocimiento y reclasificación empírica. Boletín de la Sociedad Geológica Mexicana, 58(1), 27-81.

Camus F., 2003. Geología de los sistemas porfíricos en los Andes de Chile Servicio Nacional de Geología y Minería, Santiago.

Candela, P.A. et Holland, H.D. 1984. The partitioning of Cu and Mo between silicate melts and aqueous fluids. GEOCHIM COSMOCHIM ACTA 48, 373-80.

Candela P.A., 1992. Physics of aqueous phase evolution in plutonic environments. American Mineralogist (1991) 76 (7-8): 1081-1091.

Capasso, G., Favara, R., & Inguaggiato, S. 1997. Chemical and isotopic studies of rainfall in the central Mediterranean: Implications for the origin of sulphate and nitrate in rainfall. Atmospheric Environment, 31(5), 757-766. DOI: https://doi.org/10.1016/S1352-2310(96)00241-8.

Caracciolo, P.C., Buffa, F., & Abraham, G.A., 2009. Effect of the hard segment chemistry and structure on the thermal and mechanical properties of novel biomedical segmented poly (esterurethanes). Journal of Materials Science: Materials in Medicine, 20, 145-155.

Caracciolo, L., Critelli, S., Innocenti, F., Kolios, N., Manetti, P., 2011. Unravelling provenance from Eocene-Oligocene sandstones of the Thrace Basin, North-east Greece. Sedimentology 58,1988-2011. https://doi.org/10.1111/j.1365-3091.2011.01248.x.

Caracciolo, L., Von Eynatten, H., Tolosana-Delgado, R., Critelli, S., Manetti, P., & Marchev, P., 2012. Petrological, geochemical, and statistical analysis of Eocene–Oligocene sandstones of the Western Thrace basin, Greece and Bulgaria. Journal of Sedimentary Research, 82(7), 482-498.

Caracciolo, L., Critelli, S., Cavazza, W., Meinhold, G., von Eynatten, H., & Manetti, P., 2015. The Rhodope Zone as a primary sediment source of the southern Thrace basin (NE Greece and NW Turkey): evidence from detrital heavy minerals and implications for central-eastern Mediterranean palaeogeography. International Journal of Earth Sciences, 104, 815-832.

Carrigan, C.R., Schubert, G., and Eichelberger, J.C., 1992. Thermal and dynamical regimes of single- and two-phase magmatic flow in dikes: Journal of Geophysical Research, v. 97, p. 17,377-17,392, https:// doi .org /10 .1029 / 92JB01244.
Carson, D.J., Jambor, J.L., Ogryzlo, P., & Richards, T.A., 1976. Bell copper: Geology, geochemistry and genesis of a supergene-enriched, biotized porphyry copper deposit with a superimposed phyllic zone. Canadian Institute of Mining and Metallurgy, 15, 245-263.
Catchpole, H., Kouzmanov, K., Bendezú, A., Ovtcharova, M., Spikings, R., Stein, H., & Fontboté, L., 2015. Timing of porphyry (Cu-Mo) and base metal (Zn-Pb-Ag-Cu) mineralisation in a magmatic-hydrothermal system—Morococha district, Peru. Mineralium Deposita, 50(8), 895-922.
Cernuschi, F., Dilles, J.H., Grocke, S.B., Valley, J.W., Kitajima, K., and Tepley, F.J., 2018. Rapid formation of porphyry copper deposits evidenced by diffusion of oxygen and titanium in quartz: Geology, v. 46, p. 611-614, https:// doi .org /10 .1130 /G40262 .1.
Cernuschi, F., Dilles, J.H., Osorio, J., Proffett, J.M., & Kouzmanov, K., 2023. A reevaluation of the timing and temperature of copper and molybdenum precipitation in porphyry deposits. Economic Geology, 118(5), 931-902.
Chambefort, I., Dilles, J.H., and Kent, A.J.R., 2008. Anhydrite-bearing andesite and dacite as a source for sulfur in magmatic-hydrothermal mineral deposits: Geology, v. 36, p. 719-722.
Chelle-Michou, C., Rottier, B., 2021. Transcrustal Magmatic Controls on the Size of Porphyry Cu Systems: State of Knowledge and Open Questions. https://doi.org/10.5382/SP.24.06.
Cherniak, D.J., Watson, E.B., & Wark, D.A., 2007. Ti diffusion in quartz. Chemical Geology, 236(1-2), 65-74.
Chiaradia, M., et Caricchi, L., 2017. Stochastic Modelling of Deep Magmatic Controls On Porphyry Copper Deposit Endowment.
Chin, E.J., Shimizu, K., Bybee, G.M., and Erdman, M.E., 2018. On the development of the calc-alkaline and tholeiitic magma series: A deep crustal cumulate perspective: Earth and Planetary. Science Letters, v. 482, p. 277-287, https:// doi .org /10.1016 /j.epsl .2017 .11 .016.
Chivas, A.R., 1978. Porphyry copper mineralization at the Koloula igneous complex, Guadalcanal, Solomon Islands. Economic Geology, 73(5), 645-677.
Christofides, G., Soldatos, T., Eleftheriadis, G., & Koroneos, A., 1998. Chemical and isotopic evidence for source contamination and crustal assimilation in the Hellenic Rhodope plutonic rocks. Acta Vulcanologica, 10, 305-318.
Christofides, G., Pecskay, Z., Eleftheriadis, G., Soldatos, T., Koroneos, A., 2004. The Tertiary Evros volcanic rocks (Thrace, northeastern Greece): petrology and K-Ar geochronology. Geol. Carpath. 55, 397-410. England, P.C., and Katz, R.F., 2010, Melting above the anhydrous solidus controls the location of volcanic arcs: Nature, v. 467, p. 700-703, https:// doi .org /10 .1038 /nature09417.
Clark, I. D., & Fritz, P. (1997). Environmental Isotopes in Hydrogeology. CRC Press.
Clayton, R.N., O'Neil, J.R., & Mayeda, T.K., 1972. Oxygen isotope exchange between quartz and water. Journal of Geophysical research, 77(17), 3057-3067.
Clayton, R.N., & Mayeda, T.K., 2009. Kinetic isotope effects in oxygen in the laboratory dehydration of magnesian minerals. The Journal of Physical Chemistry A, 113(10), 2212-2217.
Cline, J.S., & Bodnar, R.J., 1991. Can economic porphyry copper mineralization be generated by a typical calc-alkaline melt. Journal of Geophysical Research: Solid Earth, 96(B5), 8113-8126.
Cole, D.R., Ohmoto, H., & Jacobs, G.K., 1992. Isotopic exchange in mineral-fluid systems: III. Rates and mechanisms of oxygen isotope exchange in the system granite-H2O±NaCl±KCl at hydrothermal conditions. Geochimica et Cosmochimica Acta, 56(1), 445-466.
Cooke, D.R., Baker, M., Hollings, P., Sweet, G., Chang, Z., Danyushevsky, L., ... & Inglis, S., 2014. New advances in detecting the distal geochemical footprints of porphyry systems—epidote mineral chemistry as a tool for vectoring and fertility assessments.
Cooke, D. R., Deyell, C. L., Waters, P. J., Gonzales, R. I., & Zaw, K. (2011). Evidence for magmatic-hydrothermal fluids and ore-forming processes in epithermal and porphyry deposits of the Baguio district, Philippines. Economic Geology, 106(8), 1399-1424.Coplen, T.B, Hopple, J.A., Böhlke, J.K., Peiser, H.S., Rieder, S.E., Krouse, H.R., … & De Brivre, P., 2002. USGS Report Compilation of Minimum and MaximumIsotope Ratios of Selected Elements inNaturally Occurring Terrestrial Materialsand Reagents.

Coplen, T.B., Brand, W.A., Gehre, M., Gröning, M., Meijer, H.A., Toman, B., & Verkouteren, R.M., 2006. New guidelines for δ 13C measurements. Analytical chemistry, 78(7), 2439-2441.
Corbett, G.J., & Leach, T.M. 1998. Southwest Pacific Rim gold-copper systems: structure, alteration, and mineralization. Society of Economic Geologists.
Craig, H., 1961. Isotopic variations in meteoric waters. Science, 133(3465), 1702-1703.
Dansgaard, W. (1964). "Stable isotopes in precipitation." Tellus, 16(4), 436–468.
Del Moro, A., Innocenti, F., Kyriakopoulos, C., Manetti, P., Papadopoulos, P., 1988. Tertiary granitoids from Thrace (Northern Greece): Sr isotopic and petrochemical data. Neues Jahrb. Mineral. Abh. 159, 113-135.
Dennen, W.H., Blackburn, W.H., & Quesada, A., 1970. Aluminum in quartz as a geothermometer. Contributions to Mineralogy and Petrology, 27, 332-342.
Diamond, L. W., & Tarantola, A., 2015. Interpretation of fluid inclusions in quartz deformed by weak ductile shearing: Reconstruction of differential stress magnitudes and pre-deformation fluid properties. Earth and Planetary Science Letters, 417, 107-119.
Dilek, Y., & Altunkaynak, Ş., 2007. Cenozoic crustal evolution and mantle dynamics of post-collisional magmatism in western Anatolia. International Geology Review, 49(5), 431-453.
Dilles, J.H., & Einaudi, M.T., 1992. Wall-rock alteration and hydrothermal flow paths about the Ann-Mason porphyry copper deposit, Nevada; a 6-km vertical reconstruction. Economic Geology, 87(8), 1963-2001.
Dimou, E., Michael, K., Serment, R., 1994. Mineralogical composition of the epithermal polymetallic mineralization at Pefka area, Rhodope district. Bull Geol Soc Greece 30:533–550 (in Greek).
Dong, J., Jia, L.B., Song, M.J., Xu, S.T., Yuan, M., Li, C.L., Yang, Y.J., 2022. Trace element signature of hydrothermal quartz: a potential tracer for ore genesis. Arab J Geosci 15, 1768. https://doi.org/10.1007/s12517-022-11070-w.
Driesner, T., & Heinrich, C. A. 2019. Revised model of porphyry-Cu formation: Ore forms at the porphyry to epithermal transition, overprinting barren stockwork veining and potassic alteration. In Proceedings of the 15th SGA Biennial Meeting (Vol. 3, pp. 955-958). Society for Geology Applied to Mineral Deposits.
Duhamel-Achin, I. Substances critiques : Quel potentiel en France et en Europe ? Mines et carrières, revue de l'industrie minérale, 2022, pp.39-46.
Eglinger, A., Tarantola, A., Durand, C., Ferraina, C., Vanderhaeghe, O., André-Mayer, A. S., ... & Deloule, E., 2014. Uranium mobilization by fluids associated with Ca–Na metasomatism: AP–T–t record of fluid–rock interactions during Pan-African metamorphism (Western Zambian Copperbelt). Chemical Geology, 386, 218-237.
Eidel, J.J., Frost, J.E., and Clippinger, D.M., 1968. Copper-molybdenum mineralization at Mineral Park, Mohave County, Arizona, in Ridge, J.O., ed., Ore Deposits of the United States 1933-1968: New York, A.I.M.E., p. 1259-1281.
Einaudi, F., Godard, M., Pezard, P., Cochemé, J.J., Coulon, C., Brewer, T., & Harvey, P., 2003. Magmatic cycles and formation of the upper oceanic crust at spreading centers: Geochemical study of a continuous extrusive section in the Oman ophiolite. Geochemistry, Geophysics, Geosystems, 4(6).
England, P.C., & Katz, R.F., 2010. Melting above the anhydrous solidus controls the location of volcanic arcs. Nature, 467(7316), 700-703.
Ersoy, E.Y., Palmer, M.R., 2013. Eocene-Quaternary magmatic activity in the Aegean: implications for mantle metasomatism and magma genesis in an evolving orogeny. Lithos 180–181, 5–24.
Falkenberg, J.J., Keith, M., Melfos, V., Hohl, M., Haase, K.M., Voudouris, P., ... & Strauss, H., 2024. Insights into fluid evolution and Re enrichment by mineral micro-analysis and fluid inclusion constraints: Evidence from the Maronia Cu-Mo±Re±Au porphyry system in NE Greece. Mineralium Deposita, 1-25.
Farrell, G., Phillips, C., & Pease, K. 1995. Like taking candy: Why does repeat victimization occur? British Journal of Criminology, 35(3), 384-399.
Farver, J.R., & Yund, R.A., 1991. Measurement of oxygen grain boundary diffusion in natural, fine-grained, quartz aggregates. Geochimica et Cosmochimica Acta, 55(6), 1597-1607. (1-2), 55-70.

Federico, C., Capasso, G., Paonita, A., & Favara, R., 2010. Effects of steam-heating processes on a stratified volcanic aquifer: Stable isotopes and dissolved gases in thermal waters of Vulcano Island (Aeolian archipelago). Journal of volcanology and geothermal research, 192(3-4), 178-190.
Flem, B., & Müller, A., 2012. In situ analysis of trace elements in quartz using laser ablation inductively coupled plasma mass spectrometry. Quartz: deposits, mineralogy and analytics, 219-236.
Ford, C.E., & Green, D.H. 1977. The role of mantle metasomatism in the enrichment of Nb and Zr in lithospheric peridotites. Contributions to Mineralogy and Petrology, 64, 185-197. DOI: https://doi.org/10.1007/BF00372117.
Fournier, R.O., 1967. The porphyry copper deposit exposed in the Liberty open-pit mine near Ely, Nevada; Part 1, Syngenetic Formation. Economic Geology, 62(1), 57-81.
Fournier, R.O., 1999. Hydrothermal processes related to movement of fluid from plastic into brittle rock in the magmatic-epithermal environment: ECONOMIC GEOLOGY, v. 94, p. 1193−1211.
Franchini, M., Impiccini, A., Lentz, D., Ríos, F. J., O'Leary, S., Pons, J., & Schalamuk, A. I. (2011). Porphyry to epithermal transition in the Agua Rica polymetallic deposit, Catamarca, Argentina: An integrated petrologic analysis of ore and alteration parageneses. Ore Geology Reviews, 41(1), 49-74.
Fytikas, M., Innocenti, F., Manetti, P., Mazzuoli, R., Peccerillo, A., Villari, L., 1984. Tertiary to Quaternary evolution of volcanism in the Aegean region. Geol. Soc., London, Spec. Publ. 17, 687-699.
Gao, S., Zou, X., Hofstra, A.H., Qin, K., Marsh, E.E., Bennett, M.M., ... & Li, Z., 2022. Trace elements in quartz: Insights into source and fluid evolution in magmatic-hydrothermal systems. Economic Geology, 117(6), 1415-1428.
Gao, S., Chen, X., Zhang, Y., Zheng, Y., Long, T., Wu, S., & Jiang, X. (2021). Timing and genetic link of porphyry Mo and skarn Pb-Zn mineralization in the Chagele deposit, Western Nyainqentanglha belt, Tibet. *Ore Geology Reviews*, *129*, 103929.
Gallhofer, D., Quadt, A.V., Peytcheva, I., Schmid, S.M., & Heinrich, C.A., 2015. Tectonic, magmatic, and metallogenic evolution of the Late Cretaceous arc in the Carpathian-Balkan orogen. Tectonics, 34(9), 1813-1836.
Gat, J. R. 1996. "Oxygen and Hydrogen Isotopes in the Hydrologic Cycle." Annual Review of Earth and Planetary Sciences, 24(1), 225–262.
Gat, J.R., & Carmi, I. 1970. Evolution of the isotopic composition of atmospheric waters in the Mediterranean Sea area. Journal of Geophysical Research, 75(15), 3039-3048. DOI: https://doi.org/10.1029/JC075i015p03039.
Gerler, J., 1990. Geochemische Untersuchungen an hydrothermalen, metamorphen, granitischen und pegmatitischen Quarzen und deren Fluideinschliissen. Dissertation, Univ. Gi3ttingen, 169 pp.
Giggenbach, W.F., 1984. Mass transfer in hydrothermal systems - A conceptual approach: Geochimica et Cosmochimica Acta, v. 48, p. 2691−2711.
Giggenbach, W.F. 1992. Isotopic shifts in waters from geothermal and volcanic systems along convergent plate boundaries and their origin. Earth and Planetary Science Letters, 113(4), 495-510. DOI: https://doi.org/10.1016/0012-821X(92)90127-H.
Goff, F., & McMurtry, G.M. 2000. Tritium and stable isotopes of magmatic waters. Journal of Volcanology and Geothermal Research, 97(1-4), 347-396. DOI: https://doi.org/10.1016/S0377-0273(99)00174-7.
Goguel, R., 1983. The rare alkalies in hydrothermal alteration at Wairakei and Broadlands, geothermal fields, NZ. Geochimica et Cosmochimica Acta, 47(3), 429-437.
Goldstein, R.H.; Reynolds, T.J., 1994. Systematics of fluid inclusions in diagenetic minerals. SEPM short course notes, 31, Society for Sedimentary Geology: Broken Arrow, OK, USA, p. 1994.
Golyshev, S.I., 1981. Fractionation of stable oxygen and carbon isotopes in carbonate systems. Geokhimiya, 10, 1427-1441.
Götte, T., Pettke, T., Ramseyer, K., Koch-Müller, M., & Mullis, J., 2011. Cathodoluminescence properties and trace element signature of hydrothermal quartz: A fingerprint of growth dynamics. American Mineralogist, 96, 802–813. https://doi.org/10.2138/am.2011.3639
Götze, J., Plötze, M., & Habermann, D., 2001. Origin, spectral characteristics and practical applications of the cathodoluminescence (CL) of quartz–a review. Mineralogy and petrology, 71, 225-250.

Götze, J., Plötze, M., Graupner, T., Hallbauer, D.K., & Bray, C.J., 2004. Trace element incorporation into quartz: A combined study by ICP-MS, electron spin resonance, cathodoluminescence, capillary ion analysis, and gas chromatography. Geochimica et Cosmochimica Acta, 68(18), 3741-3759.
Götze, J., 2009. Chemistry, textures and physical properties of quartz-geological interpretation and technical application. Mineralogical Magazine, 73(4), 645-671.
Götze, J., & Möckel, R., (Eds.) 2012. Quartz: Deposits, mineralogy and analytics (p. 360).
Götze, J., Pan, Y., Müller, A., Kotova, E.L., & Cerin, D., 2017. Trace element compositions and defect structures of high-purity quartz from the Southern Ural region, Russia. Minerals, 7(10), 189.
Götze, J., Pan, Y., & Müller, A., 2021. Mineralogy and mineral chemistry of quartz: A review. mineralogical magazine, 85(5), 639-664.
Green, D.H., Hibberson, W.O., Rosenthal, A., Kovacs, I., Yaxley, G.M., Falloon, T.J., and Brink, F., 2014. Experimental study of the influence of water on melting and phase assemblages in the upper mantle: Journal of Petrology, v. 55, p. 2067-2096, https:// doi .org /10 .1093 /petrology /egu050.
Grove, T.L., Elkins-Tanton, L.T., Parman, S.W., Chatterjee, N., Muntener, O., and Gaetani, G.A., 2003. Fractional crystallization and mantle-melting controls on calc-alkaline differentiation trends: Contributions to Mineralogy and Petrology, v. 145, p. 515-533, https:// doi .org /10 .1007 /s00410 -003 -0448 -z.
Grove, T.L., Chatterjee, N., Parman, S.W., and Medard, E., 2006. The influence of H2O on mantle wedge melting: Earth and Planetary Science Letters, v. 249, p. 74-89, https:// doi .org /10 .1016 /j .epsl .2006 .06 .043.
Grujic, D., Stipp, M., & Wooden, J.L., 2011. Thermometry of quartz mylonites: Importance of dynamic recrystallization on Ti-in-quartz reequilibration. Geochemistry, Geophysics, Geosystems, 12(6).
Gustafson, L.B., & Hunt, J.P., 1975. The porphyry copper deposit at El Salvador, Chile. Economic geology, 70(5), 857-912.
Gustafson, L.B., 1978. Some major factors of porphyry copper genesis. Economic Geology, 73(5), 600-607.
Haertel, M., Herwegh, M. and Pettke, T., 2013. "Titanium-in-quartz thermometry on synkinematic quartz veins in a retrograde crustal-scale normal fault zone," Tectonophysics, vol. 608, pp. 468-481.
Halley, S., Dilles, J.H., & Tosdal, R.M., 2015. Footprints: Hydrothermal alteration and geochemical dispersion around porphyry copper deposits. SEG Discovery, (100), 1-17.
Hamlyn, P.R., Keays, R.R., Cameron, W.E., Crawford, A.J., Waldron, H.M., 1985. Precious metals in magnesian low-Ti lavas: Implications for metallogenesis and sulfur saturation in primary magmas. Geochimica et Cosmochimica Acta Volume 49, Issue 8, Pages 1797-1811.
Heaney, P.J., Veblen, D.R., & Post, J.E., 1994. Structural disparities between chalcedony and macrocrystalline quartz. American Mineralogist, 79(5-6), 452-460.
Hedenquist, J.W., & Lowenstern, J.B., 1994. The role of magmas in the formation of hydrothermal ore deposits. Nature, 370(6490), 519-527.
Hedenquist, J.W., 1995. The ascent of magmatic fluid: discharge versus mineralization. Mineralogical Association of Canada Short Course Series, 23, 263-289.
Hedenquist, J.W., Arribas, A., Jr. and Reynolds, T.J., 1998. Evolution of an intrusion-centered hydrothermal system: Far Southeast-Lepanto porphyry and epithermal Cu-Au deposits, Philippines: economic geology, v. 93, p. 373-404.
Hedenquist, J.W., Arribas, A., & Gonzalez-Urien, E., 2000. Exploration for epithermal gold deposits.
Hedenquist, J.W., 2017. Society of Economic Geologists. Economic Geology, 112, 211-218.
Heinrich, C.A., Candela, P.A. 2014. 13.1 - Fluids and Ore Formation in the Earth's Crust, Treatise on Geochemistry (Second Edition), Elsevier, p1-28, https://doi.org/10.1016/B978-0-08-095975-7.01101-3.
Helgeson, H., 1978. Mass Transfer Among Minerals and Hydrothermal. Geochemistry of hydrothermal ore deposits, 568-610.
Henley, R.W., King, P.L., Wykes, J.L., Renggli, C.J., Brink, F.J., Clark, D.A., & Troitzsch, U., 2015. Porphyry copper deposit formation by sub-volcanic sulphur dioxide flux and chemisorption. Nature Geoscience, 8(3), 210-215.
Hoefs, J. 2009. Stable Isotope Geochemistry (6th ed.). Springer-Verlag. DOI: https://doi.org/10.1007/978-3-540-70708-0.

Heynke, U., Leeder, O., & Schulz, H., 1992. On distinguishing quartz of hydrothermal or metamorphogenic origin in different monomineralic veins in the eastern part of Germany. Mineralogy and Petrology, 46, 315-329.
Hildreth, W., and Moorbath, S., 1988. Crustal contributions to arc magmatism in the Andes of central Chile: Contributions to Mineralogy and Petrology, v. 98, p. 455-489, https:// doi .org /10 .1007 /BF00372365.
Himmerkus, F., Reischmann, T., Kostopoulos, D., 2006. Late Proterozoic and Silurian basement units within the Serbo-Macedonian Massif, northern Greece: the significance of terrane accretion in the Hellenides. Geol. Soc. London, Spec. Publ. 260, 35-50.
Hoefs, J., & Hoefs, J., 2009. Stable isotope geochemistry (Vol. 285). Berlin: springer.
Hoefs, J., & Hoefs, J., 2021. Variations of stable isotope ratios in nature. Stable isotope geochemistry, 267-498.
Höss, A., Haase, K.M., Keith, M., Klemd, R., Melfos, V., Gerlach, L., Pelloth, F., Falkenberg, J.J., Voudouris, P.C., Strauss, H., Baker,T., A. Tarantola, 2024. Magmatic and hydrothermal evolution of the Skouries Au-Cu porphyry deposit, northern Greece, Ore Geology Reviews, Volume 173, 106233, ISSN 0169-1368, https://doi.org/10.1016/j.oregeorev.2024.106233.
Hong, T., Hollings, P., Gao, J., Xu, X. W., Wu, Q., Wu, C., & Mao, Q., 2020. Mineralization and petrogenesis of the Qiongheba porphyry copper deposit in Mengxi district, East Junggar, China. Ore Geology Reviews, 127, 103848.
Hong, W., R. Cooke, D., Zhang, L., Fox, N., & Thompson, J., 2019. Cathodoluminescence features, trace elements, and oxygen isotopes of quartz in unidirectional solidification textures from the Sn-mineralized Heemskirk Granite, western Tasmania. American Mineralogist, 104(1), 100-117.
Hong, W., Fox, N., Cooke, D.R., Zhang, L., & Fayek, M., 2020. B-and O-isotopic compositions of tourmaline constrain late-stage magmatic volatile exsolution in Tasmanian tin-related granite systems. Mineralium Deposita, 55, 63-78.
Hong, W., Fabris, A., Wise, T., Collins, A.S., Gilbert, S., Selby, D., ... & Reid, A.J., 2023. Metallogenic setting and temporal evolution of porphyry Cu-Mo mineralization and alteration in the Delamerian Orogen, South Australia: Insights from zircon U-Pb, molybdenite Re-Os and in situ white mica Rb-Sr geochronology. Economic Geology, 118(6), 1291-1318.
Hou, Z., Duan, L., Lu, Y., Zheng, Y., Zhu, D., Yang, Z., Yang, Z., Wang, B., Pei, Y., Zhao, Z., McCuaig, T., C., 2015. Lithospheric Architecture of the Lhasa Terrane and Its Control on Ore Deposits in the Himalayan-Tibetan Orogen. Economic Geology ; 110 (6): 1541-1575. doi: https://doi.org/10.2113/econgeo.110.6.1541.
Houston, R. A., & Dilles, J. H., 2013. Structural geologic evolution of the Butte district, Montana. Economic Geology, 108(6), 1397-1424.
Huang, R., & Audétat, A., 2012. The titanium-in-quartz (TitaniQ) thermobarometer: A critical examination and re-calibration. Geochimica et Cosmochimica Acta, 84, 75-89.
Hudson, T., Smith, J.G., & Elliott, R.L., 1979. Petrology, composition, and age of intrusive rocks associated with the Quartz Hill molybdenite deposit, southeastern Alaska. Canadian Journal of Earth Sciences, 16(9), 1805-1822.
Hutchinson, M.C., Dilles, J., 2019. Evidence for magmatic anhydrite in porphyry Cu intrusions. Econ. Geol. 114, 143-152.
Hurst, V.J., & Storch, S.P., 1981. Regional variation in the cell dimensions of metamorphic quartz. American Mineralogist, 66(1-2), 204-212.
Idrus, A., Kolb, J., & Meyer, F. M., 2007. Chemical Composition of Rock-Forming Minerals in Copper–Gold-Bearing Tonalite Porphyries at the Batu Hijau Deposit, Sumbawa Island, Indonesia: Implications for Crystallization Conditions and Fluorine–Chlorine Fugacity. Resource Geology, 57(2), 102-113.
Ihinger, P.D. & Zink, S.I., 2000. Determination of relative growth rates of natural quartz crystals, Nature, v. 404, p. 865-869.
Innocenti, F., Kolios, N., Manetti, P., Mazzuoli, R., Peccerillo, G., Rita, F., & Villari, L., 1984. Evolution and geodynamic significance of the Tertiary orogenic volcanism in northeastern Greece. Bulletin volcanologique, 47, 25-37.

Innocenti, F. Magnetti, P., Mazzuoli, R., Pertusati, P., Fykitas, M., and Kolios, N., 1994. The geology and geodynamic significance of the Isalnd of Limnos, North Aegean Sea, Greece. N. jb. Geol.Paläont. Mh., 11, 661-691.

Irarrazaval V., Sillitoe R.H., Wilson A.J., Toro J.C., Robles W., Lyall G.D., 2010. Discovery History of a Giant, High-Grade, Hypogene Porphyry Copper-Molybdenum Deposit at Los Sulfatos, Los Bronces-Río Blanco District, Central Chile.

Irvine, T. N., & Baragar, W.R.A.F., 1971. A guide to the chemical classification of the common volcanic rocks. Canadian journal of earth sciences, 8(5), 523-548.

Jébrak, M., et Marcoux, E., 2008. Geologie des ressources minerales. Ed. Gouvernement du Quebec. ISBN : 9782551237371.

Jensen, E. P., & Barton, M. D., 2000. Gold deposits related to alkaline magmatism.

Jochum, K.P., Weis, U., Stoll, B., Kuzmin, D., Yang, Q., Raczek, I., ... & Enzweiler, J., 2011. Determination of reference values for NIST SRM 610-617 glasses following ISO guidelines. Geostandards and Geoanalytical Research, 35(4), 397-429.

Jolivet, L., & Brun, J. P., 2010. Cenozoic geodynamic evolution of the Aegean. International Journal of Earth Sciences, 99(1), 109-138.

Jolivet, L., Faccenna, C., Huet, B., Labrousse, L., Le Pourhiet, L., Lacombe, O., Lecomte, E., Burov, E., Denèle, Y., Brun, J.-P., Philippon, M., Paul, A., Salaün, G., Karabulut, H., Piromallo, C., Monié, P., Gueydan, F., Okay, A.I., Oberhänsli, R., Pourteau, A., Augier, R., Gadenne, L., Driussi, O., 2013. Aegean tectonics: strain localization, slab tearing and trench retreat. Tectonophysics 597, 1–33.

Jolivet, L., Menant, A., Sternai, P., Rabillard, A., Arbaret, L., Augier, R., Laurent, V., Beaudoin, A., Grasemann, B., Huet, B., Labrousse, L., Le Pourhiet, L., 2015. The geological signature of a slab tear below the Aegean. Tectonophysics 659, 166-182.

Jolivet, L., Faccenna, C., & Becker, T.W., 2016. Mantle flow and deforming continents, the Tethys realm. In AGU Fall Meeting Abstracts (Vol. 2016, pp. T53B-07).

Jollands, M.C., Bloch, E. and Muntener, O., 2020. New Ti-in-quartz diffusivities reconcile natural Ti zoning with time scales and temperatures of upper crustal magma reservoirs, Geology, vol. 48, no. 7, pp. 654–657.

Jourdan, A.L., Venneman, T.W., Mullis, J., Ramseyer, K., 2009a. Oxygen isotope sector zoning in natural hydrothermal quartz. Mineralogical Magazine, 73(4), 615-632.

Jourdan, A.L., Vennemann, T.W., Mullis, J., Ramseyer, K., & Spiers, C.J., 2009b. Evidence of growth and sector zoning in hydrothermal quartz from Alpine veins. European Journal of Mineralogy, 21(1), 219-231.

Kaiser-Rohrmeier, M., von Quadt, A., Driesner, T., Heinrich, C.A., Handler, R., Ovtcharova, M., Ivanov, Z., Petrov, P., Sarov, S., Peytcheva, I., 2013. Post-orogenic extension and hydrothermal ore formation: high precision geochronology of the Central Rhodopian metamorphic core complex (Bulgaria-Greece). Econ. Geol. 108, 691-718.

Kalceff, M.A., 2009. Cathodoluminescence microcharacterization of point defects in α-quartz. Mineralogical Magazine, 73(4), 585-605.

Kelley, K.A., Plank, T., Newman, S., Stolper, E.M., Grove, T.L., Parman, S., and Hauri, E., 2010. Mantle melting as a function of water content beneath the Mariana Arc: Journal of Petrology, v. 51, p. 1711-1738, https:// doi .org / 10 .1093 /petrology /egq036.

Kerrich, R., 1976. Some effects of tectonic recrystallisation on fluid inclusions in vein quartz. Contributions to Mineralogy and Petrology, 59(2), 195-202.

Kesler, S.E., and Wilkinson, B.H., 2006. The role of exhumation in the temporal distribution of ore deposits: Economic Geology, v. 101, p. 919-922, https:// doi .org /10 .2113 /gsecongeo .101 .5 .919.

Kidder, S., Avouac, J.-P., and Chan, Y.-C., 2013. Application of titanium-in-quartz thermobarometry to greenschist facies veins and recrystallized quartzites in the Hsüehshan range, Taiwan. Solid Earth, 4, 1–21. doi:10.5194/se-4-1-2013.

Kilias, A., Falalakis, G., Sfeikos, A., Papadimitriou, E., Vamvaka, A., Gkarlaouni, C., 2013. The Thrace basin in the Rhodope province of NE Greece – a Tertiary supradetachment basin and its geodynamic implications. Tectonophysics 595-596, 90-105.

Klemm, A., Banerjee, A. and Hoernes, S., 1990. A new intracrystalline isotope effect, 18O under the faces of amethyst. Zeitschrift fu¨r Naturforschung, 45a, 13741376.

Klemm, A., Banerjee, A. and Hoernes, S., 1991. Fractionation of oxygen isotopes at the faces of smoky quartz. Zeitschrift fu¨r Naturforschung, 46a, 11331134.
Klemm, L.M., Pettke, T., Heinrich, C.A., and Campos, E., 2007. Hydrothermal evolution of the El Teniente deposit, Chile: Porphyry Cu-Mo ore deposition from low-salinity magmatic fluids: ECONOMIC GEOLOGY, v. 102, p. 1021-1045.
Koděra, P., Heinrich, C.A., Wälle, M., & Lexa, J., 2014. Magmatic salt melt and vapor: Extreme fluids forming porphyry gold deposits in shallow subvolcanic settings. Geology, 42(6), 495-498.
Kopp, K.0., 1965. Geologie Thrakiens. Das Tertiar zwischen Rhodope und Evros. -Ann. geol. pays Hellen .• 16; 315-362.
Korzhinsky, M.A., Tkachenko, S.I., Shmulovich, K.I., Taran, Y.A., & Steinberg, G.S., 1994. Discovery of a pure rhenium mineral at Kudriavy volcano. Nature, 369(6475), 51-52.
Kounov, A., Wüthrich, E., Seward, D., Burg, J.P., & Stockli, D., 2015. Low-temperature constraints on the Cenozoic thermal evolution of the Southern Rhodope Core Complex (Northern Greece). International journal of earth sciences, 104, 1337-1352.
Kouzmanov K. et Pokrovski G. S., 2012. Hydrothermal controls on metal distribution in porphyry Cu(-Mo-Au) systems.
Kushiro, I., Syono, Y., and Akimoto, S., 1968. Melting of a peridotite nodule at high pressures and high water pressures: Journal of Geophysical Research, v. 73, p. 6023-6029, https:// doi .org /10 .1029 /JB073i018p06023.
Kydonakis, K., Brun, J.P., & Sokoutis, D., 2015a. North Aegean core complexes, the gravity spreading of a thrust wedge. Journal of Geophysical Research: Solid Earth, 120(1), 595-616.
Kydonakis, K., Brun, J.P., Sokoutis, D., & Gueydan, F., 2015b. Kinematics of Cretaceous subduction and exhumation in the western Rhodope (Chalkidiki block). Tectonophysics, 665, 218-235.
Kydonakis, K., Moulas, E., Chatzitheodoridis, E., Brun, J.P., & Kostopoulos, D., 2015. First-report on Mesozoic eclogite-facies metamorphism preceding Barrovian overprint from the western Rhodope (Chalkidiki, northern Greece). Lithos, 220, 147-163.
Lambrecht, G., & Diamond, L.W., 2014. Morphological ripening of fluid inclusions and coupled zone-refining in quartz crystals revealed by cathodoluminescence imaging: Implications for CL-petrography, fluid inclusion analysis and trace-element geothermometry. Geochimica et Cosmochimica Acta, 141, 381-406.
Landtwing, M.R., Pettke, T., Halter, W.E., Heinrich, C.A., Redmond, P.B., Einaudi, M.T., & Kunze, K., 2005. Copper deposition during quartz dissolution by cooling magmatic–hydrothermal fluids: the Bingham porphyry. Earth and Planetary Science Letters, 235(1-2), 229-243.
Landtwing, M.R., & Pettke, T., 2005. Relationships between SEM-cathodoluminescence response and trace-element composition of hydrothermal vein quartz. American Mineralogist, 90(1), 122-131.
Landtwing, M.R., Furrer, C., Redmond, P.B., Pettke, T., Guillong, M., & Heinrich, C.A., 2010. The Bingham Canyon porphyry Cu-Mo-Au deposit. III. Zoned copper-gold ore deposition by magmatic vapor expansion.
Larsen, R.B., Henderson, I., Ihlen, P. M., & Jacamon, F., 2004. Distribution and petrogenetic behaviour of trace elements in granitic pegmatite quartz from South Norway. Contributions to Mineralogy and Petrology, 147, 615-628.
Lavrov, O.B., & Kuleshevich, L.V., 2010. The first finds of rhenium minerals in Karelia. In Doklady Earth Sciences (Vol. 432, pp. 598-601). SP MAIK Nauka/Interperiodica.
Lecumberri-Sanchez, P., Steele-MacInnis, M., & Bodnar, R.J., 2012. A numerical model to estimate trapping conditions of fluid inclusions that homogenize by halite disappearance. Geochimica et Cosmochimica Acta, 92, 14-22.
Lee C.-T.A., Luffi, P., Chin, E. J., Bouchet, R., Dasgupta, R., Morton, D. M., Le Roux, V., Yin, Q.-z., Jin, D., 2012. Copper systematics in arc magmas and implications for crust–mantle differentiation. Science, 336 , pp. 64-68.
Lee, C.-T.A., Lee, T.C., and Wu, C.-T., 2014. Modeling the compositional evolution of recharging, evacuating, and fractionating (REFC) magma chambers: Implications for differentiation of arc magmas: Geochimica et Cosmochimica Acta, v. 143, p. 8-22, https:// doi .org /10 .1016 /j .gca .2013 .08 .009.

Lehmann, K., Berger, A., Götte, T., Ramseyer, K., & Wiedenbeck, M., 2009. Growth related zonations in authigenic and hydrothermal quartz characterized by SIMS-, EPMA-, SEM-CL-and SEM-CC-imaging. Mineralogical Magazine, 73(4), 633-643.

Lescuyer, J.L., Bailly, L., Cassard, D., Lips, A.L.W., Piantone, P., McAlister, M., 2003. Sediment-hosted gold in south-eastern Europe: the epithermal deposit of Perama, Thrace, Greece. In: DG Eliopoulos et al. (eds). Mineral Exploration and Sustainable Development, Millpress, Rotterdam: 499-502.

Li Y., Audétat A., 2015. Effects of temperature, silicate melt composition, and oxygen fugacity on the partitioning of V, Mn, Co, Ni, Cu, Zn, As, Mo, Ag, Sn, Sb, W, Au, Pb, and Bi between sulfide phases and silicate melt. Geochimica et Cosmochimica Acta. Volume 162, 1 August 2015, Pages 25-45.

Lickfold, V., Cooke, D.R., Smith, S.G., and Ullrich, T.D., 2003. Endeavour copper-gold porphyry deposits, Northparkes, New South Wales: Intrusive history and fluid evolution: ECONOMIC GEOLOGY, v. 98, p. 1607-1636.

Liu, X., Richard, A., Pironon, J., & Rusk, B.G., 2023. Vein formation and reopening in a cooling yet intermittently pressurized hydrothermal system: The single-intrusion Tongchang Porphyry Cu deposit. Geosciences, 13(4), 107.

Longerich, H.P., Fryer, B.J., & Strong, D.F., 1987. Determination of lead isotope ratios by inductively coupled plasma-mass spectrometry (ICP-MS). Spectrochimica Acta Part B: Atomic Spectroscopy, 42(1-2), 39-48.

Maimon, O., Lyakhovsky, V., Melnik, O., and Navon, O., 2012. The propagation of a dyke driven by gas saturated magma: Geophysical Journal International, v. 189, p. 956–966, https:// doi .org /10 .1111 /j .1365-246X .2012 . 05342 .x.

Mao, W., Rusk, B., Yang, F., & Zhang, M., 2017. Physical and chemical evolution of the Dabaoshan porphyry Mo deposit, South China: Insights from fluid inclusions, cathodoluminescence and trace elements in quartz. Economic Geology, 112(4), 889-918.

Mao, W., Zhong, H., Zhu, W.G., Lin, X.G., & Zhao, X.Y., 2018. Magmatic-hydrothermal evolution of the Yuanzhuding porphyry Cu-Mo deposit, South China: Insights from mica and quartz geochemistry. Ore Geology Reviews, 101, 765-784.

Maravelis, A., & Zelilidis, A., 2012. Paleoclimatology and paleoecology across the eocene/Oligocene boundary, thrace basin, northeast aegean Sea, Greece. Palaeogeography, Palaeoclimatology, Palaeoecology, 365, 81-98.

Maravelis, A.G., Boutelier, D., Catuneanu, O., Seymour, K.S., Zelilidis, A., 2016. A review of tectonics and sedimentation in a forearc setting : Hellenic Thrace Basin, North Aegean Sea and Northern Greece. Tectonophysics674,1–19. https://doi.org/10.1016/j. tecto.2016.02.003.

Marchev, P., Kaiser-Rohrmeier, B., Heinrich, C., Ovtcharova, M., von Quadt, A., Raicheva, R., 2005. Hydrothermal ore deposits related to post-orogenic extensional magmatism and core complex formation: the Rhodope Massif of Bulgaria and Greece. Ore Geol. Rev. 27, 53-89.

Marchev, P., Georgiev, S., Raicheva, R., Peytcheva, I., von Quadt, A., Ovtcharova, M., Bonev, N., 2013. Adakitic magmatism in post-collisional setting: an example from the early–middle Eocene Magmatic Belt in Southern Bulgaria and Northern Greece. Lithos 180-181, 159-180.

Márton, I., Moritz, R., Spikings, R., 2010. Application of low-temperature thermochronology to hydrothermal ore deposits: formation, preservation and exhumation of epithermal gold systems from the Eastern Rhodope, Bulgaria. Tectonophysics 483, 240-254.

Mavrogonatos, C., Voudouris, P., Berndt, J., Klemme, S., Zaccarini, F., Spry, P.G., Melfos, V., Tarantola, A., Keith, M., Klemd, R., Haase, K., 2019. Trace Elements in Magnetite from the Pagoni Rachi Porphyry Prospect, NE Greece: Implications for Ore Genesis and Exploration. Minerals 2019, 9, 725. https://doi.org/10.3390/min9120725.

Mavrogonatos, C., Voudouris, P., Zaccarini, F., Klemme, S., Berndt, J., Tarantola, A., ... & Spry, P. G., 2020. Multi-stage introduction of precious and critical metals in pyrite: A case study from the Konos Hill and Pagoni Rachi porphyry/epithermal prospects, NE Greece. Minerals, 10(9), 784.

Maydagán, L., Franchini, M., Rusk, B., Lentz, D.R., McFarlane, C., Impiccini, A., ... & Rey, R., 2015. Porphyry to epithermal transition in the Altar Cu-(Au-Mo) deposit, Argentina, studied by cathodoluminescence, LA-ICP-MS and fluid inclusion analysis. Economic Geology, 110(4), 889-923.4.

McFall, K. A., 2016. Critical metals in porphyry copper deposits (Doctoral dissertation, University of Southampton).
Melfos, V., Vavelidis, M., & Theodorikas, S., 2002. Preservation of the Greek Cultural Heritage: A study of the geology and extraction techniques of two ancient quarries, Larisa prefecture, Thessaly, Greece. In Proceedings of the International Conference "Protection and Restoration of the Environment VI (pp. 1535-1544).
Melfos, V., and Voudouris P.C., 2012. Geological, Mineralogical and Geochemical Aspects for Critical and Rare Metals in Greece. Minerals 2, no. 4: 300-317. https://doi.org/10.3390/min2040300.
Melfos, V., & Voudouris, P.C., 2017. Cenozoic metallogeny of Greece and potential for precious, critical and rare metals exploration. Ore Geology Reviews, 89, 1030-1057.
Melfos, V., & Voudouris, P.C., 2022. Dépôts de Grèce (Manuel de premier cycle). Kallipos, publications académiques ouvertes. https://dx.doi.org/10.57713/kallipos-32
Menant, A., Jolivet, L., Vrielynck, B., 2016. Kinematic reconstruction and magmatic evolution illuminating crystal and mantle dynamics of the eastern Mediterranean region since the late Cretaceous. Tectonophysics 675, 103-140.
Menant, A., Jolivet L., Tuduri, J., Loiselet, C., Bertrand, G., Guillou-Frottierc, L., 2018. 3D subduction dynamics: A first-order parameter of the transition from copper- to gold-rich deposits in the eastern Mediterranean region.
Michailidis, K., 1989. Gold chemistry from the Gallikos River placer deposits, central Macedonia, Greece (No. RefW-15-13739). Aristotle University of Thessaloniki.
Mitchell, Roger H., Keays, Reid R., 1981. Abundance and distribution of gold, palladium and iridium in some spinel and garnet lherzolites: implications for the nature and origin of precious metal-rich intergranular components in the upper mantle. Geochimica et Cosmochimica Acta, 45 (12). 2425-2442 doi:10.1016/0016-7037(81)90096-x.
Moëlo, Y., Oudin, E., Makovicky, E., Karup-Møller, S., Pillard, F., Bornuat, M., & Evanghelou, E., 1985. La kirkiite, Pb10Bi3As3S19, une nouvelle espèce minérale homologue de la jordanite. Bulletin de minéralogie, 108(5), 667-677.
Monecke, T., Monecke, J., Reynolds, T.J., Tsuruoka, S., Bennett, M.M., Skewes, W B., & Palin, R.M., 2018. Quartz solubility in the H2O-NaCl system: A framework for understanding vein formation in porphyry copper deposits. Economic Geology, 113(5), 1007-1046.
Monnier, L., Lach, P., Salvi, S., Melleton, J., Bailly, L., Béziat, D., ... & Gouy, S., 2018. Quartz trace-element composition by LA-ICP-MS as proxy for granite differentiation, hydrothermal episodes and related mineralization: The Beauvoir Granite (Echassières district), France. Lithos, 320, 355-377.
Moritz, R., Márton, I., Ortelli, M., Marchev, P., Voudouris, P., Bonev, N., Spikings, R., Cosca, M., 2010. A review of age constraints of epithermal precious and base metal deposits of the Tertiary Eastern Rhodopes: coincidence with Late Eocene- Early Oligocene tectonic plate reorganization along the Tethys. In: Christofides, G., et al. (Eds.), Proceedings of the XIX Congress of the Carpathian-Balkan Geological Association, Thessaloniki. Scientific Annals of the School of Geology A.U.Th. 100, 351–358.
Müller, A., Wiedenbeck, M., Kerkhof, A.M.V.D., Kronz, A., & Simon, K., 2003. Trace elements in quartz-a combined electron microprobe, secondary ion mass spectrometry, laser-ablation ICP-MS and cathodoluminescence study. European Journal of Mineralogy, 15(4), 747-763.
Müller, A., Herrington, R., Armstrong, R., Seltmann, R., Kirwin, D.J., Stenina, N.G., & Kronz, A., 2010. Trace elements and cathodoluminescence of quartz in stockwork veins of Mongolian porphyry-style deposits. Mineralium Deposita, 45, 707-727.
Nachlas, W.O., Whitney, D.L., Teyssier, C., Bagley, B., & Mulch, A., 2014. Titanium concentration in quartz as a record of multiple deformation mechanisms in an extensional shear zone. Geochemistry, Geophysics, Geosystems, 15(4), 1374-1397.
Nachlas, W.O., & Hirth, G., 2015. Experimental constraints on the role of dynamic recrystallization on resetting the Ti-in-quartz thermobarometer. Journal of Geophysical Research: Solid Earth, 120(12), 8120-8137.
Nachlas, W.O., Thomas, J.B., & Hirth, G., 2018. TitaniQ deformed: Experimental deformation of out-of-equilibrium quartz porphyroclasts. Journal of Structural Geology, 116, 207-222.
Nesbitt, B.E., 1988. Gold deposit continuum: A genetic model for lode Au mineralization in the continental crust. Geology, 16(11), 1044-1048.

Nielsen, R.L., 1968. Hypogene texture and mineral zoning in a copper-bearing granodiorite porphyry stock, Santa Rita, New Mexico. Economic Geology, 63(1), 37-50.
Norton, D.L., and Cathles, L.M., 1973. Breccia pipes, products of exsolved vapor from magmas: Economic Geology, v. 68, p. 540-546, https:// doi .org /10 .2113 /gsecongeo .68 .4 .540.
Okay, A.I., Zattin, M., & Cavazza, W., 2010. Apatite fission-track data for the Miocene Arabia-Eurasia collision. Geology, 38(1), 35-38.
Okay, A.I., & Topuz, G., 2017. Variscan orogeny in the Black Sea region. International Journal of Earth Sciences, 106, 569-592.
Okay, A.I., Özcan, E., Hakyemez, A., Siyako, M., Sunal, G., & Kylander-Clark, A.R., 2019. The Thrace Basin and the Black Sea: the Eocene–Oligocene marine connection. Geological Magazine, 156(1), 39-61.
Onasch, C.M., & Vennemann, T.W., 1995. Disequilibrium partitioning of oxygen isotopes associated with sector zoning in quartz. Geology, 23(12), 1103-1106.
Ortelli, M., Moritz, R., Voudouris, P., & Spangenberg, J. (2009, August). Tertiary porphyry and epithermal association of the Sapes-Kassiteres district, Eastern Rhodopes, Greece. In Proceedings of the 10th biennial SGA meeting, Townsville, Australia (pp. 17-20).
Osborne, Z.R., Thomas, J.B., Nachlas, W.O., Angel, R.J., Hoff, C.M., & Watson, E.B., 2022. TitaniQ revisited: expanded and improved Ti-in-quartz solubility model for thermobarometry. Contributions to Mineralogy and Petrology, 177(3), 31.
Paquette, J.L., Ménot, R.P., Pin, C., & Orsini, J.B., 2003. Episodic and short-lived granitic pulses in a post-collisional setting: evidence from precise U–Pb zircon dating through a crustal cross-section in Corsica. Chemical Geology, 198(1-2), 1-20.
Park, J.W., Campbell, I.H., Chiaradia, M., Hao, H. and Lee, C.T., 2021. Crustal magmatic controls on the formation of porphyry copper deposits.
Passchier, C.W., & Trouw, R.A., 2005. Microtectonics. Springer Science & Business Media.
Pe-Piper, G., Piper, D.J.W., 2002. In: The Igneous Rocks of Greece. The Anatomy of an Orogen, Beiträge der regionalen Geologie der Erde 30. Berlin-Stuttgart, pp. 573.
Pe-Piper, G., Piper, D.J.W., 2006. Unique features of the Cenozoic igneous rocks of Greece. Geol. Soc. Am. Spec. Pap. 409, 259–281.
Pearce, N.J., Perkins, W.T., Westgate, J.A., Gorton, M.P., Jackson, S.E., Neal, C.R., & Chenery, S.P., 1997. A compilation of new and published major and trace element data for NIST SRM 610 and NIST SRM 612 glass reference materials. Geostandards newsletter, 21(1), 115-144.
Pecskay, Z., Lexa, J., Szakacs, A., Seghedi, I., Balogh, K., Konecny, V., ... & Cvetkovic, V., 2006. Geochronology of Neogene magmatism in the Carpathian arc and intra-Carpathian area. Geologica Carpathica-Bratislava-, 57(6), 511.
Perkins, R.J.,2018. Post-Collisional Magmatism and Porphyry Epithermal Style Mineralisation along the Maronia Magmatic Corridor, Northeastern Greece. (PhD thesis).University of Bristol.
Perny, B., Eberhardt, P., Ramseyer, K., Mullis, J., & Pankrath, R., 1992. Microdistribution of Al, Li, and Na in α quartz: Possible causes and correlation with short-lived cathodoluminescence. American Mineralogist, 77(5-6), 534-544.
Perugini, D., Poli, G., Christofides, G., Eleftheriadis, G., Koroneos, A., & Soldatos, T., 2004. Mantle-derived and crustal melts dichotomy in northern Greece: spatiotemporal and geodynamic implications. Geological Journal, 39(1), 63-80.
Peterková, T., & Dolejš, D., 2019. Magmatic-hydrothermal transition of Mo-W-mineralized granite-pegmatite-greisen system recorded by trace elements in quartz: Krupka district, Eastern Krušné hory/Erzgebirge. Chemical Geology, 523, 179-202.
Phelps, P.R., Lee, C.T.A., & Morton, D.M., 2020. Episodes of fast crystal growth in pegmatites. Nat Commun 11, 4986 (2020).
Pichavant, M., and Macdonald, R., 2007. Crystallization of primitive basaltic magmas at crustal pressures and genesis of the calc-alkaline igneous suite: experimental evidence from St. Vincent, Lesser Antilles arc: Contributions to Mineralogy and Petrology, v. 154, p. 535-558, https:// doi .org /10 .1007 /s00410 -007 -0208 -6.
Pollington, A.D., Kozdon, R., Anovitz, L.M., Georg, R.B., Spicuzza, M.J., & Valley, J.W., 2016. Experimental calibration of silicon and oxygen isotope fractionations between quartz and water at

250° C by in situ microanalysis of experimental products and application to zoned low δ30Si quartz overgrowths. Chemical Geology, 421, 127-142.
Price, J.G., Lechler, P.J., & Lear, K.G. 2013. Isotopic and elemental variations in modern precipitation and river water across the conterminous USA. Hydrological Processes, 27(16), 2315-2328. DOI: 10.1002/hyp.9365.
von Quadt, A., Moritz, R., Peytcheva, I., & Heinrich, C.A., 2005. 3: Geochronology and geodynamics of Late Cretaceous magmatism and Cu–Au mineralization in the Panagyurishte region of the Apuseni–Banat–Timok–Srednogorie belt, Bulgaria. Ore Geology Reviews, 27(1-4), 95-126.
Rabayrol, F., & Hart, C.J., 2021. Petrogenetic and tectonic controls on magma fertility and the formation of post-subduction porphyry and epithermal mineralization along the late Cenozoic Anatolian Metallogenic Trend, Turkey. Mineralium Deposita, 56, 279-306.
Raimbourg, H., Famin, V., Canizarès, A., & Le Trong, E., 2022. Fluid pressure changes recorded by trace elements in quartz. Geochemistry, Geophysics, Geosystems, 23(10), e2022GC010346.
Ramdohr, P., 1980. The Ore Minerals and Their Intergrowths, 2nd ed., 1192 p. Pergamon Press.
Redmond, P.B., Einaudi, M.T., Inan, E.E., Landtwing, M.R., & Heinrich, C.A., 2004. Copper deposition by fluid cooling in intrusion-centered systems: New insights from the Bingham porphyry ore deposit, Utah. Geology, 32(3), 217-220.
Redmond, P.B., & Einaudi, M.T., 2010. The Bingham Canyon porphyry Cu-Mo-Au deposit. I. Sequence of intrusions, vein formation and sulfide deposition.
Reed, M., Rusk, B., & Palandri, J., 2013. The Butte magmatic-hydrothermal system: One fluid yields all alteration and veins. Economic Geology, 108(6), 1379-1396.
Reischmann, T., Kostopoulos, D., 2007. Terrane accretion in the internal Hellenides. Geophys. Res. Abstracts 9, 05337.
Rice, C.M., Harmon, R.S., & Shepherd, T.J., 1985. Central City, Colorado; the upper part of an alkaline porphyry molybdenum system. Economic Geology, 80(7), 1769-1796.
Richards, J.P., 2003. Tectono-Magmatic Precursors for Porphyry Cu-(Mo-Au). Deposit Formation. Economic Geology, Vol., 95 pp. 1515-1533.
Richards, J.P., 2009. Post-subduction porphyry Cu-Au and epithermal Au deposits: products of remelting of subduction-modified lithosphere. Geology 37, 247–250.
Richards, J. P., 2011a. Magmatic to hydrothermal metal fluxes in convergent and collided margins. Author links open overlay panel. Ore Geology Reviews, Volume 40, Issue 1, Pages 1-26.
Richards, J.P., 2015. Tectonic, magmatic, and metallogenic evolution of the Tethyan orogen: from subduction to collision. Ore Geol. Rev. 70, 323-345.
Richards, J.P., 2021, Porphyry copper deposit formation in arcs: What are the odds?: Geosphere, v. 17, no. X, p. 1-26, https:// doi.org /10.1130 /GES02086.1.
Rigaudier T., 2010. Isotopic compositions of fluid inclusions in the Earth crust : determination of fluid sources and palaeoclimatic reconstructions. PhD THESIS Paleontology. Université Claude Bernard - Lyon I.
Rimstidt, J.D., & Barnes, H.L., 1980. The kinetics of silica-water reactions. Geochimica et Cosmochimica Acta, 44(11), 1683-1699.
Ring, U., Glodny, J., Will, T., & Thomson, S., 2010. The Hellenic subduction system: high-pressure metamorphism, exhumation, normal faulting, and large-scale extension. Annual Review of Earth and Planetary Sciences, 38(1), 45-76.
Robertson, A.H., 2002. Overview of the genesis and emplacement of Mesozoic ophiolites in the Eastern Mediterranean Tethyan region. Lithos 65, 1-67.
Robertson, A.H., Trivic´, B., Deric´, N., Bucurc, I.I., 2013. Tectonic development of the Vardar ocean and its margins: evidence from the Republic of Macedonia and Greek Macedonia. Tectonophysics 595-596, 25-54.
Roedder, E., 1971. Fluid inclusion studies on the porphyry-type ore deposits at Bingham, Utah, Butte, Montana, and Climax, Colorado: ECONOMIC GEOLOGY, v. 66, p. 98-120.
Roedder, E., 1984. Volume 12: fluid inclusions. Reviews in mineralogy, 12, 644.
Rohrlach, B.D., and Loucks, R.R., 2005. Multi-million-year cyclic ramp-up of volatiles in a lower crustal magma reservoirtrapped below the Tampakan copper-gold deposit by Mio-Pliocene crustal compression in the southern Philippines: InPorter, T.M. (ed.)., Super Porphyry Copper & Gold Deposits-AGlobal Perspective, PCG Publishing, Adelaide, v. 2, p. 369-407.

Rottier, B., Kouzmanov, K., Bouvier, A.S., Baumgartner, L.P., Wälle, M., Rezeau, H., ... & Fontboté, L., 2016. Heterogeneous melt and hypersaline liquid inclusions in shallow porphyry type mineralization as markers of the magmatic-hydrothermal transition (Cerro de Pasco district, Peru). Chemical Geology, 447, 93-116.

Rottier, B., Rezeau, H., Casanova, V., …, & Fontboté, L., 2017. Trace element diffusion and incorporation in quartz during heating experiments. Contrib Mineral Petrol 172, 23 (2017). https://doi.org/10.1007/s00410-017-1350-44

Rottier, B., Kouzmanov, K., Casanova, V., Wälle, M., & Fontboté, L., 2018. Cyclic dilution of magmatic metal-rich hypersaline fluids by magmatic low-salinity fluid: a major process generating the giant epithermal polymetallic deposit of Cerro de Pasco, Peru. Economic Geology, 113(4), 825-856.

Rottier, B., & Casanova, V., 2021. Trace element composition of quartz from porphyry systems: a tracer of the mineralizing fluid evolution. Mineralium Deposita, 56, 843-862.

Rottier B., Kouzmanov K., Casanova, V., Bouvier, A.S., Baumgartner, L., P., Wälle, M., Fontboté, L., 2021. Tracking fluid mixing in epithermal deposits – Insights from in-situ δ18O and trace element composition of hydrothermal quartz from the giant Cerro de Pasco polymetallic deposit, Peru, Chemical Geology, Volume 576, https://doi.org/10.1016/j.chemgeo.2021.120277.

Rusk, B., & Reed, M., 2002. Scanning electron microscope–cathodoluminescence analysis of quartz reveals complex growth histories in veins from the Butte porphyry copper deposit, Montana. Geology, 30(8), 727-730.

Rusk, B.G., Reed, M.H., Dilles, J.H., & Kent, A.J., 2006. Intensity of quartz cathodoluminescence and trace-element content in quartz from the porphyry copper deposit at Butte, Montana. American Mineralogist, 91(8-9), 1300-1312.

Rusk, B.G., Reed, M.H., & Dilles, J.H. 2008a. Fluid inclusion evidence for magmatic-hydrothermal fluid evolution in the porphyry copper-molybdenum deposit at Butte, Montana. Economic Geology, 103(2), 307-334.

Rusk, B.G., Lowers, H.A., & Reed, M.H., 2008b. Trace elements in hydrothermal quartz: Relationships to cathodoluminescent textures and insights into vein formation. Geology, 36(7), 547-550.

Rusk, B., Koenig, A., & Lowers, H., 2011. Visualizing trace element distribution in quartz using cathodoluminescence, electron microprobe and laser ablation-inductively coupled plasma-mass spectrometry. American Mineralogist, 96(5-6), 703-708.

Rusk, B., 2012. Cathodoluminescent textures and trace elements in hydrothermal quartz. Quartz: Deposits, mineralogy and analytics, 307-329.

Sander, M.V., & Black, J.E., 1988. Crystallization and recrystallization of growth-zoned vein quartz crystals from epithermal systems; implications for fluid inclusion studies. Economic Geology, 83(5), 1052-1060.

Schaarschmidt A., 2021. From the mantle wedge to the shallow crust: Magmas, fluids, and mineralizations in the Aegean subduction system -Thesis.

Schaarschmidt, A., Haase, K.M., Voudouris, P.C., Melfos, V., & Klemd, R., 2021. Migration of arc magmatism above mantle wedge diapirs with variable sediment contribution in the Aegean. Geochemistry, Geophysics, Geosystems, 22(6), e2020GC009565.

Schaarschmidt, A., Klemd, R., Regelous, M., Voudouris, P.C., Melfos, V., & Haase, K.M., 2021. The formation of shoshonitic magma and its relationship to porphyry-type mineralisation: the Maronia pluton in NE Greece. Lithos, 380, 105911.

Schirra, M., Driesner, T., & Heinrich, C.A., 2019. Relative timing of sulfide precipitation at the Batu Hijau porphyry Cu-Au deposit, Sumbawa, Indonesia. In Proceedings of the 15th SGA Biennial Meeting (Vol. 3, pp. 1009-1012). Society for Geology Applied to Mineral Deposits.

Schlöglova, K., Wälle, M., & Heinrich, C.A., 2017. LA-ICP-MS analysis of fluid inclusions: contamination effects challenging micro-analysis of elements close to their detection limit. Journal of Analytical Atomic Spectrometry, 32(5), 1052-1063.

Schmid, S. M., Bernoulli, D., Fügenschuh, B., Matenco, L., Schefer, S., Schuster, R., ... & Ustaszewski, K., 2008. The Alpine-Carpathian-Dinaridic orogenic system: correlation and evolution of tectonic units. Swiss Journal of Geosciences, 101, 139-183.

Schrön, W., Schmädicke, E., Thomas, R., Schmidt, W., 1988. Geochemische Untersuchungen an Pegmatitquarzen. Z Geol Wiss 16:229-244.

Seedorff, E., Dilles, J.H., Proffett, J.M., Jr., Einaudi, M.T., Zurcher, L., Stavast, W.J.A., Johnson, D.A., and Barton, M.D., 2005. Porphyry deposits: Characteristics and origin of hypogene features, in Hedenquist, J.W., Thompson, J.F.H., Goldfarb, R.J., and Richards, J.P., eds., Economic Geology 100th Anniversary Volume: Society of Economic Geologists, p. 251-298.

Seo, J. H., Guillong, M., & Heinrich, C.A., 2012. Separation of molybdenum and copper in porphyry deposits: The roles of sulfur, redox, and pH in ore mineral deposition at Bingham Canyon. Economic Geology, 107(2), 333-356.

Sharma, R., Srivastava, P.K. (2014). Hydrothermal Fluids of Magmatic Origin. In: Kumar, S., Singh, R. (eds) Modelling of Magmatic and Allied Processes. Society of Earth Scientists Series. Springer, Cham. https://doi.org/10.1007/978-3-319-06471-0_9

Sheppard, S.M.F., Nielsen, R.L., & Taylor, H.P. 1971. Hydrogen and oxygen isotope ratios in minerals from porphyry copper deposits. Economic Geology, 66(4), 515-542. DOI: 10.2113/gsecongeo.66.4.515.

Sheppard, S.M.F., & Gustafson, L.B. 1976. Oxygen and hydrogen isotope study of supergene and hypogene leaching and enrichment of the El Salvador porphyry copper deposit, Chile. Economic Geology, 71(8), 1569-1580. DOI: 10.2113/gsecongeo.71.8.1569.

Sheppard, S.M., 1986. Characterization and isotopic variations in natural waters. Reviews in Mineralogy and Geochemistry, 16(1), 165-183.

Shinohara, H., and Hedenquist, J.W., 1997. Constraints on magma degassing beneath the Far Southeast porphyry Cu-Au deposit, Philippines: Journal of Petrology, v. 38, p. 1741-1752.

Sillitoe, R.H., and Sawkins, F.J., 1971. Geologic, mineralogic and fluid inclusion studies relating to the origin of copper-bearing tourmaline breccia pipes, Chile: Economic Geology and the Bulletin of the Society of Economic Geologists, v. 66, p. 1028-1041, https:// doi .org /10 .2113 /gsecongeo .66 .7 .1028.

Sillitoe, R.H., 1972. A plate tectonic model for the origin of porphyry copper deposits: ECONOMIC GEOLOGY, v. 67, p. 184-197 .1998, Major regional factors favouring large size, high hypogene grade, elevated gold content and supergene oxidation and enrichment of porphyry copper deposits, in Porter, T.M., ed., Porphyry and hydrothermal copper and gold deposits: A global perspective: Adelaide, Australian Mineral Foundation, p.21-34.

Sillitoe, R. H., & Bonham, H. F., 1984. Volcanic landforms and ore deposits. *Economic Geology*, *79*(6), 1286-1298.

Sillitoe, R. H., 1985. Ore-related breccias in volcanoplutonic arcs. Economic geology, 80(6), 1467-1514.

Sillitoe, R.H, and Angeles, C.A, Jr., 1985. Geological characteristics and evolution of a gold-rich porphyry copper deposit at Guinaoang, Luzon, Philippines, in Asian Mining ’85: London, Institution of Mining and Metallurgy, p.15-26.

Sillitoe, R. H., 1994. Erosion and collapse of volcanoes: Causes of telescoping in intrusion-centered ore deposits: Geology, v. 22, p. 945-948.

Sillitoe, R. H., 1997. Characteristics and controls of the largest porphyry copper-gold and epithermal gold deposits in the circum-Pacific region. Australian Journal of Earth Sciences, 44(3), 373-388.

Sillitoe, R. H., 1998 Redmond, P.B., Einaudi, M.T., Inan, E.E., Landtwing, M.R., and Heinrich, C.A., 2004. Copper deposition by fluid cooling in intrusion-centered systems: New insights from the Bingham porphyry ore deposits, Utah. Geology, v. 32, p. 217-220.

Sillitoe, R. H., 2000. Styles of high-sulphidation gold, silver and copper mineralisation in porphyry and epithermal environments. In Proceedings of the Australasian Institute of Mining and Metallurgy (Vol. 305, No. 1, pp. 19-34). Parkville, Vic.: The Institute, [1990]-c2001.

Sillitoe, R.H., and Hedenquist, J.W., 2003, Linkages between volcanotectonic settings, ore fluid compositions, and epithermal precious metal deposits: Society of Economic Geologists Special Publication 10, p. 315-343.

Sillitoe, R.H., and Perello, J., 2005, Andean copper province: Tectonomagmatic settings, deposit types, metallogeny, exploration, and discovery: ECONOMIC GEOLOGY 100TH ANNIVERSARY VOLUME, p. 845-890.

Sillitoe, R.H., 2010. Porphyry Copper Systems. Society of Economic Geologists, Inc. Economic Geology, v. 105, pp. 3- 41.

Sillitoe, R. H. 2015. Epithermal paleosurfaces. *Mineralium Deposita*, *50*(7), 767-793.

Simon, M.F.S, H.P., Taylor, 1974. Hydrogen and Oxygen Isotope Evidence for the Origins of Water in the Boulder Batholith and the Butte Ore Deposits, Montana. Economic Geology 1974; 69 (6): 926–946. doi: https://doi.org/10.2113/gsecongeo.69.6.926

Simmons, S. T., White, N. C., John, D. A., 2005. Geological Characteristics of Epithermal Precious and Base Metal Deposits. 2005 Society of Economic Geologists, Inc., Economic Geology 100th Anniversary Volume, pp. 485-522.

Simmons, W., Falster, A., Webber, K., Roda-Robles, E., Boudreaux, A.P., Grassi, L.R., & Freeman, G., 2016. Bulk Composition of Mt. Mica Pegmatite, Maine, USA: Implications For the Origin of An Lct Type Pegmatite By Anatexis. The Canadian Mineralogist, 54(4), 1053-1070.

Siyako, M., & Huvaz, O., 2007. Eocene stratigraphic evolution of the Thrace Basin, Turkey. Sedimentary Geology, 198(1-2), 75-91.

Skarpelis, N., 1999a. The Agios Filippos ore deposit, Kirki (Western Thrace). A base-metal part of a high-sulfidation epithermal system. Bull. Geol. Soc. Greece 33, 51-60.

Skarpelis, N., 1999b. Epithermal type ores in the Aegean. The hot spring mineralization of northern Chios island. Bull. Geol. Soc. Greece 33, 61-68.

Sparks, R.S.J., Annen, C., Blundy, J.D., Cashman, K.V., Rust, A.C., & Jackson, M.D., 2019. Formation and dynamics of magma reservoirs. Philosophical Transactions of the Royal society A, 377(2139), 20180019.

Spry, P.G., Gedlinske, B.L., Skinner, B.J., 1987. Tables for the Determination of Common Opaque Minerals. https://doi.org/10.5382/EGTables

Spry, P.G., Paredes, M.M., Foster, F., Truckle, J.S., & Chadwick, T.H., 1996. Evidence for a genetic link between gold-silver telluride and porphyry molybdenum mineralization at the Golden Sunlight Deposit, Whitehall, Montana; fluid inclusion and stable isotope studies. Economic Geology, 91(3), 507-526.

Steele-MacInnis, M., Lecumberri-Sanchez, P., & Bodnar, R.J., 2012. HokieFlincs_H2O-NaCl: A Microsoft Excel spreadsheet for interpreting microthermometric data from fluid inclusions based on the PVTX properties of H2O–NaCl. Computers & Geosciences, 49, 334-337.

Stefanova, E., Driesner, T., Zajacz, Z., Heinrich, C.A., Petrov, P., & Vasilev, Z., 2014. Melt and fluid inclusions in hydrothermal veins: The magmatic to hydrothermal evolution of the Elatsite porphyry Cu-Au deposit, Bulgaria. Economic Geology, 109(5), 1359-1381.

Stern, C.R., Funk, J.A., Skewes, M.A., & Arévalo, A., 2007. Magmatic anhydrite in plutonic rocks at the El Teniente Cu-Mo deposit, Chile, and the role of sulfur-and copper-rich magmas in its formation. Economic geology, 102(7), 1335-1344.

Stipp, M., Stünitz, H., Heilbronner, R., & Schmid, S.M., 2002a. Dynamic recrystallization of quartz: correlation between natural and experimental conditions. Geological Society, London, Special Publications, 200(1), 171-190.

Stipp, M., StuÈnitz, H., Heilbronner, R., & Schmid, S.M., 2002b. The eastern Tonale fault zone: a 'natural laboratory'for crystal plastic deformation of quartz over a temperature range from 250 to 700 C. Journal of structural geology, 24(12), 1861-1884.

Streck, Martin J., Dilles, J.H., John H., 1998. Sulfur evolution of oxidized arc magmas as recorded in apatite from a porphyry copper batholith. Geology, 26 (6). 523pp. doi:10.1130/0091-7613(1998)026<0523:seooam>2.3.co;2.

Stouraiti, C., Mitropoulos, P., Tarney, J., Barreiro, B., McGrath, A.M., Baltatzis, E., 2010. Geochemistry and petrogenesis of late Miocene granitoids, Cyclades, southern Aegean: nature of source components. Lithos 114, 337-352.

Suttner, L.J., & Leininger, R.K., 1972. Comparison of the trace element content of plutonic, volcanic, and metamorphic quartz from southwestern Montana. Geological Society of America Bulletin, 83(6), 1855-1862.

Swanson, S.E., & Fenn, P.M., 1986. Quartz crystallization in igneous rocks. American Mineralogist, 71(3-4), 331-342.

Tailby, N.D., Cherniak, D.J. and Watson, E.B., 2018. "Al diffusion in quartz" American Mineralogist, vol. 103, no. 6, (2018), pp. 839-847. https://doi.org/10.2138/am-2018-5613.

Takada, A., 1994. The influence of regional stress and magmatic input on styles of monogenetic and polygenetic volcanism: Journal of Geophysical Research, v. 99, p. 13,563-13,573.

Tanner, D., Henley, R.W., Mavrogenes, J.A., & Holden, P., 2013. Combining in situ isotopic, trace element and textural analyses of quartz from four magmatic-hydrothermal ore deposits. Contributions to Mineralogy and Petrology, 166, 1119-1142.
Tarantola, A., Diamond, L.W., & Stünitz, H., 2010. Modification of fluid inclusions in quartz by deviatoric stress I: experimentally induced changes in inclusion shapes and microstructures. Contributions to Mineralogy and Petrology, 160, 825-843.
Tarantola, A., Diamond, L. W., Stünitz, H., Thust, A., & Pec, M., 2012. Modification of fluid inclusions in quartz by deviatoric stress. III: Influence of principal stresses on inclusion density and orientation. Contributions to Mineralogy and Petrology, 164, 537-550.
Tattitch, B., Chelle-Michou, C., Blundy, J. Loucks, R.R., 2021. Chemical feedbacks during magma degassing control chlorine partitioning and metal extraction in volcanic arcs. Nat Commun 12, 1774. https://doi.org/10.1038/s41467-021-21887-w
Taylor, H.P. 1974. The application of oxygen and hydrogen isotope studies to problems of hydrothermal alteration and ore deposition. Economic Geology, 69(6), 843-883. DOI: https://doi.org/10.2113/gsecongeo.69.6.843.
Taylor, H.P. 1979. Oxygen and hydrogen isotope relationships in hydrothermal mineral deposits. In H.L. Barnes (Ed.), Geochemistry of Hydrothermal Ore Deposits (2nd ed., pp. 236-277). John Wiley & Sons.Tessalina, S.G., Capmas, F., Birck, J.L., Allègre, C.J., Yudovskaya, M.A., Distler, V.V., & Chaplygin, I.V., 2005. Sources of rhenium and osmium enrichment in fumaroles, sulphide sublimates and volcanic rocks from the Kudriavy volcano. In Mineral Deposit Research: Meeting the Global Challenge (pp. 841-843). Springer, Berlin, Heidelberg.
Tessalina, S.G., Yudovskaya, M.A., Chaplygin, I.V., Birck, J.L., & Capmas, F., 2008. Sources of unique rhenium enrichment in fumaroles and sulphides at Kudryavy volcano. Geochimica et Cosmochimica Acta, 72(3), 889-909.
Thomas, J.B., Bruce Watson, E., Spear, F.S., Shemella, P.T., Nayak, S.K., & Lanzirotti, A., 2010. TitaniQ under pressure: the effect of pressure and temperature on the solubility of Ti in quartz. Contributions to Mineralogy and Petrology, 160(5), 743-759.
Thompson, A.J., Hauff, P.L., & Robitaille, A.J., 1999. Alteration mapping in exploration: application of short-wave infrared (SWIR) spectroscopy. SEG Discovery, (39), 1-27.
Tomkins, A.G., Rebryna, K.C., Weinberg, R.F., & Schaefer, B.F., 2012. Magmatic sulfide formation by reduction of oxidized arc basalt. Journal of Petrology, 53(8), 1537-1567.
Tranos, M.D., Eleftheriadis, G.E., & Kilias, A.A., 2009. Philippi granitoid as a proxy for the Oligocene and Miocene crustal deformation in the Rhodope Massif (Eastern Macedonia, Greece). Geotectonic Research, 96(1), 69-85.
Tsokas, G.N., Christofides, G. C., & Papakonstantinou, C., 1996. A geophysical study of the granites and the sedimentary basins of the Xanthi area (N. Greece). pure and applied geophysics, 146, 365-392.
Tsuruoka, S., Monecke, T., & Reynolds, T.J., 2021. Evolution of the magmatic-hydrothermal system at the Santa Rita porphyry Cu deposit, New Mexico, USA: Importance of intermediate-density fluids in ore formation. Economic Geology, 116(6), 1267-1284.
Turgut, S., Türkaslan, M., Perinçek, D., 1991. Evolution of the Thrace sedimentary basin and its hydrocarbon prospectivity. In: Spencer AM (ed) Generation, accumulation, and production of Europe's hydrocarbons. Spec Publ Eur Assoc Petrol Geosci 1 : 415-437.
Turgut, S., & Eseller, G., 2000. Sequence stratigraphy, tectonics and depositional history in eastern Thrace Basin, NW Turkey. Marine and Petroleum Geology, 17(1), 61-100.
U.S.G.S1. U.S. Geological Survey, Mineral Commodity Summaries, January 2020
U.S.G.S.2 U.S. Geological Survey, Mineral Commodity Summaries, January 2022
Urai, J.L., Means, W.D., & Lister, G.S., 1986. Dynamic recrystallization of minerals. Mineral and rock deformation: laboratory studies, 36, 161-199.
Valencia, V.A., Eastoe, C., Ruiz, J., Ochoa-Landin, L., Gehrels, G., González-Leon, C., ... & Espinoza, E., 2008. Hydrothermal evolution of the porphyry copper deposit at La Caridad, Sonora, Mexico, and the relationship with a neighboring high-sulfidation epithermal deposit. Economic Geology, 103(3), 473-491.
Van den Kerkhof, A.M., & Hein, U.F., 2001. Fluid inclusion petrography. Lithos, 55(1-4), 27-47.

Van den Kerkhof, A.M., Kronz, A., Simon, K., and Scherer, T., 2004. Fluid-controlled quartz recovery in granulite as revealed by cathodoluminescence and trace element analysis (Bamble sector, Norway). Contributions to Mineralogy and Petrology, vol. 146, no. 5, pp. 637-652.

Van Hinsbergen, D.J.J., Hafkenscheid, E., Spakman, W., Meulenkamp, J.E., & Wortel, R., 2005. Nappe stacking resulting from subduction of oceanic and continental lithosphere below Greece. Geology, 33(4), 325-328.

Vavelidis, M., Filippidis, A., Michailidis, K., Evangelou, E., 1989. The polymetallic ore mineralization of the Kirki area, Alexandroupolis district, Northeastern Greece. Geologica Rhodopica, 1, 350-365.

Vila, T., & Sillitoe, R.H., 1991. Gold-rich porphyry systems in the Maricunga belt, northern Chile. Economic Geology, 86(6), 1238-1260.

Voudouris, P.C., & Alfieris, D., 2005. New porphyry - Cu ± Mo occurrences in the north-eastern Aegean, Greece: Ore mineralogy and epithermal relationships. In Mineral deposit research: Meeting the global challenge (pp. 473-476). Springer, Berlin, Heidelberg.

Voudouris, P.C., Tarkian, M., & Arikas, K., 2006. Mineralogy of telluride-bearing epithermal ores in the Kassiteres-Sappes area, western Thrace, Greece. Mineralogy and Petrology, 87(1), 31-52.

Voudouris, P.C., Melfos, V., Spry, P. G., Bindi, L., Kartal, T., Arikas, K., ... & Ortelli, M., 2009. Rhenium-rich molybdenite and rheniite in the Pagoni Rachi Mo–Cu–Te–Ag–Au prospect, northern Greece: implications for the Re geochemistry of porphyry-style Cu–Mo and Mo mineralization. The Canadian Mineralogist, 47(5), 1013-1036.

Voudouris, P.C., Melfos, V., Spry, P.G., Moritz, R., Papavassiliou, C., & Falalakis, G., 2011. Mineralogy and geochemical environment of formation of the Perama Hill high-sulfidation epithermal Au-Ag-Te-Se deposit, Petrota Graben, NE Greece. Mineralogy and Petrology, 103(1), 79-100.

Voudouris, P.C., & Melfos, V., 2012. Aluminum-phosphate-sulfate (APS) minerals in the sericitic-advanced argillic alteration zone of the Melitena porphyry-epithermal Mo-Cu- ± Au ± Re prospect, western Thrace, Greece. N. Jb. Mineral. Abh, 190, 11-27.

Voudouris, P.C., Melfos, V., Spry, P.G., Bindi, L., Moritz, R., Ortelli, M., & Kartal, T., 2013a. Extremely Re-rich molybdenite from porphyry Cu-Mo-Au prospects in northeastern Greece: Mode of occurrence, causes of enrichment, and implications for gold exploration. Minerals, 3(2), 165-191.

Voudouris, P.C., Melfos, V., Spry, P.G., Kartal, T., Schleicher, H., Moritz, R., & Ortelli, M., 2013b. The Pagoni Rachi/Kirki Cu-Mo ± Re ± Au deposit, northern Greece: Mineralogical and fluid inclusion constraints on the evolution of a telescoped porphyry-epithermal system. The Canadian Mineralogist, 51(2), 253-284.

Voudouris, P.C., Melfos, V., Mavrogonatos, C., Tarantola, A., Götze, J., Alfieris, D., ... & Psimis, I., 2018a. Amethyst occurrences in Tertiary volcanic rocks of Greece: Mineralogical, fluid inclusion and oxygen isotope constraints on their genesis. Minerals, 8(8), 324.

Voudouris, P.C., Mavrogonatos, C., Rieck, B., Kolitsch, U., Spry, P. G., Scheffer, C., ... & Photiades, A., 2018b. The gersdorffite-bismuthinite-native gold association and the skarn-porphyry mineralization in the Kamariza mining district, Lavrion, Greece. Minerals, 8(11).

Voudouris, P.C., Mavrogonatos, C., Spry, P.G., Baker, T., Melfos, V., Klemd, R., Haase, K., Repstock, A., Djiba, A., Bismayer, U., Tarantola, A., Scheffer, C., Moritz, R., Kouzmanov, K., Alfieris, D., Papavassiliou, K., Schaarschmidt, A., Galanopoulos, E., Galanos, E., Kołodziejczyk, J., Stergiou, C., Melfou, M., 2019a. Porphyry and epithermal deposits in Greece: An overview, new discoveries, and mineralogical constraints on their genesis. Ore Geology Reviews, Volume 107, p654-691. https://doi.org/10.1016/j.oregeorev.2019.03.019.

Voudouris, P.C., Mavrogonatos, C., Graham, I., Giuliani, G., Tarantola, A., Melfos, V., Karampelas, S., Katerinopoulos, A., & Magganas, A., 2019. Gemstones of Greece: Geology and Crystallizing Environments. Minerals, 9(8), 461. https://doi.org/10.3390/min9080461.

Voudouris, P.C., Melfos, V., Mavrogonatos, C., Photiades, A., Moraiti, E., Rieck, B., ... & Zaimis, S., 2021. The Lavrion mines: A unique site of geological and mineralogical heritage. Minerals, 11(1), 76.

Walderhaug, O., 1994. Temperatures of quartz cementation in Jurassic sandstones from the Norwegian continental shelf; evidence from fluid inclusions. Journal of Sedimentary Research, 64(2a), 311-323.

Wark, D.A., & Watson, E.B., 2006. TitaniQ: a titanium-in-quartz geothermometer. Contributions to Mineralogy and Petrology, 152(6), 743-754.

Watt, G.R., Wright, P., Galloway, S., & McLean, C., 1997. Cathodoluminescence and trace element zoning in quartz phenocrysts and xenocrysts. Geochimica et Cosmochimica Acta, 61(20), 4337-4348.

Weil, J.A., 1984. A review of electron spin spectroscopy and its application to the study of paramagnetic defects in crystalline quartz. Physics and Chemistry of Minerals, Volume 10, Issue 4, pp. 149-165. 10.1007/BF00311472.

White, N.C., & Hedenquist, J.W., 1995. Epithermal gold deposits: styles, characteristics and exploration. SEG newsletter, (23), 1-13.

Wilkinson, W.H., Jr., Vega, L.A., and Titley, S.R., 1982. Geology and ore deposits at Mineral Park, Mohave County, Arizona, in Titley, S.R., ed., Advances in geology of the porphyry copper deposits, southwestern North America: Tucson, University of Arizona Press, p. 523-541.

Wilkinson, J.J., 2001. Fluid inclusions in hydrothermal ore deposits. Lithos, 55(1-4), 229-272.

Wilkinson, B.H., and Kesler, S.E., 2009. Quantitative identification of metallogenic epochs and provinces: Application to Phanerozoic porphyry copper deposits: Economic Geology, v. 104, p. 607-622, https:// doi .org /10 .2113 /gsecongeo .104 .5 .607.

Wilson, A.J., Cooke, D.R., & Harper, B.L., 2003. The Ridgeway gold-copper deposit: A high-grade alkalic porphyry deposit in the Lachlan fold belt, New South Wales, Australia. Economic Geology, 98(8), 1637-1666.

Wolfe, R.C., & Cooke, D.R., 2011. Geology of the Didipio region and genesis of the Dinkidi alkalic porphyry Cu-Au deposit and related pegmatites, northern Luzon, Philippines. Economic Geology, 106(8), 1279-1315.

Wüthrich, E., 2009. Low temperature thermochronology of the Northern Aegean Rhodope Massif. Unpublished Doctoral thesis, Zürich, Switzerland, ETH Zürich. 216 p.

Yang, Z., Chang, Z., Paquette, J., White, N.C., Hou, Z., & Ge, L., 2015. Magmatic Au mineralization at the Bilihe Au deposit, China. Economic Geology, 110(7), 1661-1668.

Zellmer, G.F., Edmonds, M., & Straub, S.M., 2015. Volatiles in subduction zone magmatism. Geological Society, London, Special Publications, 410(1), 1-17.

Zaluski, G., Kontak, D.J., & Smith, P.K. 1994. Fluid inclusion and stable isotope constraints on the origin of the East Kemptville tin deposit, Nova Scotia, Canada. Economic Geology, 89(6), 1461-1483. DOI: https://doi.org/10.2113/gsecongeo.89.6.1461.

Zhang, C., Li, X., Almeev, R.R., Horn, I., Behrens, H., & Holtz, F., 2020. Ti-in-quartz thermobarometry and TiO2 solubility in rhyolitic melts: New experiments and parametrization.

Zheng, Y.F., 1993. Calculation of oxygen isotope fractionation in hydroxyl-bearing silicates. Earth and Planetary Science Letters, 120(3-4), 247-263.

Zheng, Y.F., 1999. Oxygen isotope fractionation in carbonate and sulfate minerals. Geochemical journal, 33(2), 109-126.

Zhu, J.J., Richards, J.P., Rees, C., Creaser, R., DuFrane, S.A., Locock, A., Petrus, J.A., Lang, J., 2018. Elevated Magmatic Sulfur and Chlorine Contents in Ore-Forming Magmas at the Red Chris Porphyry Cu-Au Deposit, Northern British Columbia, Canada. Economic Geology (2018); 113 (5): 1047–1075. https://doi.org/10.5382/econgeo.2018.4581.

Zimmer, M.M., Plank, T., Hauri, E.H., Yogodzinski, G.M., Stelling, P., Larsen, J., Singer, B., Jicha, B., Mandeville, C., and Nye, C.J., 2010. The role of water in generating the calc-alkaline trend: New volatile data for Aleutian magmas and a new Tholeiitic Index: Journal of Petrology, v. 51, p. 2411-2444, https:// doi .org /10 .1093 /petrology /egq062.

ANNEXES

TABLE DES ANNEXES

Tableau des échantillons des différents sites avec commentaires et positions associées. 284
Table of ICP-MS quartz analyses for different elements in G_NIST610 standard. 288
Table of ICP-MS quartz analyses for different elements in G_NIST612 standard. 301
Table of ICP-MS quartz analyses for different elements in A-type vein. 314
Table of ICP-MS quartz analyses for different elements in B1-type veins 324
Table of ICP-MS quartz analyses for different elements in B2-type vein. 344
Table of ICP-MS quartz analyses for different elements in E1-type vein. 354
Tables of pearson correlation coefficient (Trace Element in quartz). 374
Graphical method for finding the trapping pressure using *PT* diagram ..... - 378 -
Table of analyses of fluid inclusion in A-type vein. 379
Table of analyses of fluid inclusion in B1-type vein. 384
Table of analyses of fluid inclusion in E1- and E2-type veins 392
Tableau des valeurs de températures utilisées pour le calcul du coefficient de fractionnement isotopique et coefficient de fractionnement isotopiques associés. 395
Tableau de valeurs du $\delta^{18}O$ dans les veines de type A. 396
Tableau de valeurs du $\delta^{18}O$ dans les veines de type B1. 398
Tableau de valeurs du $\delta^{18}O$ dans les veines de type B2. 402
Tableau de valeurs du $\delta^{18}O$ dans les veines de type E1. 403
Tableau de valeurs du $\delta^{18}O$ dans les veines de type E2. 404
Tableau de valeurs du $\delta^{13}C$ dans les veines de type E2. 406
Tableau d'analyses du δD par broyage des différentes veines de quartz 407
..

Tableau des échantillons des différents sites avec commentaires et positions associées.

Echantillon	Commentaires	GPS	Date
	MARONIA		
AB.01.083.01	Veines A et B dans microgranite à altération séricitique/ Argillique ?	N40°51'40";E25°32'46" (zone à veine de type B à molybdénite)	05/10/2022
AB.01.083.02	Veine ou roche encaissante ? À moly et py	N40°51'40";E25°32'46" (zone à veine de type B à molybdénite)	
AB.01.110.01	Microgranite à altération séricitique ± veines à moly, cpy, py	N40°51'57";E25°32'57"	
AB.01.112.01	Veine geodique au sein de monzodriorite	N40°51'58";E25°32'98"	
AB.01.131.01 (x3)	Greisen (?) ou épithermal (?) à milky qz et veine, matrice à grains grossier, à topaze, tourmaline, fluorite, zinwaldite, cassitérite. Dans une même colonne structurale : cette partie serait plus profonde que la rhyolite de SP. Si pyrophyllite alors serait IS lode, si Ms alors greisen	N40°51'45";E25°32'45" (vers la côte, proche du puit exploratoire)	
AB.01.132.01	veines A et B dans microgranite	N41°51'45";E25°32'44"	
AB.01.134.01 (x3)	Quartz veine (B type ou épithermal type ?)+ vacuole et glassy quartz	N40°51'46";E25°32'27" (base falaise Est)	
AB.01.134.02	E type à chalcédoine, qz et sulf	N40°51'46";E25°32'27" (base falaise Est)	
AB.01.135.01	Veine type E à carb, qz, cpy, py, sulf. +altération sericitique/carb,	N40°51'34";E25°33'00"	
	SANT DEMETRIOS		
AB.01.164.01	Vuggy silica High Sulfidation à diaspore, corrundum, pyrophyllite + supergène altération à magnétite, hématite, goethite surrounding	N41,02567°;E25,73571°	03/10/2023
	ST PHILIPPOS		
AB.01.102.01	rhyolite altérée (liée à la minéralisation ?) en dyke de 5-7m de large encaissée au sein de carbonates métamorphisés	N41°00'56'';E25°49'16" (long de la route depuis Sapes) vers SP	04/10/2022
AB.01.104.01	Breccia minéralisée à gal (HS-IS)	N41°01'06";E25°49'07"	
AB.01.104.02	Veine/breccia à gal, wurz, cass, py (HS-IS)	N41°01'06";E25°49'07"	
AB.01.128.01	Rhyolite (N80°; N80°) à stockwork à comb qz (épithermal de HT ?) parait être lié à la faille ? (N100;75N - N80;80°N)	N41°01'20";E25°48'54"	
AB.01.128.02	Veine à comb qz dans rhyolite (fluid subépithermal, quartz de type A puis après type E à carb ?)	N41°01'20";E25°48'57"	07/10/2022
AB.01.129.01	Veine à baryte, gal, tenantite	N41°01'11";E25°49'04"	
AB.01.129.02	Brèche avec veine à py, enargite +- dickite et pyrophyllite, typique HS	N41°01'11";E25°49'04" (autre coté)	

Partie 2

Echantillon	Commentaires	GPS	Date
	KONOS HILL		
TA03.140.01	Monzodiorite à altération propylitique (2eme intrusion associée à un système sub-épithermal), presque fraîche	proche N41°01.184' ; E25°46.047' le long du ruisseau.	
TA03.140.02	Monzodiorite présentant une altération séricitique et des veines à quartz rubanés, avec weathering	N41°01.184' ; E25°46.047'	
TA03.140.03	Dacite à altération séricitique en contact avec la monzodiorite à altération propylitique. La monzodiorite est plus granuleuse (texture grenue) que la dacite, malgré l'altération	N41°01.184' ; E25°46.047'	
TA03.140.04	Altération sodique se surimprime à l'altération séricitique. Roche à albite hydrothermale et séricite, avec des veines de quartz noir (à sulfures/oxydes). Veines liées à un événement précoce à molybdénite	proche de TA.03.119.02/03	
TA03.141.01	Altération séricitique se surimprime à l'altération potassique responsable du stockwork à veines de quartz rubanés	N41°01.135' ; E25°45.041'	12/04/2022
TA03.141.02	Stockwork à veines de quartz rubanés de type A (et veines de type B ?) avec molybdénite.	N41°00.973' ; E25°45.076'	
TA03.141.03	Nodules pluridécimétriques d'hém-mag-grt en proportion variable (skarn ou altération supergène ?).	N41°00.927' ; E25°45.051'	
TA03.141.04	Dacite à altération argillique avancée (lithocaps), à alunite, diaspore, APS, pyrophyllite et zunite	N41°01.301' ; E25°45.269'	
TA03.141.05	Roches à adulaire (cristal blanc rhomboédrique) et qtz améthyste. En contact avec la monzodiorite à grain fin.	Zone en surplomb dans champ à oliviers et moutons. N40°59.568' ; E25°43.259'	
AB.01.082.01	Veines A et B, altération séricitique, et weathering	N14°00'58'';E25°45'05'' (long de la creek)	
AB.01.082.02	Monzodiorite ? À altération propylitique (chl, épi, alb, et qz primaire)	N14°00'47'';E25°46'05'' (long de la route, proche d'ancienne bâtisse)	01/10/2022
MJ.01.020.11	Echantillon à patine gris/jaune à l'affleurement et minéraux gris blancs non identifiés au VNR-SWIR	41.01662°N 25.75129°E	03/10/2022

Partie 3

Echantillon	Commentaires	GPS	Date
	PAGONI RACHI		
AB.01.157.01	Andésite/granodiorite à altération propylitique	N41°00'21" E25°49'38"	01/10/2023
MB01	granodiorite à altération Sodi/calcique/potassique à veine de type A à KFds+Bi+Chl+qz+veine moly et K+py+Au (type B et C ?) (+OP propylitique)	N40°59,799' E25°50,203'	2018
MB02	Granodiorite à veine de type A et M à molybdénite	N40°59,744' E25°50,144'	2018
MB03	Altération sodicalcique/potassique à large veine (type B et réouverture type C ?) à épidote, chl, moly, Au, albite, amp	N40°59,734' E25°50,136'	2018
MB04	Stockwork de veine de type B associé à altération (albite+carb) sodique à séricitique (overprint ?) réouverture par type C ?	N40°59,725' E25°50,130'	2018
MB05	Veine à Mo, Re, chl et fl (type B/type C ?)	N40°59,721' E25°50,122'	2018
MB06	Roche lessivée avec banded qz vein enrichies en Au (similaire à ce qui est observable à KH)	N40°59,698' E25°49,824'	2018
MB08	None	None	2018
MB09	Veine de quartz à fl et chl au cœur (type B réouvert par type C ?)	N40°59,793' E25°49,932'	2018
MB11	Veine épithermale (type E) à sph, gal, tell, Mo, carb et comb quartz	N40°59,867' E25°49,932'	2018
MB12	granodiorite à altération propylitique (conservation de la structure magmatique)	None	2018
AB.01.116.01	Volant, avec un stockwork lié à la granodiorite, au contact d'une "ribon vein" à moly ? (similaire à Maroneia) type B ?	N40°59'44";E25°50'09"	
AB.01.117.01	Veines type A, M et B ? Au sein d'une granodiorite à altération potassique avec surimpression d'altération propylitique ? (pas de conservation de la structure primaire)	N40°59'44";E25°50'08"	
AB.01.118.01	Stockwork à veines type A et B avec molybdénite et rhéniite au sein de granite à altération séricitique	N40°59'43";E25°50'07"	06/10/2022
AB.01.118.02	Stockwork de veines A et B à albite et chlorite, réouverture ? veines type C ? (phyllique altération related to fault (PR to SP))	N40°59'43";E25°50'07" (10 mètres vers le Sud, long de la creek)	
AB.01.119.01	Altération phyllique importante avec veines rubanées à quartz, même système que le reste ? (PR est similaire aux veines rubanées de Konos Hill (faille : N150;90 / banded vein : N145;85°E)	N40°59'41";E25°49'49" (haut d'une petite creek)	
AB.01.119.02	Banded veins (N150;77)	N40°59'40";E25°49'52"	

Partie 4

Echantillon	Commentaires	GPS	Date
	PAGONI RACHI		
AB.01.120.01	Veines à py, carb, qtz (comb), sulf, alb (B type, C type ?, E type) : C type réouvre B type, sont recoupées par E type	N40°59'46";E25°49'56"	
AB.01.121.01	Veine type B (qtz, sericite) réouverte par type C (chl, alb, molybdénite) recoupées et décalées par E type (carb, tétraédrite)	N40°59'47";E25°49'55"	
AB.01.122.01	Veine type E à carb, qtz, tellure + altération séricitique	N40°59'50";E25°49'55"	06/10/2022
AB.01.122.02	Veine type E à gal, qtz, cal, tell, bismuth (T°C formation : 280-300°C et 2-6wt%NaCl eq)	N40°59'50";E25°49'55" (10m vers le Nord)	
AB.01.122.03	Veine type E à gal, sph, cal, qtz	N40°58'29";E25°49'56"	
AB.01.123.01	Veine type D à py massive (+Au et qtz ?)	N40°59'57";E25°49'56"	
AB.01.166.01	Banded veins alt séricitique moitié ascension de la colline, recoupé par veinlet oxydées (ancienne D type ?)	N40°59,6771;E25°49,8451	
AB.01.166.02	Limite banded veines avec veines AMB ? Altération KNaCa et prop ?	N40°59,7633';E25°49,8160'	03/10/2023
AB.01.167.01	Granodiorite altérée (KNaCa ? Avec OP propylitique ?) provenant d'un bloc éboulé à proximité de zone à veine bd	N40°59,6643'; E25°49,8557'	
AB.01.174.01	Veine de quartz +-sufides disséminés maricunga type vein +sulfides - altération séricitique N120,78E; N154,58E	N40,9967°;E25,82879°	
AB.01.177.01	Veines type E à quartz, carb, py, cpy associée à altération séricitique (voir argillique) N140,75E	N41.00312°;E25.83227°	
AB.01.177.02	Rhyolite altérée (séricitique ?) orientée N140. 3-4m de puissance au sein d'une granodiorite altérée, avec veinlets cpy, py (type C ou D ?) et cpy ou py disséminés et recpée par veine à carb, py, cpy (type E?)	N41,00237°;E25,83237°	05/10/2023
AB.01.179.01	Veines type AMB avec altération KNaCa ? SW	N40,99623°;E25,83049°	
AB.01.180.01	Zone transition alt séricitique+-KNaCa avec SW veines AMB+-bd ?	N40,99585°; E25,83033°	
AB.01.180.02	Banded veins dans roche à altération séricitique	N40,99582°; E25,83033°	
AB.01.185.01	Quartz massif au contact de veine (ribbon ?) proximité faille et zone à altération séricitique	N40,99712°;E25,83569°	06/10/2023

Table of ICP-MS quartz analyses for different elements in G_NIST610 standard.

		Li			Be			B		
		Concentration ppm	2SE (ppm)	LOD (ppm)	Concentration ppm	2SE (ppm)	LOD (ppm)	Concentration ppm	2SE (ppm)	LOD (ppm)
	G_NIST610									
Day1	610-1	425,3	24,1	0,2	466,9	25,9	0,2	379,3	17,2	2,0
	610-2	429,3	21,2	0,2	460,8	19,6	-	382,1	14,5	2,1
	610-3	485,5	28,6	0,2	471,4	25,3	-	331,5	17,3	1,7
	610-4	478,6	29,4	0,2	482,2	28,4	-	330,9	17,2	1,6
	610-5	492,3	19,4	0,2	486,9	16,5	-	336,9	11,2	2,0
	610-6	496,6	18,5	0,2	488,6	16,7	-	334,7	10,8	1,6
	610-7	493,7	22,8	0,2	473,2	22,5	-	334,0	13,1	1,6
	610-8	485,5	24,7	0,2	480,0	24,0	-	327,6	14,3	1,6
	610-9	454,6	21,1	0,3	473,1	21,2	-	362,2	14,2	2,0
	610-10	463,4	21,4	0,3	490,1	22,2	-	362,7	15,2	1,9
	610-11	471,3	22,2	0,2	478,4	22,2	-	352,2	15,2	1,9
	610-12	465,4	23,4	0,1	475,6	21,1	-	351,6	14,4	1,6
	610-13	471,8	20,1	0,2	479,8	20,9	-	357,4	14,4	1,8
	610-14	455,2	20,6	0,2	467,7	20,4	-	347,7	13,8	1,3
	610-15	460,1	25,0	0,1	469,0	22,3	-	360,7	18,8	1,4
	610-16	459,2	23,6	0,2	472,1	25,4	-	348,6	15,5	1,2
Day2	610-1	442,4	26,7	0,2	468,8	26,4	-	351,8	16,3	1,6
	610-2	453,3	19,8	0,2	470,8	18,9	-	340,5	15,3	1,4
	610-3	468,9	26,5	0,2	489,4	25,9	-	353,7	16,8	1,8
	610-4	465,2	25,3	0,2	471,0	22,8	-	358,5	15,8	2,0
	610-5	487,2	21,7	0,2	473,6	20,0	-	361,4	12,4	1,5
	610-6	488,5	20,6	0,2	481,8	18,8	-	354,9	15,5	1,3
	610-7	482,6	24,7	0,2	478,9	23,6	-	304,9	12,9	1,4
	610-8	478,4	21,3	0,2	472,0	20,2	-	343,2	14,2	1,7
	610-9	475,4	24,1	0,2	481,7	19,0	-	366,6	15,6	2,0
	610-10	457,4	17,4	0,2	479,4	17,8	-	362,7	13,6	1,9
	610-11	457,3	19,8	0,2	462,7	16,6	-	347,3	13,1	1,6
	610-12	458,9	20,9	0,2	482,0	22,5	-	354,4	15,6	1,5
	Mean	**468,0**			**476,0**			**350,0**		
	Standart Deviation	**18,3**			**7,8**			**16,3**		
	Reference Values	**468,0**			**476,0**			**350,0**		
	Precision (% RSD)	**3,9**			**1,6**			**4,6**		
	Accuracy (%)	**100,0**			**100,0**			**100,0**		

Part 2

		Na			Mg			Al		
		Concentration ppm	**2SE (ppm)**	**LOD (ppm)**	**Concentration ppm**	**2SE (ppm)**	**LOD (ppm)**	**Concentration ppm**	**2SE (ppm)**	**LOD (ppm)**
	G_NIST610									
Day1	610-1	88 182,5	3 225,0	3,7	386,9	11,4	0,1	9 799,8	181,9	0,2
	610-2	89 464,4	2 825,5	3,7	389,8	9,5	0,1	9 914,1	167,5	0,2
	610-3	103 344,5	4 367,3	4,8	447,0	14,3	0,1	11 089,2	202,6	0,3
	610-4	104 353,5	3 772,5	4,5	447,3	12,7	0,1	11 333,3	217,7	0,3
	610-5	104 668,2	2 517,9	3,5	459,3	9,7	0,1	11 229,1	153,0	0,3
	610-6	105 232,5	2 322,1	4,3	456,6	9,2	0,1	11 378,8	138,5	0,2
	610-7	105 964,1	3 488,1	4,1	453,2	11,3	0,1	11 207,0	189,0	0,2
	610-8	103 551,0	3 612,2	3,8	458,4	12,8	0,1	11 321,4	214,4	0,2
	610-9	96 362,3	2 873,1	3,9	421,1	9,3	0,1	10 592,5	153,9	0,2
	610-10	97 474,9	2 841,2	4,2	428,5	10,3	0,1	10 611,4	149,5	0,2
	610-11	99 810,1	3 221,6	4,3	433,4	10,7	0,1	10 816,1	194,7	0,2
	610-12	100 847,0	3 617,7	3,4	426,6	11,4	0,1	10 765,2	181,9	0,2
	610-13	100 371,0	2 794,3	4,6	434,9	11,9	0,1	10 892,1	194,3	0,2
	610-14	97 648,7	3 426,9	4,1	426,0	12,9	0,1	10 650,4	182,6	0,3
	610-15	97 223,9	3 454,9	3,6	418,3	12,4	0,1	10 645,6	244,5	0,2
	610-16	95 936,4	3 379,7	3,8	424,0	10,3	0,1	10 496,2	198,6	0,2
Day2	610-1	95 255,3	3 616,7	3,6	412,6	11,8	0,1	10 472,1	156,9	0,2
	610-2	96 470,3	3 081,3	4,2	425,0	10,2	0,1	10 716,7	145,0	0,2
	610-3	99 714,2	3 713,6	4,5	436,1	12,2	0,1	10 757,3	207,0	0,3
	610-4	98 418,5	3 009,8	5,2	429,5	10,7	0,1	10 691,5	163,4	0,2
	610-5	103 763,1	2 830,3	5,0	441,6	9,6	0,1	11 042,2	143,1	0,3
	610-6	102 572,4	2 740,9	4,3	445,4	9,4	0,1	11 082,3	131,1	0,3
	610-7	102 198,1	3 157,8	3,8	444,3	10,7	0,1	11 020,8	189,2	0,2
	610-8	101 118,0	2 752,9	4,9	442,0	9,7	0,1	11 099,3	157,5	0,2
	610-9	100 049,5	3 918,0	5,8	429,3	12,8	0,1	10 680,3	195,4	0,2
	610-10	98 200,3	2 835,5	4,5	421,8	10,1	0,1	10 506,3	191,9	0,2
	610-11	96 747,9	2 495,1	4,0	425,8	9,0	0,1	10 707,6	129,0	0,2
	610-12	98 416,3	3 502,2	3,7	430,5	12,2	0,1	10 785,0	183,4	0,3
	Mean	**99 405,7**			**432,0**			**10 796,6**		
	Standart Deviation	**4 300,0**			**17,6**			**377,6**		
	Reference Values	**99 415,0**			**432,0**			**10 797,0**		
	Precision (% RSD)	**4,3**			**4,1**			**3,5**		
	Accuracy (%)	**100,0**			**100,0**			**100,0**		

Part 3

		Cl			K			Ca		
		Concentration ppm	**2SE (ppm)**	**LOD (ppm)**	**Concentration ppm**	**2SE (ppm)**	**LOD (ppm)**	**Concentration ppm**	**2SE (ppm)**	**LOD (ppm)**
	G_NIST610									
Day1	610-1	299,0	12,0	8,9	416,8	10,9	1,9	71 774,9	3 013,8	18,0
	610-2	295,0	9,8	12,2	416,9	11,8	2,5	73 881,7	3 207,2	17,9
	610-3	254,8	10,5	14,7	486,5	12,4	1,8	88 390,1	3 301,0	17,7
	610-4	248,7	11,7	11,3	474,7	12,7	1,9	86 744,9	4 021,9	20,7
	610-5	282,8	10,2	11,9	489,9	9,4	2,3	86 536,5	2 122,2	16,8
	610-6	253,6	10,4	10,5	487,8	10,3	1,5	86 026,2	2 326,2	15,5
	610-7	274,3	9,3	12,4	478,2	10,7	1,9	85 358,1	2 839,7	17,8
	610-8	245,4	9,8	17,3	490,1	14,1	1,7	88 008,2	3 868,9	19,2
	610-9	319,3	7,4	12,5	461,4	10,1	1,8	78 234,7	2 280,9	14,3
	610-10	267,0	8,5	12,4	462,6	11,1	2,1	78 806,3	2 707,2	16,2
	610-11	286,2	11,0	10,4	471,6	14,1	1,8	83 375,0	3 736,3	16,4
	610-12	250,9	9,5	10,8	471,8	14,4	1,7	83 270,1	3 485,9	17,9
	610-13	296,4	10,7	12,6	468,0	11,9	1,6	83 494,2	3 552,1	15,5
	610-14	272,4	9,6	12,8	454,9	9,8	1,7	80 144,1	2 638,8	14,1
	610-15	274,9	9,5	14,7	444,9	14,7	1,7	79 733,8	4 113,0	16,8
	610-16	263,5	9,8	13,1	447,2	14,1	1,5	80 426,0	3 700,8	15,4
Day2	610-1	270,3	9,9	13,9	438,5	10,6	2,0	77 393,4	3 412,1	23,4
	610-2	270,5	8,6	15,6	444,4	9,5	1,8	78 483,8	2 787,3	22,4
	610-3	267,7	12,8	18,9	458,4	12,1	2,5	82 326,7	3 429,5	28,5
	610-4	270,1	12,0	12,7	469,9	12,6	2,5	83 102,4	3 686,5	20,4
	610-5	301,0	9,6	17,8	492,7	11,3	2,6	88 096,8	2 942,7	20,9
	610-6	277,7	11,4	17,4	483,7	9,9	2,4	86 420,5	2 723,9	17,9
	610-7	245,7	9,0	12,2	477,5	10,9	1,4	81 944,4	2 885,2	17,1
	610-8	262,7	10,4	18,8	472,7	9,5	2,3	84 095,7	2 538,9	15,6
	610-9	316,8	13,8	13,2	458,7	10,7	1,9	78 640,3	2 285,5	29,5
	610-10	275,7	9,2	20,3	457,7	8,7	1,9	80 893,2	2 534,6	21,5
	610-11	273,7	8,0	13,0	461,5	10,8	1,3	83 001,0	3 081,0	16,3
	610-12	255,7	9,4	12,3	452,0	10,7	1,7	81 302,2	3 343,2	22,6
	Mean	**274,0**			**464,0**			**82 139,5**		
	Standart Deviation	**19,9**			**20,0**			**4 166,1**		
	Reference Values	**274,0**			**464,0**			**82 144,0**		
	Precision (% RSD)	**7,3**			**4,3**			**5,1**		
	Accuracy (%)	**100,0**			**100,0**			**100,0**		

Part 4

		Ti			Mn			Fe		
		Concentration ppm	**2SE (ppm)**	**LOD (ppm)**	**Concentration ppm**	**2SE (ppm)**	**LOD (ppm)**	**Concentration ppm**	**2SE (ppm)**	**LOD (ppm)**
	G_NIST610									
Day1	610-1	409,0	19,8	-	404,2	22,7	0,1	414,4	24,4	2,9
	610-2	409,6	19,1	-	410,9	19,8	0,2	424,6	21,5	3,4
	610-3	473,1	20,3	-	461,5	20,0	0,2	483,7	23,9	2,2
	610-4	462,2	21,2	-	458,0	25,2	0,1	469,2	27,9	2,1
	610-5	474,4	14,9	-	460,1	14,5	0,1	476,1	16,7	2,0
	610-6	477,4	16,6	-	463,2	15,7	0,1	473,8	16,2	2,2
	610-7	465,8	17,7	-	456,9	19,9	0,2	475,3	23,4	2,0
	610-8	485,9	23,4	-	471,1	24,5	0,1	488,2	27,3	1,6
	610-9	446,0	16,5	-	440,9	18,6	0,1	445,8	19,8	1,9
	610-10	444,7	17,6	-	435,9	18,6	0,2	446,4	19,5	2,4
	610-11	454,3	19,6	-	452,6	21,8	0,1	465,1	24,9	1,5
	610-12	455,9	18,6	-	441,0	19,2	0,1	460,5	23,6	2,0
	610-13	451,6	18,9	-	441,3	20,8	0,1	459,1	23,4	1,8
	610-14	429,5	15,4	-	432,4	18,2	0,2	448,7	21,7	1,8
	610-15	445,9	24,0	-	434,5	22,8	0,1	444,7	24,9	1,9
	610-16	446,3	21,5	-	439,2	20,0	0,2	452,1	22,2	1,5
Day2	610-1	454,3	24,8	0,3	443,1	24,1	0,2	449,0	25,8	2,6
	610-2	437,6	14,3	-	436,4	18,3	0,2	450,1	20,0	2,5
	610-3	442,0	18,1	-	433,0	20,6	0,2	451,5	23,7	2,9
	610-4	458,3	21,8	-	454,9	24,7	0,2	467,8	26,2	3,2
	610-5	453,5	16,8	-	447,0	18,7	0,2	465,7	20,1	2,9
	610-6	463,1	15,7	-	449,2	17,1	0,2	466,6	19,4	2,4
	610-7	457,7	18,4	-	450,7	19,8	0,1	469,2	23,6	1,4
	610-8	462,6	13,8	-	453,0	16,1	0,1	458,7	18,2	2,5
	610-9	445,7	18,4	-	436,7	18,8	0,2	447,4	20,4	1,8
	610-10	451,3	16,7	-	432,7	15,1	0,2	452,7	18,9	2,2
	610-11	451,0	17,1	-	448,6	18,0	0,2	458,1	18,8	1,8
	610-12	446,7	17,2	-	442,9	18,8	0,2	459,0	22,1	1,6
	Mean	**452,0**			**444,0**			**458,0**		
	Standart Deviation	**17,3**			**14,6**			**16,0**		
	Reference Values	**452,0**			**444,0**			**458,0**		
	Precision (% RSD)	**3,8**			**3,3**			**3,5**		
	Accuracy (%)	**100,0**			**100,0**			**100,0**		

Part 5

		Co			Cu			Zn		
		Concentration ppm	**2SE (ppm)**	**LOD (ppm)**	**Concentration ppm**	**2SE (ppm)**	**LOD (ppm)**	**Concentration ppm**	**2SE (ppm)**	**LOD (ppm)**
	G_NIST610									
Day1	610-1	365,6	21,4	0,0	396,3	23,2	0,2	407,2	22,6	0,5
	610-2	379,6	19,4	0,0	416,9	22,3	0,2	422,6	22,1	0,6
	610-3	436,9	23,6	0,0	461,5	25,2	0,2	489,1	26,6	0,5
	610-4	425,8	26,1	-	461,9	28,7	0,2	482,6	28,4	0,4
	610-5	429,9	16,8	-	453,8	17,3	0,2	473,0	18,9	0,5
	610-6	421,9	15,8	-	450,9	16,3	0,2	475,5	19,1	0,5
	610-7	429,2	21,9	-	463,2	23,5	0,2	479,4	24,6	0,3
	610-8	433,6	24,7	0,0	464,2	29,0	0,2	492,7	30,5	0,3
	610-9	396,9	18,7	0,0	424,4	20,9	0,2	445,7	22,4	0,4
	610-10	400,3	19,9	-	431,1	22,4	0,2	461,1	23,8	0,4
	610-11	420,7	23,2	0,0	447,3	25,0	0,2	468,6	26,2	0,3
	610-12	403,0	21,9	0,0	447,7	25,4	0,2	451,9	24,6	0,3
	610-13	412,2	21,4	-	439,3	24,5	0,2	459,7	24,8	0,3
	610-14	397,5	19,3	-	423,3	21,6	0,2	451,6	25,4	0,3
	610-15	402,0	23,0	-	439,7	26,8	0,1	444,6	27,7	0,3
	610-16	407,0	20,5	-	434,4	23,3	0,1	454,6	24,6	0,2
Day2	610-1	407,1	25,6	0,0	444,8	29,7	0,1	455,3	30,2	0,3
	610-2	403,6	19,8	-	431,3	21,5	0,1	448,5	23,6	0,3
	610-3	404,8	22,2	-	439,5	25,6	0,2	453,9	26,7	0,3
	610-4	406,2	21,8	-	437,6	23,1	0,2	459,4	26,5	0,3
	610-5	420,5	20,2	-	438,1	20,9	0,1	475,1	25,4	-
	610-6	423,8	20,1	-	448,0	22,6	0,2	466,2	22,9	0,3
	610-7	412,2	21,3	0,0	466,9	25,2	0,1	492,8	28,0	-
	610-8	417,4	19,6	0,0	432,9	19,9	0,2	458,5	23,0	-
	610-9	399,5	18,2	0,0	435,3	22,0	0,2	446,6	25,2	0,5
	610-10	403,3	16,0	-	443,7	16,9	0,2	442,6	18,3	0,5
	610-11	415,8	18,7	-	440,9	20,5	0,1	455,7	22,4	-
	610-12	405,9	18,6	-	433,0	23,0	0,1	465,3	27,3	0,3
	Mean	**410,1**			**441,0**			**460,0**		
	Standart Deviation	**15,7**			**15,6**			**19,4**		
	Reference Values	**410,0**			**441,0**			**460,0**		
	Precision (% RSD)	**3,8**			**3,5**			**4,2**		
	Accuracy (%)	**100,0**			**100,0**			**100,0**		

Part 6

		Ga			Ge			As		
		Concentration ppm	**2SE (ppm)**	**LOD (ppm)**	**Concentration ppm**	**2SE (ppm)**	**LOD (ppm)**	**Concentration ppm**	**2SE (ppm)**	**LOD (ppm)**
	G_NIST610									
Day1	610-1	389,5	22,9	-	398,8	22,3	0,4	293,2	15,2	1,2
	610-2	398,0	20,0	-	401,3	18,9	0,4	290,6	12,4	1,1
	610-3	450,5	24,1	-	477,4	22,9	0,5	346,2	17,2	1,3
	610-4	453,7	28,2	-	463,8	26,2	0,3	341,7	18,9	1,1
	610-5	451,7	17,0	-	475,2	15,6	0,6	343,8	11,2	1,1
	610-6	452,0	15,8	-	467,0	16,7	0,4	336,1	11,8	1,2
	610-7	452,0	21,7	-	466,6	21,0	0,5	337,7	13,8	0,9
	610-8	462,9	26,0	-	472,7	24,5	0,4	346,7	15,8	0,9
	610-9	408,9	20,1	-	425,8	19,0	0,4	309,3	11,9	0,9
	610-10	427,6	21,7	-	439,9	20,4	0,4	324,2	12,8	1,2
	610-11	445,3	23,0	-	453,6	21,1	0,5	327,2	14,7	1,3
	610-12	427,7	22,5	-	447,4	23,2	0,4	317,5	14,7	1,1
	610-13	438,8	21,8	-	454,0	21,0	0,5	330,4	14,8	1,2
	610-14	419,1	21,4	-	437,0	20,8	0,5	316,5	14,9	1,1
	610-15	427,4	25,2	-	443,2	24,9	0,4	324,2	15,8	1,1
	610-16	422,7	21,4	-	427,9	22,9	0,4	314,7	15,6	0,9
Day2	610-1	420,5	26,4	-	428,0	25,3	0,5	302,8	16,8	1,2
	610-2	422,6	21,3	0,0	434,6	20,5	0,5	308,7	12,7	1,0
	610-3	436,9	23,6	-	442,3	21,9	0,5	334,9	15,8	1,2
	610-4	429,3	22,5	-	448,3	22,5	0,5	330,6	15,7	1,2
	610-5	447,2	20,8	-	467,4	20,7	0,6	344,7	14,1	1,3
	610-6	455,5	20,8	-	471,9	20,5	0,7	342,7	14,9	1,1
	610-7	435,1	22,7	-	444,5	21,6	0,3	301,8	13,4	0,9
	610-8	432,1	20,0	-	457,8	19,5	0,6	336,6	12,5	1,1
	610-9	424,5	19,5	-	440,7	18,6	0,4	323,3	14,4	1,0
	610-10	421,3	16,5	-	441,4	14,9	0,6	331,5	11,2	1,2
	610-11	438,1	19,9	-	443,4	18,3	0,4	318,3	11,8	0,7
	610-12	432,9	21,2	-	443,6	21,8	0,4	324,2	13,4	1,2
	Mean	**433,0**			**447,0**			**325,0**		
	Standart Deviation	**17,4**			**19,9**			**16,0**		
	Reference Values	**433,0**			**447,0**			**325,0**		
	Precision (% RSD)	**4,0**			**4,5**			**4,9**		
	Accuracy (%)	**100,0**			**100,0**			**100,0**		

Part 7

		Rb			Sr			Zr		
		Concentration ppm	**2SE (ppm)**	**LOD (ppm)**	**Concentration ppm**	**2SE (ppm)**	**LOD (ppm)**	**Concentration ppm**	**2SE (ppm)**	**LOD (ppm)**
	G_NIST610									
Day1	610-1	377,2	17,4	0,0	460,5	17,6	-	401,3	11,6	-
	610-2	385,7	13,9	-	468,3	13,3	-	409,6	10,5	-
	610-3	457,7	19,6	0,0	554,6	19,0	-	480,5	14,8	-
	610-4	441,0	21,8	0,0	545,1	22,5	-	461,0	13,1	-
	610-5	455,4	12,8	-	542,7	12,8	-	475,0	9,0	-
	610-6	453,5	13,2	0,0	547,5	15,4	-	472,0	10,1	-
	610-7	448,3	17,1	0,0	538,8	15,8	-	466,4	12,7	-
	610-8	444,7	18,2	-	541,5	19,9	-	471,9	13,0	-
	610-9	396,0	13,2	-	468,0	13,2	-	421,5	10,1	-
	610-10	414,1	14,0	-	495,4	13,5	-	438,7	8,8	-
	610-11	430,0	16,2	-	516,8	16,7	-	452,5	12,4	-
	610-12	417,9	16,4	-	516,6	19,4	-	443,3	12,9	-
	610-13	428,1	15,9	0,0	514,8	15,6	-	446,8	11,3	-
	610-14	415,9	17,1	0,0	511,4	20,6	-	440,1	15,2	-
	610-15	434,7	21,1	-	522,1	21,7	-	452,2	18,1	-
	610-16	410,6	17,4	-	503,8	19,7	-	435,0	14,0	-
Day2	610-1	401,3	18,4	0,0	497,1	19,9	-	432,5	12,8	-
	610-2	420,2	15,1	0,0	520,1	14,8	-	454,1	10,4	-
	610-3	425,2	17,1	0,0	511,6	15,8	-	443,8	14,0	-
	610-4	431,5	17,9	0,0	521,1	17,6	-	453,2	11,5	-
	610-5	443,9	13,9	-	530,2	13,8	-	457,6	9,2	-
	610-6	441,0	14,8	-	518,6	12,0	-	451,1	8,8	-
	610-7	426,6	15,3	-	531,4	15,2	-	459,3	11,0	-
	610-8	441,7	13,9	0,0	524,0	13,8	-	451,5	9,0	-
	610-9	409,6	15,3	-	490,7	17,7	-	433,7	13,7	-
	610-10	411,0	12,0	0,0	493,0	15,2	-	432,3	10,9	-
	610-11	422,9	12,9	0,0	515,5	13,8	-	445,2	9,3	-
	610-12	433,3	17,3	0,0	532,8	17,0	-	461,8	12,0	-
	Mean	**425,7**			**515,5**			**448,0**		
	Standart Deviation	**20,4**			**24,2**			**18,7**		
	Reference Values	**425,7**			**515,5**			**448,0**		
	Precision (% RSD)	**4,8**			**4,7**			**4,2**		
	Accuracy (%)	**100,0**			**100,0**			**100,0**		

Part 8

		Nb			Mo			Ag		
		Concentration ppm	**2SE (ppm)**	**LOD (ppm)**	**Concentration ppm**	**2SE (ppm)**	**LOD (ppm)**	**Concentration ppm**	**2SE (ppm)**	**LOD (ppm)**
	G_NIST610									
Day1	610-1	416,6	11,3	-	375,0	8,7	-	239,4	5,7	-
	610-2	429,0	10,5	-	382,5	10,0	-	248,8	6,9	-
	610-3	494,9	13,1	-	446,6	10,9	-	262,8	7,4	-
	610-4	477,5	11,1	-	430,0	10,4	-	256,4	6,9	-
	610-5	490,2	8,3	-	434,1	7,4	-	252,8	4,3	-
	610-6	491,7	8,1	-	444,7	7,5	-	254,1	4,7	-
	610-7	477,9	9,8	-	430,9	10,3	-	252,9	6,3	-
	610-8	497,3	11,4	-	437,7	10,3	-	256,0	6,9	-
	610-9	434,1	8,0	-	390,0	6,6	-	235,5	4,8	-
	610-10	448,1	7,0	-	401,1	6,8	-	242,7	5,0	-
	610-11	469,6	11,1	-	430,0	11,4	-	258,4	7,6	-
	610-12	469,8	11,9	-	419,1	11,0	-	250,4	6,4	-
	610-13	465,2	10,1	-	417,8	10,3	-	252,7	6,7	-
	610-14	473,4	13,1	-	420,7	10,6	-	249,6	6,8	-
	610-15	449,0	14,5	-	406,9	10,9	-	250,3	8,1	-
	610-16	455,6	15,2	-	404,8	13,7	-	253,1	10,3	-
Day2	610-1	449,2	11,4	-	397,4	10,6	-	244,6	6,6	-
	610-2	471,4	7,6	-	413,1	7,3	-	247,9	4,5	-
	610-3	456,6	10,0	-	411,6	9,9	-	256,6	8,4	-
	610-4	468,4	12,0	-	426,7	14,0	-	260,1	8,4	-
	610-5	479,9	6,8	-	440,8	7,5	-	255,1	5,3	-
	610-6	477,7	7,5	-	433,4	8,4	-	249,7	5,2	-
	610-7	474,1	9,0	-	410,2	7,2	-	244,8	4,9	-
	610-8	468,1	6,8	-	419,0	7,5	-	247,9	5,1	-
	610-9	439,9	11,0	-	394,3	9,3	-	242,2	6,5	-
	610-10	444,4	9,1	-	407,7	8,1	-	249,6	5,8	-
	610-11	469,8	7,5	-	421,5	7,4	-	255,9	5,2	-
	610-12	480,5	8,1	-	428,2	7,7	-	257,6	5,6	-
	Mean	**465,0**			**417,0**			**251,0**		
	Standart Deviation	**20,3**			**18,5**			**6,4**		
	Reference Values	**465,0**			**417,0**			**251,0**		
	Precision (% RSD)	**4,4**			**4,4**			**2,5**		
	Accuracy (%)	**100,0**			**100,0**			**100,0**		

Part 9

		In			Sn			Sb		
		Concentration ppm	**2SE (ppm)**	**LOD (ppm)**	**Concentration ppm**	**2SE (ppm)**	**LOD (ppm)**	**Concentration ppm**	**2SE (ppm)**	**LOD (ppm)**
	G_NIST610									
Day1	610-1	386,1	12,0	0,0	391,8	16,6	0,5	358,8	17,5	0,1
	610-2	412,7	13,7	0,0	404,2	14,8	0,4	364,0	16,1	0,1
	610-3	461,2	13,9	0,0	452,9	16,6	0,5	422,0	19,1	0,0
	610-4	442,1	15,2	0,0	438,6	18,5	0,5	409,8	20,3	0,0
	610-5	452,6	10,7	0,0	448,9	13,1	0,5	412,0	13,1	0,0
	610-6	458,5	11,1	0,0	452,8	12,8	0,3	418,4	13,7	0,1
	610-7	457,4	14,5	0,0	454,7	18,1	0,4	410,9	17,5	0,0
	610-8	456,8	16,2	-	452,3	17,6	0,4	419,1	19,7	0,0
	610-9	396,1	9,7	0,0	394,9	12,5	0,4	365,9	12,7	0,1
	610-10	411,8	11,5	0,0	402,4	12,6	0,4	376,4	14,3	0,1
	610-11	450,7	14,6	0,0	449,0	17,9	0,5	418,5	20,6	0,0
	610-12	443,6	13,8	0,0	435,8	15,0	0,4	403,9	18,5	0,1
	610-13	435,2	14,4	0,0	427,5	14,5	0,4	390,2	14,5	0,0
	610-14	427,5	11,6	0,0	429,0	14,1	0,6	388,6	14,8	0,1
	610-15	429,3	17,8	0,0	422,3	19,0	0,4	387,7	20,2	0,0
	610-16	422,2	17,2	0,0	422,9	19,6	0,4	389,8	20,0	0,0
Day2	610-1	415,6	13,7	0,0	419,6	19,9	0,6	378,6	19,0	0,1
	610-2	423,0	10,3	0,0	420,0	13,6	0,6	383,5	15,7	0,1
	610-3	432,2	16,1	0,0	430,5	18,0	0,6	399,9	17,5	0,1
	610-4	446,8	17,1	0,0	435,2	18,4	0,6	404,9	20,2	0,1
	610-5	454,2	11,9	0,0	445,7	14,4	0,6	412,8	16,0	0,1
	610-6	449,2	11,3	0,0	443,4	14,8	0,5	412,7	16,2	0,1
	610-7	435,5	11,7	0,0	439,7	16,4	0,4	402,7	17,5	0,1
	610-8	446,7	11,1	0,0	436,0	13,3	0,4	402,7	14,5	0,1
	610-9	397,7	11,0	0,0	398,7	13,8	0,7	359,1	13,7	0,1
	610-10	416,5	10,9	0,0	407,2	11,8	0,7	380,7	13,4	0,1
	610-11	444,0	11,7	-	443,1	14,9	0,5	408,8	16,1	0,0
	610-12	446,7	10,3	0,0	441,0	13,8	0,5	405,6	14,7	0,1
	Mean	**434,0**			**430,0**			**396,0**		
	Standart Deviation	**20,5**			**19,0**			**19,1**		
	Reference Values	**434,0**			**430,0**			**396,0**		
	Precision (% RSD)	**4,7**			**4,4**			**4,8**		
	Accuracy (%)	**100,0**			**100,0**			**100,0**		

Part 10

		Te			Cs			Ba		
		Concentration ppm	**2SE (ppm)**	**LOD (ppm)**	**Concentration ppm**	**2SE (ppm)**	**LOD (ppm)**	**Concentration ppm**	**2SE (ppm)**	**LOD (ppm)**
	G_NIST610									
Day1	610-1	291,7	17,7	-	333,9	21,1	0,0	407,6	26,0	-
	610-2	292,6	15,9	-	341,5	17,9	0,0	426,8	23,6	-
	610-3	313,7	15,6	-	390,6	21,1	-	487,2	26,1	-
	610-4	304,0	19,6	-	378,6	23,7	-	466,4	30,3	-
	610-5	312,4	14,0	-	385,6	14,8	-	474,1	18,0	-
	610-6	300,0	13,2	-	384,8	15,8	0,0	477,8	19,1	-
	610-7	308,2	16,0	-	371,2	17,8	-	460,6	21,2	-
	610-8	301,4	15,7	-	381,8	20,8	0,0	472,2	27,2	-
	610-9	284,4	12,2	-	332,6	14,1	0,0	405,8	19,2	-
	610-10	296,6	15,1	-	345,3	16,0	0,0	420,4	19,9	-
	610-11	330,3	17,3	-	390,5	20,9	-	474,3	25,7	-
	610-12	311,4	16,7	-	367,2	16,5	-	463,5	23,4	-
	610-13	303,3	15,2	-	369,2	19,4	-	448,7	23,0	-
	610-14	292,6	15,2	-	370,2	17,8	-	459,1	25,0	-
	610-15	291,2	16,8	-	355,5	21,1	-	435,8	27,8	-
	610-16	298,1	17,0	-	357,3	18,5	-	451,7	24,0	-
Day2	610-1	292,0	17,4	-	347,9	20,9	0,0	443,0	29,3	-
	610-2	288,4	14,5	-	352,8	17,0	-	449,3	21,6	-
	610-3	314,7	15,8	-	371,8	20,0	0,0	449,6	25,6	-
	610-4	319,0	18,2	-	372,8	20,6	-	461,8	26,5	-
	610-5	320,6	16,0	-	384,5	18,1	-	458,4	21,3	-
	610-6	314,3	15,9	-	389,0	18,1	-	470,6	22,3	-
	610-7	243,3	12,8	-	366,1	19,9	-	470,1	25,3	-
	610-8	305,7	14,9	-	371,6	17,3	0,0	451,7	20,5	-
	610-9	286,6	17,0	-	335,7	16,5	0,0	404,2	20,4	-
	610-10	303,7	11,5	-	341,1	12,6	-	412,2	16,5	-
	610-11	318,2	14,2	-	376,7	17,3	-	472,4	22,1	-
	610-12	317,5	16,1	-	382,1	18,2	-	480,6	23,8	-
	Mean	**302,0**			**366,0**			**452,0**		
	Standart Deviation	**16,5**			**18,4**			**24,2**		
	Reference Values	**302,0**			**366,0**			**452,0**		
	Precision (% RSD)	**5,5**			**5,0**			**5,4**		
	Accuracy (%)	**100,0**			**100,0**			**100,0**		

Part 11

		Ta			W			Re		
		Concentration ppm	**2SE (ppm)**	**LOD (ppm)**	**Concentration ppm**	**2SE (ppm)**	**LOD (ppm)**	**Concentration ppm**	**2SE (ppm)**	**LOD (ppm)**
	G_NIST610									
Day1	610-1	427,0	26,8	-	425,5	26,2	-	47,1	2,6	-
	610-2	439,5	22,8	-	434,2	21,6	-	48,7	2,3	-
	610-3	460,3	24,5	-	456,8	24,5	-	50,4	2,6	-
	610-4	449,3	29,7	-	454,9	33,2	-	52,9	3,5	-
	610-5	460,8	19,0	-	452,8	18,1	-	51,4	1,9	-
	610-6	461,8	18,0	-	455,9	17,4	-	52,2	1,9	-
	610-7	446,5	21,9	-	449,5	22,2	-	50,2	2,5	-
	610-8	464,9	24,8	-	469,9	24,6	-	52,2	2,6	-
	610-9	402,5	19,6	-	399,8	19,6	-	44,6	2,1	-
	610-10	420,4	21,2	-	420,9	20,7	-	46,6	2,2	-
	610-11	462,0	24,3	-	458,8	22,7	-	51,4	2,5	-
	610-12	455,7	24,5	-	444,5	23,2	-	50,4	2,8	-
	610-13	446,4	22,8	-	445,8	21,7	-	50,4	2,3	-
	610-14	447,4	23,7	-	443,4	23,8	-	49,6	2,5	-
	610-15	442,7	29,2	-	441,3	26,8	-	49,5	2,8	-
	610-16	448,8	25,3	-	450,0	26,8	-	50,9	2,8	-
Day2	610-1	445,1	29,7	-	443,5	28,2	-	48,8	3,1	-
	610-2	451,0	23,4	-	435,9	21,9	-	47,5	2,3	-
	610-3	436,5	23,5	-	431,6	23,1	-	50,9	2,8	-
	610-4	455,3	26,1	-	454,4	28,1	-	51,1	3,1	-
	610-5	456,4	22,9	-	461,2	23,4	-	53,2	2,4	-
	610-6	460,5	21,6	-	467,3	21,7	-	52,6	2,2	-
	610-7	452,5	24,5	-	449,0	24,7	-	47,0	2,7	-
	610-8	443,3	20,3	-	444,4	21,0	-	50,7	2,4	-
	610-9	390,0	20,1	-	390,8	16,9	-	44,4	2,0	-
	610-10	407,5	16,8	-	411,2	16,0	-	46,8	2,0	-
	610-11	476,0	23,2	-	468,2	22,2	-	52,2	2,2	-
	610-12	478,0	24,8	-	470,7	23,3	-	53,5	2,6	-
	Mean	**446,0**			**444,0**			**49,9**		
	Standart Deviation	**20,6**			**20,0**			**2,5**		
	Reference Values	**446,0**			**444,0**			**49,9**		
	Precision (% RSD)	**4,6**			**4,5**			**5,0**		
	Accuracy (%)	**100,0**			**100,0**			**100,0**		

Part 12

		Au			Pb			Bi		
		Concentration ppm	**2SE (ppm)**	**LOD (ppm)**	**Concentration ppm**	**2SE (ppm)**	**LOD (ppm)**	**Concentration ppm**	**2SE (ppm)**	**LOD (ppm)**
	G_NIST610									
Day1	610-1	21,8	1,2	0,1	402,8	18,6	0,0	360,3	14,1	0,0
	610-2	22,8	1,1	0,0	413,5	14,6	-	375,5	11,4	0,0
	610-3	24,2	1,2	-	444,8	20,2	0,0	393,9	14,7	0,0
	610-4	25,0	1,7	-	432,5	23,0	0,0	397,7	17,4	0,0
	610-5	24,6	0,8	-	445,0	11,9	0,0	392,0	9,9	0,0
	610-6	24,3	1,0	-	443,4	14,5	0,0	400,0	11,2	0,0
	610-7	24,6	1,4	-	430,4	18,9	0,0	392,8	15,7	0,0
	610-8	24,4	1,2	-	443,2	18,6	0,0	399,8	14,9	0,0
	610-9	21,1	0,9	-	386,3	14,2	0,0	350,7	11,4	0,0
	610-10	22,1	1,0	-	400,7	15,9	0,0	364,1	11,8	0,0
	610-11	24,4	1,2	-	436,2	18,7	-	395,4	14,9	0,0
	610-12	24,1	1,3	-	427,3	18,3	0,0	386,3	15,0	0,0
	610-13	24,4	1,1	-	429,8	17,5	-	387,6	12,7	0,0
	610-14	23,1	1,1	-	425,5	17,0	0,0	380,8	14,9	0,0
	610-15	23,2	1,3	-	430,6	21,0	0,0	383,0	17,9	0,0
	610-16	23,6	1,2	-	424,0	18,9	0,0	384,2	14,5	0,0
Day2	610-1	22,9	1,3	-	421,0	20,0	0,0	378,6	15,8	0,0
	610-2	22,7	1,0	-	415,0	14,9	0,0	374,8	10,9	0,0
	610-3	24,3	1,2	-	427,5	16,4	-	390,7	13,1	0,0
	610-4	24,3	1,4	-	417,5	19,4	-	373,9	14,8	0,0
	610-5	24,8	1,0	-	455,1	17,2	0,0	405,9	11,8	0,0
	610-6	25,4	1,0	-	447,2	14,6	0,0	409,1	12,0	0,0
	610-7	20,6	1,1	-	430,3	17,5	0,0	379,7	13,0	0,0
	610-8	23,3	1,0	-	432,5	15,7	-	388,8	11,5	0,0
	610-9	22,3	1,2	-	372,4	18,0	-	331,5	14,4	0,0
	610-10	23,1	1,0	-	402,9	12,2	-	369,2	10,9	0,0
	610-11	24,8	1,1	-	443,1	15,1	-	401,5	10,6	0,0
	610-12	24,7	1,2	-	447,4	19,2	0,0	404,2	14,1	0,0
	Mean	**23,6**			**426,0**			**384,0**		
	Standart Deviation	**1,2**			**19,4**			**17,6**		
	Reference Values	**23,6**			**426,0**			**384,0**		
	Precision (% RSD)	**5,2**			**4,6**			**4,6**		
	Accuracy (%)	**100,0**			**100,0**			**100,0**		

Part 13

		U		
		Concentration ppm	**2SE (ppm)**	**LOD (ppm)**
	G_NIST610			
Day1	610-1	444,5	14,6	-
	610-2	447,5	11,1	-
	610-3	473,0	15,1	-
	610-4	472,2	17,5	-
	610-5	471,2	10,8	-
	610-6	482,0	11,4	-
	610-7	474,7	14,1	-
	610-8	478,0	14,9	-
	610-9	417,9	10,5	-
	610-10	436,4	11,1	-
	610-11	460,5	12,1	-
	610-12	471,8	14,4	-
	610-13	471,5	13,8	-
	610-14	454,2	15,3	-
	610-15	457,0	16,2	-
	610-16	471,6	14,1	-
Day2	610-1	458,0	15,1	-
	610-2	462,5	10,0	-
	610-3	458,9	15,0	-
	610-4	450,2	15,6	-
	610-5	479,2	10,2	-
	610-6	482,4	10,8	-
	610-7	484,8	11,7	-
	610-8	465,3	11,5	-
	610-9	393,5	13,0	-
	610-10	431,5	10,2	-
	610-11	479,4	10,0	-
	610-12	492,4	12,3	-
	Mean	**461,5**		
	Standart Deviation	**21,8**		
	Reference Values	**461,5**		
	Precision (% RSD)	**4,7**		
	Accuracy (%)	**100,0**		

Table of ICP-MS quartz analyses for different elements in G_NIST612 standard.

		Li			Be			B		
		Concentration ppm	2SE (ppm)	LOD (ppm)	Concentration ppm	2SE (ppm)	LOD (ppm)	Concentration ppm	2SE (ppm)	LOD (ppm)
	G_NIST612									
Day1	612-1	37,9	2,5	0,2	37,1	3,5	-	49,7	9,5	2,2
	612-2	38,3	2,4	0,2	40,9	2,8	-	52,7	3,2	1,9
	612-3	41,2	2,2	0,2	39,2	2,5	-	36,9	2,6	2,1
	612-4	41,5	2,3	0,3	41,3	2,4	-	38,2	2,4	2,1
	612-5	42,6	2,3	0,2	39,9	2,5	-	34,9	2,0	1,4
	612-6	42,0	1,8	0,2	41,3	2,3	-	35,3	2,1	1,3
	612-7	40,2	1,9	0,2	37,5	2,2	-	36,0	2,3	1,6
	612-8	40,4	1,9	0,4	38,0	2,1	-	34,3	2,5	2,7
	612-9	38,5	1,7	0,2	38,9	2,2	-	40,1	2,1	2,1
	612-10	37,5	2,0	0,2	38,0	2,1	-	40,8	2,5	1,6
	612-11	40,2	2,0	0,2	38,9	2,4	-	36,2	2,6	1,9
	612-12	40,5	1,9	0,2	40,9	2,2	-	34,4	2,4	1,6
	612-13	41,0	2,4	0,2	38,7	2,8	-	35,9	3,0	1,6
	612-14	38,8	2,2	0,1	39,1	2,5	-	36,8	2,7	1,4
	612-15	40,0	2,0	0,2	39,5	2,4	-	36,7	2,1	1,5
	612-16	38,8	2,0	0,2	37,3	2,3	-	35,9	2,2	1,6
Day2	612-1	39,4	2,5	0,2	41,3	2,9	-	42,8	2,6	1,7
	612-2	39,1	1,6	0,2	38,5	2,0	-	41,8	2,3	1,7
	612-3	40,6	1,8	0,2	36,4	2,3	-	37,9	2,5	1,6
	612-4	41,5	1,9	0,2	36,1	2,1	-	38,5	2,3	1,7
	612-5	40,5	1,8	0,2	39,4	2,1	-	35,6	2,1	1,4
	612-6	40,6	1,7	0,3	36,3	2,0	-	36,0	2,2	2,4
	612-7	40,2	1,4	0,2	40,6	2,3	-	41,4	2,4	1,8
	612-8	39,1	1,3	0,2	39,3	1,7	-	39,1	2,0	1,9
	612-9	40,2	2,0	0,2	37,6	2,4	-	37,6	2,3	1,9
	612-10	38,8	1,6	0,2	37,5	2,3	-	37,6	2,5	1,9
	Mean	**40,0**			**38,8**			**38,6**		
	Standart Deviation	**1,3**			**1,6**			**4,4**		
	Reference Values	**40,2**			**37,5**			**34,3**		
	Precision (% RSD)	**3,2**			**4,1**			**11,4**		
	Accuracy (%)	**99,5**			**103,5**			**112,5**		

Part 2

		Na			Mg			Al		
		Concentration ppm	**2SE (ppm)**	**LOD (ppm)**	**Concentration ppm**	**2SE (ppm)**	**LOD (ppm)**	**Concentration ppm**	**2SE (ppm)**	**LOD (ppm)**
	G_NIST612									
Day1	612-1	92 990,0	3 294,3	4,7	51,8	2,1	0,1	10 465,6	211,7	0,3
	612-2	93 718,4	3 615,8	4,7	53,0	1,9	0,1	10 327,6	229,4	0,2
	612-3	105 907,9	3 556,0	5,5	56,0	1,9	0,1	11 490,5	206,3	0,3
	612-4	105 205,1	3 451,4	4,8	58,7	1,8	0,1	11 666,6	201,3	0,3
	612-5	106 051,5	4 105,7	4,0	58,9	2,0	0,1	11 715,0	281,0	0,3
	612-6	106 413,9	2 754,3	4,6	59,6	1,8	0,1	11 858,5	174,6	0,3
	612-7	103 672,3	3 258,0	5,4	57,9	1,6	0,1	11 519,8	191,9	0,3
	612-8	106 141,0	3 410,3	5,9	58,1	1,6	0,1	11 701,5	171,1	0,3
	612-9	96 688,9	2 720,2	4,4	53,4	1,1	0,1	10 684,1	173,4	0,2
	612-10	96 915,8	3 149,6	3,4	52,7	1,5	0,1	10 840,0	204,8	0,2
	612-11	100 503,3	4 153,0	5,3	55,8	2,0	0,1	11 350,2	236,1	0,3
	612-12	101 374,8	3 617,1	4,5	56,1	1,8	0,1	11 256,7	243,1	0,2
	612-13	101 305,9	3 469,3	4,5	56,5	1,9	0,1	11 276,2	223,8	0,2
	612-14	100 454,4	3 985,1	5,8	55,7	2,0	0,1	10 995,9	221,2	0,2
	612-15	100 518,7	3 175,0	4,0	55,3	1,6	0,1	11 054,3	190,4	0,2
	612-16	98 253,7	3 621,6	4,3	55,7	1,9	0,1	11 015,2	205,0	0,2
Day2	612-1	101 586,0	4 050,9	3,5	55,8	2,0	0,1	11 196,0	215,3	0,2
	612-2	99 789,0	2 832,1	4,2	54,7	1,5	0,1	11 075,7	150,8	0,3
	612-3	102 896,6	3 110,1	5,8	55,8	1,6	0,1	11 152,3	189,2	0,4
	612-4	105 073,4	2 854,5	4,9	58,0	1,8	0,1	11 406,0	185,7	0,3
	612-5	102 927,3	2 612,5	4,9	57,0	1,4	0,1	11 202,5	146,9	0,3
	612-6	102 595,0	3 131,5	6,5	55,3	1,4	0,1	11 311,1	205,6	0,3
	612-7	97 597,1	1 931,2	5,0	54,0	1,2	0,1	10 829,2	144,7	0,2
	612-8	97 412,5	2 120,4	5,7	54,4	1,3	0,1	10 772,5	149,2	0,3
	612-9	100 009,6	2 789,6	4,5	55,6	1,7	0,1	11 069,4	207,5	0,3
	612-10	101 592,4	2 517,1	4,6	56,0	1,4	0,1	11 005,6	184,4	0,3
	Mean	**101 061,3**			**55,8**			**11 163,0**		
	Standart Deviation	**3 715,4**			**1,9**			**379,0**		
	Reference Values	**103 858,0**			**68,0**			**11 167,0**		
	Precision (% RSD)	**3,7**			**3,5**			**3,4**		
	Accuracy (%)	**97,3**			**82,1**			**100,0**		

Part 3

		Cl			K			Ca		
		Concentration ppm	**2SE (ppm)**	**LOD (ppm)**	**Concentration ppm**	**2SE (ppm)**	**LOD (ppm)**	**Concentration ppm**	**2SE (ppm)**	**LOD (ppm)**
	G_NIST612									
Day1	612-1	220,7	77,1	14,0	30,8	16,7	2,4	79 054,6	3 550,7	17,8
	612-2	239,6	10,9	11,2	54,6	3,3	1,6	77 926,0	3 527,1	16,1
	612-3	243,8	11,4	16,0	64,0	2,8	2,3	91 096,9	3 728,9	19,7
	612-4	256,7	11,7	17,1	61,7	2,3	2,3	93 010,3	3 686,8	21,7
	612-5	238,8	11,1	14,4	63,7	2,9	1,8	89 296,9	3 759,8	23,8
	612-6	252,1	10,9	17,5	66,6	1,8	1,7	91 710,4	2 664,4	20,3
	612-7	264,0	12,1	13,3	64,3	2,4	2,2	89 970,5	3 248,7	20,5
	612-8	256,1	9,3	16,3	64,5	2,1	2,3	91 526,7	3 827,4	20,4
	612-9	240,3	9,5	12,3	59,3	2,1	1,8	79 843,7	2 808,4	13,9
	612-10	257,3	10,1	13,4	55,5	2,0	1,8	78 954,4	3 080,8	14,5
	612-11	255,5	10,7	13,4	60,3	2,2	2,0	85 935,4	3 759,4	17,2
	612-12	276,9	10,9	11,2	62,1	2,7	1,6	86 576,0	3 330,4	18,0
	612-13	258,4	11,4	14,8	59,5	2,0	1,7	87 285,3	3 387,1	17,7
	612-14	252,2	9,7	17,0	60,0	2,2	1,9	86 692,6	3 213,1	16,4
	612-15	236,7	9,0	16,7	58,9	2,3	1,7	81 098,5	2 621,7	17,5
	612-16	244,7	8,7	17,9	60,4	2,0	1,8	83 770,5	3 018,8	18,8
Day2	612-1	245,7	9,9	13,4	56,6	2,1	1,8	81 591,0	3 339,8	21,6
	612-2	259,0	11,2	17,1	56,4	2,3	2,4	83 335,5	2 571,6	21,5
	612-3	261,4	13,6	15,0	58,8	1,9	1,7	88 354,9	3 140,9	25,6
	612-4	249,4	10,5	21,3	61,5	2,0	2,3	92 572,2	2 264,3	18,3
	612-5	256,1	12,5	19,2	62,3	2,0	1,8	88 627,1	2 552,1	22,3
	612-6	246,8	10,4	16,1	62,6	2,2	2,0	87 429,1	3 041,3	25,5
	612-7	262,1	9,8	17,8	58,6	1,9	2,3	84 881,2	2 424,0	22,6
	612-8	239,9	8,8	16,1	56,7	1,5	2,3	82 988,0	2 078,0	18,8
	612-9	235,5	10,2	12,8	58,7	2,1	2,1	86 235,5	2 748,2	18,7
	612-10	242,0	9,2	13,1	61,3	2,7	2,1	87 493,7	3 268,8	19,2
	Mean	**249,7**			**59,2**			**86 048,3**		
	Standart Deviation	**11,7**			**6,5**			**4 445,7**		
	Reference Values	**142,0**			**62,3**			**85 002,0**		
	Precision (% RSD)	**4,7**			**11,0**			**5,2**		
	Accuracy (%)	**175,8**			**95,1**			**101,2**		

Part 4

		Ti			Mn			Fe		
		Concentration ppm	**2SE (ppm)**	**LOD (ppm)**	**Concentration ppm**	**2SE (ppm)**	**LOD (ppm)**	**Concentration ppm**	**2SE (ppm)**	**LOD (ppm)**
	G_NIST612									
Day1	612-1	34,4	3,3	0,3	35,6	2,5	0,2	3,9	24,0	3,4
	612-2	36,9	2,0	-	36,6	2,1	0,2	31,5	2,9	2,7
	612-3	43,7	2,3	-	40,3	1,7	0,2	46,4	2,6	2,3
	612-4	42,6	2,6	-	40,6	1,9	0,2	45,6	2,5	2,5
	612-5	39,7	1,9	-	39,3	1,9	0,1	45,3	2,6	2,5
	612-6	43,3	1,9	-	40,4	1,5	0,2	48,8	1,8	1,9
	612-7	40,6	1,9	-	39,8	1,8	0,2	48,5	2,7	2,9
	612-8	41,9	2,9	-	39,6	1,6	0,2	47,0	2,2	2,6
	612-9	38,4	2,1	-	35,8	1,4	0,1	44,7	2,3	2,2
	612-10	36,7	2,3	-	36,7	2,0	0,1	44,4	2,6	2,3
	612-11	37,7	2,4	-	37,9	1,9	0,2	47,0	2,9	2,0
	612-12	38,1	1,9	-	37,3	1,6	0,1	45,5	2,4	1,9
	612-13	38,2	1,8	-	38,3	1,8	0,1	47,1	2,7	1,7
	612-14	38,4	2,4	-	37,3	1,8	0,2	46,6	2,8	1,4
	612-15	37,8	2,3	-	36,1	1,5	0,1	45,0	2,2	1,9
	612-16	38,7	2,1	-	38,3	1,9	0,1	46,1	2,5	2,0
Day2	612-1	41,9	2,6	-	38,6	2,2	0,2	42,2	2,7	2,8
	612-2	41,1	2,0	-	37,9	1,5	0,2	39,5	2,0	2,9
	612-3	39,0	2,5	-	36,7	1,6	0,2	43,2	2,3	2,9
	612-4	41,6	2,3	-	38,3	1,4	0,2	45,5	2,0	2,4
	612-5	40,3	2,4	-	38,3	1,2	0,2	47,6	2,1	2,3
	612-6	40,9	2,4	0,3	39,5	1,6	0,2	45,6	1,7	2,8
	612-7	39,3	2,1	-	37,5	1,3	0,1	45,6	1,7	2,6
	612-8	37,8	2,1	-	36,9	1,0	0,2	44,2	1,5	2,5
	612-9	39,0	2,1	-	38,3	1,4	0,2	47,8	2,0	2,4
	612-10	42,1	2,6	-	38,7	1,5	0,2	48,2	1,9	2,5
	Mean	**39,6**			**38,1**			**43,6**		
	Standart Deviation	**2,3**			**1,4**			**8,8**		
	Reference Values	**44,0**			**38,7**			**51,0**		
	Precision (% RSD)	**5,7**			**3,8**			**20,2**		
	Accuracy (%)	**90,1**			**98,4**			**85,4**		

Part 5

		Co			Cu			Zn		
		Concentration ppm	**2SE (ppm)**	**LOD (ppm)**	**Concentration ppm**	**2SE (ppm)**	**LOD (ppm)**	**Concentration ppm**	**2SE (ppm)**	**LOD (ppm)**
	G_NIST612									
Day1	612-1	31,1	2,1	0,0	37,8	2,9	0,2	35,0	6,3	0,7
	612-2	33,8	2,2	0,0	38,9	2,7	0,2	32,6	2,6	0,4
	612-3	36,1	1,8	-	41,8	2,0	0,2	35,8	2,4	0,3
	612-4	37,0	1,8	-	41,9	2,1	0,2	33,7	2,2	0,5
	612-5	34,8	1,8	-	40,2	2,2	0,2	35,0	2,3	0,3
	612-6	35,0	1,3	-	40,3	1,8	0,2	37,8	1,9	0,3
	612-7	35,5	1,7	-	40,8	2,1	0,2	36,0	2,5	0,3
	612-8	36,3	1,8	-	40,4	1,9	0,3	34,9	2,3	0,5
	612-9	32,5	1,5	0,0	37,1	1,8	0,2	31,9	1,7	0,5
	612-10	32,6	1,9	-	37,9	2,4	0,2	31,4	2,2	0,4
	612-11	34,1	1,8	-	39,3	2,4	0,2	33,8	2,3	0,3
	612-12	35,0	1,8	-	39,0	2,0	0,1	33,7	2,1	0,3
	612-13	33,7	1,8	-	38,2	2,1	0,2	33,4	2,2	0,3
	612-14	35,0	2,1	-	40,8	2,4	0,1	34,0	2,4	0,3
	612-15	33,1	1,6	-	37,8	1,9	0,2	35,2	2,3	0,3
	612-16	33,7	1,8	-	38,0	2,1	0,2	34,4	2,4	0,3
Day2	612-1	34,1	2,1	-	39,3	2,4	0,1	34,2	2,5	0,3
	612-2	33,1	1,4	-	39,6	1,7	0,2	32,7	2,0	0,3
	612-3	34,0	1,7	-	38,8	1,9	0,2	32,3	2,2	0,3
	612-4	34,5	1,5	-	39,9	1,9	0,2	33,6	2,3	0,3
	612-5	35,6	1,1	0,0	39,8	1,4	0,2	36,5	1,9	-
	612-6	36,0	1,7	0,0	39,9	1,7	0,2	35,1	2,1	0,6
	612-7	34,6	1,0	-	40,9	1,6	0,2	35,0	1,8	0,4
	612-8	33,6	1,0	-	37,9	1,3	0,2	34,0	1,7	0,4
	612-9	35,0	1,6	-	40,5	1,9	0,2	34,0	2,2	0,4
	612-10	36,4	1,4	-	40,1	1,8	0,2	34,2	2,1	0,4
	Mean	**34,5**			**39,5**			**34,2**		
	Standart Deviation	**1,4**			**1,3**			**1,4**		
	Reference Values	**35,5**			**37,8**			**39,1**		
	Precision (% RSD)	**4,0**			**3,3**			**4,2**		
	Accuracy (%)	**97,1**			**104,5**			**87,6**		

Part 6

		Ga			Ge			As		
		Concentration ppm	**2SE (ppm)**	**LOD (ppm)**	**Concentration ppm**	**2SE (ppm)**	**LOD (ppm)**	**Concentration ppm**	**2SE (ppm)**	**LOD (ppm)**
	G_NIST612									
Day1	612-1	33,2	2,3	-	34,7	3,9	0,4	31,6	7,3	1,3
	612-2	34,2	2,3	0,0	34,8	2,0	0,3	31,6	2,1	1,3
	612-3	37,8	2,2	-	41,1	2,1	0,5	35,3	2,3	1,0
	612-4	37,6	1,9	-	40,5	2,0	0,4	36,6	2,3	1,2
	612-5	36,6	2,0	-	38,8	2,0	0,4	34,3	2,1	1,0
	612-6	37,8	1,6	-	40,3	1,6	0,5	37,2	1,5	0,9
	612-7	36,3	1,8	-	39,2	1,8	0,5	34,4	2,0	0,9
	612-8	37,0	1,7	-	40,4	1,9	0,5	33,0	1,5	1,0
	612-9	34,1	1,5	-	36,1	1,6	0,4	32,1	1,9	1,2
	612-10	34,1	1,9	-	35,8	1,9	0,3	31,6	1,7	1,0
	612-11	34,5	2,0	-	38,2	1,9	0,6	32,1	1,9	1,0
	612-12	34,7	1,8	-	38,1	2,1	0,4	33,2	2,0	1,1
	612-13	35,6	2,0	-	39,9	2,2	0,4	33,0	2,2	0,9
	612-14	35,5	2,1	-	40,2	2,4	0,6	34,2	2,0	1,0
	612-15	35,5	1,9	-	39,3	2,1	0,5	34,2	2,0	1,0
	612-16	34,9	1,9	-	38,2	2,0	0,5	31,8	2,0	1,1
Day2	612-1	35,3	2,0	-	38,3	2,2	0,3	34,1	2,1	1,1
	612-2	35,4	1,5	-	38,3	1,6	0,4	34,2	1,5	1,2
	612-3	35,7	1,8	-	39,9	1,9	0,4	34,5	1,8	1,2
	612-4	36,4	1,7	-	39,6	1,8	0,6	35,6	1,8	1,3
	612-5	36,2	1,3	-	39,4	1,7	0,5	35,8	1,9	1,3
	612-6	36,4	1,5	-	39,1	1,7	0,6	33,7	1,7	1,1
	612-7	35,3	1,4	-	37,5	1,4	0,4	32,9	1,5	1,2
	612-8	34,6	1,0	-	37,4	1,5	0,4	33,2	1,6	1,1
	612-9	35,7	1,7	-	39,3	1,9	0,5	34,0	2,3	1,3
	612-10	36,3	1,5	-	40,3	1,7	0,5	34,1	2,0	1,3
	Mean	**35,6**			**38,6**			**33,8**		
	Standart Deviation	**1,2**			**1,7**			**1,5**		
	Reference Values	**36,9**			**36,1**			**35,7**		
	Precision (% RSD)	**3,4**			**4,5**			**4,5**		
	Accuracy (%)	**96,6**			**107,0**			**94,6**		

Part 7

		Rb			Sr			Zr		
		Concentration ppm	**2SE (ppm)**	**LOD (ppm)**	**Concentration ppm**	**2SE (ppm)**	**LOD (ppm)**	**Concentration ppm**	**2SE (ppm)**	**LOD (ppm)**
	G_NIST612									
Day1	612-1	28,0	1,4	0,0	69,7	2,8	-	34,3	1,6	-
	612-2	29,6	1,3	0,0	72,6	2,8	-	36,1	1,3	-
	612-3	32,3	1,3	0,0	80,4	2,4	-	40,2	1,2	-
	612-4	33,3	1,3	0,0	80,6	2,6	-	40,0	1,3	-
	612-5	32,5	1,5	0,0	79,7	3,0	-	38,8	1,2	-
	612-6	33,0	1,1	-	83,2	2,4	-	41,0	1,1	-
	612-7	33,3	1,2	0,0	84,0	2,6	-	40,5	1,1	-
	612-8	32,4	1,3	0,0	79,0	2,4	-	40,8	1,3	-
	612-9	29,2	1,1	0,0	72,5	2,1	-	36,1	1,0	-
	612-10	30,1	1,2	0,0	72,9	2,7	-	36,4	1,2	-
	612-11	31,2	1,3	0,0	76,8	3,0	-	38,1	1,2	-
	612-12	31,9	1,3	0,0	80,3	2,5	-	38,8	1,2	-
	612-13	32,7	1,5	-	79,2	2,7	-	38,5	1,5	-
	612-14	31,2	1,4	-	78,3	2,7	-	38,7	1,2	-
	612-15	29,9	1,2	0,0	74,7	2,5	-	37,5	1,2	-
	612-16	30,4	1,3	0,0	73,6	2,8	-	37,7	1,2	-
Day2	612-1	31,9	1,5	0,0	80,4	3,2	-	38,8	1,5	-
	612-2	30,8	1,0	0,0	77,2	2,1	-	37,7	0,9	-
	612-3	32,1	1,2	-	78,0	2,3	-	38,2	1,3	-
	612-4	32,1	1,1	-	80,3	2,4	-	39,7	1,1	-
	612-5	32,3	1,1	-	79,6	2,4	-	38,2	1,1	-
	612-6	32,6	1,2	0,0	80,5	2,4	-	39,0	1,0	-
	612-7	30,7	0,9	0,0	75,7	1,9	-	36,8	1,0	-
	612-8	30,8	0,8	-	75,5	2,1	-	36,5	0,9	-
	612-9	32,3	1,1	0,0	80,3	2,5	-	39,6	1,3	-
	612-10	32,2	1,1	0,0	79,9	2,2	-	38,0	1,0	-
	Mean	**31,5**			**77,9**			**38,3**		
	Standart Deviation	**1,3**			**3,5**			**1,6**		
	Reference Values	**31,4**			**78,4**			**37,9**		
	Precision (% RSD)	**4,3**			**4,5**			**4,3**		
	Accuracy (%)	**100,3**			**99,3**			**101,1**		

Part 8

		Nb			Mo			Ag		
		Concentration ppm	**2SE (ppm)**	**LOD (ppm)**	**Concentration ppm**	**2SE (ppm)**	**LOD (ppm)**	**Concentration ppm**	**2SE (ppm)**	**LOD (ppm)**
	G_NIST612									
Day1	612-1	34,2	1,3	-	32,1	2,4	-	19,9	0,9	-
	612-2	35,1	0,8	-	34,6	1,2	-	20,7	0,8	-
	612-3	40,1	1,1	-	37,7	1,3	-	21,8	0,9	-
	612-4	39,9	1,1	-	38,3	1,2	-	21,8	0,7	-
	612-5	40,0	1,1	-	35,9	1,3	-	21,2	0,7	-
	612-6	40,4	1,0	-	39,5	1,4	-	22,4	0,6	-
	612-7	39,3	0,8	-	37,5	1,2	-	21,4	0,6	-
	612-8	39,4	0,9	-	38,2	1,1	-	21,5	0,7	-
	612-9	36,6	0,8	-	34,8	1,1	-	20,0	0,7	-
	612-10	35,8	1,1	-	32,8	1,0	-	18,8	0,7	-
	612-11	38,1	0,9	-	36,3	1,3	-	20,6	0,8	-
	612-12	38,7	1,1	-	36,5	1,4	-	21,5	0,8	-
	612-13	38,5	1,1	-	36,2	1,3	-	21,3	0,8	-
	612-14	38,7	1,1	-	36,4	1,1	-	20,6	0,8	-
	612-15	36,8	1,1	-	33,8	1,2	-	21,2	0,6	-
	612-16	37,8	1,2	-	34,9	1,4	-	21,5	0,8	-
Day2	612-1	38,9	1,3	-	36,0	1,5	-	21,4	0,9	-
	612-2	38,7	0,8	-	37,6	1,2	-	21,2	0,6	-
	612-3	37,5	1,1	-	35,8	1,3	-	20,8	0,7	-
	612-4	40,1	1,1	-	37,6	1,3	-	21,8	0,6	-
	612-5	38,9	0,9	-	36,9	1,2	-	22,0	0,7	-
	612-6	39,4	1,0	-	35,4	1,3	-	22,0	0,7	-
	612-7	37,6	0,9	-	35,8	1,2	-	21,3	0,7	-
	612-8	36,3	0,8	-	34,9	1,0	-	21,5	0,7	-
	612-9	38,9	1,0	-	36,5	1,1	-	21,3	0,6	-
	612-10	39,3	0,9	-	36,8	1,1	-	22,3	0,8	-
	Mean	**38,3**			**36,1**			**21,2**		
	Standart Deviation	**1,6**			**1,7**			**0,8**		
	Reference Values	**38,9**			**37,4**			**22,0**		
	Precision (% RSD)	**4,2**			**4,7**			**3,7**		
	Accuracy (%)	**98,4**			**96,6**			**96,5**		

Part 9

		In			Sn			Sb		
		Concentration ppm	**2SE (ppm)**	**LOD (ppm)**	**Concentration ppm**	**2SE (ppm)**	**LOD (ppm)**	**Concentration ppm**	**2SE (ppm)**	**LOD (ppm)**
	G_NIST612									
Day1	612-1	32,9	1,6	0,0	39,2	2,8	0,6	29,5	2,2	0,0
	612-2	33,8	1,4	0,0	41,3	2,0	0,5	31,8	1,7	0,0
	612-3	38,6	1,5	0,0	45,6	1,9	0,5	36,2	1,8	0,0
	612-4	39,2	1,2	0,0	46,3	1,7	0,5	35,8	1,6	0,0
	612-5	36,5	1,2	0,0	43,6	1,7	0,5	35,2	1,9	0,0
	612-6	38,1	1,0	0,0	45,9	1,3	0,5	36,2	1,4	0,0
	612-7	37,5	1,2	0,0	44,8	1,8	0,5	34,6	1,4	0,0
	612-8	37,2	1,1	0,0	42,9	1,5	0,6	34,2	1,5	0,0
	612-9	34,9	1,1	0,0	41,4	1,6	0,5	31,7	1,3	0,0
	612-10	33,0	1,3	0,0	41,0	2,0	0,4	31,1	1,6	0,0
	612-11	36,2	1,5	0,0	43,4	1,9	0,5	34,7	1,7	0,0
	612-12	37,1	1,2	0,0	43,4	1,7	0,5	33,7	1,4	-
	612-13	36,1	1,3	0,0	42,4	2,1	0,5	34,1	1,7	0,1
	612-14	35,6	1,2	0,0	41,2	1,7	0,5	33,2	1,6	0,1
	612-15	35,4	1,1	0,0	41,5	1,8	0,5	32,8	1,5	0,0
	612-16	36,6	1,2	0,0	43,2	1,8	0,5	33,7	1,8	0,0
Day2	612-1	35,4	1,4	0,0	41,3	1,9	0,4	32,5	1,7	0,1
	612-2	35,7	1,0	0,0	41,8	1,3	0,6	33,0	1,3	0,1
	612-3	36,3	1,0	0,0	43,8	1,7	0,5	33,4	1,5	0,0
	612-4	37,5	0,9	0,0	43,9	1,3	0,6	34,4	1,2	0,1
	612-5	37,5	0,8	0,0	43,6	1,3	0,5	34,2	1,0	0,1
	612-6	36,6	1,0	0,0	42,7	1,4	0,6	33,6	1,3	0,0
	612-7	36,2	0,9	0,0	42,4	1,4	0,5	33,0	1,1	0,1
	612-8	35,8	0,8	0,0	41,2	1,2	0,5	33,6	1,1	0,0
	612-9	37,2	1,0	-	43,9	1,8	0,5	35,3	1,5	0,1
	612-10	38,3	1,2	-	43,1	1,7	0,5	34,9	1,4	0,1
	Mean	**36,4**			**42,9**			**33,7**		
	Standart Deviation	**1,6**			**1,7**			**1,6**		
	Reference Values	**38,9**			**38,6**			**34,7**		
	Precision (% RSD)	**4,3**			**3,9**			**4,7**		
	Accuracy (%)	**93,5**			**111,1**			**97,1**		

Part 10

		Te			Cs			Ba		
		Concentration ppm	**2SE (ppm)**	**LOD (ppm)**	**Concentration ppm**	**2SE (ppm)**	**LOD (ppm)**	**Concentration ppm**	**2SE (ppm)**	**LOD (ppm)**
	G_NIST612									
Day1	612-1	30,4	3,9	-	38,8	2,8	-	35,4	3,1	-
	612-2	30,4	2,9	-	39,4	2,7	0,0	38,7	3,0	-
	612-3	35,4	3,0	-	43,5	2,3	0,0	40,8	2,5	-
	612-4	35,8	2,9	-	43,0	2,1	-	42,0	2,2	-
	612-5	35,4	3,0	-	42,8	2,4	-	40,2	2,2	-
	612-6	36,6	2,6	-	43,4	1,7	-	41,2	1,7	-
	612-7	33,8	3,0	-	43,3	2,2	0,0	41,1	2,2	-
	612-8	31,9	2,7	-	43,2	2,2	0,0	40,4	2,0	-
	612-9	32,6	2,7	-	38,3	1,7	-	36,2	1,9	-
	612-10	33,9	2,4	-	38,6	1,9	-	35,7	2,0	-
	612-11	37,3	3,3	-	41,4	2,2	0,0	40,0	2,4	-
	612-12	35,5	2,8	-	41,8	1,9	-	39,1	2,3	-
	612-13	35,0	3,4	-	42,0	2,5	0,0	38,6	2,5	-
	612-14	34,0	3,1	-	41,5	2,3	-	40,3	2,6	-
	612-15	32,9	3,0	-	40,3	2,0	-	38,6	2,1	-
	612-16	32,7	2,8	-	40,6	2,0	-	39,0	2,2	-
Day2	612-1	32,4	2,9	-	39,8	2,1	-	37,5	2,4	-
	612-2	34,4	2,3	-	39,7	1,6	-	37,5	1,8	-
	612-3	35,0	2,6	-	42,1	2,1	-	38,0	2,3	-
	612-4	32,6	2,8	-	42,1	1,5	0,0	39,6	1,5	-
	612-5	33,4	2,7	-	41,2	1,4	-	39,1	1,7	-
	612-6	35,8	3,4	-	41,5	1,6	-	37,6	1,7	-
	612-7	38,5	2,8	-	39,3	1,3	0,0	37,2	1,6	-
	612-8	36,1	2,6	-	39,3	1,2	-	37,3	1,4	-
	612-9	34,8	3,3	-	43,5	2,1	-	40,8	2,2	-
	612-10	37,2	4,0	-	43,3	1,6	-	40,4	2,0	-
	Mean	**34,4**			**41,3**			**38,9**		
	Standart Deviation	**2,0**			**1,7**			**1,8**		
	Reference Values	**/**			**42,7**			**39,3**		
	Precision (% RSD)	**6,0**			**4,1**			**4,5**		
	Accuracy (%)	**/**			**96,7**			**99,1**		

Part 11

		Ta			W			Re		
		Concentration ppm	2SE (ppm)	LOD (ppm)	Concentration ppm	2SE (ppm)	LOD (ppm)	Concentration ppm	2SE (ppm)	LOD (ppm)
	G_NIST612									
Day1	612-1	34,9	2,4	-	36,0	2,6	-	6,4	0,7	-
	612-2	37,7	2,6	-	38,0	2,6	-	6,5	0,4	-
	612-3	38,6	2,1	-	40,1	2,3	-	6,8	0,4	-
	612-4	38,3	1,9	-	38,1	1,7	-	6,7	0,4	-
	612-5	38,6	2,3	-	38,0	2,1	-	6,8	0,4	-
	612-6	38,6	1,6	-	39,1	1,8	-	6,7	0,4	-
	612-7	37,5	1,7	-	38,6	2,0	-	6,7	0,4	-
	612-8	38,4	1,9	-	38,1	2,0	-	6,7	0,4	-
	612-9	35,5	1,5	-	36,0	1,6	-	6,0	0,3	-
	612-10	34,6	1,7	-	34,7	1,7	-	6,3	0,4	-
	612-11	37,8	2,2	-	37,9	2,0	-	6,7	0,4	-
	612-12	37,3	1,9	-	38,4	2,3	-	6,5	0,4	-
	612-13	37,2	2,1	-	38,0	2,1	-	6,8	0,4	-
	612-14	38,1	2,1	-	37,4	2,1	-	6,7	0,4	-
	612-15	36,2	1,8	-	37,4	2,1	-	6,4	0,4	-
	612-16	36,6	2,0	-	36,4	2,0	-	6,4	0,4	-
Day2	612-1	37,6	2,4	-	37,8	2,4	-	6,8	0,5	-
	612-2	35,8	1,5	-	36,7	1,7	-	6,5	0,3	-
	612-3	35,7	1,7	-	37,3	2,1	-	6,5	0,4	-
	612-4	37,0	1,6	-	38,1	1,6	-	7,0	0,4	-
	612-5	37,1	1,5	-	38,1	1,4	-	6,6	0,3	-
	612-6	37,1	1,6	-	39,1	1,6	-	6,5	0,3	-
	612-7	35,2	1,2	-	36,7	1,5	-	6,6	0,3	-
	612-8	35,0	1,0	-	37,2	1,4	-	6,5	0,3	-
	612-9	37,4	1,8	-	39,2	2,2	-	6,6	0,4	-
	612-10	38,0	1,7	-	39,2	1,9	-	6,7	0,3	-
	Mean	**37,0**			**37,7**			**6,6**		
	Standart Deviation	**1,3**			**1,2**			**0,2**		
	Reference Values	**37,6**			**38,0**			**6,6**		
	Precision (% RSD)	**3,4**			**3,2**			**3,1**		
	Accuracy (%)	**98,4**			**99,3**			**99,4**		

Part 12

		Au			Pb			Bi		
		Concentration ppm	**2SE (ppm)**	**LOD (ppm)**	**Concentration ppm**	**2SE (ppm)**	**LOD (ppm)**	**Concentration ppm**	**2SE (ppm)**	**LOD (ppm)**
	G_NIST612									
Day1	612-1	4,6	0,6	0,1	35,5	1,8	0,0	31,3	1,4	0,0
	612-2	4,5	0,3	0,1	36,3	1,9	-	32,5	1,6	0,0
	612-3	4,9	0,3	-	38,5	1,9	0,0	34,8	1,3	0,0
	612-4	4,7	0,3	-	39,0	1,7	-	34,4	1,5	0,0
	612-5	4,7	0,3	-	38,9	1,8	0,0	33,3	1,3	0,0
	612-6	4,8	0,3	-	39,1	1,4	0,0	34,0	1,1	0,0
	612-7	4,7	0,2	-	37,6	1,2	0,0	34,1	1,1	0,0
	612-8	4,7	0,3	-	38,4	1,5	-	33,5	1,1	0,0
	612-9	4,3	0,2	-	35,2	1,3	0,0	31,2	1,1	0,0
	612-10	4,4	0,3	-	34,6	1,7	0,0	31,0	1,4	0,0
	612-11	4,7	0,3	-	37,6	1,7	0,0	33,5	1,3	0,0
	612-12	4,8	0,3	-	39,3	1,7	-	34,3	1,3	0,0
	612-13	4,3	0,3	0,0	37,8	1,8	-	32,9	1,5	0,0
	612-14	4,9	0,3	-	37,1	1,9	-	33,3	1,5	0,0
	612-15	4,5	0,3	-	37,7	1,5	0,0	34,4	1,2	0,0
	612-16	4,5	0,3	-	37,0	1,7	0,0	33,0	1,2	0,0
Day2	612-1	5,0	0,3	-	37,0	1,9	-	31,9	1,4	0,0
	612-2	4,6	0,3	-	37,2	1,3	-	31,8	1,0	0,0
	612-3	4,9	0,3	-	37,5	1,6	-	33,7	1,4	0,0
	612-4	5,1	0,3	-	38,6	1,7	-	34,2	1,2	0,0
	612-5	5,0	0,3	-	38,3	1,3	-	34,2	0,9	0,0
	612-6	4,9	0,3	-	37,8	1,4	0,0	33,9	1,0	0,0
	612-7	4,7	0,2	-	35,9	1,1	-	32,6	1,0	0,0
	612-8	4,7	0,3	-	36,7	1,1	0,0	33,2	0,9	0,0
	612-9	4,9	0,3	-	38,1	1,5	-	35,1	1,3	0,0
	612-10	4,9	0,3	-	37,3	1,5	-	33,9	1,1	0,0
	Mean	**4,7**			**37,5**			**33,3**		
	Standart Deviation	**0,2**			**1,2**			**1,1**		
	Reference Values	**4,8**			**38,6**			**30,2**		
	Precision (% RSD)	**4,3**			**3,3**			**3,4**		
	Accuracy (%)	**98,9**			**97,1**			**110,3**		

Part 13

		U		
		Concentration ppm	**2SE (ppm)**	**LOD (ppm)**
	G_NIST612			
Day1	612-1	35,3	1,6	-
	612-2	37,3	1,4	-
	612-3	37,7	1,2	-
	612-4	37,9	1,4	-
	612-5	38,8	1,2	-
	612-6	38,1	1,0	-
	612-7	37,1	1,1	-
	612-8	36,9	1,1	-
	612-9	35,3	1,2	-
	612-10	34,5	1,4	-
	612-11	37,3	1,2	-
	612-12	38,3	1,3	-
	612-13	37,1	1,4	-
	612-14	37,2	1,3	-
	612-15	38,1	1,0	-
	612-16	35,4	1,1	-
Day2	612-1	36,7	1,5	-
	612-2	36,0	0,8	-
	612-3	37,9	1,2	-
	612-4	38,1	1,1	-
	612-5	38,0	1,1	-
	612-6	38,2	1,1	-
	612-7	36,4	0,8	-
	612-8	36,2	0,9	-
	612-9	38,9	1,2	-
	612-10	37,7	1,1	-
	Mean	**37,2**		
	Standart Deviation	**1,2**		
	Reference Values	**37,4**		
	Precision (% RSD)	**3,1**		
	Accuracy (%)	**99,4**		

Table of ICP-MS quartz analyses for different elements in A-type vein.

			Li			Be			B			Na		
Vein type	Spot ID	CL color/intensity and quartz texture	Concentration ppm	2SE (ppm)	LOD (ppm)	Concentration ppm	2SE (ppm)	LOD (ppm)	Concentration ppm	2SE (ppm)	LOD (ppm)	Concentration ppm	2SE (ppm)	LOD (ppm)
A	0201-21	SGR	1,39	0,29	0,46	<LOD	0,00	-	<LOD	1,87	3,52	21,31	4,54	7,94
A	0201-22	SGR	1,33	0,51	0,57	<LOD	0,00	-	<LOD	2,79	4,69	34,93	7,41	13,70
A	0201-23	SGR	-	-	-	-	-	-	-	-	-	-	-	-
A	0201-24	SGR	2,23	0,40	0,39	<LOD	0,00	-	<LOD	2,32	3,72	51,50	6,68	9,05
A	0201-26	SGR/GBM	-	-	-	-	-	-	-	-	-	-	-	-
A	0201-27	SGR/GBM	3,01	0,34	0,45	<LOD	0,00	-	<LOD	1,98	4,04	8,90	4,72	7,48
A	0201-29	SGR/GBM	2,33	0,38	0,66	<LOD	0,00	-	5,38	2,99	4,59	20,00	6,47	10,82
A	0201-30	SGR/GBM	-	-	-	-	-	-	-	-	-	-	-	-
A	0201-31	SGR/GBM	-	-	-	-	-	-	-	-	-	-	-	-
A	0201-32	SGR/GBM	-	-	-	-	-	-	-	-	-	-	-	-
A	0201-33	SGR/GBM	1,57	0,49	0,64	<LOD	0,00	-	<LOD	3,66	5,68	23,52	7,21	14,40
A	0201-34	SGR/GBM	-	-	-	-	-	-	-	-	-	-	-	-
A	0201-37	SGR/GBM	2,55	0,23	0,40	<LOD	0,00	-	<LOD	1,42	3,52	29,14	4,18	8,56
A	0201-39	SGR	2,50	0,24	0,36	<LOD	0,00	-	<LOD	1,50	3,41	<LOD	3,21	7,94
A	0201-40	SGR	-	-	-	-	-	-	-	-	-	-	-	-
A	0201-41	SGR	-	-	-	-	-	-	-	-	-	-	-	-
A	0201-42	SGR	-	-	-	-	-	-	-	-	-	-	-	-
A	0201-44	SGR/GBM	1,70	0,32	0,43	<LOD	0,00	-	<LOD	2,26	4,53	107,96	9,67	11,42
A	0201-45	SGR/GBM	-	-	-	-	-	-	-	-	-	-	-	-
A	0202-20	SGR	-	-	-	-	-	-	-	-	-	-	-	-
A	0202-21	GBM/SGR	-	-	-	-	-	-	-	-	-	-	-	-
A	0202-24	GBM/SGR	-	-	-	-	-	-	-	-	-	-	-	-
A	0202-26	GBM/SGR	-	-	-	-	-	-	-	-	-	-	-	-
A	0202-27	SGR	3,23	0,56	0,44	0,14	0,27	-	<LOD	1,92	3,52	173,40	18,14	10,52
A	0202-28	GBM/SGR	2,42	0,34	0,44	<LOD	0,00	-	<LOD	1,88	3,32	37,72	8,49	11,78
A	0202-29	GBM/SGR	3,00	0,41	0,38	<LOD	0,00	-	<LOD	1,43	2,85	12,78	4,02	9,44
A	0202-30	/	2,35	0,37	0,41	<LOD	0,00	-	<LOD	1,83	3,69	13,08	4,49	9,82
A	0202-31	SGR	2,65	0,39	0,63	0,18	0,35	-	<LOD	3,08	5,03	73,28	10,91	13,75
A	0202-32	/	2,22	0,28	0,37	<LOD	0,00	-	<LOD	1,50	2,71	25,44	5,00	7,37
A	0202-33	GBM/SGR	2,69	0,48	0,53	<LOD	0,00	-	<LOD	1,77	4,58	24,42	7,78	11,48
A	0202-34	GBM/SGR	-	-	-	-	-	-	-	-	-	-	-	-
A	0202-37	SGR	2,78	0,35	0,36	<LOD	0,00	-	<LOD	1,61	4,03	16,65	3,45	9,40
A	0202-38	SGR	2,61	0,22	0,31	<LOD	0,00	-	<LOD	1,05	3,40	13,12	2,73	7,19

Part 2

			Mg			Al			Cl			K		
Vein type	Spot ID	CL color/intensity and quartz texture	Concentration ppm	2SE (ppm)	LOD (ppm)	Concentration ppm	2SE (ppm)	LOD (ppm)	Concentration ppm	2SE (ppm)	LOD (ppm)	Concentration ppm	2SE (ppm)	LOD (ppm)
A	0201-21	SGR	2,00	0,25	0,15	63,88	1,81	0,45	156,72	12,02	25,24	<LOD	1,72	3,53
A	0201-22	SGR	46,44	6,80	0,23	133,22	3,79	0,66	165,72	24,06	41,69	17,08	4,31	6,05
A	0201-23	SGR	-	-	-	-	-	-	-	-	-	-	-	-
A	0201-24	SGR	2,28	0,35	0,22	93,45	4,48	0,48	135,66	19,81	33,58	19,91	3,49	2,90
A	0201-26	SGR/GBM	-	-	-	-	-	-	-	-	-	-	-	-
A	0201-27	SGR/GBM	1,81	0,25	0,21	89,41	2,20	0,47	155,28	17,91	26,11	<LOD	1,94	4,22
A	0201-29	SGR/GBM	20,37	2,68	0,34	87,88	3,14	0,68	154,21	18,20	31,07	<LOD	3,39	6,34
A	0201-30	SGR/GBM	-	-	-	-	-	-	-	-	-	-	-	-
A	0201-31	SGR/GBM	-	-	-	-	-	-	-	-	-	-	-	-
A	0201-32	SGR/GBM	-	-	-	-	-	-	-	-	-	-	-	-
A	0201-33	SGR/GBM	3,70	0,76	0,38	114,72	7,72	0,69	147,02	27,98	51,68	7,00	4,05	6,30
A	0201-34	SGR/GBM	-	-	-	-	-	-	-	-	-	-	-	-
A	0201-37	SGR/GBM	2,77	0,86	0,23	110,98	5,90	0,47	165,82	13,50	29,44	10,37	1,64	4,54
A	0201-39	SGR	1,53	0,22	0,18	76,12	1,60	0,47	189,16	11,28	23,92	<LOD	1,45	3,97
A	0201-40	SGR	-	-	-	-	-	-	-	-	-	-	-	-
A	0201-41	SGR	-	-	-	-	-	-	-	-	-	-	-	-
A	0201-42	SGR	-	-	-	-	-	-	-	-	-	-	-	-
A	0201-44	SGR/GBM	4,05	0,37	0,25	233,22	12,64	0,72	140,98	23,86	52,18	20,70	3,59	5,58
A	0201-45	SGR/GBM	-	-	-	-	-	-	-	-	-	-	-	-
A	0202-20	SGR	-	-	-	-	-	-	-	-	-	-	-	-
A	0202-21	GBM/SGR	-	-	-	-	-	-	-	-	-	-	-	-
A	0202-24	GBM/SGR	-	-	-	-	-	-	-	-	-	-	-	-
A	0202-26	GBM/SGR	-	-	-	-	-	-	-	-	-	-	-	-
A	0202-27	SGR	19,13	3,94	0,27	371,83	24,51	0,47	187,13	22,25	35,91	24,47	2,96	4,62
A	0202-28	GBM/SGR	3,33	0,58	0,26	82,54	3,02	0,65	186,92	20,33	40,20	9,62	2,33	4,11
A	0202-29	GBM/SGR	2,49	0,55	0,17	224,07	11,80	0,50	208,59	15,72	27,02	50,68	4,99	3,61
A	0202-30	/	12,75	4,64	0,19	136,75	6,34	0,63	217,40	20,12	29,17	20,09	3,21	4,21
A	0202-31	SGR	2,05	0,51	0,32	165,71	12,36	0,88	99,05	28,64	48,30	<LOD	3,29	5,46
A	0202-32	/	2,01	0,24	0,13	96,61	6,30	0,51	165,40	18,62	26,02	<LOD	1,86	3,34
A	0202-33	GBM/SGR	2,19	0,41	0,22	114,91	5,67	0,60	185,59	27,12	45,94	<LOD	3,32	4,33
A	0202-34	GBM/SGR	-	-	-	-	-	-	-	-	-	-	-	-
A	0202-37	SGR	13,12	3,25	0,15	74,30	2,94	0,44	166,04	15,38	27,21	<LOD	1,59	4,00
A	0202-38	SGR	2,00	1,39	0,24	87,28	1,97	0,44	189,16	10,64	32,74	<LOD	1,23	3,10

Part 3

			Ca			Ti			Mn			Fe		
Vein type	Spot ID	CL color/intensity and quartz texture	Concentration ppm	2SE (ppm)	LOD (ppm)	Concentration ppm	2SE (ppm)	LOD (ppm)	Concentration ppm	2SE (ppm)	LOD (ppm)	Concentration ppm	2SE (ppm)	LOD (ppm)
A	0201-21	SGR	<LOD	17,06	31,94	34,29	1,80	-	1,56	0,20	0,24	194,46	19,95	3,34
A	0201-22	SGR	<LOD	33,27	54,96	48,59	5,24	0,36	1,99	0,37	0,41	293,00	13,23	7,61
A	0201-23	SGR	-	-	-	83,61	3,67	-	-	-	-	-	-	-
A	0201-24	SGR	36,89	19,44	31,88	56,42	3,40	-	3,29	0,50	0,28	42,60	5,18	4,96
A	0201-26	SGR/GBM	-	-	-	91,27	3,93	-	-	-	-	-	-	-
A	0201-27	SGR/GBM	<LOD	20,18	25,22	24,94	1,97	-	0,51	0,19	0,33	13,08	2,96	3,86
A	0201-29	SGR/GBM	<LOD	23,39	32,64	19,19	1,46	-	0,73	0,21	0,55	119,05	16,34	6,91
A	0201-30	SGR/GBM	-	-	-	31,23	1,67	0,42	-	-	-	-	-	-
A	0201-31	SGR/GBM	-	-	-	23,14	1,77	0,48	-	-	-	-	-	-
A	0201-32	SGR/GBM	-	-	-	99,90	4,23	-	-	-	-	-	-	-
A	0201-33	SGR/GBM	<LOD	25,98	53,41	23,95	1,84	-	1,25	0,34	0,43	288,94	39,77	6,64
A	0201-34	SGR/GBM	-	-	-	43,40	3,00	-	-	-	-	-	-	-
A	0201-37	SGR/GBM	<LOD	15,53	38,02	20,59	1,67	0,58	1,27	0,22	0,38	18,64	3,46	5,22
A	0201-39	SGR	<LOD	17,85	28,98	98,98	3,54	-	0,57	0,16	0,31	20,42	7,42	4,41
A	0201-40	SGR	-	-	-	109,52	4,63	-	-	-	-	-	-	-
A	0201-41	SGR	-	-	-	114,82	3,59	-	-	-	-	-	-	-
A	0201-42	SGR	-	-	-	51,84	2,41	-	-	-	-	-	-	-
A	0201-44	SGR/GBM	66,37	27,26	46,10	24,97	2,50	-	3,14	0,35	0,43	387,37	138,70	6,28
A	0201-45	SGR/GBM	-	-	-	20,38	1,77	-	-	-	-	-	-	-
A	0202-20	SGR	-	-	-	33,12	2,67	-	-	-	-	-	-	-
A	0202-21	GBM/SGR	-	-	-	15,79	1,60	-	-	-	-	-	-	-
A	0202-24	GBM/SGR	-	-	-	38,90	3,05	-	-	-	-	-	-	-
A	0202-26	GBM/SGR	-	-	-	20,18	2,45	-	-	-	-	-	-	-
A	0202-27	SGR	112,85	42,69	41,75	39,61	2,45	-	2,28	0,55	0,32	70,93	11,42	4,82
A	0202-28	GBM/SGR	<LOD	23,48	41,96	20,81	2,61	-	2,31	0,41	0,43	25,06	4,60	3,99
A	0202-29	GBM/SGR	33,62	19,95	27,58	28,34	2,40	-	0,36	0,19	0,30	16,47	2,40	3,27
A	0202-30	/	<LOD	23,40	40,43	21,34	2,63	-	0,69	0,25	0,35	17,93	4,30	3,34
A	0202-31	SGR	<LOD	53,22	75,55				0,49	0,35	0,44	83,41	33,46	5,93
A	0202-32	/	<LOD	19,42	31,37	10,64	1,77	-	<LOD	0,16	0,30	16,05	3,84	3,25
A	0202-33	GBM/SGR	<LOD	20,87	42,65	18,66	1,86	-	0,80	0,28	0,41	36,71	7,56	4,45
A	0202-34	GBM/SGR	-	-	-	21,64	2,99	-	-	-	-	-	-	-
A	0202-37	SGR	82,49	22,82	27,83	21,71	1,95	-	1,26	0,30	0,33	29,43	7,46	4,42
A	0202-38	SGR	<LOD	14,75	31,48	9,73	1,31	-	<LOD	0,11	0,23	6,06	1,54	4,02

Part 4

			Co			Cu			Zn			Ga		
Vein type	Spot ID	CL color/intensity and quartz texture	Concentration ppm	2SE (ppm)	LOD (ppm)	Concentration ppm	2SE (ppm)	LOD (ppm)	Concentration ppm	2SE (ppm)	LOD (ppm)	Concentration ppm	2SE (ppm)	LOD (ppm)
A	0201-21	SGR	0,05	0,02	-	0,31	0,20	0,29	0,65	0,41	0,58	<LOD	0,00	-
A	0201-22	SGR	0,03	0,04	-	3,35	0,45	0,47	1,30	0,93	0,84	0,05	0,05	-
A	0201-23	SGR	-	-	-	-	-	-	-	-	-	-	-	-
A	0201-24	SGR	<LOD	0,02	0,04	2,33	0,68	0,35	0,58	0,57	0,81	<LOD	0,00	-
A	0201-26	SGR/GBM	-	-	-	-	-	-	-	-	-	-	-	-
A	0201-27	SGR/GBM	0,01	0,01	-	<LOD	0,20	0,45	<LOD	0,34	0,68	<LOD	0,00	-
A	0201-29	SGR/GBM	<LOD	0,00	-	1,94	0,51	0,52	<LOD	0,55	0,99	<LOD	0,00	-
A	0201-30	SGR/GBM	-	-	-	-	-	-	-	-	-	-	-	-
A	0201-31	SGR/GBM	-	-	-	-	-	-	-	-	-	-	-	-
A	0201-32	SGR/GBM	-	-	-	-	-	-	-	-	-	-	-	-
A	0201-33	SGR/GBM	<LOD	0,00	-	2,64	0,61	0,59	<LOD	0,65	1,63	0,05	0,05	-
A	0201-34	SGR/GBM	-	-	-	-	-	-	-	-	-	-	-	-
A	0201-37	SGR/GBM	<LOD	0,02	0,05	2,28	1,15	0,45	0,83	0,36	0,75	<LOD	0,00	-
A	0201-39	SGR	0,06	0,02	-	0,69	0,31	0,34	<LOD	0,26	0,55	0,01	0,01	-
A	0201-40	SGR	-	-	-	-	-	-	-	-	-	-	-	-
A	0201-41	SGR	-	-	-	-	-	-	-	-	-	-	-	-
A	0201-42	SGR	-	-	-	-	-	-	-	-	-	-	-	-
A	0201-44	SGR/GBM	0,06	0,04	0,05	1,59	0,37	0,43	1,13	0,67	0,91	0,02	0,02	-
A	0201-45	SGR/GBM	-	-	-	-	-	-	-	-	-	-	-	-
A	0202-20	SGR	-	-	-	-	-	-	-	-	-	-	-	-
A	0202-21	GBM/SGR	-	-	-	-	-	-	-	-	-	-	-	-
A	0202-24	GBM/SGR	-	-	-	-	-	-	-	-	-	-	-	-
A	0202-26	GBM/SGR	-	-	-	-	-	-	-	-	-	-	-	-
A	0202-27	SGR	0,05	0,04	-	0,70	0,41	0,35	0,99	0,62	0,75	0,09	0,07	-
A	0202-28	GBM/SGR	<LOD	0,03	0,06	2,37	0,58	0,41	1,06	0,43	-	<LOD	0,00	-
A	0202-29	GBM/SGR	0,00	0,01	-	<LOD	0,19	0,32	0,67	0,31	0,56	0,07	0,04	-
A	0202-30	/	<LOD	0,00	-	<LOD	0,20	0,38	<LOD	0,47	1,20	<LOD	0,00	-
A	0202-31	SGR	0,08	0,06	-	<LOD	0,32	0,49	<LOD	0,34	1,08	<LOD	0,00	-
A	0202-32	/	0,02	0,02	-	<LOD	0,17	0,30	<LOD	0,29	0,63	<LOD	0,00	-
A	0202-33	GBM/SGR	<LOD	0,00	-	1,59	0,39	0,42	<LOD	0,53	0,85	<LOD	0,00	-
A	0202-34	GBM/SGR	-	-	-	-	-	-	-	-	-	-	-	-
A	0202-37	SGR	0,04	0,02	-	<LOD	0,14	0,25	<LOD	0,28	0,66	<LOD	0,00	-
A	0202-38	SGR	0,02	0,01	-	0,42	0,18	0,31	<LOD	0,20	0,58	<LOD	0,00	-

Part 5

			Ge			As			Rb			Sr		
Vein type	Spot ID	CL color/intensity and quartz texture	Concentration ppm	2SE (ppm)	LOD (ppm)	Concentration ppm	2SE (ppm)	LOD (ppm)	Concentration ppm	2SE (ppm)	LOD (ppm)	Concentration ppm	2SE (ppm)	LOD (ppm)
A	0201-21	SGR	3,64	0,52	0,73	<LOD	1,04	1,87	<LOD	0,01	0,03	0,12	0,04	-
A	0201-22	SGR	1,55	0,89	0,95	<LOD	1,49	2,85	<LOD	0,04	0,06	0,18	0,06	-
A	0201-23	SGR	-	-	-	-	-	-	-	-	-	-	-	-
A	0201-24	SGR	3,12	0,76	0,83	<LOD	1,20	1,87	0,11	0,04	0,04	0,12	0,04	-
A	0201-26	SGR/GBM	-	-	-	-	-	-	-	-	-	-	-	-
A	0201-27	SGR/GBM	2,51	0,65	0,91	<LOD	1,21	2,64	<LOD	0,01	0,04	0,02	0,01	-
A	0201-29	SGR/GBM	2,08	0,85	1,25	<LOD	1,81	3,33	0,03	0,03	-	0,02	0,02	-
A	0201-30	SGR/GBM	-	-	-	-	-	-	-	-	-	-	-	-
A	0201-31	SGR/GBM	-	-	-	-	-	-	-	-	-	-	-	-
A	0201-32	SGR/GBM	-	-	-	-	-	-	-	-	-	-	-	-
A	0201-33	SGR/GBM	4,54	1,13	1,45	<LOD	1,48	3,20	0,13	0,06	0,06	0,08	0,04	-
A	0201-34	SGR/GBM	-	-	-	-	-	-	-	-	-	-	-	-
A	0201-37	SGR/GBM	1,48	0,39	0,91	<LOD	0,85	2,45	0,08	0,02	-	0,22	0,04	-
A	0201-39	SGR	1,97	0,40	0,69	<LOD	0,96	2,36	0,01	0,01	-	0,03	0,01	-
A	0201-40	SGR	-	-	-	-	-	-	-	-	-	-	-	-
A	0201-41	SGR	-	-	-	-	-	-	-	-	-	-	-	-
A	0201-42	SGR	-	-	-	-	-	-	-	-	-	-	-	-
A	0201-44	SGR/GBM	3,27	0,85	1,46	<LOD	1,46	3,13	0,11	0,04	-	2,19	0,19	-
A	0201-45	SGR/GBM	-	-	-	-	-	-	-	-	-	-	-	-
A	0202-20	SGR	-	-	-	-	-	-	-	-	-	-	-	-
A	0202-21	GBM/SGR	-	-	-	-	-	-	-	-	-	-	-	-
A	0202-24	GBM/SGR	-	-	-	-	-	-	-	-	-	-	-	-
A	0202-26	GBM/SGR	-	-	-	-	-	-	-	-	-	-	-	-
A	0202-27	SGR	8,73	1,41	1,11	<LOD	1,34	2,24	0,07	0,04	-	2,19	0,26	-
A	0202-28	GBM/SGR	3,34	0,61	0,88	<LOD	0,94	2,41	0,05	0,02	-	0,17	0,05	-
A	0202-29	GBM/SGR	1,77	0,55	0,72	2,05	1,08	1,93	0,31	0,07	0,04	0,22	0,05	-
A	0202-30	/	2,15	0,55	0,86	<LOD	1,22	2,38	0,15	0,04	0,04	0,11	0,04	-
A	0202-31	SGR	1,87	1,02	1,56	<LOD	2,68	3,83	0,02	0,02	-	0,39	0,11	-
A	0202-32	/	2,82	0,55	0,91	<LOD	0,91	1,68	<LOD	0,01	0,04	0,11	0,04	-
A	0202-33	GBM/SGR	2,73	0,85	1,18	<LOD	1,40	2,93	<LOD	0,00	0,05	0,15	0,07	-
A	0202-34	GBM/SGR	-	-	-	-	-	-	-	-	-	-	-	-
A	0202-37	SGR	1,88	0,41	0,95	<LOD	0,90	1,97	<LOD	0,00	-	0,03	0,01	-
A	0202-38	SGR	1,81	0,37	1,00	<LOD	0,62	2,01	0,02	0,01	-	0,07	0,02	-

Part 6

			Zr			Nb			Mo			Ag		
Vein type	Spot ID	CL color/intensity and quartz texture	Concentration ppm	2SE (ppm)	LOD (ppm)	Concentration ppm	2SE (ppm)	LOD (ppm)	Concentration ppm	2SE (ppm)	LOD (ppm)	Concentration ppm	2SE (ppm)	LOD (ppm)
A	0201-21	SGR	-	-	-	-	-	-	0,24	0,10	-	-	-	-
A	0201-22	SGR	-	-	-	0,03	0,03	-	8,76	1,41	-	-	-	-
A	0201-23	SGR	-	-	-	-	-	-	-	-	-	-	-	-
A	0201-24	SGR	-	-	-	-	-	-	0,63	0,25	-	-	-	-
A	0201-26	SGR/GBM	-	-	-	-	-	-	-	-	-	-	-	-
A	0201-27	SGR/GBM	-	-	-	-	-	-	-	-	-	-	-	-
A	0201-29	SGR/GBM	-	-	-	-	-	-	0,81	0,26	-	-	-	-
A	0201-30	SGR/GBM	-	-	-	-	-	-	-	-	-	-	-	-
A	0201-31	SGR/GBM	-	-	-	-	-	-	-	-	-	-	-	-
A	0201-32	SGR/GBM	-	-	-	-	-	-	-	-	-	-	-	-
A	0201-33	SGR/GBM	-	-	-	-	-	-	8,29	1,33	-	-	-	-
A	0201-34	SGR/GBM	-	-	-	-	-	-	-	-	-	-	-	-
A	0201-37	SGR/GBM	-	-	-	-	-	-	-	-	-	-	-	-
A	0201-39	SGR	-	-	-	0,05	0,02	-	-	-	-	-	-	-
A	0201-40	SGR	-	-	-	-	-	-	-	-	-	-	-	-
A	0201-41	SGR	-	-	-	-	-	-	-	-	-	-	-	-
A	0201-42	SGR	-	-	-	-	-	-	-	-	-	-	-	-
A	0201-44	SGR/GBM	-	-	-	-	-	-	0,42	0,16	-	-	-	-
A	0201-45	SGR/GBM	-	-	-	-	-	-	-	-	-	-	-	-
A	0202-20	SGR	-	-	-	-	-	-	-	-	-	-	-	-
A	0202-21	GBM/SGR	-	-	-	-	-	-	-	-	-	-	-	-
A	0202-24	GBM/SGR	-	-	-	-	-	-	-	-	-	-	-	-
A	0202-26	GBM/SGR	-	-	-	-	-	-	-	-	-	-	-	-
A	0202-27	SGR	-	-	-	-	-	-	0,12	0,13	-	-	-	-
A	0202-28	GBM/SGR	-	-	-	-	-	-	0,75	0,22	-	-	-	-
A	0202-29	GBM/SGR	0,08	0,03	-	0,00	0,01	-	0,44	0,25	-	-	-	-
A	0202-30	/	-	-	-	-	-	-	-	-	-	-	-	-
A	0202-31	SGR	-	-	-	-	-	-	-	-	-	-	-	-
A	0202-32	/	-	-	-	-	-	-	-	-	-	-	-	-
A	0202-33	GBM/SGR	-	-	-	-	-	-	1,33	0,42	-	-	-	-
A	0202-34	GBM/SGR	-	-	-	-	-	-	-	-	-	-	-	-
A	0202-37	SGR	-	-	-	-	-	-	-	-	-	-	-	-
A	0202-38	SGR	-	-	-	-	-	-	-	-	-	-	-	-

Part 7

			In			Sn			Sb			Te		
Vein type	Spot ID	CL color/intensity and quartz texture	Concentration ppm	2SE (ppm)	LOD (ppm)	Concentration ppm	2SE (ppm)	LOD (ppm)	Concentration ppm	2SE (ppm)	LOD (ppm)	Concentration ppm	2SE (ppm)	LOD (ppm)
A	0201-21	SGR	0,02	0,01	0,02	1,82	0,51	0,85	<LOD	0,05	0,09	-	-	-
A	0201-22	SGR	<LOD	0,02	0,03	1,64	0,82	1,37	<LOD	0,06	0,12	-	-	-
A	0201-23	SGR	-	-	-	-	-	-	-	-	-	-	-	-
A	0201-24	SGR	<LOD	0,02	0,02	1,90	0,53	1,08	0,03	0,04	-	-	-	-
A	0201-26	SGR/GBM	-	-	-	-	-	-	-	-	-	-	-	-
A	0201-27	SGR/GBM	<LOD	0,01	0,03	2,21	0,58	1,04	<LOD	0,04	0,07	-	-	-
A	0201-29	SGR/GBM	<LOD	0,02	0,03	1,31	0,65	1,48	<LOD	0,06	0,12	-	-	-
A	0201-30	SGR/GBM	-	-	-	-	-	-	-	-	-	-	-	-
A	0201-31	SGR/GBM	-	-	-	-	-	-	-	-	-	-	-	-
A	0201-32	SGR/GBM	-	-	-	-	-	-	-	-	-	-	-	-
A	0201-33	SGR/GBM	<LOD	0,02	0,04	1,80	0,74	1,52	<LOD	0,00	0,12	-	-	-
A	0201-34	SGR/GBM	-	-	-	-	-	-	-	-	-	-	-	-
A	0201-37	SGR/GBM	<LOD	0,01	0,03	2,05	0,42	0,92	<LOD	0,02	0,09	-	-	-
A	0201-39	SGR	<LOD	0,01	0,03	2,06	0,45	0,97	0,02	0,02	-	-	-	-
A	0201-40	SGR	-	-	-	-	-	-	-	-	-	-	-	-
A	0201-41	SGR	-	-	-	-	-	-	-	-	-	-	-	-
A	0201-42	SGR	-	-	-	-	-	-	-	-	-	-	-	-
A	0201-44	SGR/GBM	<LOD	0,02	0,04	2,00	0,67	1,31	0,02	0,02	-	-	-	-
A	0201-45	SGR/GBM	-	-	-	-	-	-	-	-	-	-	-	-
A	0202-20	SGR	-	-	-	-	-	-	-	-	-	-	-	-
A	0202-21	GBM/SGR	-	-	-	-	-	-	-	-	-	-	-	-
A	0202-24	GBM/SGR	-	-	-	-	-	-	-	-	-	-	-	-
A	0202-26	GBM/SGR	-	-	-	-	-	-	-	-	-	-	-	-
A	0202-27	SGR	<LOD	0,02	0,03	2,22	0,80	1,02	0,06	0,06	-	-	-	-
A	0202-28	GBM/SGR	<LOD	0,01	0,03	2,09	0,59	1,35	0,02	0,02	-	-	-	-
A	0202-29	GBM/SGR	<LOD	0,01	0,03	1,80	0,49	0,89	0,04	0,03	-	-	-	-
A	0202-30	/	<LOD	0,02	0,03	2,72	0,59	1,41	0,03	0,03	-	-	-	-
A	0202-31	SGR	<LOD	0,03	0,05	<LOD	0,89	1,79	0,07	0,08	-	-	-	-
A	0202-32	/	<LOD	0,01	0,02	1,81	0,55	0,84	<LOD	0,03	0,09	-	-	-
A	0202-33	GBM/SGR	<LOD	0,02	0,04	1,86	0,93	1,50	<LOD	0,00	-	-	-	-
A	0202-34	GBM/SGR	-	-	-	-	-	-	-	-	-	-	-	-
A	0202-37	SGR	<LOD	0,01	0,02	1,53	0,51	1,02	0,01	0,02	-	-	-	-
A	0202-38	SGR	<LOD	0,01	0,03	2,07	0,37	1,00	0,03	0,02	-	-	-	-

Part 8

			Cs			Ba			Ta			W		
Vein type	Spot ID	CL color/intensity and quartz texture	Concentration ppm	2SE (ppm)	LOD (ppm)	Concentration ppm	2SE (ppm)	LOD (ppm)	Concentration ppm	2SE (ppm)	LOD (ppm)	Concentration ppm	2SE (ppm)	LOD (ppm)
A	0201-21	SGR	0,02	0,01	-	0,18	0,09	-	-	-	-	<LOD	0,00	-
A	0201-22	SGR	<LOD	0,02	0,02	0,13	0,14	-	-	-	-	<LOD	0,00	-
A	0201-23	SGR	-	-	-	-	-	-	-	-	-	-	-	-
A	0201-24	SGR	<LOD	0,01	0,02	0,22	0,12	-	-	-	-	<LOD	0,00	-
A	0201-26	SGR/GBM	-	-	-	-	-	-	-	-	-	-	-	-
A	0201-27	SGR/GBM	<LOD	0,00	-	-	-	-	-	-	-	<LOD	0,00	-
A	0201-29	SGR/GBM	<LOD	0,00	-	-	-	-	-	-	-	<LOD	0,00	-
A	0201-30	SGR/GBM	-	-	-	-	-	-	-	-	-	-	-	-
A	0201-31	SGR/GBM	-	-	-	-	-	-	-	-	-	-	-	-
A	0201-32	SGR/GBM	-	-	-	-	-	-	-	-	-	-	-	-
A	0201-33	SGR/GBM	0,01	0,01	-	0,24	0,18	-	-	-	-	<LOD	0,00	-
A	0201-34	SGR/GBM	-	-	-	-	-	-	-	-	-	-	-	-
A	0201-37	SGR/GBM	0,00	0,00	-	-	-	-	-	-	-	<LOD	0,00	-
A	0201-39	SGR	0,02	0,01	-	-	-	-	0,00	0,00	-	0,13	0,08	-
A	0201-40	SGR	-	-	-	-	-	-	-	-	-	-	-	-
A	0201-41	SGR	-	-	-	-	-	-	-	-	-	-	-	-
A	0201-42	SGR	-	-	-	-	-	-	-	-	-	-	-	-
A	0201-44	SGR/GBM	<LOD	0,00	-	0,72	0,24	-	-	-	-	<LOD	0,00	-
A	0201-45	SGR/GBM	-	-	-	-	-	-	-	-	-	-	-	-
A	0202-20	SGR	-	-	-	-	-	-	-	-	-	-	-	-
A	0202-21	GBM/SGR	-	-	-	-	-	-	-	-	-	-	-	-
A	0202-24	GBM/SGR	-	-	-	-	-	-	-	-	-	-	-	-
A	0202-26	GBM/SGR	-	-	-	-	-	-	-	-	-	-	-	-
A	0202-27	SGR	<LOD	0,00	-	3,66	0,54	-	-	-	-	<LOD	0,00	-
A	0202-28	GBM/SGR	0,01	0,01	-	0,38	0,18	-	-	-	-	<LOD	0,00	-
A	0202-29	GBM/SGR	0,03	0,01	-	0,20	0,12	-	0,01	0,01	-	<LOD	0,00	-
A	0202-30	/	0,01	0,01	-	0,20	0,13	-	-	-	-	<LOD	0,00	-
A	0202-31	SGR	0,01	0,01	-	0,35	0,24	-	-	-	-	<LOD	0,00	-
A	0202-32	/	0,01	0,01	-	-	-	-	-	-	-	<LOD	0,00	-
A	0202-33	GBM/SGR	<LOD	0,00	-	-	-	-	-	-	-	<LOD	0,00	-
A	0202-34	GBM/SGR	-	-	-	-	-	-	-	-	-	-	-	-
A	0202-37	SGR	0,01	0,01	-	-	-	-	-	-	-	<LOD	0,00	-
A	0202-38	SGR	<LOD	0,00	-	-	-	-	-	-	-	<LOD	0,00	-

Part 9

			Re			Au			Pb			Bi		
Vein type	Spot ID	CL color/intensity and quartz texture	Concentration ppm	2SE (ppm)	LOD (ppm)	Concentration ppm	2SE (ppm)	LOD (ppm)	Concentration ppm	2SE (ppm)	LOD (ppm)	Concentration ppm	2SE (ppm)	LOD (ppm)
A	0201-21	SGR	-	-	-	<LOD	0,00	-	0,21	0,07	0,06	<LOD	0,02	0,04
A	0201-22	SGR	-	-	-	<LOD	0,00	-	0,13	0,09	0,10	<LOD	0,06	0,10
A	0201-23	SGR	-	-	-	-	-	-	-	-	-	-	-	-
A	0201-24	SGR	-	-	-	0,01	0,02	-	0,14	0,06	0,06	<LOD	0,03	0,04
A	0201-26	SGR/GBM	-	-	-	-	-	-	-	-	-	-	-	-
A	0201-27	SGR/GBM	-	-	-	<LOD	0,00	-	<LOD	0,03	0,08	<LOD	0,03	0,05
A	0201-29	SGR/GBM	-	-	-	<LOD	0,00	-	0,10	0,06	0,09	<LOD	0,05	0,08
A	0201-30	SGR/GBM	-	-	-	-	-	-	-	-	-	-	-	-
A	0201-31	SGR/GBM	-	-	-	-	-	-	-	-	-	-	-	-
A	0201-32	SGR/GBM	-	-	-	-	-	-	-	-	-	-	-	-
A	0201-33	SGR/GBM	-	-	-	0,02	0,03	-	0,22	0,10	-	<LOD	0,05	0,08
A	0201-34	SGR/GBM	-	-	-	-	-	-	-	-	-	-	-	-
A	0201-37	SGR/GBM	-	-	-	0,01	0,01	-	<LOD	0,03	0,07	<LOD	0,02	0,06
A	0201-39	SGR	-	-	-	0,00	0,01	-	0,10	0,03	-	<LOD	0,02	0,05
A	0201-40	SGR	-	-	-	-	-	-	-	-	-	-	-	-
A	0201-41	SGR	-	-	-	-	-	-	-	-	-	-	-	-
A	0201-42	SGR	-	-	-	-	-	-	-	-	-	-	-	-
A	0201-44	SGR/GBM	-	-	-	<LOD	0,00	-	0,59	0,15	0,10	0,09	0,04	-
A	0201-45	SGR/GBM	-	-	-	-	-	-	-	-	-	-	-	-
A	0202-20	SGR	-	-	-	-	-	-	-	-	-	-	-	-
A	0202-21	GBM/SGR	-	-	-	-	-	-	-	-	-	-	-	-
A	0202-24	GBM/SGR	-	-	-	-	-	-	-	-	-	-	-	-
A	0202-26	GBM/SGR	-	-	-	-	-	-	-	-	-	-	-	-
A	0202-27	SGR	-	-	-	<LOD	0,00	-	0,24	0,12	-	0,04	0,05	-
A	0202-28	GBM/SGR	-	-	-	<LOD	0,00	-	0,28	0,08	0,07	0,07	0,03	-
A	0202-29	GBM/SGR	-	-	-	<LOD	0,00	-	0,07	0,04	-	<LOD	0,02	0,05
A	0202-30	/	-	-	-	<LOD	0,00	-	0,13	0,06	-	<LOD	0,03	0,06
A	0202-31	SGR	-	-	-	<LOD	0,00	-	0,12	0,08	-	<LOD	0,05	0,09
A	0202-32	/	-	-	-	0,01	0,01	-	0,07	0,03	0,05	<LOD	0,03	0,05
A	0202-33	GBM/SGR	-	-	-	<LOD	0,00	-	0,08	0,06	-	<LOD	0,03	0,08
A	0202-34	GBM/SGR	-	-	-	-	-	-	-	-	-	-	-	-
A	0202-37	SGR	-	-	-	<LOD	0,00	-	<LOD	0,02	0,07	<LOD	0,02	0,05
A	0202-38	SGR	-	-	-	<LOD	0,00	-	0,04	0,02	-	<LOD	0,02	0,04

Partie 10

			U		
Vein type	Spot ID	CL color/intensity and quartz texture	Concentration ppm	2SE (ppm)	LOD (ppm)
A	0201-21	SGR	<LOD	0,00	-
A	0201-22	SGR	<LOD	0,00	-
A	0201-23	SGR	-	-	-
A	0201-24	SGR	<LOD	0,00	-
A	0201-26	SGR/GBM	-	-	-
A	0201-27	SGR/GBM	<LOD	0,00	-
A	0201-29	SGR/GBM	<LOD	0,00	-
A	0201-30	SGR/GBM	-	-	-
A	0201-31	SGR/GBM	-	-	-
A	0201-32	SGR/GBM	-	-	-
A	0201-33	SGR/GBM	<LOD	0,00	-
A	0201-34	SGR/GBM	-	-	-
A	0201-37	SGR/GBM	<LOD	0,00	-
A	0201-39	SGR	<LOD	0,00	-
A	0201-40	SGR	-	-	-
A	0201-41	SGR	-	-	-
A	0201-42	SGR	-	-	-
A	0201-44	SGR/GBM	<LOD	0,00	-
A	0201-45	SGR/GBM	-	-	-
A	0202-20	SGR	-	-	-
A	0202-21	GBM/SGR	-	-	-
A	0202-24	GBM/SGR	-	-	-
A	0202-26	GBM/SGR	-	-	-
A	0202-27	SGR	<LOD	0,00	-
A	0202-28	GBM/SGR	<LOD	0,00	-
A	0202-29	GBM/SGR	<LOD	0,00	-
A	0202-30	/	<LOD	0,00	-
A	0202-31	SGR	<LOD	0,00	-
A	0202-32	/	<LOD	0,00	-
A	0202-33	GBM/SGR	<LOD	0,00	-
A	0202-34	GBM/SGR	-	-	-
A	0202-37	SGR	<LOD	0,00	-
A	0202-38	SGR	<LOD	0,00	-

Caption:

	Quartz textures
GZ	Growth Zoning
SGR	SubGrain Rotation
GBM	Grain Boundary Migration
/	undetermined texture or location
QC	Quartz Center
QM	Quartz Margin
LOD (From Longerich 1987)	Limit of Detection

CL intensity	
	dark red
	intermediate red
	dark blue
	intermediate blue
	bright blue

Table of ICP-MS quartz analyses for different elements in B1-type veins.

			Li			Be			B			Na		
Vein type	Spot ID	CL color/intensity and quartz texture	Concentration ppm	2SE (ppm)	LOD (ppm)	Concentration ppm	2SE (ppm)	LOD (ppm)	Concentration ppm	2SE (ppm)	LOD (ppm)	Concentration ppm	2SE (ppm)	LOD (ppm)
B1	0201-1	SGR	3,03	0,31	0,42	<LOD	0,00	-	<LOD	1,62	4,73	<LOD	4,48	10,25
B1	0201-2	SGR	2,34	0,29	0,41	<LOD	0,00	-	<LOD	2,09	3,65	<LOD	4,54	12,47
B1	0201-3	GZ	3,54	0,30	0,33	<LOD	0,00	-	<LOD	2,10	3,61	<LOD	4,23	9,83
B1	0201-4	GZ	2,53	0,37	0,45	<LOD	0,00	-	<LOD	1,82	4,62	<LOD	4,93	10,34
B1	0201-5	/	3,44	0,35	0,43	<LOD	0,00	-	<LOD	1,70	4,72	<LOD	3,88	8,68
B1	0201-6	/	4,35	0,45	0,48	<LOD	0,00	-	<LOD	1,75	3,88	<LOD	5,29	10,83
B1	0201-7	GZ	4,82	0,56	0,60	<LOD	0,00	-	<LOD	2,11	5,90	9,02	6,06	14,69
B1	0201-8	GZ	5,96	0,46	0,42	<LOD	0,00	-	<LOD	1,51	3,04	<LOD	3,93	9,35
B1	0201-9	GZ	3,92	0,39	0,33	<LOD	0,00	-	<LOD	1,65	3,63	<LOD	4,12	10,17
B1	0201-14	GZ	5,03	0,30	0,23	<LOD	0,00	-	<LOD	1,11	2,42	7,01	3,42	6,63
B1	0201-15	GZ	4,80	0,33	0,34	<LOD	0,00	-	<LOD	1,19	3,00	<LOD	3,32	7,93
B1	0201-16	GZ	5,95	0,46	0,45	<LOD	0,00	-	<LOD	1,73	3,02	10,82	4,26	7,60
B1	0201-17	GZ	5,26	0,36	0,26	<LOD	0,00	-	2,91	1,36	2,06	8,73	3,10	7,20
B1	0201-18	GZ/SGR	3,26	0,34	0,26	<LOD	0,00	-	<LOD	1,61	2,74	<LOD	3,67	9,21
B1	0201-19	SGR	3,01	0,35	0,38	<LOD	0,00	-	<LOD	1,49	2,67	<LOD	6,01	10,14
B1	0202-1	SGR	2,91	0,39	0,38	<LOD	0,00	-	<LOD	1,56	3,36	<LOD	4,79	8,95
B1	0202-2	GZ	3,09	0,29	0,40	<LOD	0,00	-	<LOD	1,96	3,09	9,72	4,11	9,56
B1	0202-3	GZ	2,90	0,31	0,31	<LOD	0,00	-	<LOD	1,36	2,89	7,96	3,25	7,61
B1	0202-4	GZ	4,49	0,28	0,39	<LOD	0,00	-	2,88	1,21	2,59	7,95	2,52	7,95
B1	0202-5	GZ	3,64	0,38	0,53	<LOD	0,00	-	<LOD	1,95	3,41	<LOD	4,29	9,87
B1	0202-6	GZ	5,38	0,33	0,24	<LOD	0,00	-	3,31	1,19	2,27	<LOD	2,42	6,65
B1	0202-7	GZ	4,13	0,31	0,25	<LOD	0,00	-	3,67	1,33	3,18	12,56	2,89	7,60
B1	0202-11	GZ	6,03	0,39	0,31	<LOD	0,00	-	<LOD	0,96	2,26	9,51	2,45	5,68
B1	0202-12	GZ	5,22	0,36	0,24	<LOD	0,00	-	<LOD	0,98	2,26	<LOD	3,05	6,57
B1	0202-13	GZ	3,86	0,36	0,29	<LOD	0,00	-	<LOD	1,57	3,26	<LOD	3,24	6,80
B1	0202-14	/	5,83	0,36	0,27	<LOD	0,00	-	<LOD	1,15	2,78	<LOD	2,84	8,06
B1	0202-15	GZ	3,10	0,32	0,28	<LOD	0,00	-	<LOD	1,39	3,50	<LOD	2,93	9,32
B1	0202-16	GZ	5,51	0,44	0,27	<LOD	0,00	-	<LOD	1,62	3,07	11,43	4,09	6,65
B1	0202-17	GZ	-	-	-	-	-	-	-	-	-	-	-	-
B1	0202-18	GZ	5,54	0,59	0,34	<LOD	0,00	-	<LOD	2,44	4,22	<LOD	5,67	11,67
B1	0202-19	GZ	2,81	0,38	0,35	<LOD	0,00	-	<LOD	2,10	3,92	<LOD	5,86	9,95
B1	120-01-1	SGR	1,35	0,25	0,37	0,36	0,21	-	4,07	1,85	3,29	10,39	3,75	9,00

Part 2

			Mg			Al			Cl			K		
Vein type	Spot ID	CL color/intensity and quartz texture	Concentration ppm	2SE (ppm)	LOD (ppm)	Concentration ppm	2SE (ppm)	LOD (ppm)	Concentration ppm	2SE (ppm)	LOD (ppm)	Concentration ppm	2SE (ppm)	LOD (ppm)
B1	0201-1	SGR	1,27	0,18	0,25	77,77	2,31	0,64	170,70	16,35	28,87	<LOD	1,98	4,85
B1	0201-2	SGR	1,77	0,29	0,30	89,83	2,26	0,65	146,12	18,10	32,25	<LOD	2,40	6,04
B1	0201-3	GZ	2,52	0,34	0,27	103,46	3,40	0,56	169,49	16,84	25,62	<LOD	2,34	4,17
B1	0201-4	GZ	2,56	0,39	0,38	102,74	3,45	0,64	192,74	18,31	32,17	<LOD	1,96	4,49
B1	0201-5	/	3,18	0,29	0,31	114,80	2,28	0,51	183,11	13,25	34,88	<LOD	1,86	5,13
B1	0201-6	/	3,50	0,40	0,35	132,52	3,56	0,66	181,59	23,27	32,83	<LOD	2,68	5,24
B1	0201-7	GZ	5,98	0,62	0,45	150,25	4,18	0,66	161,32	20,80	41,22	<LOD	2,89	4,62
B1	0201-8	GZ	8,07	0,69	0,25	204,52	8,27	0,55	158,60	14,01	34,28	8,44	2,04	5,22
B1	0201-9	GZ	2,10	0,21	0,32	103,52	2,04	0,51	177,59	17,48	34,19	<LOD	2,05	4,29
B1	0201-14	GZ	7,38	0,56	0,20	178,68	4,51	0,40	145,69	8,61	21,58	10,76	1,56	2,54
B1	0201-15	GZ	4,73	0,43	0,19	132,45	3,43	0,37	190,84	11,95	26,62	<LOD	1,45	3,24
B1	0201-16	GZ	7,94	0,48	0,23	216,53	4,87	0,50	144,68	12,72	37,06	15,16	1,88	4,56
B1	0201-17	GZ	9,39	0,64	0,19	213,11	8,43	0,39	122,38	10,72	25,22	25,79	2,72	3,34
B1	0201-18	GZ/SGR	2,13	0,26	0,23	97,19	2,73	0,42	146,67	11,09	22,20	<LOD	1,59	2,95
B1	0201-19	SGR	2,15	0,30	0,27	104,61	2,88	0,56	163,91	17,50	33,27	<LOD	1,57	4,14
B1	0202-1	SGR	3,17	0,36	0,21	121,53	5,83	0,50	161,60	18,73	25,41	<LOD	1,89	3,87
B1	0202-2	GZ	2,54	0,25	0,17	105,19	3,14	0,45	156,23	14,84	28,30	3,69	1,67	2,82
B1	0202-3	GZ	3,40	1,43	0,17	92,68	2,08	0,42	196,19	14,33	28,10	<LOD	1,22	3,10
B1	0202-4	GZ	5,03	0,29	0,14	157,60	2,52	0,40	188,06	10,45	25,79	9,96	1,39	3,05
B1	0202-5	GZ	3,19	0,31	0,19	116,94	2,61	0,58	167,66	15,54	36,16	<LOD	1,84	5,03
B1	0202-6	GZ	7,66	0,55	0,13	196,35	7,28	0,32	131,56	7,82	19,21	14,16	1,56	2,53
B1	0202-7	GZ	4,94	0,29	0,15	141,37	2,60	0,48	142,32	10,48	26,43	4,66	1,33	2,42
B1	0202-11	GZ	9,00	0,35	0,12	258,17	4,25	0,35	161,41	12,71	25,78	40,24	1,81	2,97
B1	0202-12	GZ	6,49	0,37	0,14	197,23	4,35	0,39	165,29	14,47	25,39	17,51	1,50	2,70
B1	0202-13	GZ	4,72	0,38	0,19	140,11	4,09	0,41	194,82	17,20	27,12	4,79	1,69	2,79
B1	0202-14	/	6,96	0,41	0,16	178,12	5,45	0,51	167,15	11,96	25,38	9,73	1,63	2,78
B1	0202-15	GZ	1,74	0,19	0,14	88,72	1,67	0,42	141,61	11,85	29,50	<LOD	1,17	2,76
B1	0202-16	GZ	7,77	0,46	0,13	260,92	4,47	0,46	182,01	16,45	32,86	43,98	3,00	3,37
B1	0202-17	GZ	-	-	-	-	-	-	-	-	-	-	-	-
B1	0202-18	GZ	4,96	0,53	0,29	180,17	5,12	0,54	203,69	16,37	29,25	21,02	2,67	3,40
B1	0202-19	GZ	1,41	0,25	0,22	81,23	2,04	0,60	219,89	18,87	40,60	<LOD	1,75	4,56
B1	120-01-1	SGR	7,40	0,74	0,15	234,63	14,19	0,42	147,64	13,75	20,64	44,93	4,99	3,54

Part 3

			Ca			Ti			Mn			Fe		
Vein type	Spot ID	CL color/intensity and quartz texture	Concentration ppm	2SE (ppm)	LOD (ppm)	Concentration ppm	2SE (ppm)	LOD (ppm)	Concentration ppm	2SE (ppm)	LOD (ppm)	Concentration ppm	2SE (ppm)	LOD (ppm)
B1	0201-1	SGR	<LOD	16,25	49,54	123,36	5,20	0,83	0,56	0,18	0,39	<LOD	3,31	6,16
B1	0201-2	SGR	<LOD	35,38	46,88	170,48	6,21	-	<LOD	0,19	0,43	<LOD	2,57	5,68
B1	0201-3	GZ	40,47	26,20	35,59	118,44	4,57	-	0,26	0,16	0,32	<LOD	1,82	4,94
B1	0201-4	GZ	<LOD	26,44	42,96	97,92	4,36	-	<LOD	0,19	0,44	22,10	6,79	4,49
B1	0201-5	/	<LOD	16,28	50,06	117,42	4,01	-	<LOD	0,18	0,34	4,63	1,69	3,94
B1	0201-6	/	<LOD	25,85	50,18	115,22	3,90	-	<LOD	0,19	0,54	<LOD	2,48	4,92
B1	0201-7	GZ	<LOD	31,97	62,66	89,92	3,58	-	<LOD	0,26	0,55	9,03	3,58	4,63
B1	0201-8	GZ	<LOD	24,62	43,94	78,79	4,13	-	0,43	0,18	0,32	12,90	2,15	4,17
B1	0201-9	GZ	<LOD	23,73	40,51	87,56	4,27	-	<LOD	0,17	0,32	<LOD	2,24	4,42
B1	0201-14	GZ	45,01	17,01	29,98	92,07	3,60	-	0,48	0,10	0,23	8,59	1,45	3,68
B1	0201-15	GZ	30,91	15,05	28,55	98,81	3,57	-	<LOD	0,12	0,24	5,92	1,63	3,93
B1	0201-16	GZ	<LOD	17,33	39,09	110,93	5,75	-	0,66	0,17	0,32	12,85	2,39	4,21
B1	0201-17	GZ	<LOD	12,52	27,95	100,76	4,48	-	1,47	0,18	0,27	219,82	17,69	3,59
B1	0201-18	GZ/SGR	<LOD	15,31	33,09	113,03	4,00	-	<LOD	0,11	0,30	5,06	1,73	3,94
B1	0201-19	SGR	37,62	17,55	37,23	181,21	9,81	-	<LOD	0,16	0,35	37,83	5,77	4,81
B1	0202-1	SGR	<LOD	18,91	25,86	94,30	3,87	-	0,35	0,17	0,29	7,06	3,13	3,15
B1	0202-2	GZ	<LOD	20,05	34,99	113,78	5,18	-	0,51	0,15	0,25	5,80	3,57	3,71
B1	0202-3	GZ	<LOD	16,64	27,33	125,13	4,92	-	<LOD	0,13	0,28	3,08	1,61	2,99
B1	0202-4	GZ	<LOD	14,32	29,71	87,11	3,45	-	0,47	0,13	0,26	18,85	2,06	3,19
B1	0202-5	GZ	<LOD	16,20	39,92	113,99	5,28	-	0,48	0,18	0,34	<LOD	2,11	3,86
B1	0202-6	GZ	<LOD	11,36	23,12	80,54	3,30	-	0,49	0,10	0,20	7,30	1,50	2,88
B1	0202-7	GZ	48,53	16,20	32,86	85,30	3,45	-	0,58	0,13	0,22	6,02	1,36	3,81
B1	0202-11	GZ	37,54	16,01	26,36	81,50	3,41	-	0,80	0,11	0,19	14,76	1,49	2,60
B1	0202-12	GZ	28,70	14,45	26,27	100,80	3,56	-	0,51	0,10	0,22	11,52	1,16	2,42
B1	0202-13	GZ	<LOD	16,90	31,81	97,12	3,87	-	<LOD	0,13	0,28	8,40	1,65	3,42
B1	0202-14	/	<LOD	14,05	32,03	100,38	3,85	-	0,46	0,14	0,26	9,28	1,37	2,62
B1	0202-15	GZ	29,08	12,97	26,28	50,62	3,26	-	<LOD	0,13	0,23	<LOD	1,36	3,28
B1	0202-16	GZ	<LOD	18,74	32,31	92,56	3,77	-	0,81	0,15	0,25	24,72	1,82	3,18
B1	0202-17	GZ	-	-	-	109,96	5,01	0,38	-	-	-	-	-	-
B1	0202-18	GZ	<LOD	19,46	31,87	160,02	9,21	-	0,41	0,19	0,35	15,81	2,06	4,85
B1	0202-19	GZ	52,43	19,70	42,07				0,51	0,23	0,44	8,74	3,77	4,60
B1	120-01-1	SGR	59,33	25,34	30,12	44,56	10,60	-	0,69	0,13	0,28	5,88	3,68	5,15

Part 4

			Co			Cu			Zn			Ga		
Vein type	Spot ID	CL color/intensity and quartz texture	Concentration ppm	2SE (ppm)	LOD (ppm)	Concentration ppm	2SE (ppm)	LOD (ppm)	Concentration ppm	2SE (ppm)	LOD (ppm)	Concentration ppm	2SE (ppm)	LOD (ppm)
B1	0201-1	SGR	0,04	0,02	-	1,60	1,03	0,52	<LOD	0,34	0,85	<LOD	0,00	-
B1	0201-2	SGR	<LOD	0,02	0,05	0,60	0,26	0,50	<LOD	0,41	0,84	<LOD	0,00	-
B1	0201-3	GZ	<LOD	0,01	0,03	<LOD	0,21	0,36	<LOD	0,38	0,65	0,01	0,01	-
B1	0201-4	GZ	0,30	0,12	-	<LOD	0,21	0,51	<LOD	0,34	1,28	0,01	0,01	-
B1	0201-5	/	0,01	0,01	-	0,91	0,24	0,31	<LOD	0,32	1,10	<LOD	0,00	-
B1	0201-6	/	0,02	0,02	-	<LOD	0,24	0,45	<LOD	0,51	1,19	<LOD	0,00	-
B1	0201-7	GZ	0,06	0,04	-	<LOD	0,30	0,65	<LOD	0,56	0,89	<LOD	0,00	-
B1	0201-8	GZ	0,02	0,01	-	<LOD	0,17	0,39	<LOD	0,38	0,73	0,00	0,01	-
B1	0201-9	GZ	<LOD	0,01	0,05	<LOD	0,25	0,41	<LOD	0,43	0,77	<LOD	0,00	-
B1	0201-14	GZ	<LOD	0,01	0,04	1,51	0,56	0,19	0,54	0,31	0,43	0,00	0,00	-
B1	0201-15	GZ	0,00	0,00	-	<LOD	0,13	0,33	<LOD	0,32	0,96	<LOD	0,00	-
B1	0201-16	GZ	0,00	0,01	-	<LOD	0,14	0,35	<LOD	0,30	0,67	<LOD	0,00	-
B1	0201-17	GZ	0,02	0,01	-	0,97	0,19	0,24	0,90	0,39	0,50	0,29	0,06	-
B1	0201-18	GZ/SGR	<LOD	0,00	-	<LOD	0,14	0,26	<LOD	0,32	0,48	<LOD	0,00	-
B1	0201-19	SGR	<LOD	0,00	-	5,90	2,13	0,44	<LOD	0,37	0,67	<LOD	0,00	-
B1	0202-1	SGR	<LOD	0,00	-	<LOD	0,17	0,33	<LOD	0,35	0,66	<LOD	0,00	-
B1	0202-2	GZ	0,03	0,02	0,04	<LOD	0,28	0,30	<LOD	0,29	0,59	0,01	0,01	-
B1	0202-3	GZ	0,02	0,02	-	<LOD	0,13	0,31	<LOD	0,27	0,63	<LOD	0,00	-
B1	0202-4	GZ	0,01	0,01	0,03	<LOD	0,09	0,27	<LOD	0,23	0,52	0,00	0,00	-
B1	0202-5	GZ	<LOD	0,00	0,05	<LOD	0,19	0,39	<LOD	0,29	0,76	0,02	0,02	-
B1	0202-6	GZ	0,02	0,01	-	<LOD	0,08	0,25	<LOD	0,19	0,44	<LOD	0,00	-
B1	0202-7	GZ	0,01	0,01	-	0,67	0,22	0,29	0,64	0,32	0,53	<LOD	0,00	-
B1	0202-11	GZ	0,01	0,01	-	<LOD	0,13	0,23	<LOD	0,29	0,51	<LOD	0,00	-
B1	0202-12	GZ	<LOD	0,00	0,04	<LOD	0,11	0,33	<LOD	0,24	0,52	0,01	0,01	-
B1	0202-13	GZ	<LOD	0,00	-	<LOD	0,11	0,27	<LOD	0,30	0,52	0,02	0,02	-
B1	0202-14	/	<LOD	0,01	0,04	0,32	0,16	0,29	<LOD	0,24	0,53	<LOD	0,00	-
B1	0202-15	GZ	<LOD	0,00	-	<LOD	0,14	0,28	<LOD	0,25	0,54	<LOD	0,00	-
B1	0202-16	GZ	0,05	0,03	-	<LOD	0,14	0,33	<LOD	0,41	0,56	0,01	0,01	-
B1	0202-17	GZ	-	-	-	-	-	-	-	-	-	-	-	-
B1	0202-18	GZ	0,02	0,02	-	<LOD	0,21	0,31	<LOD	0,29	0,75	0,05	0,04	-
B1	0202-19	GZ	0,06	0,03	-	<LOD	0,19	0,40	<LOD	0,42	0,80	<LOD	0,00	-
B1	120-01-1	SGR	<LOD	0,02	0,04	<LOD	0,15	0,35	<LOD	0,42	0,77	0,01	0,01	-

Part 5

			Ge			As			Rb			Sr		
Vein type	Spot ID	CL color/intensity and quartz texture	Concentration ppm	2SE (ppm)	LOD (ppm)	Concentration ppm	2SE (ppm)	LOD (ppm)	Concentration ppm	2SE (ppm)	LOD (ppm)	Concentration ppm	2SE (ppm)	LOD (ppm)
B1	0201-1	SGR	1,25	0,48	1,20	<LOD	1,07	2,59	<LOD	0,02	0,04	<LOD	-	-
B1	0201-2	SGR	1,30	0,52	1,05	<LOD	1,05	2,70	<LOD	0,02	0,05	<LOD	-	-
B1	0201-3	GZ	1,22	0,47	0,80	2,68	0,92	1,75	<LOD	0,02	0,04	0,01	0,01	-
B1	0201-4	GZ	1,93	0,48	1,06	<LOD	1,01	2,27	<LOD	0,02	0,05	0,05	0,02	-
B1	0201-5	/	1,41	0,45	0,89	<LOD	1,10	2,21	<LOD	0,02	0,04	<LOD	-	-
B1	0201-6	/	0,76	0,46	1,41	<LOD	1,20	2,67	<LOD	0,01	0,04	<LOD	-	-
B1	0201-7	GZ	0,89	0,73	1,26	<LOD	1,83	3,64	<LOD	0,02	0,07	<LOD	-	-
B1	0201-8	GZ	1,66	0,46	1,03	<LOD	0,96	2,52	0,01	0,01	-	<LOD	-	-
B1	0201-9	GZ	1,85	0,54	0,80	<LOD	0,83	2,58	<LOD	0,01	0,04	0,01	0,01	-
B1	0201-14	GZ	1,42	0,34	0,77	<LOD	0,70	1,49	0,05	0,02	-	0,03	0,01	-
B1	0201-15	GZ	1,66	0,38	0,71	<LOD	0,87	2,12	0,02	0,01	-	<LOD	-	-
B1	0201-16	GZ	1,29	0,41	1,05	<LOD	0,92	2,09	0,05	0,02	0,04	0,04	0,02	-
B1	0201-17	GZ	2,46	0,37	0,75	<LOD	0,69	1,47	0,11	0,03	0,03	0,02	0,01	-
B1	0201-18	GZ/SGR	1,70	0,52	0,69	<LOD	0,88	1,52	0,02	0,01	-	<LOD	-	-
B1	0201-19	SGR	1,90	0,69	1,15	<LOD	1,02	2,64	<LOD	0,02	0,05	0,06	0,02	-
B1	0202-1	SGR	1,79	0,56	0,86	<LOD	1,26	1,92	0,04	0,02	-	0,10	0,05	-
B1	0202-2	GZ	1,17	0,39	0,94	<LOD	0,89	1,93	0,02	0,01	-	0,00	0,01	-
B1	0202-3	GZ	1,82	0,38	0,94	<LOD	0,79	1,53	<LOD	0,01	0,03	<LOD	-	-
B1	0202-4	GZ	1,35	0,33	0,67	<LOD	0,71	1,95	0,05	0,02	-	<LOD	-	-
B1	0202-5	GZ	1,28	0,54	0,75	<LOD	0,89	2,14	<LOD	0,01	0,04	0,00	0,01	-
B1	0202-6	GZ	0,99	0,23	0,64	<LOD	0,57	1,43	0,07	0,02	-	0,04	0,01	-
B1	0202-7	GZ	1,07	0,32	0,76	<LOD	0,71	2,01	0,03	0,01	0,02	0,01	0,01	-
B1	0202-11	GZ	1,52	0,37	0,66	<LOD	0,70	1,85	0,17	0,03	0,02	0,06	0,02	-
B1	0202-12	GZ	1,06	0,30	0,72	<LOD	0,75	1,67	0,08	0,02	-	0,04	0,01	-
B1	0202-13	GZ	1,38	0,34	0,86	<LOD	1,05	1,58	0,00	0,01	-	<LOD	-	-
B1	0202-14	/	0,70	0,36	0,66	<LOD	0,83	1,86	0,04	0,02	0,03	<LOD	-	-
B1	0202-15	GZ	0,98	0,37	0,71	<LOD	0,79	1,58	<LOD	0,01	0,03	<LOD	-	-
B1	0202-16	GZ	1,66	0,37	0,81	<LOD	0,88	2,10	0,20	0,05	0,04	0,08	0,02	-
B1	0202-17	GZ	-	-	-	-	-	-	-	-	-	-	-	-
B1	0202-18	GZ	1,61	0,46	0,85	<LOD	1,20	2,96	0,12	0,05	-	0,01	0,01	-
B1	0202-19	GZ	2,63	0,67	1,17	<LOD	0,90	2,61	0,02	0,02	-	0,01	0,01	-
B1	120-01-1	SGR	3,34	0,55	0,53	<LOD	0,98	1,75	0,20	0,04	0,03	0,05	0,02	-

Part 6

			Zr			Nb			Mo			Ag		
Vein type	Spot ID	CL color/intensity and quartz texture	Concentration ppm	2SE (ppm)	LOD (ppm)	Concentration ppm	2SE (ppm)	LOD (ppm)	Concentration ppm	2SE (ppm)	LOD (ppm)	Concentration ppm	2SE (ppm)	LOD (ppm)
B1	0201-1	SGR	-	-	-	-	-	-	-	-	-	-	-	-
B1	0201-2	SGR	-	-	-	0,00	0,01	-	-	-	-	-	-	-
B1	0201-3	GZ	0,01	0,01	-	-	-	-	0,09	0,09	-	-	-	-
B1	0201-4	GZ	-	-	-	-	-	-	-	-	-	-	-	-
B1	0201-5	/	-	-	-	-	-	-	-	-	-	-	-	-
B1	0201-6	/	-	-	-	-	-	-	-	-	-	-	-	-
B1	0201-7	GZ	-	-	-	-	-	-	-	-	-	-	-	-
B1	0201-8	GZ	-	-	-	-	-	-	-	-	-	-	-	-
B1	0201-9	GZ	0,02	0,02	-	-	-	-	-	-	-	-	-	-
B1	0201-14	GZ	0,01	0,01	-	-	-	-	-	-	-	-	-	-
B1	0201-15	GZ	-	-	-	-	-	-	-	-	-	-	-	-
B1	0201-16	GZ	-	-	-	-	-	-	-	-	-	-	-	-
B1	0201-17	GZ	0,01	0,01	-	0,22	0,04	-	0,04	0,03	-	-	-	-
B1	0201-18	GZ/SGR	-	-	-	-	-	-	-	-	-	-	-	-
B1	0201-19	SGR	-	-	-	-	-	-	0,20	0,11	-	-	-	-
B1	0202-1	SGR	-	-	-	-	-	-	0,95	0,39	-	-	-	-
B1	0202-2	GZ	0,00	0,01	-	-	-	-	1,14	1,23	-	-	-	-
B1	0202-3	GZ	-	-	-	-	-	-	-	-	-	-	-	-
B1	0202-4	GZ	-	-	-	-	-	-	-	-	-	-	-	-
B1	0202-5	GZ	-	-	-	-	-	-	0,15	0,08	-	-	-	-
B1	0202-6	GZ	-	-	-	-	-	-	-	-	-	-	-	-
B1	0202-7	GZ	0,00	0,00	-	-	-	-	0,02	0,02	-	-	-	-
B1	0202-11	GZ	-	-	-	-	-	-	-	-	-	-	-	-
B1	0202-12	GZ	0,00	0,00	-	-	-	-	-	-	-	-	-	-
B1	0202-13	GZ	-	-	-	-	-	-	-	-	-	-	-	-
B1	0202-14	/	-	-	-	-	-	-	-	-	-	-	-	-
B1	0202-15	GZ	0,00	0,01	-	-	-	-	-	-	-	-	-	-
B1	0202-16	GZ	-	-	-	-	-	-	-	-	-	-	-	-
B1	0202-17	GZ	-	-	-	-	-	-	-	-	-	-	-	-
B1	0202-18	GZ	-	-	-	-	-	-	-	-	-	-	-	-
B1	0202-19	GZ	-	-	-	-	-	-	-	-	-	-	-	-
B1	120-01-1	SGR	-	-	-	-	-	-	-	-	-	-	-	-

Part 7

			In			Sn			Sb			Te		
Vein type	Spot ID	CL color/intensity and quartz texture	Concentration ppm	2SE (ppm)	LOD (ppm)	Concentration ppm	2SE (ppm)	LOD (ppm)	Concentration ppm	2SE (ppm)	LOD (ppm)	Concentration ppm	2SE (ppm)	LOD (ppm)
B1	0201-1	SGR	<LOD	0,01	0,03	2,18	0,47	1,24	0,06	0,03	-	-	-	-
B1	0201-2	SGR	<LOD	0,01	0,04	1,84	0,61	1,07	<LOD	0,04	0,10	-	-	-
B1	0201-3	GZ	<LOD	0,01	0,03	2,76	0,55	0,92	0,08	0,04	-	-	-	-
B1	0201-4	GZ	<LOD	0,02	0,04	1,97	0,59	1,49	<LOD	0,05	0,12	-	-	-
B1	0201-5	/	<LOD	0,01	0,03	2,27	0,57	0,89	0,01	0,01	-	-	-	-
B1	0201-6	/	<LOD	0,02	0,03	2,74	0,68	1,19	0,07	0,04	-	-	-	-
B1	0201-7	GZ	0,06	0,02	-	1,98	0,70	1,25	0,02	0,03	-	-	-	-
B1	0201-8	GZ	0,06	0,02	0,03	2,87	0,57	1,14	0,03	0,02	-	-	-	-
B1	0201-9	GZ	<LOD	0,01	0,03	2,93	0,56	1,09	0,01	0,01	-	-	-	-
B1	0201-14	GZ	0,03	0,01	0,02	2,14	0,29	0,69	<LOD	0,03	0,06	-	-	-
B1	0201-15	GZ	<LOD	0,01	0,03	2,90	0,40	0,84	<LOD	0,01	0,08	-	-	-
B1	0201-16	GZ	<LOD	0,01	0,03	2,21	0,62	1,06	<LOD	0,04	0,08	-	-	-
B1	0201-17	GZ	<LOD	0,01	0,02	1,75	0,48	0,86	0,08	0,03	-	-	-	-
B1	0201-18	GZ/SGR	<LOD	0,01	0,02	2,01	0,39	0,89	<LOD	0,00	0,05	-	-	-
B1	0201-19	SGR	0,01	0,01	-	1,66	0,61	1,16	0,06	0,04	-	-	-	-
B1	0202-1	SGR	<LOD	0,01	0,02	2,49	0,51	0,93	<LOD	0,03	0,09	-	-	-
B1	0202-2	GZ	<LOD	0,01	0,02	1,46	0,60	0,87	0,01	0,01	-	-	-	-
B1	0202-3	GZ	<LOD	0,01	0,03	2,64	0,44	0,98	0,08	0,04	-	-	-	-
B1	0202-4	GZ	<LOD	0,01	0,02	2,05	0,37	0,69	0,07	0,03	0,07	-	-	-
B1	0202-5	GZ	<LOD	0,01	0,03	1,59	0,55	1,02	0,10	0,05	0,10	-	-	-
B1	0202-6	GZ	<LOD	0,01	0,02	1,90	0,35	0,77	0,05	0,02	-	-	-	-
B1	0202-7	GZ	<LOD	0,01	0,03	2,15	0,36	0,84	0,04	0,02	-	-	-	-
B1	0202-11	GZ	<LOD	0,01	0,02	2,07	0,34	0,79	0,03	0,02	-	-	-	-
B1	0202-12	GZ	<LOD	0,01	0,02	2,01	0,35	0,92	<LOD	0,02	0,07	-	-	-
B1	0202-13	GZ	<LOD	0,01	0,02	2,36	0,48	0,96	0,02	0,02	-	-	-	-
B1	0202-14	/	<LOD	0,01	0,03	2,34	0,41	0,81	<LOD	0,00	-	-	-	-
B1	0202-15	GZ	<LOD	0,01	0,02	1,89	0,40	0,76	0,04	0,03	-	-	-	-
B1	0202-16	GZ	<LOD	0,01	0,02	1,57	0,36	0,92	<LOD	0,00	-	-	-	-
B1	0202-17	GZ	-	-	-	-	-	-	-	-	-	-	-	-
B1	0202-18	GZ	<LOD	0,02	0,03	2,14	0,53	0,98	0,00	0,00	-	-	-	-
B1	0202-19	GZ	0,03	0,02	-	2,24	0,53	1,25	0,11	0,06	-	-	-	-
B1	120-01-1	SGR	<LOD	0,01	0,02	4,91	0,48	0,69	0,10	0,05	-	-	-	-

Part 8

			Cs			Ba			Ta			W		
Vein type	Spot ID	CL color/intensity and quartz texture	Concentration ppm	2SE (ppm)	LOD (ppm)	Concentration ppm	2SE (ppm)	LOD (ppm)	Concentration ppm	2SE (ppm)	LOD (ppm)	Concentration ppm	2SE (ppm)	LOD (ppm)
B1	0201-1	SGR	0,00	0,00	-	-	-	-	-	-	-	<LOD	0,00	-
B1	0201-2	SGR	<LOD	0,00	0,02	-	-	-	-	-	-	<LOD	0,00	-
B1	0201-3	GZ	<LOD	0,00	-	-	-	-	-	-	-	0,02	0,03	-
B1	0201-4	GZ	0,00	0,01	-	-	-	-	-	-	-	<LOD	0,00	-
B1	0201-5	/	<LOD	0,00	-	-	-	-	-	-	-	<LOD	0,00	-
B1	0201-6	/	<LOD	0,00	-	-	-	-	-	-	-	<LOD	0,00	-
B1	0201-7	GZ	0,02	0,01	-	-	-	-	-	-	-	<LOD	0,00	-
B1	0201-8	GZ	<LOD	0,00	-	-	-	-	-	-	-	<LOD	0,00	-
B1	0201-9	GZ	<LOD	0,00	-	-	-	-	-	-	-	<LOD	0,00	-
B1	0201-14	GZ	<LOD	0,00	-	0,03	0,03	-	0,00	0,00	-	<LOD	0,00	-
B1	0201-15	GZ	0,00	0,00	-	-	-	-	-	-	-	<LOD	0,00	-
B1	0201-16	GZ	0,00	0,00	-	0,08	0,07	-	-	-	-	<LOD	0,00	-
B1	0201-17	GZ	<LOD	0,00	0,02	0,01	0,01	-	-	-	-	<LOD	0,00	-
B1	0201-18	GZ/SGR	<LOD	0,00	-	-	-	-	-	-	-	<LOD	0,00	-
B1	0201-19	SGR	0,01	0,01	-	-	-	-	-	-	-	<LOD	0,00	-
B1	0202-1	SGR	0,02	0,01	-	-	-	-	-	-	-	<LOD	0,00	-
B1	0202-2	GZ	<LOD	0,00	-	0,01	0,02	-	-	-	-	<LOD	0,00	-
B1	0202-3	GZ	<LOD	0,00	-	-	-	-	-	-	-	<LOD	0,00	-
B1	0202-4	GZ	<LOD	0,00	0,02	-	-	-	-	-	-	<LOD	0,00	-
B1	0202-5	GZ	<LOD	0,00	-	-	-	-	-	-	-	<LOD	0,00	-
B1	0202-6	GZ	0,01	0,01	-	0,06	0,04	-	-	-	-	<LOD	0,00	-
B1	0202-7	GZ	<LOD	0,00	-	-	-	-	-	-	-	<LOD	0,00	-
B1	0202-11	GZ	<LOD	0,00	-	-	-	-	-	-	-	<LOD	0,00	-
B1	0202-12	GZ	0,00	0,00	-	-	-	-	-	-	-	<LOD	0,00	-
B1	0202-13	GZ	<LOD	0,00	-	-	-	-	-	-	-	<LOD	0,00	-
B1	0202-14	/	<LOD	0,00	-	0,07	0,06	-	-	-	-	<LOD	0,00	-
B1	0202-15	GZ	<LOD	0,00	-	-	-	-	-	-	-	<LOD	0,00	-
B1	0202-16	GZ	<LOD	0,00	-	0,05	0,06	-	-	-	-	<LOD	0,00	-
B1	0202-17	GZ	-	-	-	-	-	-	-	-	-	-	-	-
B1	0202-18	GZ	<LOD	0,00	-	-	-	-	-	-	-	<LOD	0,00	-
B1	0202-19	GZ	<LOD	0,00	-	-	-	-	-	-	-	<LOD	0,00	-
B1	120-01-1	SGR	0,02	0,01	-	0,24	0,09	-	-	-	-	<LOD	0,00	-

Part 9

			Re			Au			Pb			Bi		
Vein type	Spot ID	CL color/intensity and quartz texture	Concentration ppm	2SE (ppm)	LOD (ppm)	Concentration ppm	2SE (ppm)	LOD (ppm)	Concentration ppm	2SE (ppm)	LOD (ppm)	Concentration ppm	2SE (ppm)	LOD (ppm)
B1	0201-1	SGR	-	-	-	<LOD	0,00	-	0,03	0,02	-	<LOD	0,02	0,06
B1	0201-2	SGR	-	-	-	<LOD	0,00	-	0,16	0,05	-	<LOD	0,02	0,06
B1	0201-3	GZ	-	-	-	0,01	0,01	-	<LOD	0,00	-	<LOD	0,02	0,05
B1	0201-4	GZ	-	-	-	<LOD	0,00	-	<LOD	0,02	0,08	<LOD	0,03	0,06
B1	0201-5	/	-	-	-	0,00	0,01	-	0,02	0,01	-	<LOD	0,02	0,06
B1	0201-6	/	-	-	-	<LOD	0,00	-	0,00	0,00	-	<LOD	0,03	0,07
B1	0201-7	GZ	-	-	-	<LOD	0,00	-	<LOD	0,04	0,10	<LOD	0,00	0,07
B1	0201-8	GZ	-	-	-	0,01	0,01	-	0,01	0,01	-	<LOD	0,02	0,06
B1	0201-9	GZ	-	-	-	<LOD	0,00	-	0,05	0,03	-	<LOD	0,03	0,06
B1	0201-14	GZ	-	-	-	<LOD	0,00	-	<LOD	0,02	0,05	<LOD	0,01	0,04
B1	0201-15	GZ	-	-	-	<LOD	0,00	-	<LOD	0,02	0,06	<LOD	0,02	0,04
B1	0201-16	GZ	-	-	-	0,01	0,01	-	0,06	0,03	-	<LOD	0,02	0,04
B1	0201-17	GZ	-	-	-	0,01	0,01	-	0,07	0,03	-	<LOD	0,02	0,03
B1	0201-18	GZ/SGR	-	-	-	<LOD	0,00	-	0,04	0,02	-	<LOD	0,02	0,04
B1	0201-19	SGR	-	-	-	<LOD	0,00	-	0,05	0,03	-	<LOD	0,03	0,06
B1	0202-1	SGR	-	-	-	<LOD	0,00	-	0,01	0,01	-	<LOD	0,02	0,05
B1	0202-2	GZ	-	-	-	<LOD	0,00	-	0,05	0,03	-	<LOD	0,03	0,04
B1	0202-3	GZ	-	-	-	<LOD	0,00	-	0,02	0,02	-	<LOD	0,02	0,05
B1	0202-4	GZ	-	-	-	<LOD	0,00	-	0,02	0,01	-	<LOD	0,02	0,05
B1	0202-5	GZ	-	-	-	<LOD	0,00	-	0,01	0,01	-	<LOD	0,02	0,05
B1	0202-6	GZ	-	-	-	<LOD	0,00	-	0,04	0,02	-	<LOD	0,02	0,03
B1	0202-7	GZ	-	-	-	<LOD	0,00	-	0,23	0,07	-	<LOD	0,02	0,04
B1	0202-11	GZ	-	-	-	<LOD	0,00	-	0,06	0,03	-	<LOD	0,02	0,04
B1	0202-12	GZ	-	-	-	<LOD	0,00	-	0,02	0,01	-	<LOD	0,02	0,05
B1	0202-13	GZ	-	-	-	<LOD	0,00	-	<LOD	0,00	-	<LOD	0,02	0,05
B1	0202-14	/	-	-	-	<LOD	0,00	-	0,07	0,03	0,06	<LOD	0,02	0,05
B1	0202-15	GZ	-	-	-	<LOD	0,00	-	0,00	0,01	-	<LOD	0,02	0,04
B1	0202-16	GZ	-	-	-	<LOD	0,00	-	0,08	0,04	-	<LOD	0,02	0,05
B1	0202-17	GZ	-	-	-	-	-	-	-	-	-	-	-	-
B1	0202-18	GZ	-	-	-	<LOD	0,00	-	0,04	0,03	-	<LOD	0,03	0,06
B1	0202-19	GZ	-	-	-	0,00	0,00	-	<LOD	0,04	0,09	<LOD	0,03	0,06
B1	120-01-1	SGR	-	-	-	<LOD	0,02	0,06	0,04	0,02	-	<LOD	0,02	0,04

Part 10

			U		
Vein type	Spot ID	CL color/intensity and quartz texture	Concentration ppm	2SE (ppm)	LOD (ppm)
B1	0201-1	SGR	<LOD	0,00	-
B1	0201-2	SGR	0,03	0,02	-
B1	0201-3	GZ	0,01	0,01	-
B1	0201-4	GZ	<LOD	0,00	-
B1	0201-5	/	<LOD	0,00	-
B1	0201-6	/	<LOD	0,00	-
B1	0201-7	GZ	<LOD	0,00	-
B1	0201-8	GZ	<LOD	0,00	-
B1	0201-9	GZ	<LOD	0,00	-
B1	0201-14	GZ	<LOD	0,00	-
B1	0201-15	GZ	<LOD	0,00	-
B1	0201-16	GZ	<LOD	0,00	-
B1	0201-17	GZ	0,17	0,04	-
B1	0201-18	GZ/SGR	0,06	0,03	-
B1	0201-19	SGR	0,01	0,01	-
B1	0202-1	SGR	<LOD	0,00	-
B1	0202-2	GZ	0,00	0,00	-
B1	0202-3	GZ	<LOD	0,00	-
B1	0202-4	GZ	<LOD	0,00	-
B1	0202-5	GZ	<LOD	0,00	0,02
B1	0202-6	GZ	<LOD	0,00	-
B1	0202-7	GZ	<LOD	0,00	-
B1	0202-11	GZ	<LOD	0,00	-
B1	0202-12	GZ	<LOD	0,00	-
B1	0202-13	GZ	<LOD	0,00	-
B1	0202-14	/	<LOD	0,00	-
B1	0202-15	GZ	<LOD	0,00	-
B1	0202-16	GZ	<LOD	0,00	-
B1	0202-17	GZ	-	-	-
B1	0202-18	GZ	<LOD	0,00	-
B1	0202-19	GZ	<LOD	0,00	-
B1	120-01-1	SGR	<LOD	0,00	-

Part 11 second part of samples

			Li			Be			B			Na		
Vein type	Spot ID	CL color/intensity and quartz texture	Concentration ppm	2SE (ppm)	LOD (ppm)	Concentration ppm	2SE (ppm)	LOD (ppm)	Concentration ppm	2SE (ppm)	LOD (ppm)	Concentration ppm	2SE (ppm)	LOD (ppm)
B1	120-01-2	SGR	-	-	-	-	-	-	-	-	-	-	-	-
B1	120-01-3	SGR	0,74	0,32	0,43	<LOD	0,00	-	3,61	2,41	3,45	44,95	7,44	8,03
B1	120-01-4	/	-	-	-	-	-	-	-	-	-	-	-	-
B1	120-01-5	/	-	-	-	-	-	-	-	-	-	-	-	-
B1	120-01-7	GZ	2,40	0,30	0,38	<LOD	0,00	-	5,04	1,82	3,07	54,31	5,18	7,68
B1	120-01-8	GZ	1,63	0,30	0,54	<LOD	0,00	-	<LOD	3,26	5,18	72,16	10,08	10,08
B1	120-01-9	GZ	1,66	0,36	0,35	<LOD	0,00	-	<LOD	2,04	4,16	199,73	21,98	8,27
B1	120-01-10	GZ	1,60	0,43	0,42	<LOD	0,00	-	5,18	3,36	3,97	200,60	19,63	7,86
B1	120-01-11	GZ	1,63	0,24	0,70	0,25	0,23	-	<LOD	1,70	6,32	146,53	7,57	16,22
B1	120-01-14	GZ	2,18	0,25	0,44	<LOD	0,00	-	4,39	1,87	3,29	65,32	8,05	8,27
B1	120-01-15	/	-	-	-	-	-	-	-	-	-	-	-	-
B1	120-01-16	/	2,17	0,41	0,44	<LOD	0,00	-	4,67	2,09	4,03	11,41	4,70	10,32
B1	120-01-17	/	1,96	0,46	0,63	<LOD	0,00	-	<LOD	3,55	6,05	30,12	9,93	13,54
B1	120-01-18	/	0,60	0,44	0,56	<LOD	0,00	-	<LOD	3,03	4,79	28,35	8,27	11,65
B1	120-01-19	GZ	-	-	-	-	-	-	-	-	-	-	-	-
B1	120-01-20	GZ	-	-	-	-	-	-	-	-	-	-	-	-
B1	120-01-21	GZ	1,91	0,21	0,30	<LOD	0,00	-	<LOD	1,37	3,00	44,64	4,22	7,00
B1	120-01-22	GZ	1,74	0,32	0,48	<LOD	0,00	-	<LOD	2,93	5,63	149,56	12,01	11,26
B1	120-01-23	GZ	1,61	0,21	0,32	0,03	0,06	-	3,62	1,75	3,55	35,32	4,30	9,67
B1	120-01-24	/	1,81	0,30	0,43	<LOD	0,00	-	<LOD	2,47	4,82	20,61	4,49	11,50
B1	120-01-25	/	-	-	-	-	-	-	-	-	-	-	-	-
B1	120-01-26	GZ	3,22	0,50	0,39	<LOD	0,00	-	4,77	1,95	4,04	82,58	6,89	9,54
B1	120-01-27	GZ	1,75	0,39	0,36	<LOD	0,00	-	<LOD	1,80	3,59	29,87	5,66	7,65
B1	120-01-28	/	-	-	-	-	-	-	-	-	-	-	-	-
B1	120-01-29	GZ	2,03	0,25	0,35	<LOD	0,00	-	<LOD	1,59	2,93	61,29	3,84	8,83
B1	120-01-30	GZ	-	-	-	-	-	-	-	-	-	-	-	-
B1	120-01-31	GZ	-	-	-	-	-	-	-	-	-	-	-	-
B1	120-01-32	GZ	1,71	0,33	0,41	<LOD	0,00	-	<LOD	1,96	4,38	73,36	7,38	10,79
B1	120-01-33	GZ	1,81	0,27	0,37	<LOD	0,00	-	<LOD	1,87	3,90	72,46	3,85	6,97
B1	120-01-34	GZ	1,33	0,56	0,54	<LOD	0,00	-	<LOD	4,17	4,85	81,30	8,74	17,32
B1	120-01-35	SGR	0,88	0,40	0,55	<LOD	0,00	-	<LOD	2,60	5,75	25,67	8,56	14,69
B1	120-01-36	SGR	1,43	0,36	0,42	<LOD	0,00	-	<LOD	2,03	4,04	59,04	10,04	10,96
B1	120-01-37	SGR	1,10	0,38	0,50	<LOD	0,00	-	<LOD	2,83	4,55	73,81	10,35	11,12
B1	120-01-38	SGR	0,90	0,23	0,44	<LOD	0,00	-	<LOD	1,44	3,26	42,13	3,66	7,37

Part 12

			Mg			Al			Cl			K		
Vein type	Spot ID	CL color/intensity and quartz texture	Concentration ppm	2SE (ppm)	LOD (ppm)	Concentration ppm	2SE (ppm)	LOD (ppm)	Concentration ppm	2SE (ppm)	LOD (ppm)	Concentration ppm	2SE (ppm)	LOD (ppm)
B1	120-01-2	SGR	-	-	-	-	-	-	-	-	-	-	-	-
B1	120-01-3	SGR	8,59	0,66	0,23	172,73	3,95	0,56	153,69	18,34	30,22	33,26	3,02	3,79
B1	120-01-4	/	-	-	-	-	-	-	-	-	-	-	-	-
B1	120-01-5	/	-	-	-	-	-	-	-	-	-	-	-	-
B1	120-01-7	GZ	13,13	0,54	0,19	459,31	7,47	0,47	191,65	11,38	26,12	157,90	6,34	3,55
B1	120-01-8	GZ	14,73	1,30	0,26	530,89	14,47	0,59	169,91	23,06	30,05	208,54	7,88	4,83
B1	120-01-9	GZ	23,93	1,21	0,19	571,33	13,98	0,43	190,78	16,56	24,54	290,43	13,15	4,42
B1	120-01-10	GZ	17,24	1,28	0,24	677,43	19,21	0,46	174,96	28,49	29,24	292,99	10,47	4,08
B1	120-01-11	GZ	20,86	0,78	0,35	655,33	10,47	1,38	207,26	13,16	34,69	232,58	6,06	5,12
B1	120-01-14	GZ	21,26	1,74	0,26	588,82	35,93	0,65	216,45	18,07	29,51	219,43	17,90	4,12
B1	120-01-15	/	-	-	-	-	-	-	-	-	-	-	-	-
B1	120-01-16	/	6,22	0,40	0,24	197,15	3,94	0,70	219,24	20,18	36,41	26,82	3,04	3,38
B1	120-01-17	/	13,42	1,91	0,31	272,05	16,46	0,77	183,67	34,19	39,50	41,97	3,36	5,70
B1	120-01-18	/	23,34	1,43	0,30	234,92	8,03	0,54	182,72	22,67	32,95	67,87	3,42	4,10
B1	120-01-19	GZ	-	-	-	-	-	-	-	-	-	-	-	-
B1	120-01-20	GZ	-	-	-	-	-	-	-	-	-	-	-	-
B1	120-01-21	GZ	12,16	0,61	0,24	383,27	4,93	0,46	208,16	13,01	23,31	117,31	4,48	3,99
B1	120-01-22	GZ	18,32	1,27	0,32	515,24	15,54	0,58	259,59	23,70	41,41	208,68	8,46	4,77
B1	120-01-23	GZ	14,40	0,58	0,22	425,21	5,05	0,48	234,20	13,77	27,01	115,45	2,74	3,38
B1	120-01-24	/	11,87	0,70	0,30	324,05	6,65	0,78	226,23	15,69	27,73	93,33	4,41	4,24
B1	120-01-25	/	-	-	-	-	-	-	-	-	-	-	-	-
B1	120-01-26	GZ	16,35	0,67	0,24	542,63	13,44	0,53	257,22	21,09	24,17	133,62	4,05	4,26
B1	120-01-27	GZ	25,43	1,30	0,28	454,61	7,07	0,39	234,92	16,59	20,07	206,50	7,52	3,97
B1	120-01-28	/	-	-	-	-	-	-	-	-	-	-	-	-
B1	120-01-29	GZ	13,54	0,45	0,20	511,16	6,72	0,41	205,83	12,27	28,69	150,19	3,18	3,43
B1	120-01-30	GZ	-	-	-	-	-	-	-	-	-	-	-	-
B1	120-01-31	GZ	-	-	-	-	-	-	-	-	-	-	-	-
B1	120-01-32	GZ	15,92	0,86	0,29	554,31	8,62	0,61	163,16	16,76	31,18	217,90	5,51	5,42
B1	120-01-33	GZ	19,64	0,88	0,20	549,39	11,31	0,45	173,96	15,10	25,87	202,97	5,98	3,46
B1	120-01-34	GZ	10,56	1,05	0,37	342,78	14,35	0,83	191,27	23,17	47,85	128,13	9,20	6,25
B1	120-01-35	SGR	7,61	0,67	0,42	266,24	7,23	0,69	186,67	23,43	36,80	62,60	4,45	5,18
B1	120-01-36	SGR	16,98	2,67	0,22	241,05	7,39	0,45	197,68	19,67	33,12	75,04	3,55	4,61
B1	120-01-37	SGR	21,95	1,50	0,29	349,82	6,86	0,60	175,98	24,62	35,17	141,13	4,01	6,08
B1	120-01-38	SGR	42,18	1,23	0,20	606,52	8,27	0,62	157,38	15,07	27,51	259,40	5,61	4,30

Part 13

			Ca			Ti			Mn			Fe		
Vein type	Spot ID	CL color/intensity and quartz texture	Concentration ppm	2SE (ppm)	LOD (ppm)	Concentration ppm	2SE (ppm)	LOD (ppm)	Concentration ppm	2SE (ppm)	LOD (ppm)	Concentration ppm	2SE (ppm)	LOD (ppm)
B1	120-01-2	SGR	-	-	-	146,73	6,10	-	-	-	-	-	-	-
B1	120-01-3	SGR	<LOD	26,25	49,31	135,04	5,87	0,49	3,53	0,44	0,40	32,56	4,08	6,68
B1	120-01-4	/	-	-	-	211,64	7,93	0,50	-	-	-	-	-	-
B1	120-01-5	/	-	-	-	223,82	7,44	-	-	-	-	-	-	-
B1	120-01-7	GZ	53,21	17,92	27,81	236,43	9,70	-	3,11	0,32	0,28	32,29	3,14	4,37
B1	120-01-8	GZ	78,52	27,19	45,58	311,41	9,47	-	1,99	0,29	0,33	33,16	3,59	7,40
B1	120-01-9	GZ	81,48	17,05	42,05	334,47	12,55	-	14,02	1,43	0,32	102,91	9,45	5,94
B1	120-01-10	GZ	87,94	30,27	40,30	408,74	11,74	-	11,72	1,66	0,37	67,03	8,47	4,70
B1	120-01-11	GZ	37,99	23,00	68,88	378,45	11,20	-	7,50	0,59	0,80	57,71	4,33	8,68
B1	120-01-14	GZ	53,13	20,90	44,78	288,20	13,63	-	1,87	0,22	0,35	40,50	3,63	6,26
B1	120-01-15	/	-	-	-	356,58	8,33	0,50	-	-	-	-	-	-
B1	120-01-16	/	<LOD	27,60	45,44	363,20	11,55	-	1,03	0,20	0,38	5,83	3,23	5,04
B1	120-01-17	/	<LOD	29,58	58,44	304,25	8,65	0,54	3,09	0,68	0,43	15,89	5,29	6,77
B1	120-01-18	/	131,68	101,34	53,22	349,84	11,76	-	3,20	0,75	0,42	40,64	6,22	7,43
B1	120-01-19	GZ	-	-	-	411,66	13,76	-	-	-	-	-	-	-
B1	120-01-20	GZ	-	-	-	410,73	15,54	-	-	-	-	-	-	-
B1	120-01-21	GZ	<LOD	13,49	31,34	270,94	8,57	-	1,52	0,17	0,23	15,29	1,96	4,78
B1	120-01-22	GZ	56,39	29,51	56,29	365,10	12,99	-	8,15	1,16	0,49	66,33	7,24	6,34
B1	120-01-23	GZ	<LOD	15,46	36,42	269,15	9,37	-	1,75	0,22	0,28	20,18	2,02	3,93
B1	120-01-24	/	51,65	26,94	45,48	194,17	10,89	0,69	1,23	0,26	0,30	15,79	2,52	6,04
B1	120-01-25	/	-	-	-	289,99	10,48	-	-	-	-	-	-	-
B1	120-01-26	GZ	116,27	44,47	34,01	285,59	12,50	-	2,35	0,44	0,29	25,97	2,82	3,60
B1	120-01-27	GZ	<LOD	28,40	39,75	262,36	9,64	-	2,82	0,34	0,28	61,24	3,99	4,57
B1	120-01-28	/	-	-	-	290,39	7,68	-	-	-	-	-	-	-
B1	120-01-29	GZ	65,53	20,25	33,56	272,13	9,60	-	1,35	0,19	0,35	22,66	1,81	4,19
B1	120-01-30	GZ	-	-	-	358,46	12,16	-	-	-	-	-	-	-
B1	120-01-31	GZ	-	-	-	250,45	6,77	-	-	-	-	-	-	-
B1	120-01-32	GZ	<LOD	22,17	47,41	416,44	10,48	-	1,39	0,24	0,35	32,98	2,33	5,03
B1	120-01-33	GZ	44,44	21,36	32,94	364,50	8,67	-	1,04	0,20	0,25	29,28	3,12	4,64
B1	120-01-34	GZ	<LOD	38,63	57,12	199,64	7,41	0,62	6,18	1,20	0,50	84,32	25,74	7,09
B1	120-01-35	SGR	<LOD	31,24	45,59	127,60	5,15	-	2,58	0,48	0,35	7,89	3,68	6,12
B1	120-01-36	SGR	<LOD	18,31	45,77	203,41	9,53	-	6,44	0,90	0,32	42,70	5,07	4,89
B1	120-01-37	SGR	54,99	36,37	54,80	189,99	8,37	-	10,98	1,16	0,45	54,02	6,82	6,20
B1	120-01-38	SGR	72,83	18,44	34,98	331,17	9,11	-	1,64	0,18	0,31	64,28	2,85	5,08

Part 14

			Co			Cu			Zn			Ga		
Vein type	Spot ID	CL color/intensity and quartz texture	Concentration ppm	2SE (ppm)	LOD (ppm)	Concentration ppm	2SE (ppm)	LOD (ppm)	Concentration ppm	2SE (ppm)	LOD (ppm)	Concentration ppm	2SE (ppm)	LOD (ppm)
B1	120-01-2	SGR	-	-	-	-	-	-	-	-	-	-	-	-
B1	120-01-3	SGR	0,03	0,02	-	1,00	0,26	0,46	<LOD	0,62	1,17	<LOD	0,00	-
B1	120-01-4	/	-	-	-	-	-	-	-	-	-	-	-	-
B1	120-01-5	/	-	-	-	-	-	-	-	-	-	-	-	-
B1	120-01-7	GZ	<LOD	0,00	0,03	<LOD	0,17	0,35	0,93	0,47	0,76	<LOD	0,00	-
B1	120-01-8	GZ	<LOD	0,03	0,06	<LOD	0,28	0,60	<LOD	0,65	1,17	0,03	0,03	-
B1	120-01-9	GZ	<LOD	0,02	0,04	0,71	0,26	0,41	2,35	0,72	0,96	0,07	0,05	-
B1	120-01-10	GZ	0,02	0,03	-	<LOD	0,28	0,52	3,18	1,39	0,88	0,05	0,05	-
B1	120-01-11	GZ	0,01	0,01	-	<LOD	0,19	0,89	1,41	0,67	1,01	0,05	0,03	-
B1	120-01-14	GZ	0,01	0,01	-	<LOD	0,25	0,41	1,06	0,67	0,99	0,06	0,04	-
B1	120-01-15	/	-	-	-	-	-	-	-	-	-	-	-	-
B1	120-01-16	/	<LOD	0,00	0,04	<LOD	0,18	0,52	<LOD	0,57	0,90	0,01	0,02	-
B1	120-01-17	/	<LOD	0,00	-	<LOD	0,39	0,62	1,27	1,16	1,47	<LOD	0,00	-
B1	120-01-18	/	0,06	0,04	0,06	<LOD	0,22	0,53	<LOD	0,95	1,28	0,05	0,05	-
B1	120-01-19	GZ	-	-	-	-	-	-	-	-	-	-	-	-
B1	120-01-20	GZ	-	-	-	-	-	-	-	-	-	-	-	-
B1	120-01-21	GZ	<LOD	0,01	0,04	<LOD	0,18	0,37	<LOD	0,35	0,83	0,00	0,01	-
B1	120-01-22	GZ	0,06	0,04	-	0,75	0,42	0,53	0,96	0,89	0,99	0,02	0,03	-
B1	120-01-23	GZ	0,04	0,02	-	<LOD	0,15	0,37	0,69	0,43	0,65	0,01	0,01	-
B1	120-01-24	/	0,05	0,03	-	<LOD	0,23	0,47	<LOD	0,52	1,03	0,02	0,02	-
B1	120-01-25	/	-	-	-	-	-	-	-	-	-	-	-	-
B1	120-01-26	GZ	<LOD	0,02	0,04	0,40	0,30	0,37	<LOD	0,60	0,91	0,02	0,02	-
B1	120-01-27	GZ	0,03	0,03	-	<LOD	0,28	0,37	<LOD	0,45	0,89	0,04	0,04	-
B1	120-01-28	/	-	-	-	-	-	-	-	-	-	-	-	-
B1	120-01-29	GZ	0,02	0,02	-	<LOD	0,17	0,38	<LOD	0,34	0,61	0,00	0,01	-
B1	120-01-30	GZ	-	-	-	-	-	-	-	-	-	-	-	-
B1	120-01-31	GZ	-	-	-	-	-	-	-	-	-	-	-	-
B1	120-01-32	GZ	<LOD	0,00	0,05	<LOD	0,24	0,37	<LOD	0,55	0,99	0,01	0,02	-
B1	120-01-33	GZ	0,05	0,03	-	<LOD	0,18	0,33	<LOD	0,55	0,58	<LOD	0,00	-
B1	120-01-34	GZ	0,07	0,05	-	1,26	0,77	0,64	1,86	1,18	1,44	<LOD	0,00	-
B1	120-01-35	SGR	<LOD	0,00	0,06	<LOD	0,27	0,36	<LOD	0,86	1,29	<LOD	0,00	-
B1	120-01-36	SGR	0,07	0,04	-	0,37	0,29	0,37	2,31	0,98	0,80	0,04	0,04	-
B1	120-01-37	SGR	0,06	0,04	-	<LOD	0,26	0,46	2,36	1,00	1,24	<LOD	0,00	-
B1	120-01-38	SGR	0,05	0,02	0,04	<LOD	0,16	0,31	<LOD	0,39	0,89	0,05	0,03	-

Part 15

			Ge			As			Rb			Sr		
Vein type	Spot ID	CL color/intensity and quartz texture	Concentration ppm	2SE (ppm)	LOD (ppm)	Concentration ppm	2SE (ppm)	LOD (ppm)	Concentration ppm	2SE (ppm)	LOD (ppm)	Concentration ppm	2SE (ppm)	LOD (ppm)
B1	120-01-2	SGR	-	-	-	-	-	-	-	-	-	-	-	-
B1	120-01-3	SGR	1,09	0,49	0,91	<LOD	1,24	3,24	0,15	0,06	0,04	0,13	0,04	-
B1	120-01-4	/	-	-	-	-	-	-	-	-	-	-	-	-
B1	120-01-5	/	-	-	-	-	-	-	-	-	-	-	-	-
B1	120-01-7	GZ	1,27	0,41	0,62	<LOD	0,92	2,06	0,28	0,06	-	0,13	0,03	-
B1	120-01-8	GZ	1,80	0,52	0,98	<LOD	1,88	2,93	0,29	0,07	0,04	0,08	0,04	-
B1	120-01-9	GZ	1,44	0,45	0,78	<LOD	1,60	2,21	0,83	0,11	0,04	0,46	0,08	-
B1	120-01-10	GZ	1,39	0,66	0,78	<LOD	1,85	2,58	0,37	0,08	0,04	0,40	0,09	-
B1	120-01-11	GZ	1,33	0,48	0,71	<LOD	1,03	2,35	0,27	0,06	0,08	0,14	0,04	-
B1	120-01-14	GZ	1,28	0,49	0,63	<LOD	1,44	2,44	0,08	0,04	0,04	0,03	0,02	-
B1	120-01-15	/	-	-	-	-	-	-	-	-	-	-	-	-
B1	120-01-16	/	1,95	0,56	0,96	<LOD	1,20	2,77	0,07	0,03	0,05	0,06	0,03	-
B1	120-01-17	/	1,65	0,92	0,98	<LOD	2,95	3,74	0,32	0,12	-	0,16	0,07	-
B1	120-01-18	/	2,27	0,75	1,02	<LOD	1,71	3,12	0,31	0,09	0,05	0,17	0,05	-
B1	120-01-19	GZ	-	-	-	-	-	-	-	-	-	-	-	-
B1	120-01-20	GZ	-	-	-	-	-	-	-	-	-	-	-	-
B1	120-01-21	GZ	1,46	0,42	0,78	<LOD	0,78	2,32	0,22	0,04	0,03	0,07	0,02	-
B1	120-01-22	GZ	1,34	0,69	1,18	<LOD	1,83	2,87	0,56	0,11	0,04	0,22	0,08	-
B1	120-01-23	GZ	1,64	0,42	0,89	<LOD	0,83	2,48	0,29	0,05	0,04	0,07	0,02	-
B1	120-01-24	/	1,29	0,46	0,89	<LOD	1,36	2,49	0,26	0,06	-	0,07	0,03	-
B1	120-01-25	/	-	-	-	-	-	-	-	-	-	-	-	-
B1	120-01-26	GZ	2,06	0,59	0,90	<LOD	1,03	2,13	0,30	0,07	0,04	0,68	0,11	-
B1	120-01-27	GZ	1,13	0,40	0,73	<LOD	1,20	2,03	0,49	0,11	0,04	0,24	0,06	-
B1	120-01-28	/	-	-	-	-	-	-	-	-	-	-	-	-
B1	120-01-29	GZ	1,18	0,41	0,71	<LOD	0,77	2,27	0,31	0,05	0,04	0,58	0,05	-
B1	120-01-30	GZ	-	-	-	-	-	-	-	-	-	-	-	-
B1	120-01-31	GZ	-	-	-	-	-	-	-	-	-	-	-	-
B1	120-01-32	GZ	1,58	0,53	0,88	<LOD	1,21	2,19	0,08	0,03	0,03	0,07	0,03	-
B1	120-01-33	GZ	1,97	0,56	0,66	<LOD	1,31	1,72	0,07	0,03	0,03	0,08	0,03	-
B1	120-01-34	GZ	2,04	1,07	1,41	<LOD	1,30	3,46	0,28	0,11	0,06	0,57	0,13	-
B1	120-01-35	SGR	1,64	1,01	1,05	<LOD	1,50	2,88	0,17	0,08	0,06	0,17	0,05	-
B1	120-01-36	SGR	1,20	0,61	0,90	<LOD	1,71	2,15	0,27	0,09	0,03	0,22	0,06	-
B1	120-01-37	SGR	2,03	0,83	1,41	<LOD	1,64	2,99	0,49	0,11	0,06	0,39	0,10	-
B1	120-01-38	SGR	1,45	0,43	0,73	<LOD	0,99	2,15	1,00	0,09	0,04	0,25	0,04	-

Part 16

			Zr			Nb			Mo			Ag		
Vein type	Spot ID	CL color/intensity and quartz texture	Concentration ppm	2SE (ppm)	LOD (ppm)	Concentration ppm	2SE (ppm)	LOD (ppm)	Concentration ppm	2SE (ppm)	LOD (ppm)	Concentration ppm	2SE (ppm)	LOD (ppm)
B1	120-01-2	SGR	-	-	-	-	-	-	-	-	-	-	-	-
B1	120-01-3	SGR	0,05	0,03	-	-	-	-	-	-	-	-	-	-
B1	120-01-4	/	-	-	-	-	-	-	-	-	-	-	-	-
B1	120-01-5	/	-	-	-	-	-	-	-	-	-	-	-	-
B1	120-01-7	GZ	0,02	0,02	-	-	-	-	-	-	-	-	-	-
B1	120-01-8	GZ	0,03	0,03	-	-	-	-	-	-	-	-	-	-
B1	120-01-9	GZ	0,05	0,03	-	-	-	-	-	-	-	0,05	0,04	-
B1	120-01-10	GZ	0,03	0,03	-	-	-	-	-	-	-	-	-	-
B1	120-01-11	GZ	0,05	0,03	-	-	-	-	-	-	-	-	-	-
B1	120-01-14	GZ	0,03	0,02	-	-	-	-	-	-	-	-	-	-
B1	120-01-15	/	-	-	-	-	-	-	-	-	-	-	-	-
B1	120-01-16	/	-	-	-	-	-	-	-	-	-	-	-	-
B1	120-01-17	/	0,05	0,05	-	-	-	-	-	-	-	-	-	-
B1	120-01-18	/	-	-	-	-	-	-	-	-	-	-	-	-
B1	120-01-19	GZ	-	-	-	-	-	-	-	-	-	-	-	-
B1	120-01-20	GZ	-	-	-	-	-	-	-	-	-	-	-	-
B1	120-01-21	GZ	0,02	0,01	-	-	-	-	-	-	-	-	-	-
B1	120-01-22	GZ	-	-	-	-	-	-	-	-	-	-	-	-
B1	120-01-23	GZ	0,03	0,02	-	-	-	-	-	-	-	-	-	-
B1	120-01-24	/	-	-	-	-	-	-	-	-	-	-	-	-
B1	120-01-25	/	-	-	-	-	-	-	-	-	-	-	-	-
B1	120-01-26	GZ	0,06	0,03	-	-	-	-	-	-	-	-	-	-
B1	120-01-27	GZ	0,02	0,02	-	-	-	-	-	-	-	-	-	-
B1	120-01-28	/	-	-	-	-	-	-	-	-	-	-	-	-
B1	120-01-29	GZ	0,01	0,01	-	-	-	-	-	-	-	-	-	-
B1	120-01-30	GZ	-	-	-	-	-	-	-	-	-	-	-	-
B1	120-01-31	GZ	-	-	-	-	-	-	-	-	-	-	-	-
B1	120-01-32	GZ	-	-	-	-	-	-	-	-	-	-	-	-
B1	120-01-33	GZ	0,08	0,04	-	-	-	-	-	-	-	-	-	-
B1	120-01-34	GZ	0,04	0,05	-	-	-	-	-	-	-	-	-	-
B1	120-01-35	SGR	0,01	0,02	-	-	-	-	-	-	-	-	-	-
B1	120-01-36	SGR	-	-	-	-	-	-	-	-	-	-	-	-
B1	120-01-37	SGR	0,01	0,01	-	-	-	-	-	-	-	-	-	-
B1	120-01-38	SGR	0,04	0,02	-	-	-	-	-	-	-	-	-	-

Part17

			In			Sn			Sb			Te		
Vein type	Spot ID	CL color/intensity and quartz texture	Concentration ppm	2SE (ppm)	LOD (ppm)	Concentration ppm	2SE (ppm)	LOD (ppm)	Concentration ppm	2SE (ppm)	LOD (ppm)	Concentration ppm	2SE (ppm)	LOD (ppm)
B1	120-01-2	SGR	-	-	-	-	-	-	-	-	-	-	-	-
B1	120-01-3	SGR	<LOD	0,02	0,03	4,54	0,92	0,95	<LOD	0,00	-	-	-	-
B1	120-01-4	/	-	-	-	-	-	-	-	-	-	-	-	-
B1	120-01-5	/	-	-	-	-	-	-	-	-	-	-	-	-
B1	120-01-7	GZ	<LOD	0,01	0,02	4,79	0,46	0,66	<LOD	0,03	0,05	-	-	-
B1	120-01-8	GZ	<LOD	0,02	0,03	4,28	0,98	1,18	<LOD	0,03	0,09	-	-	-
B1	120-01-9	GZ	0,03	0,02	0,02	4,92	0,59	0,90	<LOD	0,04	0,08	-	-	-
B1	120-01-10	GZ	<LOD	0,02	0,02	4,03	0,64	0,95	<LOD	0,00	-	-	-	-
B1	120-01-11	GZ	<LOD	0,01	0,05	4,14	0,57	1,31	0,02	0,02	-	-	-	-
B1	120-01-14	GZ	<LOD	0,02	0,02	3,79	0,78	0,99	0,02	0,02	-	-	-	-
B1	120-01-15	/	-	-	-	-	-	-	-	-	-	-	-	-
B1	120-01-16	/	<LOD	0,02	0,03	5,21	0,64	1,26	0,06	0,05	-	-	-	-
B1	120-01-17	/	<LOD	0,03	0,04	3,77	0,80	1,22	0,10	0,08	-	-	-	-
B1	120-01-18	/	<LOD	0,02	0,04	3,89	1,30	1,36	<LOD	0,06	0,11	-	-	-
B1	120-01-19	GZ	-	-	-	-	-	-	-	-	-	-	-	-
B1	120-01-20	GZ	-	-	-	-	-	-	-	-	-	-	-	-
B1	120-01-21	GZ	<LOD	0,01	0,04	3,46	0,39	0,87	0,09	0,04	-	-	-	-
B1	120-01-22	GZ	<LOD	0,02	0,03	4,08	0,84	1,32	<LOD	0,05	0,09	-	-	-
B1	120-01-23	GZ	<LOD	0,01	0,02	3,65	0,47	1,02	0,12	0,05	0,08	-	-	-
B1	120-01-24	/	<LOD	0,02	0,03	3,02	0,71	1,04	0,06	0,04	-	-	-	-
B1	120-01-25	/	-	-	-	-	-	-	-	-	-	-	-	-
B1	120-01-26	GZ	<LOD	0,02	0,02	3,95	0,45	0,76	0,17	0,08	-	-	-	-
B1	120-01-27	GZ	<LOD	0,02	0,02	3,33	0,66	0,68	0,07	0,05	-	-	-	-
B1	120-01-28	/	-	-	-	-	-	-	-	-	-	-	-	-
B1	120-01-29	GZ	0,02	0,01	0,01	3,34	0,44	0,88	0,08	0,03	-	-	-	-
B1	120-01-30	GZ	-	-	-	-	-	-	-	-	-	-	-	-
B1	120-01-31	GZ	-	-	-	-	-	-	-	-	-	-	-	-
B1	120-01-32	GZ	<LOD	0,01	0,03	2,90	0,69	1,09	<LOD	0,00	-	-	-	-
B1	120-01-33	GZ	<LOD	0,01	0,02	3,06	0,47	0,76	0,05	0,04	-	-	-	-
B1	120-01-34	GZ	<LOD	0,00	-	2,50	0,95	1,38	<LOD	0,00	-	-	-	-
B1	120-01-35	SGR	<LOD	0,02	0,04	2,17	1,08	1,35	0,17	0,11	-	-	-	-
B1	120-01-36	SGR	0,03	0,02	0,02	2,81	0,50	0,85	<LOD	0,00	-	-	-	-
B1	120-01-37	SGR	0,04	0,02	-	2,67	0,61	1,40	0,07	0,06	-	-	-	-
B1	120-01-38	SGR	0,03	0,01	0,03	2,24	0,43	0,94	0,05	0,03	-	-	-	-

Part 18

			Cs			Ba			Ta			W		
Vein type	Spot ID	CL color/intensity and quartz texture	Concentration ppm	2SE (ppm)	LOD (ppm)	Concentration ppm	2SE (ppm)	LOD (ppm)	Concentration ppm	2SE (ppm)	LOD (ppm)	Concentration ppm	2SE (ppm)	LOD (ppm)
B1	120-01-2	SGR	-	-	-	-	-	-	-	-	-	-	-	-
B1	120-01-3	SGR	0,05	0,02	-	0,43	0,20	-	-	-	-	<LOD	0,00	-
B1	120-01-4	/	-	-	-	-	-	-	-	-	-	-	-	-
B1	120-01-5	/	-	-	-	-	-	-	-	-	-	-	-	-
B1	120-01-7	GZ	0,01	0,01	-	0,43	0,15	-	-	-	-	<LOD	0,00	-
B1	120-01-8	GZ	<LOD	0,00	0,02	0,18	0,14	-	-	-	-	<LOD	0,00	-
B1	120-01-9	GZ	0,02	0,02	-	1,72	0,38	-	-	-	-	<LOD	0,00	-
B1	120-01-10	GZ	0,09	0,03	-	2,41	0,61	-	-	-	-	<LOD	0,00	-
B1	120-01-11	GZ	0,01	0,01	-	0,63	0,18	-	-	-	-	<LOD	0,00	-
B1	120-01-14	GZ	<LOD	0,00	-	-	-	-	-	-	-	<LOD	0,00	-
B1	120-01-15	/	-	-	-	-	-	-	-	-	-	-	-	-
B1	120-01-16	/	0,02	0,01	-	0,17	0,12	-	-	-	-	<LOD	0,00	-
B1	120-01-17	/	<LOD	0,00	-	2,21	1,04	-	-	-	-	<LOD	0,00	-
B1	120-01-18	/	0,02	0,02	-	0,51	0,22	-	-	-	-	<LOD	0,00	-
B1	120-01-19	GZ	-	-	-	-	-	-	-	-	-	-	-	-
B1	120-01-20	GZ	-	-	-	-	-	-	-	-	-	-	-	-
B1	120-01-21	GZ	0,00	0,00	-	0,23	0,09	-	-	-	-	<LOD	0,00	-
B1	120-01-22	GZ	0,02	0,02	-	1,22	0,30	-	-	-	-	<LOD	0,00	-
B1	120-01-23	GZ	<LOD	0,00	-	0,50	0,15	-	-	-	-	<LOD	0,00	-
B1	120-01-24	/	<LOD	0,00	-	0,33	0,14	-	-	-	-	<LOD	0,00	-
B1	120-01-25	/	-	-	-	-	-	-	-	-	-	-	-	-
B1	120-01-26	GZ	0,02	0,01	-	2,34	0,48	-	-	-	-	<LOD	0,00	-
B1	120-01-27	GZ	0,03	0,02	0,02	1,28	0,29	-	-	-	-	<LOD	0,00	-
B1	120-01-28	/	-	-	-	-	-	-	-	-	-	-	-	-
B1	120-01-29	GZ	0,01	0,01	-	0,87	0,21	-	-	-	-	<LOD	0,00	-
B1	120-01-30	GZ	-	-	-	-	-	-	-	-	-	-	-	-
B1	120-01-31	GZ	-	-	-	-	-	-	-	-	-	-	-	-
B1	120-01-32	GZ	<LOD	0,00	0,03	0,18	0,11	-	-	-	-	<LOD	0,00	-
B1	120-01-33	GZ	<LOD	0,00	-	-	-	-	-	-	-	<LOD	0,00	-
B1	120-01-34	GZ	0,02	0,02	-	1,57	0,75	-	-	-	-	0,29	0,20	-
B1	120-01-35	SGR	0,02	0,02	-	0,25	0,19	-	-	-	-	0,03	0,05	-
B1	120-01-36	SGR	0,03	0,02	-	1,83	0,53	-	-	-	-	<LOD	0,00	-
B1	120-01-37	SGR	0,07	0,03	-	1,30	0,32	-	-	-	-	<LOD	0,00	0,06
B1	120-01-38	SGR	0,02	0,01	-	1,19	0,24	-	-	-	-	<LOD	0,00	-

Part 19

			Re			Au			Pb			Bi		
Vein type	Spot ID	CL color/intensity and quartz texture	Concentration ppm	2SE (ppm)	LOD (ppm)	Concentration ppm	2SE (ppm)	LOD (ppm)	Concentration ppm	2SE (ppm)	LOD (ppm)	Concentration ppm	2SE (ppm)	LOD (ppm)
B1	120-01-2	SGR	-	-	-	-	-	-	-	-	-	-	-	-
B1	120-01-3	SGR	-	-	-	<LOD	0,05	0,10	0,26	0,08	-	<LOD	0,03	0,05
B1	120-01-4	/	-	-	-	-	-	-	-	-	-	-	-	-
B1	120-01-5	/	-	-	-	-	-	-	-	-	-	-	-	-
B1	120-01-7	GZ	-	-	-	0,06	0,03	-	0,07	0,03	0,05	<LOD	0,01	0,04
B1	120-01-8	GZ	-	-	-	0,08	0,06	-	<LOD	0,00	0,07	<LOD	0,04	0,06
B1	120-01-9	GZ	-	-	-	0,07	0,04	0,07	0,65	0,14	-	<LOD	0,02	0,04
B1	120-01-10	GZ	-	-	-	<LOD	0,04	0,06	1,24	0,28	-	<LOD	0,03	0,04
B1	120-01-11	GZ	-	-	-	<LOD	0,04	0,31	0,30	0,07	0,13	<LOD	0,03	0,09
B1	120-01-14	GZ	-	-	-	<LOD	0,00	0,08	0,13	0,06	-	<LOD	0,03	0,04
B1	120-01-15	/	-	-	-	-	-	-	-	-	-	-	-	-
B1	120-01-16	/	-	-	-	<LOD	0,00	0,06	<LOD	0,00	-	<LOD	0,03	0,04
B1	120-01-17	/	-	-	-	0,00	0,00	-	0,64	0,26	-	<LOD	0,04	0,07
B1	120-01-18	/	-	-	-	<LOD	0,00	-	0,08	0,05	0,08	<LOD	0,04	0,06
B1	120-01-19	GZ	-	-	-	-	-	-	-	-	-	-	-	-
B1	120-01-20	GZ	-	-	-	-	-	-	-	-	-	-	-	-
B1	120-01-21	GZ	-	-	-	0,00	0,01	-	0,09	0,03	0,05	<LOD	0,02	0,04
B1	120-01-22	GZ	-	-	-	<LOD	0,00	-	0,35	0,12	0,08	<LOD	0,00	0,07
B1	120-01-23	GZ	-	-	-	<LOD	0,00	-	0,06	0,03	-	<LOD	0,01	0,05
B1	120-01-24	/	-	-	-	<LOD	0,00	-	0,06	0,04	-	<LOD	0,03	0,06
B1	120-01-25	/	-	-	-	-	-	-	-	-	-	-	-	-
B1	120-01-26	GZ	-	-	-	<LOD	0,00	-	0,15	0,07	-	<LOD	0,03	0,05
B1	120-01-27	GZ	-	-	-	<LOD	0,00	-	0,14	0,05	0,07	<LOD	0,03	0,04
B1	120-01-28	/	-	-	-	-	-	-	-	-	-	-	-	-
B1	120-01-29	GZ	-	-	-	<LOD	0,00	-	0,06	0,03	-	0,04	0,02	0,04
B1	120-01-30	GZ	-	-	-	-	-	-	-	-	-	-	-	-
B1	120-01-31	GZ	-	-	-	-	-	-	-	-	-	-	-	-
B1	120-01-32	GZ	-	-	-	<LOD	0,00	-	0,10	0,04	0,07	<LOD	0,02	0,05
B1	120-01-33	GZ	-	-	-	<LOD	0,00	-	0,06	0,04	-	<LOD	0,03	0,03
B1	120-01-34	GZ	-	-	-	<LOD	0,00	-	1,32	0,35	-	<LOD	0,05	0,08
B1	120-01-35	SGR	-	-	-	<LOD	0,00	-	0,14	0,08	-	<LOD	0,04	0,07
B1	120-01-36	SGR	-	-	-	<LOD	0,00	-	1,15	0,25	-	<LOD	0,02	0,05
B1	120-01-37	SGR	-	-	-	<LOD	0,00	-	0,91	0,16	-	<LOD	0,03	0,05
B1	120-01-38	SGR	-	-	-	<LOD	0,00	-	0,10	0,03	-	<LOD	0,02	0,05

Part 20

			U		
Vein type	Spot ID	CL color/intensity and quartz texture	Concentration ppm	2SE (ppm)	LOD (ppm)
B1	120-01-2	SGR	-	-	-
B1	120-01-3	SGR	<LOD	0,00	-
B1	120-01-4	/	-	-	-
B1	120-01-5	/	-	-	-
B1	120-01-7	GZ	<LOD	0,00	-
B1	120-01-8	GZ	<LOD	0,00	-
B1	120-01-9	GZ	<LOD	0,00	-
B1	120-01-10	GZ	0,01	0,02	-
B1	120-01-11	GZ	<LOD	0,00	-
B1	120-01-14	GZ	<LOD	0,00	-
B1	120-01-15	/	-	-	-
B1	120-01-16	/	<LOD	0,00	-
B1	120-01-17	/	<LOD	0,00	-
B1	120-01-18	/	<LOD	0,00	-
B1	120-01-19	GZ	-	-	-
B1	120-01-20	GZ	-	-	-
B1	120-01-21	GZ	<LOD	0,00	-
B1	120-01-22	GZ	<LOD	0,00	-
B1	120-01-23	GZ	<LOD	0,00	-
B1	120-01-24	/	<LOD	0,00	-
B1	120-01-25	/	-	-	-
B1	120-01-26	GZ	<LOD	0,00	-
B1	120-01-27	GZ	<LOD	0,00	-
B1	120-01-28	/	-	-	-
B1	120-01-29	GZ	<LOD	0,00	-
B1	120-01-30	GZ	-	-	-
B1	120-01-31	GZ	-	-	-
B1	120-01-32	GZ	<LOD	0,00	-
B1	120-01-33	GZ	<LOD	0,00	-
B1	120-01-34	GZ	<LOD	0,00	-
B1	120-01-35	SGR	0,02	0,02	-
B1	120-01-36	SGR	<LOD	0,00	-
B1	120-01-37	SGR	<LOD	0,00	-
B1	120-01-38	SGR	<LOD	0,00	-

Caption:

	Quartz textures
GZ	Growth Zoning
SGR	SubGrain Rotation
GBM	Grain Boundary Migration
/	undetermined texture or location
QC	Quartz Center
QM	Quartz Margin
LOD (From Longerich 1987)	Limit of Detection

CL intensity	
	dark red
	intermediate red
	dark blue
	intermediate blue
	bright blue

Table of ICP-MS quartz analyses for different elements in B2-type vein.

			Li			Be			B			Na		
Vein type	Spot ID	CL color/intensity and quartz texture	Concentration ppm	2SE (ppm)	LOD (ppm)	Concentration ppm	2SE (ppm)	LOD (ppm)	Concentration ppm	2SE (ppm)	LOD (ppm)	Concentration ppm	2SE (ppm)	LOD (ppm)
B2	11902-1		1,59	0,23	0,46	-	-	-	4,36	1,65	3,06	86,62	6,40	9,25
B2	11902-2		1,25	0,34	0,63	-	-	-	<LOD	2,18	4,48	26,19	4,85	8,46
B2	11902-3		2,08	0,37	0,42	0,34	0,26	-	6,40	1,89	3,55	116,30	7,79	10,02
B2	11902-4		57,04	3,58	0,58	-	-	-	<LOD	3,05	4,87	187,01	10,19	11,38
B2	11902-5		0,85	0,24	0,43	-	-	-	4,42	1,91	3,97	26,20	4,20	9,57
B2	11902-6		-	-	-	-	-	-	-	-	-	-	-	-
B2	11902-7		2,12	0,36	0,57	-	-	-	<LOD	2,54	4,15	170,86	8,35	11,08
B2	11902-8		0,69	0,16	0,36	-	-	-	<LOD	1,52	3,00	29,74	8,77	9,37
B2	11902-9		0,72	0,19	0,40	-	-	-	<LOD	1,34	3,05	22,25	3,52	8,53
B2	11902-10		2,84	0,35	0,39	0,64	0,36	-	<LOD	1,74	3,43	121,12	6,08	9,17
B2	11902-11		-	-	-	-	-	-	-	-	-	-	-	-
B2	11902-12		1,44	0,30	0,39	-	-	-	<LOD	1,73	3,85	12,87	4,45	11,53
B2	11902-13		0,48	0,22	0,46	-	-	-	<LOD	1,87	5,05	<LOD	4,87	11,32
B2	11902-14		2,41	0,26	0,37	-	-	-	<LOD	1,27	2,84	38,25	3,95	8,70
B2	11902-15		2,45	0,40	0,49	1,27	0,60	-	<LOD	1,48	4,03	118,43	6,81	10,14
B2	11902-16		2,89	0,36	0,46	-	-	-	4,19	1,49	3,90	72,29	5,36	10,76
B2	11902-17		0,64	0,17	0,33	-	-	-	<LOD	1,20	3,36	20,20	3,16	8,71
B2	11902-18		0,20	0,22	0,46	-	-	-	<LOD	1,68	3,46	<LOD	4,30	9,94
B2	11902-19		0,30	0,21	0,58	-	-	-	<LOD	1,90	3,31	22,92	4,86	12,88
B2	11902-20		2,06	0,32	0,38	-	-	-	<LOD	1,60	3,21	22,18	4,81	8,41
B2	11902-21		2,57	0,31	0,34	0,08	0,11	-	3,08	1,49	2,55	117,20	5,95	9,55
B2	11902-22		0,33	0,20	0,43	-	-	-	<LOD	1,42	3,29	49,31	6,31	8,64
B2	11902-23		-	-	-	-	-	-	-	-	-	-	-	-
B2	11902-24		0,30	0,17	0,34	-	-	-	<LOD	1,18	3,12	71,56	5,84	8,89
B2	11902-25		0,69	0,15	0,30	-	-	-	2,63	1,17	2,31	37,34	2,99	7,40
B2	11902-26		-	-	-	-	-	-	-	-	-	-	-	-

Part 2

			Mg			Al			Cl			K		
Vein type	Spot ID	CL color/intensity and quartz texture	Concentration ppm	2SE (ppm)	LOD (ppm)	Concentration ppm	2SE (ppm)	LOD (ppm)	Concentration ppm	2SE (ppm)	LOD (ppm)	Concentration ppm	2SE (ppm)	LOD (ppm)
B2	11902-1		8,12	0,74	0,20	693,85	14,29	0,49	172,35	14,36	28,81	97,64	4,02	5,07
B2	11902-2		3,65	0,42	0,26	342,50	8,54	0,74	175,69	21,22	38,35	31,36	2,88	5,57
B2	11902-3		10,92	0,83	0,22	1 725,62	78,47	0,61	166,88	16,17	39,71	256,47	12,60	5,11
B2	11902-4		11,03	0,79	0,41	4 098,61	129,58	0,78	118,99	29,77	56,64	180,60	7,41	8,14
B2	11902-5		1,04	0,21	0,21	384,83	15,18	0,64	124,59	18,50	41,79	<LOD	2,85	6,63
B2	11902-6		-	-	-	-	-	-	-	-	-	-	-	-
B2	11902-7		3,34	0,44	0,29	2 447,47	60,76	0,56	142,93	26,04	44,91	105,62	4,52	7,91
B2	11902-8		7,38	1,12	0,20	109,44	3,83	0,50	142,59	18,83	34,28	- 5,92	1,64	4,08
B2	11902-9		1,44	0,23	0,19	119,14	10,56	0,53	146,37	15,17	39,98	17,34	2,59	3,33
B2	11902-10		5,31	0,59	0,18	1 803,43	31,82	0,48	176,75	17,51	35,85	128,42	3,24	4,94
B2	11902-11		-	-	-	-	-	-	-	-	-	-	-	-
B2	11902-12		3,35	0,45	0,22	485,52	16,95	0,68	154,79	17,78	40,47	50,72	3,00	5,84
B2	11902-13		0,68	0,19	0,25	132,68	15,49	0,73	123,88	19,77	41,07	9,28	3,58	5,99
B2	11902-14		0,71	0,15	0,19	592,31	17,31	0,63	158,97	14,17	25,89	68,19	4,12	3,88
B2	11902-15		3,63	0,45	0,23	1 969,35	37,75	0,64	145,06	18,78	46,53	76,59	3,87	5,50
B2	11902-16		12,61	0,79	0,21	1 564,26	50,26	0,65	188,99	22,18	37,32	220,94	6,67	5,60
B2	11902-17		0,76	0,14	0,17	156,85	3,86	0,45	206,69	14,59	32,52	9,05	1,70	4,02
B2	11902-18		0,46	0,16	0,31	55,62	3,25	0,50	194,30	19,25	39,74	<LOD	2,17	5,31
B2	11902-19		1,12	0,26	0,25	200,09	8,99	0,66	214,22	21,81	40,75	27,49	3,00	6,06
B2	11902-20		1,06	0,21	0,24	562,20	10,57	0,65	177,88	16,57	36,19	45,86	2,79	5,16
B2	11902-21		4,04	0,31	0,19	2 001,03	33,45	0,48	163,28	16,93	31,31	152,69	4,28	3,96
B2	11902-22		0,96	0,24	0,19	103,82	3,59	0,54	212,05	23,96	33,08	<LOD	2,68	4,49
B2	11902-23		-	-	-	-	-	-	-	-	-	-	-	-
B2	11902-24		1,23	0,19	0,18	114,98	3,82	0,50	163,26	12,15	32,10	7,42	2,03	3,87
B2	11902-25		0,76	0,17	0,16	168,31	5,97	0,42	171,04	13,59	26,53	4,41	1,37	3,17
B2	11902-26		-	-	-	-	-	-	-	-	-	-	-	-

Part 3

			Ca			Ti			Mn			Fe		
Vein type	Spot ID	CL color/intensity and quartz texture	Concentration ppm	2SE (ppm)	LOD (ppm)	Concentration ppm	2SE (ppm)	LOD (ppm)	Concentration ppm	2SE (ppm)	LOD (ppm)	Concentration ppm	2SE (ppm)	LOD (ppm)
B2	11902-1		150,48	36,74	39,79	88,06	3,44	-	5,62	0,43	0,41	57,26	5,22	6,21
B2	11902-2		<LOD	22,20	47,50	83,13	3,20	-	3,13	0,29	0,53	88,83	10,16	7,64
B2	11902-3		<LOD	26,66	43,47	38,57	2,96	-	6,27	0,45	0,40	210,95	26,65	7,03
B2	11902-4		111,25	39,98	62,63	2,22	0,48	-	<LOD	0,25	0,63	158,30	16,72	9,08
B2	11902-5		<LOD	21,25	64,55	2,58	0,53	-	0,65	0,28	0,47	24,15	5,62	7,21
B2	11902-6		-	-	-	95,31	3,77	-	-	-	-	-	-	-
B2	11902-7		<LOD	30,56	64,39	5,59	1,01	-	0,91	0,35	0,54	<LOD	3,48	7,89
B2	11902-8		<LOD	15,61	40,52	1,30	0,35	-	<LOD	0,15	0,38	<LOD	2,06	4,73
B2	11902-9		47,94	20,96	40,01	101,52	4,22	-	1,05	0,23	0,38	29,15	3,33	5,18
B2	11902-10		54,21	23,10	31,32	9,88	1,30	-	1,21	0,24	0,35	<LOD	2,64	6,11
B2	11902-11		-	-	-	105,67	7,92	-	-	-	-	-	-	-
B2	11902-12		57,40	20,15	43,70	108,35	3,56	-	1,14	0,29	0,29	94,96	8,37	5,68
B2	11902-13		<LOD	30,84	46,66	108,12	4,24	-	0,61	0,22	0,45	24,59	3,07	5,64
B2	11902-14		45,21	13,59	35,73	122,65	4,26	-	1,89	0,29	0,33	27,44	2,32	5,30
B2	11902-15		<LOD	24,68	38,02	4,60	0,89	-	0,72	0,28	0,52	<LOD	3,28	6,12
B2	11902-16		<LOD	25,74	42,32	46,37	3,60	-	4,14	0,39	0,39	219,06	23,08	7,41
B2	11902-17		<LOD	17,84	40,96	106,35	4,00	-	0,91	0,19	0,38	34,51	2,64	4,79
B2	11902-18		<LOD	25,14	43,94	90,22	4,99	-	<LOD	0,20	0,43	11,11	3,40	6,48
B2	11902-19		<LOD	25,84	52,89	96,61	4,52	-	0,61	0,28	0,43	27,28	4,27	6,20
B2	11902-20		<LOD	22,35	44,14	112,91	4,88	-	1,31	0,20	0,42	42,88	3,30	5,97
B2	11902-21		<LOD	15,32	38,69	13,26	1,59	-	1,35	0,21	0,34	22,00	2,87	5,29
B2	11902-22		<LOD	25,17	37,98	86,91	3,91	-	1,82	0,31	0,40	28,34	4,65	5,00
B2	11902-23		-	-	-	94,07	3,80	-	-	-	-	-	-	-
B2	11902-24		36,88	17,17	28,77	92,23	3,92	-	2,85	0,35	0,29	23,84	3,29	4,99
B2	11902-25		42,50	17,05	44,08	102,69	4,42	-	2,63	0,38	0,29	17,45	1,84	3,92
B2	11902-26		-	-	-	87,72	3,99	-	-	-	-	-	-	-

Part 4

			Co			Cu			Zn			Ga		
Vein type	Spot ID	CL color/intensity and quartz texture	Concentration ppm	2SE (ppm)	LOD (ppm)	Concentration ppm	2SE (ppm)	LOD (ppm)	Concentration ppm	2SE (ppm)	LOD (ppm)	Concentration ppm	2SE (ppm)	LOD (ppm)
B2	11902-1		0,01	0,01	-	17,01	1,94	0,34	1,16	0,45	0,65	0,11	0,04	-
B2	11902-2		0,04	0,03	-	5,14	0,53	0,45	<LOD	0,37	0,89	0,10	0,05	-
B2	11902-3		0,03	0,02	-	3,41	0,46	0,44	0,91	0,51	0,82	0,08	0,04	-
B2	11902-4		0,11	0,05	-	0,56	0,30	0,56	<LOD	0,63	0,97	0,09	0,07	-
B2	11902-5		0,05	0,03	-	<LOD	0,21	0,49	<LOD	0,36	0,84	- 0,00	0,00	-
B2	11902-6		-	-	-	-	-	-	-	-	-	-	-	-
B2	11902-7		0,01	0,01	0,09	8,00	3,38	0,54	<LOD	0,51	0,91	0,17	0,08	-
B2	11902-8		0,01	0,01	0,05	<LOD	0,16	0,39	<LOD	0,27	0,64	0,00	0,01	-
B2	11902-9		0,01	0,01	-	0,83	0,19	0,34	<LOD	0,27	0,58	0,14	0,04	-
B2	11902-10		0,07	0,03	0,05	0,49	0,19	0,32	<LOD	0,35	0,68	0,26	0,07	-
B2	11902-11		-	-	-	-	-	-	-	-	-	-	-	-
B2	11902-12		<LOD	0,01	0,07	2,35	0,46	0,42	1,22	0,48	0,86	0,07	0,04	-
B2	11902-13		- 0,00	0,00	-	1,68	0,32	0,41	<LOD	0,39	0,80	0,01	0,02	-
B2	11902-14		0,01	0,01	-	1,83	0,31	0,33	1,44	0,34	-	0,09	0,04	-
B2	11902-15		0,01	0,01	-	0,52	0,24	0,48	<LOD	0,36	0,83	0,13	0,07	-
B2	11902-16		0,02	0,02	-	2,05	0,37	0,43	0,86	0,42	0,76	0,34	0,10	-
B2	11902-17		0,03	0,02	-	1,70	0,35	0,33	<LOD	0,22	0,72	0,16	0,04	-
B2	11902-18		0,00	0,00	-	<LOD	0,19	0,39	<LOD	0,31	1,42	0,12	0,05	-
B2	11902-19		- 0,00	0,00	-	<LOD	0,22	0,42	<LOD	0,35	0,76	0,16	0,07	-
B2	11902-20		0,01	0,01	-	1,39	0,38	0,39	<LOD	0,32	0,72	0,09	0,04	-
B2	11902-21		0,01	0,01	-	2,36	0,51	0,37	<LOD	0,22	0,51	0,15	0,05	-
B2	11902-22		0,01	0,01	-	18,26	1,83	0,38	<LOD	0,58	0,74	0,03	0,03	-
B2	11902-23		-	-	-	-	-	-	-	-	-	-	-	-
B2	11902-24		0,00	0,01	-	4,15	0,56	0,31	<LOD	0,29	0,64	0,06	0,03	-
B2	11902-25		- 0,00	0,00	-	0,69	0,16	0,29	0,92	0,34	0,57	0,06	0,03	-
B2	11902-26		-	-	-	-	-	-	-	-	-	-	-	-

Part 5

			Ge			As			Rb			Sr		
Vein type	Spot ID	CL color/intensity and quartz texture	Concentration ppm	2SE (ppm)	LOD (ppm)	Concentration ppm	2SE (ppm)	LOD (ppm)	Concentration ppm	2SE (ppm)	LOD (ppm)	Concentration ppm	2SE (ppm)	LOD (ppm)
B2	11902-1		3,39	0,61	0,96	<LOD	0,97	2,45	0,74	0,08	-	0,56	0,16	-
B2	11902-2		3,15	0,71	1,34	<LOD	1,53	3,22	0,22	0,06	0,05	0,46	0,09	-
B2	11902-3		5,42	0,78	1,35	<LOD	1,20	2,70	1,48	0,15	0,05	0,66	0,08	-
B2	11902-4		0,97	0,77	1,23	<LOD	1,55	3,10	1,48	0,24	-	10,60	0,68	-
B2	11902-5		1,57	0,53	1,29	<LOD	1,25	2,42	0,05	0,02	-	0,05	0,02	-
B2	11902-6		-	-	-	-	-	-	-	-	-	-	-	-
B2	11902-7		3,73	0,85	1,13	<LOD	1,50	3,74	0,13	0,05	-	0,26	0,07	-
B2	11902-8		1,57	0,37	0,73	<LOD	0,83	2,40	<LOD	0,01	0,04	0,08	0,03	-
B2	11902-9		2,42	0,50	0,84	<LOD	0,77	2,34	0,17	0,04	0,04	0,12	0,03	-
B2	11902-10		4,75	0,55	0,87	<LOD	1,19	2,11	0,58	0,09	0,03	0,16	0,04	-
B2	11902-11		-	-	-	-	-	-	-	-	-	-	-	-
B2	11902-12		2,10	0,59	1,14	<LOD	1,16	3,07	0,39	0,07	-	0,04	0,02	-
B2	11902-13		2,43	0,65	1,28	<LOD	1,14	3,17	0,15	0,05	-	0,08	0,03	-
B2	11902-14		2,83	0,45	0,83	<LOD	0,90	1,94	0,35	0,05	0,04	0,13	0,03	-
B2	11902-15		3,14	0,77	1,01	<LOD	1,35	2,94	0,10	0,04	0,05	0,33	0,05	-
B2	11902-16		5,05	0,76	1,18	3,50	1,41	2,88	1,43	0,16	-	0,47	0,09	-
B2	11902-17		2,83	0,45	0,96	<LOD	0,88	2,15	0,13	0,03	0,05	0,08	0,02	-
B2	11902-18		2,98	0,70	1,20	<LOD	1,24	2,81	0,07	0,03	-	-	-	-
B2	11902-19		2,83	0,66	1,29	3,77	1,29	2,60	0,22	0,05	-	0,05	0,02	-
B2	11902-20		2,15	0,54	1,04	<LOD	1,04	2,18	0,51	0,07	0,05	0,05	0,02	-
B2	11902-21		5,16	0,52	0,94	3,07	0,91	2,84	0,70	0,10	0,05	0,15	0,04	-
B2	11902-22		2,71	0,63	1,10	2,72	1,14	2,20	0,07	0,03	-	0,21	0,06	-
B2	11902-23		-	-	-	-	-	-	-	-	-	-	-	-
B2	11902-24		2,23	0,47	0,89	2,83	0,81	1,47	0,10	0,03	-	0,41	0,06	-
B2	11902-25		2,15	0,39	0,65	<LOD	0,80	1,66	0,07	0,02	-	0,25	0,04	-
B2	11902-26		-	-	-	-	-	-	-	-	-	-	-	-

Part 6

			Zr			Nb			Mo			Ag		
Vein type	Spot ID	CL color/intensity and quartz texture	Concentration ppm	2SE (ppm)	LOD (ppm)	Concentration ppm	2SE (ppm)	LOD (ppm)	Concentration ppm	2SE (ppm)	LOD (ppm)	Concentration ppm	2SE (ppm)	LOD (ppm)
B2	11902-1		0,05	0,02	-	0,06	0,02	-	0,45	0,15	-	-	-	-
B2	11902-2		0,06	0,03	-	-	-	-	0,02	0,03	-	-	-	-
B2	11902-3		-	-	-	-	-	-	0,18	0,10	-	0,01	0,01	-
B2	11902-4		-	-	-	-	-	-	-	-	-	-	-	-
B2	11902-5		-	-	-	-	-	-	-	-	-	-	-	-
B2	11902-6		-	-	-	-	-	-	-	-	-	-	-	-
B2	11902-7		-	-	-	-	-	-	-	-	-	-	-	-
B2	11902-8		0,01	0,01	-	-	-	-	-	-	-	-	-	-
B2	11902-9		0,06	0,03	-	0,06	0,02	-	-	-	-	-	-	-
B2	11902-10		-	-	-	-	-	-	-	-	-	-	-	-
B2	11902-11		-	-	-	-	-	-	-	-	-	-	-	-
B2	11902-12		0,11	0,04	-	0,02	0,01	-	-	-	-	-	-	-
B2	11902-13		-	-	-	-	-	-	-	-	-	-	-	-
B2	11902-14		0,28	0,05	-	0,03	0,01	-	-	-	-	-	-	-
B2	11902-15		-	-	-	-	-	-	-	-	-	-	-	-
B2	11902-16		0,02	0,02	-	-	-	-	-	-	-	-	-	-
B2	11902-17		0,07	0,02	-	0,10	0,03	-	-	-	-	-	-	-
B2	11902-18		-	-	-	0,03	0,02	-	-	-	-	-	-	-
B2	11902-19		-	-	-	0,04	0,02	-	-	-	-	-	-	-
B2	11902-20		0,16	0,04	-	0,00	0,00	-	-	-	-	-	-	-
B2	11902-21		-	-	-	-	-	-	-	-	-	-	-	-
B2	11902-22		0,04	0,03	-	-	-	-	0,04	0,06	-	-	-	-
B2	11902-23		-	-	-	-	-	-	-	-	-	-	-	-
B2	11902-24		0,05	0,02	-	-	-	-	-	-	-	-	-	-
B2	11902-25		0,07	0,02	-	-	-	-	0,01	0,02	-	-	-	-
B2	11902-26		-	-	-	-	-	-	-	-	-	-	-	-

Part 7

			In			Sn			Sb			Te		
Vein type	Spot ID	CL color/intensity and quartz texture	Concentration ppm	2SE (ppm)	LOD (ppm)	Concentration ppm	2SE (ppm)	LOD (ppm)	Concentration ppm	2SE (ppm)	LOD (ppm)	Concentration ppm	2SE (ppm)	LOD (ppm)
B2	11902-1		<LOD	0,01	0,03	2,52	0,52	1,18	0,13	0,08	0,11	-	-	-
B2	11902-2		<LOD	0,02	0,04	2,68	0,69	1,49	<LOD	0,05	0,14	-	-	-
B2	11902-3		<LOD	0,01	0,03	1,69	0,53	1,40	0,56	0,13	0,12	-	-	-
B2	11902-4		<LOD	0,02	0,04	<LOD	0,78	1,57	0,16	0,09	0,12	-	-	-
B2	11902-5		<LOD	0,02	0,04	1,89	0,56	1,29	<LOD	0,06	0,11	-	-	-
B2	11902-6		-	-	-	-	-	-	-	-	-	-	-	-
B2	11902-7		<LOD	0,02	0,04	<LOD	0,97	1,53	0,64	0,19	0,13	-	-	-
B2	11902-8		<LOD	0,01	0,03	1,51	0,43	1,26	<LOD	0,04	0,11	-	-	-
B2	11902-9		<LOD	0,01	0,03	2,37	0,45	0,94	0,11	0,04	-	-	-	-
B2	11902-10		<LOD	0,01	0,02	1,81	0,40	0,95	0,69	0,11	0,07	-	-	-
B2	11902-11		-	-	-	-	-	-	-	-	-	-	-	-
B2	11902-12		<LOD	0,02	0,04	1,93	0,53	1,13	0,14	0,05	-	-	-	-
B2	11902-13		<LOD	0,02	0,03	<LOD	0,66	1,40	0,15	0,07	-	-	-	-
B2	11902-14		<LOD	0,01	0,03	1,44	0,43	0,94	0,12	0,04	0,08	-	-	-
B2	11902-15		<LOD	0,02	0,04	1,27	0,62	1,23	0,35	0,11	0,12	-	-	-
B2	11902-16		<LOD	0,02	0,04	1,70	0,59	1,25	0,58	0,13	0,10	-	-	-
B2	11902-17		<LOD	0,01	0,03	1,87	0,45	1,17	<LOD	0,04	0,08	-	-	-
B2	11902-18		<LOD	0,02	0,03	2,28	0,56	1,39	<LOD	0,05	0,11	-	-	-
B2	11902-19		<LOD	0,02	0,03	2,84	0,67	1,60	<LOD	0,06	0,12	-	-	-
B2	11902-20		<LOD	0,01	0,03	2,60	0,58	1,18	0,08	0,04	-	-	-	-
B2	11902-21		<LOD	0,01	0,03	1,30	0,56	0,99	0,62	0,11	-	-	-	-
B2	11902-22		<LOD	0,02	0,03	1,88	0,58	1,37	0,11	0,06	-	-	-	-
B2	11902-23		-	-	-	-	-	-	-	-	-	-	-	-
B2	11902-24		<LOD	0,01	0,03	2,42	0,47	0,93	0,13	0,05	0,10	-	-	-
B2	11902-25		<LOD	0,01	0,02	2,14	0,37	0,65	0,08	0,03	-	-	-	-
B2	11902-26		-	-	-	-	-	-	-	-	-	-	-	-

Part 8

			Cs			Ba			Ta			W		
Vein type	Spot ID	CL color/intensity and quartz texture	Concentration ppm	2SE (ppm)	LOD (ppm)	Concentration ppm	2SE (ppm)	LOD (ppm)	Concentration ppm	2SE (ppm)	LOD (ppm)	Concentration ppm	2SE (ppm)	LOD (ppm)
B2	11902-1		0,11	0,03	-	1,17	0,22	-	-	-	-	0,92	0,18	-
B2	11902-2		0,05	0,02	-	0,27	0,13	-	0,02	0,01	-	0,47	0,14	-
B2	11902-3		0,11	0,03	-	3,46	0,48	-	-	-	-	-	-	-
B2	11902-4		1,05	0,14	-	3,93	0,51	-	-	-	-	-	-	-
B2	11902-5		0,00	0,00	-	0,16	0,09	-	-	-	-	-	-	-
B2	11902-6		-	-	-	-	-	-	-	-	-	-	-	-
B2	11902-7		0,04	0,02	-	2,32	0,57	-	-	-	-	-	-	-
B2	11902-8		- 0,00	0,00	-	-	-	-	-	-	-	-	-	-
B2	11902-9		0,03	0,01	-	0,27	0,10	-	-	-	-	0,14	0,07	-
B2	11902-10		0,03	0,01	-	1,37	0,28	-	-	-	-	-	-	-
B2	11902-11		-	-	-	-	-	-	-	-	-	-	-	-
B2	11902-12		0,04	0,02	-	0,28	0,12	-	0,01	0,01	-	-	-	-
B2	11902-13		0,03	0,02	-	-	-	-	-	-	-	-	-	-
B2	11902-14		0,07	0,02	-	-	-	-	0,10	0,02	-	-	-	-
B2	11902-15		0,00	0,01	-	2,01	0,50	-	-	-	-	-	-	-
B2	11902-16		0,15	0,04	-	1,80	0,41	-	-	-	-	-	-	-
B2	11902-17		0,05	0,01	-	0,16	0,08	-	0,00	0,00	-	0,16	0,05	-
B2	11902-18		0,00	0,01	-	-	-	-	-	-	-	-	-	-
B2	11902-19		0,01	0,01	-	0,28	0,14	-	0,01	0,01	-	-	-	-
B2	11902-20		0,05	0,02	-	-	-	-	0,04	0,01	-	0,01	0,01	-
B2	11902-21		0,05	0,01	-	1,60	0,26	-	-	-	-	-	-	-
B2	11902-22		0,03	0,02	-	0,41	0,21	-	-	-	-	-	-	-
B2	11902-23		-	-	-	-	-	-	-	-	-	-	-	-
B2	11902-24		0,02	0,01	-	0,50	0,16	-	-	-	-	0,09	0,05	-
B2	11902-25		0,02	0,01	-	0,26	0,09	-	0,03	0,01	-	0,08	0,04	-
B2	11902-26		-	-	-	-	-	-	-	-	-	-	-	-

Part 9

			Re			Au			Pb			Bi		
Vein type	Spot ID	CL color/intensity and quartz texture	Concentration ppm	2SE (ppm)	LOD (ppm)	Concentration ppm	2SE (ppm)	LOD (ppm)	Concentration ppm	2SE (ppm)	LOD (ppm)	Concentration ppm	2SE (ppm)	LOD (ppm)
B2	11902-1		-	-	-	- 0,00	0,00	-	0,74	0,11	0,07	0,05	0,03	0,05
B2	11902-2		-	-	-	0,00	0,00	-	0,47	0,12	0,07	<LOD	0,04	0,06
B2	11902-3		-	-	-	- 0,00	0,00	-	0,61	0,08	-	<LOD	0,04	0,07
B2	11902-4		-	-	-	0,00	0,00	-	<LOD	0,00	0,11	<LOD	0,04	0,06
B2	11902-5		-	-	-	- 0,00	0,00	-	0,21	0,07	0,08	<LOD	0,03	0,06
B2	11902-6		-	-	-	-	-	-	-					
B2	11902-7		-	-	-	- 0,00	0,00	-	0,10	0,06	-	<LOD	0,03	0,08
B2	11902-8		-	-	-	0,00	0,00	-	0,06	0,03	-	<LOD	0,03	0,05
B2	11902-9		-	-	-	- 0,00	0,00	-	0,10	0,04	-	<LOD	0,02	0,06
B2	11902-10		-	-	-	0,00	0,00	-	0,08	0,04	-	<LOD	0,03	0,05
B2	11902-11		-	-	-	-	-	-	-	-	-	-	-	-
B2	11902-12		-	-	-	0,00	0,00	-	0,11	0,04	0,08	<LOD	0,03	0,06
B2	11902-13		-	-	-	0,02	0,02	-	0,11	0,05	-	<LOD	0,02	0,05
B2	11902-14		-	-	-	0,00	0,01	-	0,27	0,06	-	<LOD	0,02	0,05
B2	11902-15		-	-	-	- 0,00	0,00	-	0,08	0,05	-	<LOD	0,01	0,06
B2	11902-16		-	-	-	0,00	0,00	-	0,26	0,07	-	<LOD	0,03	0,06
B2	11902-17		-	-	-	- 0,00	0,00	-	0,15	0,04	-	<LOD	0,02	0,05
B2	11902-18		-	-	-	0,00	0,00	-	0,02	0,02	-	<LOD	0,03	0,06
B2	11902-19		-	-	-	- 0,00	0,00	-	0,14	0,05	0,07	<LOD	0,03	0,07
B2	11902-20		-	-	-	0,00	0,00	-	0,21	0,06	-	<LOD	0,02	0,05
B2	11902-21		-	-	-	- 0,00	0,00	-	0,07	0,03	-	<LOD	0,02	0,05
B2	11902-22		-	-	-	0,00	0,00	-	0,25	0,08	0,08	0,06	0,04	0,05
B2	11902-23		-	-	-	-	-	-	-					
B2	11902-24		-	-	-	0,00	0,00	-	0,24	0,06	0,05	<LOD	0,02	0,05
B2	11902-25		-	-	-	- 0,00	0,00	-	0,50	0,09	-	<LOD	0,02	0,04
B2	11902-26		-	-	-	-	-	-	-	-	-	-	-	-

Part 10

			U		
Vein type	Spot ID	CL color/intensity and quartz texture	Concentration ppm	2SE (ppm)	LOD (ppm)
B2	11902-1		0,90	0,18	-
B2	11902-2		1,33	0,24	-
B2	11902-3		0,12	0,03	-
B2	11902-4		-	-	-
B2	11902-5		-	-	-
B2	11902-6				
B2	11902-7		-	-	-
B2	11902-8		-	-	-
B2	11902-9		6,91	1,02	-
B2	11902-10		0,09	0,03	-
B2	11902-11		-	-	-
B2	11902-12		2,43	0,69	-
B2	11902-13		2,43	0,35	-
B2	11902-14		5,04	0,57	-
B2	11902-15		0,04	0,02	-
B2	11902-16		3,20	0,82	-
B2	11902-17		5,70	0,42	-
B2	11902-18		3,76	0,64	-
B2	11902-19		2,79	0,77	-
B2	11902-20		4,71	0,81	-
B2	11902-21		0,04	0,02	-
B2	11902-22		0,27	0,07	-
B2	11902-23				
B2	11902-24		5,89	1,46	-
B2	11902-25		1,52	0,18	-
B2	11902-26		-	-	-

Table of ICP-MS quartz analyses for different elements in E1-type vein.

			Li			Be			B			Na		
Vein type	Spot ID	CL color/intensity and quartz texture	Concentration ppm	2SE (ppm)	LOD (ppm)	Concentration ppm	2SE (ppm)	LOD (ppm)	Concentration ppm	2SE (ppm)	LOD (ppm)	Concentration ppm	2SE (ppm)	LOD (ppm)
E	12203-1	QM	11,05	0,62	0,44	-	-	-	<LOD	1,71	4,15	13,62	3,31	8,40
E	12203-2	/	35,91	1,42	0,33	-	-	-	<LOD	1,50	2,31	23,87	4,21	7,25
E	12203-3	/	52,37	1,95	0,39	-	-	-	<LOD	2,02	3,40	38,54	3,78	8,24
E	12203-4	QC	5,46	0,37	0,39	-	-	-	<LOD	1,44	2,27	<LOD	2,93	7,24
E	12203-5	QM	14,19	0,60	0,38	-	-	-	<LOD	1,23	3,00	<LOD	2,73	7,35
E	12203-6	QC	22,22	1,28	0,46	-	-	-	<LOD	1,78	5,04	12,38	4,47	10,14
E	12203-7	/	17,59	0,95	0,48	-	-	-	<LOD	1,62	3,07	42,20	7,69	7,32
E	12203-8	/	-	-	-	-	-	-	-	-	-	-	-	-
E	12203-9	/	3,01	0,43	0,36	-	-	-	<LOD	1,57	3,83	<LOD	4,01	10,26
E	12203-10	/	6,35	0,51	0,46	-	-	-	<LOD	2,35	4,76	<LOD	6,06	11,44
E	12203-11	/	6,21	0,67	0,36	-	-	-	<LOD	1,72	3,57	<LOD	5,39	9,71
E	12203-12	/	36,71	2,36	0,51	0,24	0,25	-	<LOD	2,36	3,99	106,22	9,51	11,01
E	12203-13	/	40,33	1,12	0,40	-	-	-	<LOD	1,87	4,34	48,14	4,90	7,11
E	12203-14	QM	37,54	1,28	0,39	-	-	-	<LOD	1,81	3,30	64,06	6,40	9,57
E	12203-15	QM	69,99	2,75	0,30	0,14	0,16	-	3,43	1,48	2,82	45,50	4,70	8,45
E	12203-16	QM	39,56	1,69	0,29	-	-	-	3,38	1,69	2,72	41,89	4,01	6,02
E	12203-17	QC	12,46	0,76	0,41	-	-	-	<LOD	1,82	4,46	10,61	4,96	8,83
E	12203-18	QC	4,26	0,39	0,41	-	-	-	<LOD	1,37	2,77	8,20	3,23	7,93
E	12203-19	QC	8,29	0,53	0,42	-	-	-	<LOD	2,48	4,33	39,96	8,88	10,45
E	12203-20	/	10,01	0,90	0,43	-	-	-	<LOD	1,85	2,74	21,40	6,98	7,24
E	12203-21	/	61,47	2,02	0,47	-	-	-	<LOD	1,49	3,29	53,54	4,84	8,68
E	12203-22	/	14,90	0,96	0,52	-	-	-	<LOD	2,28	3,24	44,62	6,54	10,76
E	12203-23	/	22,22	1,37	0,59	-	-	-	<LOD	2,02	4,29	26,63	6,01	10,03
E	12203-24	/	2,53	0,31	0,33	-	-	-	<LOD	1,31	3,69	<LOD	3,62	9,56
E	12203-25	/	1,87	0,50	0,48	-	-	-	<LOD	2,87	3,98	19,05	5,26	9,56
E	12203-26	/	3,22	0,30	0,36	-	-	-	<LOD	1,20	2,16	9,91	6,45	7,39
E	12203-27	/	30,42	1,94	0,38	-	-	-	<LOD	1,56	2,78	7,57	5,04	7,39
E	12203-28	/	51,69	2,57	0,35	-	-	-	<LOD	1,66	2,78	11,45	3,79	6,84
E	12203-29	/	54,97	1,82	0,28	-	-	-	<LOD	1,37	2,28	13,05	3,29	6,93
E	12203-30	QC	1,54	0,26	0,32	-	-	-	<LOD	1,50	3,01	9,53	3,22	8,94
E	12203-31	QM	6,27	0,52	0,37	-	-	-	<LOD	1,89	3,33	<LOD	3,89	8,71
E	12203-32	QM	50,45	1,40	0,30	-	-	-	<LOD	1,12	2,04	9,90	2,51	7,45
E	110201-1	QC	12,10	0,56	0,37	-	-	-	<LOD	1,18	3,05	<LOD	3,03	9,75
E	110201-2	/	25,14	1,22	0,44	-	-	-	<LOD	1,86	3,38	20,77	4,52	12,60
E	110201-3	/	69,32	2,07	0,56	-	-	-	<LOD	2,14	4,05	24,94	5,47	10,83

Part 2

			Mg			Al			Cl			K		
Vein type	Spot ID	CL color/intensity and quartz texture	Concentration ppm	2SE (ppm)	LOD (ppm)	Concentration ppm	2SE (ppm)	LOD (ppm)	Concentration ppm	2SE (ppm)	LOD (ppm)	Concentration ppm	2SE (ppm)	LOD (ppm)
E	12203-1	QM	<LOD	0,09	0,22	663,48	10,48	0,50	155,32	14,61	21,27	7,00	1,60	3,94
E	12203-2	/	2,23	0,90	0,20	1 064,10	38,25	0,44	182,11	11,08	21,05	<LOD	1,24	4,14
E	12203-3	/	6,42	9,15	0,21	2 027,08	46,68	0,51	146,37	15,31	24,85	7,83	2,52	3,77
E	12203-4	QC	0,35	0,15	0,15	188,77	5,64	0,43	150,26	12,30	21,73	<LOD	1,24	2,79
E	12203-5	QM	<LOD	0,10	0,17	428,06	7,52	0,47	103,41	13,33	25,59	<LOD	1,23	2,85
E	12203-6	QC	0,11	0,13	0,25	736,67	19,43	0,49	165,48	20,70	35,17	<LOD	1,69	4,60
E	12203-7	/	6,04	1,21	0,19	596,90	13,66	0,44	184,75	14,76	30,47	<LOD	2,07	3,51
E	12203-8	/	-	-	-	-	-	-	-	-	-	-	-	-
E	12203-9	/	1,44	0,58	0,25	236,64	7,49	0,54	134,09	16,23	35,30	<LOD	1,76	3,20
E	12203-10	/	0,64	0,23	0,26	442,51	10,36	0,72	187,05	18,04	35,89	<LOD	2,38	4,82
E	12203-11	/	0,37	0,18	0,28	442,65	32,97	0,57	129,89	17,05	35,11	<LOD	1,82	4,10
E	12203-12	/	24,62	1,59	0,21	3 183,90	128,15	0,74	107,78	16,35	37,77	173,48	9,87	4,68
E	12203-13	/	1,98	0,41	0,19	342,62	4,99	0,56	134,52	16,20	32,84	41,04	2,14	4,91
E	12203-14	QM	7,55	2,14	0,27	306,16	6,96	0,57	131,91	16,06	38,77	33,86	2,33	4,14
E	12203-15	QM	1,65	0,39	0,15	472,73	10,11	0,51	158,69	13,21	20,91	30,29	2,68	3,26
E	12203-16	QM	1,07	0,26	0,21	307,21	6,73	0,57	150,58	13,00	23,89	35,36	2,47	2,53
E	12203-17	QC	0,76	0,23	0,26	761,14	18,02	0,61	172,52	16,82	28,37	9,39	2,40	3,65
E	12203-18	QC	2,77	0,39	0,18	316,47	13,04	0,51	177,77	13,05	26,20	4,51	1,62	3,42
E	12203-19	QC	7,64	1,39	0,31	465,54	11,97	0,57	180,68	21,83	29,69	<LOD	2,31	5,57
E	12203-20	/	2,45	0,62	0,19	500,18	24,95	0,46	173,03	13,08	26,42	<LOD	1,52	3,25
E	12203-21	/	1,09	0,27	0,18	2 947,18	37,93	0,51	168,20	12,09	30,42	<LOD	1,42	3,65
E	12203-22	/	3,19	0,38	0,25	1 569,95	30,15	0,60	141,47	16,70	31,53	67,77	2,94	3,21
E	12203-23	/	1,37	0,29	0,27	1 685,17	37,17	0,60	149,06	18,88	36,43	19,95	3,28	5,22
E	12203-24	/	<LOD	0,11	0,18	236,63	9,34	0,48	154,20	16,08	22,28	<LOD	1,71	3,35
E	12203-25	/	0,23	0,22	0,31	232,89	12,17	0,64	176,33	28,94	46,16	<LOD	1,77	5,36
E	12203-26	/	0,19	0,12	0,18	222,23	10,58	0,49	181,27	11,71	27,03	<LOD	1,36	2,85
E	12203-27	/	0,85	0,21	0,16	678,88	35,18	0,46	143,99	12,16	20,90	<LOD	1,78	3,26
E	12203-28	/	<LOD	0,09	0,17	1 182,55	23,15	0,45	141,25	14,65	29,96	<LOD	1,62	3,23
E	12203-29	/	<LOD	0,07	0,15	1 335,74	17,50	0,42	156,81	12,35	22,03	<LOD	1,35	2,77
E	12203-30	QC	0,30	0,10	0,21	172,25	4,31	0,49	167,63	14,62	28,41	<LOD	1,57	3,50
E	12203-31	QM	<LOD	0,12	0,16	415,75	9,94	0,56	171,61	14,98	28,52	<LOD	2,62	3,60
E	12203-32	QM	<LOD	0,05	0,14	1 211,18	12,96	0,37	154,25	10,60	22,66	<LOD	1,33	2,63
E	110201-1	QC	0,65	0,17	0,19	870,08	13,42	0,45	160,32	14,70	37,70	<LOD	1,71	4,68
E	110201-2	/	2,87	0,45	0,28	1 020,61	21,72	0,64	141,14	20,73	44,04	28,87	4,03	4,65
E	110201-3	/	0,44	0,22	0,24	2 087,36	39,59	0,67	191,43	31,03	49,71	<LOD	2,77	5,46

Part 3

			Ca			Ti			Mn			Fe		
Vein type	Spot ID	CL color/intensity and quartz texture	Concentration ppm	2SE (ppm)	LOD (ppm)	Concentration ppm	2SE (ppm)	LOD (ppm)	Concentration ppm	2SE (ppm)	LOD (ppm)	Concentration ppm	2SE (ppm)	LOD (ppm)
E	12203-1	QM	<LOD	17,27	41,65	0,74	0,28	-	<LOD	0,14	0,30	<LOD	1,78	4,46
E	12203-2	/	30,28	15,78	25,43	2,81	0,51	-	<LOD	0,12	0,28	<LOD	1,46	4,02
E	12203-3	/	60,24	23,03	39,54	7,44	1,30	-	<LOD	0,14	0,26	<LOD	2,23	4,90
E	12203-4	QC	<LOD	14,02	35,74	0,84	0,28	-	<LOD	0,11	0,28	<LOD	1,39	3,55
E	12203-5	QM	<LOD	15,78	34,74	1,27	0,54	-	<LOD	0,08	0,24	<LOD	1,41	3,64
E	12203-6	QC	<LOD	22,50	43,14	0,99	0,37	-	0,45	0,21	0,31	<LOD	2,38	4,38
E	12203-7	/	56,99	20,41	34,72	1,06	0,32	-	<LOD	0,14	0,30	<LOD	1,52	4,49
E	12203-8	/	-	-	-	0,73	0,45	0,62	-	-	-	-	-	-
E	12203-9	/	<LOD	20,32	40,67	0,81	0,34	-	<LOD	0,15	0,38	<LOD	1,65	5,44
E	12203-10	/	<LOD	22,74	49,14	0,24	0,26	-	<LOD	0,16	0,32	<LOD	3,03	5,68
E	12203-11	/	<LOD	16,72	37,52	0,97	0,39	-	<LOD	0,18	0,33	<LOD	2,03	4,33
E	12203-12	/	85,87	33,62	56,02	0,43	0,27	-	<LOD	0,24	0,40	<LOD	2,13	5,94
E	12203-13	/	<LOD	21,57	48,75	0,39	0,23	-	<LOD	0,14	0,41	<LOD	2,38	5,17
E	12203-14	QM	<LOD	20,29	45,59	1,06	0,41	0,73	<LOD	0,13	0,33	<LOD	1,80	5,30
E	12203-15	QM	<LOD	19,96	35,67	0,53	0,25	-	<LOD	0,14	0,29	<LOD	2,26	3,28
E	12203-16	QM	43,30	26,28	40,15	0,22	0,17	-	<LOD	0,13	0,27	<LOD	2,07	2,91
E	12203-17	QC	<LOD	23,61	42,01	0,87	0,34	-	<LOD	0,18	0,38	<LOD	2,15	3,93
E	12203-18	QC	<LOD	22,96	43,33	0,74	0,32	-	0,52	0,18	0,30	513,11	79,18	3,43
E	12203-19	QC	<LOD	19,16	38,11	2,02	0,58	-	<LOD	0,19	0,33	43,37	5,01	4,31
E	12203-20	/	<LOD	20,43	38,27	55,50	5,44	-	<LOD	0,15	0,28	12,21	2,81	3,49
E	12203-21	/	<LOD	14,68	42,09	8,70	1,26	-	<LOD	0,13	0,30	<LOD	2,08	4,04
E	12203-22	/	74,95	22,91	51,33	0,57	0,34	-	0,98	0,29	0,36	44,45	4,90	4,03
E	12203-23	/	<LOD	29,15	44,87	0,88	0,44	-	<LOD	0,25	0,36	<LOD	2,41	5,01
E	12203-24	/	37,41	18,95	33,25	0,80	0,35	-	<LOD	0,14	0,32	<LOD	1,47	3,65
E	12203-25	/	<LOD	34,80	48,36	1,34	0,47	-	<LOD	0,24	0,42	37,30	24,65	5,47
E	12203-26	/	38,05	26,92	34,89	1,03	0,35	-	<LOD	0,13	0,29	<LOD	1,34	3,59
E	12203-27	/	47,48	20,61	37,59	2,63	0,62	-	<LOD	0,12	0,33	<LOD	1,38	3,73
E	12203-28	/	<LOD	16,13	30,40	3,12	0,51	-	<LOD	0,11	0,30	<LOD	1,63	3,64
E	12203-29	/	32,57	13,08	29,70	2,29	0,47	-	<LOD	0,11	0,28	<LOD	1,40	3,44
E	12203-30	QC	<LOD	15,31	30,14	0,42	0,22	-	<LOD	0,12	0,25	<LOD	1,32	3,64
E	12203-31	QM	36,35	17,71	30,29	0,76	0,28	-	<LOD	0,18	0,31	<LOD	2,05	3,87
E	12203-32	QM	<LOD	10,81	30,88	3,37	0,52	-	0,24	0,10	0,22	<LOD	1,21	2,56
E	110201-1	QC	<LOD	14,44	40,63	1,45	0,39	-	<LOD	0,13	0,32	<LOD	1,73	4,83
E	110201-2	/	<LOD	19,45	38,48	1,46	0,35	-	0,44	0,16	0,37	<LOD	2,58	5,71
E	110201-3	/	<LOD	24,40	40,20	2,99	0,65	-	<LOD	0,23	0,38	<LOD	2,89	6,42

Part 4

			Co			Cu			Zn			Ga		
Vein type	Spot ID	CL color/intensity and quartz texture	Concentration ppm	2SE (ppm)	LOD (ppm)	Concentration ppm	2SE (ppm)	LOD (ppm)	Concentration ppm	2SE (ppm)	LOD (ppm)	Concentration ppm	2SE (ppm)	LOD (ppm)
E	12203-1	QM	0,01	0,01	-	<LOD	0,13	0,33	<LOD	0,32	0,66	0,05	0,03	-
E	12203-2	/	0,01	0,01	-	<LOD	0,11	0,28	<LOD	0,26	0,44	<LOD	0,00	-
E	12203-3	/	<LOD	0,00	-	<LOD	0,17	0,33	<LOD	0,36	0,65	<LOD	0,00	-
E	12203-4	QC	<LOD	0,00	0,04	<LOD	0,10	0,22	<LOD	0,20	0,49	<LOD	0,00	-
E	12203-5	QM	<LOD	0,00	-	<LOD	0,13	0,26	<LOD	0,23	0,47	<LOD	0,00	-
E	12203-6	QC	<LOD	0,00	-	<LOD	0,20	0,34	<LOD	0,43	0,81	<LOD	0,00	-
E	12203-7	/	<LOD	0,00	-	<LOD	0,13	0,30	<LOD	0,30	0,63	<LOD	0,00	-
E	12203-8	/	-	-	-	-	-	-	-	-	-	-	-	-
E	12203-9	/	0,04	0,03	-	<LOD	0,16	0,29	<LOD	0,26	0,67	<LOD	0,00	-
E	12203-10	/	<LOD	0,00	-	<LOD	0,22	0,37	<LOD	0,45	0,79	<LOD	0,00	-
E	12203-11	/	<LOD	0,00	-	<LOD	0,17	0,43	<LOD	0,32	0,65	<LOD	0,00	-
E	12203-12	/	<LOD	0,00	-	<LOD	0,23	0,47	<LOD	0,48	0,84	<LOD	0,00	-
E	12203-13	/	0,01	0,01	-	<LOD	0,15	0,32	<LOD	0,26	0,74	<LOD	0,00	-
E	12203-14	QM	0,00	0,01	-	<LOD	0,14	0,39	<LOD	0,30	0,64	<LOD	0,00	-
E	12203-15	QM	<LOD	0,00	-	<LOD	0,13	0,22	0,54	0,32	0,44	0,02	0,02	-
E	12203-16	QM	<LOD	0,00	-	<LOD	0,15	0,31	<LOD	0,32	0,53	0,08	0,04	-
E	12203-17	QC	<LOD	0,00	-	<LOD	0,14	0,41	0,73	0,35	-	<LOD	0,00	-
E	12203-18	QC	0,06	0,03	-	0,25	0,15	0,24	15,42	2,41	-	<LOD	0,00	-
E	12203-19	QC	<LOD	0,00	-	<LOD	0,19	0,37	1,05	0,43	0,66	<LOD	0,00	-
E	12203-20	/	0,00	0,01	-	<LOD	0,14	0,36	1,01	0,39	0,60	<LOD	0,00	-
E	12203-21	/	0,03	0,02	-	<LOD	0,13	0,30	0,72	0,30	-	<LOD	0,00	-
E	12203-22	/	<LOD	0,00	-	<LOD	0,22	0,36	4,62	1,16	0,44	<LOD	0,00	-
E	12203-23	/	0,05	0,04	-	<LOD	0,20	0,38	<LOD	0,39	0,95	<LOD	0,00	-
E	12203-24	/	0,03	0,02	-	<LOD	0,14	0,36	<LOD	0,27	0,66	<LOD	0,00	-
E	12203-25	/	0,05	0,04	-	<LOD	0,25	0,50	4,35	4,59	0,75	<LOD	0,00	-
E	12203-26	/	<LOD	0,01	0,05	<LOD	0,14	0,28	<LOD	0,25	0,58	<LOD	0,00	-
E	12203-27	/	<LOD	0,00	-	<LOD	0,14	0,28	<LOD	0,28	0,49	<LOD	0,00	-
E	12203-28	/	<LOD	0,00	-	<LOD	0,13	0,37	<LOD	0,08	-	<LOD	0,00	-
E	12203-29	/	<LOD	0,00	-	<LOD	0,12	0,22	<LOD	0,18	0,49	<LOD	0,00	-
E	12203-30	QC	<LOD	0,00	-	<LOD	0,11	0,23	0,60	0,26	-	<LOD	0,00	-
E	12203-31	QM	<LOD	0,00	-	<LOD	0,18	0,39	<LOD	0,00	0,69	<LOD	0,00	-
E	12203-32	QM	<LOD	0,00	-	<LOD	0,10	0,21	0,56	0,21	0,45	<LOD	0,00	-
E	110201-1	QC	<LOD	0,02	0,05	<LOD	0,12	0,31	<LOD	0,23	0,62	<LOD	0,00	-
E	110201-2	/	0,08	0,03	-	<LOD	0,19	0,46	0,88	0,38	-	<LOD	0,00	-
E	110201-3	/	0,08	0,04	-	<LOD	0,20	0,41	<LOD	0,47	0,85	<LOD	0,00	-

Part 5

			Ge			As			Rb			Sr		
Vein type	Spot ID	CL color/intensity and quartz texture	Concentration ppm	2SE (ppm)	LOD (ppm)	Concentration ppm	2SE (ppm)	LOD (ppm)	Concentration ppm	2SE (ppm)	LOD (ppm)	Concentration ppm	2SE (ppm)	LOD (ppm)
E	12203-1	QM	<LOD	0,37	0,99	<LOD	1,10	2,61	0,04	0,02	0,04	0,85	0,08	-
E	12203-2	/	0,60	0,42	0,67	<LOD	0,87	1,81	0,03	0,01	0,02	0,07	0,02	-
E	12203-3	/	1,08	0,47	0,80	2,18	1,27	2,15	0,07	0,03	0,04	0,07	0,03	-
E	12203-4	QC	0,32	0,25	0,65	<LOD	0,69	1,74	<LOD	0,00	0,03	<LOD	-	-
E	12203-5	QM	<LOD	0,34	0,73	<LOD	0,79	1,94	0,04	0,02	-	0,03	0,01	-
E	12203-6	QC	0,28	0,54	1,13	<LOD	1,16	2,40	0,06	0,03	-	0,34	0,07	-
E	12203-7	/	0,34	0,31	0,83	<LOD	1,01	2,49	0,04	0,02	0,04	0,12	0,03	-
E	12203-8	/	-	-	-	-	-	-	-	-	-	-	-	-
E	12203-9	/	<LOD	0,45	1,12	<LOD	0,98	1,87	<LOD	0,02	0,04	0,11	0,03	-
E	12203-10	/	<LOD	0,71	1,14	<LOD	1,58	3,20	0,07	0,03	0,05	0,32	0,08	-
E	12203-11	/	0,79	0,51	1,12	<LOD	1,20	2,41	0,06	0,03	-	0,20	0,04	-
E	12203-12	/	1,14	0,73	1,38	<LOD	1,34	3,00	1,10	0,14	0,05	7,45	0,47	-
E	12203-13	/	0,78	0,46	1,02	<LOD	1,04	2,62	0,27	0,05	0,04	0,37	0,05	-
E	12203-14	QM	<LOD	0,43	1,10	<LOD	1,04	2,80	0,20	0,05	0,05	0,26	0,05	-
E	12203-15	QM	1,00	0,34	0,82	<LOD	0,98	1,79	0,20	0,04	-	0,25	0,05	-
E	12203-16	QM	1,74	0,40	0,91	<LOD	1,37	1,77	0,22	0,05	-	0,31	0,08	-
E	12203-17	QC	0,84	0,40	0,97	<LOD	1,04	2,81	0,08	0,03	-	0,49	0,08	-
E	12203-18	QC	0,47	0,34	0,68	<LOD	0,99	2,04	0,07	0,02	-	0,15	0,03	-
E	12203-19	QC	1,69	0,61	0,94	<LOD	1,26	2,35	0,05	0,03	-	0,05	0,02	-
E	12203-20	/	1,17	0,35	0,95	<LOD	0,97	1,89	0,03	0,02	-	0,18	0,04	-
E	12203-21	/	1,61	0,43	0,79	1,81	1,00	1,67	0,03	0,02	-	0,11	0,03	-
E	12203-22	/	0,96	0,58	0,92	<LOD	1,54	1,92	0,41	0,09	-	3,55	0,24	-
E	12203-23	/	1,47	0,60	1,04	2,86	1,41	2,57	0,20	0,07	0,05	1,02	0,13	-
E	12203-24	/	0,54	0,30	0,96	<LOD	0,84	2,08	0,03	0,02	-	0,09	0,03	-
E	12203-25	/	<LOD	0,47	1,37	<LOD	1,64	2,74	0,05	0,03	-	0,04	0,03	-
E	12203-26	/	0,41	0,33	0,74	<LOD	0,97	1,90	0,05	0,02	-	0,08	0,03	-
E	12203-27	/	0,79	0,34	1,04	<LOD	0,88	1,99	0,04	0,02	-	0,07	0,02	-
E	12203-28	/	1,49	0,44	0,68	<LOD	1,02	2,28	0,03	0,02	-	<LOD	-	-
E	12203-29	/	0,56	0,38	0,73	<LOD	0,81	2,08	<LOD	0,01	0,03	0,00	0,01	-
E	12203-30	QC	<LOD	0,33	0,86	<LOD	0,78	1,99	<LOD	0,00	-	0,04	0,02	-
E	12203-31	QM	0,68	0,59	0,88	<LOD	1,33	2,01	0,07	0,03	-	0,13	0,04	-
E	12203-32	QM	0,61	0,30	0,79	<LOD	0,68	1,68	<LOD	0,00	0,04	0,00	0,00	-
E	110201-1	QC	0,50	0,31	1,02	<LOD	0,76	2,41	0,06	0,02	0,05	0,09	0,02	-
E	110201-2	/	0,57	0,49	1,25	2,66	1,17	2,40	0,15	0,04	-	0,29	0,05	-
E	110201-3	/	1,12	0,74	1,06	<LOD	1,98	3,16	<LOD	0,02	0,05	0,05	0,03	-

Part 6

			Zr			Nb			Mo			Ag		
Vein type	Spot ID	CL color/intensity and quartz texture	Concentration ppm	2SE (ppm)	LOD (ppm)	Concentration ppm	2SE (ppm)	LOD (ppm)	Concentration ppm	2SE (ppm)	LOD (ppm)	Concentration ppm	2SE (ppm)	LOD (ppm)
E	12203-1	QM	-	-	-	-	-	-	-	-	-	-	-	-
E	12203-2	/	-	-	-	-	-	-	-	-	-	-	-	-
E	12203-3	/	-	-	-	-	-	-	-	-	-	-	-	-
E	12203-4	QC	-	-	-	-	-	-	-	-	-	-	-	-
E	12203-5	QM	-	-	-	-	-	-	-	-	-	-	-	-
E	12203-6	QC	-	-	-	-	-	-	-	-	-	-	-	-
E	12203-7	/	-	-	-	-	-	-	-	-	-	-	-	-
E	12203-8	/	-	-	-	-	-	-	-	-	-	-	-	-
E	12203-9	/	-	-	-	-	-	-	-	-	-	-	-	-
E	12203-10	/	-	-	-	-	-	-	-	-	-	-	-	-
E	12203-11	/	-	-	-	-	-	-	-	-	-	-	-	-
E	12203-12	/	-	-	-	-	-	-	-	-	-	-	-	-
E	12203-13	/	-	-	-	-	-	-	-	-	-	-	-	-
E	12203-14	QM	-	-	-	-	-	-	-	-	-	-	-	-
E	12203-15	QM	0,00	0,01	-	-	-	-	-	-	-	-	-	-
E	12203-16	QM	-	-	-	-	-	-	-	-	-	-	-	-
E	12203-17	QC	-	-	-	-	-	-	-	-	-	-	-	-
E	12203-18	QC	-	-	-	-	-	-	0,01	0,02	-	-	-	-
E	12203-19	QC	-	-	-	-	-	-	-	-	-	-	-	-
E	12203-20	/	-	-	-	-	-	-	-	-	-	-	-	-
E	12203-21	/	-	-	-	-	-	-	-	-	-	-	-	-
E	12203-22	/	-	-	-	-	-	-	-	-	-	-	-	-
E	12203-23	/	-	-	-	-	-	-	-	-	-	-	-	-
E	12203-24	/	-	-	-	-	-	-	-	-	-	-	-	-
E	12203-25	/	-	-	-	-	-	-	-	-	-	-	-	-
E	12203-26	/	-	-	-	-	-	-	-	-	-	-	-	-
E	12203-27	/	-	-	-	-	-	-	-	-	-	-	-	-
E	12203-28	/	-	-	-	-	-	-	-	-	-	-	-	-
E	12203-29	/	-	-	-	-	-	-	-	-	-	-	-	-
E	12203-30	QC	-	-	-	-	-	-	-	-	-	-	-	-
E	12203-31	QM	-	-	-	-	-	-	-	-	-	0,01	0,02	-
E	12203-32	QM	-	-	-	-	-	-	-	-	-	-	-	-
E	110201-1	QC	-	-	-	-	-	-	-	-	-	-	-	-
E	110201-2	/	-	-	-	-	-	-	-	-	-	-	-	-
E	110201-3	/	-	-	-	-	-	-	-	-	-	-	-	-

Part 7

			In			Sn			Sb			Te		
Vein type	Spot ID	CL color/intensity and quartz texture	Concentration ppm	2SE (ppm)	LOD (ppm)	Concentration ppm	2SE (ppm)	LOD (ppm)	Concentration ppm	2SE (ppm)	LOD (ppm)	Concentration ppm	2SE (ppm)	LOD (ppm)
E	12203-1	QM	<LOD	0,01	0,02	1,99	0,56	0,96	0,62	0,13	0,10	-	-	-
E	12203-2	/	<LOD	0,01	0,02	2,41	0,41	0,88	1,70	0,19	0,08	-	-	-
E	12203-3	/	<LOD	0,02	0,02	1,68	0,48	0,94	1,92	0,24	0,09	-	-	-
E	12203-4	QC	<LOD	0,01	0,02	2,68	0,42	0,75	0,07	0,03	0,07	-	-	-
E	12203-5	QM	<LOD	0,01	0,02	1,18	0,35	0,81	0,40	0,08	-	-	-	-
E	12203-6	QC	<LOD	0,02	0,03	2,03	0,80	0,93	1,06	0,19	0,11	-	-	-
E	12203-7	/	<LOD	0,01	0,03	1,73	0,43	1,04	1,08	0,14	-	-	-	-
E	12203-8	/	-	-	-	-	-	-	-	-	-	-	-	-
E	12203-9	/	<LOD	0,01	0,03	1,93	0,48	1,08	0,11	0,05	-	-	-	-
E	12203-10	/	<LOD	0,02	0,03	2,70	0,69	1,57	0,13	0,07	-	-	-	-
E	12203-11	/	0,02	0,01	-	<LOD	0,55	1,39	0,09	0,05	-	-	-	-
E	12203-12	/	<LOD	0,02	0,04	<LOD	0,60	1,16	0,19	0,07	-	-	-	-
E	12203-13	/	<LOD	0,01	0,03	<LOD	0,57	1,31	6,74	0,44	0,09	-	-	-
E	12203-14	QM	<LOD	0,01	0,03	1,91	0,53	1,26	4,23	0,39	-	-	-	-
E	12203-15	QM	<LOD	0,01	0,03	2,30	0,52	0,80	4,43	0,51	-	-	-	-
E	12203-16	QM	<LOD	0,02	0,03	2,26	0,53	0,81	2,17	0,26	-	-	-	-
E	12203-17	QC	0,02	0,01	-	1,41	0,54	1,11	0,14	0,05	-	-	-	-
E	12203-18	QC	0,03	0,01	0,02	1,63	0,50	1,07	0,11	0,05	-	-	-	-
E	12203-19	QC	0,03	0,02	-	1,95	0,62	1,35	0,29	0,10	-	-	-	-
E	12203-20	/	<LOD	0,01	0,03	1,94	0,50	1,03	0,28	0,08	-	-	-	-
E	12203-21	/	<LOD	0,01	0,03	<LOD	0,48	1,02	0,91	0,12	-	-	-	-
E	12203-22	/	<LOD	0,02	0,03	<LOD	0,79	1,16	0,91	0,23	-	-	-	-
E	12203-23	/	<LOD	0,01	0,03	<LOD	0,63	1,49	1,13	0,23	-	-	-	-
E	12203-24	/	0,02	0,01	0,02	2,16	0,53	0,91	0,10	0,04	-	-	-	-
E	12203-25	/	<LOD	0,02	0,04	2,00	0,98	1,20	0,14	0,08	-	-	-	-
E	12203-26	/	0,02	0,01	0,02	1,68	0,47	0,79	0,09	0,04	-	-	-	-
E	12203-27	/	0,02	0,01	-	<LOD	0,46	0,97	0,34	0,09	-	-	-	-
E	12203-28	/	<LOD	0,01	0,02	1,59	0,39	0,86	0,15	0,07	-	-	-	-
E	12203-29	/	<LOD	0,01	0,03	1,17	0,38	0,99	0,27	0,07	0,07	-	-	-
E	12203-30	QC	<LOD	0,01	0,03	2,29	0,54	0,96	0,00	0,01	-	-	-	-
E	12203-31	QM	<LOD	0,02	0,03	1,41	0,56	1,00	0,16	0,10	-	-	-	-
E	12203-32	QM	0,02	0,01	0,02	1,24	0,38	0,87	0,36	0,07	-	-	-	-
E	110201-1	QC	<LOD	0,01	0,03	1,66	0,40	0,96	0,11	0,04	0,09	-	-	-
E	110201-2	/	<LOD	0,02	0,03	2,13	0,71	1,51	1,60	0,19	0,11	-	-	-
E	110201-3	/	<LOD	0,02	0,03	<LOD	0,60	1,40	1,04	0,18	-	-	-	-

Part 8

			Cs			Ba			Ta			W		
Vein type	Spot ID	CL color/intensity and quartz texture	Concentration ppm	2SE (ppm)	LOD (ppm)	Concentration ppm	2SE (ppm)	LOD (ppm)	Concentration ppm	2SE (ppm)	LOD (ppm)	Concentration ppm	2SE (ppm)	LOD (ppm)
E	12203-1	QM	0,00	0,00	-	2,72	0,40	-	-	-	-	-	-	-
E	12203-2	/	0,00	0,00	-	0,24	0,09	-	-	-	-	-	-	-
E	12203-3	/	<LOD	0,00	-	0,11	0,08	-	-	-	-	-	-	-
E	12203-4	QC	<LOD	0,00	-	-	-	-	-	-	-	-	-	-
E	12203-5	QM	<LOD	0,00	-	-	-	-	-	-	-	-	-	-
E	12203-6	QC	<LOD	0,00	-	0,94	0,26	-	-	-	-	-	-	-
E	12203-7	/	<LOD	0,00	-	0,28	0,11	-	-	-	-	-	-	-
E	12203-8	/	-	-	-	-	-	-	-	-	-	-	-	-
E	12203-9	/	0,00	0,01	-	0,29	0,13	-	-	-	-	-	-	-
E	12203-10	/	<LOD	0,00	-	0,88	0,29	-	-	-	-	-	-	-
E	12203-11	/	<LOD	0,00	-	0,66	0,19	-	-	-	-	-	-	-
E	12203-12	/	0,50	0,08	-	6,55	0,71	-	-	-	-	-	-	-
E	12203-13	/	0,19	0,04	-	0,05	0,06	-	-	-	-	-	-	-
E	12203-14	QM	0,15	0,03	-	0,18	0,10	-	-	-	-	-	-	-
E	12203-15	QM	0,18	0,04	-	0,13	0,09	-	-	-	-	-	-	-
E	12203-16	QM	0,12	0,03	-	-	-	-	-	-	-	-	-	-
E	12203-17	QC	0,02	0,01	-	1,27	0,35	-	-	-	-	-	-	-
E	12203-18	QC	0,01	0,01	-	0,30	0,12	-	-	-	-	-	-	-
E	12203-19	QC	<LOD	0,00	-	-	-	-	-	-	-	-	-	-
E	12203-20	/	<LOD	0,00	0,03	0,18	0,11	-	-	-	-	-	-	-
E	12203-21	/	0,01	0,01	-	0,31	0,13	-	-	-	-	-	-	-
E	12203-22	/	0,09	0,03	-	11,75	1,00	-	-	-	-	-	-	-
E	12203-23	/	0,03	0,02	-	5,01	0,92	-	-	-	-	-	-	-
E	12203-24	/	<LOD	0,01	0,02	0,14	0,08	-	-	-	-	-	-	-
E	12203-25	/	<LOD	0,00	-	0,04	0,07	-	-	-	-	-	-	-
E	12203-26	/	0,00	0,00	-	0,03	0,04	-	-	-	-	-	-	-
E	12203-27	/	0,02	0,01	-	-	-	-	-	-	-	-	-	-
E	12203-28	/	<LOD	0,00	-	-	-	-	-	-	-	-	-	-
E	12203-29	/	0,00	0,00	-	-	-	-	-	-	-	-	-	-
E	12203-30	QC	0,00	0,00	-	-	-	-	-	-	-	-	-	-
E	12203-31	QM	0,02	0,01	-	0,44	0,21	-	-	-	-	-	-	-
E	12203-32	QM	<LOD	0,00	-	-	-	-	-	-	-	-	-	-
E	110201-1	QC	0,01	0,01	-	0,31	0,10	-	-	-	-	-	-	-
E	110201-2	/	0,03	0,01	-	1,25	0,26	-	-	-	-	-	-	-
E	110201-3	/	0,00	0,01	-	0,42	0,19	-	-	-	-	-	-	-

Part 9

			Re			Au			Pb			Bi		
Vein type	Spot ID	CL color/intensity and quartz texture	Concentration ppm	2SE (ppm)	LOD (ppm)	Concentration ppm	2SE (ppm)	LOD (ppm)	Concentration ppm	2SE (ppm)	LOD (ppm)	Concentration ppm	2SE (ppm)	LOD (ppm)
E	12203-1	QM	-	-	-	<LOD	0,00	-	0,02	0,02	-	<LOD	0,02	0,05
E	12203-2	/	-	-	-	<LOD	0,00	-	0,06	0,03	-	<LOD	0,02	0,04
E	12203-3	/	-	-	-	<LOD	0,00	-	0,00	0,01	-	<LOD	0,03	0,05
E	12203-4	QC	-	-	-	<LOD	0,00	-	0,04	0,02	-	<LOD	0,02	0,04
E	12203-5	QM	-	-	-	<LOD	0,00	-	0,02	0,02	-	<LOD	0,02	0,04
E	12203-6	QC	-	-	-	<LOD	0,00	-	0,03	0,03	-	<LOD	0,03	0,06
E	12203-7	/	-	-	-	<LOD	0,00	-	0,12	0,05	-	<LOD	0,02	0,05
E	12203-8	/	-	-	-	-	-	-	-	-	-	-	-	-
E	12203-9	/	-	-	-	<LOD	0,00	-	0,04	0,03	-	<LOD	0,02	0,06
E	12203-10	/	-	-	-	<LOD	0,00	-	0,07	0,05	-	<LOD	0,04	0,06
E	12203-11	/	-	-	-	<LOD	0,00	-	0,05	0,03	-	<LOD	0,03	0,06
E	12203-12	/	-	-	-	<LOD	0,00	-	0,11	0,05	-	<LOD	0,04	0,06
E	12203-13	/	-	-	-	<LOD	0,00	-	<LOD	0,02	0,09	<LOD	0,01	0,07
E	12203-14	QM	-	-	-	<LOD	0,00	-	<LOD	0,02	0,08	<LOD	0,02	0,05
E	12203-15	QM	-	-	-	<LOD	0,00	-	0,10	0,06	-	0,05	0,02	-
E	12203-16	QM	-	-	-	<LOD	0,00	-	0,04	0,03	-	0,05	0,03	0,05
E	12203-17	QC	-	-	-	<LOD	0,00	-	0,10	0,04	0,08	<LOD	0,03	0,06
E	12203-18	QC	-	-	-	<LOD	0,00	-	1,21	0,32	0,05	0,05	0,02	0,04
E	12203-19	QC	-	-	-	0,05	0,05	-	0,14	0,07	0,09	0,08	0,04	-
E	12203-20	/	-	-	-	<LOD	0,00	-	0,19	0,08	-	<LOD	0,02	0,04
E	12203-21	/	-	-	-	<LOD	0,00	-	0,03	0,02	-	<LOD	0,02	0,05
E	12203-22	/	-	-	-	<LOD	0,00	-	0,69	0,18	-	0,04	0,03	-
E	12203-23	/	-	-	-	<LOD	0,00	-	<LOD	0,00	-	0,05	0,03	-
E	12203-24	/	-	-	-	<LOD	0,00	-	0,05	0,03	-	<LOD	0,02	0,05
E	12203-25	/	-	-	-	<LOD	0,00	-	0,20	0,13	-	<LOD	0,01	0,07
E	12203-26	/	-	-	-	<LOD	0,00	-	<LOD	0,00	-	<LOD	0,01	0,04
E	12203-27	/	-	-	-	<LOD	0,00	-	0,04	0,03	-	<LOD	0,02	0,05
E	12203-28	/	-	-	-	0,01	0,01	-	0,08	0,04	0,07	<LOD	0,02	0,05
E	12203-29	/	-	-	-	<LOD	0,00	-	0,04	0,02	-	0,04	0,02	-
E	12203-30	QC	-	-	-	<LOD	0,00	-	0,06	0,03	-	0,05	0,02	0,04
E	12203-31	QM	-	-	-	<LOD	0,00	-	0,04	0,04	-	<LOD	0,00	0,05
E	12203-32	QM	-	-	-	<LOD	0,00	-	<LOD	0,00	-	<LOD	0,02	0,04
E	110201-1	QC	-	-	-	<LOD	0,00	-	<LOD	0,00	0,08	0,07	0,02	-
E	110201-2	/	-	-	-	<LOD	0,00	-	<LOD	0,00	-	<LOD	0,02	0,07
E	110201-3	/	-	-	-	0,03	0,04	-	0,09	0,05	-	<LOD	0,03	0,08

Part 10

			U		
Vein type	Spot ID	CL color/intensity and quartz texture	Concentration ppm	2SE (ppm)	LOD (ppm)
E	12203-1	QM	-	-	-
E	12203-2	/	-	-	-
E	12203-3	/	-	-	-
E	12203-4	QC	-	-	-
E	12203-5	QM	-	-	-
E	12203-6	QC	-	-	-
E	12203-7	/	-	-	-
E	12203-8	/	-	-	-
E	12203-9	/	-	-	-
E	12203-10	/	-	-	-
E	12203-11	/	-	-	-
E	12203-12	/	-	-	-
E	12203-13	/	-	-	-
E	12203-14	QM	-	-	-
E	12203-15	QM	-	-	-
E	12203-16	QM	-	-	-
E	12203-17	QC	-	-	-
E	12203-18	QC	-	-	-
E	12203-19	QC	-	-	-
E	12203-20	/	-	-	-
E	12203-21	/	-	-	-
E	12203-22	/	-	-	-
E	12203-23	/	-	-	-
E	12203-24	/	-	-	-
E	12203-25	/	-	-	-
E	12203-26	/	-	-	-
E	12203-27	/	-	-	-
E	12203-28	/	-	-	-
E	12203-29	/	-	-	-
E	12203-30	QC	-	-	-
E	12203-31	QM	-	-	-
E	12203-32	QM	-	-	-
E	110201-1	QC	-	-	-
E	110201-2	/	-	-	-
E	110201-3	/	-	-	-

Part 11, second part of samples.

			Li			Be			B			Na		
Vein type	Spot ID	CL color/intensity and quartz texture	Concentration ppm	2SE (ppm)	LOD (ppm)	Concentration ppm	2SE (ppm)	LOD (ppm)	Concentration ppm	2SE (ppm)	LOD (ppm)	Concentration ppm	2SE (ppm)	LOD (ppm)
E	110201-4	/	48,08	2,43	0,53	-	-	-	<LOD	2,77	3,99	20,68	5,12	10,95
E	110201-5	/	26,83	1,10	0,30	-	-	-	<LOD	1,35	3,18	25,91	4,29	8,08
E	110201-6	/	44,88	1,53	0,39	-	-	-	<LOD	1,10	2,72	23,58	2,98	8,91
E	110201-7	/	56,70	1,85	0,44	0,25	0,20	-	<LOD	1,53	3,14	25,31	4,37	8,15
E	110201-8	/	40,14	2,33	0,47	-	-	-	<LOD	1,27	3,09	11,60	5,72	8,89
E	110201-9	/	85,91	2,90	0,31	-	-	-	3,03	1,10	2,63	36,73	3,28	5,88
E	110201-10	/	98,57	2,79	0,57	-	-	-	<LOD	1,50	2,50	60,05	5,03	10,40
E	110201-11	/	97,49	2,61	0,34	-	-	-	<LOD	0,95	2,90	75,87	2,85	7,05
E	110201-12	/	31,82	1,65	0,31	-	-	-	<LOD	1,14	2,73	20,15	2,81	6,83
E	110201-13	/	24,81	2,48	0,54	-	-	-	<LOD	2,73	6,03	14,42	8,50	11,92
E	110201-14	/	36,79	1,69	0,34	-	-	-	<LOD	1,61	2,56	<LOD	3,96	10,38
E	110201-15	/	46,08	1,68	0,40	-	-	-	<LOD	1,56	2,55	38,96	3,92	9,68
E	110201-16	QM	55,67	1,36	0,33	-	-	-	<LOD	1,12	2,10	29,83	3,04	7,11
E	110201-17	QM	20,67	0,66	0,29	-	-	-	<LOD	1,05	1,99	7,55	2,93	7,46
E	110201-18	/	13,88	1,27	0,52	-	-	-	<LOD	2,87	4,06	20,50	6,57	13,87
E	110201-19	QC	-	-	-	-	-	-	-	-	-	-	-	-
E	110201-20	/	21,13	1,01	0,43	-	-	-	<LOD	1,82	3,53	24,70	3,94	8,18
E	110201-21	QM	11,25	0,94	0,59	-	-	-	4,02	3,03	3,80	<LOD	6,27	11,11
E	110201-22	/	8,52	0,54	0,45	-	-	-	<LOD	2,06	3,14	11,31	3,04	9,32
E	110201-23	/	12,46	0,85	0,49	-	-	-	<LOD	1,88	4,63	32,13	5,51	9,29
E	110201-24	/	23,11	1,02	0,37	-	-	-	<LOD	1,15	2,74	18,14	2,99	7,44
E	110201-25	/	7,29	0,57	0,49	-	-	-	<LOD	1,39	3,38	16,75	3,34	7,96
E	110201-26	QM	10,60	0,63	0,39	-	-	-	<LOD	1,55	3,66	19,50	3,66	7,11
E	110201-27	/	7,94	0,55	0,28	-	-	-	<LOD	1,25	2,20	16,41	3,48	6,91
E	110201-28	/	6,69	0,82	0,43	-	-	-	<LOD	2,17	2,65	24,14	3,51	11,93
E	110201-29	QC	7,07	0,50	0,43	-	-	-	<LOD	1,61	3,03	12,36	4,77	8,95
E	110201-30	QM	9,98	0,60	0,32	-	-	-	<LOD	0,92	3,07	11,90	2,85	8,37
E	110201-31	QM	25,96	1,63	0,53	-	-	-	<LOD	2,10	4,32	28,52	7,07	12,83
E	110201-32	QC	11,47	0,54	0,40	-	-	-	<LOD	1,06	2,60	15,83	3,12	7,79

Part 12

			Mg			Al			Cl			K		
Vein type	Spot ID	CL color/intensity and quartz texture	Concentration ppm	2SE (ppm)	LOD (ppm)	Concentration ppm	2SE (ppm)	LOD (ppm)	Concentration ppm	2SE (ppm)	LOD (ppm)	Concentration ppm	2SE (ppm)	LOD (ppm)
E	110201-4	/	0,35	0,18	0,27	1 492,53	27,29	0,70	134,04	20,51	35,30	<LOD	2,52	4,99
E	110201-5	/	<LOD	0,09	0,18	859,40	21,84	0,40	153,25	15,81	29,17	7,28	2,01	3,81
E	110201-6	/	<LOD	0,07	0,17	1 770,54	40,23	0,41	175,26	11,55	23,95	<LOD	1,33	3,30
E	110201-7	/	<LOD	0,09	0,24	1 825,70	26,22	0,53	160,95	19,01	33,65	<LOD	1,89	4,33
E	110201-8	/	<LOD	0,12	0,21	1 065,35	22,31	0,54	153,75	24,01	37,95	<LOD	2,36	4,18
E	110201-9	/	<LOD	0,06	0,16	2 440,61	25,91	0,41	174,35	12,87	29,17	<LOD	1,24	3,63
E	110201-10	/	0,54	0,16	0,21	3 100,92	38,80	0,63	143,05	16,90	35,72	5,22	2,19	4,57
E	110201-11	/	<LOD	0,06	0,13	3 458,72	28,67	0,46	148,95	12,19	24,29	<LOD	1,21	3,59
E	110201-12	/	0,30	0,09	0,16	856,54	43,13	0,40	143,27	11,84	25,02	6,96	1,80	3,44
E	110201-13	/	<LOD	0,20	0,32	620,62	28,62	0,87	176,19	31,86	46,09	<LOD	4,12	6,15
E	110201-14	/	<LOD	0,09	0,14	1 266,14	19,62	0,55	156,13	13,62	33,19	<LOD	1,48	4,65
E	110201-15	/	<LOD	0,11	0,18	2 266,12	44,23	0,48	175,48	17,73	33,86	<LOD	2,19	4,70
E	110201-16	QM	<LOD	0,08	0,16	1 779,90	17,53	0,36	150,93	13,45	27,67	<LOD	1,15	3,30
E	110201-17	QM	1,05	1,72	0,13	1 125,71	13,42	0,32	140,68	11,87	22,57	<LOD	1,20	3,21
E	110201-18	/	0,36	0,27	0,26	1 031,36	39,66	0,75	161,26	26,92	47,60	<LOD	3,63	5,39
E	110201-19	QC	-	-	-	-	-	-	-	-	-	-	-	-
E	110201-20	/	0,94	0,22	0,19	1 473,49	21,72	0,56	159,79	17,13	43,26	7,04	3,93	4,19
E	110201-21	QM	<LOD	0,12	0,28	687,76	14,79	0,72	208,13	32,34	53,37	<LOD	2,80	6,59
E	110201-22	/	0,95	0,38	0,20	692,68	9,03	0,64	189,30	21,71	33,67	5,92	2,90	4,72
E	110201-23	/	0,25	0,16	0,24	1 096,80	24,01	0,61	215,65	22,71	34,13	9,61	2,30	4,32
E	110201-24	/	42,95	7,58	0,20	1 253,10	20,08	0,40	177,64	13,57	28,08	5,96	1,62	3,94
E	110201-25	/	<LOD	0,10	0,21	624,88	30,25	0,51	168,93	16,23	27,97	<LOD	1,96	3,12
E	110201-26	QM	0,22	0,13	0,20	733,35	20,31	0,55	145,88	17,18	34,52	<LOD	1,88	3,68
E	110201-27	/	0,16	0,09	0,14	610,52	12,89	0,54	190,39	12,08	26,89	4,20	1,42	3,32
E	110201-28	/	4,02	0,64	0,24	647,71	34,12	0,53	139,52	23,78	41,23	34,21	4,66	3,76
E	110201-29	QC	0,24	0,12	0,19	602,58	14,27	0,57	180,23	19,74	33,05	<LOD	1,91	4,30
E	110201-30	QM	<LOD	0,07	0,17	672,99	29,17	0,48	174,14	11,02	36,53	<LOD	1,23	3,22
E	110201-31	QM	1,00	0,35	0,23	1 748,06	45,25	0,83	161,99	16,73	39,32	<LOD	3,43	5,03
E	110201-32	QC	1,94	3,52	0,16	818,18	27,15	0,44	183,06	16,10	22,85	<LOD	1,45	3,94

Part 13

			Ca			Ti			Mn			Fe		
Vein type	Spot ID	CL color/intensity and quartz texture	Concentration ppm	2SE (ppm)	LOD (ppm)	Concentration ppm	2SE (ppm)	LOD (ppm)	Concentration ppm	2SE (ppm)	LOD (ppm)	Concentration ppm	2SE (ppm)	LOD (ppm)
E	110201-4	/	<LOD	28,39	64,43	2,86	0,59	-	<LOD	0,23	0,48	<LOD	2,85	6,28
E	110201-5	/	<LOD	20,58	34,14	0,70	0,29	-	0,48	0,16	0,35	<LOD	2,04	3,72
E	110201-6	/	<LOD	14,43	34,41	2,36	0,53	-	<LOD	0,12	0,26	<LOD	1,56	3,02
E	110201-7	/	<LOD	32,58	47,84	2,42	0,58	-	<LOD	0,16	0,35	<LOD	2,62	6,20
E	110201-8	/	<LOD	23,41	40,31	1,70	0,45	-	<LOD	0,20	0,43	<LOD	2,16	4,53
E	110201-9	/	<LOD	13,05	31,69	6,16	0,88	-	<LOD	0,12	0,27	<LOD	1,56	3,52
E	110201-10	/	<LOD	18,05	44,09	8,70	1,31	-	<LOD	0,18	0,37	<LOD	1,96	4,37
E	110201-11	/	<LOD	11,06	25,15	7,46	1,05	-	<LOD	0,10	0,28	<LOD	1,41	2,85
E	110201-12	/	<LOD	13,82	31,05	1,85	0,58	-	<LOD	0,10	0,25	<LOD	1,60	3,52
E	110201-13	/	<LOD	33,17	56,87	2,11	0,53	-	<LOD	0,24	0,46	<LOD	4,63	6,81
E	110201-14	/	<LOD	18,01	34,83	2,64	0,56	-	<LOD	0,12	0,29	<LOD	2,13	5,07
E	110201-15	/	<LOD	16,50	36,05	2,97	0,57	0,56	<LOD	0,18	0,36	<LOD	2,02	5,09
E	110201-16	QM	<LOD	11,80	34,41	1,35	0,40	-	<LOD	0,11	0,26	<LOD	1,33	3,82
E	110201-17	QM	<LOD	14,51	28,49	2,85	0,53	-	<LOD	0,10	0,30	<LOD	1,45	2,74
E	110201-18	/	<LOD	44,31	71,96	1,59	0,49	-	<LOD	0,28	0,46	<LOD	4,33	7,38
E	110201-19	QC	-	-	-	3,87	1,04	-	-	-	-	-	-	-
E	110201-20	/	<LOD	21,63	41,15	3,31	1,29	-	<LOD	0,17	0,45	<LOD	2,79	5,25
E	110201-21	QM	<LOD	30,36	64,32	1,11	0,37	-	<LOD	0,23	0,41	<LOD	2,92	6,94
E	110201-22	/	<LOD	25,36	39,68	1,58	0,48	-	<LOD	0,21	0,39	<LOD	2,47	4,77
E	110201-23	/	<LOD	26,73	45,24	1,72	0,55	-	<LOD	0,19	0,43	<LOD	2,94	4,58
E	110201-24	/	<LOD	14,39	34,44	2,65	0,55	-	0,96	0,19	0,29	9,99	2,46	5,25
E	110201-25	/	<LOD	17,77	42,44	0,67	0,31	0,54	<LOD	0,13	0,45	<LOD	1,98	4,17
E	110201-26	QM	<LOD	19,39	38,80	0,89	0,32	-	<LOD	0,18	0,47	201,74	30,27	5,28
E	110201-27	/	<LOD	16,50	36,94	0,60	0,31	-	<LOD	0,15	0,31	<LOD	2,55	4,00
E	110201-28	/	59,72	30,49	42,42	0,99	0,44	-	1,83	0,30	0,39	1 445,76	208,39	4,00
E	110201-29	QC	<LOD	20,30	43,11	0,95	0,34	-	<LOD	0,14	0,38	<LOD	3,31	4,72
E	110201-30	QM	<LOD	10,97	34,17	1,15	0,32	-	<LOD	0,10	0,31	<LOD	1,51	4,26
E	110201-31	QM	<LOD	30,06	51,65	2,27	0,87	-	<LOD	0,24	0,48	<LOD	3,26	5,74
E	110201-32	QC	<LOD	15,21	33,90	1,16	0,36	-	<LOD	0,13	0,28	<LOD	1,30	3,19

Part 14

			Co			Cu			Zn			Ga		
Vein type	Spot ID	CL color/intensity and quartz texture	Concentration ppm	2SE (ppm)	LOD (ppm)	Concentration ppm	2SE (ppm)	LOD (ppm)	Concentration ppm	2SE (ppm)	LOD (ppm)	Concentration ppm	2SE (ppm)	LOD (ppm)
E	110201-4	/	0,07	0,04	0,08	<LOD	0,21	0,35	0,98	0,45	0,83	<LOD	0,00	-
E	110201-5	/	0,05	0,03	-	<LOD	0,19	0,35	0,40	0,23	-	<LOD	0,00	-
E	110201-6	/	0,06	0,02	-	<LOD	0,13	0,34	<LOD	0,17	0,60	0,01	0,01	-
E	110201-7	/	0,09	0,04	-	<LOD	0,15	0,46	<LOD	0,28	0,67	<LOD	0,00	-
E	110201-8	/	0,04	0,03	-	<LOD	0,17	0,36	<LOD	0,38	0,65	0,01	0,03	-
E	110201-9	/	0,04	0,02	-	<LOD	0,13	0,29	<LOD	0,19	0,50	<LOD	0,00	-
E	110201-10	/	<LOD	0,02	0,08	<LOD	0,17	0,41	<LOD	0,30	0,71	<LOD	0,00	-
E	110201-11	/	0,06	0,02	-	0,27	0,12	0,23	<LOD	0,16	0,47	0,03	0,02	-
E	110201-12	/	0,00	0,00	-	<LOD	0,12	0,28	<LOD	0,21	0,48	<LOD	0,00	-
E	110201-13	/	0,11	0,06	-	<LOD	0,32	0,55	<LOD	0,03	1,09	<LOD	0,00	-
E	110201-14	/	<LOD	0,02	0,05	<LOD	0,14	0,36	<LOD	0,28	0,68	<LOD	0,00	-
E	110201-15	/	0,02	0,02	-	<LOD	0,20	0,36	<LOD	0,34	0,58	0,01	0,02	-
E	110201-16	QM	<LOD	0,00	-	<LOD	0,10	0,31	<LOD	0,17	0,50	0,01	0,01	-
E	110201-17	QM	0,03	0,01	-	<LOD	0,11	0,23	<LOD	0,18	0,49	<LOD	0,00	-
E	110201-18	/	<LOD	0,00	-	<LOD	0,29	0,58	<LOD	0,58	1,01	<LOD	0,00	-
E	110201-19	QC	-	-	-	-	-	-	-	-	-	-	-	-
E	110201-20	/	0,04	0,03	-	<LOD	0,24	0,41	<LOD	0,30	0,62	0,01	0,02	-
E	110201-21	QM	0,01	0,02	-	0,46	0,31	0,36	<LOD	0,01	0,73	<LOD	0,00	-
E	110201-22	/	<LOD	0,00	-	<LOD	0,19	0,38	0,49	0,32	-	<LOD	0,00	0,07
E	110201-23	/	0,02	0,02	-	<LOD	0,19	0,33	0,36	0,27	-	<LOD	0,00	-
E	110201-24	/	0,05	0,02	-	<LOD	0,12	0,32	<LOD	0,13	0,55	0,01	0,01	-
E	110201-25	/	0,05	0,02	-	<LOD	0,13	0,36	<LOD	0,23	0,64	<LOD	0,00	-
E	110201-26	QM	0,08	0,03	-	<LOD	0,13	0,40	13,79	2,54	0,73	0,02	0,02	-
E	110201-27	/	0,04	0,02	-	<LOD	0,13	0,31	<LOD	0,16	0,60	<LOD	0,00	-
E	110201-28	/	0,35	0,12	-	<LOD	0,18	0,31	110,57	19,52	-	0,01	0,03	-
E	110201-29	QC	0,04	0,03	-	<LOD	0,17	0,35	1,39	0,52	0,55	<LOD	0,00	-
E	110201-30	QM	0,07	0,02	0,05	<LOD	0,09	0,33	<LOD	0,17	0,64	<LOD	0,00	-
E	110201-31	QM	<LOD	0,05	0,16	<LOD	0,22	0,39	<LOD	0,30	0,76	<LOD	0,00	-
E	110201-32	QC	0,12	0,04	0,06	<LOD	0,13	0,30	<LOD	0,26	0,59	<LOD	0,00	-

Part 15

			Ge			As			Rb			Sr		
Vein type	Spot ID	CL color/intensity and quartz texture	Concentration ppm	2SE (ppm)	LOD (ppm)	Concentration ppm	2SE (ppm)	LOD (ppm)	Concentration ppm	2SE (ppm)	LOD (ppm)	Concentration ppm	2SE (ppm)	LOD (ppm)
E	110201-4	/	1,24	0,60	1,32	<LOD	1,14	2,96	0,05	0,03	-	0,04	0,02	-
E	110201-5	/	<LOD	0,43	0,88	<LOD	0,88	2,13	0,08	0,02	-	0,54	0,07	-
E	110201-6	/	0,67	0,31	0,86	<LOD	0,76	2,10	<LOD	0,01	0,04	0,04	0,01	-
E	110201-7	/	0,63	0,45	1,10	<LOD	1,01	2,62	<LOD	0,02	0,04	0,32	0,47	-
E	110201-8	/	0,63	0,49	1,13	<LOD	1,48	2,56	<LOD	0,00	-	<LOD	-	-
E	110201-9	/	0,95	0,35	0,69	<LOD	0,73	1,90	0,02	0,01	-	0,01	0,01	-
E	110201-10	/	0,63	0,48	0,86	2,60	1,09	2,36	0,03	0,02	-	0,03	0,02	-
E	110201-11	/	1,55	0,34	0,71	1,90	0,75	1,66	0,00	0,00	-	0,05	0,01	-
E	110201-12	/	0,64	0,28	0,94	<LOD	0,80	1,69	0,07	0,02	0,04	0,32	0,05	-
E	110201-13	/	1,07	0,83	1,39	<LOD	2,39	3,84	<LOD	0,02	0,06	<LOD	-	-
E	110201-14	/	1,67	0,47	0,97	<LOD	1,04	2,29	<LOD	0,01	0,04	<LOD	-	-
E	110201-15	/	1,33	0,54	0,95	<LOD	1,13	2,33	<LOD	0,02	0,04	0,25	0,05	-
E	110201-16	QM	0,55	0,33	0,73	2,16	0,96	1,95	0,04	0,02	-	0,34	0,05	-
E	110201-17	QM	0,65	0,27	0,65	<LOD	0,84	1,63	0,04	0,01	-	0,00	0,00	-
E	110201-18	/	<LOD	0,98	1,48	<LOD	1,54	3,77	0,10	0,05	-	0,27	0,08	-
E	110201-19	QC	-	-	-	-	-	-	-	-	-	-	-	-
E	110201-20	/	1,02	0,49	1,20	<LOD	1,21	3,03	0,05	0,03	-	0,08	0,03	-
E	110201-21	QM	0,94	0,73	1,32	<LOD	1,76	3,23	<LOD	0,03	0,06	0,05	0,03	-
E	110201-22	/	0,54	0,51	0,95	<LOD	1,32	2,41	0,05	0,03	-	0,11	0,03	-
E	110201-23	/	1,05	0,69	1,14	<LOD	1,16	2,68	0,11	0,05	0,05	0,53	0,09	-
E	110201-24	/	1,26	0,38	0,72	<LOD	0,85	2,05	<LOD	0,02	0,04	0,02	0,01	-
E	110201-25	/	0,58	0,39	0,99	<LOD	0,93	2,44	0,06	0,02	-	0,32	0,06	-
E	110201-26	QM	0,78	0,46	0,71	<LOD	1,04	2,81	<LOD	0,02	0,05	0,14	0,04	-
E	110201-27	/	<LOD	0,34	0,95	<LOD	0,96	1,94	0,03	0,02	-	0,18	0,04	-
E	110201-28	/	0,54	0,51	0,90	<LOD	1,16	2,19	0,11	0,06	-	0,48	0,08	-
E	110201-29	QC	<LOD	0,40	0,99	<LOD	1,04	2,62	0,04	0,02	-	0,13	0,04	-
E	110201-30	QM	0,52	0,31	0,93	<LOD	0,64	2,38	<LOD	0,01	0,04	0,04	0,01	-
E	110201-31	QM	<LOD	0,72	1,04	<LOD	1,46	2,53	<LOD	0,01	0,06	0,13	0,05	-
E	110201-32	QC	<LOD	0,38	0,91	<LOD	0,86	1,85	0,01	0,01	-	0,04	0,02	-

Part 16

			Zr			Nb			Mo			Ag		
Vein type	Spot ID	CL color/intensity and quartz texture	Concentration ppm	2SE (ppm)	LOD (ppm)	Concentration ppm	2SE (ppm)	LOD (ppm)	Concentration ppm	2SE (ppm)	LOD (ppm)	Concentration ppm	2SE (ppm)	LOD (ppm)
E	110201-4	/	-	-	-	-	-	-	-	-	-	-	-	-
E	110201-5	/	-	-	-	-	-	-	-	-	-	-	-	-
E	110201-6	/	-	-	-	-	-	-	-	-	-	-	-	-
E	110201-7	/	-	-	-	-	-	-	-	-	-	-	-	-
E	110201-8	/	-	-	-	-	-	-	-	-	-	-	-	-
E	110201-9	/	-	-	-	-	-	-	-	-	-	-	-	-
E	110201-10	/	-	-	-	-	-	-	-	-	-	-	-	-
E	110201-11	/	-	-	-	-	-	-	-	-	-	-	-	-
E	110201-12	/	-	-	-	-	-	-	-	-	-	-	-	-
E	110201-13	/	-	-	-	-	-	-	-	-	-	-	-	-
E	110201-14	/	-	-	-	-	-	-	-	-	-	-	-	-
E	110201-15	/	-	-	-	-	-	-	-	-	-	-	-	-
E	110201-16	QM	-	-	-	-	-	-	-	-	-	-	-	-
E	110201-17	QM	-	-	-	-	-	-	-	-	-	-	-	-
E	110201-18	/	-	-	-	-	-	-	-	-	-	-	-	-
E	110201-19	QC	-	-	-	-	-	-	-	-	-	-	-	-
E	110201-20	/	-	-	-	-	-	-	-	-	-	-	-	-
E	110201-21	QM	-	-	-	-	-	-	-	-	-	-	-	-
E	110201-22	/	-	-	-	-	-	-	-	-	-	-	-	-
E	110201-23	/	-	-	-	-	-	-	-	-	-	-	-	-
E	110201-24	/	7,84	1,92	-	-	-	-	-	-	-	-	-	-
E	110201-25	/	-	-	-	-	-	-	-	-	-	-	-	-
E	110201-26	QM	-	-	-	-	-	-	-	-	-	-	-	-
E	110201-27	/	-	-	-	-	-	-	-	-	-	-	-	-
E	110201-28	/	-	-	-	-	-	-	0,15	0,12	-	-	-	-
E	110201-29	QC	-	-	-	-	-	-	-	-	-	-	-	-
E	110201-30	QM	-	-	-	-	-	-	-	-	-	-	-	-
E	110201-31	QM	-	-	-	-	-	-	-	-	-	-	-	-
E	110201-32	QC	-	-	-	-	-	-	-	-	-	-	-	-

Part 17

			In			Sn			Sb			Te		
Vein type	Spot ID	CL color/intensity and quartz texture	Concentration ppm	2SE (ppm)	LOD (ppm)	Concentration ppm	2SE (ppm)	LOD (ppm)	Concentration ppm	2SE (ppm)	LOD (ppm)	Concentration ppm	2SE (ppm)	LOD (ppm)
E	110201-4	/	<LOD	0,02	0,04	<LOD	0,66	1,13	0,36	0,11	0,10	-	-	-
E	110201-5	/	<LOD	0,01	0,03	1,21	0,44	0,95	1,42	0,17	0,10	-	-	-
E	110201-6	/	<LOD	0,01	0,03	1,75	0,37	0,70	1,61	0,16	0,08	-	-	-
E	110201-7	/	<LOD	0,01	0,03	1,77	0,62	0,91	1,84	0,17	0,09	-	-	-
E	110201-8	/	<LOD	0,02	0,03	1,16	0,77	1,03	0,46	0,13	-	-	-	-
E	110201-9	/	<LOD	0,01	0,02	1,04	0,32	0,88	2,34	0,18	0,08	-	-	-
E	110201-10	/	<LOD	0,01	0,02	1,41	0,54	1,21	3,07	0,28	0,08	-	-	-
E	110201-11	/	0,02	0,01	0,02	<LOD	0,34	0,91	4,08	0,23	-	-	-	-
E	110201-12	/	0,02	0,01	-	2,20	0,37	0,84	0,43	0,09	0,08	-	-	-
E	110201-13	/	<LOD	0,02	0,04	1,72	0,94	1,40	0,37	0,18	-	-	-	-
E	110201-14	/	<LOD	0,01	0,03	<LOD	0,43	0,93	0,14	0,05	-	-	-	-
E	110201-15	/	<LOD	0,02	0,03	<LOD	0,63	1,10	3,28	0,30	-	-	-	-
E	110201-16	QM	<LOD	0,01	0,03	1,30	0,35	0,92	1,75	0,15	-	-	-	-
E	110201-17	QM	<LOD	0,01	0,02	1,31	0,33	0,65	0,12	0,04	-	-	-	-
E	110201-18	/	<LOD	0,02	0,04	<LOD	0,69	1,57	2,45	0,36	-	-	-	-
E	110201-19	QC	-	-	-	-	-	-	-	-	-	-	-	-
E	110201-20	/	<LOD	0,01	0,03	1,35	0,56	1,22	1,79	0,20	0,09	-	-	-
E	110201-21	QM	<LOD	0,02	0,04	<LOD	0,90	1,45	0,18	0,09	-	-	-	-
E	110201-22	/	<LOD	0,02	0,03	1,40	0,50	1,01	0,75	0,13	-	-	-	-
E	110201-23	/	0,01	0,01	-	<LOD	0,55	1,08	1,22	0,20	-	-	-	-
E	110201-24	/	<LOD	0,01	0,03	1,49	0,41	0,88	0,49	0,08	-	-	-	-
E	110201-25	/	<LOD	0,01	0,03	1,66	0,43	1,03	0,76	0,16	-	-	-	-
E	110201-26	QM	<LOD	0,01	0,03	1,62	0,48	0,95	0,83	0,16	0,11	-	-	-
E	110201-27	/	<LOD	0,01	0,03	1,81	0,37	0,98	0,80	0,12	-	-	-	-
E	110201-28	/	<LOD	0,02	0,03	1,67	0,64	1,07	0,54	0,19	0,10	-	-	-
E	110201-29	QC	<LOD	0,02	0,02	<LOD	0,48	1,19	1,63	0,19	0,09	-	-	-
E	110201-30	QM	<LOD	0,01	0,02	1,52	0,36	0,84	0,52	0,08	-	-	-	-
E	110201-31	QM	<LOD	0,02	0,04	<LOD	0,52	1,18	0,65	0,15	-	-	-	-
E	110201-32	QC	<LOD	0,01	0,03	1,99	0,44	1,13	0,47	0,10	-	-	-	-

Part 18

			Cs			Ba			Ta			W		
Vein type	Spot ID	CL color/intensity and quartz texture	Concentration ppm	2SE (ppm)	LOD (ppm)	Concentration ppm	2SE (ppm)	LOD (ppm)	Concentration ppm	2SE (ppm)	LOD (ppm)	Concentration ppm	2SE (ppm)	LOD (ppm)
E	110201-4	/	<LOD	0,00	-	0,02	0,05	-	-	-	-	-	-	-
E	110201-5	/	0,03	0,01	-	1,50	0,33	-	-	-	-	-	-	-
E	110201-6	/	<LOD	0,00	-	0,04	0,04	-	-	-	-	-	-	-
E	110201-7	/	<LOD	0,00	-	-	-	-	0,01	0,01	-	-	-	-
E	110201-8	/	0,01	0,01	-	-	-	-	-	-	-	-	-	-
E	110201-9	/	0,00	0,00	-	-	-	-	-	-	-	-	-	-
E	110201-10	/	<LOD	0,00	-	0,34	0,13	-	-	-	-	-	-	-
E	110201-11	/	<LOD	0,00	-	0,37	0,10	-	-	-	-	-	-	-
E	110201-12	/	0,01	0,01	-	1,24	0,24	-	-	-	-	-	-	-
E	110201-13	/	<LOD	0,00	0,03	-	-	-	-	-	-	-	-	-
E	110201-14	/	<LOD	0,00	-	-	-	-	-	-	-	-	-	-
E	110201-15	/	0,00	0,01	-	1,13	0,32	-	-	-	-	-	-	-
E	110201-16	QM	<LOD	0,00	-	1,15	0,19	-	-	-	-	-	-	-
E	110201-17	QM	<LOD	0,00	0,02	-	-	-	-	-	-	-	-	-
E	110201-18	/	0,04	0,02	-	1,00	0,36	-	-	-	-	-	-	-
E	110201-19	QC	-	-	-	-	-	-	-	-	-	-	-	-
E	110201-20	/	<LOD	0,01	0,03	0,57	0,22	-	-	-	-	-	-	-
E	110201-21	QM	<LOD	0,00	-	0,15	0,14	-	-	-	-	-	-	-
E	110201-22	/	<LOD	0,00	-	0,47	0,16	-	-	-	-	-	-	-
E	110201-23	/	<LOD	0,00	-	1,81	0,44	-	-	-	-	-	-	-
E	110201-24	/	<LOD	0,00	-	0,33	0,11	-	-	-	-	-	-	-
E	110201-25	/	0,01	0,01	-	0,51	0,16	-	-	-	-	-	-	-
E	110201-26	QM	<LOD	0,00	-	0,48	0,14	-	-	-	-	-	-	-
E	110201-27	/	0,00	0,00	-	0,37	0,12	-	-	-	-	-	-	-
E	110201-28	/	0,04	0,02	-	1,44	0,43	-	-	-	-	-	-	-
E	110201-29	QC	0,00	0,00	-	0,25	0,12	-	-	-	-	-	-	-
E	110201-30	QM	0,00	0,00	-	0,20	0,07	-	-	-	-	-	-	-
E	110201-31	QM	<LOD	0,00	-	0,44	0,20	-	-	-	-	-	-	-
E	110201-32	QC	0,00	0,00	-	0,09	0,06	-	-	-	-	-	-	-

Part 19

			Re			Au			Pb			Bi		
Vein type	Spot ID	CL color/intensity and quartz texture	Concentration ppm	2SE (ppm)	LOD (ppm)	Concentration ppm	2SE (ppm)	LOD (ppm)	Concentration ppm	2SE (ppm)	LOD (ppm)	Concentration ppm	2SE (ppm)	LOD (ppm)
E	110201-4	/	0,01	0,02	-	<LOD	0,00	-	0,03	0,03	-	0,06	0,03	-
E	110201-5	/	-	-	-	<LOD	0,00	-	0,03	0,02	-	<LOD	0,02	0,05
E	110201-6	/	-	-	-	<LOD	0,00	-	<LOD	0,00	-	<LOD	0,02	0,04
E	110201-7	/	-	-	-	<LOD	0,00	-	<LOD	0,00	-	0,08	0,05	0,06
E	110201-8	/	-	-	-	<LOD	0,00	-	<LOD	0,00	-	<LOD	0,03	0,05
E	110201-9	/	-	-	-	<LOD	0,00	-	0,05	0,03	-	<LOD	0,01	0,04
E	110201-10	/	-	-	-	<LOD	0,00	-	0,04	0,03	-	<LOD	0,02	0,05
E	110201-11	/	-	-	-	<LOD	0,00	-	0,00	0,01	-	<LOD	0,01	0,04
E	110201-12	/	-	-	-	<LOD	0,00	-	<LOD	0,00	-	<LOD	0,02	0,04
E	110201-13	/	-	-	-	<LOD	0,00	-	<LOD	0,00	-	<LOD	0,03	0,07
E	110201-14	/	-	-	-	<LOD	0,00	-	<LOD	0,00	-	<LOD	0,02	0,06
E	110201-15	/	-	-	-	<LOD	0,00	-	0,01	0,01	-	<LOD	0,02	0,05
E	110201-16	QM	-	-	-	<LOD	0,00	-	<LOD	0,02	0,06	<LOD	0,02	0,05
E	110201-17	QM	-	-	-	<LOD	0,00	0,05	0,01	0,01	-	<LOD	0,02	0,04
E	110201-18	/	-	-	-	<LOD	0,00	-	0,04	0,04	-	<LOD	0,04	0,07
E	110201-19	QC	-	-	-	-	-	-	-	-	-	-	-	-
E	110201-20	/	-	-	-	<LOD	0,00	-	0,05	0,04	-	<LOD	0,03	0,06
E	110201-21	QM	-	-	-	<LOD	0,00	-	<LOD	0,00	0,11	<LOD	0,02	0,08
E	110201-22	/	-	-	-	<LOD	0,00	-	<LOD	0,00	-	<LOD	0,02	0,05
E	110201-23	/	-	-	-	0,02	0,03	-	<LOD	0,02	0,07	<LOD	0,03	0,06
E	110201-24	/	-	-	-	<LOD	0,00	-	0,05	0,03	-	<LOD	0,02	0,05
E	110201-25	/	-	-	-	<LOD	0,00	-	0,06	0,03	-	<LOD	0,02	0,05
E	110201-26	QM	-	-	-	<LOD	0,00	-	0,94	0,19	-	<LOD	0,02	0,05
E	110201-27	/	-	-	-	<LOD	0,00	-	<LOD	0,01	0,07	<LOD	0,02	0,05
E	110201-28	/	-	-	-	<LOD	0,00	-	10,07	1,76	-	0,02	0,02	-
E	110201-29	QC	-	-	-	<LOD	0,00	-	0,07	0,04	-	<LOD	0,03	0,06
E	110201-30	QM	-	-	-	<LOD	0,00	-	0,06	0,02	-	0,07	0,02	0,04
E	110201-31	QM	-	-	-	<LOD	0,00	-	0,09	0,05	-	0,00	0,00	-
E	110201-32	QC	-	-	-	<LOD	0,00	-	0,01	0,01	-	<LOD	0,02	0,05

Part 20

			U		
Vein type	Spot ID	CL color/intensity and quartz texture	Concentration ppm	2SE (ppm)	LOD (ppm)
E	110201-4	/	-	-	-
E	110201-5	/	-	-	-
E	110201-6	/	-	-	-
E	110201-7	/	-	-	-
E	110201-8	/	-	-	-
E	110201-9	/	-	-	-
E	110201-10	/	-	-	-
E	110201-11	/	-	-	-
E	110201-12	/	-	-	-
E	110201-13	/	-	-	-
E	110201-14	/	-	-	-
E	110201-15	/	-	-	-
E	110201-16	QM	-	-	-
E	110201-17	QM	-	-	-
E	110201-18	/	-	-	-
E	110201-19	QC	-	-	-
E	110201-20	/	0,00	0,01	-
E	110201-21	QM	-	-	-
E	110201-22	/	-	-	-
E	110201-23	/	-	-	-
E	110201-24	/	0,22	0,05	-
E	110201-25	/	-	-	-
E	110201-26	QM	-	-	-
E	110201-27	/	-	-	-
E	110201-28	/	-	-	-
E	110201-29	QC	-	-	-
E	110201-30	QM	-	-	-
E	110201-31	QM	-	-	-
E	110201-32	QC	0,00	0,00	-

Caption:

	Quartz textures
GZ	Growth Zoning
SGR	SubGrain Rotation
GBM	Grain Boundary Migration
/	undetermined texture or location
QC	Quartz Center
QM	Quartz Margin
LOD (From Longerich 1987)	Limit of Detection

CL intensity	
	dark red to brown
	dark red
	bright red
	bright red to orange

Tables of pearson correlation coefficient (Trace Element in quartz).

A-type vein

	Li	B	Na	Mg	Al	Cl	K	CA	Ti	Mn	Fe	Co	Cu	Zn	Ga	Ge	As	Rb	Sr	Zr	Nb	Mo	In	Sn	Sb	Cs	Ba	Ta	Au	Pb	Bi
Li	1,00																														
B	-0,06	1,00																													
Na	0,13	-0,21	1,00																												
Mg	-0,28	0,29	0,17	1,00																											
Al	0,30	-0,27	0,84	0,20	1,00																										
Cl	0,31	-0,08	-0,23	0,09	0,11	1,00																									
K	0,21	-0,42	0,23	0,11	0,61	0,42	1,00																								
CA	0,14	-0,17	0,68	0,44	0,65	0,16	0,31	1,00																							
Ti	-0,09	-0,16	0,06	0,11	0,01	-0,01	0,42	0,02	1,00																						
Mn	-0,36	-0,32	0,58	0,21	0,29	-0,26	0,23	0,55	0,22	1,00																					
Fe	-0,78	-0,03	0,30	0,36	0,20	-0,41	0,02	0,24	0,04	0,49	1,00																				
Co	-0,16	-0,12	0,50	0,02	0,22	-0,49	-0,40	0,19	0,29	0,27	0,35	1,00																			
Cu	-0,51	0,10	0,06	0,41	-0,09	-0,17	0,01	0,08	0,11	0,55	0,48	0,07	1,00																		
Zn	-0,14	-0,26	0,50	0,42	0,47	0,10	0,45	0,35	0,04	0,60	0,32	0,25	0,37	1,00																	
Ga	0,53	0,53	0,40	0,29	0,67	0,45	0,38	0,56	-0,44	-0,07	-0,36	-0,46	-0,17	0,19	1,00																
Ge	0,12	-0,03	0,76	0,04	0,65	0,03	0,14	0,60	0,04	0,42	0,17	0,20	0,02	0,15	0,58	1,00															
As	0,31	0,05	0,35	-0,29	0,41	-0,28	0,10	0,09	0,21	0,03	0,02	0,55	-0,07	-0,21	0,31	0,22	1,00														
Rb	0,15	-0,38	-0,06	-0,00	0,38	0,36	0,90	0,19	-0,10	0,05	0,05	-0,48	0,03	0,14	0,38	-0,06	0,22	1,00													
Sr	0,07	-0,33	0,91	0,11	0,85	-0,09	0,33	0,69	0,01	0,54	0,42	0,43	-0,00	0,51	0,16	0,66	0,28	0,07	1,00												
Zr	0,29	-0,16	-0,15	-0,12	0,30	0,36	0,77	-0,03	-0,03	-0,23	-0,16	-0,47	-0,21	0,04	0,36	-0,16	0,31	0,81	-0,05	1,00											
Nb	-0,18	-0,07	-0,19	0,31	-0,14	0,18	0,18	-0,10	0,84	-0,08	0,08	0,13	0,15	0,04	-0,51	-0,22	-0,07	-0,16	-0,14	-0,03	1,00										
Mo	-0,61	0,10	-0,08	0,56	-0,04	-0,13	0,01	0,04	0,09	0,17	0,63	-0,09	0,68	0,10	0,04	0,04	-0,08	0,15	-0,12	-0,07	0,26	1,00									
In	-0,76	0,27	0,16	0,29	-0,04	-0,34	-0,07	0,05	-0,04	0,48	0,75	0,10	0,33	0,32	-0,42	0,03	-0,40	-0,20	0,22	-0,18	-0,08	0,27	1,00								
Sn	0,12	-0,39	-0,00	-0,12	0,12	0,69	0,35	0,15	0,05	0,13	-0,20	-0,39	-0,06	0,32	0,06	0,25	-0,56	0,23	0,16	-0,04	0,03	-0,16	-0,19	1,00							
Sb	0,30	0,46	0,22	-0,12	0,25	-0,34	-0,05	-0,17	-0,11	-0,27	-0,11	0,14	-0,36	0,02	0,90	0,29	0,60	-0,11	0,06	0,08	-0,32	-0,24	-0,09	-0,32	1,00						
Cs	-0,02	0,13	-0,52	0,04	0,36	0,56	0,68	-0,02	0,27	-0,21	0,09	-0,43	-0,28	0,14	0,39	0,00	0,21	0,54	-0,13	0,69	0,28	0,01	0,21	0,21	0,14	1,00					
Ba	0,30	-0,09	0,89	0,22	0,85	0,10	0,32	0,73	0,10	0,39	0,09	0,29	-0,07	0,37	0,64	0,90	0,24	0,01	0,79	-0,04	-0,13	-0,08	-0,04	0,21	0,30	0,15	1,00				
Ta	0,30	-0,18	-0,20	-0,15	0,25	0,41	0,77	-0,07	0,17	-0,28	-0,20	-0,41	-0,23	-0,02	0,22	-0,19	0,33	0,75	-0,08	0,97	0,18	-0,10	-0,23	-0,01	0,03	0,74	-0,07	1,00			
Au	-0,58	0,51	0,46	0,95	0,90	-0,70	0,33	0,73	-0,55	0,43	0,68	-0,10	0,92	0,26	1,00	0,49	0,27	0,92	0,49	#####	-0,70	0,68	0,07	-0,32	0,99	-0,51	0,65	-0,70	1,00		
Pb	-0,43	-0,35	0,59	-0,02	0,42	-0,21	0,19	0,34	0,02	0,69	0,71	0,46	0,27	0,51	-0,36	0,41	0,30	0,05	0,74	-0,15	-0,11	0,09	0,59	0,14	-0,17	0,12	0,37	-0,17	0,59	1,00	
Bi	-0,30	-0,45	0,44	0,24	0,40	0,10	0,43	0,35	-0,10	0,65	0,49	0,04	0,34	0,72	-0,13	0,25	-0,33	0,29	0,58	0,03	-0,09	0,15	0,49	0,34	-0,37	0,20	0,28	-0,04	0,08	0,78	1,00

Table of pearson correlation coefficient (Trace Element in quartz) in B1-type vein.

B1-type vein

	Li	Be	B	Na	Mg	Al	Cl	K	CA	Ti	Mn	Fe	Co	Cu	Zn	Ga	Ge	As	Rb	Sr	Zr	Nb	Mo	Ag	In	Sn	Sb	Cs	Ba	Ta	W	Au	Pb	Bi	U
Li	1,00																																	
Be	-0,72	1,00																																
B	-0,33	0,12	1,00																															
Na	-0,51	-0,00	0,37	1,00																														
Mg	-0,52	-0,37	0,37	0,62	1,00																													
Al	-0,48	-0,29	0,43	0,81	0,83	1,00																												
Cl	-0,35	-0,93	0,22	0,36	0,30	0,41	1,00																											
K	-0,60	-0,21	0,37	0,84	0,82	0,97	0,39	1,00																										
CA	-0,42	0,97	0,50	0,52	0,55	0,54	0,27	0,52	1,00																									
Ti	-0,64	-0,52	0,38	0,74	0,73	0,82	0,51	0,82	0,53	1,00																								
Mn	-0,49	0,02	0,31	0,88	0,57	0,60	0,26	0,65	0,42	0,55	1,00																							
Fe	-0,19	-0,10	0,26	0,48	0,49	0,44	-0,00	0,42	0,24	0,34	0,52	1,00																						
Co	-0,26	-0,64	-0,03	-0,04	-0,00	-0,08	0,15	-0,07	0,07	0,02	0,02	0,05	1,00																					
Cu	-0,01	-1,00	-0,14	-0,05	-0,16	-0,18	-0,11	-0,05	-0,01	-0,04	-0,02	0,15	0,02	1,00																				
Zn	-0,38	-0,10	0,26	0,75	0,42	0,47	0,14	0,46	0,28	0,41	0,89	0,48	0,25	0,02	1,00																			
Ga	0,12	0,13	0,17	0,11	0,19	0,09	-0,30	0,08	-0,00	0,02	0,20	0,92	-0,10	0,41	0,28	1,00																		
Ge	-0,25	0,67	0,21	-0,01	0,03	0,01	0,06	0,01	0,31	0,09	0,03	0,24	0,22	0,08	0,09	0,29	1,00																	
As	-0,16	1,00	0,08	0,19	0,00	0,08	0,11	0,11	0,21	0,13	0,13	0,09	0,11	0,20	0,25	0,06	0,03	1,00																
Rb	-0,52	-0,86	0,29	0,65	0,86	0,70	0,32	0,72	0,53	0,59	0,68	0,49	0,02	-0,08	0,45	0,14	0,04	-0,01	1,00															
Sr	-0,40	-0,11	0,17	0,61	0,47	0,53	0,38	0,48	0,53	0,41	0,61	0,31	0,01	-0,05	0,50	-0,03	0,02	0,17	0,59	1,00														
Zr	-0,45	-0,35	0,24	0,60	0,56	0,66	0,22	0,61	0,37	0,57	0,43	0,33	-0,06	-0,04	0,38	0,17	0,09	0,24	0,46	0,46	1,00													
Nb	0,19	#####	0,08	-0,08	-0,01	-0,05	-0,27	-0,11	-0,10	-0,11	-0,03	0,75	-0,03	0,08	0,05	0,92	0,27	0,04	-0,04	-0,11	-0,02	1,00												
Mo	0,01	#####	0,01	-0,14	-0,21	-0,21	-0,17	-0,21	-0,14	-0,16	-0,13	-0,10	-0,01	0,03	-0,14	-0,08	-0,03	-0,05	-0,17	-0,16	-0,13	-0,01	1,00											
Ag	-0,12	#####	-0,01	0,48	0,23	0,23	0,05	0,34	0,23	0,19	0,53	0,30	-0,09	0,03	0,36	0,15	-0,03	-0,20	0,44	0,29	0,25	-0,02	-0,03	1,00										
In	-0,03	0,53	-0,21	0,08	0,24	0,07	0,03	0,08	0,14	0,02	0,24	0,09	0,35	-0,09	0,29	-0,03	0,04	-0,15	0,26	0,41	-0,03	-0,04	-0,17	0,17	1,00									
Sn	-0,55	0,96	0,58	0,58	0,46	0,58	0,45	0,53	0,47	0,63	0,49	0,16	-0,14	-0,17	0,35	-0,08	0,21	0,09	0,44	0,31	0,48	-0,16	-0,23	0,29	-0,04	1,00								
Sb	-0,31	-0,36	0,17	-0,03	0,03	0,06	0,26	-0,04	0,30	0,11	-0,02	-0,00	0,21	0,02	-0,02	-0,07	0,32	0,22	0,08	0,31	0,13	0,08	-0,21	-0,13	0,04	0,10	1,00							
Cs	-0,52	1,00	0,45	0,53	0,36	0,39	0,04	0,44	0,36	0,38	0,66	0,12	-0,03	-0,14	0,66	-0,08	0,05	0,30	0,35	0,41	0,31	-0,19	-0,05	0,01	0,28	0,32	0,09	1,00						
Ba	-0,49	-0,53	0,32	0,70	0,61	0,59	0,40	0,55	0,48	0,57	0,74	0,39	0,06	-0,06	0,72	0,06	0,06	0,29	0,71	0,81	0,54	-0,08	-0,14	0,27	0,23	0,45	0,33	0,63	1,00					
Ta	0,17	#####	-0,16	-0,08	-0,05	-0,07	-0,16	-0,13	0,03	-0,12	-0,07	-0,07	-0,08	0,17	-0,02	-0,11	-0,03	-0,09	-0,08	-0,11	-0,03	-0,02	-0,03	-0,02	0,18	-0,10	0,01	#####	-0,08	1,00				
W	-0,38	#####	-0,06	0,98	0,79	0,76	0,68	1,00	0,54	1,00	0,93	1,00	1,00	1,00	0,96	#####	0,87	-0,15	0,83	0,97	1,00	#####	-0,52	#####	1,00	0,04	1,00	1,00	0,99	#####	1,00			
Au	-0,46	#####	0,33	0,56	0,63	0,62	-0,04	0,63	0,69	0,32	0,50	0,19	0,01	0,10	0,22	-0,04	-0,28	-0,27	0,66	0,46	0,55	-0,15	-0,22	0,49	0,10	0,61	-0,54	0,14	0,19	#####	#####	1,00		
Pb	-0,42	0,07	0,19	0,63	0,35	0,36	0,14	0,39	0,20	0,39	0,79	0,39	0,09	0,01	0,89	0,11	0,04	0,30	0,43	0,57	0,35	-0,05	-0,12	0,21	0,24	0,28	0,08	0,68	0,77	-0,07	1,00	0,25	1,00	
Bi	-0,41	1,00	-0,06	0,11	0,12	0,12	0,03	0,23	0,23	0,33	0,01	0,06	0,51	-0,09	-0,03	0,06	0,33	0,00	0,02	0,09	0,15	0,02	0,16	-0,06	-0,01	0,05	0,06	0,08	-0,04	#####	1,00	- 0,09	0,01	1,00
U	0,70	#####	0,07	-0,20	0,19	-0,06	-0,81	-0,26	-0,40	-0,31	-0,13	0,86	0,11	-0,12	0,02	0,99	0,82	-0,30	-0,01	-0,23	-0,09	0,94	-0,29	#####	-0,11	-0,25	-0,04	-0,50	-0,20	#####	1,00	- 0,37	- 0,25	- 0,25	1,00

Table of pearson correlation coefficient (Trace Element in quartz) in B2-type vein.

B2-type veins

	Li	Be	B	Na	Mg	Al	Cl	K	Ca	Ti	Mn	Fe	Co	Cu	Zn	Ga	Ge	As	Rb	Sr	Zr	Nb	Mo	Ag	Sn	Sb	Cs	Ba	Ta	W	Au	Pb	Bi	U
Li	1,00																																	
Be	-0,03	1,00																																
B	0,76	0,59	1,00																															
Na	0,55	0,39	0,80	1,00																														
Mg	0,47	0,16	0,77	0,61	1,00																													
Al	0,72	0,37	0,70	0,92	0,66	1,00																												
Cl	-0,06	0,07	0,87	0,26	0,24	0,11	1,00																											
K	0,39	0,25	0,88	0,73	0,83	0,78	0,32	1,00																										
Ca	0,47	0,03	0,95	0,70	0,88	0,57	0,64	0,75	1,00																									
Ti	-0,35	-0,45	-0,65	-0,71	-0,56	-0,70	-0,05	-0,58	-0,40	1,00																								
Mn	0,37	-0,02	0,82	0,37	0,78	0,26	0,45	0,64	0,89	-0,08	1,00																							
Fe	0,41	0,51	0,72	0,59	0,92	0,67	0,29	0,86	0,71	-0,48	0,73	1,00																						
Co	0,74	0,13	0,71	0,49	0,52	0,65	0,11	0,51	0,46	-0,53	0,17	0,56	1,00																					
Cu	-0,13	-0,18	0,49	0,15	0,13	-0,08	0,40	0,17	0,74	0,02	0,44	0,00	-0,17	1,00																				
Zn	0,80	0,12	0,89	0,57	0,41	0,51	0,92	0,44	0,71	0,00	0,60	0,41	0,53	0,45	1,00																			
Ga	0,04	0,27	0,46	0,42	0,45	0,43	0,54	0,57	0,46	-0,24	0,26	0,53	0,24	-0,05	0,47	1,00																		
Ge	-0,16	0,31	0,83	0,52	0,49	0,38	0,71	0,70	0,53	-0,33	0,60	0,53	0,11	0,23	0,70	0,72	1,00																	
As	0,58	0,26	0,99	0,73	0,54	0,54	0,98	0,62	1,00	-0,50	0,70	0,52	0,55	0,46	1,00	0,74	0,88	1,00																
Rb	0,55	0,05	0,76	0,57	0,94	0,69	0,24	0,92	0,80	-0,41	0,75	0,90	0,55	-0,01	0,46	0,45	0,50	0,58	1,00															
Sr	1,00	-0,05	0,82	0,55	0,48	0,70	-0,06	0,38	0,48	-0,33	0,91	0,42	0,73	-0,09	0,49	0,01	-0,17	0,66	0,55	1,00														
Zr	-0,10	-0,20	0,17	-0,30	-0,23	-0,21	0,25	-0,17	0,08	0,52	0,08	-0,09	-0,11	-0,01	0,69	-0,00	-0,01	0,40	-0,06	-0,13	1,00													
Nb	-0,12	-0,18	0,25	-0,24	-0,16	-0,26	0,34	-0,21	0,51	0,41	0,03	-0,16	-0,08	0,12	0,63	0,24	0,07	0,43	-0,12	-0,12	0,29	1,00												
Mo	-0,05	-0,01	0,47	0,18	0,39	0,03	0,14	0,28	0,72	0,05	0,70	0,21	-0,06	0,64	0,33	-0,01	0,25	0,18	0,32	-0,01	-0,02	0,26	1,00											
Ag	-0,03	0,18	0,58	0,23	0,42	0,19	0,07	0,55	#####	-0,14	0,59	0,55	0,09	-0,00	0,12	-0,05	0,39	#####	0,50	0,00	-0,12	-0,11	0,33	1,00										
Sn	0,17	-0,11	0,84	0,19	0,15	0,00	0,86	0,10	0,74	0,09	0,43	0,21	0,19	0,38	0,89	0,36	0,47	0,92	0,17	0,34	0,24	0,32	0,21	-0,01	1,00									
Sb	-0,03	0,40	0,75	0,69	0,57	0,62	0,45	0,75	0,27	-0,79	0,29	0,67	0,32	-0,00	0,39	0,77	0,86	0,78	0,48	-0,05	-0,32	-0,25	-0,01	0,32	0,18	1,00								
Cs	0,99	-0,08	0,73	0,55	0,54	0,72	-0,01	0,46	0,52	-0,31	0,82	0,50	0,74	-0,08	0,63	0,08	-0,10	0,56	0,63	0,99	-0,07	-0,08	0,04	0,04	0,28	-0,01	1,00							
Ba	0,62	0,37	0,79	0,90	0,77	0,92	0,13	0,86	0,66	-0,65	0,55	0,79	0,55	0,05	0,29	0,38	0,46	0,67	0,77	0,63	-0,32	-0,23	0,23	0,49	0,03	0,63	0,65	1,00						
Ta	-0,06	-0,14	-0,02	-0,22	-0,23	-0,13	0,16	-0,12	-0,04	0,41	0,04	-0,11	-0,09	-0,13	0,55	-0,02	-0,00	0,43	-0,06	-0,09	0,91	0,10	-0,11	-0,08	0,13	-0,23	-0,05	-0,27	1,00					
W	-0,08	-0,13	0,25	-0,01	0,19	-0,12	0,18	-0,05	0,72	0,19	0,53	0,02	-0,02	0,56	0,30	0,05	0,12	0,20	0,06	-0,03	0,10	0,39	0,80	-0,08	0,37	-0,17	-0,01	-0,03	-0,02	1,00				
Au	-0,06	-0,08	0,02	-0,08	-0,18	-0,14	-0,06	-0,17	-0,03	0,24	-0,14	-0,12	-0,15	-0,09	0,47	-0,22	-0,02	0,21	-0,10	-0,06	0,05	-0,08	-0,07	-0,05	-0,08	-0,12	-0,05	-0,18	0,11	-0,09	1,00			
Pb	0,24	-0,08	0,75	0,20	0,47	0,09	0,41	0,38	0,83	0,10	0,90	0,49	0,15	0,51	0,64	0,06	0,39	0,79	0,49	0,79	0,23	0,10	0,74	0,45	0,49	0,04	0,64	0,34	0,21	0,68	-0,08	1,00		
Bi	0,60	#####	1,00	0,87	0,53	0,55	1,00	1,00	1,00	-1,00	0,69	0,82	0,99	1,00	1,00	0,66	0,96	1,00	0,50	0,73	0,97	0,43	0,50	#####	0,95	0,97	0,64	0,71	#####	0,43	0,57	0,70	1,00	
U	-0,21	-0,31	0,11	-0,45	-0,37	-0,45	0,31	-0,38	-0,27	0,67	-0,07	-0,22	-0,28	-0,24	0,64	0,18	-0,08	0,43	-0,21	-0,21	0,54	0,58	-0,19	-0,18	0,42	-0,40	-0,17	-0,45	0,35	0,02	0,10	- 0,09	0,67	1,00

Table of pearson correlation coefficient (Trace Element in quartz) in E1-type vein.

E1-type veins	Li	Be	B	Na	Mg	Al	Cl	K	CA	Ti	Mn	Fe	Co	Cu	Zn	Ga	Ge	As	Rb	Sr	Zr	Mo	Ag	In	Sn	Sb	Cs	Ba	Ta	Re	Au	Pb	Bi	U
Li	1,00																																	
Be	0,22	1,00																																
B	0,13	0,09	1,00																															
Na	0,55	0,42	-0,05	1,00																														
Mg	-0,02	0,26	-0,18	0,33	1,00																													
Al	0,76	0,27	-0,16	0,63	0,17	1,00																												
Cl	-0,19	-0,21	-0,13	-0,25	-0,11	-0,14	1,00																											
K	0,10	0,79	-0,08	0,73	0,40	0,33	-0,61	1,00																										
CA	-0,16	0,23	-0,05	0,38	0,30	0,05	-0,18	0,66	1,00																									
Ti	0,10	-0,05	0,08	0,08	0,00	0,11	0,06	-0,24	-0,11	1,00																								
Mn	-0,19	-0,16	0,02	0,01	0,32	-0,09	-0,09	0,12	0,34	-0,12	1,00																							
Fe	-0,28	#####	0,26	-0,15	-0,08	-0,25	-0,37	0,16	0,38	-0,15	0,78	1,00																						
Co	-0,08	0,10	-0,05	-0,03	0,03	0,01	-0,13	0,35	0,50	-0,15	0,76	0,90	1,00																					
Cu	-0,03	-0,22	0,15	-0,08	-0,19	0,09	0,41	-0,41	-0,23	0,21	-0,16	-0,25	-0,07	1,00																				
Zn	-0,17	-0,05	0,09	-0,02	0,02	-0,11	-0,15	0,08	0,28	-0,04	0,78	0,98	0,88	-0,13	1,00																			
Ga	0,05	-0,09	0,22	0,26	-0,16	-0,27	-0,33	0,44	0,01	-0,17	-0,23	-0,00	-0,20	-0,10	-0,19	1,00																		
Ge	0,38	0,06	0,19	0,36	0,19	0,41	-0,07	0,22	-0,01	0,22	-0,05	-0,40	-0,12	0,18	-0,09	0,66	1,00																	
As	0,38	-0,08	0,20	0,30	-0,10	0,44	-0,04	0,11	0,27	-0,01	0,03	-0,18	0,10	0,22	-0,01	-0,07	0,18	1,00																
Rb	-0,00	0,57	-0,04	0,63	0,43	0,22	-0,41	0,99	0,61	-0,11	0,09	0,02	-0,01	-0,29	0,02	0,47	0,14	0,12	1,00															
Sr	-0,01	0,56	-0,19	0,56	0,40	0,33	-0,36	0,93	0,61	-0,08	0,10	-0,03	0,09	-0,26	0,01	0,42	0,15	0,12	0,95	1,00														
Zr	-0,03	-0,03	-0,14	-0,04	0,84	0,03	0,10	-0,07	-0,02	-0,00	0,34	-0,12	-0,01	-0,10	-0,03	-0,18	0,15	-0,10	-0,04	-0,05	1,00													
Mo	-0,12	-0,03	0,05	-0,00	0,04	-0,08	-0,12	0,09	0,26	-0,04	0,76	0,95	0,85	-0,13	0,99	-0,14	-0,08	-0,01	0,02	0,01	-0,02	1,00												
Ag	-0,12	-0,03	0,18	-0,14	-0,05	-0,11	0,07	-0,10	0,07	-0,04	0,00	#####	#####	-0,09	#####	#####	-0,03	0,02	-0,02	-0,03	-0,02	-0,02	1,00											
In	-0,07	0,06	-0,04	0,21	0,32	0,04	0,07	0,44	0,24	-0,10	0,19	0,06	0,02	0,12	0,05	-0,03	0,36	0,12	0,30	0,30	0,20	0,04	-0,03	1,00										
Sn	-0,26	0,05	0,07	-0,19	0,00	-0,51	0,03	-0,08	0,00	0,02	-0,01	0,12	-0,02	-0,29	0,04	0,49	-0,37	-0,08	-0,07	-0,15	-0,00	0,04	-0,02	-0,10	1,00									
Sb	0,55	0,13	0,31	0,58	-0,04	0,27	-0,14	0,04	-0,06	-0,01	-0,09	-0,23	-0,14	-0,03	-0,09	0,08	0,12	0,23	0,11	-0,07	-0,06	-0,06	-0,09	-0,09	-0,10	1,00								
Cs	0,22	0,86	0,09	0,84	0,89	0,29	-0,65	0,93	0,59	-0,25	-0,01	0,13	-0,06	-0,34	-0,01	0,33	0,27	-0,08	0,94	0,82	0,24	-0,01	-0,05	0,41	-0,06	0,31	1,00							
Ba	-0,10	0,21	-0,13	0,36	0,20	0,26	-0,24	0,61	0,53	-0,10	0,30	-0,06	0,09	-0,17	0,06	0,11	0,12	0,20	0,66	0,77	-0,03	0,04	-0,02	0,14	-0,21	-0,05	0,41	1,00						
Ta	0,15	0,67	0,18	0,01	-0,05	0,12	0,00	#####	-0,13	-0,01	-0,11	#####	0,10	-0,04	-0,03	#####	-0,05	-0,01	-0,04	-0,01	-0,02	-0,02	-0,02	-0,14	0,06	0,08	#####	-0,06	1,00					
Re	0,11	-0,03	0,01	-0,02	-0,04	0,07	-0,16	#####	-0,10	0,00	#####	#####	0,04	#####	-0,02	#####	0,14	#####	-0,03	-0,04	-0,02	-0,02	-0,02	-0,19	-0,10	-0,07	#####	-0,05	-0,02	1,00				
Au	-0,50	#####	0,64	0,87	0,92	-0,46	0,30	#####	-0,59	-0,48	0,58	#####	1,00	1,00	0,86	#####	0,45	-0,42	0,06	-0,67	#####	#####	#####	0,41	0,51	-0,10	#####	-0,25	#####	#####	1,00			
Pb	-0,15	-0,03	0,08	-0,02	0,03	-0,09	-0,13	0,09	0,29	-0,04	0,80	0,97	0,89	-0,14	1,00	-0,19	-0,09	0,02	0,04	0,03	-0,03	0,99	-0,03	0,07	0,04	-0,09	-0,02	0,10	#####	-0,03	0,68	1,00		
Bi	0,02	0,28	0,16	0,04	-0,14	-0,10	0,12	0,16	-0,17	0,03	-0,14	-0,24	0,03	-0,11	-0,09	0,76	0,19	0,04	0,07	0,03	-0,20	-0,09	#####	-0,10	0,13	-0,03	0,03	0,05	0,35	0,22	0,90	- 0,08	1,00	
U	-0,03	-0,03	-0,14	-0,04	0,84	0,03	0,10	-0,07	-0,02	-0,00	0,34	-0,13	-0,01	-0,09	-0,03	-0,19	0,15	-0,10	-0,04	-0,05	1,00	-0,02	-0,02	0,20	-0,00	-0,06	-0,08	-0,03	-0,02	-0,02	#####	- 0,03	- 0,20	1,00

Graphical method for finding the trapping pressure using *PT* diagram

Pressure vs salinity diagram (from Bodnar 1985), and pressure projection from fluid inclusion data (here Th = 500°C and salinity = 35wt%)

Red curves isothermal curves L+V

Yellow doted lines projection lines

Blue point fluid inclusion

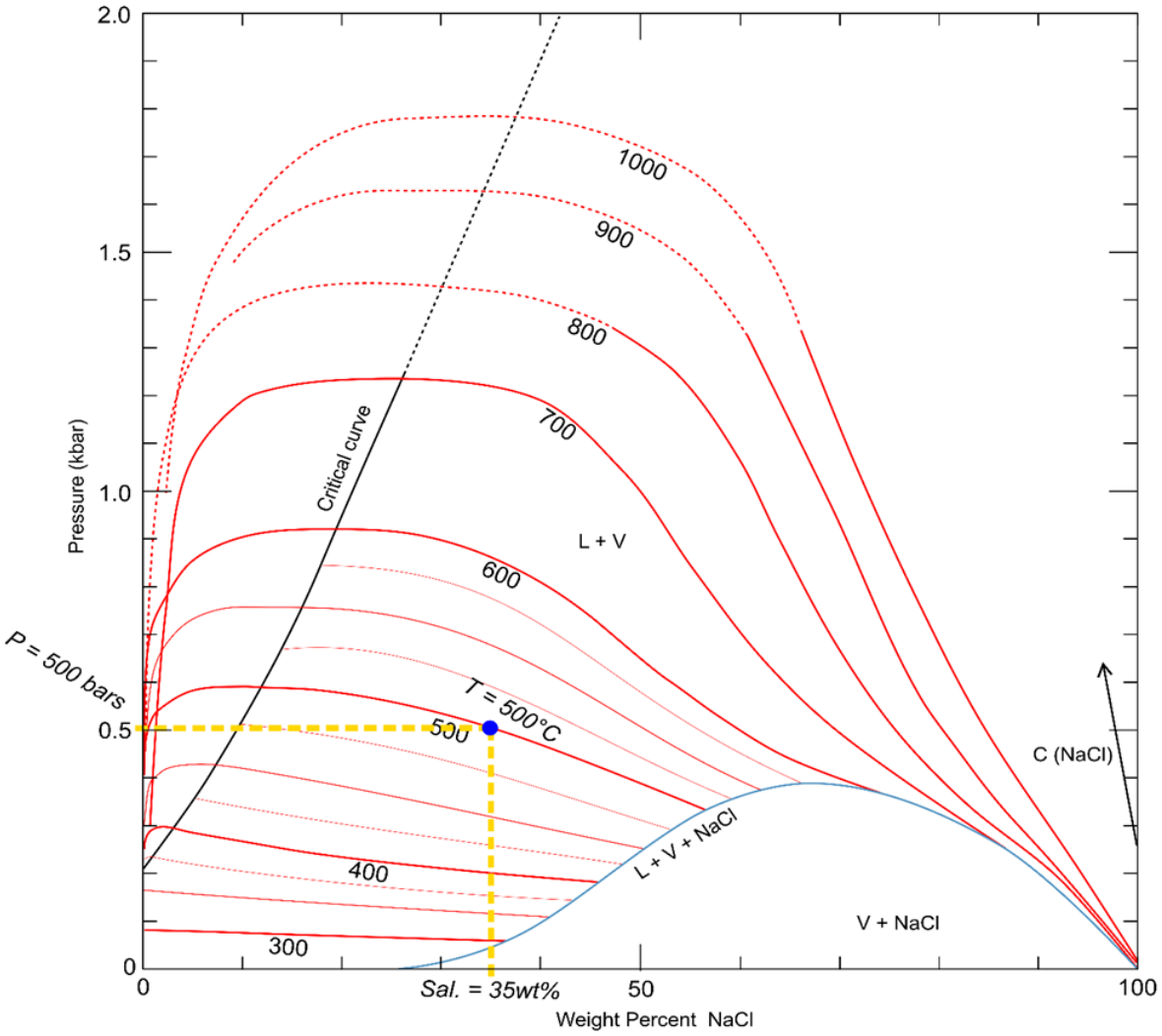

A vertical line passing through the salinity scale at the salinity value of the fluid inclusion was constructed (35.0 $wt\%_{equiv.NaCl}$) and plot the fluid inclusion point at the intersection between the corresponding isothermal curves (*T*h = 500°C) and the vertical line (Salinity = 35.0 $wt\%_{equiv.NaCl}$). The pressure was determined by drawing a horizontal line from the crossing of the fluid inclusion point and *P* scale and reporting the *P* value at the intersection between both lines (~ 500 bars).

Table of analyses of fluid inclusion in A-type vein.

Vein type	A															
Fluid inclusion type	Type 1					Type 2						Type 3				
	Th	Tm(ice)	sal Bodnar (wt% equiv NaCl)	sal Steele–McInnis (wt% equiv NaCl)	P Steele–McInnis (bars)	Th	Th Steele–McInnis	Tm (hal)	sal Bodnar (wt% equiv NaCl)	sal Steele–McInnis (wt% equiv NaCl)	P Steele–McInnis (bars)	Th	Tm (ice)	sal Bodnar (wt% equiv NaCl)	sal Steele–McInnis (wt% equiv NaCl)	P Steele–McInnis (bars)
Fluid inclusion data from Voudouris et al. 2013a	265	–1,6	2,7	2,7	50	360	360	347	42,1	42,1	120	371	–4,2	6,7	6,7	201
	391	–4,4	7,0	7,0	249	391	391	320	39,3	39,7	173	379	–3	5,0	5,0	223
	312	–2,4	4,0	4,0	99	385	385	315	38,9	39,3	164	412	–7	10,4	10,5	295
	384	–4,1	6,6	6,6	232	467	491	491	58,6	58,6	497	389	–6,4	9,7	9,7	238
	397	–4,9	7,7	7,7	262	457	457	407	47,9	48,1	273	407	–5,4	8,4	8,4	288
	407	–5,2	8,1	8,1	288	473	473	438	51,7	51,7	293	395	–6,8	10,2	10,2	252
	265	–1,4	2,4	2,4	50	492	492	395	46,6	46,6	338	390	–4,7	7,5	7,4	245
	382	–3,9	6,3	6,3	228	481	481	394	46,5	46,5	318	387	–3,4	5,6	5,6	241
	379	–2,8	4,7	4,6	223	494	494	440	51,9	51,8	327					
	411	–2,5	4,2	4,2	312	474	474	399	47,0	47,1	305	*433*	*–5,9*	*9,1*	*9,1*	*362*
	409	–3,7	6,0	6,0	300	505	505	502	60,2	60,0	327	*421*	*–4,1*	*6,6*	*6,6*	*335*
	388	–5,1	8,0	8,0	239	510	510	488	58,2	58,0	338	*438*	*–3,9*	*6,3*	*6,3*	*392*
	378	–4,5	7,2	7,2	217	507	507	469	55,7	55,5	339	*442*	*–5,6*	*8,7*	*8,7*	*393*
	404	–4,4	7,0	7,0	283	481	481	404	47,6	47,6	315	*428*	*–6,2*	*9,5*	*9,5*	*345*
	348	–4	6,5	6,4	155	495	495	448	52,9	52,8	326	*432*	*–5,1*	*8,0*	*8,0*	*364*
	367	–3,8	6,2	6,2	193							*477*	*–6,4*	*9,7*	*9,7*	*512*

Part 2

Vein type	A															
Fluid inclusion type	Type 1					Type 2						Type 3				
	Th	Tm(ice)	sal Bodnar (wt% equiv NaCl)	sal Steele–McInnis (wt% equiv NaCl)	P Steele–McInnis (bars)	Th	Th Steele–McInnis	Tm (hal)	sal Bodnar (wt% equiv NaCl)	sal Steele–McInnis (wt% equiv NaCl)	P Steele–McInnis (bars)	Th	Tm (ice)	sal Bodnar (wt% equiv NaCl)	sal Steele–McInnis (wt% equiv NaCl)	P Steele–McInnis (bars)
Fluid inclusion data from Voudouris et al. 2013a	405	–5,1	8,0	8,0	283	*428*	*456*	*456*	*54,0*	*54,3*	*478*					
	367	–4	6,5	6,4	193	*398*	*434*	*434*	*51,3*	*51,7*	*517*					
	375	–2,7	4,5	4,5	214	*499*	*503*	*503*	*60,2*	*60,5*	*359*					
	379	–2,9	4,8	4,8	223	*474*	*501*	*501*	*59,9*	*59,8*	*534*					
	381	–3,9	7,7	6,3	225	*467*	*494*	*494*	*59,0*	*59,0*	*523*					
	253	–2,6	4,4	4,3	40	*376*	*474*	*474*	*55,9*	*55,9*	*1 210*					
	302	–2,7	4,5	4,5	86	*385*	*465*	*465*	*54,9*	*55,0*	*965*					
	450	–6	9,2	9,2	417	*378*	*481*	*481*	*56,8*	*56,7*	*1 286*					
	389	–5,2	8,1	8,1	241	*354*	*465*	*465*	*54,7*	*54,8*	*1 443*					
	369	–4,4	7,0	7,0	196	*369*	*457*	*457*	*53,8*	*54,0*	*1 074*					
	394	–2,8	4,7	4,6	262	*461*	*502*	*502*	*60,0*	*59,8*	*638*					
	399	–3,5	5,7	5,7	273	*371*	*461*	*461*	*54,3*	*54,5*	*1 099*					
	420	–6	9,2	9,2	322	*361*	*451*	*451*	*53,1*	*53,4*	*1 110*					
	425	–5,9	9,1	9,1	337	*381*	*463*	*463*	*54,6*	*54,8*	*990*					
	419	–7,2	10,7	10,7	314	*373*	*480*	*480*	*56,7*	*56,5*	*1 353*					
	372	–5,5	8,6	8,5	201	*368*	*478*	*478*	*56,4*	*56,3*	*1 408*					
	410	–5,8	9,0	8,9	294	*385*	*470*	*470*	*55,5*	*55,5*	*1 027*					
	487	–6,8	10,2	10,2	549	*502*	*576*	*576*	*69,9*	*68,5*	*1 183*					
	380	–6,3	9,6	9,6	217	*479*	*555*	*555*	*67,1*	*65,9*	*1 095*					
	375	–5,6	8,7	8,7	207	*484*	*519*	*519*	*62,4*	*62,0*	*622*					
	469	–6,5	9,9	9,9	481	*470*	*528*	*528*	*63,5*	*62,8*	*824*					
	464	–6,3	9,6	9,6	464											
	465	–6,6	10,0	10,0	465											

Part 3

Vein type	A															
Fluid inclusion type	Type 1					Type 2						Type 3				
	Th	Tm(ice)	sal Bodnar (wt% equiv NaCl)	sal Steele–McInnis (wt% equiv NaCl)	P Steele–McInnis (bars)	Th	Th Steele–McInnis	Tm (hal)	sal Bodnar (wt% equiv NaCl)	sal Steele–McInnis (wt% equiv NaCl)	P Steele–McInnis (bars)	Th	Tm (ice)	sal Bodnar (wt% equiv NaCl)	sal Steele–McInnis (wt% equiv NaCl)	P Steele–McInnis (bars)
Fluid inclusion data from Voudouris et al. 2013a	458	–5,1	8,0	8,0	453											
	395	–4,9	7,7	7,7	257											
	377	–5	7,9	7,9	213											
	435	–7	10,5	10,5	362											
	265	–2	3,4	3,4	50											
	263	–1,7	2,9	2,9	48											
	299	–1,9	3,2	3,2	83											
	279	–2,2	3,7	3,7	62											
	284	–1,4	2,4	2,4	67											
	286	–2	3,4	3,4	69											
	291	–2,2	3,7	3,7	74											
	274	–1,7	2,9	2,9	57											
	454	–4,7	7,5	7,4	443											
	444	–5,6	8,7	8,7	400											
	419	–6,1	9,3	9,3	319											
	435	–4,2	6,7	6,7	379											
	467	–7	10,5	10,5	469											
	454	–6	9,2	9,2	431											
	449	–6,6	10,0	10,0	409											
	482	–6,9	10,4	10,4	526											
	507	–7,9	11,6	11,6	616											

Part 4

Vein type	A															
Fluid inclusion type	Type 1					Type 2						Type 3				
	Th	Tm(ice)	sal Bodnar (wt% equiv NaCl)	sal Steele–McInnis (wt% equiv NaCl)	P Steele–McInnis (bars)	Th	Th Steele–McInnis	Tm (hal)	sal Bodnar (wt% equiv NaCl)	sal Steele–McInnis (wt% equiv NaCl)	P Steele–McInnis (bars)	Th	Tm (ice)	sal Bodnar (wt% equiv NaCl)	sal Steele–McInnis (wt% equiv NaCl)	P Steele–McInnis (bars)
This study	320	–2	3,4	3,4	111	*>550*	*>550*	/	/	/	/	409	–5,95	9,1	9,1	291
	425	–1,4	2,4	2,4	366	*>550*	*>550*	/	/	/	/	419	–5,85	9,0	9,0	319
						>550	*>550*	/	/	/	/	381	–5,95	9,1	9,1	220
	372,5	#DIV/0!				*>550*	*>550*	/	/	/	/	386	–0,74	1,3	1,3	249
		#DIV/0!										378	–0,42	0,8	0,8	230
												376	–0,76	1,3	1,3	223
												487	–4,35	7,1	7,0	592
												470	–5,65	8,9	8,8	495
												490	–4,40	7,0	7,0	605
												>550	*–2,9*	/	*4,8*	/
												>550	*–2,1*	/	*3,5*	/
												>550	*–9,3*	/	*13,2*	/
												>550	*–2*	/	*3,4*	/
												>550	*–16,3*	/	*19,7*	/

Part 5

Caption:																	
	Fluid inclusion data																
		Fluid event															
		P1			*Reequilibrated fluid inclusion*												
		P2															
		E															
	Type 1	**Type 2**	**Type 3**														
Homogenization type	L–V–>L	L–V–H–>L	V–L–>V														

T_e the first melting temperature (eutectic)

T_m(ice) the ice melting temperature

T_m(hal) the dissolution temperature of halite

T_h (L+V→L) or T_h (L+V→V) the temperature of total homogenization

Steele Mc using Steele McInnis et al. 2012 spreadsheet

Bodnar using Bodnar 1993 formula

sal salinity

Table of analyses of fluid inclusion in B1-type vein.

Vein type		B1													
Fluid inclusion type		Type 1				Type 2						Type 3				
		Th	Tm(ice)	sal Bodnar (wt% equiv NaCl)	sal Steele–McInnis (wt% equiv NaCl)	P Steele–McInnis (bars)	Th	Th Steele–McInnis	Tm(hal)	sal Bodnar (wt% equiv NaCl)	sal Steele–McInnis (wt% equiv NaCl)	P Steele–McInnis (bars)	Th	Tm(ice)	sal Bodnar (wt% equiv NaCl)	sal Steele–McInnis (wt% equiv NaCl)	P Steele–McInnis (bars)
Fluid inclusion data from Voudouris et al. 2013a		310	–1,1	1,9	1,9	98	408	408	323	39,6	39,9	202	385	–4,5	7,2	7,2	233
		363	–6	9,2	9,2	181	415	415	317	39,1	39,4	215	370	–3,1	5,1	5,1	202
		380	–4,9	7,7	7,7	220	398	398	282	36,4	36,8	190	390	–6	9,2	9,2	241
		374	–4	6,5	6,4	208	432	432	291	37,1	37,4	250	394	–5,8	9,0	8,9	252
		398	–4,9	7,7	7,7	265							410	–4,6	7,3	7,3	299
		394	–4,8	7,6	7,6	255	*391*	*401*	*401*	*47,6*	*48,1*	*255*	400	–4,1	6,6	6,6	273
		378	–5,4	8,4	8,4	214	*393*	*401*	*401*	*47,6*	*48,1*	*237*	371	–3,8	6,2	6,2	202
		391	–5,6	8,7	8,7	245	*389*	*414*	*414*	*49,0*	*49,5*	*403*	394	–5,1	8,0	8,0	254
		384	–2,1	3,6	3,5	238	*394*	*411*	*411*	*46,8*	*49,2*	*330*	383	–4,7	7,5	7,4	228
		393	–3,6	5,9	5,9	256	*406*	*417*	*417*	*49,3*	*49,9*	*288*	409	–4,9	7,7	7,7	295
		405	–4,7	7,5	7,4	285	*394*	*410*	*410*	*48,5*	*49,0*	*320*	415	–5,7	8,8	8,8	309
		308	–1,4	2,4	2,4	95	*399*	*410*	*410*	*48,5*	*49,1*	*277*	401	–4	6,5	6,4	276
		374	–4	6,5	6,4	208	*407*	*421*	*421*	*49,8*	*50,3*	*319*	420	–4,9	7,7	7,7	327
		361	–3,7	6,0	6,0	181	*420*	*437*	*437*	*51,7*	*52,1*	*367*	414	–4,9	7,7	7,7	310
		391	–5,4	8,4	8,4	246	*371*	*469*	*469*	*55,3*	*55,3*	*1213*	387	–4,1	6,6	6,6	239
		366	–4,1	6,6	6,6	191	*389*	*449*	*449*	*52,9*	*53,3*	*743*	407	–3,5	5,7	5,7	295

Part 2

Vein type	B1															
Fluid inclusion type	Type 1					Type 2						Type 3				
	Th	Tm(ice)	sal Bodnar (wt% equiv NaCl)	sal Steele–McInnis (wt% equiv NaCl)	P Steele–McInnis (bars)	Th	Th Steele–McInnis	Tm(hal)	sal Bodnar (wt% equiv NaCl)	sal Steele–McInnis (wt% equiv NaCl)	P Steele–McInnis (bars)	Th	Tm(ice)	sal Bodnar (wt% equiv NaCl)	sal Steele–McInnis (wt% equiv NaCl)	P Steele–McInnis (bars)
Fluid inclusion data from Voudouris et al. 2013a	381	–4,6	7,3	7,3	223	*398*	*474*	*474*	*56,1*	*56,1*	*919*	394	–2,8	4,7	4,6	262
	408	–5,7	8,8	8,8	289	*385*	*456*	*456*	*53,8*	*54,0*	*860*	394	–4	6,5	6,4	258
	394	–4,1	6,6	6,6	257	*399*	*479*	*479*	*56,7*	*56,6*	*966*	412	–3,6	5,9	5,9	310
	359	–3,7	6,0	6,0	177	*381*	*467*	*467*	*55,1*	*55,2*	*1041*	398	–3,5	5,7	5,7	270
	398	–4,3	6,9	6,9	267	*390*	*450*	*450*	*53,1*	*53,4*	*744*	414	–2,9	4,8	4,8	320
	371	–4	6,5	6,4	202	*389*	*466*	*466*	*55,0*	*55,1*	*929*	371	–4,5	7,2	7,2	201
	382	–5,2	8,1	8,1	224	*399*	*470*	*470*	*55,6*	*55,6*	*862*	379	–4,4	7,0	7,0	219
	317	–1,2	2,1	2,1	107	*361*	*465*	*465*	*54,7*	*54,8*	*1316*	391	–4,7	7,5	7,4	248
	380	–4,9	7,7	7,7	220	*374*	*478*	*478*	*56,4*	*56,3*	*1304*	411	–3,7	6,0	6,0	306
	366	–3,9	6,3	6,3	191	*409*	*480*	*480*	*56,9*	*56,8*	*868*	381	–3,9	6,3	6,3	225
	381	–5	7,9	7,9	222	*391*	*444*	*444*	*52,3*	*52,7*	*674*	391	–4,6	7,3	7,3	248
	364	–4,7	7,5	7,4	185	*389*	*465*	*465*	*54,9*	*55,0*	*917*	407	–5,7	8,8	8,8	286
	379	–3,8	6,2	6,2	221	*402*	*448*	*448*	*53,0*	*53,2*	*613*	410	–4,6	7,3	7,3	299
	319	–2	3,4	3,4	109	*394*	*435*	*435*	*51,4*	*51,8*	*560*	400	–3,7	6,0	6,0	275
	397	–6	9,2	9,2	259	*409*	*497*	*497*	*59,1*	*58,7*	*1076*	367	–3,5	5,7	5,7	194
	401	–4,2	6,7	6,7	276	*384*	*449*	*449*	*52,9*	*53,3*	*795*	371	–4,4	7,0	7,0	201
	411	–5,3	8,3	8,3	299	*374*	*450*	*450*	*53,0*	*53,3*	*921*	428	–4,1	6,6	6,6	357
	384	–4,8	7,6	7,6	230							376	–5,6	8,7	8,7	209
	397	–4,4	7,0	7,0	264							384	–4,1	6,6	6,6	232
	374	–3,3	5,4	5,4	210							366	–3,9	6,3	6,3	191
	357	–3,6	5,9	5,9	173							408	–5,2	8,1	8,1	291
	369	–4	6,5	6,4	197							371	–3,7	6,0	6,0	202
	385	–5,4	8,4	8,4	231							387	–5,1	8,0	8,0	236
	379	–5,3	8,3	8,3	217							395	–6	9,2	9,2	254
	387	–6	9,2	9,2	234							397	–5,9	9,1	9,1	259

Part 3

Vein type	B1														
Fluid inclusion type	Type 1					Type 2						Type 3				
	Th	Tm(ice)	sal Bodnar (wt% equiv NaCl)	sal Steele–McInnis (wt% equiv NaCl)	P Steele–McInnis (bars)	Th	Th Steele–McInnis	Tm(hal)	sal Bodnar (wt% equiv NaCl)	sal Steele–McInnis (wt% equiv NaCl)	P Steele–McInnis (bars)	Th	Tm(ice)	sal Bodnar (wt% equiv NaCl)	sal Steele–McInnis (wt% equiv NaCl)	P Steele–McInnis (bars)
Fluid inclusion data from Voudouris et al. 2013a	395	–5,6	8,7	8,7	255							399	–6	9,2	9,2	264
	247	–1	1,7	1,7	37							406	–5,1	8,0	8,0	286
	227	–1,2	2,1	2,1	26							411	–5,8	9,0	8,9	297
	367	–3,3	5,4	5,4	194											
	373	–4,4	7,0	7,0	205											
	379	–5,5	8,6	8,5	216											
	399	–3,7	6,0	6,0	272											
	372	–4,6	7,3	7,3	203											
	285	–1,9	3,2	3,2	68											
	297	–2,3	3,9	3,9	80											
	271	–1,7	2,9	2,9	55											
	273	–1,9	3,2	3,2	56											
	396	–4	6,5	6,4	263											
	401	–4,4	7,0	7,0	275											
	361	–2,4	4,0	4,0	183											
	388	–3,1	5,1	5,1	245											
	383	–4,2	6,7	6,7	229											
	381	–5,1	8,0	8,0	222											
	406	–3,9	6,3	6,3	291											
	378	–4,9	7,7	7,7	216											
	271	–1,6	2,7	2,7	55											
	309	–2,1	3,6	3,5	95											
	266	–1,2	2,1	2,1	51											
	273	–1,4	2,4	2,4	57											
	389	–4,2	6,7	6,7	244											

Part 4

Vein type	B1															
Fluid inclusion type	Type 1					Type 2						Type 3				
	Th	Tm(ice)	sal Bodnar (wt% equiv NaCl)	sal Steele–McInnis (wt% equiv NaCl)	P Steele–McInnis (bars)	Th	Th Steele–McInnis	Tm(hal)	sal Bodnar (wt% equiv NaCl)	sal Steele–McInnis (wt% equiv NaCl)	P Steele–McInnis (bars)	Th	Tm(ice)	sal Bodnar (wt% equiv NaCl)	sal Steele–McInnis (wt% equiv NaCl)	P Steele–McInnis (bars)
Fluid inclusion data from Voudouris et al. 2013a	393	–4,6	7,3	7,3	253											
	375	–4,3	6,9	6,9	210											
	383	–4,6	7,3	7,3	228											
	385	–5,4	8,4	8,4	231											
	291	–1,1	1,9	1,9	74											
	297	–1,8	3,1	3,1	81											
	322	–1,2	2,1	2,1	115											
	330	–2,5	4,2	4,2	126											
	405	–3,8	6,2	6,2	288											
	374	–4	6,5	6,4	208											
	380	–5,7	8,8	8,8	218											
	392	–5,4	8,4	8,4	248											
	395	–5,7	8,8	8,8	255											
	431	–4,1	6,6	6,6	367											
	399	–4	6,5	6,4	271											
	410	–4,8	7,6	7,6	298											
	369	–3,9	6,3	6,3	198											
	418	–5,5	8,6	8,5	319											
	399	–5,7	8,8	8,8	265											
	354	–3,9	6,3	6,3	166											
	349	–3,1	5,1	5,1	158											
	411	–5,9	9,1	9,1	297											
	415	–4	6,5	6,4	317											
	421	–3,8	6,2	6,2	336											
	387	–3,7	6,0	6,0	241											

Part 6

Vein type	B1															
Fluid inclusion type	Type 1					Type 2						Type 3				
	Th	Tm(ice)	sal Bodnar (wt% equiv NaCl)	sal Steele–McInnis (wt% equiv NaCl)	P Steele–McInnis (bars)	Th	Th Steele–McInnis	Tm(hal)	sal Bodnar (wt% equiv NaCl)	sal Steele–McInnis (wt% equiv NaCl)	P Steele–McInnis (bars)	Th	Tm(ice)	sal Bodnar (wt% equiv NaCl)	sal Steele–McInnis (wt% equiv NaCl)	P Steele–McInnis (bars)
Fluid inclusion data from Voudouris et al. 2013a	394	–4,4	7,0	7,0	256											
	305	–1,9	3,2	3,2	90											
	356	–3,9	6,3	6,3	170											
	361	–4,2	6,6	6,7	180											
	368	–4,8	7,6	7,6	193											
	379	–5,4	8,4	8,4	217											
	385	–3,1	5,1	5,1	237											
	376	–4,1	6,6	6,6	213											
	214	–2,8	4,7	4,6	20											
	394	–4,4	7,0	7,0	256											
	422	–4,2	6,7	6,7	337											
	410	–3,7	6,0	6,0	303											
	454	–6,6	10,0	10,0	426											
	468	–6,5	9,9	9,9	477											
	487	–6,9	10,4	10,4	547											
	402	–3,4	5,6	5,6	282											
	392	–1,6	2,7	2,7	261											
	396	–5,7	8,8	8,8	257											
	402	–4,2	6,7	6,7	278											
	411	–4,9	7,7	7,7	301											
	418	–4,5	7,2	7,2	323											
	405	–4,1	6,6	6,6	287											
	425	–5,8	9,0	8,9	338											
	389	–5,3	8,3	8,3	241											
	419	–2,4	4,0	4,0	338											

Part 7

Vein type	B1															
Fluid inclusion type	Type 1					Type 2						Type 3				
	Th	Tm(ice)	sal Bodnar (wt% equiv NaCl)	sal Steele–McInnis (wt% equiv NaCl)	P Steele–McInnis (bars)	Th	Th Steele–McInnis	Tm(hal)	sal Bodnar (wt% equiv NaCl)	sal Steele–McInnis (wt% equiv NaCl)	P Steele–McInnis (bars)	Th	Tm(ice)	sal Bodnar (wt% equiv NaCl)	sal Steele–McInnis (wt% equiv NaCl)	P Steele–McInnis (bars)
Fluid inclusion data from Voudouris et al. 2013a	419	–4,7	7,5	7,4	325											
	406	–1,6	2,7	2,7	302											
	400	–4,6	7,3	7,3	271											
	390	–3,3	5,4	5,4	250											
	395	–5,2	8,1	8,1	256											

Part 8

Vein type	B1														
Fluid inclusion type	Type 1					Type 2						Type 3				
	Th	Tm(ice)	sal Bodnar (wt% equiv NaCl)	sal Steele–McInnis (wt% equiv NaCl)	P Steele–McInnis (bars)	Th	Th Steele–McInnis	Tm(hal)	sal Bodnar (wt% equiv NaCl)	sal Steele–McInnis (wt% equiv NaCl)	P Steele–McInnis (bars)	Th	Tm(ice)	sal Bodnar (wt% equiv NaCl)	sal Steele–McInnis (wt% equiv NaCl)	P Steele–McInnis (bars)
This study	301	–4,64222614840989	7,4	7,4	83	418		287	37,1	37,1	225	389	–6,30491877256317	9,6	9,6	237
	125	–0,620318021201413	1,1	1,1	2	427		288	37,2	37,2	241	398	–4,12554151624548	6,6	6,6	267
	287	–4,54646643109541	7,2	7,2	68	424		274	36,2	36,2	238	386	–3,8908393501805	6,3	6,3	236
						436		279	36,5	36,5	260					
						>550	*>550*	/	/	/	/					
						>550	*>550*	/	/	/	/					
						>550	*>550*	/	/	/	/					
						>550	*>550*	/	/	/	/					
						>550	*>550*	/	/	/	/					
						>550	*>550*	/	/	/	/					
						>550	*>550*	/	/	/	/					

Part 9

Caption:																
	Fluid inclusion data															
		Fluid event								T_e the first melting temperature (eutectic)						
		P1			*Reequilibrated fluid inclusion*					T_m(ice) the ice melting temperature						
		P2								T_m(hal) the dissolution temperature of halite						
		E								T_h (L+V→L) or T_h (L+V→V) the temperature of total homogenization						
										Steele Mc	using Steele McInnis et al. 2012 spreadsheet					
	Type 1	**Type 2**	**Type 3**							Bodnar	using Bodnar 1993 formula					
Homogenization type	L–V–>L	L–V–H–>L	V–L–>V							sal	salinity					
Pressure	pressure	pressure	pressure	pressure	pressure	pressure	pressure	pressure	pressure	pressure	pressure					

Table of analyses of fluid inclusion in E1- and E2-type veins.

Vein type	E1					E2				
Fluid inclusion type	Type 1					Type 1				
	Th	Tm(ice)	sal Bodnar (wt% equiv NaCl)	sal Steele–McInnis (wt% equiv NaCl)	P Steele–McInnis (bars)	Th	Tm(ice)	sal Bodnar (wt% equiv NaCl)	sal Steele–McInnis (wt% equiv NaCl)	P Steele–McInnis (bars)
Fluid inclusion data from Voudouris et al. 2013a	269	–1,3	2,2	2,2	53	263	-1,0	1,74	1,7	48
	249	–1,7	2,9	2,9	38	239	-1,5	2,57	2,6	32
	254	–1,1	1,9	1,9	42	255	-1,2	2,07	2,1	42
	261	–1,2	2,1	2,1	47	259	-1,7	2,90	2,9	45
	245	–1,4	2,4	2,4	36	260	-0,8	1,40	1,4	46
	247	–0,9	1,6	1,6	37	261	-1,1	1,90	1,9	47
	231	–1,5	2,6	2,6	28	245	-1,4	2,41	2,4	36
	245	–1,6	2,7	2,7	36	249	-0,9	1,57	1,6	38
	239	–1,7	2,9	2,9	32	254	-1,2	2,07	2,1	42
	258	–0,8	1,4	1,4	45	257	-1,0	1,74	1,7	44
	331	–1,4	2,4	2,4	129	258	-1,4	2,41	2,4	44
	219	–1,6	2,7	2,7	22	277	-0,9	1,57	1,6	60
	224	–0,6	1,1	1,1	25	265	-1,3	2,24	2,2	50
	264	–0,9	1,6	1,6	49	264	-1,5	2,57	2,6	49
	269	–1	1,7	1,7	53	271	-1,6	2,74	2,7	55
	247	–0,9	1,6	1,6	37	269	-1,2	2,07	2,1	53

Part 2

Vein type	E1					E2				
Fluid inclusion type	Type 1					Type 1				
	Th	Tm(ice)	sal Bodnar (wt% equiv NaCl)	sal Steele–McInnis (wt% equiv NaCl)	P Steele–McInnis (bars)	Th	Tm(ice)	sal Bodnar (wt% equiv NaCl)	sal Steele–McInnis (wt% equiv NaCl)	P Steele–McInnis (bars)
Fluid inclusion data from Voudouris et al. 2013a	231	–1,1	1,9	1,9	28	273	-0,9	1,57	1,6	57
	254	–1,2	2,1	2,1	42					
	227	–0,8	1,4	1,4	26					
	322	–1,3	2,2	2,2	115					
	334	–1,5	2,6	2,6	134					
	319	–1,2	2,1	2,1	110					
	320	–1	1,7	1,7	112					
	284	–0,9	1,6	1,6	67					
	230	–0,7	1,2	1,2	28					
	224	–1,1	1,9	1,9	25					
	257	–1,5	2,6	2,6	44					
	284	–1	1,7	1,7	67					
	310	–1,4	2,4	2,4	97					
Vein type	E1					E2				
Fluid inclusion type	Type 1					Type 1				
	Th	Tm(ice)	sal Bodnar (wt% equiv NaCl)	sal Steele–McInnis (wt% equiv NaCl)	P Steele–McInnis (bars)	Th	Tm(ice)	sal Bodnar (wt% equiv NaCl)	sal Steele–McInnis (wt% equiv NaCl)	P Steele–McInnis (bars)
This study	/	–0,7	/	1,2	/					
	/	–0,8	/	1,4	/					

Part 3

Caption:																
	Fluid inclusion data															
		Fluid event								T_e the first melting temperature (eutectic)						
		P1			*Reequilibrated fluid inclusion*					T_m(ice) the ice melting temperature						
		P2								T_m(hal) the dissolution temperature of halite						
		E								T_h (L+V→L) or T_h (L+V→V) the temperature of total homogenization						
										Steele Mc	using Steele McInnis et al. 2012 spreadsheet					
	Type 1	**Type 2**	**Type 3**							Bodnar	using Bodnar 1993 formula					
Homogenization type	L–V–>L	L–V–H–>L	V–L–>V							sal	salinity					
Pressure	pressure	pressure	pressure	pressure	pressure	pressure	pressure	pressure	pressure	pressure	pressure					

Tableau des valeurs de températures utilisées pour le calcul du coefficient de fractionnement isotopique et coefficient de fractionnement isotopiques associés.

	EXTREMA T (C°)			*EXTREMA Coefficient de fractionnement / ‰*					
Type de veines	*MIN*	*MAX*		*MIN T*	*MAX T*	Isotope	*Références*	Equilibre	
A	457	510	*From Voudouris et al. 2013a and Abiven et al. Submitted*	3,58	3,20	Oxygène	*Zheng 1993a*	qz<=>H20	1000 lnα=4.48(10^6/T^2)−4.77(10^3/T)+1.71
B1	366	398	*From Voudouris et al. 2013a and Abiven et al. Submitted*	5,21	4,55	Oxygène	*Zheng 1993a*	qz<=>H20	1000 lnα=4.48(10^6/T^2)−4.77(10^3/T)+1.71
B2	220	350	*From similar veins of Maricunga Belt, called "banded veins" (by Muntean and Einaudi, 2000)*	10,46	5,59	Oxygène	*Zheng 1993a*	qz<=>H20	1000 lnα=4.48(10^6/T^2)−4.77(10^3/T)+1.71
E1	219	334	*From Voudouris et al. 2013a and Abiven et al. Submitted*	10,51	6,01	Oxygène	*Zheng 1993a*	qz<=>H20	1000 lnα=4.48(10^6/T^2)−4.77(10^3/T)+1.71
E2	239	277	*From Voudouris et al. 2013a*	7.91	6.5	Oxygène	*Zheng 1999*	cal<=>H20	1000 lnα=4,01*(10^6/T^2)-4,66*(10^3/T)+1,71
E2	239	277	*From Voudouris et al. 2013a*	9.58	9.1	Oxygène	*Zheng 1999*	cal<=>C02	1000 $ln\alpha$ = - 1.71 × (106 / T2) + 10.01 × (103 / T) – 3.45
E2	239	277	*From Voudouris et al. 2013a*	- 0.87	- 1,39	Carbone	*Golyshev et al., 1981*	cal<=>C02	1000 lnα =0.05855*(10^18/T^6)−4.09568*(10^12/T^4)+20.76421* (10^9/T^3)−35.8984*(10^6/T^2)+19.1975*(10^3/T)+0.2204

Températures en Kelvin

Tableau de valeurs du $\delta^{18}O$ dans les veines de type A.

Type de veines	Nom échantillon	N° analyse	N° analyse planche photo	CL intensité	δ18Oquartz	2σ	δ18OH20 min	δ18OH2O max
A	MB0201	1	1		10,8	0,3	7,2	7,6
A	MB0201	2	2		10,3	0,3	6,7	7,1
A	MB0201	3	3		10,0	0,3	6,5	6,8
A	MB0201	4	4		10,4	0,3	6,8	7,2
A	MB0201	5	5		8,5	0,4	4,9	5,3
A	MB0201	6	6		7,8	0,5	4,2	4,6
A	MB0201	7	7		7,4	0,5	3,8	4,2
A	MB0201	8	8		7,1	0,5	3,5	3,9
A	MB0201	9	9		7,5	0,5	3,9	4,3
A	MB0201	10	10		10,5	0,3	6,9	7,3
A	MB0201	11	11		10,4	0,3	6,9	7,2
A	MB0201	12	12		10,2	0,3	6,6	7,0
A	MB0201	13	13		10,3	0,3	6,8	7,1
A	MB0201	14	14		9,9	0,3	6,4	6,7
A	MB0201	15	15		10,1	0,3	6,5	6,9
A	MB0201	16	16		10,0	0,3	6,4	6,8
A	MB0201	17	17		10,1	0,3	6,6	6,9
A	MB0201	18	18		10,2	0,3	6,7	7,0
A	MB0201	19	19		10,1	0,3	6,5	6,9
A	MB0201	20	20		10,4	0,3	6,8	7,2
A	MB0201	21	21		9,9	0,3	6,4	6,7
A	MB0201	22	22		10,4	0,3	6,8	7,2
A	MB0201	23	23		10,4	0,3	6,8	7,2
A	MB0201	24	24		9,9	0,3	6,3	6,7
A	MB0201	25	25		9,8	0,4	6,3	6,6
A	MB0201	26	26		9,4	0,3	5,8	6,2
A	MB0201	27	27		9,8	0,3	6,2	6,6
A	MB0201	28	28		9,5	0,3	5,9	6,3
A	MB0201	29	29		9,8	0,3	6,3	6,6
A	MB0201	30	30		9,8	0,3	6,2	6,6
A	MB0201	31	31		9,8	0,3	6,2	6,6
A	MB0201	32	32		8,6	0,3	5,0	5,4
A	MB0201	33	33		8,1	0,3	4,5	4,9
A	MB0201	34	34		9,8	0,3	6,3	6,6
A	MB0201	35	35		9,5	0,3	5,9	6,3
A	MB0201	36	36		9,5	0,3	5,9	6,3
A	MB0201	37	37		9,9	0,3	6,3	6,7
A	MB0201	38	38		9,2	0,3	5,6	6,0
A	MB0201	39	39		9,9	0,3	6,3	6,7
A	MB0201	40	40		9,9	0,3	6,3	6,7

Partie 2

Type de veines	Nom échantillon	N° analyse	N° analyse planche photo	CL intensité	δ18Oquartz	2σ	δ18OH20 min	δ18OH2O max
A	MB0201	41	41		9,4	0,3	5,9	6,2
A	MB0201	42	42		9,4	0,3	5,8	6,2
A	MB0201	43	43		9,7	0,3	6,1	6,5
A	MB0201	44	44		9,7	0,3	6,1	6,5
A	MB0201	45	45		9,9	0,3	6,3	6,7
A	MB0201	46	46		9,7	0,3	6,1	6,5
A	MB0201	47	47		9,4	0,3	5,8	6,2
A	MB0201	48	48		9,2	0,3	5,6	6,0
A	MB0201	49	49		10,0	0,3	6,4	6,8
A	MB0201	50	50		10,4	0,3	6,9	7,2
A	MB0201	51	51		10,4	0,3	6,9	7,2
A	MB0201	52	52		9,9	0,3	6,3	6,7
A	MB0201	53	53		9,8	0,4	6,2	6,6
A	MB0201	54	54		9,5	0,3	5,9	6,3
A	MB0201	55	55		9,6	0,3	6,0	6,4
A	MB0201	56	56		10,1	0,3	6,5	6,9
A	MB0202	1	57		11,5	0,3	7,9	8,3
A	MB0202	2	58		11,6	0,2	8,1	8,4
A	MB0202	3	59		11,4	0,2	7,8	8,2
A	MB0202	4	60		11,5	0,2	7,9	8,3
A	MB0202	5	61		11,1	0,2	7,5	7,9
A	MB0202	6	62		11,2	0,3	7,6	8,0
A	MB0202	6	63		11,2	0,3	7,6	8,0
A	MB0202	7	64		11,1	0,3	7,5	7,9
A	MB0202	8	65		11,2	0,2	7,6	8,0
A	MB0202	9	66		11,0	0,3	7,4	7,8
A	MB0202	10	67		11,0	0,2	7,5	7,8
A	MB0202	11	68		11,0	0,3	7,4	7,8
A	MB0202	12	69		10,9	0,2	7,3	7,7

Tableau de valeurs du $\delta^{18}O$ dans les veines de type B1.

Type de veines	Nom échantillon	N° analyse	N° analyse planche photo	CL intensité	δ18Oquartz	2σ	δ18OH20 min	δ18OH2O max
B1	MB0201	1	1		10,9	0,3	5,6	6,3
B1	MB0201	2	2		11,3	0,3	6,1	6,8
B1	MB0201	3	3		9,9	0,3	4,7	5,4
B1	MB0201	4	4		10,0	0,3	4,8	5,5
B1	MB0201	5	5		10,0	0,3	4,7	5,4
B1	MB0201	6	6		9,8	0,3	4,6	5,3
B1	MB0201	7	7		10,0	0,3	4,7	5,4
B1	MB0201	8	8		10,0	0,3	4,8	5,5
B1	MB0201	9	9		9,9	0,3	4,7	5,3
B1	MB0201	10	10		9,8	0,3	4,6	5,3
B1	MB0201	11	11		9,8	0,3	4,6	5,3
B1	MB0201	12	12		9,3	0,3	4,0	4,7
B1	MB0201	13	13		10,0	0,3	4,8	5,5
B1	MB0201	14	14		9,8	0,3	4,6	5,3
B1	MB0201	15	15		9,4	0,3	4,2	4,9
B1	MB0201	16	16		9,5	0,3	4,3	4,9
B1	MB0201	17	17		9,7	0,3	4,4	5,1
B1	MB0201	18	18		10,3	0,3	5,0	5,7
B1	MB0201	19	19		10,0	0,3	4,8	5,5
B1	MB0201	20	20		10,1	0,3	4,9	5,6
B1	MB0201	21	21		10,2	0,3	4,9	5,6
B1	MB0201	22	22		10,0	0,3	4,8	5,5
B1	MB0201	23	23		9,7	0,3	4,5	5,2
B1	MB0201	24	24		9,7	0,3	4,5	5,1
B1	MB0201	25	25		10,1	0,3	4,9	5,5
B1	MB0201	26	26		9,8	0,3	4,5	5,2
B1	MB0201	27	27		9,5	0,3	4,3	5,0
B1	MB0202	28	1		11,7	0,3	6,5	7,2
B1	MB0202	29	2		11,1	0,3	5,9	6,6
B1	MB0202	30	3		10,8	0,3	5,6	6,2
B1	MB0202	31	4		10,8	0,3	5,6	6,2
B1	MB0202	32	5		10,7	0,2	5,5	6,2
B1	MB0202	33	6		10,6	0,2	5,4	6,0
B1	MB0202	34	7		10,5	0,2	5,3	5,9
B1	MB0202	35	8		10,4	0,2	5,2	5,8
B1	MB0202	36	9		10,4	0,3	5,2	5,8
B1	MB0202	37	10		10,8	0,3	5,6	6,2
B1	MB0202	38	11		10,9	0,3	5,7	6,4
B1	AB.120.01	39	1		9,4	0,2	4,2	4,8
B1	AB.120.01	40	2		9,5	0,2	4,3	4,9

Partie 2

Type de veines	Nom échantillon	N° analyse	N° analyse planche photo	CL intensité	δ18Oquartz	2σ	δ18OH20 min	δ18OH2O max
B1	MB0201	1	1		10,9	0,3	5,6	6,3
B1	MB0201	2	2		11,3	0,3	6,1	6,8
B1	MB0201	3	3		9,9	0,3	4,7	5,4
B1	MB0201	4	4		10,0	0,3	4,8	5,5
B1	MB0201	5	5		10,0	0,3	4,7	5,4
B1	MB0201	6	6		9,8	0,3	4,6	5,3
B1	MB0201	7	7		10,0	0,3	4,7	5,4
B1	MB0201	8	8		10,0	0,3	4,8	5,5
B1	MB0201	9	9		9,9	0,3	4,7	5,3
B1	MB0201	10	10		9,8	0,3	4,6	5,3
B1	MB0201	11	11		9,8	0,3	4,6	5,3
B1	MB0201	12	12		9,3	0,3	4,0	4,7
B1	MB0201	13	13		10,0	0,3	4,8	5,5
B1	MB0201	14	14		9,8	0,3	4,6	5,3
B1	MB0201	15	15		9,4	0,3	4,2	4,9
B1	MB0201	16	16		9,5	0,3	4,3	4,9
B1	MB0201	17	17		9,7	0,3	4,4	5,1
B1	MB0201	18	18		10,3	0,3	5,0	5,7
B1	MB0201	19	19		10,0	0,3	4,8	5,5
B1	MB0201	20	20		10,1	0,3	4,9	5,6
B1	MB0201	21	21		10,2	0,3	4,9	5,6
B1	MB0201	22	22		10,0	0,3	4,8	5,5
B1	MB0201	23	23		9,7	0,3	4,5	5,2
B1	MB0201	24	24		9,7	0,3	4,5	5,1
B1	MB0201	25	25		10,1	0,3	4,9	5,5
B1	MB0201	26	26		9,8	0,3	4,5	5,2
B1	MB0201	27	27		9,5	0,3	4,3	5,0
B1	MB0202	28	1		11,7	0,3	6,5	7,2
B1	MB0202	29	2		11,1	0,3	5,9	6,6
B1	MB0202	30	3		10,8	0,3	5,6	6,2
B1	MB0202	31	4		10,8	0,3	5,6	6,2
B1	MB0202	32	5		10,7	0,2	5,5	6,2
B1	MB0202	33	6		10,6	0,2	5,4	6,0
B1	MB0202	34	7		10,5	0,2	5,3	5,9
B1	MB0202	35	8		10,4	0,2	5,2	5,8
B1	MB0202	36	9		10,4	0,3	5,2	5,8
B1	MB0202	37	10		10,8	0,3	5,6	6,2
B1	MB0202	38	11		10,9	0,3	5,7	6,4
B1	AB.120.01	39	1		9,4	0,2	4,2	4,8
B1	AB.120.01	40	2		9,5	0,2	4,3	4,9
B1	AB.120.01	41	3		8,9	0,2	3,7	4,4
B1	AB.120.01	42	4		9,4	0,2	4,2	4,9

Partie 3

Type de veines	Nom échantillon	N° analyse	N° analyse planche photo	CL intensité	δ18Oquartz	2σ	δ18OH20 min	δ18OH2O max
B1	AB.120.01	43	5		10,4	0,2	5,2	5,9
B1	AB.120.01	44	6		9,9	0,2	4,7	5,3
B1	AB.120.01	45	7		10,1	0,2	4,8	5,5
B1	AB.120.01	46	8		9,9	0,2	4,7	5,4
B1	AB.120.01	47	9		10,0	0,2	4,8	5,5
B1	AB.120.01	48	10		9,6	0,2	4,4	5,1
B1	AB.120.01	49	11		9,9	0,2	4,7	5,3
B1	AB.120.01	50	12		10,0	0,2	4,8	5,4
B1	AB.120.01	51	13		9,7	0,2	4,5	5,2
B1	AB.120.01	52	14		9,2	0,2	4,0	4,7
B1	AB.120.01	53	15		9,6	0,2	4,4	5,0
B1	AB.120.01	54	16		10,0	0,2	4,8	5,5
B1	AB.120.01	55	17		9,2	0,2	4,0	4,6
B1	AB.120.01	56	18		9,4	0,2	4,2	4,8
B1	AB.120.01	57	19		9,0	0,2	3,8	4,5
B1	AB.120.01	58	20		10,7	0,2	5,5	6,1
B1	AB.120.01	59	21		9,1	0,2	3,9	4,6
B1	AB.120.01	60	22		9,2	0,2	3,9	4,6
B1	AB.120.01	61	23		8,5	0,2	3,3	3,9
B1	AB.120.01	62	24		9,6	0,2	4,4	5,0
B1	AB.120.01	63	25		9,1	0,2	3,8	4,5
B1	AB.120.01	64	26		9,5	0,2	4,2	4,9
B1	AB.120.01	65	27		9,5	0,2	4,3	4,9
B1	AB.120.01	66	28		9,7	0,2	4,5	5,1
B1	AB.120.01	67	29		9,2	0,2	4,0	4,6
B1	AB.120.01	68	30		9,4	0,2	4,2	4,9
B1	AB.120.01	69	31		9,1	0,2	3,8	4,5
B1	AB.120.01	70	32		9,6	0,2	4,3	5,0
B1	AB.120.01	71	33		9,6	0,2	4,3	5,0
B1	AB.120.01	72	34		10,0	0,2	4,8	5,5
B1	AB.120.01	73	35		9,4	0,2	4,2	4,8
B1	AB.120.01	74	36		10,0	0,2	4,8	5,5
B1	AB.120.01	75	37		9,2	0,2	3,9	4,6
B1	AB.120.01	76	38		9,3	0,2	4,1	4,8
B1	AB.120.01	77	39		9,4	0,2	4,1	4,8
B1	AB.120.01	78	40		9,8	0,2	4,6	5,2
B1	AB.120.01	79	41		9,8	0,2	4,6	5,3
B1	AB.120.01	80	42		9,9	0,2	4,7	5,4
B1	AB.120.01	81	43		10,0	0,2	4,8	5,5
B1	AB.120.01	82	44		10,1	0,2	4,9	5,5
B1	AB.120.01	83	45		9,9	0,2	4,7	5,4
B1	AB.120.01	84	46		10,0	0,2	4,8	5,5

Partie 4

Type de veines	Nom échantillon	N° analyse	N° analyse planche photo	CL intensité	δ18Oquartz	2σ	δ18OH20 min	δ18OH2O max
B1	AB.120.01	85	47		9,9	0,2	4,7	5,4
B1	AB.120.01	86	48		9,6	0,2	4,4	5,0
B1	AB.120.01	87	49		9,7	0,2	4,5	5,1
B1	AB.120.01	88	50		10,5	0,2	5,3	5,9

Tableau de valeurs du $\delta^{18}O$ dans les veines de type B2.

Type de veines	Nom échantillon	N° analyse	CL intensité	δ18Oqtz	2σ	δ18OH20 min	δ18OH2O max
B2	AB119.02	1		9,4	0,2	- 1,1	3,8
B2	AB119.02	2		8,4	0,2	- 2,1	2,8
B2	AB119.02	3		8,3	0,2	- 2,1	2,7
B2	AB119.02	4		9,9	0,2	- 0,6	4,3
B2	AB119.02	5		11,7	0,2	1,3	6,2
B2	AB119.02	6		12,5	0,2	2,1	7,0
B2	AB119.02	7		9,6	0,2	- 0,8	4,0
B2	AB119.02	8		8,8	0,2	- 1,7	3,2
B2	AB119.02	9		7,9	0,2	- 2,5	2,3
B2	AB119.02	10		8,1	0,2	- 2,4	2,5
B2	AB119.02	11		8,9	0,2	- 1,6	3,3
B2	AB119.02	12		7,6	0,2	- 2,9	2,0
B2	AB119.02	13		8,3	0,2	- 2,2	2,7
B2	AB119.02	14		9,3	0,2	- 1,2	3,7

Tableau de valeurs du $\delta^{18}O$ dans les veines de type E1.

Type de veines	Nom échantillon	N° analyse	N° analyse planche photo	δ18Oquartz	2σ	δ18OH20 min	δ18OH2O max
E1	MB110201	1	1	12,7	0,2	2,2	6,7
E1	MB110201	2	2	9,7	0,2	- 0,8	3,7
E1	MB110201	3	3	8,3	0,2	- 2,2	2,3
E1	MB110201	4	4	8,4	0,2	- 2,1	2,4
E1	MB110201	5	5	9,0	0,2	- 1,5	3,0
E1	MB110201	6	6	8,9	0,2	- 1,6	2,9
E1	MB110201	7	7	9,9	0,2	- 0,6	3,9
E1	MB110201	8	8	10,0	0,2	- 0,6	3,9
E1	AB122.03	9	1	11,4	0,3	0,9	5,4
E1	AB122.03	10	2	11,5	0,4	1,0	5,5
E1	AB122.03	11	3	11,7	0,3	1,2	5,7
E1	AB122.03	12	4	8,1	0,3	- 2,4	2,1
E1	AB122.03	13	5	7,8	0,3	- 2,7	1,8
E1	AB122.03	14	6	8,4	0,4	- 2,1	2,4
E1	AB122.03	15	7	7,0	0,3	- 3,5	1,0
E1	AB122.03	16	8	8,2	0,3	- 2,3	2,2
E1	AB122.03	17	9	9,0	0,3	- 1,5	3,0
E1	AB122.03	18	10	8,8	0,3	- 1,7	2,8
E1	AB122.03	19	11	8,8	0,3	- 1,7	2,8
E1	AB122.03	20	12	8,4	0,3	- 2,1	2,4
E1	AB122.03	21	13	11,8	0,4	1,3	5,8
E1	AB122.03	22	14	12,2	0,3	1,7	6,2
E1	AB122.03	23	15	9,2	0,3	- 1,3	3,2
E1	AB122.03	24	16	7,9	0,3	- 2,6	1,9
E1	AB122.03	25	17	10,0	0,3	- 0,6	4,0
E1	AB122.03	26	18	9,7	0,3	- 0,8	3,7
E1	AB122.03	27	19	8,1	0,3	- 2,4	2,1
E1	AB122.03	28	20	9,6	0,3	- 0,9	3,6

Tableau de valeurs du $\delta^{18}O$ dans les veines de type E2.

Type de veines	Nom échantillon	N° analyse	N° analyse planche photo	δ18Ocal	2σ(cal)	δ18H2O min	δ18OH20 max	δ18CO2 min	δ18CCO2 max	
E2 Cal2	AB122.01	1	1	5,48	0,38	-2,4	-0,3	-4,1	-3,3	
E2 Cal2	AB122.01	2	2	3,00	0,38	-4,9	-2,8	-6,6	-5,8	
E2 Cal3	AB122.01	3	3	6,43	0,37	-1,5	0,6	-3,1	-2,4	
E2 Cal3	AB122.01	4	4	5,66	0,38	-2,3	-0,2	-3,9	-3,2	
E2 Cal3	AB122.01	5	5	- 5,50	0,86	-13,4	-11,3	-15,1	-14,3	
E2 Cal3	AB122.01	6	6	4,36	0,38	-3,5	-1,5	-5,2	-4,5	
E2 Cal3	AB122.01	7	7	1,06	0,73	-6,8	-4,8	-8,5	-7,8	
E2 Cal3	AB122.01	8	8	- 0,42	0,38	-8,3	-6,2	-10,0	-9,2	
E2 Cal3	AB122.01	9	9	- 0,79	0,42	-8,7	-6,6	-10,4	-9,6	
E2 Cal3	AB122.01	10	10	- 0,15	0,38	-8,1	-6,0	-9,7	-9,0	
E2 Cal3	AB122.01	11	11	- 2,00	0,63	-7,9	-5,8	-9,6	-8,8	
E2 Cal3	AB122.01	12	12	5,18	0,37	-2,7	-0,6	-4,4	-3,6	
E2 Cal3	AB122.01	13	13	0,43	0,38	-7,5	-5,4	-9,1	-8,4	
E2 Cal3	AB122.01	14	14	3,57	0,38	-4,3	-2,3	-6,0	-5,3	
E2 Cal2	AB122.01	15	15	5,55	0,37	-2,4	-0,3	-4,0	-3,3	
E2 Cal2	AB122.01	16	16	3,55	0,38	-4,4	-2,3	-6,0	-5,3	
E2 Cal2	AB122.01	17	17	3,22	0,38	-4,7	-2,6	-6,4	-5,6	
E2 Cal4	AB122.01	18	18	7,33	0,38	-0,6	1,5	-2,2	-1,5	
E2 Cal4	AB122.01	19	19	8,03	0,38	0,1	2,2	-1,5	-0,8	
E2 Cal4	AB122.01	20	20	6,76	0,37	-1,1	0,9	-2,8	-2,1	
E2 Cal4	AB122.01	21	21	7,38	0,38	-0,5	1,6	-2,2	-1,4	
E2 Cal3	MB110201	22	1	- 0,58	0,30	-8,5	-6,4	-10,2	-9,4	
E2 Cal3	MB110201	23	2	- 1,35	0,29	-9,3	-7,2	-10,9	-10,2	
E2 Cal3	MB110201	24	3	1,69	0,30	-6,2	-4,1	-7,9	-7,1	
E2 Cal3	MB110201	25	4	1,30	0,31	-6,6	-4,5	-8,3	-7,5	
E2 Cal3	MB110201	26	5	1,63	0,30	-6,3	-4,2	-7,9	-7,2	

Type de veines	Nom échantillon	N° analyse	N° analyse planche photo	δ18Ocal	2σ(cal)	δ18OH2O min	δ18OH20 max	δ18OCO2 min	δ18OCO2 max	
E2 Cal3	MB110201	27	6	- 0,24	0,90	-8,1	-6,1	-9,8	-9,1	
E2 Cal3	MB110201	28	7	3,53	0,36	-4,4	-2,3	-6,0	-5,3	
E2 Cal3	MB110201	29	8	- 1,60	0,30	-9,5	-7,4	-11,2	-10,4	
E2 Cal1	MB110201	30	9	8,48	0,18	0,6	2,7	-1,1	-0,3	
E2 Cal1	MB110201	31	10	7,14	0,16	-0,8	1,3	-2,4	-1,7	
E2 Cal1	MB110201	32	11	7,90	0,16	0,0	2,1	-1,7	-0,9	
E2	AB120.01	33	51	7,29	0,32	-0,6	1,5	-2,3	-1,5	
E2	AB120.01	34	52	8,39	0,29	0,5	2,6	-1,2	-0,4	
E2	AB120.01	35	53	7,41	0,31	-0,5	1,6	-2,2	-1,4	
E2	AB120.01	36	54	7,82	0,29	-0,1	2,0	-1,8	-1,0	
E2	AB120.01	37	55	7,03	0,30	-0,9	1,2	-2,5	-1,8	
E2	AB120.01	38	56	11,75	0,29	3,8	5,9	2,2	2,9	
E2	AB120.01	39	57	12,44	0,29	4,5	6,6	2,9	3,6	
E2	AB120.01	40	58	10,09	0,30	2,2	4,3	0,5	1,3	
E2	AB120.01	41	59	9,17	0,30	1,3	3,3	-0,4	0,3	
E2	AB120.01	42	60	9,35	0,30	1,4	3,5	-0,2	0,5	
E2	AB120.01	43	61	9,79	0,30	1,9	4,0	0,2	1,0	
E2	AB120.01	44	62	10,06	0,29	2,2	4,2	0,5	1,2	
E2	AB120.01	45	63	10,92	0,29	3,0	5,1	1,3	2,1	
E2	AB120.01	46	64	11,40	0,29	3,5	5,6	1,8	2,6	
E2	AB120.01	47	65	22,12	0,30	14,2	16,3	12,5	13,3	outliers
E2	AB120.01	48	66	21,29	0,29	13,4	15,5	11,7	12,5	outliers

Tableau de valeurs du $\delta^{13}C$ dans les veines de type E2.

Type de veine	Nom échantillon	N° analyse	δ13Ccal	2σ(cal)	$\delta 13CCO_2$ max	$\delta 13CCO_2$ min	
E2 Cal3	MB110201	1	- 4,7	0,6	-3,8	-3,1	
E2 Cal3	MB110201	2	- 3,6	0,6	-2,7	-2,0	
E2 Cal3	MB110201	3	- 21,8	0,6	-20,9	-20,2	outlier
E2 Cal3	MB110201	4	- 7,1	0,5	-6,3	-5,6	
E2 Cal3	MB110201	5	- 0,1	0,9	0,8	1,5	
E2 Cal3	MB110201	6	- 3,9	0,6	-3,0	-2,3	
E2 Cal3	MB110201	7	- 3,8	0,6	-3,0	-2,3	
E2 Cal3	MB110201	8	- 2,6	0,6	-1,7	-1,0	
E2 Cal3	MB110201	9	- 4,7	0,8	-3,8	-3,1	
E2 Cal1	MB110201	10	- 10,8	0,5	-9,9	-9,2	
E2 Cal1	MB110201	11	- 9,0	0,4	-8,1	-7,4	
E2 Cal1	MB110201	12	- 12,5	0,5	-11,6	-10,9	
E2 Cal2	AB122.01	1	- 4,3	0,7	-3,4	-2,7	
E2 Cal3	AB122.01	2	- 5,4	0,6	-4,5	-3,8	
E2 Cal3	AB122.01	3	- 5,7	0,5	-4,8	-4,1	
E2 Cal3	AB122.01	4	- 5,1	0,4	-4,2	-3,5	
E2 Cal3	AB122.01	5	- 4,2	0,6	-3,4	-2,7	
E2 Cal3	AB122.01	7	- 7,4	0,5	-6,6	-5,8	
E2 Cal3	AB122.01	8	- 4,3	0,5	-3,5	-2,8	
E2 Cal3	AB122.01	9	- 2,4	0,5	-1,5	-0,8	
E2 Cal2	AB122.01	10	- 3,7	0,6	-2,8	-2,1	
E2 Cal2	AB122.01	11	- 6,3	0,5	-5,4	-4,7	
E2 Cal2	AB122.01	12	- 5,7	0,5	-4,9	-4,2	
E2 Cal4	AB122.01	13	- 4,8	0,7	-4,0	-3,3	
E2 Cal4	AB122.01	14	- 7,4	0,6	-6,5	-5,8	
E2 Cal4	AB122.01	15	- 8,6	0,7	-7,7	-7,0	
E2 Cal4	AB122.01	16	- 8,5	0,5	-7,7	-7,0	

Tableau d'analyses du δD par broyage des différentes veines de quartz

Date préparation	Date piège	Date analyse	Echantillon	Minéral	Veine	Masse	N° analyse	Température	Calibration volume	GNC	H2	P20°	n	CO2	P20°	n	δD	**δDcorr**	Commentaires
	B. Abiven	T. Rigaudier				mg		°C		mbar	mbar	mbar	µmol	mbar	mbar	µmol	‰	‰	
/	22/08/2023	08/30/23	ED4	eau		6 µL	H5701	22,5	GV	0,060	235,4	233,4	100,6	/	/	/	-56,20	/	
		08/31/23					H5701										-55,5	/	
/	22/08/2023	08/31/23	OH tropical mix	eau		6 µL	H5702	23	PV	0,050	867,4	858,6	370,1	/	/	/	1,1	/	
							H5702										2,4	/	
21/08/2023	*22/08/2023*	*08/30/23*	*AB122.03*	*qz*	*E1*	*6785*	*H5703*	*22*	*PV*	*0,045*	*26,4*	*26,2*	*11,3*	*0,2*	*0,2*	*0,1*	*5,3*	*5,1*	**n < 30 µmol**
21/08/2023	*22/08/2023*	*08/31/23*	*AB122.03*	*qz*	*E1*	*6762*	*H5704*	*22*	*PV*	*1,000*	*13,0*	*12,9*	*5,6*	*0,2*	*0,2*	*0,1*	*17,6*	*17,0*	**n < 30 µmol**
		08/31/23															*22,7*	*21,9*	**n < 30 µmol**
21/08/2023	*23/08/2023*	*08/30/23*	*AB122.01*	*cal*	*E2*	*7603*	*H5705*	*23*	*PV*	*0,055*	*218,9*	*216,7*	*93,4*	*3,2*	*3,2*	*1,4*	*-13,2*	***- 12,8***	
21/08/2023	23/08/2023	08/30/23	AB122.01	cal	E2	8098	H5706	22	PV	0,055	245,8	244,1	105,2	3,5	3,5	1,5	-24,2	- 23,5	
21/08/2023	23/08/2023	*08/30/23*	*AB122.03*	*cal*	*E1*	*8215*	*H5707*	*22,5*	*PV*	*0,055*	*868,8*	*861,4*	*371,3*	*12,4*	*12,3*	*5,3*	*XX*		**vide**
23/08/2023	24/08/2023	08/30/23	AB122.03	cal	E1	8215	H5708	22	PV	0,045	639,5	635,2	273,8	9,4	9,3	4,0	-42,6	- 41,2	
23/08/2023	24/08/2023	08/30/23	AB119.02	qz	B2	7251	H5709	22	PV	0,065	86,7	86,1	37,1	1,0	1,0	0,4	2,1	**2,0**	
23/08/2023	24/08/2023	*08/30/23*	*AB119.02*	*qz*	*B2*	*6554*	*H5710*	*22*	*PV*	*0,090*	*74,0*	*73,5*	*31,7*	*0,8*	*0,8*	*0,3*	*-62,8*	*- 60,8*	**pollué**
23/08/2023	24/08/2023	08/30/23	AB120.01	qz	B1	10374	H5711	23	PV	0,065	154,1	152,5	65,7	0,6	0,6	0,3	-24,6	**- 23,8**	
23/08/2023	24/08/2023	08/30/23	AB120.01	qz	B1	10423	H5712	23	PV	0,065	211,0	208,9	90,0	0,8	0,8	0,3	-10,8	**- 10,5**	
		08/31/23															-12	**- 11,7**	
24/08/2023	28/08/2023	08/31/23	MB02	qz	B1	4152	*H5713*	23	PV	0,090	63,4	62,8	27,0	0,4	0,4	0,2	-8,1	- 7,9	**n < 30 µmol**
24/08/2023	28/08/2023	08/31/23	MB02	qz	B1	4125	*H5714*	23	PV	0,070	51,1	50,6	21,8	0,3	0,3	0,1	-19,6	- 19,0	**n < 30 µmol**
24/08/2023	28/08/2023	*08/31/23*	*MB02*	*qz*	*A*	*4046*	*H5715*	*23*	*PV*	*0,060*	*179,1*	*177,3*	*76,4*	*0,3*	*0,3*	*0,1*	*-42,4*	*- 41,0*	**pollué**
24/08/2023	28/08/2023	08/31/23	MB02	qz	A	4095	*H5716*	22	PV	0,075	361,5	359,0	154,8	0,7	0,7	0,3	-24,8	**- 24,0**	

Partie 2

Date préparation	Date piège	Date analyse	Echantillon	Minéral	Veine	Masse	N° analyse	Température	Calibration volume	GNC	H2	P20°	n	CO2	P20°	n	δD	**δDcorr**	Commentaires
	B. Abiven	T. Rigaudier				mg		°C		mbar	mbar	mbar	µmol	mbar	mbar	µmol	‰	‰	
/	23/01/2024	25/03/2024	THALASSA	eau		2µL	H5720	22	PV	0,065	417,8	415,0	178,9	/	/	/	3,7	/	
		02/04/2024															3,6	/	
/	23/01/2024	25/03/2024		eau		6µL	H5721	22	PV	0,160	833,6	827,9	356,8	/	/	/	2,8	/	
19/01/2024	24/01/2024	26/03/2024	AB.122.03	qz	E1	7079	H5722	22	PV	0,045	124,3	123,5	53,2	0,8	0,8	0,3	-40,0	**- 41,6**	
19/01/2024	24/01/2024	26/03/2024	AB.122.03	qz	E1	7010	H5723	22	PV	0,060	143,8	142,8	61,6	0,8	0,8	0,3	-33,5	**- 35,4**	
19/01/2024	24/01/2024	26/03/2024	AB.122.03	qz	E1	7037	H5724	23	PV	0,110	89,5	88,6	38,2	0,7	0,7	0,3	-37,9	**- 39,6**	
19/01/2024	24/01/2024	26/03/2024	AB.180.01	qz	B2	11789	H5725	23	PV	0,750	6,6	6,5	2,8	0,1	0,1	0,0	-67,2	- 67,6	**n < 30 µmol**
19/01/2024	24/01/2024	26/03/2024	AB.180.01	qz	B2	11877	H5726	23,5	PV	0,130	32,0	31,6	13,6	0,4	0,4	0,2	-67,1	- 67,5	**n < 30 µmol**
24/01/2024	25/01/2024	28/03/2024	AB.122.01	cal	E2	13222	H5727	23	PV	0,085	569,2	563,4	242,8	7,1	7,0	3,0	-45,6	**- 47,0**	
24/01/2024	25/01/2024	28/03/2024	AB.122.01	cal	E2	13222	H5728	23	PV	0,150	714,9	707,7	305,0	8,5	8,4	3,6	-48,4	**- 49,6**	
24/01/2024	25/01/2024	28/03/2024	AB.122.01	cal	E2	13668	H5729	24	PV	0,500	725,8	716,0	308,6	8,1	8,0	3,4	XX		**pollué**
24/01/2024	25/01/2024	29/03/2024	MB09	qz	B1	11710	H5730	24	PV	0,150	251,6	248,2	107,0	0,7	0,7	0,3	-3,7	**- 6,9**	
24/01/2024	25/01/2024	29/03/2024	MB09	qz	B1	12154	H5731	24	PV	0,100	308,2	308,2	132,8	0,8	0,8	0,3	0,6	**- 2,8**	
25/01/2024	26/01/2024	29/03/2024	MB09	qz	B1	11107	H5732	23	PV	0,130	249,3	249,3	107,4	1,0	1,0	0,4	XX		**pollué**
25/01/2024	26/01/2024	29/03/2024	MB09	qz	A	6520	H5733	24	PV	0,150	501,4	494,6	213,2	1,4	1,4	0,6	-23,1	**- 25,4**	
25/01/2024	26/01/2024	29/03/2024	MB09	qz	A	6582	H5734	24	PV	0,130	317,7	313,4	135,1	1,1	1,1	0,5	XX		**pollué**
25/01/2024	26/01/2024	29/03/2024	MB09	qz	A	4786	H5735	24	PV	0,095	190,8	188,2	81,1	0,3	0,3	0,1	-18,4	**- 21,0**	
/	26/01/2024		ED4	eau		6µL	H5736	24	PV	0,070	887,3	875,3	377,3	/	/	/	XX		**pollué**
		26/03/2024	IAEA OH-26 Vienna TW	eau			*H5737*										-78,00	/	
		28/03/2024		eau			*H5738*										-78,10	/	
		02/04/2024		eau													-78,10	/	
		29/03/2024	IAEA OH-29 Tropical Mix				*H5739*										2,30	/	

Partie 3, STANDARTS et légende.

STANDARTS	Valeurs théoriques / ‰	Valeurs mesurées 08/23 / ‰	Valeurs mesurées 03/24 / ‰
THALASSA	0,0	/	3,4
IAEA OH-29 tropical mix	1,8	1,8	2,3
ED4	-54,0	-55,8	/
IAEA OH-26 VIENNA TW	-78,0	/	-78,1

GNC	Pression Gaz Non Condensables
H2	Pression hydrogène
P20°	Pression hydrogène à 20 °C
n	Quantité hydrogène
CO2	Pression CO2
P20°	Pression CO2 à 20 °C
δD	Valeurs isotopiques hydrogène
δDcorr	Valeurs isotopiques hydrogène corrigées